



DEPARTMENT OF PHYSICS  
 COLLEGE OF WILLIAM AND MARY  
 FOUNDED IN 1693  
 WILLIAMSBURG, VIRGINIA

FACILITY FORM 802

|  |  |
|--|--|
| <p><b>N66 32726</b></p> <p>(ACCESSION NUMBER)</p> <p><u>515</u></p> <p>(PAGES)</p> <p><u>CR-76991</u></p> <p>(NASA CR OR TMX OR AD NUMBER)</p> | <p><b>N66 32754</b></p> <p>(THRU)</p> <p><u>1</u></p> <p>(CODE)</p> <p><u>24</u></p> <p>(CATEGORY)</p> |
|--|--|

GPO PRICE \$ \_\_\_\_\_

CFSTI PRICE(S) \$ \_\_\_\_\_

Hard copy (HC) 5.65

Microfiche (MF) 2.50

Volume I

February, 1966

ff 653 July 65

# Intermediate Energy Physics

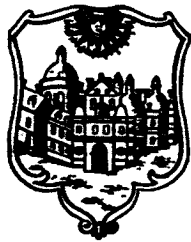
PROCEEDINGS OF THE

# WILLIAMSBURG CONFERENCE

on

## Intermediate Energy Physics

February 10-12, 1966



VOLUME I

*Sponsored By:*

NATIONAL AERONAUTICS AND SPACE ADMINISTRATION

U. S. AIR FORCE OFFICE OF SCIENTIFIC RESEARCH

U. S. ATOMIC ENERGY COMMISSION

U. S. NATIONAL SCIENCE FOUNDATION

THE COLLEGE OF WILLIAM AND MARY

WILLIAMSBURG, VIRGINIA

## FOREWARD

In the last ten years particle physics in the energy range between 100 MeV and 1000 MeV has enjoyed a continuing growth even while large programs were developing at higher energy machines. This activity at intermediate energies has been due to significant theoretical contributions, most notably the prediction of parity non-conservation in weak interactions, and to advances in particle detectors, accelerators and beam handling devices. Recently, intermediate energy physics has shown particularly vigorous activity in a new direction, the use of pions as nuclear probes, and in the rejuvenation of mesic x-ray research by application of new techniques.

It was felt that the growth and diversification of intermediate energy physics precluded a thorough treatment of even the most vital phases of this field in existing conferences, and thus a Conference on Intermediate Energy Particle Physics was organized and held in Williamsburg, Virginia, on February 10-12, 1966. The Conference was open to all physicists, both experimental and theoretical, interested in the physics of protons, pions and muons in this energy range. The response to the Conference, and the substance of the papers presented, indicates the extent to which intermediate energy physics is developing as an active field of research.

In preparing these proceedings, it was not possible to submit all the discussions to the participants before publication. Therefore, any errors which persist are the responsibility of the Editor.

Our thanks to the Sponsors, the Scientific Secretaries, the Conference Registrars and typists, and those students who aided in various aspects of the Conference.

H. Funsten  
R. Siegel  
R. Welsh  
R. Winter

**Organizing Committee**

R. T. Siegel (Chairman)  
H. O. Funsten  
R. E. Welsh  
R. G. Winter

**Scientific Secretariat**

H. O. Funsten (Editor)  
M. Eckhause  
K. Gotow  
D. Hopp  
J. Kane  
R. Klein  
D. Koltun  
R. Silbar

TABLE OF CONTENTS

## VOLUME I

Page

## WELCOME TO VISITORS

Davis Y. Paschall, President, College of William and Mary . . . . . xiii

Session A

## EFFECTS OF NUCLEAR STRUCTURE IN MU-ATOMIC SPECTRA

H. L. Anderson, R. J. McKee, C. K. Hargrove, E. P. Hincks . . . . . 1

## HIGH RESOLUTION MUONIC X-RAY STUDIES

S. Devons . . . . . 15

## REMARKS ON THE THEORY OF MU-MESIC ATOMS

D. G. Ravenhall . . . . . 37

X-RAYS FROM MUONIC ATOMS WITH SPHERICAL OR NEARLY SPHERICAL NUCLEI  
and  
STUDIES OF MUONIC ATOMS OF NON-SPHERICAL NUCLEI

R. E. Coté, W. J. Prestwich, S. Raboy, C. C. Trail,  
R. A. Carrigan, Jr., A. Gaigalas and R. B. Sutton . . . . . 51

MEASUREMENTS OF THE M1 AND E2 MUONIC h.f.s. OF  $\text{Bi}^{209}$ , AND OF THE  
MUONIC ISOTOPE SHIFTS FOR  $\text{Pb}^{206}$ ,  $\text{Pb}^{207}$  AND  $\text{Pb}^{208}$

V. L. Telegdi . . . . . 77

## THE ANOMALOUS INTENSITY RATIOS IN MUONIC LEAD AND BISMUTH

J. Hüfner . . . . . 87

## MUONIC X-RAY SPECTRA AND CHARGE DISTRIBUTION IN DEFORMED NUCLEI

H. L. Acker . . . . . 91

## MUONIC X-RAY STUDIES OF SPHERICAL NUCLEI

C. Daum, G. Backenstoss, J. C. Sens, S. A. deWit, and H. L. Acker . . . 99

DETAILED ANALYSIS OF MUONIC X-RAY SPECTRUM FROM STRONGLY DEFORMED  
e-e NUCLEI

K. Runge, T. T. Bardin, R. Barrett, S. Devons, D. Hitlin,  
E. R. Macagno, C. Nissim-Sabat, J. Rainwater, and C. S. Wu . . . . . 135

Session B

## PI-MESIC X-RAYS

K. M. Crowe . . . . . 145

## POLARIZATION IN PION-PROTON SCATTERING

P. D. Grannis . . . . . 175

## PION INTERACTIONS WITH NUCLEI

T. E. O. Ericson . . . . . 187

## TWO-NUCLEON EMISSION FOLLOWING ABSORPTION OF STOPPED NEGATIVE PIONS

M. E. Nordberg, Jr., K. F. Kinsey and R. L. Burman . . . . . 207

## PION CAPTURE AND NUCLEAR STRUCTURE

H. Davis, H. Muirhead, and J. N. Woulds  
(Paper presented by P. T. Andrews). . . . . 223

## THEORY OF PION ABSORPTION ON LIGHT NUCLEI

D. Koltun and A. Reitan . . . . . 241

## RADIATIVE PION ABSORPTION IN COMPLEX NUCLEI

D. K. Anderson and J. M. Eisenberg . . . . . 253

 $\pi^-$  ABSORPTION BY UNCORRELATED NUCLEONS IN  $O^{16}$ 

J. LeTourneux . . . . . 259

## DOUBLE CHARGE EXCHANGE

J. Solomon . . . . . 269

## THE PRODUCTION OF CHARGED PIONS BY 600 MeV PROTONS ON VARIOUS NUCLEI

E. Heer, W. Hirt, M. Martin, E. G. Michaelis,  
C. Serre, P. Skarek, B. T. Wright . . . . . 277

Session C

## MUON CAPTURE AND NUCLEAR STRUCTURE

J. D. Walecka . . . . . 297

## MUON CAPTURE AND NUCLEAR GIANT RESONANCES

H. Überall . . . . . 327

## MUONIUM

V. W. Hughes . . . . . 377

## MUON CAPTURE RATES IN COMPLEX NUCLEI

R. E. Welsh, M. Eckhause, R. T. Siegel, and T. A. Filippas . . . . . 411

## COMPARISON OF THE LIFETIMES OF POSITIVE AND NEGATIVE PIONS

D. S. Ayres, R. D. Eandi, A. S. Greenberg, R. W. Kenney  
R. J. Kurz, and B. Macdonald . . . . . 419

## A MEASUREMENT OF THE LIFETIME OF THE POSITIVE PION

K. F. Kinsey, L. Lobkowitz, and M. E. Nordberg, Jr. . . . . 427

## OPTICAL MODELS FOR PION-NUCLEUS SCATTERING

M. M. Sternheim and E. Auerbach . . . . . 439

PHASE SHIFT ANALYSIS FOR ELASTIC  $\pi^+$  -  $\text{He}^4$  SCATTERING IN THE  
ENERGY INTERVAL 100-160 MeV/cM. M. Block, I. Kenyon, J. Keren, D. Koetke, P. K. Malhotra.  
R. Walker, and H. Winzeler . . . . . 447INELASTIC  $\pi^+$  -  $\text{He}^4$  REACTIONS IN THE MOMENTUM RANGE 100-160 MeV/cM. M. Block, I. Kenyon, J. Keren, D. Koetke, P. K. Malhotra,  
P. Mazur, R. Walker, H. Winzeler . . . . . 455

PARTICIPANTS . . . . . 461

INDEX OF CONTRIBUTORS . . . . . 467

## VOLUME II

Session D

## NUCLEON-NUCLEON SCATTERING

G. Breit . . . . . 471

## PION-NUCLEON PHASE SHIFT ANALYSES

L. D. Roper . . . . . 495

## NON-DYNAMICAL STRUCTURE OF PARTICLE REACTIONS

M. J. Moravcsik . . . . . 517

PHOTOPRODUCTION OF  $N^*$  RESONANCES IN THE QUARK MODEL

R. G. Moorhouse . . . . . 545

A COMPARISON OF RESONANCE FORMULAS FOR THE (1236 MeV, 3/2)  
PION NUCLEON RESONANCE

S. R. Deans and W. G. Holladay . . . . . 551

n-n S-WAVE SCATTERING LENGTH FROM THE NEUTRON SPECTRA OF THE  
REACTION  $\pi^- + d \rightarrow 2n + \gamma$ 

R. W. Salter, Jr., R. P. Haddock, M. Zeller, J. B. Czirr,  
and D. R. Nygren . . . . . 569

MEASUREMENTS OF THE DIFFERENTIAL CROSS-SECTION AND POLARIZATION  
IN PROTON-PROTON SCATTERING AT ABOUT 143 MeV

O. N. Jarvis, G. F. Cox, G. H. Eaton, B. Rose, and C. P. Van Zyl. . . 595

Session EEXPERIMENTAL ASPECTS OF NUCLEON-NUCLEON SCATTERING AND  
POLARIZATION BELOW 1 BEV

B. Rose . . . . . 603

## p-p BREMSSTRAHLUNG AT 160 MeV

B. Gottschalk, W. J. Shlaer and K. H. Wang . . . . . 649

## P-P BREMSSTRAHLUNG CALCULATIONS

P. Signell and D. Marker . . . . . 667

## NUCLEON-NUCLEON BREMSSTRAHLUNG AT 200 MeV

K. W. Rothe, P. F. M. Koehler, E. H. Thorndike . . . . . 677

## NEUTRON-PROTON INTERACTIONS AT 205 MeV

E. H. Thorndike, N. W. Reay, D. Spalding, and A. R. Thomas . . . . . 691

## QUASI-FREE PROTON SCATTERING AT 160 MeV

B. Gottschalk, W. J. Shlaer, K. Strauch and K. H. Wang . . . . . 703

A SHELL-MODEL CALCULATION OF THE QUASI-ELASTIC SCATTERING OF  
PROTONS FROM COMPLEX NUCLEI

N. S. Wall . . . . . 719



CHANGES IN RADII BETWEEN NEIGHBORING NUCLIDES

L. R. B. Elton and A. Swift . . . . . 731

COHERENT NEUTRON-PROTON HOLE EXCITATIONS IN NUCLEI

S. Fallieros, T. A. Hughes and B. Goulard . . . . . 743

NUCLEAR STRUCTURE MEASUREMENTS WITH THE BROOKHAVEN COSMOTRON

J. L. Friedes, H. Palevsky, R. J. Sutter and G. W. Bennett. . . . . 749  
R. L. Stearns, D. M. Corley, N. S. Wall, G. C. Phillips  
and W. D. Simpson

Session F

SUMMARY OF CONFERENCE - NUCLEAR STRUCTURE

D. H. Wilkinson . . . . . 757

SUMMARY OF CONFERENCE - FUNDAMENTAL PROCESSES

L. Wolfenstein . . . . . 775

PARTICIPANTS . . . . . 793

INDEX OF CONTRIBUTORS . . . . . 799

## WELCOME ADDRESS

Davis Y. Paschall

President of the College of William and Mary

Gentlemen of the Williamsburg Conference:

The College of William and Mary is honored to serve as host for the first - and, we hope, highly productive - Williamsburg Conference on Intermediate Energy Physics. We look forward to your visiting with us for the next several days, especially since the College will on Saturday be celebrating Charter Day, the two hundred seventy-third anniversary of the founding of this institution by the British Monarchs for whom it is named.

In the informational material which was prepared for your use, you may already have read some of the history of this institution, and of the man who was certainly one of our most notable graduates - Thomas Jefferson. You have also perhaps seen in your informational material the description of the now - almost - forgotten scientist who was Jefferson's great teacher and whose name has been ascribed to the new Physical Laboratory -- William Small. It may not have come to your attention that one of the three original buildings of the College is one called the Brafferton. This edifice - still in use - was constructed to house a school for the Aborigines established in a bequest by Robert Boyle, who I am told, did some original research in the behavior of particles moving at energies considerably lower than those you will consider during this conference.

In mentioning these names, I would simply make the point that Jefferson, so renowned as a statesman, was in his time the example of the broadly educated man -- scientist, craftsman, literary creator, and philosopher -- that we take

as our standard of excellence today. Jefferson viewed man in his infinite potential, and set the basic image and purpose of this college to be that of providing the broadly educated person.

Jefferson's other insistent standard was that education should keep at least abreast, and preferably in advance, of the continually changing need of society. Therefore, in his reorganization of this College in 1779 he introduced what were then radical concepts of education--including a greatly expanded curriculum in "natural philosophy" which was developed into the science faculties of our present college--and a break in general with the university oriented system of the European tradition.

In the eighteenth century, this campus and this community rode the crest of the wave of the enlightenment. The Society for the Advancement of Useful Knowledge was a group which stimulated a continuing dialogue on all dimensions of human knowledge. The founding of Phi Beta Kappa on this campus is a well-known story. The role played by college students and faculty in the movement for independence and a new nation is also well known.

But in welcoming you today I wish to emphasize that we consider a conference such as this to be perfectly in keeping with the Jeffersonian tradition. Both in its subject-matter and in its response to the intellectual needs of the twentieth century. In Jefferson's day, the times called for intellectual boldness and the scientific mind. Can we seriously dispute that the need is still the same today?

The College greets you cordially, and assures you of our joy in the stimulating association made possible by your presence here.

MUONIC X-RAYS

Chairman, J. Rainwater

EFFECTS OF NUCLEAR STRUCTURE IN MU-ATOMIC SPECTRA

H. L. Anderson and R. J. McKee

Enrico Fermi Institute for Nuclear Studies, University of Chicago

C. K. Hargrove and E. P. Hincks

Division of Pure Physics, National Research Council of Canada, Ottawa

Presented by H. L. Anderson

It is appropriate to remark at the beginning of this conference that we are seeing a revival in the subject of mu-mesic x-rays, and that in view of the fact that our chairman is Professor Rainwater, I am impelled to remind you that his was the original classic work on the subject. It was Fitch and Rainwater in 1953 who made a careful study of mu mesic x-rays and used them to show that the charge radius of nuclei was some 20% smaller than was thought previously. The same conclusion emerged from the Stanford electron scattering measurements at just about the same time. Thus, both experiments showed that the radius of the nuclear charge is given by  $R = r_0 A^{1/3}$  with  $r_0 = 1.20$  fermis. I think it is quite remarkable that this value of  $r_0$  has changed very little over the years. I also remind you that the importance of the muon as a nuclear probe was pointed out as early as 1949 by John Wheeler who wrote about it in a number of remarkable papers that still serve as the basic guide to the subject today. Wheeler pointed out that from measurements of mu mesic x-rays one could determine such things as the nuclear quadrupole moment as well as the fine structure splitting. Subsequent papers by Wilets and by Jacobsohn showed that even for a nucleus whose spin was zero, dynamic quadrupole effects due to the nuclear rotational states would produce a particularly complex hyperfine structure whose study could reveal a number of features of the nuclear structure.

The revival occurred as a consequence of the successful development of the Li-drift Ge-detector a little more than two years ago by Dr. A. J. Tavendale at the Canadian Chalk River Laboratories. Tavendale's detector gave an improvement in resolution by a factor of 10 or even more over sodium iodide and made accessible many of the interesting phenomena that had been anticipated by Wheeler, by Willets, and by Jacobsohn. This session is devoted to these new investigations.

I'd like now to describe some of our work at Chicago done with my Canadian collaborators and one of my graduate students. About a year and a half ago we persuaded Dr. A. J. Tavendale to bring down one of his better Li-drift Ge-detectors, and our work began. I'd like to show on the first slide (Figure 1) why the muon is so useful in exploring the shape of the nuclear charge distribution. The dotted curve shows the distribution of the nuclear charge density in Pb, while the solid curves show the various mu-atomic wave functions. You see that the 1s wave function penetrates quite deeply into the nucleus in a heavy element like Pb. The  $2p_{1/2}$  wave function also penetrates a fair amount, the  $2p_{3/2}$  also penetrates a good deal, but a different amount. Even the d state wave functions penetrate a small amount. By measuring the 2p - 1s transition energies and the d-p transition energies carefully, it is possible to obtain more about the charge distribution than its mean square radius. Additional detail about the shape of the nuclear charge distribution can be obtained as Hill and Ford pointed out many years ago. The additional detail in the muonic x-ray analysis makes more meaningful a comparison with the kind of analysis that Hahn, Hofstadter, and Ravenhall carried out on the electron scattering measurements.

The next slide (Figure 2) shows some of our spectra obtained in the region of the 2p  $\rightarrow$  1s transitions. This is just the actual data as seen in a 1024 channel analyser set to take the upper part of the spectrum at 2 kev per channel. The lowest curve is for Au. The  $2p_{1/2} - 1s_{1/2}$  transition is labelled (1), the  $2p_{3/2} - 1s_{1/2}$  transition is labelled (2). These are the double escape peaks, so-called. The lines labelled (3), (4) are the same lines in single escape. Here you see the same in Pb 206 and here you see the same for the case of Bi.

The next slide (Figure 3) shows the lower region between 1000 and 2400 kilovolts set to obtain the d - p lines. The labels (1) and (2) mark the f - d transitions; their splitting is clearly seen here. The labels 5 and 6 mark the d - p lines in double escape. No. 7 is one of the d - p lines in single escape, the other one is there also but not too evident in this slide. No. 8 marks the Compton edge due to the  $3d_{5/2} - 2p_{3/2}$  transition. No. 9 is the other Compton edge due to  $3d_{3/2} - 2p_{1/2}$ . No. 10 is the full energy peak of the  $3d_{5/2} - 2p_{3/2}$  transition. These little peaks 3 and 4 are crossover transitions corresponding to  $5f - 3d$ . In our work we used 2048 channels, 1024 of them set in the region of the  $2p \rightarrow 1s$  transitions, and 1024 set in the  $3d - 2p$  region. We also had another 800 channel analyzer to explore other parts of the spectrum at the same time.

One problem that we had was that the peaks were not quite symmetric. This can be seen in the data of Figure 4. We believe this was due to an inefficiency in charge collection due to imperfections of our crystal. In analyzing these curves we supposed that the line shape was basically Gaussian in form but with a fraction of the events reduced in amplitude according to an exponential law. We could obtain good fits by suitable adjustment of the three parameters such a description makes available. In the case  $2p_{1/2} - 1s_{1/2}$  transition in Pb 206, the fit shown in Figure 4 is the fit that was obtained by superimposing similar curves with amplitudes adjusted to take into account the isotopic composition of our particular sample of the Pb 206. (We had a sample of Pb 206 with 88% of 206 and smaller amounts of 207, 208, and 204.) We allowed the shape parameters to vary, and we introduced an isotope shift that was proportional to the difference in the atomic weight of the isotopes, and then tried to fit simultaneously the Pb 206, and a sample of natural Pb. In Figure 4A, the large peak belongs to the isotope 206. In Figure 4B, the large peak belongs to the isotope 208, and I think it is almost evident from these two curves, one above the other, that there is a shift and that the energy of the transition in Pb 206 is higher than that of Pb 208. Figure 4C and 4D show analogous fits for the  $2p_{3/2} - 1s_{1/2}$  transitions. The isotope shift is clearly evident here as well.

The value found for the isotope shift was 8.4 kev. On the other hand, if the  $A^{1/3}$  rule were to hold strictly, i.e. if the particle density were the same in both isotopes, you would expect the Pb 206 - Pb 208 isotope shift to be 15 kev. The result is that the shift is less than the constant density rule by about 55%. This is actually in very close agreement to numbers that have been obtained much earlier by Brix and Kupfermann from optical spectra analysis. We have here a confirmation of the result of the isotope shift measurements known for sometime from optical spectra.

Figure 5A shows our analysis in the case of the d lines (of Pb 206); Figure 5B the analysis in the case of the f lines. Our method is to take the six energies, two for  $2p - 1s$ , two for  $3d - 2p$  and two for  $4f - 3d$  and use them to determine two parameters of the nuclear shape assuming this to be of the Fermi type,

$$\rho(r) = \rho_0 \left\{ 1 + e^{n\left(\frac{r}{R} - 1\right)} \right\}$$

(The electron scattering people use a slightly different notation writing:  $n\left(\frac{r}{R} - 1\right) = \left(\frac{r - c}{a}\right)$ )

In our analysis we used as parameters,  $r_0$  and  $1/n$ , where  $r_0$  is the reduced equivalent radius,

$$r_0 = \sqrt{\frac{5}{3}} \langle r^2 \rangle_{av}^{1/2} A^{-1/3}$$

we use  $r_0$  because it is this quantity that is primarily determined from the muonic x-rays energies.

Figure 6 shows how one can take the energies of the lower p line and the upper d line to determine  $r_0$ . For the isotope Pb 208 we could determine from such a plot that  $r_0 = 1.196$  and a little less than 15. Pb 206 really requires a slightly different scale here, in the ratio of the cube roots of the atomic weights. The circle indicates where Pb 206 should lie if both 206 and 208 were spherical and had the same particle density. Figure 6 shows that the observed shift is 55% of that expected from the simple model. Our final determination of the shape parameters were obtained from a least squares fit to the six energies mentioned, instead of only the two represented in Figure 6.



Figure 7 shows some of our results in the case of Au. As you know Au has a nuclear spin of  $3/2$  and a quadrupole moment. The upper  $2p \rightarrow 1s$  line is broadened and split by quadrupole interaction, and there are four lines, with total angular momentum  $F = 3, 2, 1, 0$ . Our analysis uses the same shape as the ones deduced from the analysis of the Pb isotopes. The quadrupole splitting is left as a free parameter in finding the best fit. The result of the analysis is given in Figure 12.

Figure 8 shows the lower line in Au which again is slightly split. There are two states  $F = 2$  and  $F = 1$ . These are normally taken as degenerate, but if account is taken of the interaction between the states with the same  $F$  values in  $p_{1/2}$  as well as in  $p_{3/2}$  the degeneracy is removed. The splitting is too small to be observable, but anyway the analysis takes it into account.

Figure 9 shows the  $3d \rightarrow 2p$  transitions in Au. The upper line seems relatively simple, but there are 4 lines which are, however, only slightly split. The lower line (Figure 10) is more complicated and has 8 components. The fit uses two free parameters, the fine structure splitting and the quadrupole splitting.

Figure 11 shows a determination of the quadrupole moment from the quadrupole moment from the quadrupole splitting. We write the quadrupole splitting energy,

$$E_Q = \frac{e^2}{10} Q_0 \langle n' l' m' | f(r) | n l m \rangle$$

The observed splittings are  $E_Q$  times angular momentum factors. Our measurement really determines the product of the intrinsic quadrupole moment  $Q_0$  and a penetration factor. The penetration factor is model dependent and our determination of  $Q_0$  assumed the nucleus to be a uniformly charged ellipsoid. This allows us to avail ourselves of the formalism of the theory of Bohr - Mottelson for the purpose of calculating the matrix element. The penetration function depends on value of the nucleus radius, which in turn can be determined from the transition energies of the main lines.

Figure 12 summarizes our results for the four nuclei: Au 197 and Pb 206, 208, and Bi 209. We have given six energies here; the  $2p_{1/2} - 1s_{1/2}$  transition energy, and the p splitting. We've

given the  $3d_{3/2} - 2p_{1/2}$  energy and the difference between the p and d fine structure splittings which is the number that's measured experimentally, and similarly for the f energies. Taking these numbers with these errors, we made a least squares fit to determine the parameters of the charge distributions in each case. The energies calculated with these parameters may now be compared with those observed. The difference between the experiment and the calculation is given in the brackets. It is seen that the fit is on the whole pretty good. We have been puzzled by the small inconsistency obtained in the value of  $\Delta p$  for Au 197 and for Pb 206.

Figure 13 summarizes the interpretation of the data in terms of the two parameters of the Fermi type of nuclear charge distribution. Note the high precision in the determination of  $r_0$  and the remarkable consistency of this quantity among the four nuclides studied. The shape parameter  $\frac{1}{n}$  is less well determined by these measurements. The errors in  $r_0$  and  $1/n$  are strongly correlated so we give the correlation error for these quantities. Using this we can deduce the alternative parameters  $r$ , and  $t$  for a direct comparison with electron scattering values. The discrepancy between these results and those from the electron scattering analysis becomes apparent if one uses the electron scattering parameters to calculate the muonic x-ray energies. The discrepancy is small in the case of Bi but for Au the  $2p - 1s$  transition energy is 90 kev higher if one uses the parameters from electron scattering. In the case of Pb 208 the discrepancy is 70 kev. Such calculations are model dependent as Ravenhall will show later in this session.

Finally, we show a number of slides showing how the dynamic quadrupole effect reveals itself in thorium. Hincks, Johnson, and I had seen evidence of this effect in our early work with a NaI spectrometer but we were unable to make a useful analysis. Telegdi and his collaborators working with Raboy and Trail's superior NaI spectrometer made a clear observation of the effect and could establish the sign of the quadrupole moment. Here we show the additional detail made possible with Ge detectors. We are not satisfied with the present data---we need much better statistics to do a

proper job of the analysis. Figure 14 shows the lower  $2p - 1s$  complex of lines and our fit according to the theory of the dynamic quadrupole effect. The upper  $2p - 1s$  line shown in Figure 15 is even more complex. Figure 16 shows how the calculated spectrum depends on the value of the intrinsic quadrupole moment of Th 232. Our best fit to the data is shown above. It corresponds to a value  $Q_0 = 8.9$  barns. This may be compared with the value of 10 barns obtained from coulomb excitation measurements.

Figures 17, 18, 19, and 20 show our data for Bi and its analysis in terms of a static quadrupole moment. (There wasn't time to show these.) The value  $\epsilon_Q$  for Bi given in Figure 12 corresponds to  $A_2 = -3.15$  (in the notation of LeBellac, Nucl. Physics 40, 645 (1963) ).

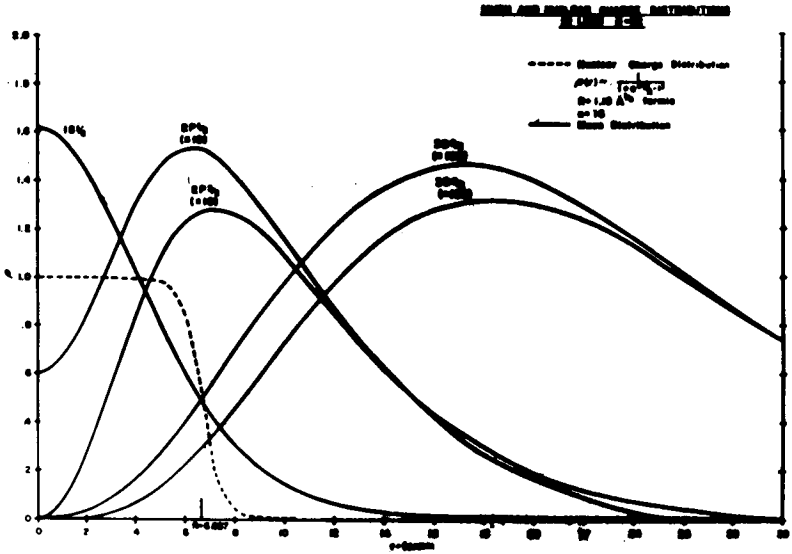


Figure 1. Muon and nuclear charge distribution in lead.

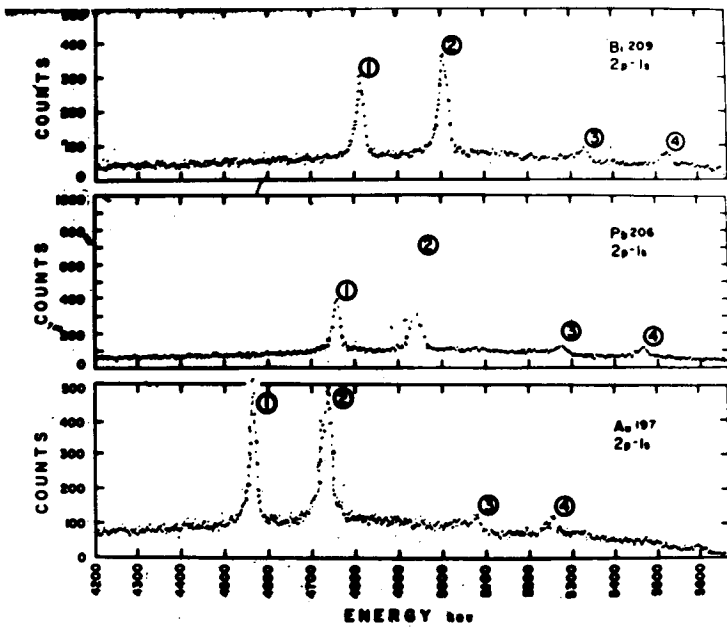


Figure 2.  $2p - 1s$  muon x-rays in bismuth 209, lead 206 and gold 197.

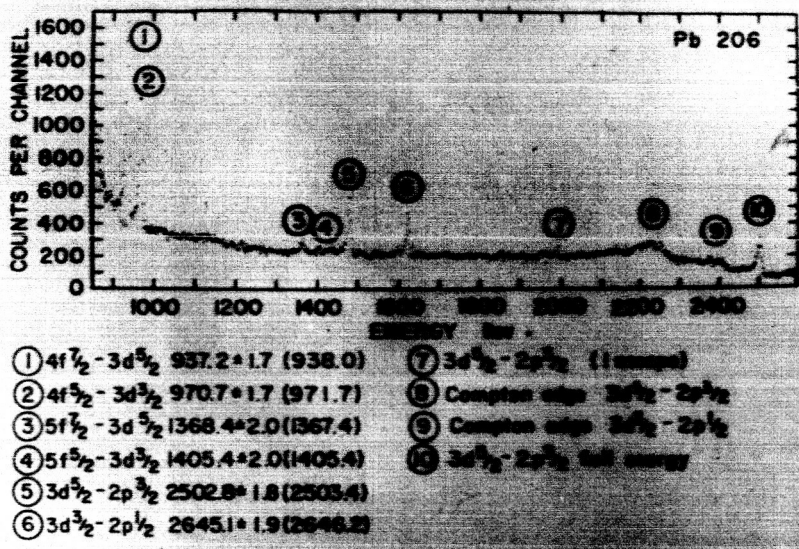


Figure 3. Muon x-ray spectra from lead 206.

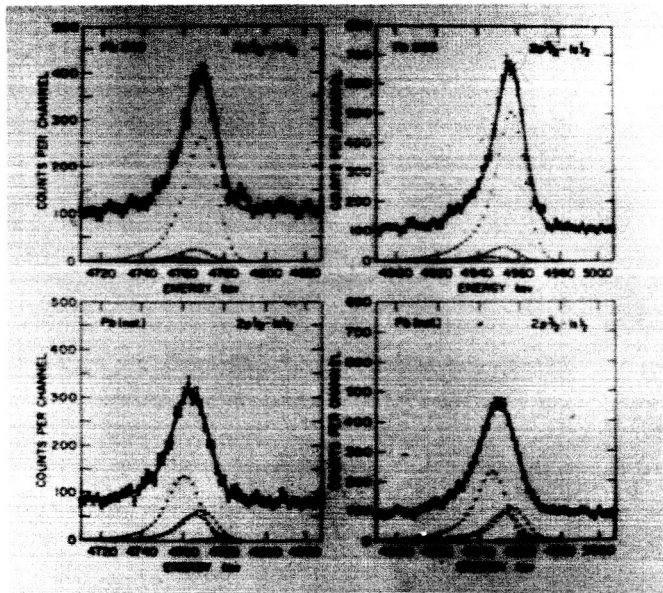


Figure 4.  $2p_{3/2} - 1s_{1/2}$  muon x-ray spectra for lead isotopes showing data reduction methods.

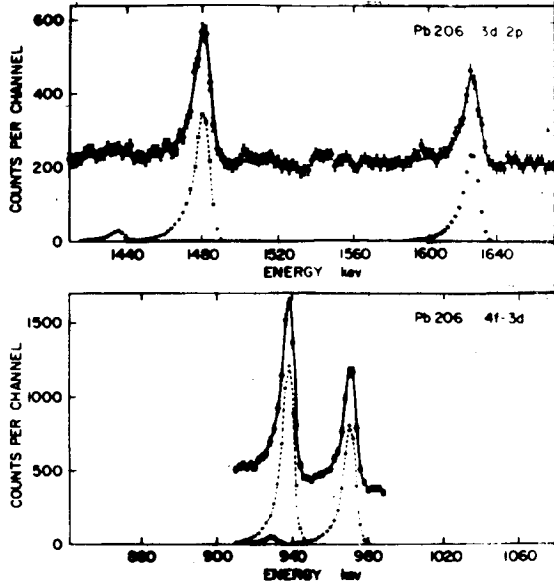


Figure 5. Upper - Muon x-ray spectra from lead 206 3d - 2p transition. Lower - 4f - 3d transition.

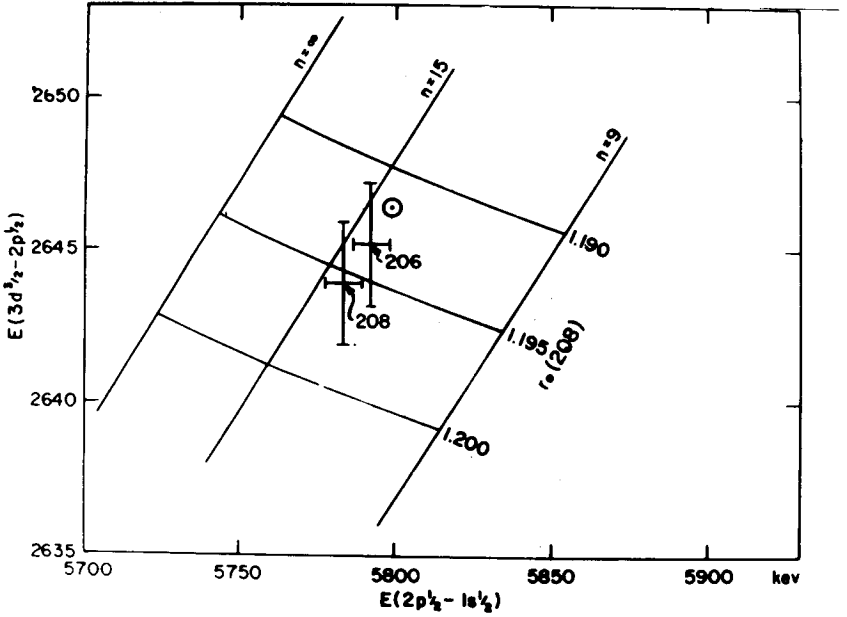
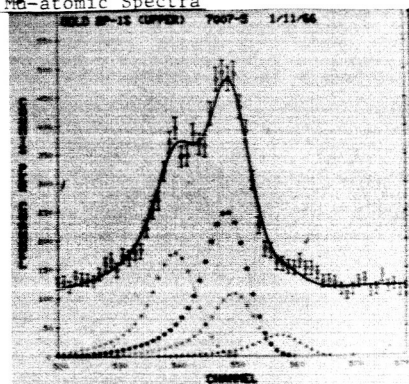


Figure 6. Calculation of  $r_0$  for the lead isotopes 206 and 208.

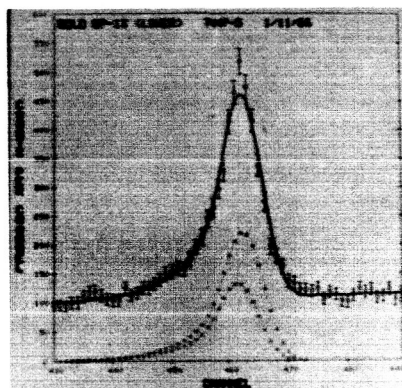
## Mo-atomic Spectra



RUN NUMBER 7007

GOLD 2P-1S (UPPER) 7007-5 1/11/66  
 CHANNELS-PARAM=111 CHISQ=104  
 FWHM=14.7 KEV HALF ENERGY=8.3 KEV  
 E(2P1/2-1S1/2)=4567.8 KEV (DOUBLE ESCAPE)  
 P SPLITTING=167.4 KEV

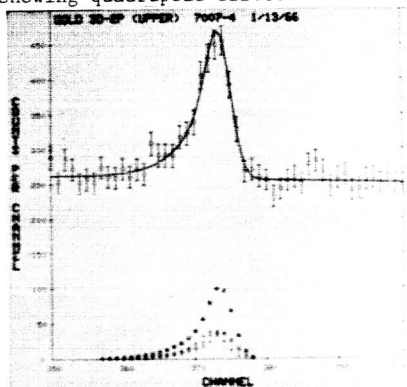
Figure 7. Muon x-ray spectra for the  $2p_{3/2} - 1s_{1/2}$  transition in gold, showing quadrupole effect.



RUN NUMBER 7007

GOLD 2P-1S (LOWER) 7007-5 1/11/66  
 CHANNELS-PARAM=111 CHISQ=104  
 FWHM=14.7 KEV HALF ENERGY=8.3 KEV  
 E(2P1/2-1S1/2)=4567.8 KEV (DOUBLE ESCAPE)  
 P SPLITTING=167.4 KEV

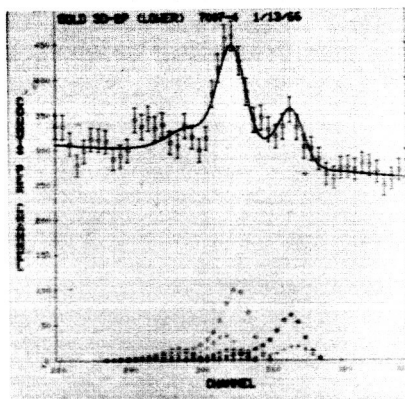
Figure 8.  $2p_{1/2} - 1s_{1/2}$  transition in gold.



RUN NUMBER 7007

GOLD 3D-2P (UPPER) 7007-4 1/13/66  
 CHANNELS-PARAM=91 CHISQ=73  
 FWHM=7.4 KEV HALF ENERGY=5.2 KEV  
 E(3D3/2-2P1/2)=1447.8 KEV (DOUBLE ESCAPE)  
 P-D SPLITTING 131.3 KEV

Figure 9.  $3d_{3/2} - 2p_{1/2}$  transition in gold.



RUN NUMBER 7007

GOLD 3D-2P (LOWER) 7007-4 1/13/66  
 CHANNELS-PARAM=91 CHISQ=73  
 FWHM=7.4 KEV HALF ENERGY=5.2 KEV  
 E(3D3/2-2P1/2)=1447.8 KEV (DOUBLE ESCAPE)  
 P-D SPLITTING 131.3 KEV

Figure 10.  $3d-2p$  transition in gold, lower lines.

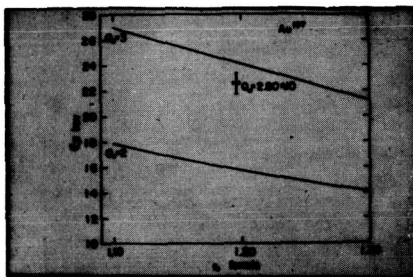


Figure 11. Quadrupole moment in Au 197 deduced from quadrupole splitting and  $r_0$ .

Muon X Ray Transition Energies, Splittings and Intensity Ratios

|                       | Au 197           | Pb 206           | Pb 208           | Bi 209          |
|-----------------------|------------------|------------------|------------------|-----------------|
| $2p_{3/2} - 1s_{1/2}$ | 5998.7±4.8 (2.2) | 5792.1±5.0(-1.7) | 5783.7±5.0(-1.9) | 5848.7±5.0(1.4) |
| $3d_{5/2} - 2p_{3/2}$ | 2677.8±2.0(10.0) | 2645.1±1.9(-0.2) | 2643.9±2.0(-0.2) | 2703.3±2.2(0.3) |
| $4f_{7/2} - 3d_{5/2}$ | 900.0±1.7(10.8)  | 970.7±1.7(-1.0)  | 970.7±1.7(-1.0)  | 936.7±1.7(-0.1) |
| $\Delta p$            | 187.7±1.4(-2.3)  | 187.6±1.4(2.0)   | 185.9±1.4(0.8)   | 191.0±1.4(0.3)  |
| $\Delta p - \Delta d$ | 13.3±1.4(-1.6)   | 142.3±1.4(-0.5)  | 143.7±1.4(1.2)   | 165.4±1.4(-0.4) |
| $\Delta d - \Delta p$ | 23.2±1.4(0.0)    | 33.5±1.4(-0.2)   | 33.5±1.4(-0.2)   | 34.9±1.4(-0.4)  |
| $\Delta f$            | (7.8)            | (9.1)            | (9.1)            | (9.5)           |
| $Q_0$                 | 22.8±1.4         | —                | —                | -3.8±1.4        |
| $Q_0$                 | 2.8±0.2          | —                | —                | -0.7±0.2        |
| $R_p$                 | 1.7±0.3          | 2.0±0.3          | 1.8±0.3          | 1.5±0.3         |
| $R_d$                 | 1.5±0.3          | 1.8±0.3          | 1.9±0.3          | 1.5±0.3         |
| $R_f$                 | 1.4±0.2          | 1.5±0.2          | 1.5±0.2          | 1.4±0.2         |

Energies in keV. (E capt. - E det.) in brackets.  $Q_0$  in  $10^{-28}$  cm<sup>2</sup>. Includes a correction for detector efficiency of 7%, 10% and 6% for Pb, Bi, and Bi respectively.

Figure 12. Muon x-ray energies in Au 197, Pb 206, Pb 208, Bi 209.

Nuclear Shape Parameters

|                                       | Au 197              | Pb 206               | Pb 208               | Bi 209               |
|---------------------------------------|---------------------|----------------------|----------------------|----------------------|
| $\delta$                              | 1.19±0.005          | 1.197±0.005          | 1.199±0.005          | 1.198±0.005          |
| $\beta_2$                             | 0.061±0.015         | 0.073±0.009          | 0.078±0.010          | 0.089±0.010          |
| $\langle \delta^2, \beta_2^2 \rangle$ | $36 \times 10^{-3}$ | $1.8 \times 10^{-3}$ | $2.2 \times 10^{-3}$ | $2.4 \times 10^{-3}$ |
| $\delta$                              | 1.19±0.005          | 1.190±0.005          | 1.191±0.005          | 1.191±0.007          |
| $\beta_2$                             | 1.19±0.5            | 2.1±0.5              | 2.1±0.5              | 1.9±0.5              |

Lengths in fermis.

Figure 13. Nuclear shape parameters deduced from muon x-ray energies.



## Mu-atomic Spectra

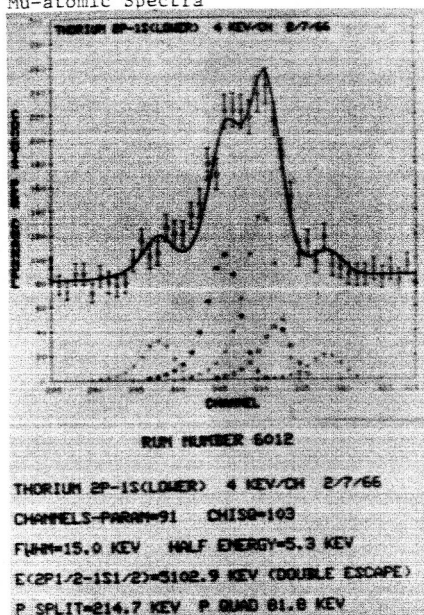


Figure 14. 2p - 1s transitions in thorium, lower lines showing quadrupole effect due to interaction with rotation states.

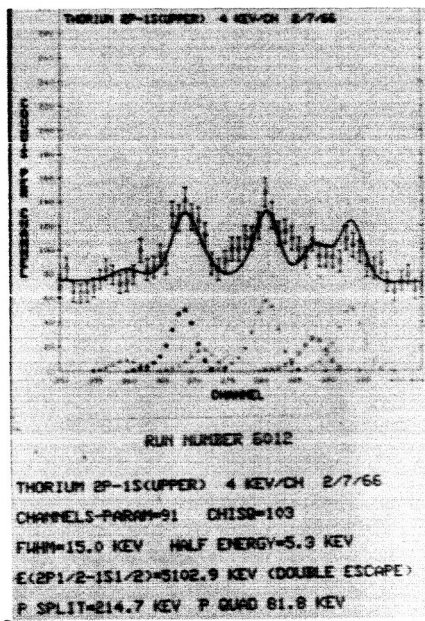


Figure 15. Upper lines of the 2p - 1s transitions in Th 232.

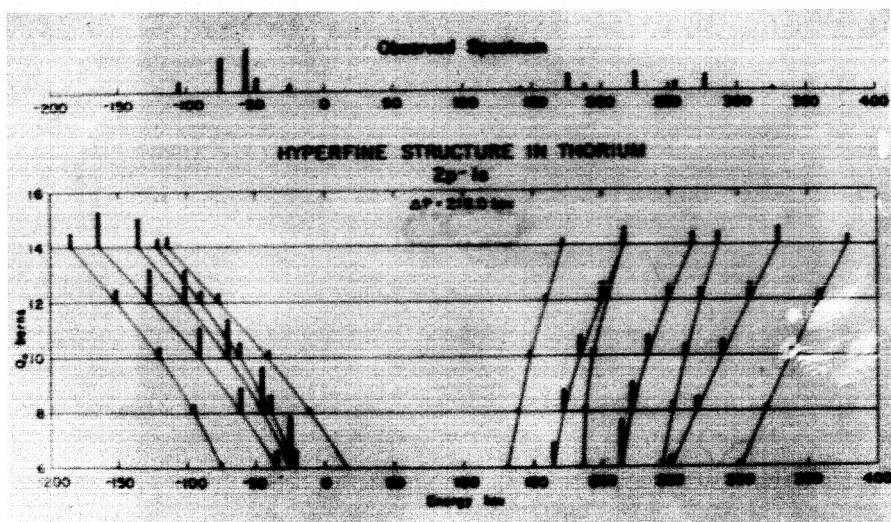


Figure 16. Comparison of observed fit with calculated spectrum of Th 232 2p - 1s transitions.

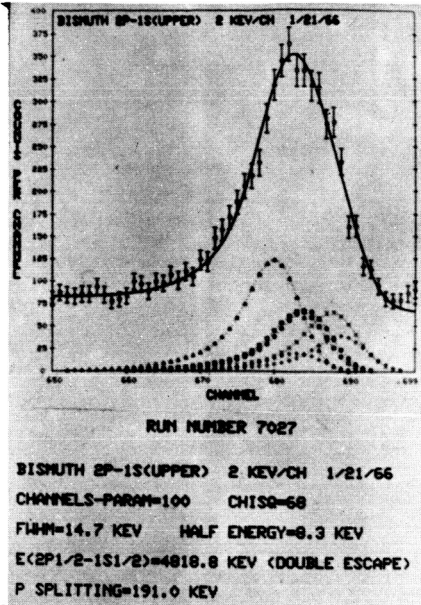


Figure 17. 2p - 1s upper lines in Bi 209 showing quadrupole broadening.

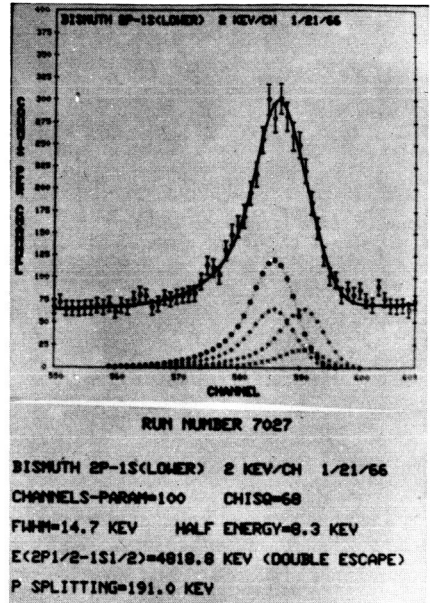


Figure 18. 2p - 1s lower lines in Bi 209 showing magnetic dipole effect.

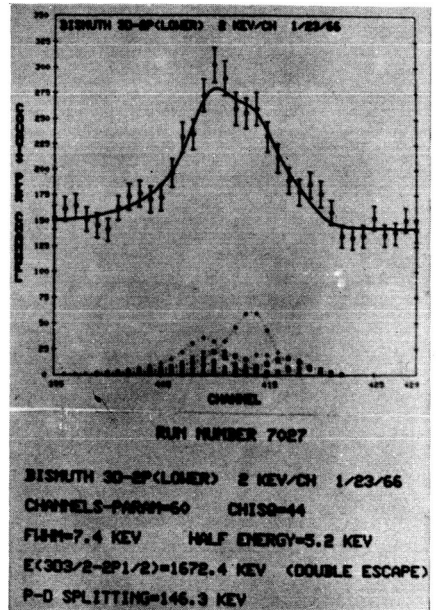
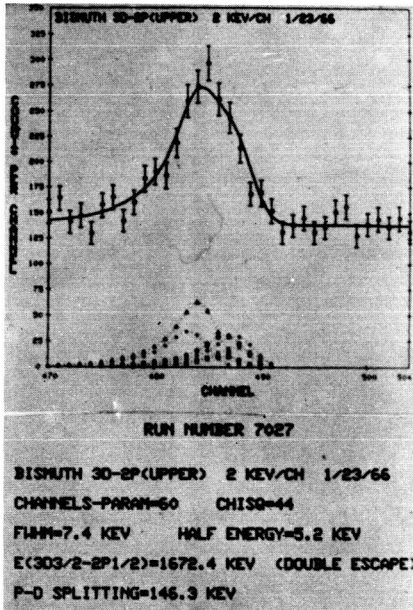


Figure 19. 3d - 2p upper lines in Bi 209. Figure 20. 3d - 2p lower lines in Bi 209.

NSA 32728-15

High Resolution Muonic X-Ray Studies\*

S. Devons

Columbia University

I must confess to a certain diffidence in talking to you on this subject when there are clearly so many experts in the audience. My own involvement in this type of work has been maintained by the very enjoyable nature of this type of experiment - a certain old-fashioned charm which is not always a feature of contemporary experimental physics, and especially experiments requiring large accelerators.

I'm sure that any of you who have done this kind of experiment, and I hope there are lots of you who will do more, will find that it is really a very pleasurable occupation.

You might ask then, why is it necessary to have such large teams of people to do this work. Well, Dr. Anderson gave the answer. He said, "You have to work round the clock because of the competitors nowadays." And nobody can work 24 hours a day. I think the nature of the work is also such that it's not the sort of thing that you can put on a computer and hope for the best, because things happen in front of your eyes and you want to be there to see and change them. So, of the people involved, let's say that some worked while others slept and others slept while others worked. And so in this way both the fun and the burden were shared. But everybody was awake when they were in the lab, I think! Now, it's quite impossible in the 29 odd minutes left to do justice to all the work that has been done; much of it analyzed and the rest being analyzed. So, I propose instead to try and do a service here by putting down some of the salient

---

\*This report is based on work done in collaboration with D. Hitlin, E. Macagno, K. Runge, T. Tchao and C. S. Wu, Department of Physics, Columbia University, Pegram Laboratory and R. C. Cohen, C. Nissim-Sabat and J. Rainwater, Department of Physics, Columbia University, Nevis Laboratories and supported by A.E.C. Contract AT 30-GEN 72 and O.N.R. Contract 266(72).

features. The work we've done has been rather in the nature of a survey of many problems of different sorts, ranging from muonic x-rays in carbon to those in uranium. The interesting features, I think, that are worth putting on record this morning, are just those that indicate where the real high resolution is important, where precision is important, where accuracy is important. So if you'll allow me, I'll just make a little table here.

| Quantity  | Electronic Atom                     | Muonic Atom                          | Ratio                        | Typical Values for Muonic Atoms     |
|---|-------------------------------------|--------------------------------------|------------------------------|-------------------------------------|
| Atomic radius $\langle r \rangle$ (1s state)  | $\frac{\hbar^2}{e^2} \frac{1}{Z m}$ | $\frac{\hbar^2}{e^2} \frac{1}{Z m'}$ | $\frac{1}{207}$              | $5 \times 10^{-13}$ cm for $Z = 50$ |
| Electric Monopole<br>$\left\langle \frac{Ze^2}{r} \right\rangle$  | $Z^2 m$                             | $Z^2 m'$                             | 207                          | 6 Mev                               |
| Electric Quadrupole (Hyperfine)<br>$\left\langle \frac{[Q_N] e}{r^3} \right\rangle$                         | $[Q_N] Z^3 m^3$                     | $[Q_N] Z^3 m'^3$                     | $(207)^3 \sim 10^7$          | $\sim 100$ kev in the rare earths   |
| Magnetic Dipole Splitting (Hyperfine)<br>$\left\langle \frac{[M_N] M_{\mu, e}}{r^3} \right\rangle$          | $[M_N] Z^3 m^2$                     | $[M_N] Z^3 m'^2$                     | $(207)^2 \sim 4 \times 10^4$ | 1 kev in heavy elements             |
| Fine Structure Splitting<br>$\left\langle \frac{\vec{L} \cdot \vec{\sigma} \cdot Z}{m^2 r^3} \right\rangle$ | $Z^4 m$                             | $Z^4 m'$                             | 207                          | $\sim 200$ kev in heavy elements    |

$m, m'$  are electron and muon mass, respectively:  $[M_N], [Q_N]$  represent nuclear properties.

These factors which occur in expressions for the muon-nuclear interaction, and their variation with atomic number, clearly indicate the sort of domain of the subject; and the numbers indicate the sort of resolution that is necessary, and why it is that germanium Li-drift detectors, which have resolutions of the order of kilovolts, make possible resolution and precise measurement of these interactions, something which was previously quite unattainable. And this is what has brought about the big change in the subject. Now in the experiments which I will describe, we used detectors of about six cm<sup>3</sup>'s. The resolution was pretty good. The resolution of these detectors varies, of course, with energy. Our resolution was 7 to 8 kev in the energy range 5 to 6 Mev, and better at lower energies (2 to 3 kev at 100 kev). Efficiency, also, varies throughout the spectrum, but one can study energies all the way from 100 kilovolts or less to 7 Mev, and it's as good a detector as any, I think, in all that region except, of course, for the present limited size, which limits the efficiency.

Since the ideal monopole is clearly a bad approximation because the size of the orbit is comparable with the size of the nucleus, the departures from the point charge are very significant and even the differences in this effect from isotope to isotope ("isotope shift") can become quite large in heavy elements. Contributions to isotope shift can come from any of the terms, of course. But the predominant effect in isotope shifts is usually the change in the effective monopole field. To exploit the extraordinary resolution of these detectors to the full we have, therefore always used single or separated isotopes.

I think we have made measurements essentially of all these terms in various elements. Isotope shifts are quite large in many cases. We have seen the electric hyperfine structure effects, both static and dynamic; the magnetic hyperfine structure effects; and, of course, the fine structure splitting is quite clearly seen. I think we've seen it down to a Z of about 28. Figure 1 shows the standard layout. Figure 2 shows the arrangement we used on our muon beam which was not a

record breaker, at least not for high intensity anyway, so we used our detectors directly in the beam. We took extreme precautions to eliminate electrons which are rather obnoxious with these detectors, (more so than with NaI counters). We had a pair of detectors which operated essentially independently. Figure 3 is a picture of the detector system. "Gemini" indicates that there are two detectors. There is a constant feed of liquid nitrogen.

Figure 4 is a standard  $\text{Co}^{60}$  calibration spectrum. This energy is a difficult region for these detectors, but here you can see an overall picture of the response of the detector.

Figure 5 is a montage of different spectra for calibration purposes, ranging from  $\text{O}^{16}$  down to  $\text{Co}^{60}$ ; and there were other spectra taken in the region from 1 Mev down to 50 kev.

Figure 6 illustrates a pleasing technique which was possible, and convenient because the resolution is so high. You don't have to do each element at the time. You can do like Moseley did, in ordinary x-ray spectra. You can put a whole string of materials in and easily pick out all the separate lines. You can avoid a lot of systematic errors this way.

Figure 7 lists some of the results of measurements of K and L x-rays using these "sandwiches" and comparison with calculations.

Figure 8 shows a rather more detailed analysis of a deformed nucleus -  $\text{W}^{182}$  - which has a sizable quadrupole moment. It has correspondingly low lying  $2^+$  states, of the order of 100 kilovolts. I should mention here that excitation of the nucleus can occur, (dynamic quadrupole interaction) and so to regard the nucleus as a static object is, as has been predicted many years ago by Wilets and by Jacobsen and we now know from many experiments, no longer an approximation. But the dynamic effects vary greatly, depending on the level structure of the nuclei. In this case, where the level structure of the nuclei is comparable with the fine structure splitting, the interaction is highly developed. When the muon comes

down to the 1s level, sometimes the nucleus is excited, sometimes it isn't. In fact, the odd labelled lines represent one state of the nucleus and the even labelled lines the other. These effects are noticeably different even for the similar nuclei  $W^{182}$ ,  $W^{184}$  and  $W^{186}$ , and a detailed discussion of this will be presented later this morning by Dr. Runge.

Figure 9 shows isotope effect in K-x-rays of  $Nd^{142}$ ,  $Nd^{144}$ , and  $Nd^{146}$ .

Figures 10 and 11 illustrate the  $Bi^{209}$  lines and a calibration line of  $O^{16}$  at 6.13 Mev. You can see (Fig. 10) the widths of these two "lines" are quite obviously different, as is the structure of the lines. This width of the Bi line is attributed to magnetic hyperfine interaction. To analyze this in terms of an experimental line that is itself broad naturally places a great premium on getting the highest possible resolution. We had a resolution there of about 8 kilovolts. So magnetic hyperfine structure, even in favorable places, is close to the limit of the resolution of the technique. I think this is about as high a resolution as anybody has achieved in this energy region; about 8 kilovolts. But even this is none too good.

Figure 12 is an attempt to analyze the bismuth line. The analysis is based, (as well as on the commoner quadrupole interaction), on certain models about the magnetic moment, how it is distributed over the nuclear volume - whether it's given by single-particle model with or without configuration mixing. The components of the line which build up this broad line are given. You see the difference between the line width and the actual line. There is some evidence of a double bump here; this is actually a point. There's some evidence from the structure of configurational mixing, but you see the difficulties as well as the possibilities of the method. I should also remark that this example,  $Bi^{209}$  which has a large magnetic moment is one of the most favorable cases for studying this effect - the so called Bohr-Weisskopf effect.

Figure 13 shows the L x-rays of Bi<sup>209</sup> which again have a rather interesting feature. Here are the broad lines due to hyperfine effects and fortunately there's a nuclear excited line from the actual mu capture by Bi<sup>209</sup> leading to an excited Pb<sup>208</sup> nucleus that is 2.6 Mev. This gives a nice sharp line right in this region, so one can see quite clearly there that the broadening is not instrumental at all there! There's a real gamma ray line with the zero broadening and the two "broadened" muonic x-ray lines. So one can actually do a fairly precise measurement; although still limited by statistical fluctuations which were nearly always an all important feature of our measurements.

Figure 14 is a rather complicated spectra where the limitation is not only due to resolution but clearly statistical. The deformed uranium nucleus yields lots of components in the 2p-1s transition, and the analysis is here quite clearly limited largely by fluctuations.

Figure 15 is a comparison of some observed and estimated energy differences between components of the transition. For example, the number 44.7 kev, as compared with 44.2 kev and 45.0 kev, represents the excitation of the first rotational state of U<sup>238</sup>. This number 44.7 kev is taken from nuclear tables, the other two values are from the x-ray spectrum. There is no significant difference. But there is no reason why the two numbers should be identical because these are not the same objects. In one case there is a bare uranium nucleus (one can ignore electrons!), and in the other there is a uranium nucleus with a muon around it - and thereby hangs an interesting tale which I don't have time to recount. Suffice to say that with a little more statistical accuracy and a little more resolution, one could in fact study the difference between these two energies, which is now just at the limit of what the experiment can seek.

Figure 16 is a curve showing optical isotope shifts which have been measured over the last couple of decades and showing how the measured isotope shift varies and compares with the so-called "theoretical" value just using A<sup>13</sup> law. You see



marked changes, due to shell effects particularly in the region of the deformed nuclei. One knows the general interpretation of the effect. One is measuring the apparent mean square radius, and this varies both because of a change in density of the nucleus and because of a change of sphericity, or departure from sphericity, and sometimes there is one and sometimes there is the other. Sometimes they add; sometimes they subtract and you get the characteristic variation of the isotope shift with a number of neutrons. The crosses are some measurements we have made with muonic x-rays. The other points of the curve are the optical ones. Below is the attempted theoretical curve to explain the optical curves. Now you see the crosses generally, (although the analysis is not complete in the stage, and there are many subtleties which one has to look into carefully) agree with the optical values. And this brings me to one of the general remarks I'd like to make: namely the relation of this type of study to optical spectroscopy and particularly isotope shifts. The optical isotope shifts have still, in the best measurements, a higher accuracy than the muonic x-ray ones. Moreover, they can be made with samples on the order of 100-thousand times smaller than required for the muonic x-ray measurements, or at least a thousand times in these experiments that we've done. And as I mentioned, we always used either single occurring isotopes or single isotopes separated because with a high resolution, if you mix isotopes you can smear everything out. However, this means having 50 or 100, or at least 20 grams of isotope which is not always feasible. The optical measurements, on the other hand, are limited by the knowledge of the electronic wave functions whereas, in principal, the muon wave functions are much simpler. They're not entirely simple because the departure from the coulomb field is much bigger here and you must be very careful. At least somebody has to be very careful. In the optical case, one has the many-electron problem, which is in principal more complicated - so you might say a big function of the muon work will be to normalize some of these optical data and make them much more

valuable. And then you can extend the measurements using the optical method to the isotopes which are in too small abundance to be practical for the muonic x-ray work.

There is another feature, of course: the approximations that enter in interpreting the two sorts of data are quite different. Dr. Anderson mentioned that polarization effects, which involve, in principle, all the higher states of the nuclei are quite different in these two energy regions of optical and muonic x-rays. And as far as I know there is no evidence here as to just how different; maybe somebody at the conference will tell us just how small these effects are, judged by theory; and even more important in this context, how different they are from one isotope to the next. The estimates made so far indicate that they're very small; of the order of few kev; and one assumes that in going, for example, from tungsten 182 to tungsten 184 the change in polarization effect must be in order of magnitude less than the polarization effect itself. And that brings you down into the level of experimental error, so you don't worry about it! There appears then to be a very strong interaction, between the optical data and the nuclear data, and to a large extent, you might say fortunately, this is complementary and not competitive. I hope we'll hear more about this.

One final remark: In many cases, which I haven't time to discuss, for the muonic as distinct from the optical (electronic) atom, it's quite inappropriate to consider this sort of system as a nucleus and the muon as an object which interacts with it 'occasionally.' One is dealing now with a new type of object which is a new sort of nucleus - nucleus plus muon. And this object as a whole has excited states, it has properties and one has to consider it very often in this way. Now in most cases one can try to separate this thing out naturally into two parts in order to make it tractable. However, there are some interesting cases where this separation is, in a sense, false - one has to look at interaction of

the muon and the structured nucleus all as one object. These interesting cases are just about at the moment at the edge of what is resolvable or what is possible by virtue of the limited intensity of muon beams. But no doubt here or in other places there will be better muon beams, better Li-drifted detectors, more people and these problems will soon be explored and they will be discussed at the next conference.

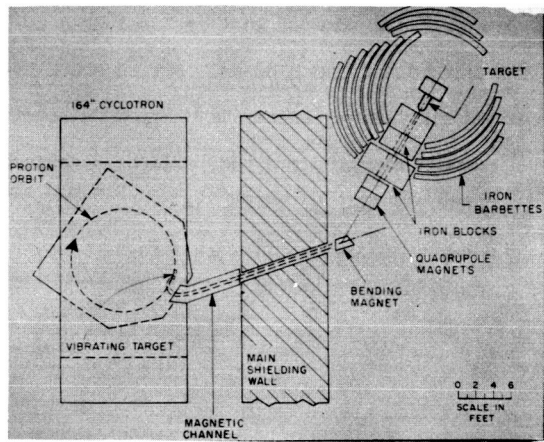


Figure 1 - Plan view of Cyclotron and experimental room showing beam line.

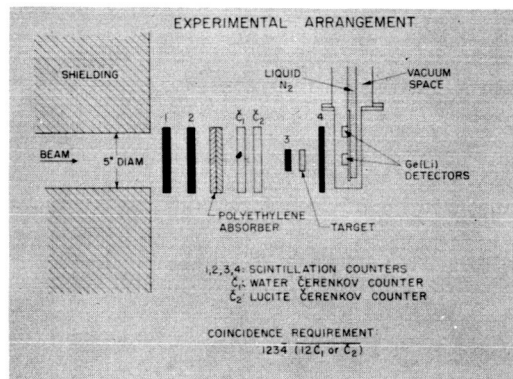


Figure 2 - Experimental counter arrangement.

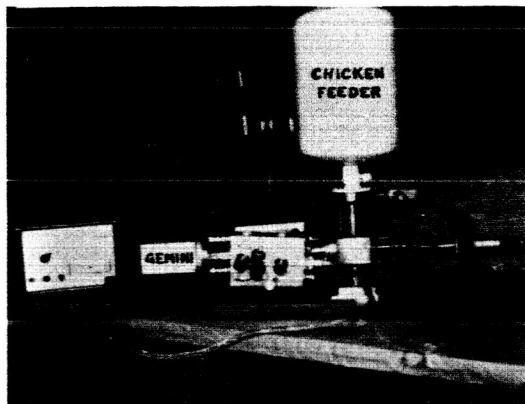


Figure 3 - Detector system - two detectors are enclosed in Gemini; Chicken Feeder is a constant feed of liquid nitrogen.

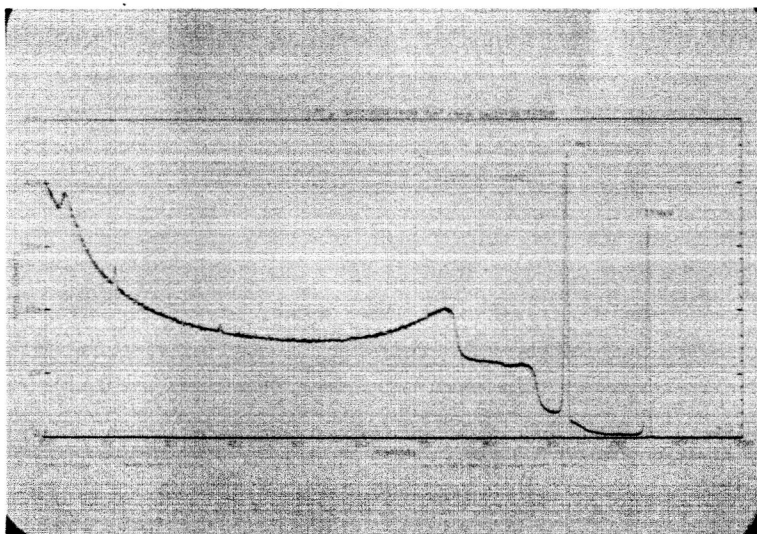


Figure 4 -  $\text{Co}^{60}$  calibration spectrum using a Ge Li-drifted detector

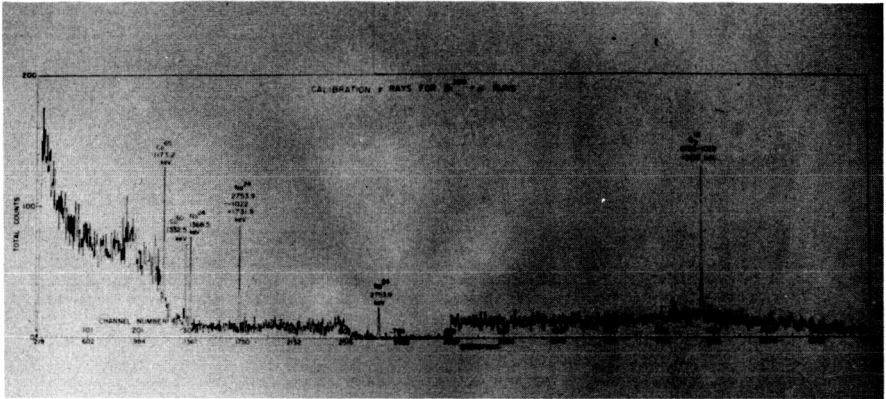


Figure 5 - Montage of different spectra for calibration purposes.

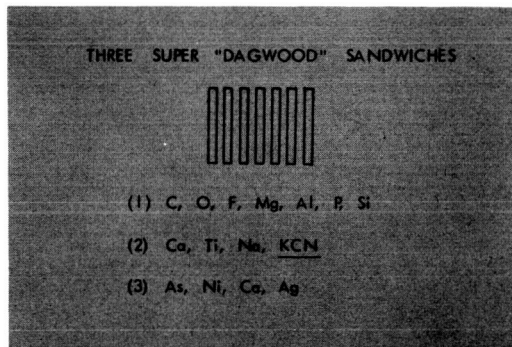


Figure 6 - Multiple element target assembly.

|    |         | K X-rays                    |                                 | L X-ray     |                                 |
|----|---------|-----------------------------|---------------------------------|-------------|---------------------------------|
|    |         | 2p - 1s                     |                                 | 3d - 2p     |                                 |
| Z  | Element | Theoretical<br>(Pustovalov) | Experimental<br>(Columbia 1965) | Theoretical | Experimental<br>(Columbia 1965) |
| 28 | Ni      | 1421                        | 1422.1                          | 309.6       | 309.97                          |
|    |         | 1426                        | 1427.4                          |             |                                 |
| 29 | Cu      | 1504                        | 1506.61                         | 332.1       | 330.26                          |
|    |         | 1510                        | 1512.78                         |             | 334.8                           |
| 33 | As      | 1859.4                      | 1855.8                          | 431.1       | 427.5                           |
|    |         | 1869.3                      | 1866.9                          |             | 436.6                           |

Figure 7 - Results of K and L muonic x-ray spectra with theoretical estimates.

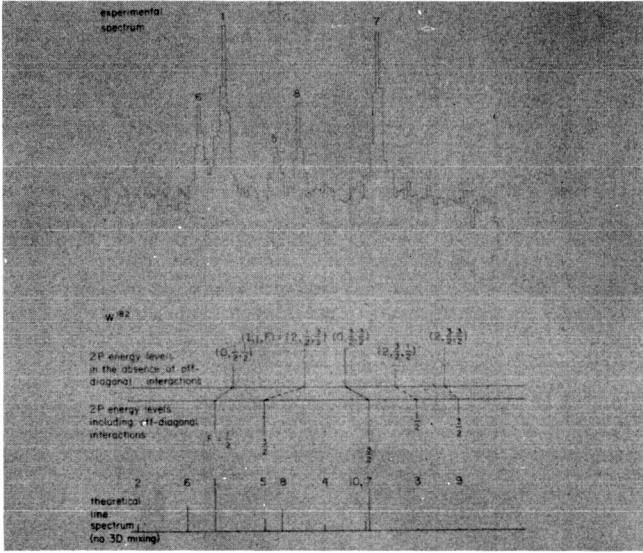


Figure 8 -  $W^{182}$  experimental muon x-ray spectra and energy level diagram.



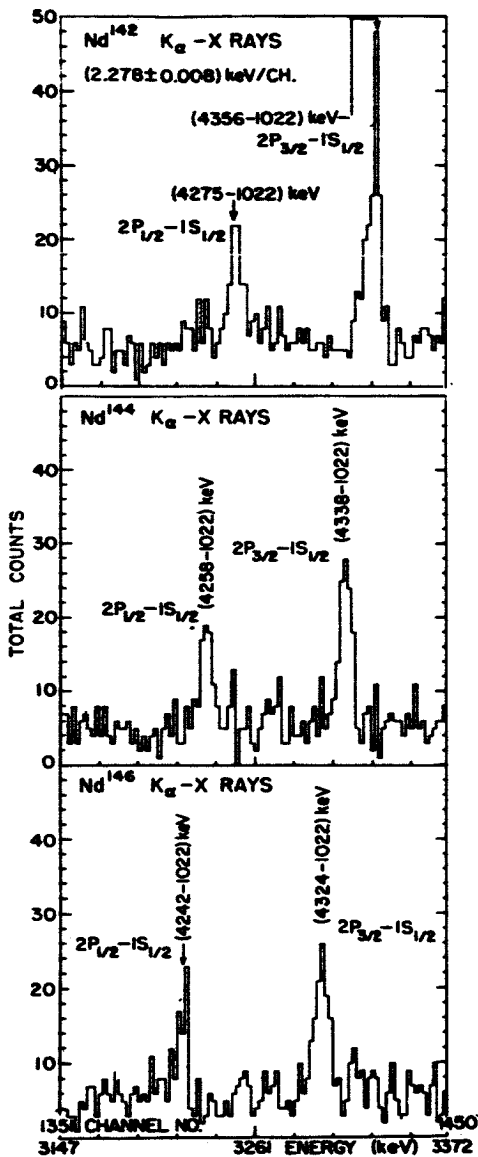


Figure 9 -  $Nd^{142}$ ,  $144$ ,  $146$  muon x-ray spectra.

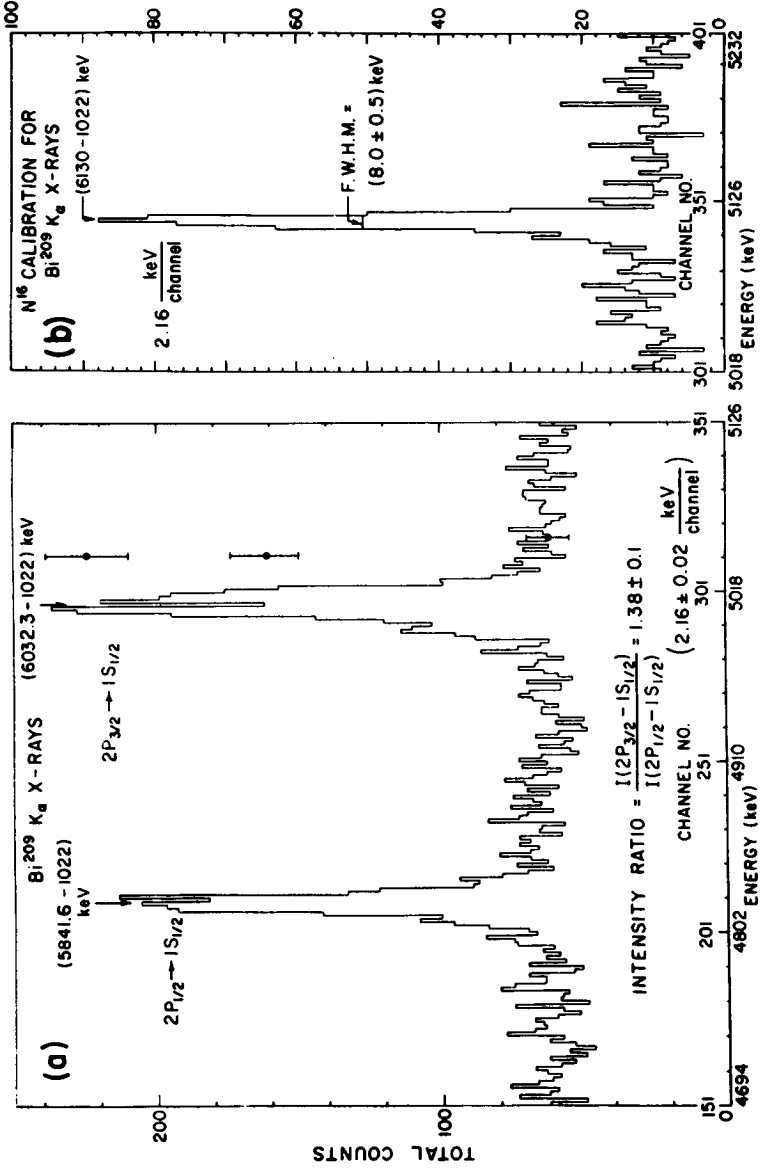
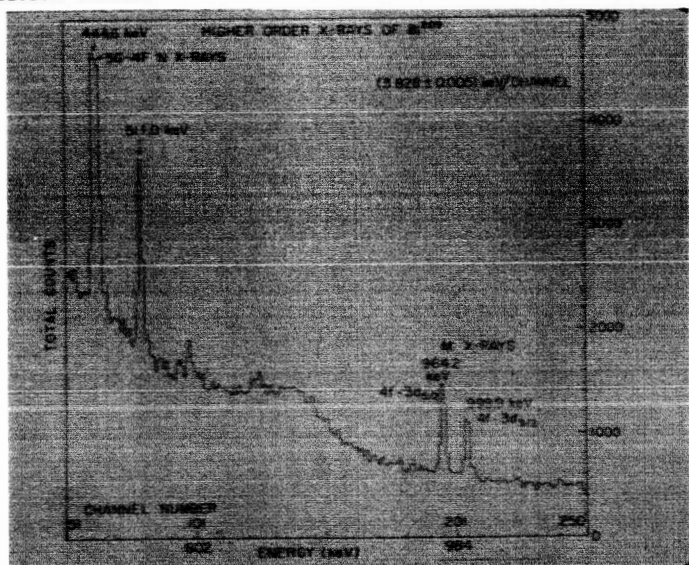
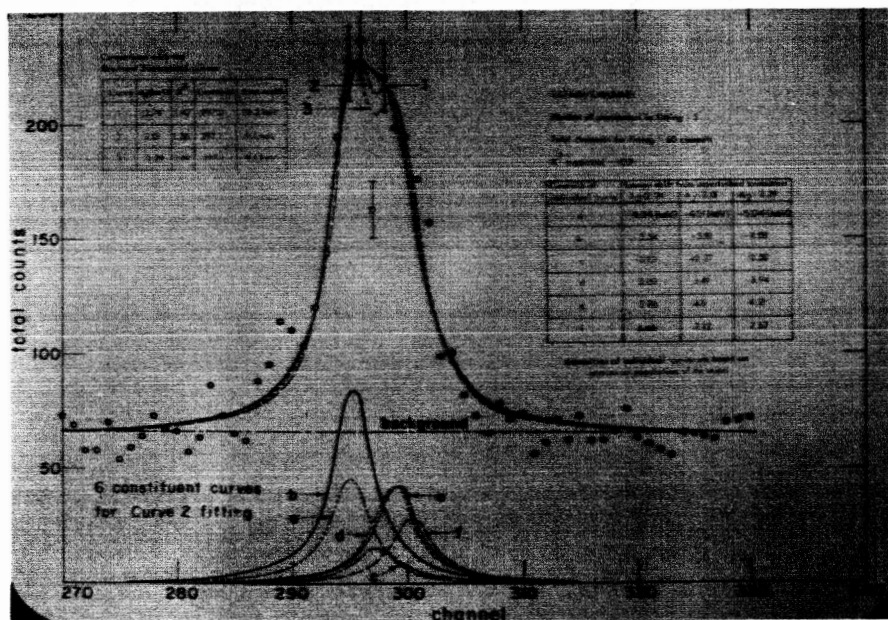
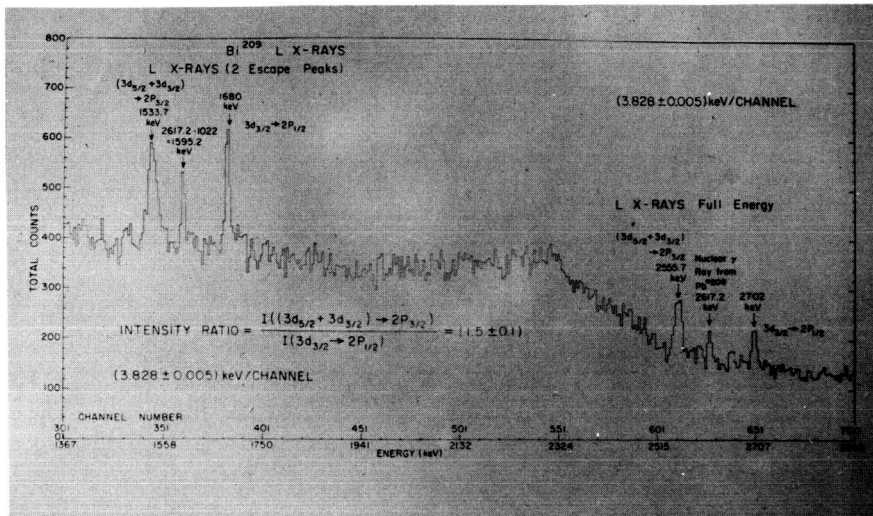
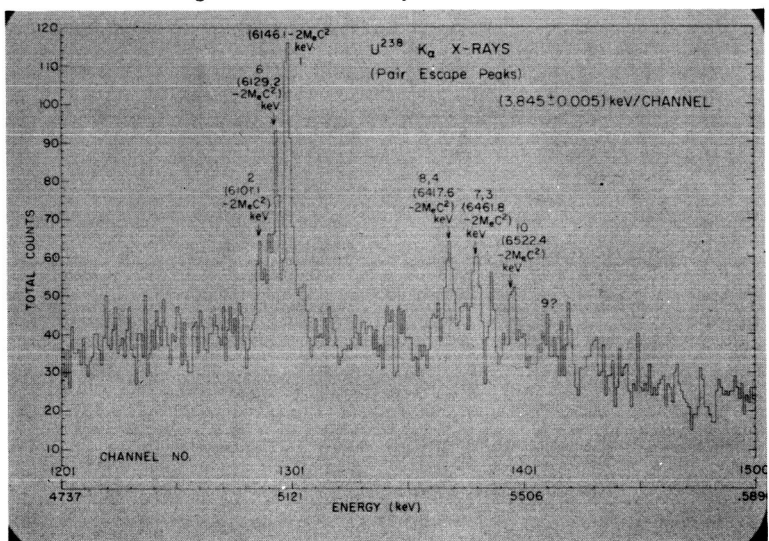


Figure 10 -  $\text{Bi}^{209}$  A muon x-ray spectra together with  $\text{N}^{16}$  calibration spectra.

## High Resolution Studies

Figure 11 - Higher order muon x-rays from  $\text{Bi}^{209}$ .Figure 12 - Analysis of  $\text{Bi}^{209}$   $2p_{3/2}$  to  $1s_{1/2}$  line.

Figure 13 - L x-rays from Bi<sup>209</sup>.Figure 14 - U<sup>238</sup> muon x-rays.

| U <sup>238</sup> K X-RAYS |                    |                   |
|---------------------------|--------------------|-------------------|
| ENERGY DIFFERENCES        |                    |                   |
|                           | EXPERIMENTAL (KeV) | THEORETICAL (KeV) |
| Δ 2-1                     | 35.7               | 36.1              |
| Δ 3-2                     | 26.5               | 26.3              |
| Δ 3-3                     | 288.5              | 288.9             |
| Δ 10-3                    | 108.8              | 108.7             |
| Δ 7-2                     | 44.2               | 44.7              |
| Δ 1-2                     | 45.0               | 44.7              |
| Δ 4-2                     | 21.1               | 27.2              |

|            |  |     |
|------------|--|-----|
| PARAMETERS | $E_{K\alpha} = 44.7$                     | KeV |
|            | $E_{K\beta} = 234$                       | KeV |
|            | $E_{K\gamma} = 94.5$                     | KeV |
|            | $n_{O_2} = 10.5$                         | b.  |
|            | then $\langle \phi f(r) \rangle = 88.57$ |     |

Figure 15 - U<sup>238</sup> K x-ray energy differences, experimental and theoretical.

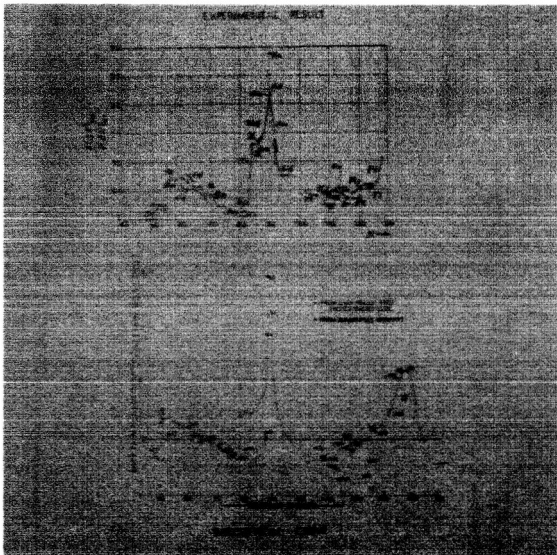


Figure 16 - Optical isotope shifts showing variation with theoretical fit using A<sup>1/3</sup> Law. (From: Elton, L. R. B., Nuclear Sizes, Oxford, 1961)

HUGHES: I'm wondering whether the lines that the Columbia group saw were asymmetric like the ones Anderson mentioned.

DEVONS: In first approximation - no.

WILKINSON - I'd like to ask Dr. Anderson whether the sense of the discrepancy between the predicted energy from the electron measurements and the muon energy measurements was the sense that you expect from polarization effect.

ANDERSON: I don't really know.

TELEGDI: I would like to ask my colleague, Prof. Anderson, what he meant when he said that lead 206 and lead 208 were measured simultaneously, or ordinary lead and lead 206 were measured simultaneously.

ANDERSON: The lead 206 and lead 208 were not measured simultaneously, they were analyzed simultaneously - that is the computer was asked to find the best fit in both spectra, looking at the data of lead 206 and lead 208 and asking for a best simultaneous fit of that data. The measurements were not taken simultaneously in the mode of the Columbia or of your own work, but the measurements were taken interspersed.

BREIT: I have a few things to remark on, all short. The first is that the smaller radius of the charge distribution actually was strongly suspected and definitely down in form of numbers, in connection with the old measurements of Shuler and Shuler and Kupferman on the atomic spectroscopic shift. The value of rho that was used from alpha particle information was definitely too large and I remember that fits had to be made using not just quadratic parabolas but higher order parabolas for the charge distribution. On the other hand one should

## High Resolution Studies

remark that in the atomic spectroscopy one gets a combination of the change of radius, and the value of the radius, and the great advantage of the mu mesic atom is that one gets the total isotope shift and not the change in the isotope shift as one increases  $A$ . Another thing that occurs to one is that the remarks on polarization in both papers so far do not seem to distinguish between even and odd isotopes and that even the description of what the experimentalists apparently understand by polarization is the standard thing that one usually finds in print. There is a closely related phenomenon consisting of the excitation of low lying levels in work at Yale by Gendenan, Arkin and others showing that there are conditions in the atomic problem in which low lying levels can produce appreciable effects provided there are correlation effects in the wave functions. In connection with the isotopes of lead, there is the fact that lead 207 - at least I didn't hear it mentioned in the Chicago description - does not really indicate a polarization effect. Because the levels of odd-even nuclei fall lower, there are some excited levels falling lower than those of the even-even. A third point which is not a question is that atomic spectroscopists have used separated lead 208 which has been possible to obtain from manufacturers. There was a concern on Long Island where one can get it. Presumably you need here a much larger quantity and for that reason there is more difficulty but I thought I would mention it in case it might be a help in separating the effects of the three isotopes.

TELEGDI: Pb 208 and 206 and 207 are available both from natural sources and from Oak Ridge. The three isotopes have been measured separately and the data will be shown to you in a contributed paper.

DEVONS: I didn't show all these data, but we have other examples of odd-even shifts too, in tin isotopes and one or two others. The odd-even effect is just

similar to what one expects from atomic spectroscopy. I think the polarization effects is a cover up term for the sum over all the highest states which one can't see as individual dynamic effects. I think everybody is aware of the rather crude term, but how big it is or how much it changes from one nucleus to a neighboring isotope is really the problem that one is faced with. One assumed that it is small.

ANDERSON: First about the isotope shift. In our experiment we had only two samples but we assumed that the isotope shift of the lead 207 was shifted somewhat less than that taking the optical spectra value from a paper of Itrudel and using that as part of the analysis. So we make no claim about the odd-even effect, but as you've already heard Telegdi's group has made such measurements with properly separated isotopes. I wanted to also correct my Answer to Wilkinson's remark. I think the direction is right but I have no statement to make about the magnitude.

MRS. WU: We saw lines distinctly in  $\text{Sn}^{118}$ ,  $\text{Sn}^{119}$ , and  $\text{Sn}^{120}$ . In  $\text{Sn}^{119}$  all lines are level with  $\text{Sn}^{118}$ . There is a 6 kev difference between  $\text{Sn}^{118}$  and  $\text{Sn}^{120}$ . This is the first very pronounced example of the even-odd staggering effect. The second effect is the polarization effect. Now this is very difficult. In order to see this effect, apart from other effects, we have chosen something which is particularly sensitive to the deformation effect and this we have also seen. This will also be published.



Remarks on the Theory of Mu-Mesic Atoms\*

D. G. Ravenhall

Department of Physics, University of Illinois, Urbana, Illinois

I would like to associate myself with the sentiments expressed by the previous speakers. The audience contains many people who have contributed much more to this topic than I have. My remarks will be confined to a couple of aspects of the problem.

The model which forms the basis for the mu-mesic atom calculations presented at this conference represents the nucleus as a charge distribution, and the meson as a Dirac particle which interacts through the Coulomb interaction. The basic physical picture is very simple. It is this simplicity which makes mu-mesic atoms such an attractive tool for exploring nuclear structure. The degree of sophistication with which the model has been applied has depended very much on the accuracy and extent of the experimental results available. Now that electric quadrupole and even magnetic dipole hyperfine structure is observed so clearly, the application of the model, with its assumed charge and current densities, can be carried out to an appropriate degree of accuracy. Calculations of such a kind are reported at this conference. The difficulties encountered are mainly computational, so far as I am aware, and there is no point in my discussing them here. They are best considered

---

\* Work supported by the National Science Foundation, Contract No. NSF-G-17428.

as part of an analysis of particular experiments, and there are a number of these that we shall enjoy during this session. My contribution will be to comment on the basic model and to remind you of the level of accuracy beyond which a more refined description of the nucleus may be needed.

The basic assumption that the muon is in all observable respects a heavy electron is well borne out by measurement of its spin and total magnetic moment. As regards its interactions, the most recent comparison of muon-proton scattering with electron-proton scattering, by Cool et al.,<sup>1)</sup> puts the upper limit on any difference in structure of the interaction at 0.3 F. In replacing the nucleus by a static, perhaps deformed, charge distribution an additional approximation, neglect of nuclear polarization, is involved. It produces the largest contribution to the uncertainty in the theoretical predictions. The same approximation is made also in electron-nucleus scattering, and a comparison of results obtained from the two methods may show to what extent this omission is detectable. That comparison will be made later in this paper. Some comments on calculation of the vacuum polarization contribution to energy shifts will be made also.

Whatever dynamic model is used to describe the nucleus itself, the Coulomb interaction between its constituent parts and the muon will cause virtual transitions to excited nuclear states. It also induces virtual transitions of the muon to other Coulomb orbits. Physically the effect is the distortion or polarization of the nucleus by the Coulomb field of the muon, and the effect of the extra electric field so caused on the motion, and energy eigenvalue, of the muon. Nuclear polarization was

originally estimated to be a large effect, but the most detailed and reliable calculations of it, by Lakin<sup>2)</sup> and recently by Scheck,<sup>3)</sup> give for nuclei around Lead an energy shift for the  $1s$  state of order 3-6 Kev. These calculations were made with non-relativistic, point-nucleus Coulomb wave functions for the muon states and they are for the  $1s$  state only. Lakin's calculation employed for the electric dipole contribution the photo-nuclear giant resonance cross section, through sum rule techniques. He relates the monopole contribution to a classical nuclear compressibility. Scheck considered the additional contribution arising from the single proton states of Bismuth, which contribute about the same shift as the collective effects considered by Lakin. At a stage where, in experimental measurement of  $K_{\alpha}$  lines, precision has reached this order of magnitude, a re-examination of this question is very desirable.<sup>4)</sup>

The other large correction needed by the simple model is due to vacuum polarization. The strong Coulomb field of the nucleus creates virtual electron-positron pairs which form a space charge around the nucleus, modifying the Coulomb field a little. Usually an approximation is used which treats only to lowest order the interaction of the electron-positron pair with the nuclear Coulomb field (the Uehling term). The expectation value of the modifications in the Coulomb potential is calculated for each muon state. The presence of this effect in the precisely known  $3d-2p$  transition in phosphorus, where finite-size effects are unimportant, is already well established.<sup>5)</sup> The effect of vacuum polarization on the  $1s_{1/2}$  state is large:  $\sim 80$  Kev in Lead. One would expect that the Born approximation for the electron-pair and the nucleus would

be very poor for heavy nuclei, since the expansion parameter is  $(Z\alpha)^2$ , which can be almost 0.4 and that here might be an important uncertainty. But a calculation by Wickmann and Kroll<sup>6)</sup> of the higher terms shows that in Lead they are less than 1 Kev. Point-Coulomb Dirac states are employed for the electron pair, but probably that is not a bad approximation for electrons. I cannot give a physical reason for the tremendous reduction in magnitude of these higher terms, but am glad that it enables us to use the simpler forms of the Uehling term with confidence.

Despite the earlier promise to eschew computational details, the method by which Clark, Herman and I<sup>7)</sup> include the vacuum polarization effect is perhaps worth mentioning. Calculation of an expectation value involves an extra process after the eigenvalue of the desired muon state has been found. From the foregoing physical picture, it is reasonable to add the vacuum polarization potential to the nuclear Coulomb potential in the Dirac equation. The eigenvalue obtained now includes automatically the vacuum polarization shift. (It also includes all the higher order effects of the Uehling term--all ladder diagrams--but since the expansion parameter is  $Z\alpha^2$  these higher terms are very small, of order 0.1 Kev in Gold.) One can show that to a good approximation this potential is

$$V_{v.p.}(r) = (2\alpha/3\pi) [\ln(\kappa_e/Cr) - 5/6] V_{coul}(r) ,$$

where  $\kappa_e$  is the electron Compton wavelength, C is Euler's constant, and  $V_{coul}(r)$  is the nuclear Coulomb potential. This is only an approximation to the Uehling term, and the remainder, which can be evaluated occasionally to check, is around 0.6 Kev for the 1s state in Gold. It should be possible to include the effect of the nuclear quadrupole field on the vacuum polarization<sup>8)</sup> in the same way.

It is interesting to conclude by making a comparison, in as detailed and accurate a manner as is presently possible, of the mesic atom results with the electron-scattering conclusions. In this way we can see to what extent the corrections we have discussed have yet become appreciable. Electron-scattering experiments up to now are useful mainly for spherical nuclei. Two nuclei which are spherical, and for which data exists from both kinds of experiments, are Gold and Calcium.

In Gold, an early analysis of electron scattering cross sections<sup>9)</sup> led to a series of possible charge distribution profiles, all pretty much equally preferable. They can be arranged in a linear fashion with a variation essentially describing the amount of charge in the tail of the distribution. The mu-mesic x-ray energies for the  $2p_{1/2} \rightarrow 1s_{1/2}$  and  $3d_{3/2} \rightarrow 2p_{1/2}$  transitions, and the fine-structure splitting  $2p_{3/2} - 2p_{1/2}$ , predicted by this progression of charge distributions are seen in Fig. 1 to vary monotonically. The experimental values of these energies,<sup>10)</sup> when plotted on that figure, then select three separate places in the progression. It is a measure of the agreement of the electron-scattering and mu-mesic x-ray techniques that the region selected, in between the Fermi and the parabolic Fermi shapes, is the same for all three energies. We note that the uncertainty in the  $2p_{1/2} \rightarrow 1s$  transition energy as predicted from electron scattering is about  $\pm 35$  Kev. (This comes from the uncertainties in the parameter values of, for example, the Fermi distribution.) This compares with the experimental uncertainty of  $\pm 9$  Kev.<sup>11)</sup> It will be useful to have new, more extensive electron scattering measurements on some spherical nucleus in this region to improve the precision.

Nuclear polarization effects of order 3 Kev are still small compared to these errors, but not too small to worry about. The vacuum polarization contributions to the calculated levels are quite large,  $\sim 29$  Kev for the  $2p_{1/2} \rightarrow 1s_{1/2}$  transition. It is interesting to note that for these transitions also, omission of vacuum polarization would significantly impair this agreement.

Calcium is a spherical nucleus (probably) which has received extensive attention from electron scatterers, and there are mesic x-ray measurements. The two effects we have dwelt on, vacuum and nuclear polarization, are reduced from their values in Gold, but the precision of the predictions and experiments is also improved. The two experimental values for the  $\text{Ca}^{40}$   $2p \rightarrow 1s$  energy are  $(782.8 \pm 3)$  Kev<sup>12)</sup> and  $(780.7 \pm 0.8)$  Kev.<sup>13)</sup> The electron-scattering result predicts  $(782.1 \pm 2)$  Kev<sup>14)</sup> which is in fine agreement. Vacuum polarization contributes 6.0 Kev to this value, and without it there would be discrepancy of about two standard deviations.

Nuclear polarization effects are expected to be smaller than in Gold, and if the calculations there are scaled according to  $Z^2$ , they predict around 0.2 Kev shifts. This is still small compared to the errors quoted above. More detailed and precise measurements are possible on the difference between the charge densities of the isotopes  $\text{Ca}^{40}$  and  $\text{Ca}^{44}$ . The level structure of these two isotopes is quite different, and to the extent that low-lying levels contribute to nuclear polarization in either type of experiment, one might expect perhaps to see such an effect in the difference. The measured difference in  $2p \rightarrow 1s$  x-rays is  $(0.6 \pm 0.3)$  Kev<sup>15)</sup>,  $(0.9 \pm 0.3)$  Kev.<sup>16)</sup> From electron scattering one obtains charge distribution differences which then give for this difference  $(0.7 \pm 0.3)$  Kev.<sup>17)</sup> The

-7-

agreement is good, but the errors are large enough still to leave room for a nuclear polarization effect. Vacuum polarization makes a negligible (0.02 Kev) contribution.

Thus nuclear polarization, not an especially welcome complication of our simple mu-mesic atom model, is not as yet an essential element of the theory. But it is just around the corner, and more complete investigations of it are very desirable.

## References

1. R. Cool, A. Maschke, L. M. Lederman, M. Tannenbaum, R. Ellsworth, A. Melissinos, J. H. Tinlot, and T. Yamanouchi, Phys. Rev. Letters 14, 535 (1965).
2. W. Lakin, Technical Report No. 2, OOR No. 116-53, Carnegie Institute of Technology (unpublished).
3. F. Scheck, Z. Physik 172, 239 (1963).
4. Added later: In a preprint given to me later, H. L. Acker, G. Backenstoss, C. Daum, J. C. Sens, and S. A. de Wit (Nuclear Physics, to be published) calculate the  $E(0)$  and  $E(1)$  contributions to the nuclear polarizability with accurate muon wave functions. (They also give references to work by Nuding and Greiner which I was not aware of.) Their results for  $E(1)$  are considerably smaller than those reported above, but for  $E(0)$  they are in agreement. The importance of the  $E(2)$  nuclear polarization for deformed nuclei has been pointed out by L. Chinn and L. Wilets (preprint). As was emphasized to me by D. H. Wilkinson, a complete calculation of the effect, including contributions from all of the nuclear giant resonances as well as individual levels where appropriate, using accurate muon wave functions, and for all relevant muon states, is very desirable.
5. A. Petermann and Y. Yamaguchi, Phys. Rev. Letters 2, 359 (1959). I am grateful to V. L. Telegdi for pointing out the omission of this remark in the talk as given.
6. E. Wickmann and N. Kroll, Phys. Rev. 96, 239 (1954). The result quoted includes finite-size effects on the muon wave function, by comparing it with the Uehling term.



7. B. C. Clark, R. Herman, and D. G. Ravenhall, report in preparation. The calculations used in this paper are the work of these three authors.
8. J. M. Pearson, Nucl. Phys. 45, 401 (1963).
9. B. Hahn, D. G. Ravenhall, and R. Hofstadter, Phys. Rev. 101, 1131 (1956).
10. H. L. Acker, G. Backenstoss, C. Daum, J. C. Sens, and S. A. de Wit, Phys. Letters 14, 317 (1965). Data communicated privately to us by H. Anderson and S. Raboy (reported at this Conference) are in close agreement with the CERN data, the final version of which is in reference 4.
11. The most recent CERN results, reference 4, now give the errors as  $\pm 5.0$  keV.
12. D. Quitmann, R. Engfer, U. Hegel, P. Brix, G. Backenstoss, K. Goebel, and B. Stadler, Nucl. Phys. 51, 609 (1964). In reference 4 the CERN group now give the value  $783.8 \pm 1.5$  keV, which does not significantly change the quality of the agreement.
13. J. A. Bjorkland, S. Raboy, C. C. Trail, R. D. Ehrlich, and R. J. Powers, Nucl. Phys. 69, 161 (1965).
14. M. Croissiaux, R. Hofstadter, A. E. Walker, M. R. Yearian, D. G. Ravenhall, B. C. Clark, and R. Herman, Phys. Rev. 137, B865 (1965).
15. R. C. Cohen, S. Devons, A. D. Kanaris, and C. Nissim-Sabat, Phys. Letters 11, 70 (1964).
16. J. A. Bjorkland, S. Raboy, C. C. Trail, R. D. Ehrlich, and R. J. Powers, Phys. Rev. 136, B341 (1964).
17. R. Hofstadter, G. K. Nöldeke, K. J. van Oostrum, L. R. Suelzle, M. R. Yearian, B. C. Clark, R. Herman, and D. G. Ravenhall, Phys. Rev. Letters 15, 758 (1965).

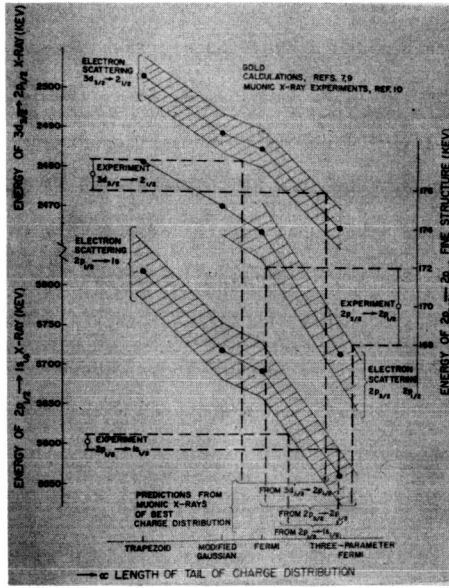


Fig. 1 A comparison of the electron scattering predictions<sup>7,9)</sup> for energies of gold mu-mesic atom states with experimental measurements.<sup>10)</sup> The abscissa is a conceptual parameter which characterizes the difference between the various acceptable charge distribution in reference 9. There are various ordinate scales for the different transitions. There is complete agreement among the three energy differences as to the "best" charge distribution.

RAINWATER: I thought the presence or nonpresence of vacuum polarization had been settled in our measurement on the 3P-2P phosphorus x-ray. Do you feel that it isn't completely settled?

RAVENHALL: No, I only wish to comment on it in this particular context. I guess that it is much more sensible than to worry about whether it really were there or not, to look at it where the nuclear effects are quite small. I'm sorry, I should have mentioned that.

TELEGDI: I would like to make a comment to Dr. Ravenhall, and in particular, also to the audience, that these numbers that you have discussed on the isotope shift in calcium. Somebody in the light of the two previous papers might think that they were obtained by the most recent techniques. As a matter of fact, they were obtained by the old-fashioned techniques, and there is large room for improvement, which will come, at least a factor ten. Secondly, I have been extremely attracted by one sentence that you dropped casually that had to do with the quadrupole vacuum polarization effect. I have been puzzled myself by the following physical problem. Namely, if you have an ellipsoidal nucleus, the gradients of the electrical field near the tips of this ellipsoid are larger than they would be if it were spherical, and I believe that the mean gradient comes out to be larger. Now vacuum polarization to some extent is the consequence of how much gradient you have over a Compton wave length, and I would like you to confirm that if one takes this formalism and simply introduces a spheroidal electro-static field one get the correct vacuum polarization. What is the real theoretical situation to allow for this particular distribution? Now before your answer, I would like to make a third statement, which is quite along

the lines of our chairman. The Columbia work has established vacuum polarization quite conclusively. Now if you take the mass of the muon for granted, say from  $g-2$ , accepting quantum electrodynamics at that level, then both the measurements performed at Columbia and Chicago on that famous Phosphorus transition by a further extension of Rainwater's critical absorber technique, verify the vacuum polarization in that particular phosphorus transition to 5%, which in itself is a valuable physical result. And I expect your answer to the second point.

RAVENHALL: The point about the fact that the data on calcium was obtained with sodium-iodide crystals: I would like very much to find out just how much the accuracy there can be improved, and to what extent does it depend on other things. But on the vacuum polarization problem, I'm referring to the fact that if you expand the nuclear field, there is a monopole contribution, the vacuum polarization term, and then there's a quadrupole contribution, which is then presumably to be included in the quadrupole charge density, which is the thing you take matrix elements of when you do the splitting. I think both of those can be included in this way. I have not, as yet, included the quadrupole term that way but the monopole term we have included for some time that way.

ELTON: I just want to point out the uncertainty between the various charge distributions can be looked at from a slightly more fundamental point of view. The Fermi distribution isn't God given, it isn't even Fermi given. To me it seems a much better way to get distribution by generating wave functions in a shell model potential, a Saxon-Woods potential and then getting the charge distribution from that. Such a distribution fits the data of the electron scattering very well. It is interesting that it has a shorter tail than the Fermi distribution. It's more nearly like the Gaussian distribution for which

have a hankering because I looked at it twelve years ago. I think that analyses really ought to be done in terms of wave function and I will talk re about that when I give my contribution, which happens to be a totally fferent session.

REIT: All I wanted to say is that as long as the calculation of nuclear olarizability effects is made with a single proton, one does not really settle the question of even the order of magnitude because of possible correlations of the motions of protons within the nucleus. The calculation I had been referring to for the optical case dealt with the difference in effects similar to those in the calcium isotopes, but for heavier nuclei where the effects become larger and were not confined to an expansion around the nucleus but were concerned to what happens within the nucleus, particularly with the monopole effect.

HUGHES: Polarization of the nucleus by its interaction with the muon in muonic atoms contributes significantly to the g-value of the muon in muonic atoms. M1 transition type nuclear polarization may have been marginally observed for one or two low  $Z$  nuclei.

X-rays from Muonic Atoms with Spherical or Nearly Spherical Nuclei

R. E. Cote', W. J. Prestwich, S. Raboy\* and C. C. Trail\*\*

Argonne National Laboratory

R. A. Carrigan, Jr., A. Gaigalas and R. B. Sutton

Carnegie Institute of Technology

and

Studies of Muonic Atoms of Non-Spherical Nuclei

R. B. Sutton, A. Gaigalas and R. A. Carrigan, Jr.

Carnegie Institute of Technology

R. E. Cote', W. J. Prestwich, S. Raboy\* and C. C. Trail\*\*

Argonne National Laboratory

Since the previous speakers have discussed the theoretical background of muonic x-ray experiments and made the comparison between electronic and muonic spectra I shall limit my remarks to comments on the experimental data we have obtained. However, before doing that let me just mention the way in which we plan to interpret our data. For extensive help and guidance in this part of the work we are deeply indebted to Dr. D. G. Ravenhall of The University of Illinois, who must indeed be considered as one of our collaborators.

The Dirac equation is solved for a point muon in the field of a finite nuclear charge distribution to get the unperturbed muonic wave functions and energy levels. A correction to the potential for the effects of vacuum polarization is made in the manner described by Dr. Ravenhall. The final eigenvalues and eigenvectors include the effects of the mixing of nuclear levels through the matrix elements of the quadrupole interaction. The intensities are derived in the usual way under the assumption that (1) only E1 radiation gives an appreciable contribution, (2) the  $4f_{7/2}$  and  $4f_{5/2}$  levels are not split by hyperfine interactions, (3) these levels are

PRECEDING PAGE BLANK NOT FILMED.

N66 51 32730

populated as  $2J + 1$ , and (4) the only mode of deexcitation is from  $f \rightarrow d \rightarrow p \rightarrow s$  states.

Let us now look at some spectra. The spectrum shown in Figure 1 of the K x-rays from  $\text{Pr}^{141}$  is one of the simplest. Since praseodymium is mono-isotopic, the spectrum is not complicated by isotopic shift and since the nucleus has a very small quadrupole moment there is no observable broadening caused by quadrupole interaction. In fact, the lines shown here, as well as the  $L$  lines, do not appear to be broader than the corresponding calibration lines. The magnetic interaction in spite of the rather large  $\mu = 4.5$  is not large enough to be readily observable.

For those nuclides with large quadrupole moments the spectra are much more complex. Several examples are shown in the next few figures. In Figure 2 is shown the K x-ray spectrum of muonic  $\text{Ho}^{165}$ . The strong line at the left arises mainly from  $2p_{1/2} \rightarrow 1s_{1/2}$  transitions that result in the nucleus being left in its ground state. The overall spread of the spectrum is determined mainly by the fine structure splitting of the 2p levels. However, a knowledge of the effects of nuclear excitation (the dynamic quadrupole effect) and of the splitting of the muonic levels caused by the static quadrupole interaction is necessary to interpret the spectrum completely. The peak at 3754.3 keV, where this value is the full energy minus 1022 keV, is caused by several transitions all dependent upon the excited state of  $\text{Ho}^{165}$  at 94.7 keV. The  $\text{Ho}^{165}$  nucleus is left in this state about 27% of the time.

The next two figures show more examples of similar spectra. The K x-ray spectrum of  $\text{Tb}^{159}$  is shown in Figure 3. Terbium is mono-isotopic and has a ground state spin of  $3/2$  and excited states at 58 and 137.5 keV. The intrinsic quadrupole moments of  $\text{Tb}^{159}$  and  $\text{Ho}^{165}$  are very nearly the same.

The more compact appearance of the terbium spectrum is the result of the smaller fine structure splitting of the  $2p$  levels. The K x-ray spectrum of  $Ta^{181}$  is shown in Figure 4. Tantalum is also monoisotopic. Its ground state spin is  $7/2$  and it has nuclear levels at 136 and 301 keV.  $Ta^{181}$  is considerably more distorted than  $Tb^{159}$  or  $Ho^{165}$  and its  $A$  and  $Z$  are much greater. Both of these properties produce a spectrum that has a greater spread in energy than those of  $Ho^{165}$  and  $Tb^{159}$ . It should be noted that whereas the fine-structure splitting for  $Ta^{181}$  would be about 136 keV if the nuclide were spherical, the energy difference between lines that result basically from  $2p_{1/2} \rightarrow 1s_{1/2}$  transitions and those from  $2p_{3/2} \rightarrow 1s_{1/2}$  transitions is about 192 keV.

The next figure illustrates two different effects, the isotope shift and a higher order K x-ray line. In Figure 5 are shown the  $K_{\alpha}$  and  $K_{\beta}$  spectra for natural cerium. It should be noted that the  $K_{\alpha}$  spectrum is shown through its full energy peaks, that for the  $K_{\beta}$  through its double escape peaks. Natural cerium is composed four isotopes, but two of these make up 99.5% of it.  $Ce^{140}$  makes up about 88.5% and  $Ce^{142}$  about 11% of the natural element. The shoulder on each of the  $K_{\alpha}$  lines corresponds to the spectrum for  $Ce^{142}$ . A better measure of this effect is of course, available from the double escape peaks that correspond to these transitions, but this portion of the observed spectrum was chosen because it allowed the inclusion of the  $K_{\beta}$  spectrum as well. The separation of the two peaks in the latter shows the fine-structure separation of the  $3p$  levels in cerium. This separation is about 20 keV.

In Figure 6 is shown the K spectrum for indium which is 95%  $In^{115}$ . Any deviations from a simple two component spectrum must therefore be interpreted in terms of additional interactions between the muon and the  $In^{115}$  nucleus. It is clear that a definite bulge appears on the high energy



side of the  $2p_{3/2} \rightarrow 1s_{1/2}$  line. A comparison of the  $2p_{1/2} \rightarrow 1s_{1/2}$  line with a calibration line of nearly the same energy proves that this x-ray line is broader than a single line should be. Since the  $J = 1/2$  levels involved in this transition are not split by electric quadrupole interaction, a splitting arising from the magnetic dipole interaction is required to explain the additional width. This will be discussed in more detail later. The next figure, Figure 7, shows the  $L$  x-ray spectrum for indium recorded at the same time as the K spectrum just discussed. Here the structure of the  $3d_{5/2} \rightarrow 2p_{3/2}$  line is immediately noticeable. Such a splitting appears to be consistent with the known nuclear properties of  $\text{In}^{115}$ . Both  $\text{In}^{113}$  and  $\text{In}^{115}$  have similar nuclear properties; the magnetic moments are about 5.5 nuclear magnetons, the ground state spin is  $J = 9/2$  for both, and the quadrupole moments are about + 0.8 barns.

The K x-ray spectrum of iodine is shown in Figure 8. Two points are to be noticed here. As with indium, but in a more noticeable way, there is structure in the  $2p_{3/2} \rightarrow 1s_{1/2}$  line. There is, perhaps, some slight broadening of the  $2p_{1/2} \rightarrow 1s_{1/2}$  line. Higher resolution studies are needed to explore this point more fully. The second point to notice is the nearly equal intensities of the two K lines. The ratio of the integrated intensities is about 1.2, far from the statistical 2.0 one might expect. The  $L$  x-ray spectrum of iodine is shown in Figure 9. This spectrum was recorded with 0.863 keV per channel rather than the 3.30 keV/channel used for the K lines. The  $3d_{3/2} \rightarrow 2p_{1/2}$  line is about the same width as the nearest calibration line, the 1173 keV line of  $\text{Co}^{60}$ . The  $3d_{5/2} \rightarrow 2p_{3/2}$  transition shows considerable structure. The  $3d_{3/2} \rightarrow 2p_{3/2}$  transition which is weak is, in this case, not even resolved from the structure in the  $3d_{5/2} \rightarrow 2p_{3/2}$  transition. A very preliminary analysis of the structure observed in the K and  $L$  lines of iodine is only in qualitative agreement with what is expected on the basis of the known nuclear parameters.

Let us now turn to two heavy nearly spherical nuclides, Au<sup>197</sup> and Bi<sup>209</sup>. Both have small static quadrupole moments and it should be possible to interpret their spectra rather well in terms of the fairly simple model given by Wheeler many years ago. The K x-ray spectrum of Au<sup>197</sup> is shown in Figure 10. Here for the first time we see the structure of the  $2p_{3/2} \rightarrow 1s_{1/2}$  transition fairly well resolved for what we may consider to be a nearly spherical nucleus. Au<sup>197</sup> has a ground state spin of  $J = 3/2$  and a quadrupole moment of  $Q = +0.58$ . The pattern of lines in the  $2p_{3/2} \rightarrow 1s_{1/2}$  transition should consist of basically three components in the ratio 5:10:1, with a spacing of about 14 keV between each of the weaker lines and the strong one. The measured value of this separation is  $18.9 \pm 0.4$  keV.

Before moving on to the last element to be discussed let us examine one particular calibration line that was used for many of the measurements. This is the 6.128 MeV line that follows the beta decay of N<sup>16</sup>. The spectrum is shown in Figure 11 in which incidentally, the value of the energy of the line is an old one. The ordinate has a logarithmic scale and four distinct peaks are clearly evident. The first peak on the left is the double escape peak of the 6.128 MeV line, the next peak is its first escape and the peak on the far right is the full energy peak. The peak to the left of this full energy peak is the double escape peak of the much weaker transition at 7.120 MeV. The observation of the full set of peaks corresponding to a particular gamma ray provides a fine set of calibration points for spectra in this region.

Besides calibration measurements and the measurement of the spectrum that arises from accidental coincidences one other spectrum is of interest in the study of muonic x-rays. This is the capture gamma ray spectrum. It is studied primarily to be sure that no capture lines are counted as x-rays, but it is clear that a knowledge of the capture gamma rays can lead to a better understanding of the process of muon capture as well. This most well

known capture line is that at 2.614 MeV observed in the middle of the x-ray spectrum of bismuth (this can be seen in Figure 16). In Figure 12 can be seen two other capture gamma rays that follow the capture of a muon in bismuth. The line at 583 keV is directly related to the 2.614 MeV line. The former feeds the level in  $\text{Pb}^{208}$  from which the latter arises. The line at 571 keV corresponds to the transition from the first excited state of  $\text{Pb}^{207}$  to its ground state. Thus it is clear that at least two different nuclides are formed following muon capture in bismuth.

Let us now consider the muonic x-ray spectrum of bismuth in some detail. The M x-rays are shown in Figure 13. Under the assumption that any hyperfine splitting of the 4f and 3d levels can be ignored, the spectrum should consist of three lines with relative intensities of 1, 20 and 14 in order of increasing energy. The actual integrated intensities of the three lines shown in Figure 13 are 1.9, 20, 13.9 in good agreement with those just noted. This agreement is known to vanish for the K lines. The spectrum of K x-rays in bismuth is shown in Figure 14. It is clear that the line formed from the  $2p_{3/2} \rightarrow 1s_{1/2}$  transitions is not nearly twice that of the  $2p_{1/2} \rightarrow 1s_{1/2}$  line. In fact the ratio of integrated intensities is only about 1.4. Careful observation of the K lines of Figure 14 along with a comparison with the calibration line shows two other features of the data. First, the line at the higher energy is split into two peaks. On the basis of Wheeler's simple prescription, four lines are expected with a spacing between high and low energy pairs of about 7 keV. The observed spectrum is roughly consistent with this prediction. Another reason must be found for the added width of

the line that corresponds to the  $2p_{1/2} \rightarrow 1s_{1/2}$  transition. The magnetic dipole interaction can provide the mechanism. LeBellac has computed the energy level shifts for the  $2p$  and  $1s$  levels in bismuth. This splitting is shown in Figure 15; no quadrupole interaction is included. An examination of the x-ray spectrum might be expected to show more of the detail of the spectrum that, of course, is the result of both magnetic dipole and electric quadrupole interactions. The  $L$  spectrum is shown in Figure 16. Here, the splitting of the  $2p_{3/2}$  level is clearly shown in the line formed from the  $3d_{5/2} \rightarrow 2p_{3/2}$  transitions, the  $Pb^{208}$  capture line is a dominant feature of the central part of the spectrum, and some indication is seen for the weak  $3d_{3/2} \rightarrow 2p_{3/2}$  transitions. There is also a slight suggestion of structure in the  $3d_{3/2} \rightarrow 2p_{1/2}$  line. Preliminary attempts to fit these data with the published nuclear quadrupole moment and the magnetic splitting as evaluated by LeBellac have not been successful. Some examples that show the effect of varying  $Q$ , the quadrupole moment are shown in Figure 17. (The ordinate is logarithmic.) The lower curve is the computed spectrum with a line shape, obtained simultaneously, folded in for a value of  $Q = -0.34$ , a value listed in the recent compilation of Fuller and Cohen. The upper curve represents the same spectrum, but with  $Q$  increased by about 30%. That this is nearly consistent with the data is clear, but it certainly does not give a quantitative fit to the data. A further increase in  $Q$  is clearly needed. Another way in which the fit could be improved is through a reduction in the magnetic splitting since this interaction does tend to wash out the pattern. Such a reduction would, of course, be constrained by the requirement that the computed width of the  $2p_{1/2} \rightarrow 1s_{1/2}$  be compatible with experiment. This analysis will be done in the near future. As a final point it should be noted that the intensity ratios of the various components of the  $L$  x-ray spectrum of bismuth

are not compatible with the simple statistical expectation. The ratio, corrected for changes in counter efficiency, of the transitions from the  $3d_{5/2}$  level to those from the  $3d_{3/2}$  level is only 1.09. It is certain that some of the simple assumptions made about the mode of deexcitation are wrong.

\* S. Raboy now at Harper College, State University of New York, Binghamton, N.Y.

\*\* C. C. Trail now at Brooklyn College, Brooklyn, N.Y.

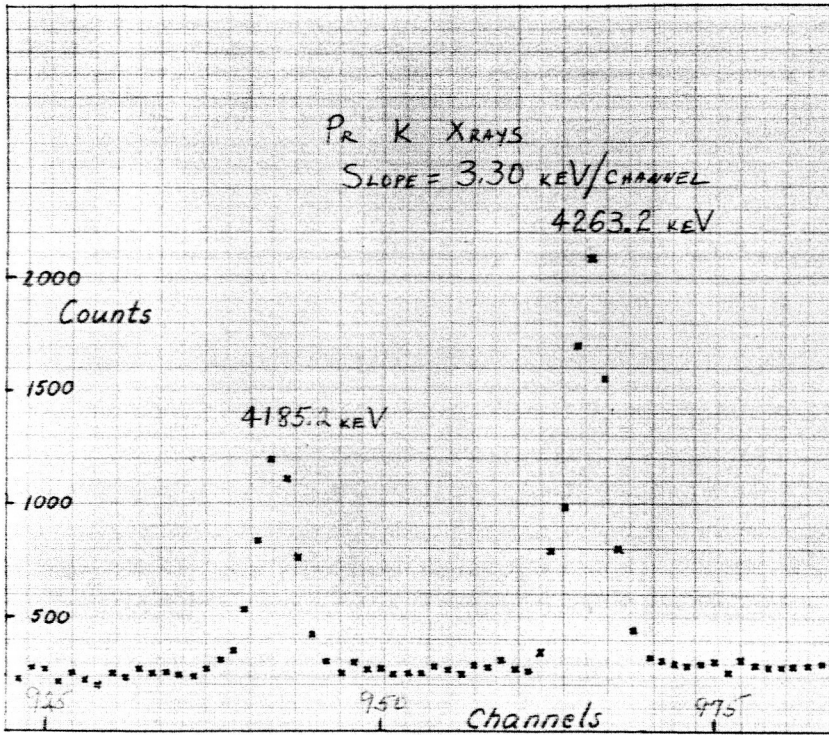
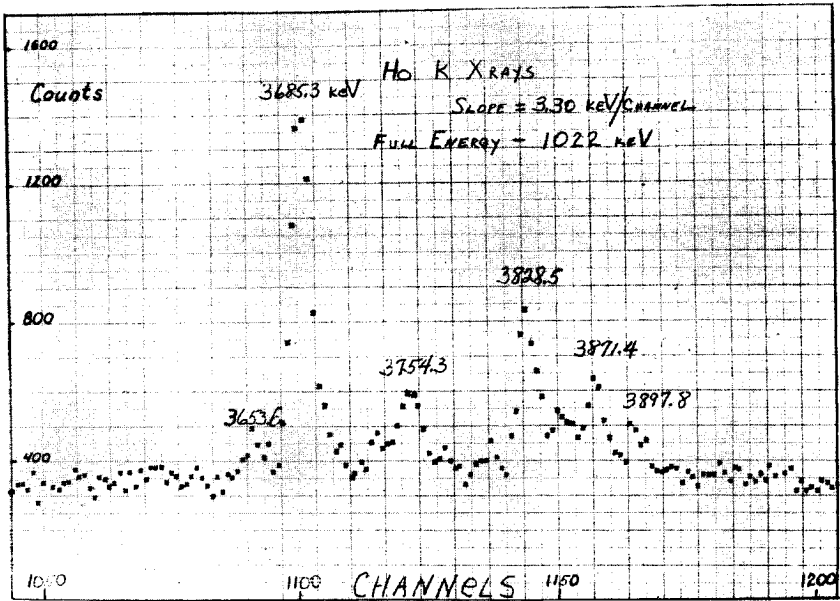


Figure 1 - Pr<sup>141</sup> K X-rays

Figure 2 - Ho<sup>165</sup> K X-rays

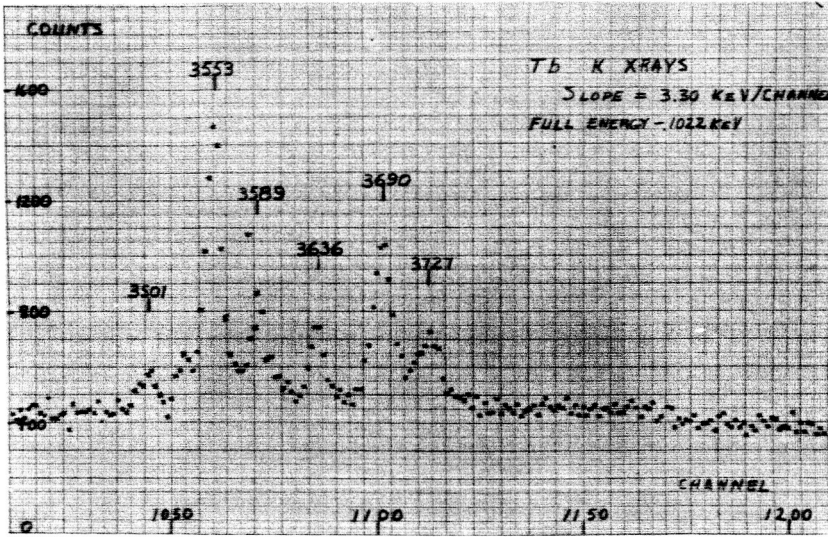


Figure 3 - Tb<sup>159</sup> K X-rays



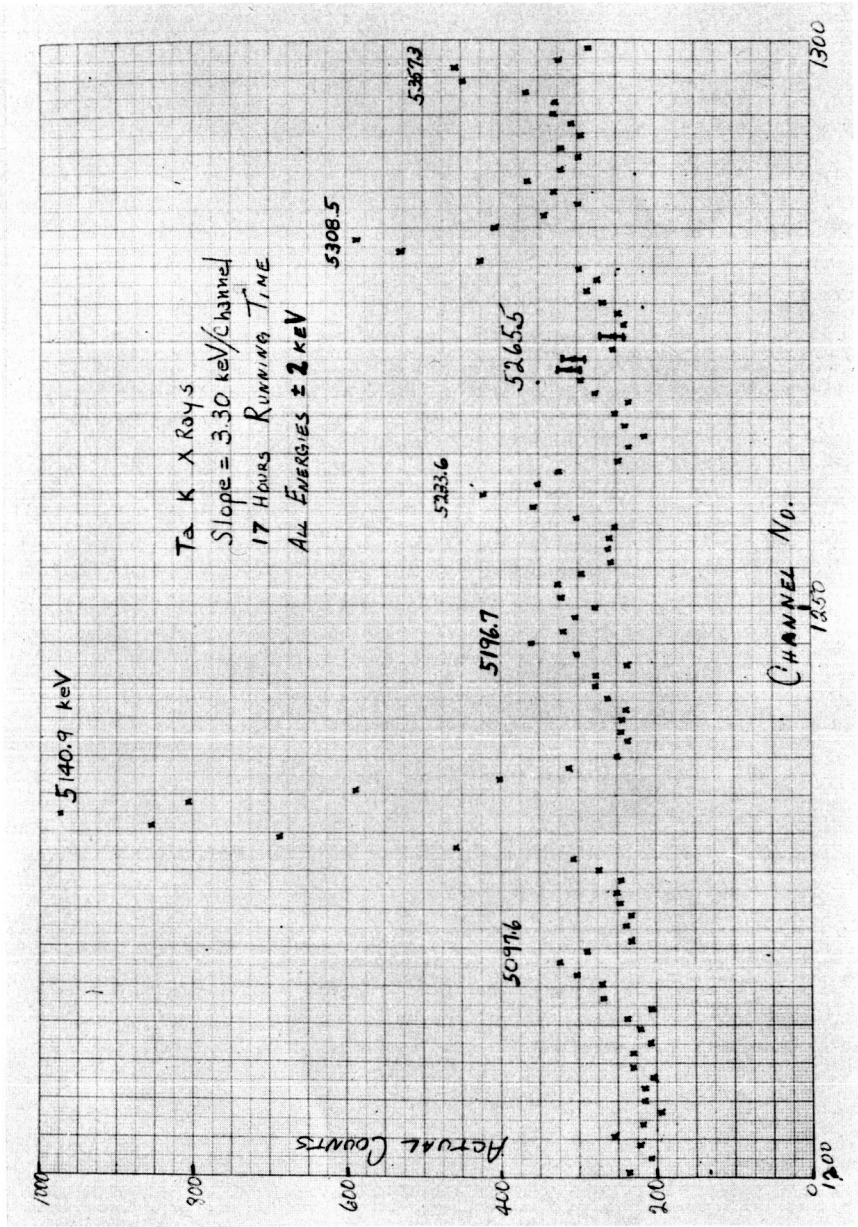


Figure 4 - Ta K X-rays

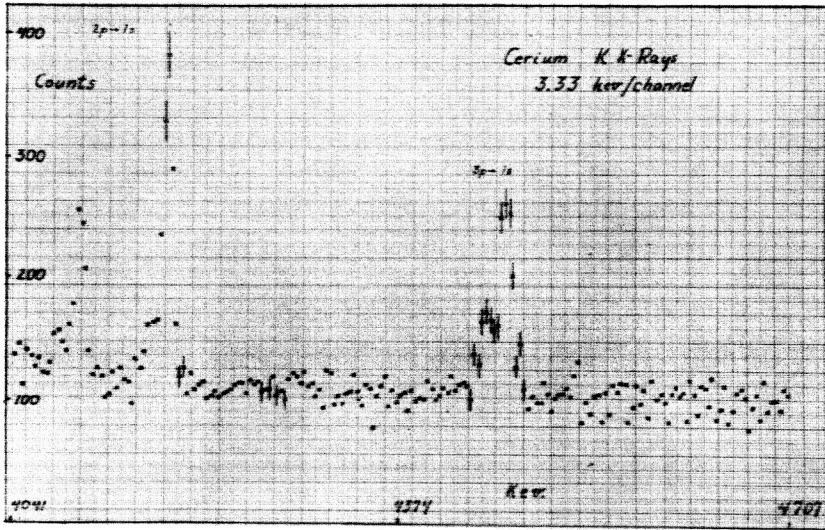


Figure 5 - K X-rays from cerium

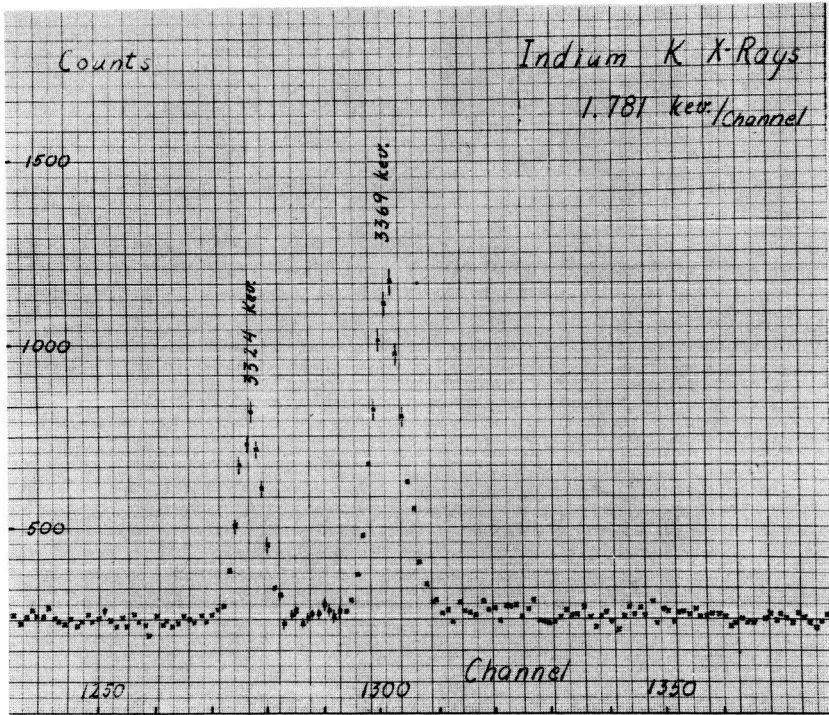


Figure 6 - K X-rays from indium

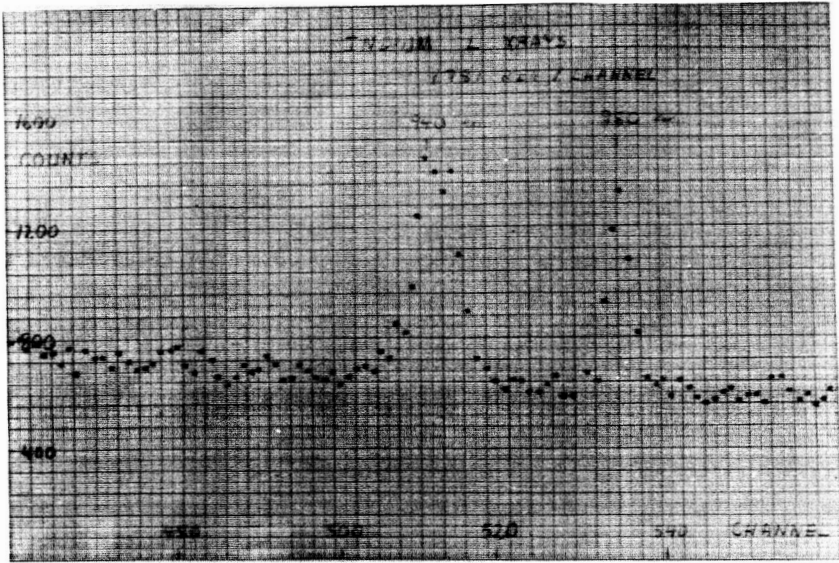


Figure 7 - L X-rays from indium

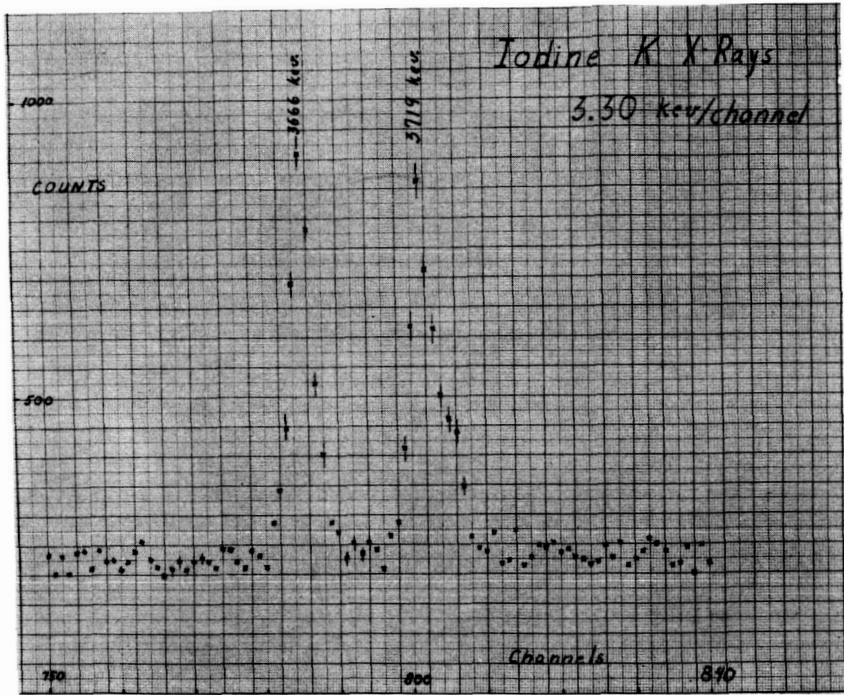


Figure 8 - K X-rays from iodine

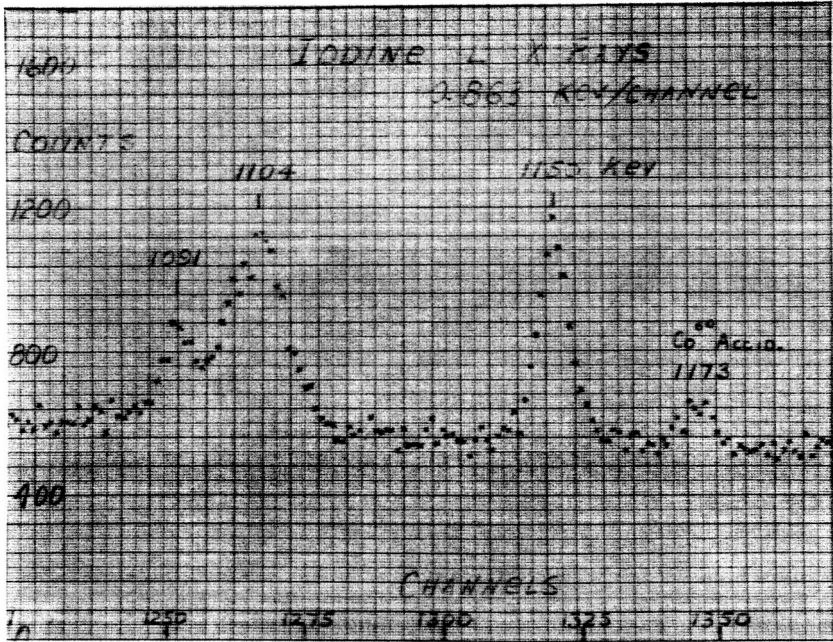
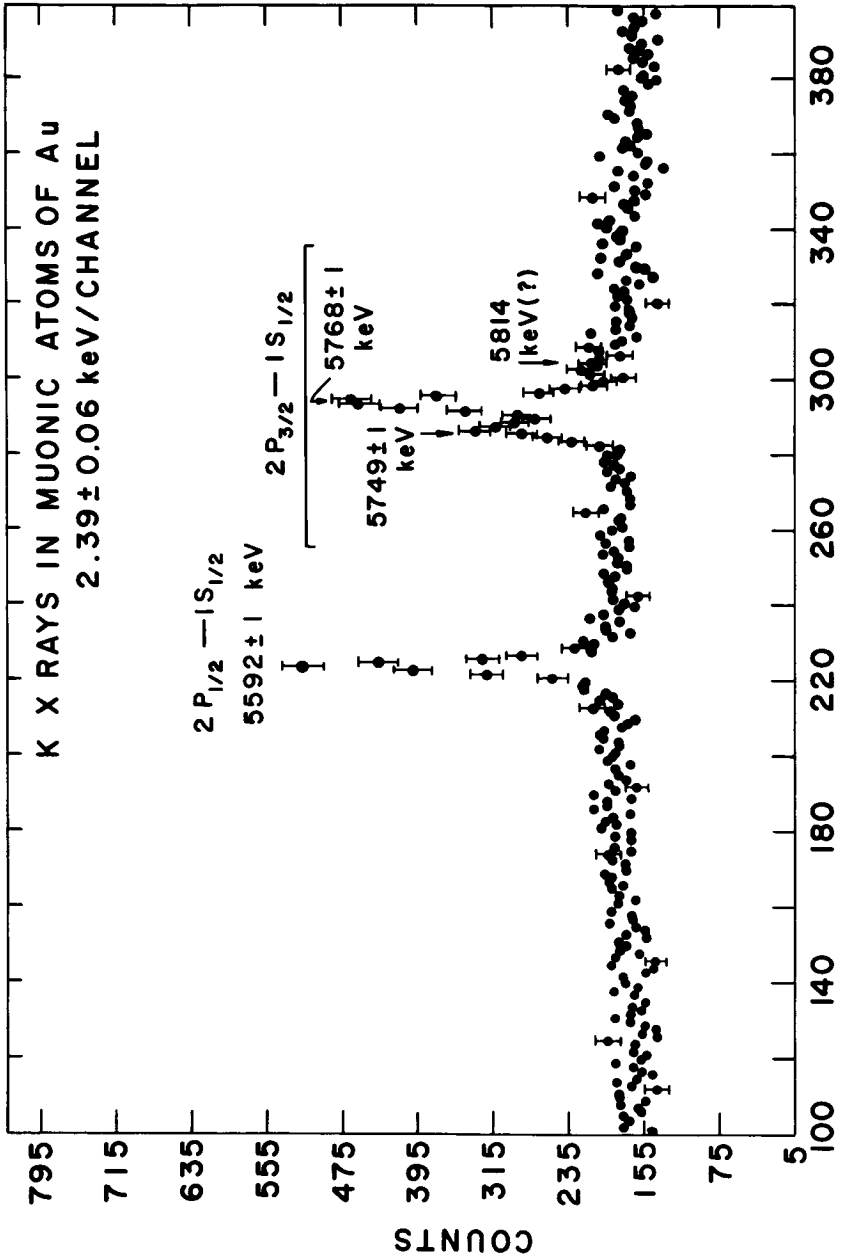


Figure 9 - L. X-rays from iodine



**Figure 10 - K X-rays in muonic atoms of Au<sup>197</sup>**

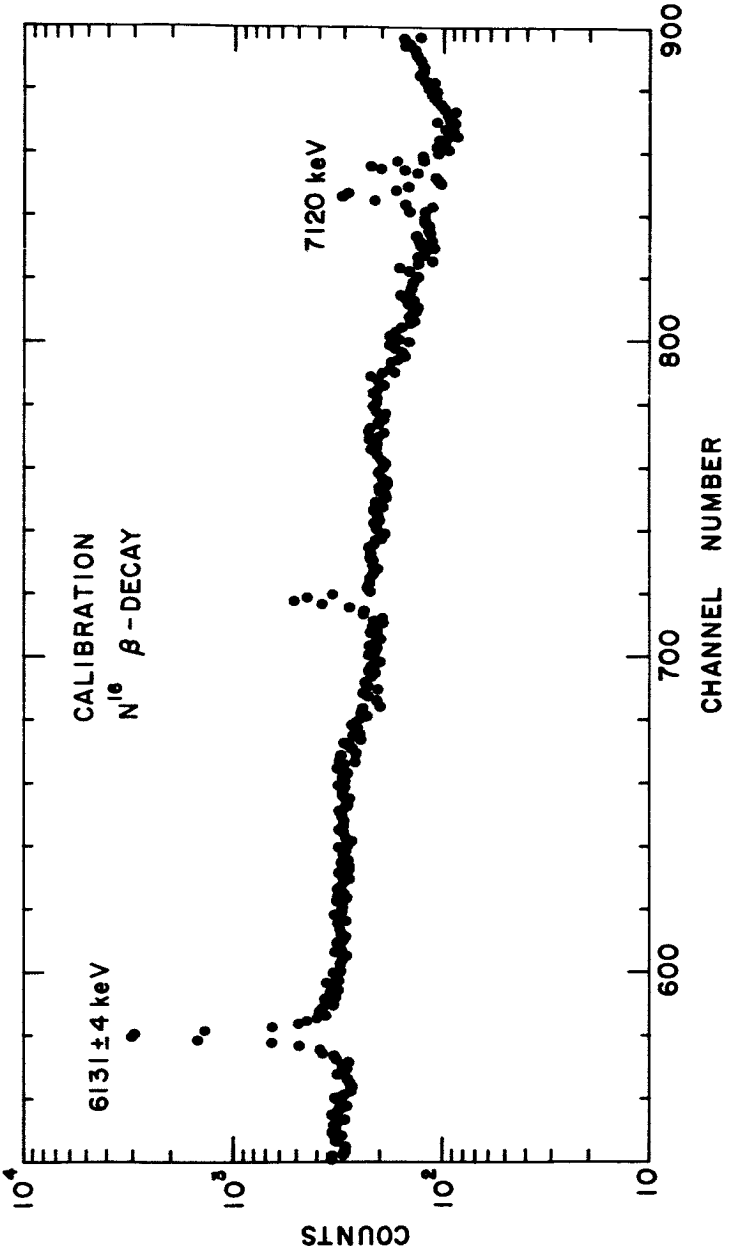


Figure 11 - Calibration spectrum



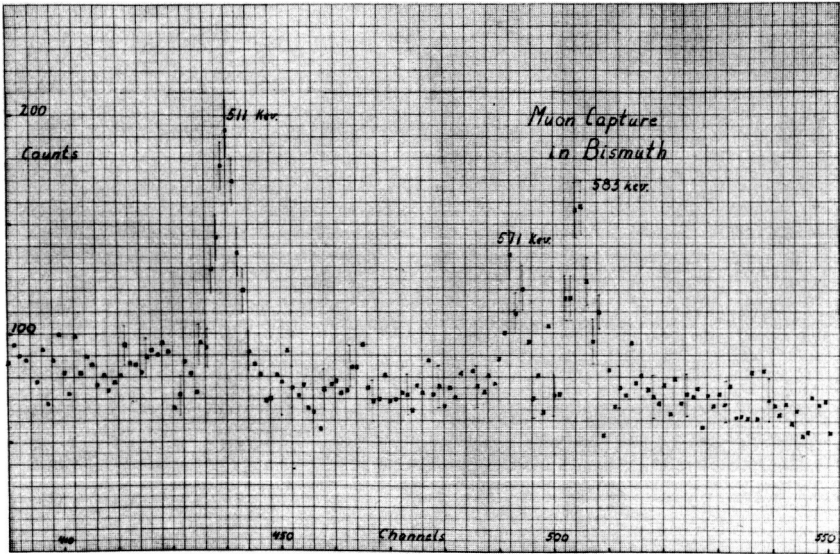


Figure 12 - Muon Capture in Bismuth Spectrum

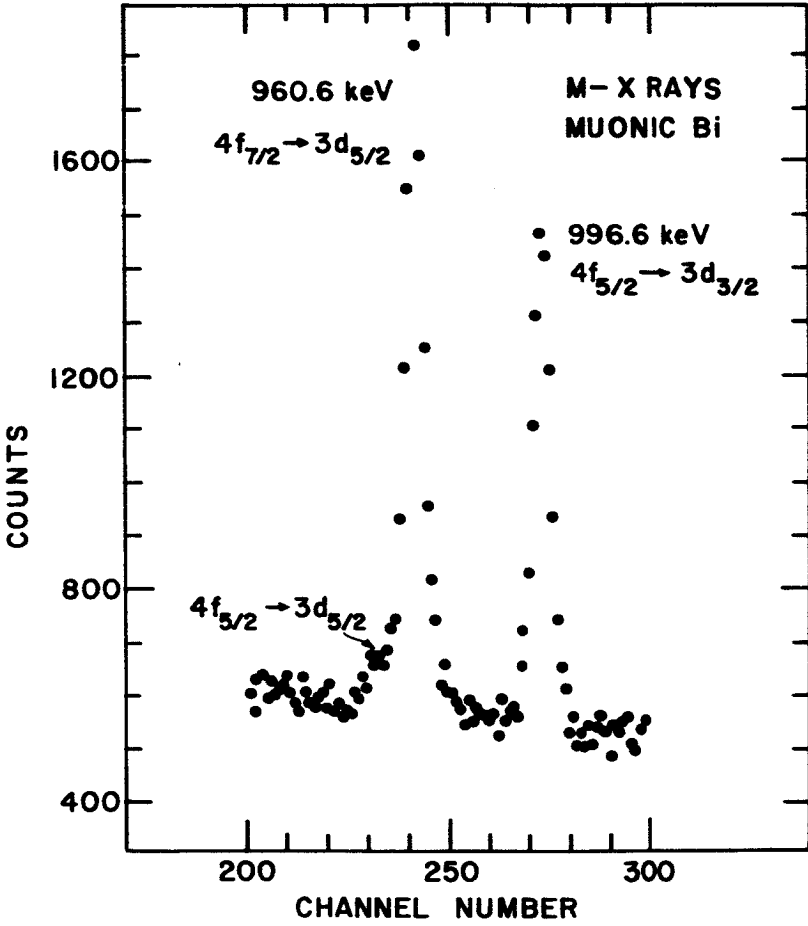


Figure 13 - Example of the M lines in bismuth

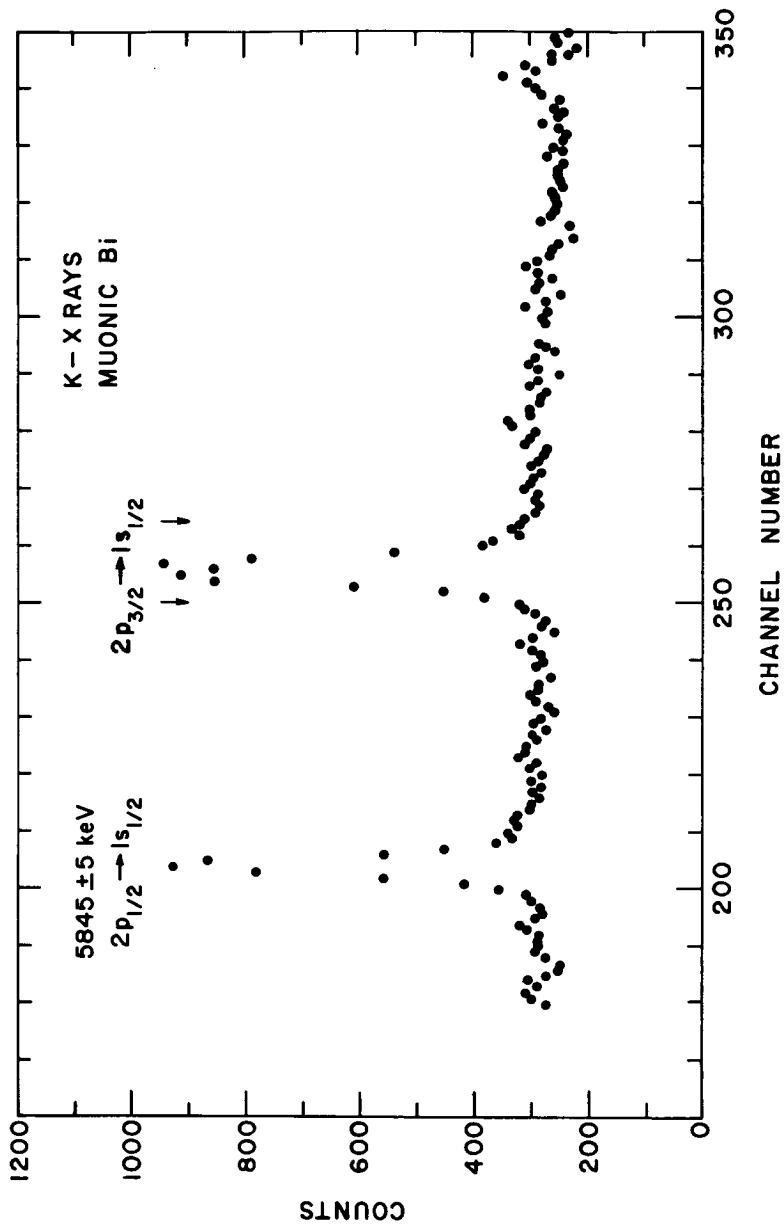
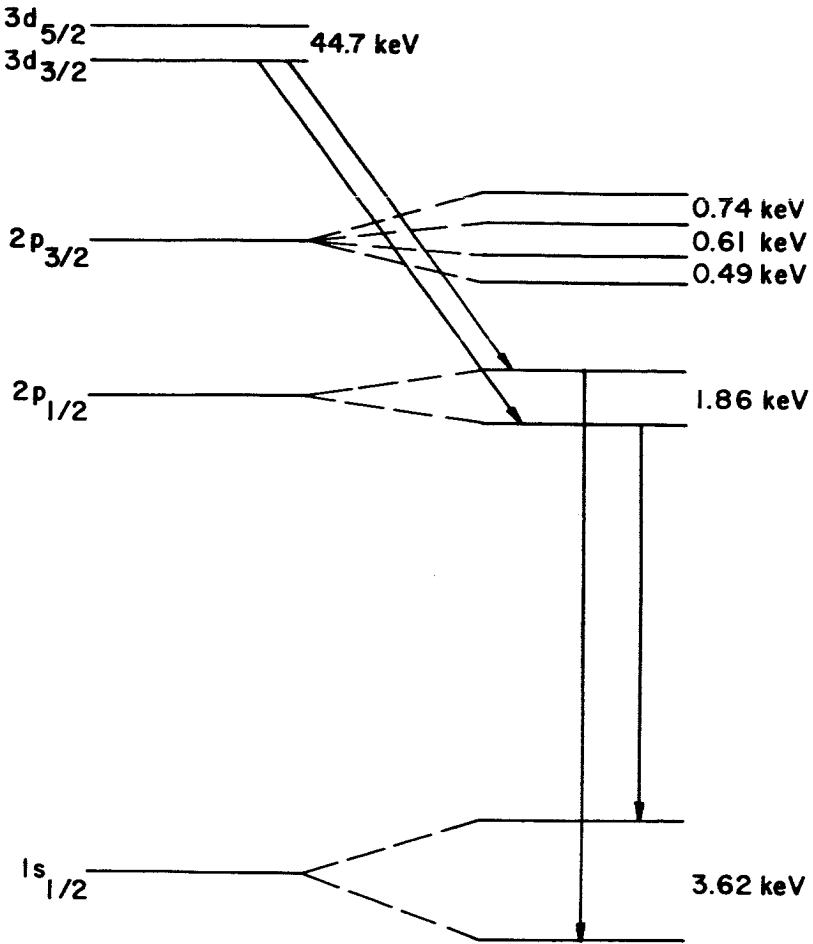


Figure 14 - K X-rays in bismuth



MAGNETIC HYPERFINE SPLITTING  
FROM Le Bellac  
 $\text{Bi}^{209}$

Figure 15 - Theoretical magnetic hyperfine splitting in  $\text{Bi}^{209}$

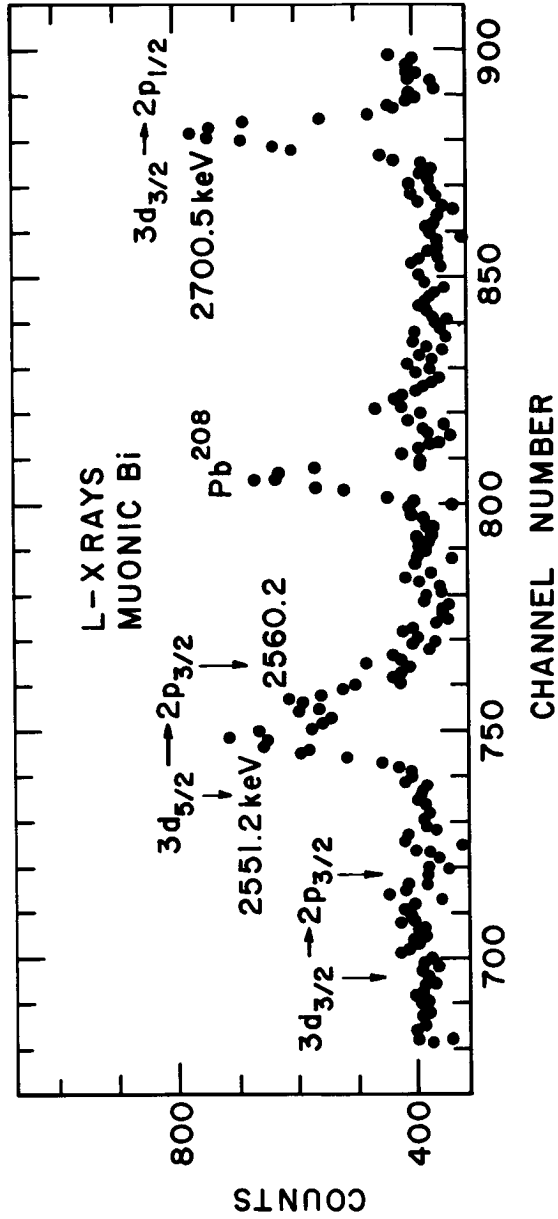


Figure 16 - L X-rays in bismuth

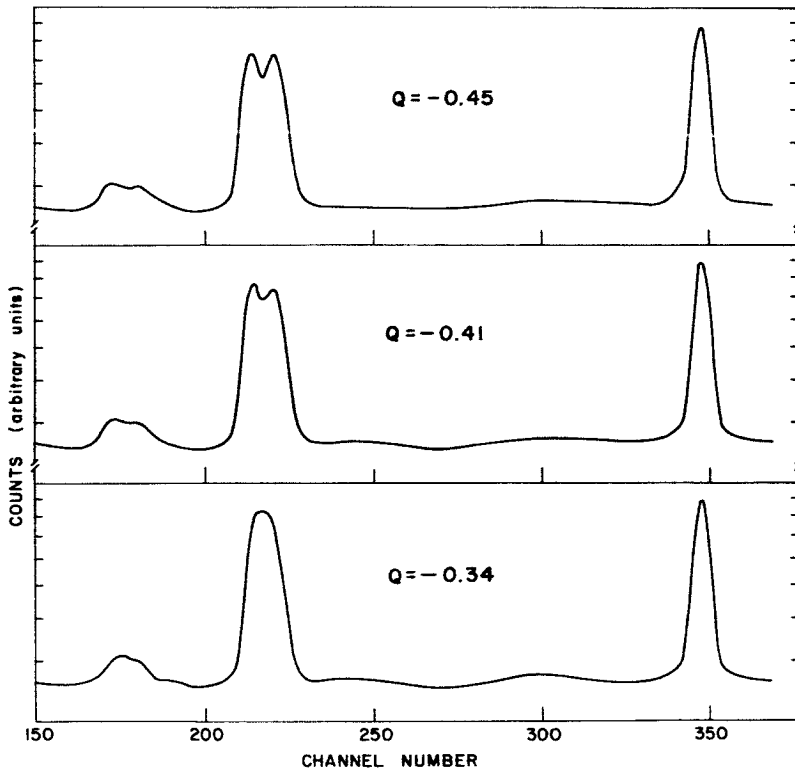


Figure 17 - Spectra for various values of  $Q_0$

: N6E 32731

MEASUREMENTS OF THE M1 AND E2 MUONIC h.f.s.  
OF Bi<sup>209</sup>, AND OF THE MUONIC ISOTOPE SHIFTS FOR  
Pb<sup>206</sup>, Pb<sup>207</sup> and Pb<sup>208</sup>

V. L. Telegdi

University of Chicago and Harvard University

I will talk about an experiment, or rather two muonic x-ray experiments, which we (R.D. Ehrlich, D. Fryberger, D. A. Jensen, C. Nissim-Sabat, R. J. Powers, B. A. Sherwood and myself) have carried out at Chicago. There considerable overlap between this material and that presented by previous speakers.

The two topics that I wish to discuss now are: (1) the muonic hyperfine structure in bismuth (this was also covered by the preceding contributed paper as well as by Professor Devons) and (2) the muonic isotope shifts in the lead isotopes 206, 207, and 208.

In both these investigations, for reasons which will become quite apparent and which I will try to be specific about, we used a technique which was originated by Devons, Cohen, Kanaris, and Nissim-Sabat at Columbia. This technique was originated in a study of muonic isotope shifts, turned out to be particularly useful in studying the hyperfine structure of muonic bismuth, where the emphasis is on the (very small) dipole splitting. The technique consists in having a variety of targets, in our particular case up to four, bombarded by a single muon beam and, by the arrangement of suitable counter, tagging the stopping muons according to the target which they hit. The rate is low enough that one can do this and view, with a single x-ray detector, an

PRECEDING PAGE BLANK NOT FILMED.

ensemble of targets which yield either muonic x-rays of very similar energies (as in the measurement of isotope shifts) or use muonic x-rays from one of the targets as a line shape calibration for the others (as in the case of the magnetic hfs in Bi, where the splitting is of the order of the line width). Let me briefly mention one more technical point, one which has been made easy to explain by the talk of the preceding speaker: when you stop a muon in matter, especially in a heavy element like bismuth, you get both muonic x-rays which are prompt and capture gamma rays which are delayed. While these captured gamma rays are on the one-hand a nuisance, they can on the other hand be used as an energy and line shape calibration. Generally one takes the muonic x-rays with as short delay as possible with respect to the muon stop signal so as to not include the capture as a background gamma ray; one then has to make separate delayed runs in order to record the captured gamma rays. In our experiments, not only did we look at several targets at once (for instance, in the case of Bi, we combined a bismuth target with a  $\text{Pb}^{206}$  target), but we measured for every photon event simultaneously by the pulse height and the time. So we obtained two dimensional spectra; the information derived electronically was stored on magnetic tape which can then be analyzed either for a fixed time interval, or a fixed energy interval sequentially. This proved to be very convenient.

Let me now turn to the case of the hfs of bismuth. As Professor Devons pointed out, the magnetic dipole (M1) hfs effects are generally much smaller in a mesic atom than are the electric



## Muonic X-rays

quadrupole effects, a situation which is inverted with respect to the atomic case. As Professor Devons said, the M1 splittings that one has here, are of the order of a few kilovolts. It is clear that if you wish to determine splittings of this sort, you have to have the highest resolution. Now, the very best Ge(Li) crystals used in this field, such as in particular the one used in the Columbia work, have 8 kilovolts resolution (FWHM). The Ge(Li) detector used in our experiments does not exhibit this exceptional resolution, but gives only 12 kilovolts. There is, however, a second problem, namely that one has to know the precise shape of the line shape for the analysis of the Bi spectrum, we are not using the famous  $O^{16*}$  line, which all the speakers have talked about, but rather another muonic x-ray, the  $Pb^{206} K_{\alpha}$  line. Our  $Pb^{206}$  sample is practically monoisotopic, 88% ( I should thank here Professor Siegel for the loan of a radio-lead target.) We thus determine, under identical conditions, the line shape of a muonic x-ray that is not perturbed by any kind of hyperfine effect, and the corresponding transition in the element for which we wish to establish the broadening due to M1 hfs. Let me say just a few words about the physics of the M1 hyperfine structure. The splitting, i.e. the interaction energy  $E(M1)$  if you wish, is proportional to  $\psi^2(0)$  in the case of a point-like moment. This is the famous contact interaction in an s-state. Now if you want to work out the interaction energy for a finite nucleus, you have to average this over the entire nuclear magnetization. This yields

$$E(M1) \sim \langle \psi^2(\vec{r}_{\mu}) \delta(r_{\mu} - \vec{R}) \rangle_{\text{mag}}$$

where  $\vec{R}$  is a nuclear coordinate and  $r_\mu$  is the muon coordinate. Now this averaging leads to a reduction, because the magnetization  $\vec{M}(\vec{R})$  is extended. So (1) leads to a reduction due to the finite extension. This reduction may to first order be computed by assuming that the nuclear magnetization  $\vec{M}(\vec{R})$ , is distributed like the nuclear charge  $\rho(\vec{R})$ . This assumption is obviously a patent falsehood since the charge distribution  $\rho(\vec{R})$  is due to all the nucleons, whereas the magnetisation is due just to a few. Sometimes, a reduction so computed is called the Bohr-Weisskopf effect. What I would propose to call the true Bohr-Weisskopf effect, is however a more subtle effect, namely the dependence of the hyperfine interaction on the specific details of the nuclear magnetization, viz. orbital vs. spin magnetization. Unfortunately, both in our experiment and to my knowledge, in every other muonic x-ray experiment, one can detect the reduction of the M1 hyperfine interaction from a "point" value (which it would of course be idiotic to assume) to the "extended" value which is reasonable; but we cannot detect reliably, and I don't think anyone else can either, the difference between the predicted values based on the simplified assumption ( $M \sim \rho$ ) and on more realistic assumptions based on specific nuclear models. So this point may perhaps be the subject for some future investigation if further technical break-throughs should occur. And let me say that Bi, having a large Z, a large magnetic moment and a small quadrupole moment is the most favorable nucleus for these investigations. In fact, it is interesting and amusing to note that the atomic (M1) hyperfine structure was also first

studied in a quantitative way in a pioneering paper, I think by Goudsmit and Back, in the bismuth spectrum, probably for the same reasons.

The first figure is at best of some entertainment value. You see the chicken feeder ( $N_2$  reservoir), as it is called at Columbia. Below it the crystal is positioned in the muon channel beam of the Chicago cyclotron. The thing specific to our setup is that the entire linear system, save the preamplifier, is thermostated; this we found to be very useful. The four-target arrangement mentioned earlier is barely visible - note the two tagging counters on either side.

In Figure 2 you see the muonic K spectra simultaneously recorded from  $Bi^{209}$  and  $Pb^{206}$  targets. Lead 206 is spinless, and serves as the reference line. We are not particularly interested in the absolute energies, but we happen to agree with those measured by other people. The line widths of the two  $Pb^{206}$  K-lines, both unaffected by magnetic or other hyperfine effects, should be the same; they are so to within 0.5 kilovolt. Now, a  $K\alpha_2$  transition, takes place between two levels of  $j < 3/2$ , and should hence exhibit a purely M1 (as opposed to E2!) hfs. Therefore, the lower Bi K-line should be broader than the two  $Pb^{206}$  K-lines that are equal, and the upper Bi K-line, which connects the  $p_{3/2}$  state to the  $s_{1/2}$  state should be broader than either of them because it is affected electric quadrupole (E2) and magnetic dipole (M1) effects. The spectra are indeed as predicted, using essentially hfs interaction constants as computed by LeBellac.

The E2 constant scales however with the "known" quadrupole moment of Bi, and I warn you that atomic quadrupole moments are uncertain to at least 15% because of various uncertain corrections. The punch line of Fig. 2 is that we use the  $\text{Pb}^{206}$  lines as a calibration for our instrumental line shape under real running conditions. The Bi and Pb prompt spectra are taken simultaneously. Included in Fig. 2 is the predicted line shape (14.5 keV width) for a nucleus with extended magnetization, and the predicted line shape for a point nuclear magnetic dipole (18.9 keV width). We can clearly rule out the point magnetic dipole, as the finite dipole gives a much better chi-square fit; but we cannot make any safe statements about refined nuclear models.

Further corroboration of the same effects is obtained by looking at the L x-rays (Fig. 3) roughly in the manner covered by the preceding contributed paper. Here you see two things. Between the two L-peaks, in the long region where nothing is supposed to occur, and you see in the prompt spectrum a delayed gamma-ray (2.615 keV), which is the one everybody has been mentioning. Now if we extract from our two-dimensional spectra events falling in this energy region at late times, we see very beautifully that this is indeed a capture gamma-ray. So, whereas in the Bi K-spectrum we use a simultaneous  $\text{Pb}^{206}$  spectrum for line shape calibration, we use in the L-spectrum this capture gamma ray, delayed, for the same purpose. The summary of our Bi data is that we do have good, quite solid evidence for the finite magnetization; but who could have doubted that? Also our data indicate a preference for 0.45 barns, for the quadrupole moment of  $\text{Bi}^{209}$  (this is a rather high value).

I shall now turn to the muonic isotope shifts in lead. Fig. 4 shows a superposition of the muonic  $K\alpha_1$  lines from the lead isotopes 206, 207, 208. Our targets (thanks to the AEC) were all of 90% or higher purity, and these lines are the actual data taken simultaneously, following the technique introduced by Devons et al. Fig. 4 shows only the statistically most important  $K\alpha_1$  line, but we have corresponding data on the  $K\alpha_2$  line, and for the L x-rays as well. In this Figure see very clearly the shifts from one isotope to the next, and by determining the centroids of the lines one can determine them quite accurately. I shall summarize our results in the form of a Table.

The payoff in this business comes in comparing these results to the corresponding ones obtained in optical spectroscopy. In the latter field, the shifts are usually expressed as a ratio of two constants,  $C_{\text{obs}}/C_{\text{th}}$ . The theoretical value,  $C_{\text{th}}$ , is computed assuming the  $A^{1/3}$  law, and is plagued by uncertainties (a) in the extrapolation to the series limit, (b) in the normalization of the electronic wave functions. The comparison with muonic data can hence serve to (a) check the extrapolation procedure, (b) determine the absolute normalization of the wave functions. It is interesting to note that our shifts depart from theory (which here is presumably reliable) in good agreement with the atomic data. In particular, for the (206-207)/(206-208) ratio, where the normalization drops out in the atomic case, we have excellent agreement with the optical data. The old time spectroscopists seem to do a good job. In particular the fudge factor  $\beta$ , which is put equal to unity in determining the individual atomic shift within a given isotope pair in desiring  $C_{\text{obs}}/C_{\text{th}}$ , seems to have been guessed right.

TABLE I

Muonic  $K\alpha_1$  Isotope Shift (keV)

|         | Observed       | Theory** |
|---------|----------------|----------|
| 206-207 | $3.74 \pm .32$ | 7.0      |
| 206-208 | $9.41 \pm .30$ | 14.0     |

## Muonic Isotope Shift Ratios

| Muonic  | Atomic*  |
|---|--|
| $\frac{(206-207)_{\text{obs}}}{(206-207)_{\text{th}}} = 0.53 \pm 0.04$    | $\beta \frac{C_{\text{obs}}}{C_{\text{th}}} = 0.46 \pm 0.07$           |
| $\frac{(206-208)_{\text{obs}}}{(206-208)_{\text{th}}} = 0.67 \pm 0.02$    | $\beta \frac{C_{\text{exp}}}{C_{\text{th}}} = 0.60 \pm 0.07$           |
| $\frac{(206-207)_{\text{obs}}}{(206-208)_{\text{obs}}} = 0.397 \pm 0.036$ | $\frac{(206-207)_{\text{obs}}}{(206-208)_{\text{obs}}} = 0.38 \pm .01$ |

\*\* Assumed Fermi charge distribution with half density radius  $c = 1.11 \times A^{1/3}$  fm. and skin thickness  $t = 2.4$  fm.

\* From a review by Brix and Kopfermann, Rev. Mod. Phys. 30, 517 (1958) based on optical measurements by Steudel, Z. Physik 132, 429 (1952).

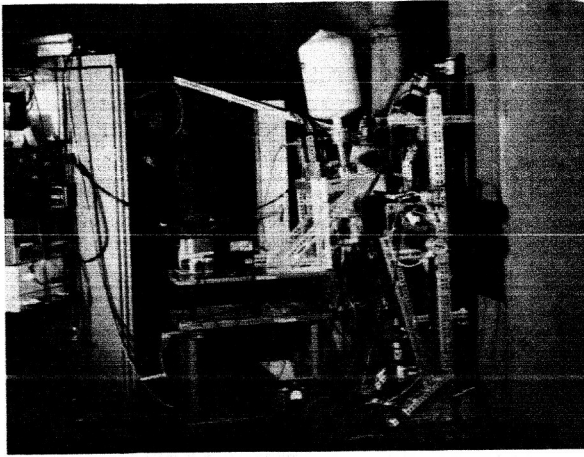


Figure 1. Chicken feeder.

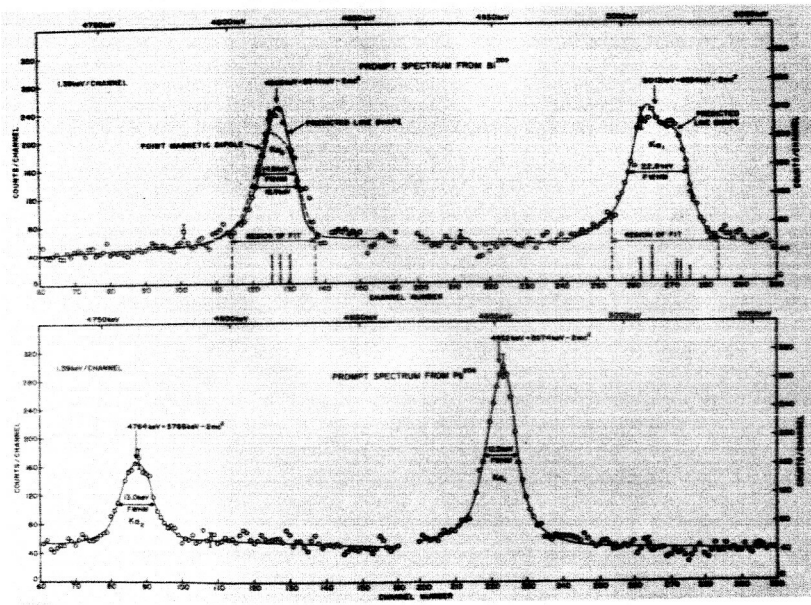


Figure 2. K spectra of bismuth and lead.

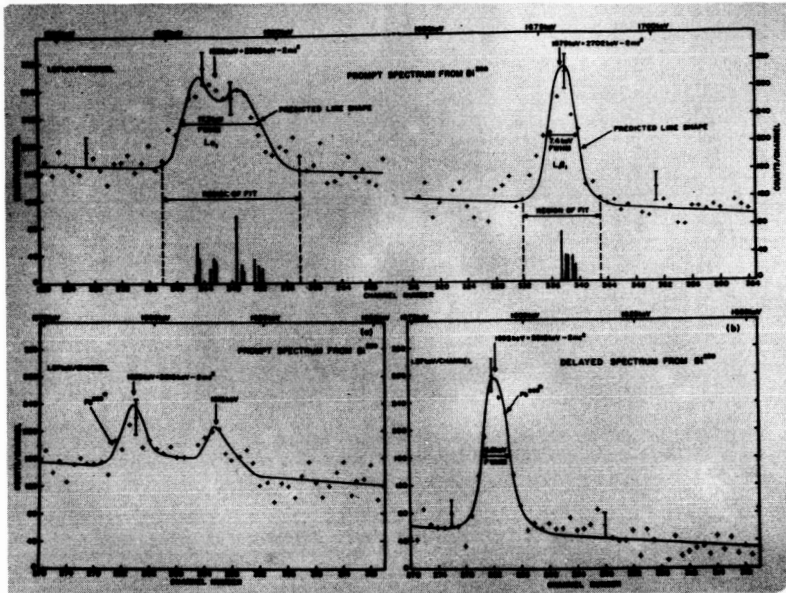
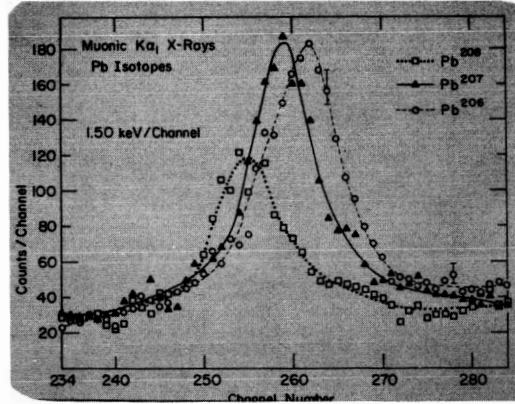


Figure 3. L x-rays

Figure 4. Muonic  $K\alpha_1$  x-rays of the lead isotopes.



THE ANOMALOUS INTENSITY RATIOS IN MUONIC LEAD AND BISMUTH

Jorg Hüfner

University of Heidelberg, Germany

1466 87  
32732

The energies of the muonic X-rays are quite well understood in terms of parameters of the nuclear charge distribution. But there are some problems concerning the intensities of the muonic X-rays. In Pb and Bi, e.g., the intensity ratio  $\frac{I(2p_{3/2} + 1s_{1/2})}{I(2p_{1/2} + 1s_{1/2})}$  is expected to be 1.9 (using statistical arguments). But the most recent experiments yield about 1.5. Within the experimental error this value is the same for different Pb isotopes and for Bi(e.g.<sup>1</sup>).

The calculation, which is reported here was intended to explain this phenomenon. It started from the following idea: The free muon is slowed down in the target and finally captured into some bound state of the muonic atom. It then cascades from level to level, emitting  $\gamma$ -radiation and Auger electrons. The  $\gamma$ -transitions (essentially E 1) depend strongly on the transition energy. How this energy dependence affects the intensity ratio (1), is illustrated with the help of Figure 1. The figure shows the lowest levels of muonic Pb. The 2s + 2p transition is a good example for the energy dependence. If the energy dependence of this E-2 transition is neglected two thirds of the intensity go to the 2 p<sub>3/2</sub> state and only one third to the 2p<sub>1/2</sub> state. But the intensities get nearly equal if the E<sup>3</sup> dependence of the transition is taken into account. The same effect was expected to happen several times during the cascade of the muon and to add up. The resulting intensity ratio (1) would then be smaller than 1.9. The Auger <sup>2)</sup> and radiative transitions (only those with  $|\Delta l| = 1$ ) were calculated with nonrelativistic wave functions (but the correct relativistic energies were used). The intensity ratio (1) was evaluated for each state with quantum numbers

$n$  and  $l$  ( $n \leq 14$ ,  $l \leq n-1$ ) into which the free muon could be captured. (The two states of each fine structure doublet were assumed to be fed proportional to  $(2j + 1)$ ).

A typical result is shown in Figure 2. The full line shows the intensity ratio (1) as a function of  $l$ , the orbital momentum of the captured muon (for  $n = 10$  and  $Z = 82$ ). The ratio (1) takes the experimentally observed value of 1.5 only if the muon is initially captured into states with  $l = 0$  or  $l = 1$ . Our calculation also shows, that if the muon is captured into  $l = 0$  or  $l = 1$  one should observe a strong  $2s \rightarrow 2p$  transition and a weak  $3d \rightarrow 2p$  transition (Figure 3). This is not confirmed by experiment, but the reverse holds true, as the  $2s \rightarrow 2p$  transition has not yet been found.

It is not yet known, whether the 2 s-state is deexcited to the 2 p-state via E 1 radiation or to the 1 s-state via electron pair creation. In the latter case, one does not observe the  $2s \rightarrow 2p$  transition, but the intensity ratio (1) never takes values as low as 1.5 (broken line in Figure 2).

---

#### References:

- 1) G. Backenstoss, C. Daum, J. C. Seus, S. A. deWit, to be published in Nucl. Phys.
- 2) A. H. deBorde, Proc. Phys. Soc., London, 67, 57 (1954).

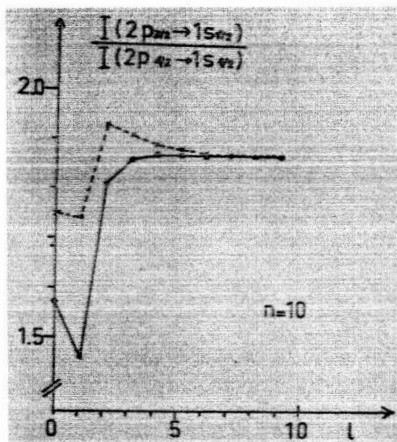
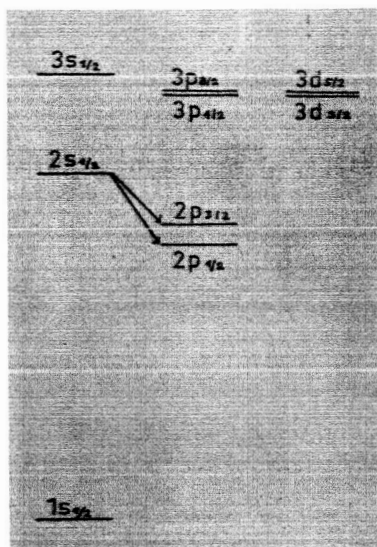


Figure 2 - The intensity ratio  $\frac{I(2p_{3/2} + 1s_{1/2})}{I(2p_{1/2} + 1s_{1/2})}$  as a function of the angular momentum  $l$  of the captured muon.

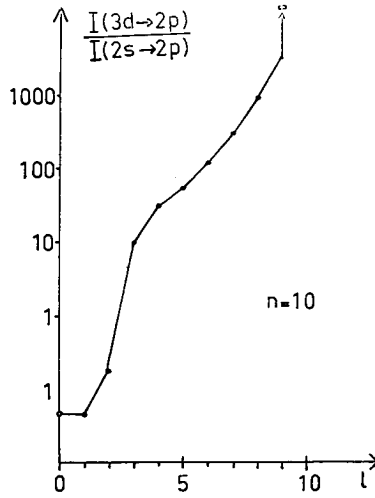


Figure 3 - The intensity ratio  $\frac{I(3d \rightarrow 2p)}{I(2s \rightarrow 2p)}$  as a function of the angular momentum  $l$  of the captured muon.

H. L. Acker

University of Virginia, Charlottesville, Virginia<sup>††</sup>

N66-91  
32733

The elastic scattering of high energy electrons and the X-ray spectra of muonic atoms have yielded much information about the charge distribution in spherical nuclei. For deformed nuclei, however, very little is known about their charge distribution. Here precise electron scattering experiments are not yet available. The quadrupole hyperfine structure of muonic X-ray spectra seems to give at present the only experimental information. The aim of our investigations is to show what details of the charge distribution of deformed nuclei may be expected from muonic hfs.

The hfs in muonic atoms has first been treated by Willets<sup>1)</sup> and by Jacobsohn<sup>2)</sup>. They have already pointed out that due to the proximity of the muon to the nucleus, finite nuclear size effects are very important. Thus the usual approximation for the quadrupole interaction

$$H_Q = \frac{1}{2} e^2 Q P_2(\cos \vartheta) \frac{1}{r^3}$$

is no longer appropriate, but  $r^{-3}$  has to be replaced by

$$f(r) = \frac{Z}{eQ} \left\{ r^2 \int_r^\infty \rho(\vec{r}') P_2(\cos \vartheta') \frac{d\vec{r}'}{r'^3} + \frac{1}{r^3} \int_0^r \rho(\vec{r}') P_2(\cos \vartheta') r'^2 d\vec{r}' \right\}$$

For long distances,  $f(r) \rightarrow r^{-3}$ , but close to the nucleus, its form depends on the charge distribution  $\rho(\vec{r}')$  of the deformed nucleus. It is this dependence which gives us the information about the charge distribution. The hyperfine structure of the spectra is determined by

the matrix elements of  $H_Q$  with the muonic and nuclear wave functions.

These matrix elements have the structure

$$\langle \dots | H_Q | \dots \rangle = Q \langle \varphi_{\ell, n}(r) | f(r) | \varphi_{\ell', n'}(r) \rangle \times \\ \times (\text{angular momentum factors})$$

It is the product of the quadrupole moment with the matrix element of  $f(r)$  which determines the hfs shift and hfs splitting, and it is this product which is deduced from experiment. It has already been shown<sup>3,4)</sup> that quadrupole effects are important only in the 2p and 3d states of the muon. The spectra are determined by 2 parameters--the radial matrix elements of  $f(r)$  with the muonic 2p and the 3d wave functions.

What is now the accuracy in determining these parameters by experiment? Fig. 1 shows the 4f-3d and the 2p-1s spectra for  $U^{238}$ . The 4f-3d spectrum depends only on the 3d matrix elements. Here, an accuracy of 1keV in measuring the energy difference A-B or A-C leads to an uncertainty of 5% in the 3d matrix elements. From the 2p-1s spectrum we may determine the 2p matrix element up to 1/2%, measuring the energy difference D-E with 1keV accuracy.

It is, however, always the product of the quadrupole moment with the matrix elements, which is determined with this accuracy. The accuracy of the matrix elements themselves is limited by the uncertainty of  $Q$ , which is often not known very accurately. The ratio of the 2p to the 3d matrix elements, however, is not affected by uncertainties of  $Q$ , and an experimental determination of this ratio up to a few percent seems possible.

Having studied the muonic quadrupole splitting and having deduced the relevant parameters, we have now to consider what different nuclear

models predict for these parameters, the radial matrix elements of  $f(r)$ . In treating spherical nuclei, the Fermi distribution

$$\rho(r) \propto \left(1 + \exp 4.4 \frac{r-c}{t}\right)^{-1}$$

has been quite successful. We generalize this distribution, giving the radial parameter  $c$  and the surface thickness  $t$  an angular dependence:

$$\rho(\vec{r}) \propto \left(1 + \exp 4.4 \frac{r-c(1+\beta Y_{20})}{t(1+\beta Y_{20})}\right)^{-1}$$

The deformation parameter  $\beta$  determines the quadrupole moment, whereas the shape parameter  $\gamma$  specifies the distribution of the quadrupole producing charge. Fig. 2 shows the lines of equal charge density for different values of  $\gamma$ , all for the nucleus  $U^{238}$  with  $Q = 11$  barn. These different charge distributions lead to different radial functions  $f(r)$ , as shown in fig. 3. The functions  $f(r)$  differ, however, only inside the nucleus. Comparing with the probability density of the muon in the  $2p_{3/2}$  and  $3d_{3/2}$  states, also shown in fig. 3, we expect a distinct sensitivity of the  $2p$  matrix elements on variations of  $\gamma$ . This is shown in fig. 4, we see, too, that the  $3d$  matrix elements depend much less on  $\gamma$ . Thus, the ratio of the  $2p$  to the  $3d$  matrix elements is quite sensitive to  $\gamma$ , an accuracy of 1% in this ratio yields an uncertainty of  $\pm 0.5$  in  $\gamma$ . The comparison with experimental data for  $U^{238}$  leads to a value  $\gamma \approx 0.5^\circ$ , i.e. a charge distribution where the surface thickness does not vary with angle.

Besides this generalized Fermi distribution we have also studied a multipole expansion

$$\rho(\vec{r}) = \rho_0(r) + Y_{20}(\vartheta) \rho_2(r)$$

choosing a Fermi distribution for the monopole part  $\varphi_0(r)$  and a Gaussian for the quadrupole distribution  $\varphi_2(r)$ . Whereas the generalized Fermi distribution had only one additional parameter besides the quadrupole moment - the shape parameter  $\gamma$  - this Gaussian is determined by 2 additional parameters - the position of its maximum,  $c_2$ , and its width,  $t_2$ . The calculations have shown<sup>6)</sup>, that it is, however, not possible to determine these two parameters by the 2 radial matrix elements: In a  $c_2$ - $t_2$ -plot the curves for fixed values of the matrix elements give no clear point of intersection (fig. 5).

Summarizing our calculations we may say that muonic hfs is indeed a sensitive tool for investigating the charge distribution of deformed nuclei. Besides the quadrupole moment, at least one additional parameter may be determined, specifying the distribution of the quadrupole producing charge.

+ Work supported in part by the U.S. Atomic Energy Commission

++ On leave from the University of Freiburg, Freiburg, Germany

- 1) L. Wilets, Mat. Fys. Medd. Dan.Vid. Selsk. 29, No 1 (1956)
- 2) B. A. Jacobsohn, Physical Review 96 (1954) 1637
- 3) R. D. Ehrlich, R. J. Powers, V. L. Telegdi, J. A. Bjorkland, S. Raboy and C. C. Trail, Physical Review Letters 13 (1964) 550
- 4) H. L. Acker, H. Marschall, G. Backenstoss and D. Quitmann, Nuclear Physics 62 (1965) 477
- 5) H. L. Acker and H. Marschall, Physics Letters 19 (1965) 127
- 6) H. L. Acker, "The Study of the Charge Distribution in Deformed Nuclei by Muonic Hyperfine Structure", preprint University of Virginia (to be published in Nuclear Physics)



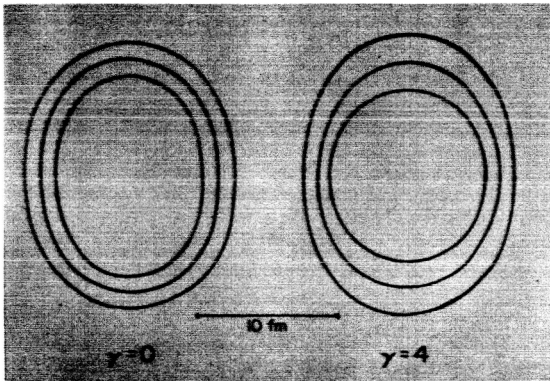
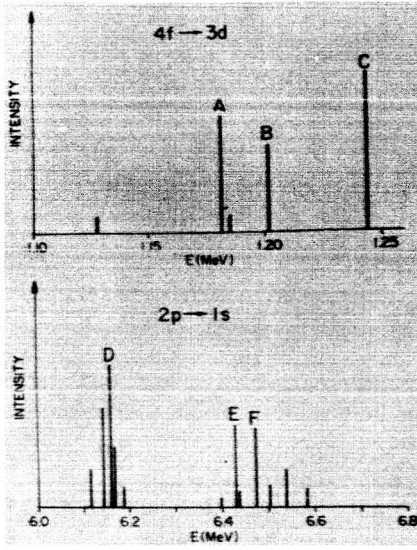


Figure 2 - Lines of constant charge density ( $\rho=0.9\rho(Q)$ ,  $0.5\rho(Q)$ ,  $0.1\rho(Q)$ ) for  $U^{238}$ ,  $Q=11$  barns.

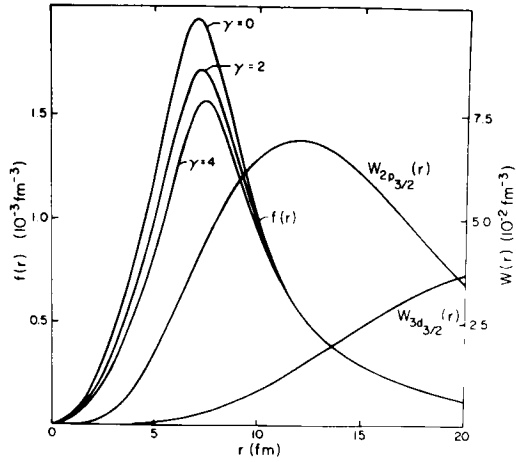


Figure 3 - Radial functions  $f(r)$  of the quadrupole interaction for  $\gamma = 0, 2, 4$  and probability density  $W(r)$  of the muon in the  $2p_{3/2}$  and  $3d_{3/2}$  state ( $U^{238}$ ,  $Q=11$  barns)

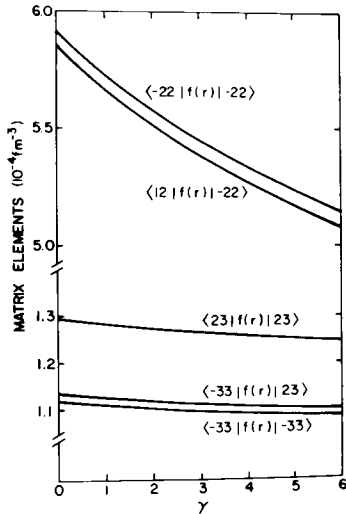


Figure 4 - Dependence of the 2p and 3d matrix elements  $\langle H n | f(r) | H^1 n^1 \rangle$  on the shape parameter  $\gamma$  for  $U^{238}$ ,  $Q=11$  barns.

## Spectra in Deformed Nuclei

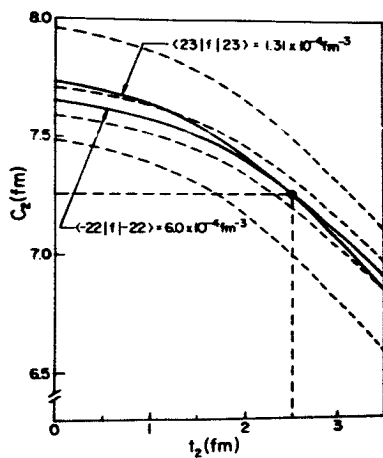


Figure 5 -  $C_2$ - $t_2$  diagram for the radial matrix elements. The curves correspond to values of  $6.0 \times 10^{-4} \text{ fm}^{-3} \pm 1\%$  for the  $2p$  matrix element  $\langle -22|f(r)|-22 \rangle$ , respectively  $1.31 \times 10^{-4} \text{ fm}^{-3} \pm 1\%$  for the  $3d$  matrix element  $\langle 23|f(r)|23 \rangle$

## MUONIC X-RAY STUDIES OF SPHERICAL NUCLEI

C. Daum, G. Backenstoss, J. C. Sens, and S. A. deWit

CERN, Geneva, Switzerland

and

H. L. Acker

Physikalisches Institut der Universität, Freiburg, Germany

In this joint paper, a few data on the experiment will be given. Then, the analysis of muonic X-ray spectra for spherical and deformed nuclei will be discussed.

## Experiment.

A flux of  $50000 \text{ sec}^{-1}$  negative muons of the 124 Mev/c is obtained from the muon channel at the stochastically operated 600 Mev CERN Synchrocyclotron. The particles are formed on a spot of  $10 \times 10 \text{ cm}^2$ . They are the backward-decaying muons of 220 Mev/c pions. The pion contamination is less than 0.5% of the muons, the electron contamination is still smaller. The targets have an area of  $7 - 50 \text{ cm}^2$  and a thickness of  $2-13 \text{ g/cm}^2$ ; 6000 - 32000 muons are stopped per second. The Ge(Li) detector has an area of about  $3.5 \text{ cm}^2$  and a thickness of 6 mm. It has been made by Professor E. Baldinger and Mr. G. Matile at the University of Basle. The detector was placed a few mm behind the target in the beam line in order to have the maximum possible solid angle. The resolution ranges from 7 keV at 0.5 Mev to 18 keV at 6 Mev.

## Spherical nuclei.

Measurements have been made on Cl, Ca, Fe, on all nuclei between Sn and Nd, except Xenon, and on all nuclei between Au and Bi. All elements have the natural isotope composition. In addition, a sample of  $^{206}\text{Pb}$  has been used.

PRECEDING PAGE BLANK NOT FILMED.

Except for the three lightest nuclei,  $2p \rightarrow 1s$  and  $3d \rightarrow 2p$  spectra have been measured, as well as many spectra of higher transitions. Figure 1 shows some typical  $2p \rightarrow 1s$  and  $3d \rightarrow 2p$  spectra. The background has been subtracted. It is typically  $1/3$  of the peak height. Several capture gamma rays have also been observed, which yield incidentally better energy values for several nuclear levels than available up to now. Tables 1, 2, and 3 list the measured transition energies, table 4 and 5 the calibration lines, used in the experiment.

For the theoretical analysis, the Dirac equation is solved numerically for a Fermi-type charge distribution with radial parameter  $C$  and skin thickness parameter  $t$ . The precision on the energy is better than  $0.01$  kev. The most important correction is due to the vacuum polarization. It has been calculated with the expression of Ford and Wills in perturbation theory and added to the above obtained energies. The  $4f - 3d$  and higher transitions are in good agreement with the calculated energies, thus providing a check on the consistency of the finite size corrections, which are small for the  $3d$  and higher levels, and of the vacuum polarization correction. Other corrections are assumed to be negligibly small.

The data are presented in the form of  $c-t$  diagrams. A transition energy determines an iso-energetic line in this diagram. In general, four transitions are measured, two  $2p \rightarrow 1s$  and two  $3d \rightarrow 2p$  lines, yielding six energy differences, and, hence, six iso-energetic lines, or, when errors are also considered, six bands in the  $c-t$  diagram. Two parameters, i.e.  $e$  and  $t$ , have to be determined. Therefore, the problem is overdetermined. The common area of all bands determines the pairs of  $c$ ,  $t$  values consistent with the data. This overdetermination provides again a consistency check on the finite size correction and the vacuum polarization correction.

The sensitivity of the energy bands is quite different for medium  $Z$  and high  $Z$  nuclei, e. g. Sn and Bi. In Figure 2, this is demonstrated. The  $2p \rightarrow 1s$  bands, 6 kev wide in Su and 10 kev in Bi, are very narrow. The  $3d \rightarrow 2p$  bands are both 4 - 6 bev wide. In Bi a small common area is determined. In Su the  $3d \rightarrow 2p$  band is not effective. A five to ten times smaller error is needed for Su to obtain a similar result as in Bi. A c-t diagram can also be made for the energy levels. Starting from the calculated value for the 4f level, one obtains the absolute level energies. The result is also in Figure 2. It shows clearly, that the  $2p \rightarrow 1s$  band is completely dominated by the 1s level, the  $3d \rightarrow 2p$  band by the 2p level. In Bi the 3d band is already very wide, in Su the limits of the 3d band are completely off-scale.

The Figures 3, 4, 5 and 6 show the c-t diagrams of Ca, Sb, Au, Hg, Tl,  $^{206}\text{Pb}$ , Pb(nat) and Bi. The  $2p_{3/2} \rightarrow 1s_{1/2}$  bands are not shown, because the bands are indistinguishable from the  $2p_{1/2} \rightarrow 1s_{1/2}$  bands. The results of electron scattering data are also shown. In Ca and Sb both methods determine a common area, in Au, Pb and Bi they do not. We have estimated, that for the muonic X-rays the correction due to nuclear polarization is smaller than the experimental errors. No explanation for the discrepancy is known to us. Tables 6 and 7 show the c, t combinations for muonic X-ray data and electron scattering data.

Elton has made a systematic analysis of electron scattering data, assuming: 1) proton and nuclear distributions have the same shape, 2) the surface thickness is constant at  $t = 2.49$  fm, 3) the maximum nuclear density (at  $\gamma = 0$ ) is constant,  $\rho_n = 0.168 \text{ fm}^{-3}$ . These assumptions are consistent with the short range character and the saturation properties of nuclear forces.

We have made a similar, systematic analysis of our data. The surface

thickness has a common region for the heavy  $Z$  nuclei, i.e.  $t = 2.21 \begin{smallmatrix} +0.14 \\ -0.21 \end{smallmatrix}$  fm. Imposing this value upon all nuclei,  $\rho_n = 0.158 \text{ fm}^{-3}$ , and  $C_0 = CA^{-1/3}$  follows Elton's curve for these values of  $t$  and  $\rho_n$ , i.e.  $C_0 = (1.149 - 0.715 A^{-2/3}) \text{ fm}$ . Figure 7 shows the result and also the lines for the electron scattering data.

The muonic X-ray data agree surprisingly well with this simple model. The difference between the two sets of data may be due to our choice of  $t$  at the high  $Z$  nuclei, for which agreement with electron scattering is poor in the individual cases. A combined analysis of both sets of data is needed for a more definite conclusion. It is, moreover, interesting to remark that our data on the deformed nuclei show agreement with the systematics of  $c$  and  $t$  values of the spherical nuclei.

For nuclei with electric quadrupole moment and magnetic dipole moment one can expect to observe hyperfine structure effects, i. e. at least the peaks will show a broadening. We have observed such broadening for I, An and Bi. In Nd the isotope effect causes a broadening. Figure 8 shows the  $2p + 1s$  spectrum of Au. We measure a hyperfine splitting of  $(19.8 \pm 2) \text{ kev}$ , whereas the theoretical prediction is  $(17 \pm 2) \text{ kev}$ . The calculation is done with the wave functions of the finite size nucleus.

Nuclear polarization effects are essentially all electromagnetic couplings between muon and nucleus. The effect has been estimated by several authors. It has been decreasing from around 60 kev on the  $1s$  state in Pb to about 1 kev in successive estimates. We have made an estimate, that the electric monopole term yields a contribution of less than 3 kev on the  $1s$  state for all nuclei between Sn and Bi, the electric dipole term less than 0.4 kev, i.e. the effects are well within the experimental error. All higher order terms are negligible and all higher states than the  $1s$  state are less affected.

An interesting subject are the relative intensities of the  $E_1$  transitions between fine structure multiplets. Table 8 lists the results. We find that for all nuclei between Sn and Nd the intensities agree with a statistical population of the muonic levels, except in the  $2p \rightarrow 1s$  transitions of I and Nd. A resonance between the  $\Delta(2p)$  splitting and the energy difference between ground and first excited state of the nucleus may be responsible for the reduction of the  $2p \rightarrow 1s$  intensity ratio. A maximum resonance condition decreases the ratio in I to 1.32, instead of 1.95 for a statistical theory, whereas the observed ratio is  $1.06 \pm 0.08$ . In the heavy Z nuclei all  $3d \rightarrow 2p$  and  $2p \rightarrow 1s$  intensity ratios deviate from a statistical theory. Processes, competing with the  $E_1$  transitions, are e.g. other electromagnetic radiative transitions, non-radiative transitions like pair formation, photonuclear effect, nuclear excitation followed by particle emission, induced fission or nuclear Auger effect, and resonances with nuclear levels. We have estimated, that all these effects are negligible, except possibly  $E_1$  couplings with unknown nuclear levels at 6 to 8 Mev excitation.

#### Deformed nuclei.

Measurements have been made on fourteen elements between Sn and Pu. A preliminary result on the analysis of eight mono-isotope elements has been performed. Targets of  $^{233}\text{U}$ ,  $^{235}\text{U}$  and Pu were kindly made available by the UKAEA of Harwell, England.

Acker and Marschall have developed a method to compare the data with two models for the deformed charge distribution, the modified c-model and the hard core model. We have started for each model a search for the best fit to the data, taking  $c$ ,  $t$  and  $Q_0$ , the intrinsic quadrupole moment as free parameters. For each set of  $c$ ,  $t$  and  $Q_0$ , the monopole part and the quadrupole part of the charge distribution are computed numerically. The first yields parameters  $c^1$



and  $t^1$ , which are used as the parameters of a Fermi-type charge distribution for the calculation of the unperturbed energies, in the same way as for the spherical nuclei. The second yields the deformation  $B$ , corresponding with  $Q_0$ . The program also yields muonic wave functions, with which the muonic quadrupole matrix elements are computed. Then, the energy matrices are diagonalized and the perturbed level scheme is obtained.

The population of the  $4f$  levels or sub-levels is assumed to be statistical. Then, the whole cascade of  $E1$  transitions between the  $4f$  state and the lowest states is calculated. A list of transition energies and intensities is obtained. The line shape of calibration lines in the corresponding energy ranges is folded into the theoretical spectrum and a comparison with the experimental spectrum is made.

In all nuclei the three lowest levels of the rotational bands are taken into account and their final population is calculated. Only in Pu, it was necessary to use the five lowest levels of the rotational band. Figures 9 - 20 show the results for Tb, Ho, Ta, Th,  $^{233}\text{U}$ ,  $^{235}\text{U}$ ,  $^{238}\text{U}$  and Pu for both models. Final adjustments have to be made, but the general agreement for energies as well as intensities is remarkably good. At the present stage of the analysis, it is impossible to make a choice between the two models on the basis of the muonic X-ray data alone. For these preliminary fits, both models have very closely the same unperturbed energies and the same products of the radial matrix elements with the quadrupole moments.

However, several facts are in favour of the modified  $c$ -model. The general trend of  $c$  and  $t$  values in this model agrees better with the systematics, obtained for the spherical nuclei, than that for the hard core model. The quadrupole moments in the modified  $c$ -model are in closer agreement with other

## Studies of Spherical Nuclei

measurements than those in the hard core model.

No indication is present in the analysis of these spectra, that it is necessary to abandon the assumption, that the intrinsic quadrupole moment is constant within a rotational band, i.e. the Bohr-Mottelson model for the rotational structure of these nuclei holds extremely well.

The good fit of the line intensities between experimental and theoretical spectrum suggests strongly, that the durations of the relation intensities in the  $2p \rightarrow 1s$  and  $3d \rightarrow 2p$  spectra of spherical nuclei from a statistical theory is due to coupling with nuclear levels.

Table 1

Energies of muonic  $2p-1s$  transitions  
(all energies except for  $Z = 17, 20, 26$   
are obtained from the double escape peaks)

| Element           | Z  | $A^a)$ | Present data                    |                                 |                     |                                      | Previous data                               |   | Ref.   |  |
|-------------------|----|--------|---------------------------------|---------------------------------|---------------------|--------------------------------------|---|---|--|--|
|                   |    |        | $E(2p_{1/2} + 1s_{1/2})$<br>keV | $E(2p_{3/2} + 1s_{1/2})$<br>keV | $\Delta(2p)$<br>keV | Calibration<br>lines, see<br>Table 2 | $E(2p + 1s)$<br>centre of<br>gravity<br>keV | $E(2p + 1s)$<br>centre of<br>gravity<br>keV   |  |  |
| Cl                | 17 | 35.46  |                                 |                                 |                     |                                      | 578.6 ± 1.5                                 | 582.8 ± 1.3   | 12)  |  |
| Ca                | 20 | 40.08  |                                 |                                 |                     |                                      | 783.8 ± 1.5                                 | 782.8 ± 3.0<br>790.8 ± 1.6<br>780.7 ± 0.8   | 14)<br>14)<br>25)  |  |
| Fe                | 26 | 55.85  |                                 |                                 |                     |                                      | 1256.4 ± 2.4                                | 1255.5 ± 2.4<br>1255.4 ± 3.0<br>1261.4 ± 5.3<br>1254.5 ± 4.0  | 14)<br>14)<br>17)<br>25)   |  |
| Sn                | 50 | 118.84 | 3657.3 ± 3.0                    | 3612.8 ± 3.0                    | 44.5 ± 1.5          | 9,10                                 | 3641.6 ± 3.5                                | 3649 ± 15 d)  | 23)  |  |
| Sb                | 51 | 121.86 | 3563.3 ± 2.0                    | 3554.7 ± 2.0                    | 48.6 ± 1.5          | 9,10                                 | 3526.5 ± 3.0                                | 3646.4 ± 6.4<br>3544 ± 15   | 12)<br>23)   |  |
| Te                | 52 | 127.46 | 3625.6 ± 2.5                    | 3575.5 ± 2.5                    | 50.1 ± 1.5          | 9,10                                 | 3608.6 ± 4.0                                | 3622 ± 17   | 23)  |  |
| I                 | 53 | 127.00 | 3721.6 ± 2.5                    | 3667.6 ± 3.0                    | 54.0 ± 3.0          | 10,14                                | 3695.5 ± 4.0                                | 3712 ± 16   | 23)  |  |
| Ca                | 55 | 133.00 | 3899.1 ± 3.5                    | 3836.1 ± 3.0                    | 63.0 ± 3.5          | 10,11                                | 3875.7 ± 4.5                                | 3888 ± 15   | 23)  |  |
| Ba                | 56 | 137.38 | 3979.8 ± 4.0                    | 3915.4 ± 4.0                    | 64.4 ± 3.5          | 10,11                                | 3958.8 ± 7.0                                | 3981 ± 30   | 13)  |  |
| La                | 57 | 139.00 | 4071.2 ± 4.0                    | 4001.3 ± 4.0                    | 69.9 ± 2.0          | 10,11                                | 4047.7 ± 5.0                                | 4065 ± 15   | 23)  |  |
| Ce                | 58 | 140.22 | 4160.3 ± 5.0                    | 4087.3 ± 5.0                    | 73.0 ± 2.5          | 10,11                                | 4134.8 ± 6.0                                | 4164 ± 25   | 23)  |  |
| Pr                | 59 | 141.00 | 4258.8 ± 5.5                    | 4184.3 ± 5.0                    | 74.5 ± 2.5          | 10,11                                | 4232.6 ± 7.0                                | 4244 ± 35   | 23)  |  |
| Nd                | 60 | 144.33 | 4335.0 ± 6.0                    | 4257.2 ± 5.5                    | 77.8 ± 2.5          | 10,11                                | 4305.2 ± 6.5                                |   |  |  |
| Au                | 79 | 197.00 | 5762.5 ± 5.0                    | 5592.8 ± 5.0                    | 169.7 ± 2.0         | 14,15;10,14                          |   | $E(2p_{1/2} + 1s_{1/2})$<br>{ 5772 ± 9 <sup>b)</sup><br>5789<br>5930 ± 11 <sup>b)</sup>   | $\Delta(2p)$<br>170 ± 2<br>187.6 ± 4.3                                     | 30)<br>31)<br>10)                      |
| Hg                | 80 | 200.58 | 5817.2 ± 5.0                    | 5645.1 ± 10.0                   | 172.1 ± 2.5         | 10,14                                |   |   |  |  |
| Tl                | 81 | 204.41 | 5897.9 ± 5.0                    | 5716.6 ± 5.0                    | 181.3 ± 2.0         | 14,15;10,14                          |   |   |  |  |
| <sup>208</sup> Pb | 82 | 206.15 | 5972.3 ± 5.0                    | 5786.9 ± 5.0                    | 185.4 ± 2.0         | 10,14;11,14                          |   |   |  |  |
| Pb(nat)           | 82 | 207.21 | 5966.0 ± 5.0                    | 5780.1 ± 5.0                    | 185.9 ± 2.0         | 14,15;10,14                          |   | { 5990 ± 11 <sup>b)</sup><br>6002 ± 16 <sup>b)</sup><br>5972 ± 7 <sup>b)</sup><br>6053 ± 5 <sup>b)</sup><br>6062 ± 20 <sup>c)</sup><br>6041 ± 7 <sup>b)</sup> | 185.9 ± 6.0<br>186 ± 7<br>185 ± 2<br>189.7 ± 4.4<br>194.5 ± 7.2<br>194 ± 5 | 10)<br>23)<br>30)<br>14)<br>23)<br>30) |
| Bi                | 83 | 209.00 | 6032.2 ± 5.0                    | 5899.7 ± 5.5                    | 192.5 ± 3.0         | 10,14;11,14                          |   |   |  |  |

a) A is sum of abundance times number of nucleons for all isotopes of an element

b) 61% ± 6 keV taken for the <sup>14</sup>N calibration line.

c) 6135 ± 10 keV taken for the <sup>16</sup>N calibration line.

d) 44.25 ± 20 keV taken for the PoBe calibration line

e) 4132 ± 11 keV taken for the <sup>66</sup>Ge calibration line, see text.

Table 2

Energies of muonic  $3d-2p$  transitions (energies are obtained from photo peaks for  $Z = 50-60$  and from double escape peaks for  $Z = 79-83$ )

| Present data      |    |        |                                 |                                 |                                  |                                      | Previous data           |                           |      |
|-------------------|----|--------|---------------------------------|---------------------------------|----------------------------------|--------------------------------------|-------------------------|---------------------------|------|
| Element           | Z  | A      | $E(3d_{5/2} - 2p_{3/2})$<br>keV | $E(3d_{3/2} - 2p_{1/2})$<br>keV | $\Delta(2p) - \Delta(3d)$<br>keV | Calibration<br>lines, see<br>Table 2 | $E(3d-2p)$<br>keV       | $\Delta(2p) - \Delta(3d)$ | Ref. |
| Sn                | 50 | 118.04 | 982.5 ± 3.0                     | 1022.6 ± 3.0                    | 40.1 ± 1.5                       | 4,5                                  | ---                     | ---                       | -    |
| Sb                | 51 | 121.86 | 1019.6 ± 3.0                    | 1062.8 ± 3.0                    | 43.2 ± 1.5                       | 4,5                                  | ---                     | ---                       | -    |
| Te                | 52 | 127.66 | 1060.0 ± 3.0                    | 1104.3 ± 3.0                    | 44.3 ± 1.5                       | 3,9                                  | ---                     | ---                       | -    |
| I                 | 53 | 127.00 | 1098.0 ± 3.0                    | 1146.7 ± 3.5                    | 48.7 ± 3.0                       | 4,5                                  | ---                     | ---                       | -    |
| Ce                | 55 | 133.00 | 1188.6 ± 3.0                    | 1241.6 ± 3.0                    | 53.0 ± 2.0                       | 5,8                                  | ---                     | ---                       | -    |
| Ba                | 56 | 137.38 | 1229.2 ± 3.0                    | 1289.2 ± 3.5                    | 60.0 ± 3.5                       | 5,8                                  | 1247 ± 11 <sup>a)</sup> | ---                       | 13)  |
| La                | 57 | 139.00 | 1266.8 ± 3.0                    | 1328.4 ± 3.0                    | 61.6 ± 2.0                       | 5,8                                  | ---                     | ---                       | -    |
| Ce                | 58 | 140.22 | 1314.9 ± 3.0                    | 1376.7 ± 3.0                    | 61.8 ± 2.5                       | 8,9                                  | ---                     | ---                       | -    |
| Pr                | 59 | 141.00 | 1356.7 ± 3.0                    | 1422.6 ± 3.0                    | 65.9 ± 2.0                       | 8,9                                  | ---                     | ---                       | -    |
| Nd                | 60 | 144.33 | 1401.1 ± 3.0                    | 1469.8 ± 3.0                    | 68.7 ± 2.5                       | 8,9                                  | ---                     | ---                       | -    |
| Au                | 79 | 197.00 | 2343.1 ± 2.5                    | 2474.4 ± 2.0                    | 131.3 ± 3.0                      | 8,9                                  | 2342 ± 4 <sup>d)</sup>  | 136 ± 6                   | 30)  |
| Hg                | 80 | 200.58 | 2388.5 ± 4.5                    | 2523.6 ± 4.5                    | 135.1 ± 3.5                      | 8,9                                  | ---                     | ---                       | -    |
| Tl                | 81 | 204.41 | 2446.6 ± 2.0                    | 2589.0 ± 2.0                    | 138.4 ± 2.0                      | 8,9                                  | 2458 ± 5 <sup>b)</sup>  | 146 ± 5 <sup>b)</sup>     | 10)  |
| <sup>208</sup> Pb | 82 | 206.15 | 2500.6 ± 1.5                    | 2643.2 ± 3.0                    | 142.6 ± 2.5                      | 8,9                                  | ---                     | ---                       | -    |
| Pb                | 82 | 207.21 | 2499.7 ± 1.5                    | 2641.8 ± 1.5                    | 142.1 ± 1.5                      | 8,9                                  | 2498 ± 4 <sup>b)</sup>  | 147 ± 4 <sup>b)</sup>     | 10)  |
|                   |    |        |                                 |                                 |                                  |                                      | 2500 ± 4 <sup>d)</sup>  | 147 ± 6                   | 23)  |
|                   |    |        |                                 |                                 |                                  |                                      | 2502 ± 3 <sup>d)</sup>  | 141 ± 5                   | 30)  |
| Bi                | 83 | 209.00 | 2554.8 ± 2.0                    | 2700.2 ± 2.5                    | 145.4 ± 2.0                      | 8,9                                  | 2555 ± 4 <sup>b)</sup>  | 148 ± 4 <sup>b)</sup>     | 10)  |
|                   |    |        |                                 |                                 |                                  |                                      | 2553 ± 7 <sup>d)</sup>  | 146 ± 6                   | 30)  |

a) centre of gravity of  $3d-2p$  group

b)  $E(3d_{5/2} - 2p_{3/2}) - 0.9 \Delta(3d)$

c)  $\Delta(2p) - 0.9 \Delta(3d)$

d)  $E(3d_{3/2} - 2p_{1/2})$

Table 3

Results on 4f - 3d, 5g - 4f, 6h - 5g and 7i - 6h transition energies from the muonic X-ray data

| Element Z | c    | s    | E(6f - 5d) (keV)      |                                  |                            | E(5g - 4f) (keV) |                                  |      | E(7i - 6h) (keV) |                                  |      |  |
|-----------|------|------|-----------------------|----------------------------------|----------------------------|------------------|----------------------------------|------|------------------|----------------------------------|------|--|
|           |      |      | Point nucleus         | Finite nucleus - var. pol. corr. | Exp.                       | Point nucleus    | Finite nucleus - var. pol. corr. | Exp. | Point nucleus    | Finite nucleus - var. pol. corr. | Exp. |  |
| oO        | 5.46 | 2-25 | 345.95                | 346.00                           | 346.5 ± 1.2                |                  |                                  |      |                  |                                  |      |  |
|           | 5.54 | "    | 359.46                | 361.05                           | 360.3 ± 1.21               |                  |                                  |      |                  |                                  |      |  |
| sS        | 5.60 | "    | 375.91                | 375.06                           | 375.5 ± 1.25               |                  |                                  |      |                  |                                  |      |  |
|           | 5.81 | "    | 396.44                | 396.56                           | 397.7 ± 1.32               |                  |                                  |      |                  |                                  |      |  |
| tT        | 5.79 | "    | 418.58                | 418.05                           | 417.2 ± 1.40               |                  |                                  |      |                  |                                  |      |  |
|           | 5.79 | "    | 434.44                | 434.44                           | 434.5 ± 1.35               |                  |                                  |      |                  |                                  |      |  |
| uU        | 5.62 | "    | 466.61                | 466.05                           | 466.1 ± 1.34               |                  |                                  |      |                  |                                  |      |  |
|           | 5.89 | "    | 493.10                | 492.36                           | 492.5 ± 1.25               |                  |                                  |      |                  |                                  |      |  |
| vV        | 6.71 | 1-0  | 559.51 <sup>a)</sup>  | 559.04 <sup>a)</sup>             | 559.6 ± 1.4 <sup>a)</sup>  |                  |                                  |      |                  |                                  |      |  |
|           | 6.46 | 2-1  | 605.14 <sup>b)</sup>  | 605.50 <sup>b)</sup>             | 605.1 ± 1.6 <sup>b)</sup>  |                  |                                  |      |                  |                                  |      |  |
| wW        | 6.63 | 2-2  | 644.32 <sup>a)</sup>  | 644.05 <sup>a)</sup>             | 644.3 ± 1.4 <sup>a)</sup>  |                  |                                  |      |                  |                                  |      |  |
|           | 6.67 | 2-2  | 695.00 <sup>a)</sup>  | 695.00 <sup>a)</sup>             | 695.0 ± 1.4 <sup>a)</sup>  |                  |                                  |      |                  |                                  |      |  |
| xX        | 6.63 | 2-2  | 733.16 <sup>b)</sup>  | 733.63 <sup>b)</sup>             | 733.7 ± 1.6 <sup>b)</sup>  |                  |                                  |      |                  |                                  |      |  |
|           | 6.87 | 2-2  | 794.20 <sup>b)</sup>  | 794.54 <sup>b)</sup>             | 794.2 ± 1.6 <sup>b)</sup>  |                  |                                  |      |                  |                                  |      |  |
| yY        | 6.72 | 2-1  | 856.43 <sup>b)</sup>  | 856.92 <sup>b)</sup>             | 856.5 ± 1.5 <sup>b)</sup>  |                  |                                  |      |                  |                                  |      |  |
|           | 6.71 | 1-0  | 919.57 <sup>a)</sup>  | 919.04 <sup>a)</sup>             | 919.1 ± 1.4 <sup>a)</sup>  |                  |                                  |      |                  |                                  |      |  |
| zZ        | 6.46 | 2-1  | 987.51 <sup>b)</sup>  | 987.76 <sup>b)</sup>             | 988.1 ± 1.6 <sup>b)</sup>  |                  |                                  |      |                  |                                  |      |  |
|           | 6.63 | 2-2  | 1044.32 <sup>a)</sup> | 1044.05 <sup>a)</sup>            | 1044.3 ± 1.4 <sup>a)</sup> |                  |                                  |      |                  |                                  |      |  |
| aa        | 6.63 | 2-2  | 1100.19 <sup>b)</sup> | 1100.79 <sup>b)</sup>            | 1100.1 ± 1.4 <sup>b)</sup> |                  |                                  |      |                  |                                  |      |  |
|           | 6.87 | 2-2  | 1166.00 <sup>a)</sup> | 1166.00 <sup>a)</sup>            | 1166.0 ± 1.4 <sup>a)</sup> |                  |                                  |      |                  |                                  |      |  |
| bb        | 6.63 | 2-2  | 1233.16 <sup>b)</sup> | 1233.63 <sup>b)</sup>            | 1233.7 ± 1.6 <sup>b)</sup> |                  |                                  |      |                  |                                  |      |  |
|           | 6.87 | 2-2  | 1304.20 <sup>b)</sup> | 1304.54 <sup>b)</sup>            | 1304.2 ± 1.6 <sup>b)</sup> |                  |                                  |      |                  |                                  |      |  |
| cc        | 6.72 | 2-1  | 1376.43 <sup>b)</sup> | 1376.92 <sup>b)</sup>            | 1376.5 ± 1.5 <sup>b)</sup> |                  |                                  |      |                  |                                  |      |  |
|           | 6.71 | 1-0  | 1444.32 <sup>a)</sup> | 1444.05 <sup>a)</sup>            | 1444.3 ± 1.4 <sup>a)</sup> |                  |                                  |      |                  |                                  |      |  |

a) E(4f - 3d) - 5g,  
b) E(4f - 3d) - 5g.

Table 4  
Energies of calibration lines

| Source                              | Energy<br>keV                          | Reference                         | Line No. |
|-------------------------------------|--|-----------------------------------|----------|
| $^{57}\text{Co}$                    | $122.05 \pm 0.05$                      | 43)                               | (1)      |
| $^{22}\text{Na}$ and $\text{ThC}''$ | $511.006 \pm 0.005$                    | 43)                               | (2)      |
| $\text{ThC}''$                      | $583.139 \pm 0.023$                    | 43)                               | (3)      |
| $^{137}\text{Cs}$                   | $661.595 \pm 0.076$                    | 43)                               | (4)      |
| $^{60}\text{Co}$                    | $1173.226 \pm 0.04$                    | 43)                               | (5)      |
| $^{14}\text{N}$                     | $1290.0 \pm 1.2$ (double escape peak)  | } 44)                             | (6)      |
|                                     | $2312.0 \pm 1.2$ (photopeak)           |                                   | (7)      |
| $^{60}\text{Co}$                    | $1332.38 \pm 0.05$ (photopeak)         | 43)                               | (8)      |
|                                     | $1592.46 \pm 0.1$ (double escape peak) | } 43)                             | (9)      |
| $\text{ThC}''$                      | $2614.47 \pm 0.1$ (photopeak)          |                                   | (10)     |
|                                     | $\text{PoBe}$                          | $3411 \pm 5$ (double escape peak) | } 44)    |
| $4433 \pm 5$ (photopeak)            |  | (12)                              |          |
| $^{66}\text{Ca}$                    | $4679.3 \pm 2.0$ (photopeak)           | see Table 4.                      | (13)     |
|                                     | $5109 \pm 4$ (double escape peak)      | } 45)                             | (14)     |
| $^{16}\text{N}$                     | $5620 \pm 4$ (single escape peak)      |                                   | (15)     |
|                                     | $6131 \pm 4$ (photopeak)               |                                   | (16)     |

Table 5

$\gamma$  rays above 2.5 MeV from decay of  $^{66}\text{Ga}$  ( $\tau_{1/2} = 9.5\text{h}$ )

| $E_{\gamma}^{(46)}$<br>keV | $E_{\gamma}^{(47)}$<br>keV | $E_{\gamma}^{(48)}$<br>keV | $E_{\gamma}^{(49)}$<br>keV | $E_{\gamma}$ (this paper)<br>keV |                      |
|----------------------------|----------------------------|----------------------------|----------------------------|----------------------------------|----------------------|
| 4800                       | $4830 \pm 50$              | $4833 \pm 30$              | $4832 \pm 7$               | $4798.6 \pm 2.8$                 | (photopeak)          |
| -                          | -                          | $4450 \pm 60$              | $(4485 \pm 10)^*$          | $(4453.0 \pm 3.5)^*$             | (photopeak)          |
| 4250                       | $4330 \pm 50$              | $4300 \pm 5$               | $4314 \pm 10$              | $4285.7 \pm 2.7$                 | (photopeak)          |
| -                          | $4120 \pm 50$              | $4100 \pm 40$              | $4132 \pm 11$              | $4079.3 \pm 2.0$                 | (photopeak)          |
| -                          | $3780 \pm 30$              | $3790 \pm 30$              | $3810 \pm 10$              | $3776.6 \pm 2.8$                 | (double escape peak) |
| -                          | -                          | -                          | -                          | $(3771.3 \pm 2.0)^*$             | (photopeak)          |
| -                          | $3410 \pm 40$              | $3400 \pm 20$              | $3463 \pm 10$              | $3431.0 \pm 3.5$                 | (double escape peak) |
| 3300                       | $3240 \pm 40$              | $3240 \pm 40$              | $3251 \pm 10$              | $3263.7 \pm 2.3$                 | (double escape peak) |
| -                          | -                          | $3030 \pm 50$              | -                          | $3057.3 \pm 2.0$                 | (double escape peak) |
| 2750                       | 2750                       | $2748 \pm 4$               | -                          | $2749.3 \pm 2.0$                 | (double escape peak) |

\* ) Values in brackets are energies of not observed photopeaks derived from the corresponding double-escape peaks.

Table 6

Low and medium Z nuclei.

Radial parameter  $a$  and central proton density  $\rho_p$  for various values of  $t$  from the muonic X-ray data. For comparison, electron scattering data<sup>24,25</sup> are included. ( $a, t$  in fm,  $\rho_p$  in protons/fm<sup>3</sup>).

| Element          | $t = 0.0$                          |                    | $t = 1.0$                          |                    | $t = 2.0$                          |                    | $t = 3.0$                          |                    | electron scattering |                       |
|------------------|------------------------------------|--------------------|------------------------------------|--------------------|------------------------------------|--------------------|------------------------------------|--------------------|---------------------|-----------------------|
|                  | $a$                                | $\rho_p$           | $a$                                | $\rho_p$           | $a$                                | $\rho_p$           | $a$                                | $\rho_p$           | $a$                 | $t$                   |
| <sup>17</sup> Cl | 4.265 ± 0.0910<br>± 0.110 ± 0.0042 | 0.0416<br>± 0.0042 | 4.154 ± 0.0550<br>± 0.113 ± 0.0049 | 0.0550<br>± 0.0049 | 5.710 ± 0.0682<br>± 0.129 ± 0.0070 | 0.0682<br>± 0.0070 | 5.931 ± 0.1050<br>± 0.137 ± 0.0121 | 0.1050<br>± 0.0121 |                     |                       |
| <sup>20</sup> Ca | 4.454 ± 0.075<br>± 0.0028          | 0.0542<br>± 0.0028 | 4.319 ± 0.077<br>± 0.074 ± 0.0030  | 0.0577<br>± 0.0030 | 5.900 ± 0.0710<br>± 0.082 ± 0.0042 | 0.0710<br>± 0.0042 | 5.125 ± 0.1064<br>± 0.096 ± 0.0080 | 0.1064<br>± 0.0080 | 3.60 ± 0.83         | 2.50 ± 0.16<br>- 0.11 |
| <sup>26</sup> Fe | 4.772 ± 0.042<br>± 0.0016          | 0.0571<br>± 0.0016 | 4.652 ± 0.0602<br>± 0.045 ± 0.0018 | 0.0602<br>± 0.0018 | 4.271 ± 0.0716<br>± 0.049 ± 0.0024 | 0.0716<br>± 0.0024 | 5.509 ± 0.1003<br>± 0.057 ± 0.0041 | 0.1003<br>± 0.0041 |                     |                       |
| <sup>30</sup> Zn | 5.940 ± 0.010<br>± 0.0003          | 0.0570<br>± 0.0003 | 5.048 ± 0.0508<br>± 0.011 ± 0.0003 | 0.0508<br>± 0.0003 | 5.507 ± 0.0649<br>± 0.010 ± 0.0003 | 0.0649<br>± 0.0003 | 5.067 ± 0.0778<br>± 0.012 ± 0.0005 | 0.0778<br>± 0.0005 |                     |                       |
| <sup>51</sup> Sb | 5.998 ± 0.007<br>± 0.0002          | 0.0564<br>± 0.0002 | 5.908 ± 0.0582<br>± 0.007 ± 0.0002 | 0.0582<br>± 0.0002 | 5.630 ± 0.0641<br>± 0.007 ± 0.0002 | 0.0641<br>± 0.0002 | 5.138 ± 0.0764<br>± 0.008 ± 0.0004 | 0.0764<br>± 0.0004 | 5.32 ± 0.11         | 2.50 ± 0.25           |
| <sup>52</sup> Te | 6.050 ± 0.008<br>± 0.0002          | 0.0559<br>± 0.0002 | 5.967 ± 0.0576<br>± 0.008 ± 0.0002 | 0.0576<br>± 0.0002 | 5.693 ± 0.0633<br>± 0.008 ± 0.0002 | 0.0633<br>± 0.0002 | 5.208 ± 0.0751<br>± 0.009 ± 0.0004 | 0.0751<br>± 0.0004 |                     |                       |
| <sup>53</sup> I  | 6.077 ± 0.009<br>± 0.0003          | 0.0564<br>± 0.0003 | 5.988 ± 0.0581<br>± 0.009 ± 0.0003 | 0.0581<br>± 0.0003 | 5.715 ± 0.0638<br>± 0.010 ± 0.0003 | 0.0638<br>± 0.0003 | 5.233 ± 0.0756<br>± 0.011 ± 0.0004 | 0.0756<br>± 0.0004 |                     |                       |
| <sup>55</sup> Cs | 6.157 ± 0.011<br>± 0.0003          | 0.0563<br>± 0.0003 | 6.070 ± 0.0579<br>± 0.008 ± 0.0002 | 0.0579<br>± 0.0002 | 5.802 ± 0.0634<br>± 0.009 ± 0.0003 | 0.0634<br>± 0.0003 | 5.330 ± 0.0746<br>± 0.010 ± 0.0004 | 0.0746<br>± 0.0004 |                     |                       |
| <sup>56</sup> Ba | 6.206 ± 0.011<br>± 0.0003          | 0.0559<br>± 0.0003 | 6.120 ± 0.0575<br>± 0.011 ± 0.0003 | 0.0575<br>± 0.0003 | 5.855 ± 0.0629<br>± 0.011 ± 0.0003 | 0.0629<br>± 0.0003 | 5.389 ± 0.0737<br>± 0.013 ± 0.0005 | 0.0737<br>± 0.0005 |                     |                       |
| <sup>57</sup> La | 6.235 ± 0.010<br>± 0.0003          | 0.0561<br>± 0.0003 | 6.149 ± 0.0577<br>± 0.010 ± 0.0003 | 0.0577<br>± 0.0003 | 5.886 ± 0.0630<br>± 0.011 ± 0.0004 | 0.0630<br>± 0.0004 | 5.424 ± 0.0737<br>± 0.012 ± 0.0005 | 0.0737<br>± 0.0005 |                     |                       |
| <sup>58</sup> Ce | 6.261 ± 0.012<br>± 0.0003          | 0.0564<br>± 0.0003 | 6.176 ± 0.0580<br>± 0.013 ± 0.0004 | 0.0580<br>± 0.0004 | 5.915 ± 0.0632<br>± 0.013 ± 0.0004 | 0.0632<br>± 0.0004 | 5.456 ± 0.0738<br>± 0.015 ± 0.0006 | 0.0738<br>± 0.0006 |                     |                       |
| <sup>59</sup> Pr | 6.259 ± 0.012<br>± 0.0004          | 0.0574<br>± 0.0004 | 6.174 ± 0.0591<br>± 0.012 ± 0.0004 | 0.0591<br>± 0.0004 | 5.913 ± 0.0644<br>± 0.013 ± 0.0004 | 0.0644<br>± 0.0004 | 5.455 ± 0.0732<br>± 0.014 ± 0.0005 | 0.0732<br>± 0.0005 |                     |                       |
| <sup>60</sup> Nd | 6.313 ± 0.013<br>± 0.0004          | 0.0569<br>± 0.0004 | 6.229 ± 0.0585<br>± 0.013 ± 0.0004 | 0.0585<br>± 0.0004 | 5.971 ± 0.0636<br>± 0.014 ± 0.0005 | 0.0636<br>± 0.0005 | 5.520 ± 0.0740<br>± 0.015 ± 0.0006 | 0.0740<br>± 0.0006 |                     |                       |



Table 7

Elements  $^{79}\text{Au}$  to  $^{83}\text{Bi}$ .

Radial parameter  $c$ , surface thickness parameter  $t$ , and proton density  $\rho_p$  for the muonic X-ray data. For comparison, electron scattering data<sup>3,4,5,6</sup> are included. ( $c, t$  in fm;  $\rho$  in protons/fm<sup>3</sup>)

| Element          | $c_1$             | $t_1$ | $\rho_{p_1}$ | $c \pm (bc) t$    | $t$  | $\rho_p$ | $c_2$    | $t_2$ | $\rho_{p_2}$ | Electron scattering |                 |
|------------------|-------------------|-------|--------------|-------------------|------|----------|----------|-------|--------------|---------------------|-----------------|
|                  |                   |       |              |                   |      |          |          |       |              | $c$                 | $t$             |
| $^{79}\text{Au}$ | 6.79              | 1.50  | 0.0588       | $6.71 \pm 0.01$   | 1.80 | 0.0602   | 6.55     | 2.36  | 0.0622       | $5.38 \pm 0.06$     | $2.35 \pm 0.12$ |
| $^{80}\text{Hg}$ | 6.75              | 1.89  | 0.0597       | $6.46 \pm 0.02$   | 2.68 | 0.0651   | 6.20     | 3.22  | 0.0704       |                     |                 |
| $^{81}\text{Tl}$ | 6.75              | 1.90  | 0.0604       | $6.62^s \pm 0.01$ | 2.28 | 0.0627   | $6.53^s$ | 2.50  | 0.0645       |                     |                 |
| $^{82}\text{Pb}$ | 6.74 <sup>s</sup> | 1.97  | 0.0611       | $6.62^s \pm 0.01$ | 2.31 | 0.0634   | 6.55     | 2.51  | 0.0643       |                     |                 |
| $^{82}\text{Pb}$ | 6.74 <sup>s</sup> | 2.00  | 0.0610       | $6.67 \pm 0.01$   | 2.21 | 0.0624   | 6.56     | 2.50  | 0.0645       | $5.5 \pm 0.13$      | $2.3 \pm 0.23$  |
| $^{83}\text{Bi}$ | 6.84 <sup>s</sup> | 1.72  | 0.0598       | $6.72^s \pm 0.01$ | 2.14 | 0.0619   | 6.62     | 2.42  | 0.0635       | $6.47 \pm 0.13$     | $2.7 \pm 0.27$  |

Table 8

Intensity ratios of transitions between fine structure multiplets in nuclei atoms

| Element    | Present data  |             |   |             |   |           | Previous data |             | Ref. |   |   |                   |
|------------|---|-------------|---|-------------|---|-----------|---------------|-------------|------|---|---|-------------------|
|            | Exp.  |             | Th  |             | Th  |           | 2p + 1s       | 3d + 2p     |      |   |   |                   |
|            | Uncorr.   | Corrected   | Uncorr.   | Corrected   | Uncorr.   | Corrected |               |             |      |   |   |                   |
|            | $I(3P_{3/2} \rightarrow 1s_{1/2}) / I(3P_{1/2} \rightarrow 1s_{1/2})$ |             | $I(3S_{1/2} \rightarrow 3d_{3/2}) / I(3P_{3/2} \rightarrow 2p_{3/2})$ |             | $I(4S_{1/2} \rightarrow 4p_{3/2}) / I(4S_{1/2} \rightarrow 3d_{3/2})$ |           |               |             |      |   |   |                   |
| 10Be       | 1.86  | 1.83 ± 0.11 | 1.993   | 1.73 ± 0.15 | 1.953   |           |               |             |      |   |   |                   |
| 10B        | 1.91  | 1.90 ± 0.10 | 1.953   | 2.76        | 2.57 ± 0.30   | 1.953     |               |             |      |   |   |                   |
| 11B        | 1.96  | 1.95 ± 0.13 | 1.953   | 2.01        | 1.86 ± 0.20   | 1.953     |               |             |      |   |   |                   |
| 11C        | 1.07  | 1.06 ± 0.08 | 1.953   | 3.20        | 3.00 ± 0.30   | 1.953     |               |             |      |   |   |                   |
| 12C        | 1.70  | 1.68 ± 0.11 | 1.951   | 2.15        | 2.08 ± 0.30   | 1.951     |               |             |      |   |   |                   |
| 13C        | 4.07  | 2.05 ± 0.23 | 1.953   | 1.87        | 1.78 ± 0.50   | 1.953     |               |             |      |   |   |                   |
| 14C        | 1.98  | 1.95 ± 0.10 | 1.951   | 2.23        | 2.00 ± 0.25   | 1.951     |               |             |      |   |   |                   |
| 16O        | 1.87  | 1.86 ± 0.12 | 1.950   | 4.29        | 2.10 ± 0.50   | 1.950     |               |             |      |   |   |                   |
| 17O        | 1.86  | 1.81 ± 0.16 | 1.950   | 2.76        | 2.56 ± 0.40   | 1.950     |               |             |      |   |   |                   |
| 18O        | 1.01  | 1.29 ± 0.08 | 1.969   | 1.91        | 1.71 ± 0.20   | 1.969     |               |             |      |   |   |                   |
| 18Ne       | 1.52  | 1.50 ± 0.10 | 1.826   | 1.17        | 1.40 ± 0.16   | 1.758     | 1.73          | 1.71 ± 0.10 | 1.49 | 1.98 ± 0.10 <sup>a)</sup><br>(1.70 ± 0.11)<br>1.65 ± 0.30 | 31)                                     |                   |
| 20Ne       | 1.15  | 1.29 ± 0.06 | 1.823   | 1.51        | 1.75 ± 0.15   | 1.731     | 1.58          | 1.56 ± 0.12 | 1.49 | 1.03 ± 0.10   | 10)                                     |                   |
| 21Ne       | 1.06  | 1.09 ± 0.10 | 1.983   | 1.20        | 1.59 ± 0.28   | 1.730     | 1.89          | 1.79 ± 0.24 | 1.49 |   |   |                   |
| 21P        | 1.50  | 1.45 ± 0.10 | 1.982   | 1.35        | 1.57 ± 0.15   | 1.769     | 1.61          | 1.56 ± 0.25 | 1.49 |   |   |                   |
| 22Ne(m.s.) | 1.95  | 1.50 ± 0.15 | 1.922   | 1.35        | 1.57 ± 0.20   | 1.769     | 1.72          | 1.63 ± 0.12 | 1.49 | 1.8 ± 0.4<br>2.08 ± 0.29<br>1.78 ± 0.10                   | 1.6 ± 0.5<br>1.28 ± 0.12<br>1.08 ± 0.08 | 30)               |
| 20Ne       | 1.25  | 1.31 ± 0.20 | 1.800   | 1.25        | 1.44 ± 0.20   | 1.748     | 1.35          | 1.18 ± 0.12 | 1.49 | 1.53 ± 0.09<br>1.86 ± 0.16<br>1.2 ± 0.5                   | 1.69 ± 0.08<br>1.6<br>1.2               | 16)<br>16)<br>30) |

a) The first value is calculated, omitting the weak 50% hot lines; the value in brackets shows the observational intensity for this line into account.

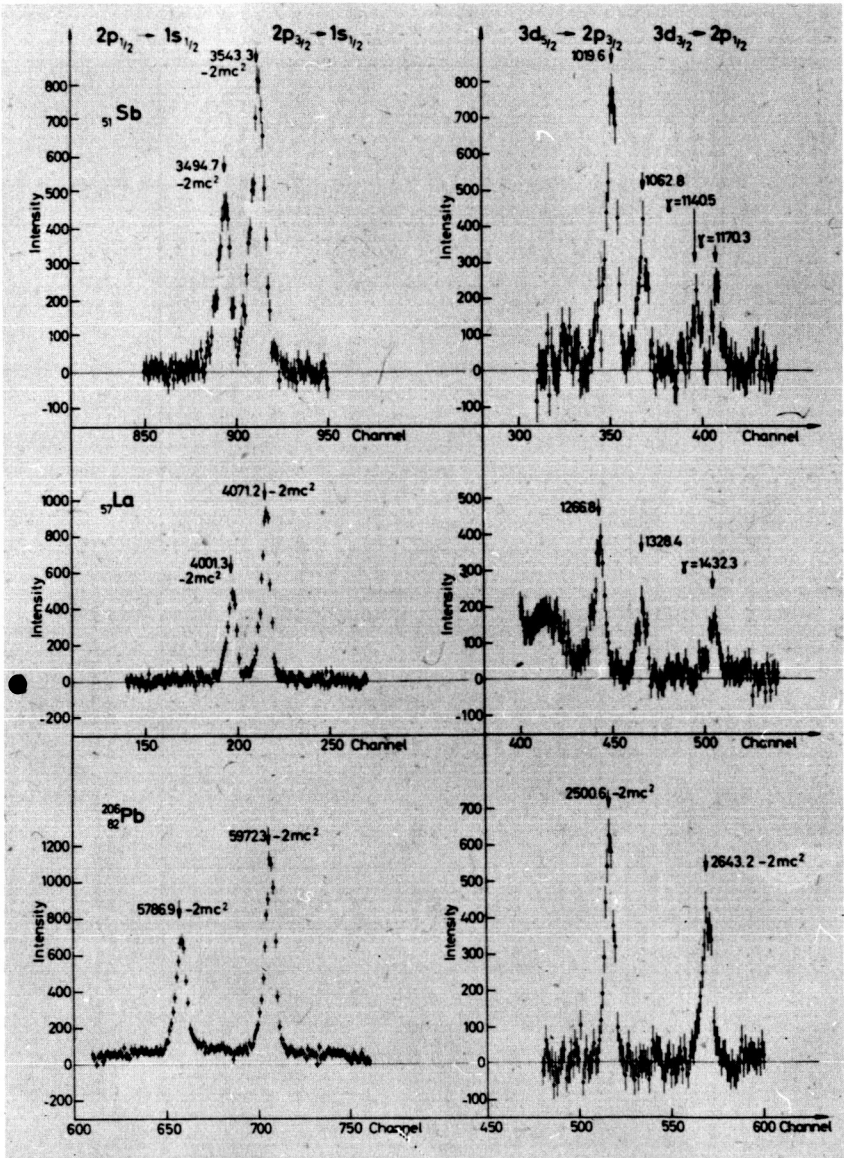


Figure 1

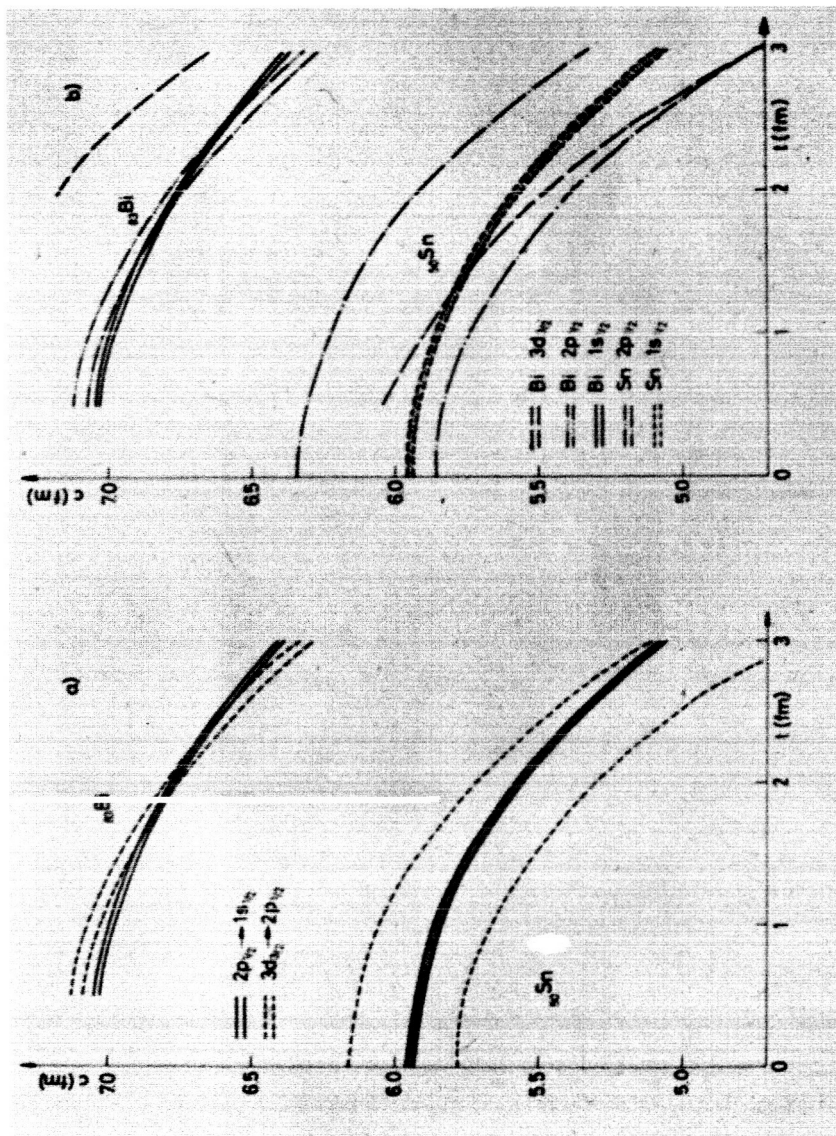


Figure 2

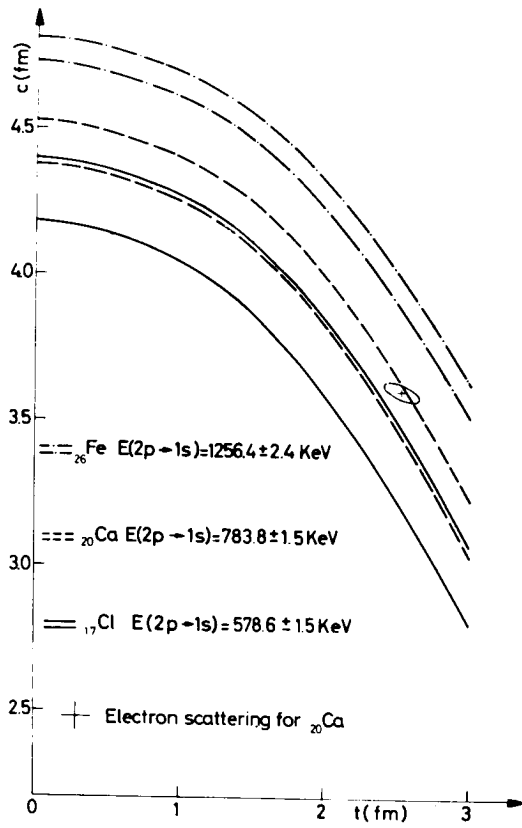


Figure 3

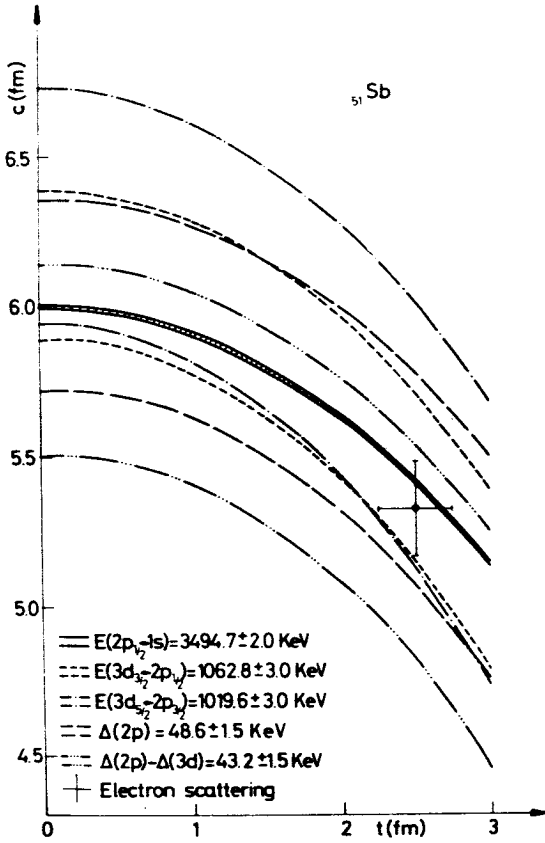


Figure 4

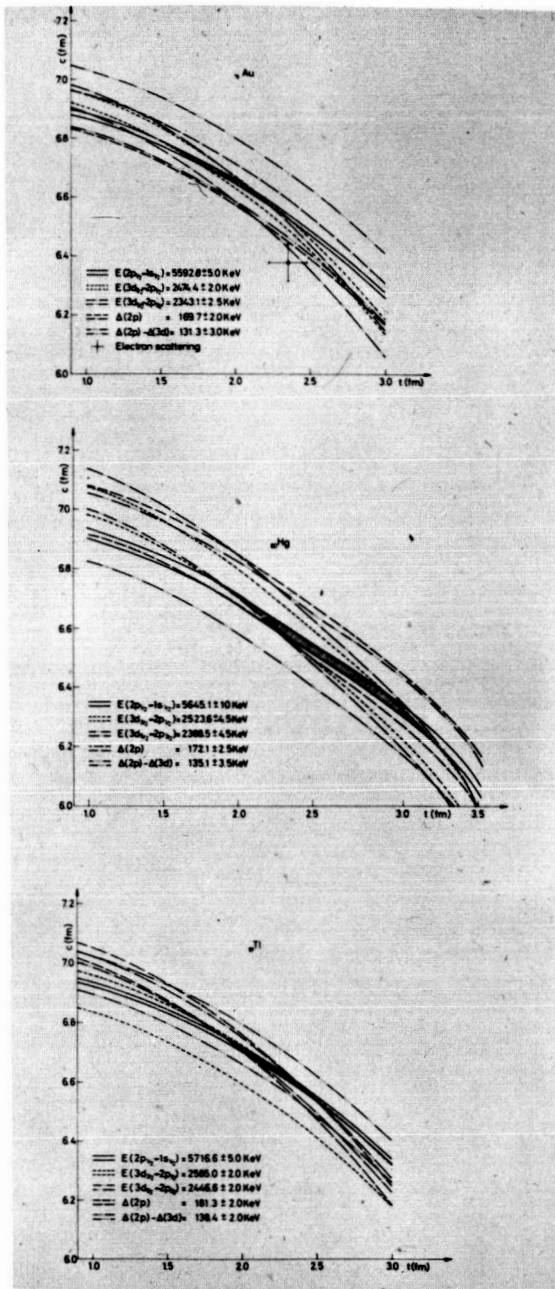


Figure 5

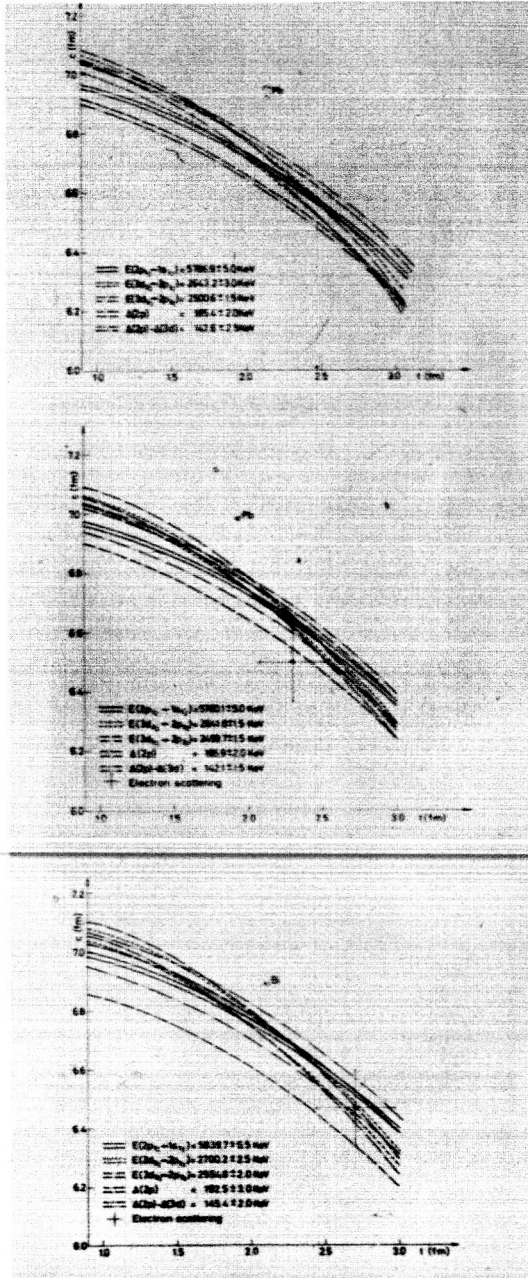


Figure 6



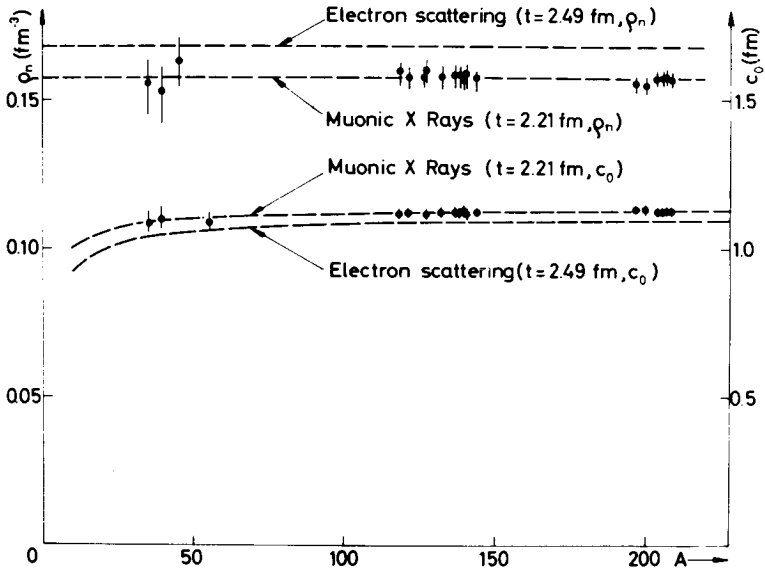


Figure 7

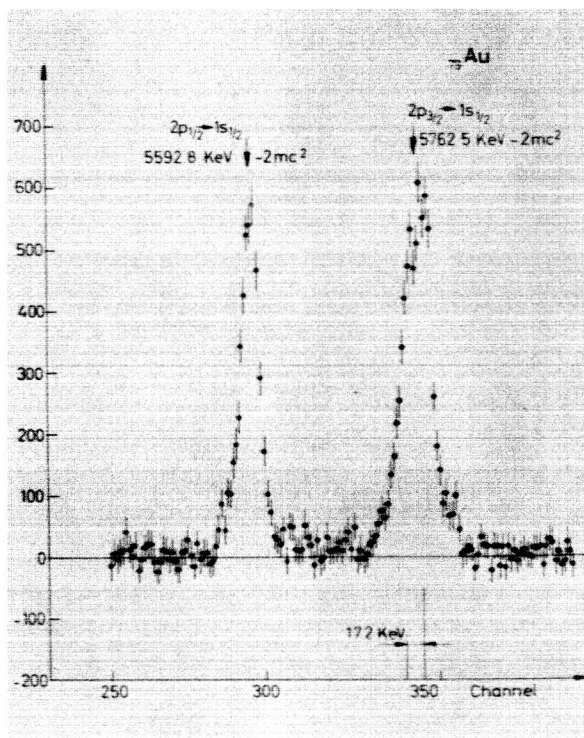


Figure 8

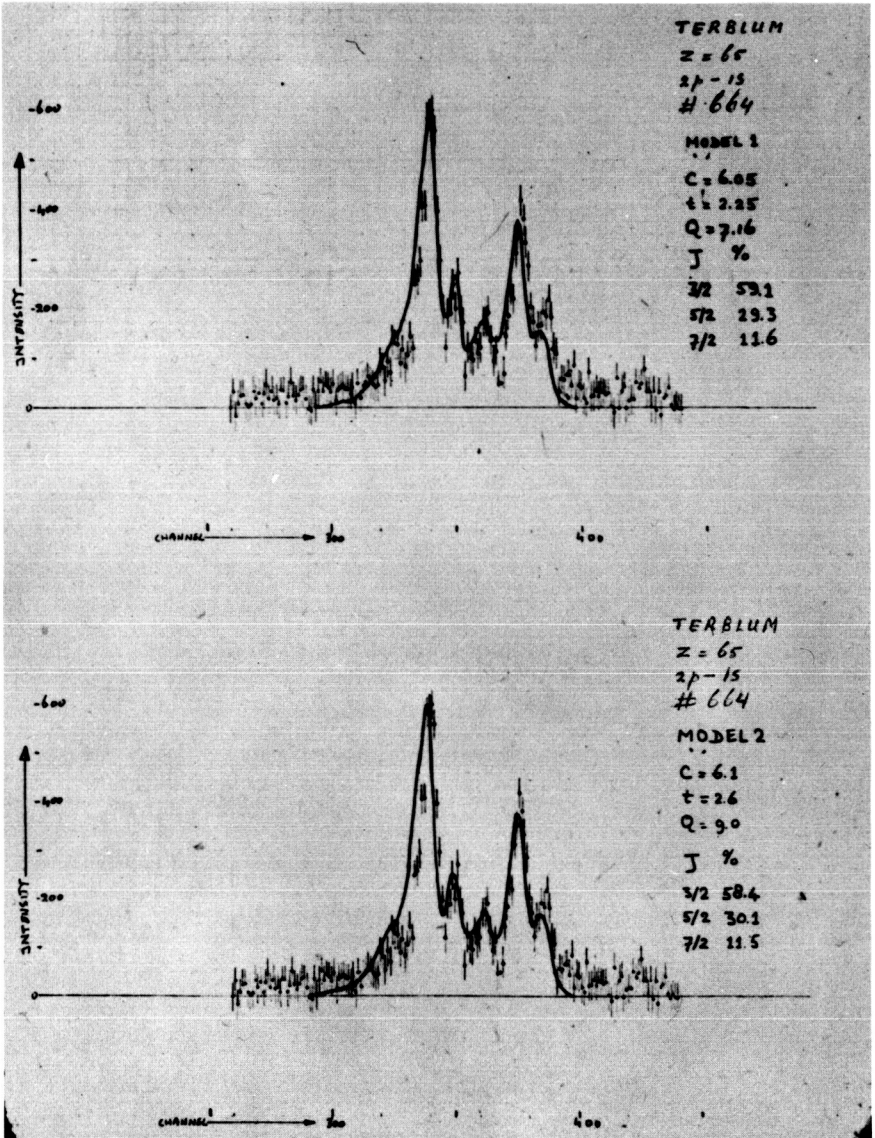


Figure 9

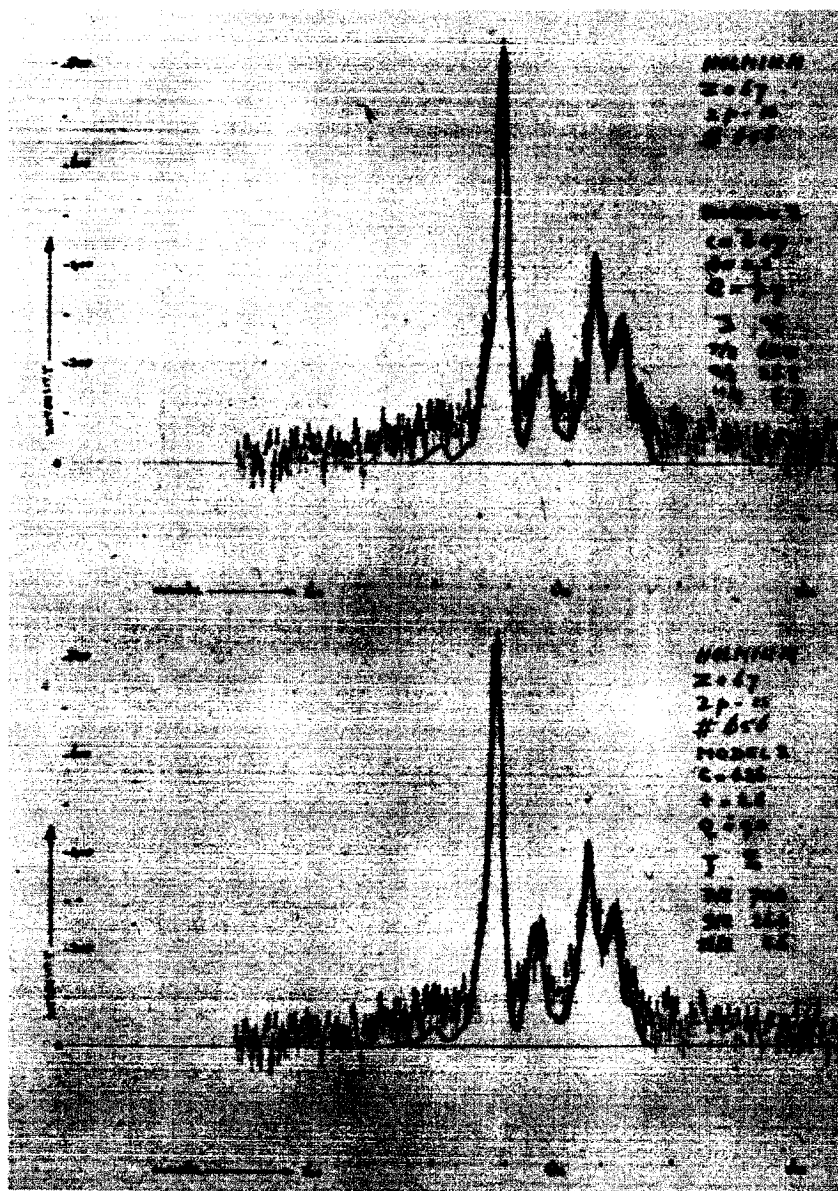


Figure 10

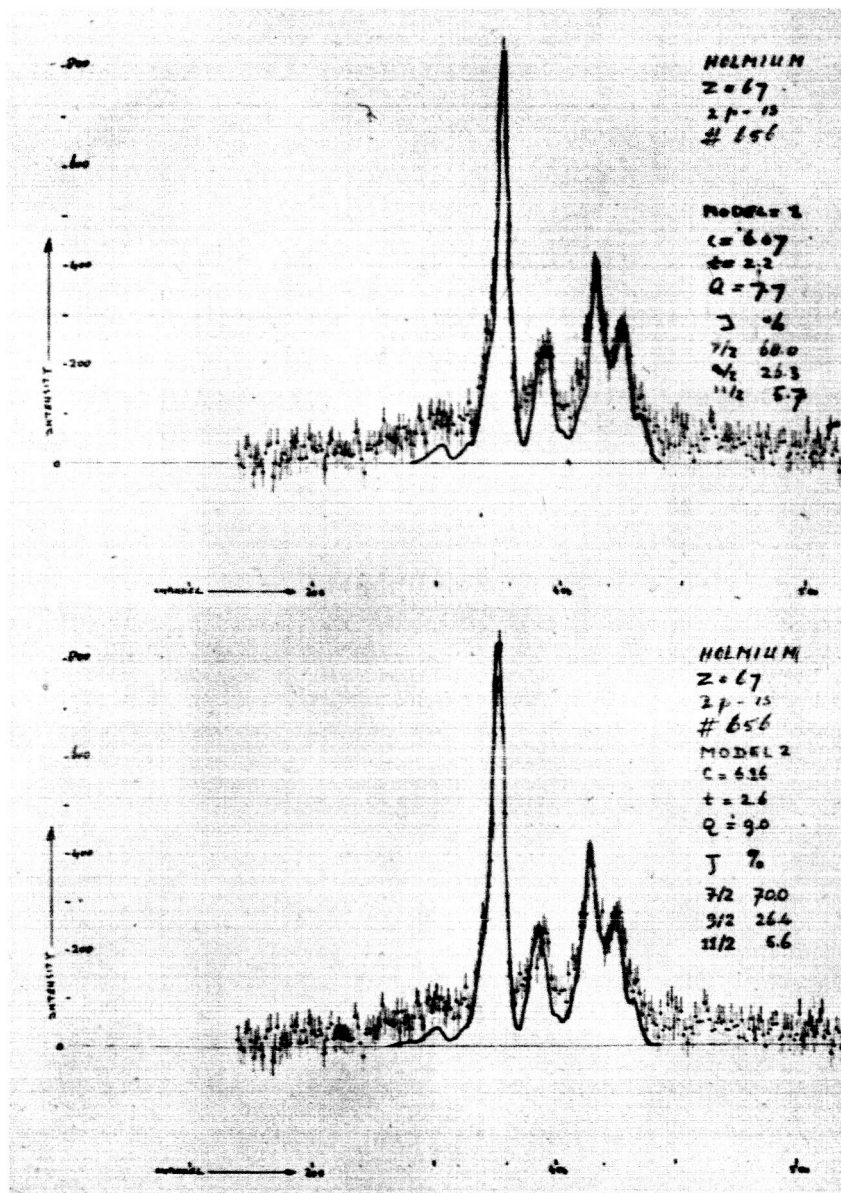


Figure 10

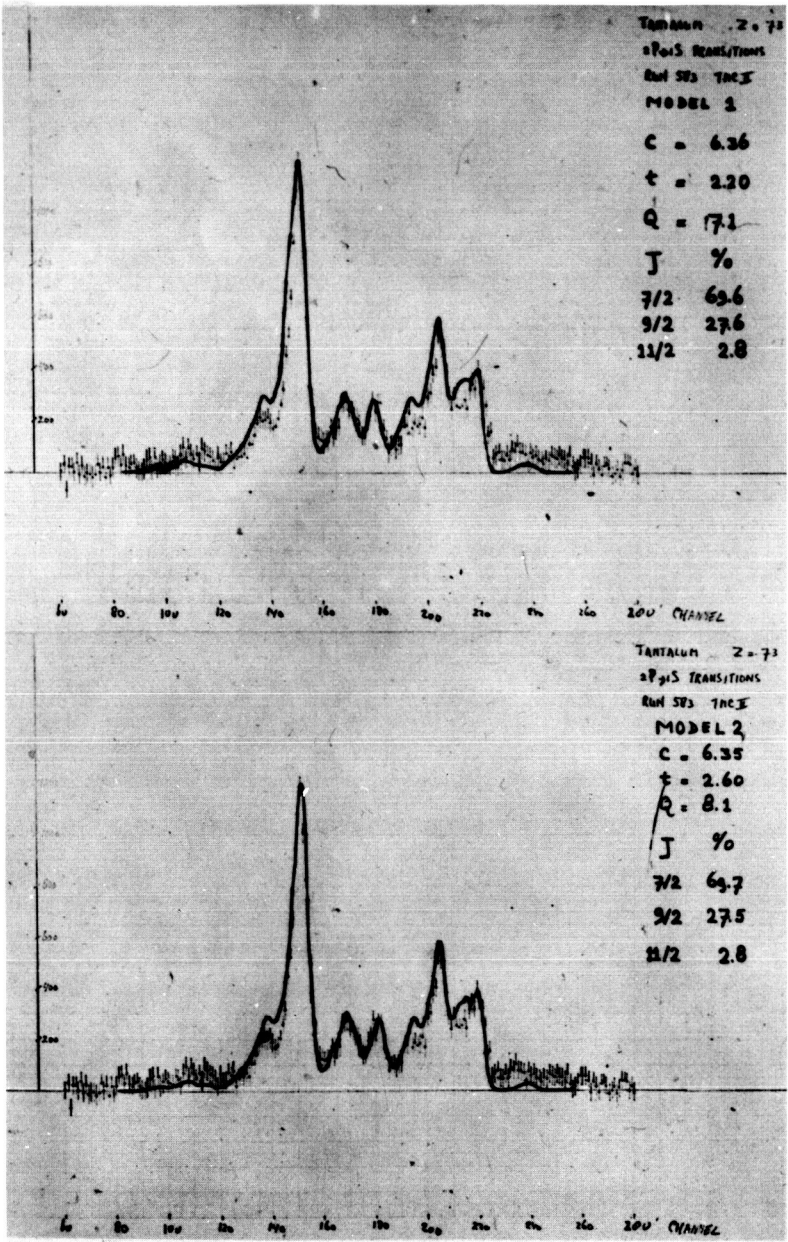


Figure 11

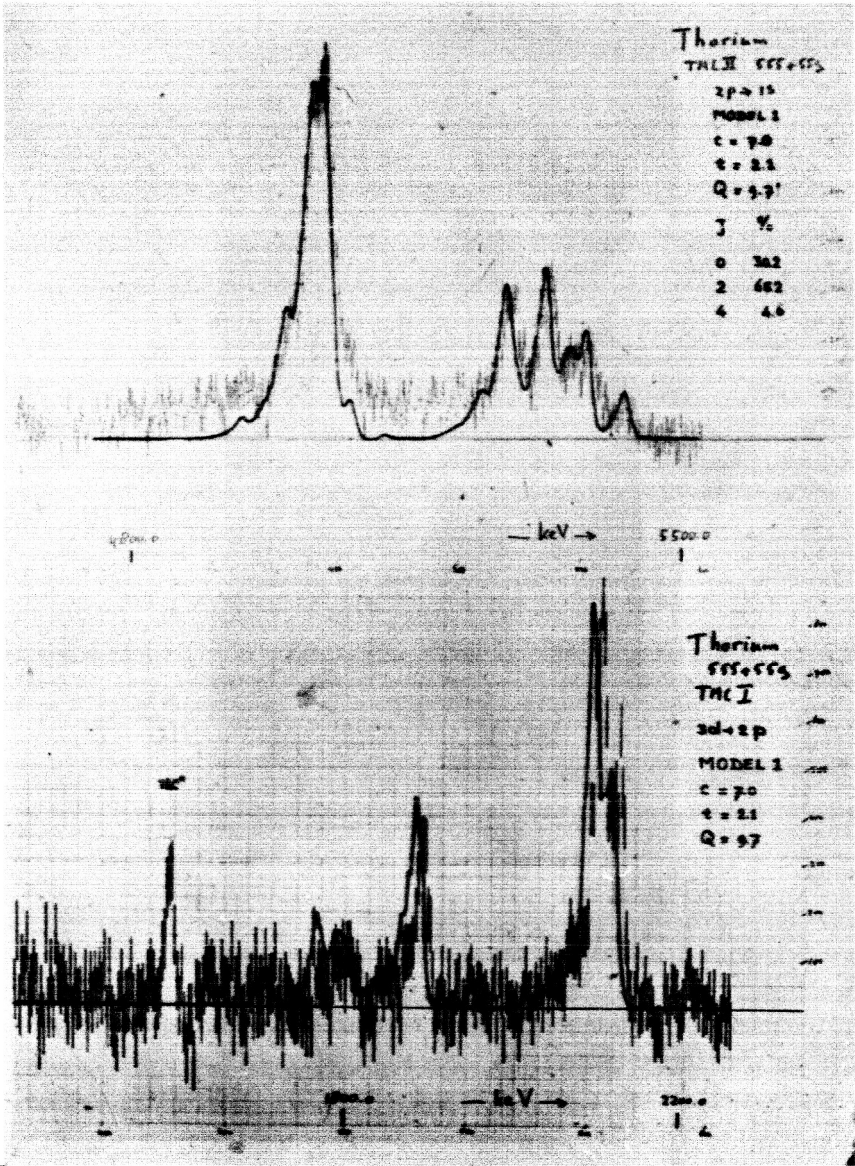


Figure 12

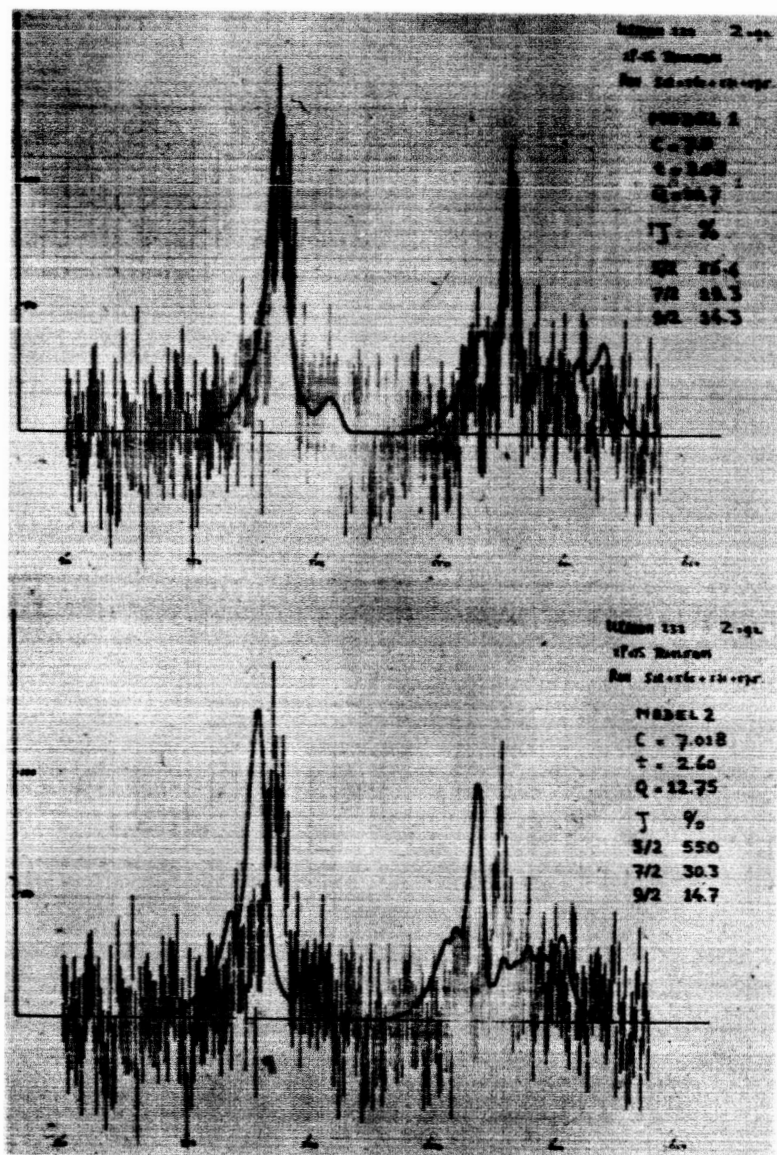


Figure 14



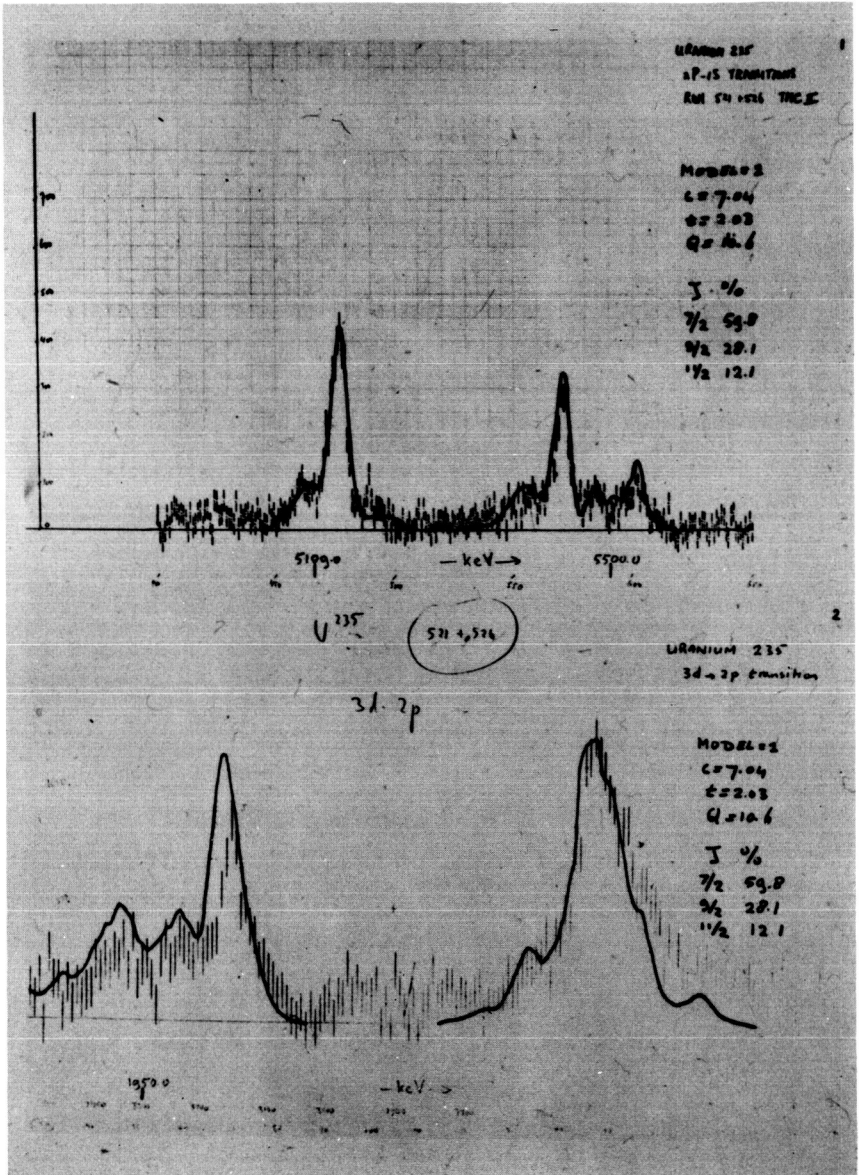


Figure 15

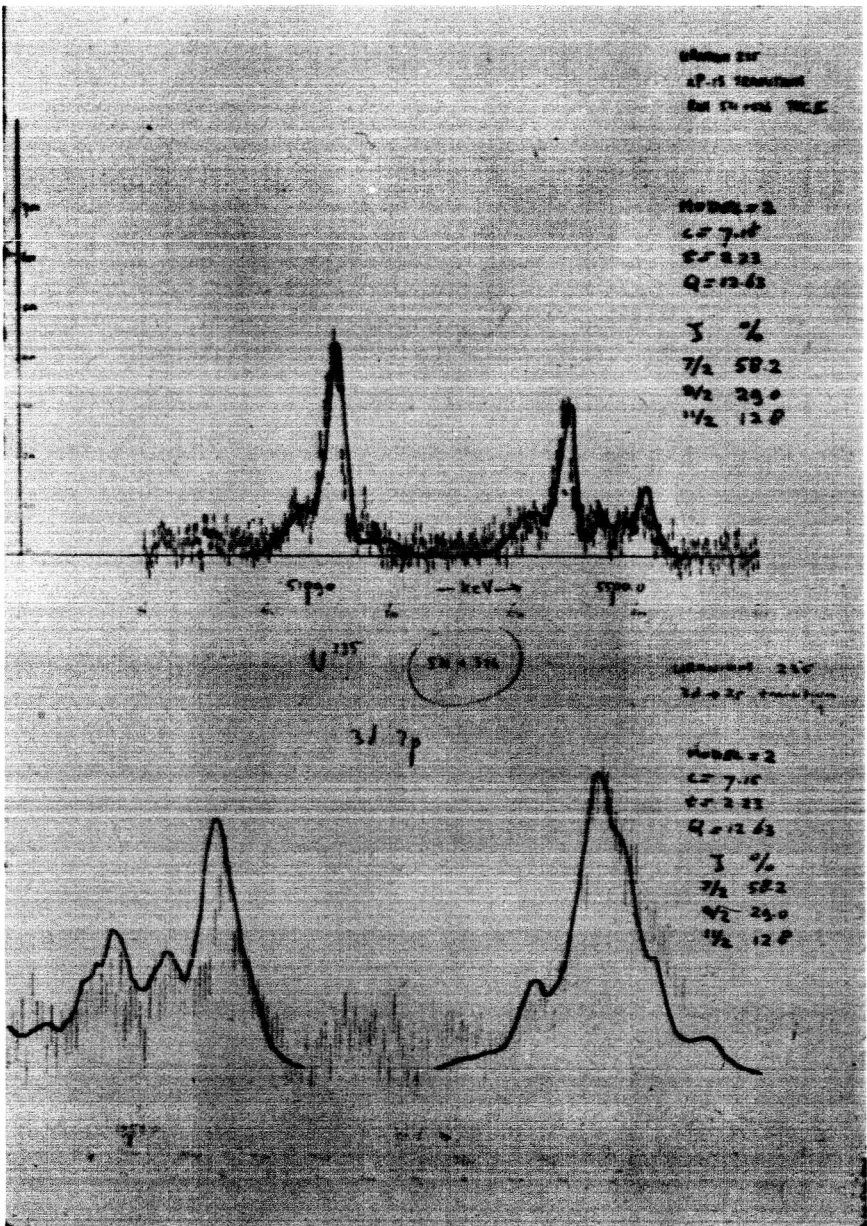


Figure 16

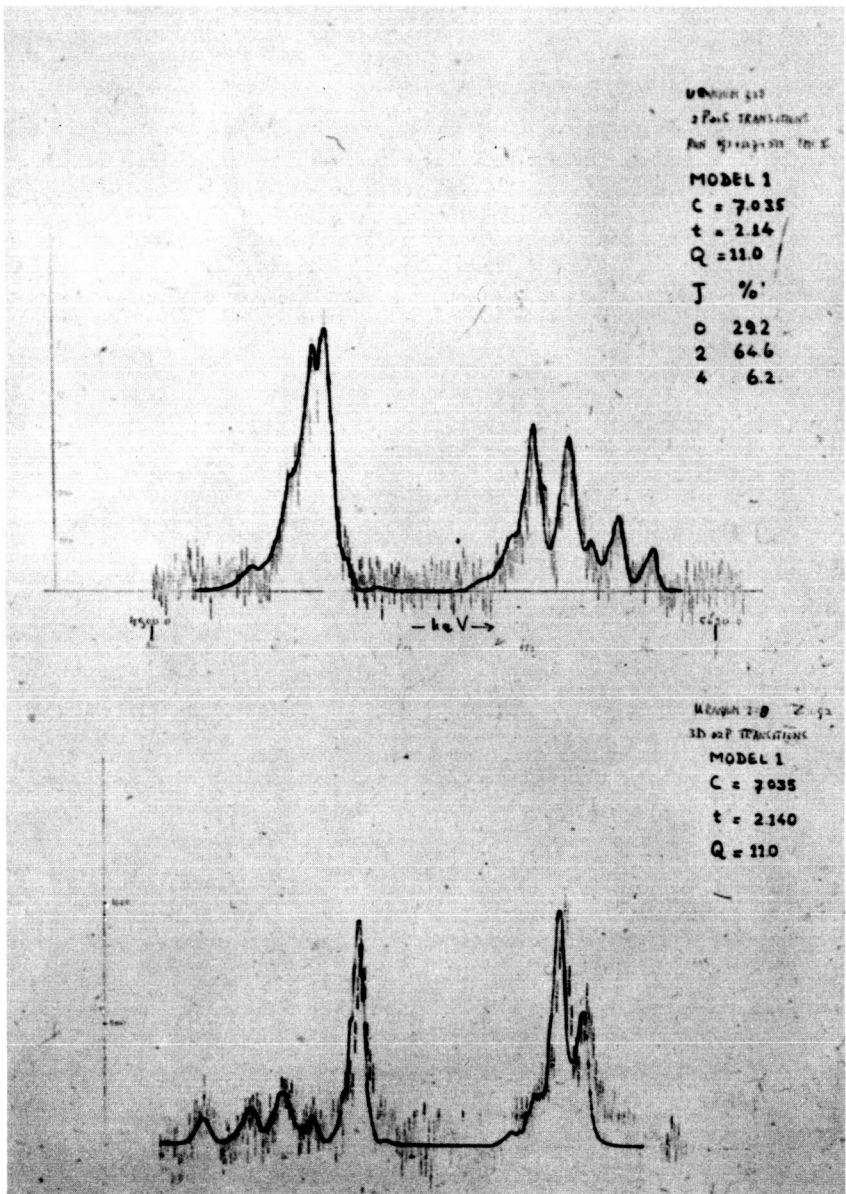


Figure 17

## Studies of Spherical Nuclei

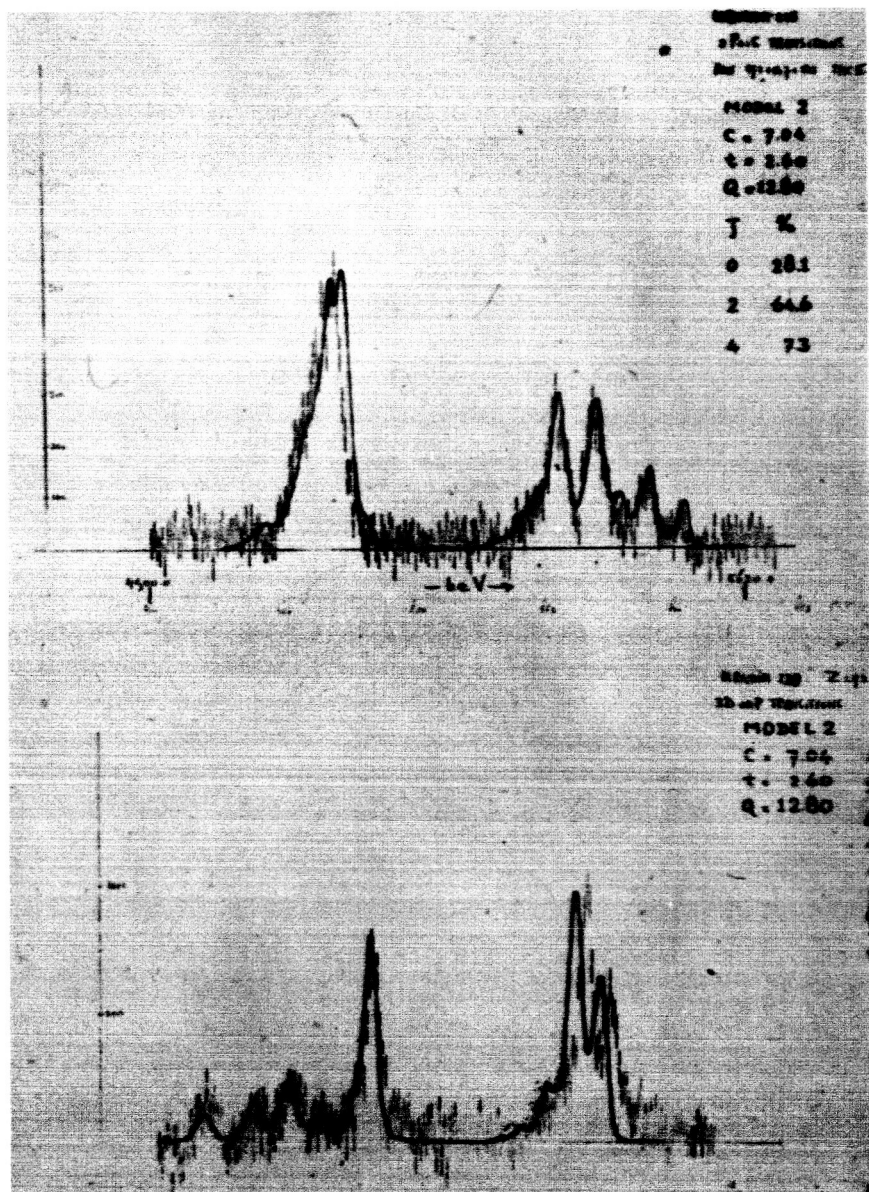


Figure 18

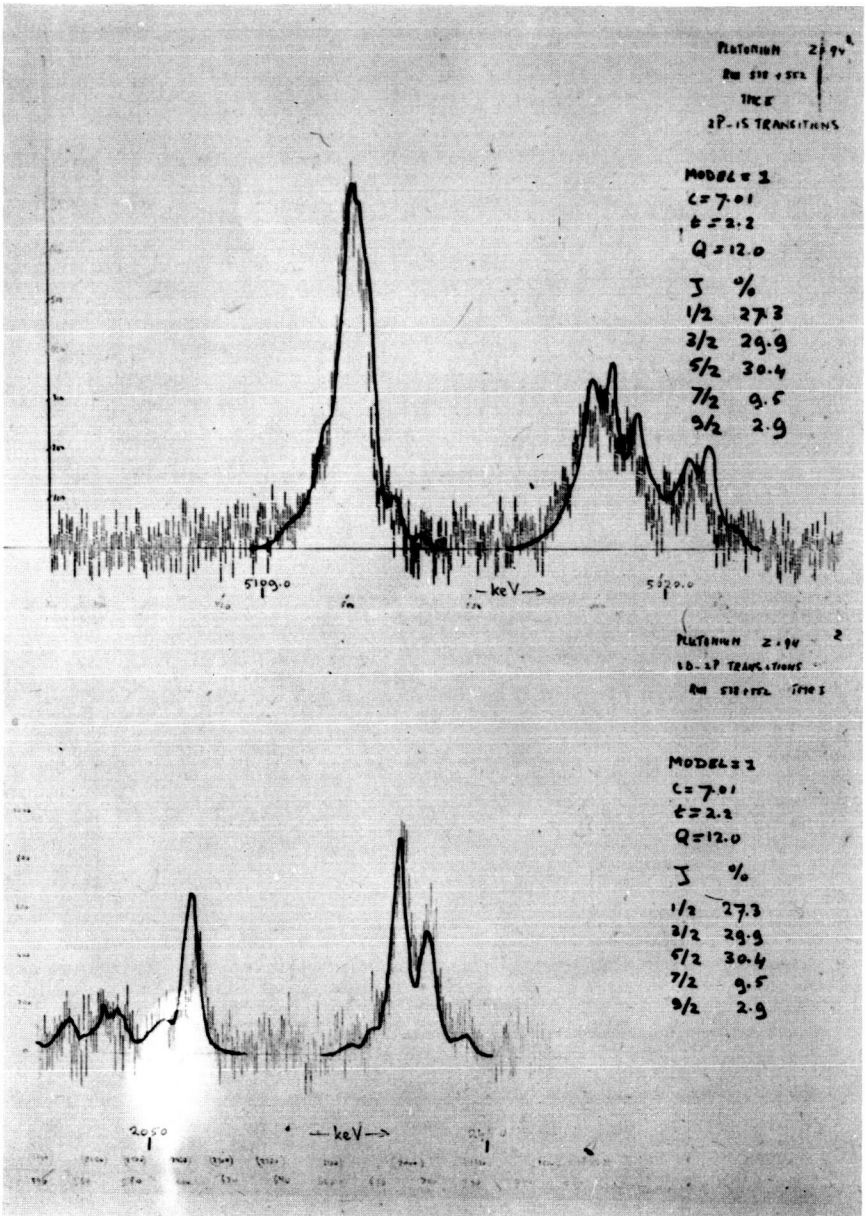


Figure 19

## Studies of Spherical Nuclei

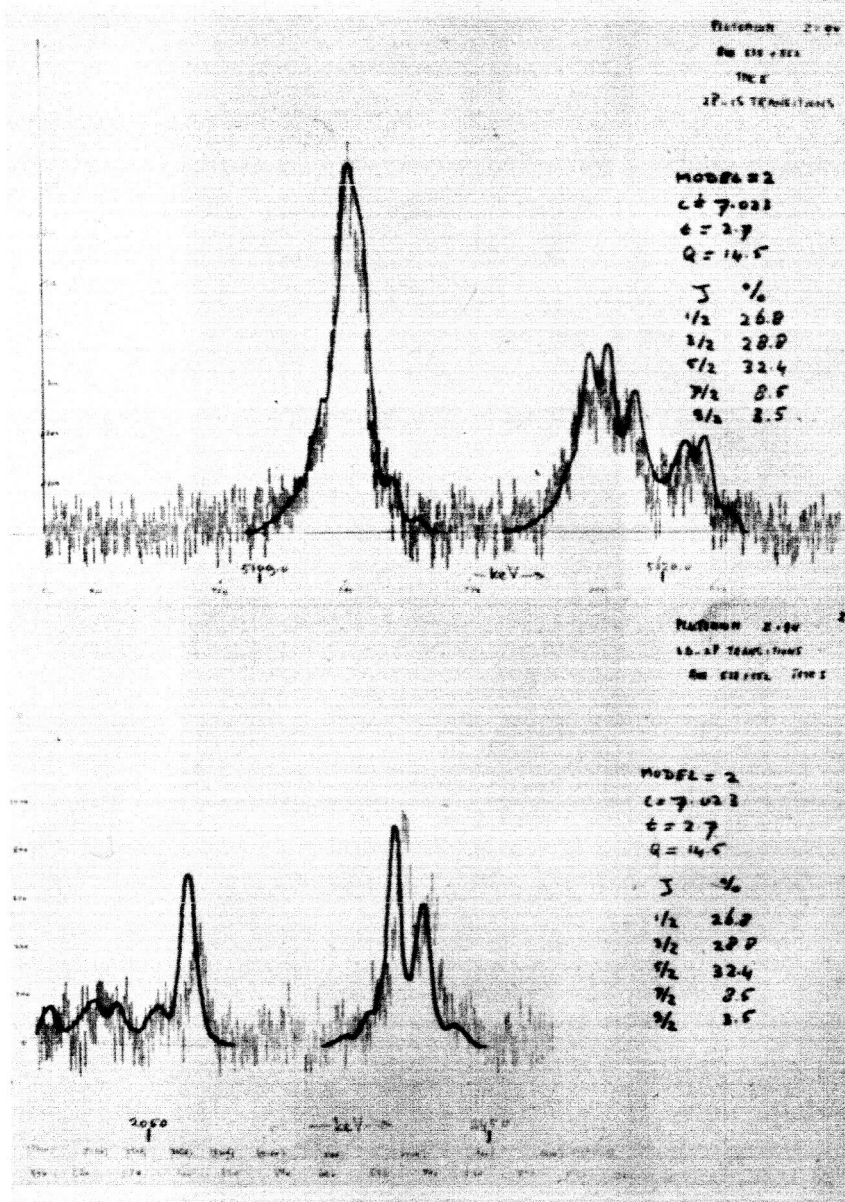


Figure 20

N66-135  
32735

DETAILED ANALYSIS OF MUONIC X-ray SPECTRUM FROM STRONGLY DEFORMED e-e NUCLEI.

K. Runge, T. T. Bardin, R. Barrett, S. Devons, D. Hitlin,

E. R. Macagno, C. Nissim-Sabat, J. Rainwater, and C.S.Wu

Columbia University

The study of dynamic E2 interaction in  $\mu$ -mesic atoms yields important information about the quadrupole moments of deformed nuclei.<sup>1)2)3)</sup> Here, as opposed to the quadrupole h.f.s. splitting of electronic atoms, however, not only the sign and size of the ground state moments are responsible for the h.f.s. splitting, but also the sign and size of the quadrupole moments of the excited states and the transition probabilities  $B(E2)$  to these and the ground state. This way one observes an E2 splitting pattern even for  $I=0$  or  $I=1/2$  ground state spin nuclei in the case of  $\mu$ -mesic atoms.

The matrix element of the interaction can be written as

$$\langle I_n e_j, FM | H_Q | I_n' e_j', FM \rangle = -\frac{1}{2} e^2 Q_0 \times \langle \phi_n e | F(r) | \phi_n' e \rangle \times \text{ang. man. factors}$$

The reduced matrix element  $\langle \phi_n e | F(r) | \phi_n' e \rangle$  which we might call a quadrupole form factor contains the important information about the radial distribution of the quadrupole moment in the nucleus. The size of the quadrupole interaction depends on the product of the quadrupole moment and the form factor so that it is impossible to determine the two separately from  $\mu$ -mesic transitions having the same or approximately the same radial wave functions in the initial,

\* This work is partially supported by the United States Atomic Energy Commission and the Office of Naval Research.

PRECEDING PAGE BLANK NOT FILMED.

respectively in the final state. In order to have an independent determination one has to measure d-state and p-state h.f.s splitting as well. The accurate determination of the d-state splitting, however, is generally quite difficult.

In a different approach, one might take the  $B(E2)$  values as determined by life time measurements of nuclear states or by coulomb excitation and compute only the radial matrix elements from the h.f.s. experimental splitting. Here then, the limiting factor of the accuracy of the so determined matrix elements is the accuracy of the coulomb excitation measurements.

I want to present here results of measurements on the three even Tungsten isotopes,  $W^{182}$ ,  $184$ ,  $186$ , on  $U^{238}$ , and on  $Sm^{152}$ . The Tungsten isotopes lie rather at the end of the deformed nuclei and their nuclear spectroscopic features are well described by the Bohr-Mottelson theory. They all have low lying excited rotational states with large transition probabilities  $B(E2)$  to the ground states. We therefore expect to see the dynamic hyperfine structure very clearly. Moreover, since we keep  $Z$  constant and vary the number of neutrons, we will get information on the isotope shift and changes in the nuclear structure as neutrons are added, in addition to those known from nuclear spectroscopy.

$Sm^{152}$  is on the lower end of the deformed nuclear region and has high deformation and a large quadrupole moment. The dynamic h.f.s. is again expected to be large.  $U^{238}$  finally should show a dynamic  $E2$  mixing not only in the p-states, but also in the d-states which then strongly affects the intensities in the h.f.s. lines of the  $2p \rightarrow 1s$  transition.



The experimental setup used was described earlier this morning by Prof. Devons. We used the W-isotopes as a metallic powder. The amounts were  $W^{182} \sim 80g$ ;  $W^{184} \sim 59g$ ;  $W^{186} \sim 44g$ .  $Sm^{152}$  was in the form of  $Sm_2O_3$  and a total of about 30g was used in the experiment. Typically about 100 h of running time was required for each isotope to accumulate enough counts.

In the first figure, I would like to show the spectrum of the K X-rays from  $W^{182}$ . We clearly resolve five lines, the energy of which we can determine accurately without complicated folding. The resolution of the detector is  $8 \pm .5$  keV in this energy region.

Figure 2 shows the spectra which we got for the three isotopes  $W^{182}$ ,  $184$ , and  $186$ . There is one peculiarity in these seemingly very similar spectra. Line 5 and 8 are in this order visible in the  $W^{182}$ . They change position as we go to  $W^{186}$ . In  $W^{184}$  they just pass each other and could not be resolved. Furthermore, you might keep in mind the size of the line number 7 for later comparison.

We have done some calculations in order to extract some of the features of these nuclei. The results are given in the Figure 3.

Because, the nucleus can be left in an excited state, preferentially in the first rotational state, this energy should therefore appear as an energy difference between pairs of lines in the h.f.s. spectrum. One such pair is number 5 and number 6 which shows within the experimental errors the energy listed for each isotope.

As input data for the calculations we used the intrinsic quadrupole moments measured by coulomb excitation. We furthermore assumed the quadrupole moments of the first excited state to be equal

to the transition E2 moment in size. We then obtained values for the radial matrix element  $\langle \phi_{n_e} | f(r) | \phi_{n_e'} \rangle$ . These calculations are very sensitive to the B(E2) values which are published by Hansen, Olsen, and Skilbreit.<sup>4)</sup> It seems, however, that there is quite a discrepancy between the results of different groups measuring B(E2) in coulomb excitation. More accurate values are highly desirable.

With this now it is possible to demonstrate a few features of these nuclei. As we add neutrons to  $W^{182}$  the nucleus becomes less deformed as we approach the magic neutron shell 126, or, reach the nuclei of the transition region and leave the really deformed nuclei. The moment of inertia becomes smaller and the energies of the first excited states higher. This is equally reflected in the radial matrix elements, which become smaller as the nuclei become more spherical, i.e. the overlap between the quadrupole distribution  $f(r)$  and the muon wave functions become smaller. Equally the quadrupole moments become smaller and follow the trend.

We are now undertaking a program in calculating various charge distributions in order to find the proper description of  $f(r)$  for the three nuclei. This is especially designed to shed some light onto the relationship between the radial charge distribution or quadrupole moments and the moments of inertia.

We furthermore varied the ratio

$$g = Q_0(02)/Q_0(22) ; Q_0(02) = 4\sqrt{\frac{2}{5}} B(E2)$$

by a total of 30 percent and adjusted

$$d = e^2/10 Q_0(02) \langle \phi_{n_e} | f(r) | \phi_{n_e'} \rangle$$

so to give an optimum fit to the experimental data. From this we

can say, that with the shown experimental data we cannot fix to better than 10 percent, which is still too uncertain to be of interest to the Bohr-Mottelson model.

In Figure 4 we see the  $K_{\alpha}$  - spectrum of  $\text{Sm}^{152}$ . As you will notice in line number 7 it is not visible at all. The energy of the first excited state is 121.8 keV and the fine structure 88 keV; a best fit was obtained with  $a=31.5$  keV and  $Q_0=5.93$ . These values are still somewhat tentative, however.

The last two Figures deal with  $\text{U}^{235}$ . The quadrupole moment is very large here, 10.5 barn. Figure 5 shows the experimental spectrum. The agreement between the calculated energies and the experimental ones is very good once we fixed the values for the radial matrix element. There is, however, a not very good agreement in the intensities of the h.f.s. lines, although we included the mixing in the 3d-states. This is an important correction at this high Z.

Figure 6 shows the comparison between calculated and experimental values. The agreement is very good if we use the experimentally known quadrupole moment and the energy of the first excited state as input data to calculate the radial matrix element.

#### REFERENCES

- 1) J. A. Wheeler, Phys. Rev. 92, 812 (1953)
- 2) L. Willets, Dan. Mat. Fys. Medd. 29, No. 3 (1954)
- 3) B. Jacobsohn, Phys. Rev. 96, 1637 (1954)
- 4) O. Hansen, M. C. Olesen, O. Skilbreit and B. Elbek, Nuclear Physics 25, 634 (1961)

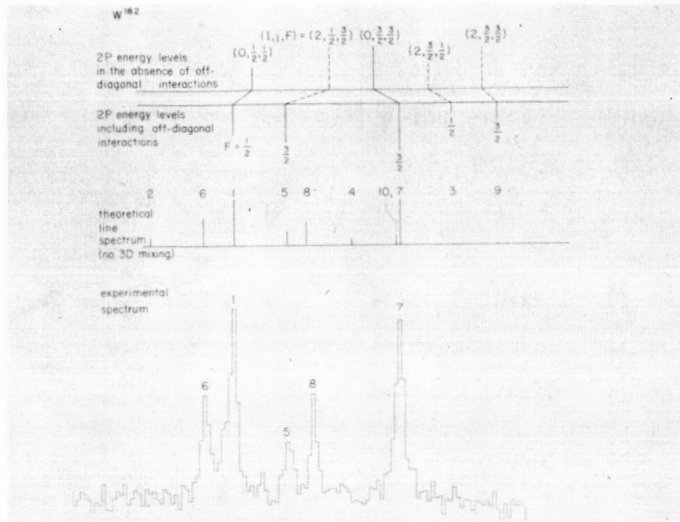


Figure 1. Muonic x-ray spectra and energy levels from  $W^{182}$ .

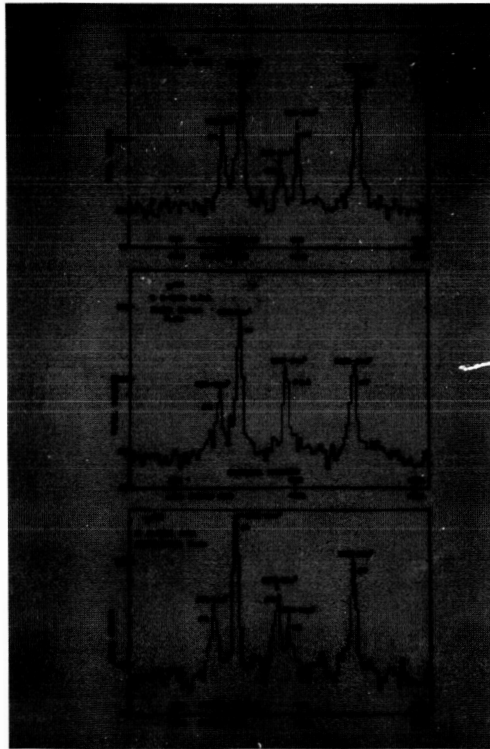


Figure 2. Muonic x-ray spectra from tungsten<sup>182</sup>, <sup>184</sup> and <sup>186</sup>.

X-ray Spectrum from Strongly Deformed e-e Nuclei

LIFE-LINE  $\alpha$  X-RAYS

(1)  $\alpha$  X-RAY SPECTRUM (2)  $\alpha$  X-RAY SPECTRUM

$\alpha = Q_0 \times (\frac{1}{2} + \frac{1}{2} \cos^2 \theta)$   $Q_0$  Transition Probability Moment

$\langle \phi | T | \phi \rangle$  The Expectation Value of the Rank-2 Dipole Operator  $T(2)$

| L <sub>1</sub> | 4f92      |           | 4f64      |           | 4f36      |           |
|----------------|-----------|-----------|-----------|-----------|-----------|-----------|
|                | Exp.      | Theo.     | Exp.      | Theo.     | Exp.      | Theo.     |
| 1              | 142.6 KeV | 142.6 KeV | 142.6 KeV | 142.6 KeV | 142.6 KeV | 142.6 KeV |
| 2              | 142.6 KeV | 142.6 KeV | 142.6 KeV | 142.6 KeV | 142.6 KeV | 142.6 KeV |
| 3              | 142.6 KeV | 142.6 KeV | 142.6 KeV | 142.6 KeV | 142.6 KeV | 142.6 KeV |
| 4              | 142.6 KeV | 142.6 KeV | 142.6 KeV | 142.6 KeV | 142.6 KeV | 142.6 KeV |
| 5              | 142.6 KeV | 142.6 KeV | 142.6 KeV | 142.6 KeV | 142.6 KeV | 142.6 KeV |
| 6              | 142.6 KeV | 142.6 KeV | 142.6 KeV | 142.6 KeV | 142.6 KeV | 142.6 KeV |
| 7              | 142.6 KeV | 142.6 KeV | 142.6 KeV | 142.6 KeV | 142.6 KeV | 142.6 KeV |

Figure 3. Table of tungsten K  $\alpha$  x-rays, theoretical and experimental.

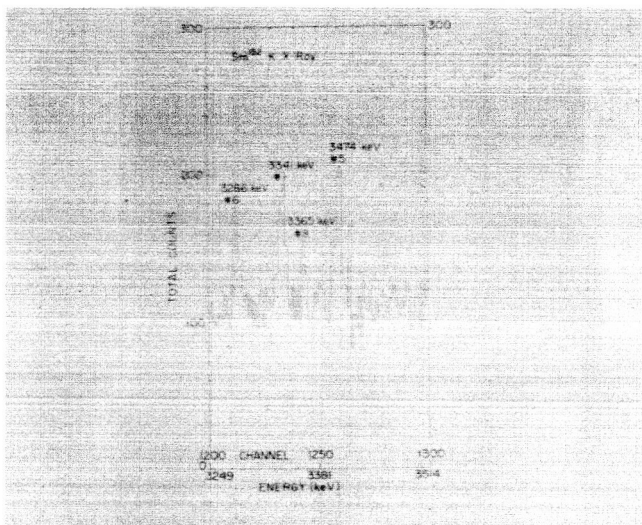


Figure 4. Sm<sup>152</sup> K muon x-rays.

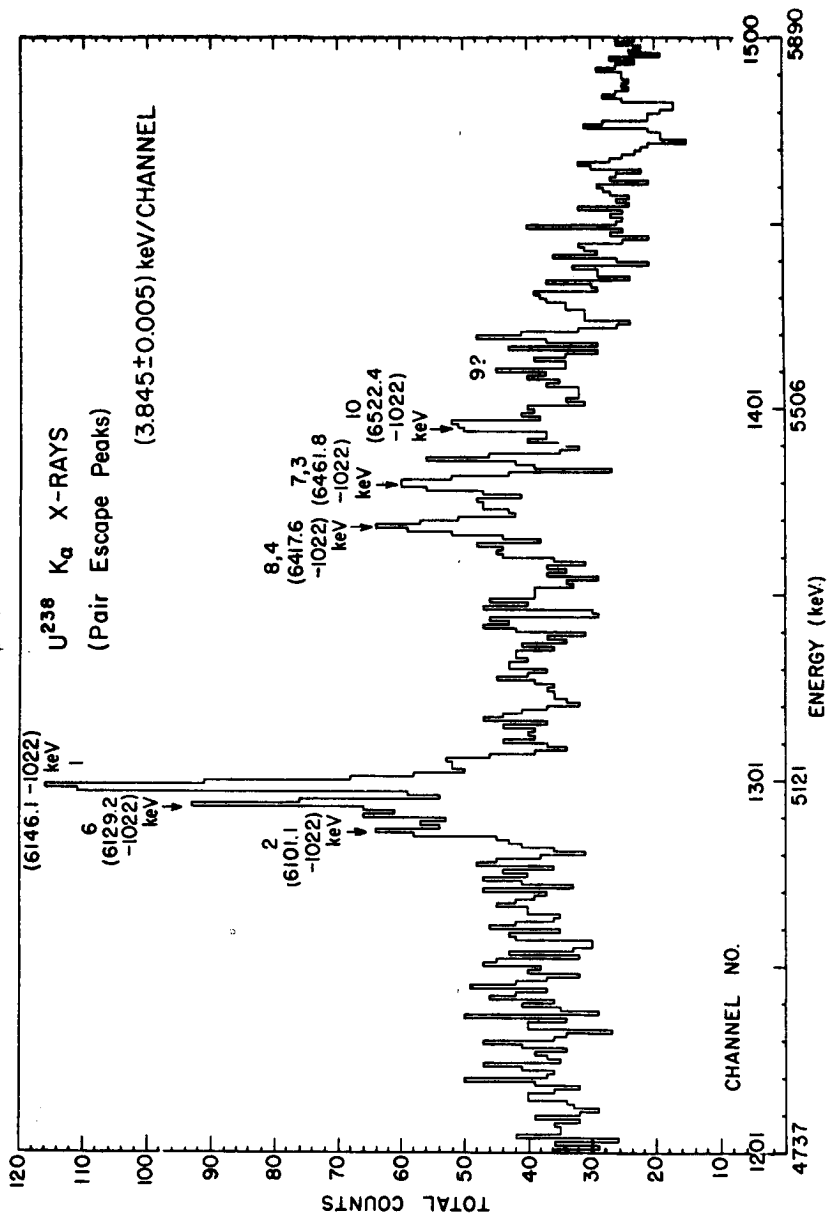


Figure 5.  $U^{238}$  muonic x-ray spectra and energy level diagram.

| $U^{238}$ K X-RAYS<br>ENERGY DIFFERENCES  |       |                   |
|---|-------|-------------------|
| EXPERIMENTAL (KeV)  |       | THEORETICAL (KeV) |
| $\Delta$ 7-1  | 315.7 | 316.1             |
| $\Delta$ 8-2  | 316.5 | 316.1             |
| $\Delta$ 8-6  | 288.5 | 288.9             |
| $\Delta$ 10-8   | 104.8 | 108.7             |
| $\Delta$ 7-8  | 44.2  | 44.7              |
| $\Delta$ 1-2  | 45.0  | 44.7              |
| $\Delta$ 6-2  | 28.1  | 27.2              |
| PARAMETERS: $E_n = 44.7$ KeV<br>$E_s = 234$ KeV<br>$\alpha = 94.5$ KeV<br>$\therefore$ if $Q_0 = 10.5$ b.<br>then $\langle \phi   f(r)   \phi \rangle = 6.26$ |       |                   |

Figure 6.  $U^{238}$  K x-rays tabulated (experimental and theoretical).

SESSION B

STRONG INTERACTIONS OF PIONS

Chairman, P. C. Gugelot



## PI-MESIC X-RAYS

K. M. Crowe

University of California, Berkeley

N66-32736-1

The work on pi-mesic x-rays that has been going on at the 184" Cyclotron in Berkeley can be broken into three experiments. One is an improvement on the pion mass value made with the 7.7 m curved quartz spectrometer which has been done by Mr. Robert Shafer for his Ph.D. Thesis at Berkeley. The second is the measurement of the strong interaction shift in the 3d-2p transition due to a shift in the 2p level. This measurement was done by A. Astbury, J. Deutch, R. Taylor, R. Shafer and myself with the same instrument. The third, on which I am afraid I will not be able to spend as much time as I would like, is work that is being done concurrently by Dr. David Jenkins. He would be here himself discussing this experiment for the fact that he is actually running the experiment now. We are using the semi-conductor technique in the study of pi-mesic x-rays and I will show preliminary data on the energy shifts for the s, p, d, and f states for a number of elements.

This program of research was begun before the 184" conversion to 740 MeV by Dr. Jesse DuMond, Mr. Ralph Peters, a mechanical engineer at the radiation laboratory, and myself. The object was to build a spectrometer to make precision measurements in the mesonic x-ray field. We had in mind at the time the problem of the masses, the vacuum polarization corrections and the nuclear shifts. The s state shift was the only known shift at the time; the p state shifts were shown to be small and in fact were not believed to be significant at that time. We also had some hope of extracting nuclear parameters out of these data.

It was clear that at that time it was necessary for us to make a substantial improvement in the resolution of the detectors and Dr. DuMond suggested that we copy the Argonne 7.7 m spectrometer and apply it to the mesic x-ray problem.

Figure 1 shows the crystal which is bent to a radius equal to the 7.7 m. The x-rays strike the crystal and are diffracted through a small angle, pass through the collimator and are counted in the detector. The basic resolution of the instrument is determined by the quality of the crystal. The collimator only acts as a shield to prevent direct gamma rays from being detected.

Figure 2 shows the geometry. The crystal can be tilted with respect to the axis of the beam by the sine screw mechanism. The arm is moved by microscope screw, and if one knows the distance to the contact point of this arm and the calibration of the screw, then one can convert it to the sine to the angle and hence, measure the wavelength relative to the crystal spacing. As the crystal is moved through an angle  $\theta$  with respect to the incidence direction, the collimator is moved through an angle  $2\theta$  such that the rays that leave will pass down the axis of the collimator. The collimator is approximately three feet long. The detector is surrounded with heavy shielding, and a counterweight balances out the excess weight on the detector arm. The whole system rotates on a gun mount which sets on a 30 ton concrete block cast into the floor. The quartz crystal is bent on a stainless steel block accurately ground with a cylindrical convex surface by a very ingenious method which was used by the Argonne group for their spectrometer and this crystal block was made with the same machine. The concave block is ground to match the convex block. The crystal is then imprisoned between two blocks as shown in Figure 3. There is a rubber gasket to distribute the load on the crystal. One observes the Newton fringes when the crystal is bent and the dark central fringe spreads uniformly toward the edge. The crystal is 6 mm thick,

8.8 inches on a side. The first Argonne crystal was 6 mm thick and 12 x 12 inches and it broke on bending. Subsequently they went to a 4 mm crystal. So far we have been lucky enough to have ours survive for about two or three years.

A calibration source, whose dimension is small compared to the resolution of this device measures the crystal quality. In Figure 4 the full width at half maximum is 17' of arc. This compares favorably with the half dozen other spectrometers in the world.

Table 1 is a summary of the details of the apparatus.

The spectrometer resolution is calculated as

$$\Delta E = 1.6 \times 10^{-5} E^2 \text{ (keV)},$$

in other words, the higher the energy, the poorer the present resolution which is just the opposite to the Ge-detector situation where the higher the energy the better the resolution. And for our energies, for example 100 keV, it turns out to be 0.16 percent.

Figure 5 is a picture of the tower in which the crystal is mounted. Note the microscope screw which rotates the crystal holder.

Figure 6 shows the overall layout. The beam for the pions is extracted, collimated, bent and re-focused on to the target which is about 8 inches high. The gamma rays which are produced pass through an additional concrete shield to the spectrometer. Notice that the x-rays are diffracted either to the right or to the left to cancel out uncertainty the zero of the device. Figure 7 shows the details of the target. The beam is brought in at about a momentum 200 meV/c., slowed down, the electrons are anti-coincided out and about  $10^6$  pions emerge from the degrader per second and about  $10^4$  stop in the target. Finally there are two anti-coincidence counters, to reject the pions which did not stop. The depth of field of the spectrometer is larger than the target dimensions. The main reason why

we restrict the dimension to 1/4 inch is the self-absorption of the out-going x-rays in the target material itself. The transverse dimension contributes to the resolution. The size of this target is matched to the crystal resolution.

In Figure 8, the efficiency of curve crystal spectrometer shows two effects. For high energy there is a  $1/E^2$  loss due to loss of reflectivity and it very seriously limits what we can do with this device. In order to go up to several hundred keV we sacrifice a factor of approximately 10 yield from our maximum. On the other hand in the lower energy direction we are limited by the self-absorption of the quartz crystal itself. For these reasons we limited ourselves to the region from 30 to 100 keV in our primary work. You notice that the efficiency is of  $10^{-6}$  so that the rate is  $10^{-2}$  counts per second. The data comes in at a very low rate.

Figure 9 shows the measurements of the 4f-3d transition in both Ca and Ti which are used for the mass measurements. The large background is associated with an accidental coincidence between the real stopping pions and the singles counting rate due to radioactivity in the Sodium Iodide detector itself. In the future, we plan to change detectors when we can obtain big enough semi-conductor detectors to put in place of present Sodium Iodide.

The positions of the peaks are converted into x-ray energy and we've measured several sources which have been measured in other laboratories; we find that our crystal seems to also have an overall absolute calibration which is quite comparable again with the other instruments of this type. Therefore, we have confidence in the accuracy of the sine screw, the quality of the crystal, the temperature controls, etc.

Table II gives a conversion of position of the line to energy. Table III shows the calculations of the energies of the level for a Ca line and a Ti line

for the 4f-3d transition. The second order of vacuum polarization correction is calculated and we estimated the fourth order of vacuum polarization correction. The estimate of the strong interaction correction is based on the data which comes from the shifts which will be discussed later. The result of the two measurements is  $M_{\pi} = 139.577 \pm .014$  mev.

Now the best previous value consisted taking the mass measurement of the muon, which was mentioned by Telegdi, and the difference between the pi and the mu which is measured by Barkas, Birnbaum and Smith in a photographic emulsion experiment to obtain  $M_{\pi} = 139.60 \pm .05$  MeV which is in good agreement with our value. There is a possibility of taking the mass of the pi and the mass of the mu and using energy conservation in the decay to evaluate the mass of the mu neutrino,

$$M_{\nu}^2 = (M_{\pi} - M_{\mu})^2 - 2M_{\pi}T_{\mu} .$$

In Figure 10 the results are shown graphically for various neutrino masses. The mass of the pi is known well enough that most of the error in the ordinate comes from the measurement of the kinetic energy obtained in the emulsion measurement which gives a spread as indicated. On the other hand, measurements of the mass difference restricts us to an elliptical zone. The likelihood for surfaces 68% confidence gives

$$M_{\nu} = 0 \pm 2.1 \text{ mev}$$

whereas the 90% confidence gives us 2.7. The error is somewhat improved over the previous measurements and comes almost entirely from the emulsion value of  $T_{\mu}$ .

The strong interaction part of the energy level has been observed for the aluminum transition of the energy shift in the p state in another experiment. The 3d-2p transition in aluminum has an energy of 87 keV and various corrections can be calculated accurately with the exception of the strong interaction. Table IV shows the results. There is a net discrepancy for the transition which amounts to  $244 \pm 80$  volts.

The major source of error in the measurement is statistical. Figure 11 shows the data. These data were taken before the mass data with two or three times more background. The changes made between the two measurements were that the collimator slits were opened up to factor of 3 and there was improvement in the timing of the electronics.

The recent work with semi-conductors is going on at this time. Figure 12 is a picture of the geometry. The defector is a 6 cm<sup>3</sup> Ge Li-drifted detector which has a resolution of about 3-5 keV at the energies that we are talking about and these energies range from 30 or 40 keV up to 700 keV. Figure 13 shows an example of the spectra one obtains from a Ta target.

In Figure 14 the data is shown for the difference between the calculated energy for the 3d-2p transition and the measured energy, the lower curve represents the correction due to the vacuum polarization and the top curve is drawn through the points. Based on the  $\pi$  nucleon 3-3 state, an approximate formula was given by Wolfenstein in 1956 -

$$\frac{\delta E}{E} = - \frac{\delta_{33}}{\eta^3} \left( \frac{Z}{3} + N \right) (Z\alpha)^3$$

The predicted shift corresponds to attractive potential as observed. Recently Ericson has reanalyzed in detail the shift in the p state using a multiple scattering approach including the small phase shifts, the Lorentz Lorenz effect and numerous other corrections. His results are in substantial agreement with the data. In terms of a local s state potential and non-local p state potential we can write

$$\delta E = V_L \int \psi^2 \rho(r) d\tau + V_{NL} \int |\nabla \psi_\pi|^2 \rho(r) d\tau$$

where  $V_L = +10 \pm 2$  Mev and  $V_{NL} = -80 \pm 20$  Mev (Fermi)<sup>2</sup>, using conventional

density parameters for the nucleus. For s, p, and d states it fits the data adequately. Further details of his calculations will appear in his paper at this meeting.

Figure 15 shows the shift in the 4f-3d transitions and Figure 16 shows the presence of a residual shift in the 5g-4f transitions. Here the magnitude of the shift is larger than calculated with the potentials, although it is possible that the nuclear parameters are not chosen to fit up to uranium.

Figure 17 shows the kind of yield data which we obtain for the 5g-4f transitions. The detailed analysis and interpretation of this and similar results are going on presently.

In summary measurements of the energy levels in II - nucleus atoms are being remeasured with higher accuracy. Currently significant line widths are also observed. The study of relative yields of specific transitions is underway.

Table I. Important Parameters of the Bent Crystal Spectrometer

|   |   |   |
|---|---|---|
| Crystal:                                    | Type  | quartz (310)                                      |
|   | Dimensions  | 20 x 20 x 0.6 cm <sup>3</sup>                     |
|   | Aperture  | 160 cm <sup>2</sup>                               |
|   | Focal Circle Diameter                               | 764 cm  |
|   | Intrinsic Resolution <sup>a</sup> (fwhm)            | 17 sec of arc                                     |
|   | Corresponding Energy Resolution (fwhm) <sup>b</sup> | $\Delta E = 1.6 \times 10^{-5} E^2 \text{ keV}$   |
|   | Projected Resolution at Target (fwhm)               | 0.063 cm  |
|   | Depth of Field                                      | 8 cm  |
|   | Maximum Overall Efficiency                          | $\sim 2.5 \times 10^{-6}$ at 50 keV               |
|   | Sine Screw:   | Maximum Measurable Angle <sup>a</sup>             |
| Corresponding Minimum Energy <sup>c</sup>   |   | 40 keV  |
| Precision Presently Obtainable <sup>a</sup> |   | $\pm 0.4$ sec                                     |
| Corresponding Energy Precision <sup>b</sup> |   | $\sigma = \pm 3.8 \times 10^{-7} E^2 \text{ keV}$ |
| Collimator:                                 | Overall Dimensions                                  | 18 x 18 x 94 cm                                   |
|   | Plates  | 44 Pb alloy plates 1 mm thick                     |
|   | Gaps  | 3 mm (tapered)                                    |
|   | Resolution (fwhm)                                   | 900 sec of arc                                    |
| Detector:                                   | Type  | NaI (Tl)  |
|   | Dimensions  | 17 x 17 x 0.63 cm <sup>3</sup>                    |
|   | P.M. Tubes  | 9 RCA 6810's                                      |

<sup>a</sup> 1 sec  $\approx$  0.011  $\mu$

<sup>b</sup> At 50 keV, the resolution is 40 eV (fwhm) and the obtainable precision about  $\pm 1$  eV.

<sup>c</sup> First order both sides



Table II. Results of Experiment.

| <u>Parameter</u>                       | <u>Calcium 4F-3D</u>                     | <u>Titanium 4F-3D</u>                   |
|--|--|---|
| Diffraction peak location:             |  |   |
| Left (turns)                           | $-50.6829 \pm 0.0089$                    | $-41.7517 \pm 0.0057$                   |
| Right (turns)                          | $+51.5585 \pm 0.0068$                    | $+42.6462 \pm 0.0042$                   |
| Midpoint (turns)                       | $+0.438 \pm 0.006$                       | $+0.447 \pm 0.004$                      |
| Separation $\times 0.5$ (turns)        | $51.1207 \pm 0.0056$                     | $42.1989 \pm 0.0036$                    |
| $\sin \theta_B$ ( $18^\circ\text{C}$ ) | $0.0726120 \pm 119 \text{ ppm}$          | $0.0599388 \pm 84 \text{ ppm}$          |
| Wavelength                             | $171.004 \text{ xu} \pm 126 \text{ ppm}$ | $141.155 \text{ xu} \pm 98 \text{ ppm}$ |
| Energy                                 | $72.352 \text{ keV} \pm 127 \text{ ppm}$ | $87.651 \text{ keV} \pm 99 \text{ ppm}$ |

Table III. Calculation of the 4F-3D Pionic Calcium and Titanium Transition Energies Using  $M_\pi c^2 = 139.580$  MeV.

| <u>Effect</u>                                | <u>Calcium</u>         | <u>Titanium</u>        |
|--|------------------------|------------------------|
| Klein-Gordon Equation                        | $72.388 \pm 0.001$ keV | $87.622 \pm 0.001$ keV |
| Reduced Mass                                 | $- 0.270 \pm 0.001$    | $- 0.273 \pm 0.001$    |
| Vacuum Polarization (Second-Order)           | $+ 0.230 \pm 0.002$    | $+ 0.301 \pm 0.002$    |
| Vacuum Polarization (Fourth-Order)           | $+ 0.002 \pm 0.002$    | $+ 0.002 \pm 0.002$    |
| Strong-Interaction Shift                     | $+ 0.002 \pm 0.002$    | $+ 0.004 \pm 0.004$    |
| Orbital-Electron Screening                   | $- 0.001 \pm 0.001$    | $- 0.001 \pm 0.001$    |
| Electromagnetic Form Factors                 | negligible             | negligible             |
| Lamb Shift                                   | negligible             | negligible             |
| $\pi$ -Atomic Recoil                         | negligible             | negligible             |
| Calculated Transition Energy                 | $72.351 \pm 0.004$ keV | $87.655 \pm 0.005$ keV |
| Scale Factor:                                |                        |                        |
| $\frac{M_\pi c^2}{\text{Transition Energy}}$ | $1929.21 \pm 55$ ppm   | $1592.38 \pm 57$ ppm   |

Table IV  
Calculation of the 3D-2p  $\pi$ -Mesic Transition Energy in Aluminum [  $E_{\alpha} = 139.59 \pm 0.05$  keV ]

| Calculation                 | 2P Level      | 3D Level   | 3D-2p Transition      |
|-----------------------------|---------------|------------|-----------------------|
| Schrödinger                 | 157.027 keV   | 69.790 keV | 87.237 keV            |
| Reduced Mass                | -0.869        | -0.386     | -0.483                |
| Klein Gordon                | +0.206        | +0.031     | +0.175                |
| Vacua Polarization (Koslov) | +0.112        | +0.083     | +0.359                |
| Finite Charge Distribution  | -0.003        | .000       | -0.003                |
| Electron Screening          | -0.001        | -0.002     | +0.001                |
| Total E. M. Calculation:    | 156.802       | 69.516     | 87.286                |
| Error (from $E_{\alpha}$ )  |               |            | $\pm 0.030$           |
| Measurement, this expt.:    |               |            | 87.530 $\pm$ .070 keV |
| Difference                  | Exp. - Theory |            | 0.244 $\pm$ .030      |

Strong Interaction Shift

$$V(r) = \frac{V_0}{1 + \exp\left[\frac{r - r_0}{\alpha}\right]}$$

Saxon Woods Potential:  $V_0 = -18 \pm 6$  keV

Perturbation Theory Calculation Yields  $R_0 = 1.2A^{1/3}$  f. ;  $\alpha = 0.6$  f.

MU.36764

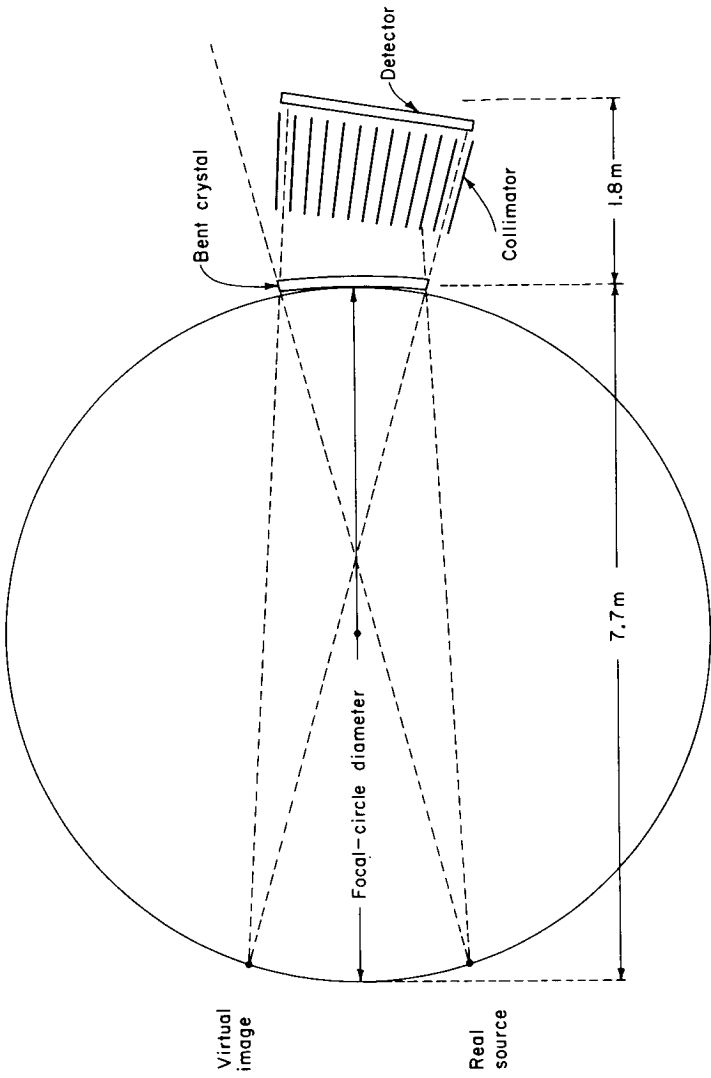


Figure 1. Bent crystal spectrometer.

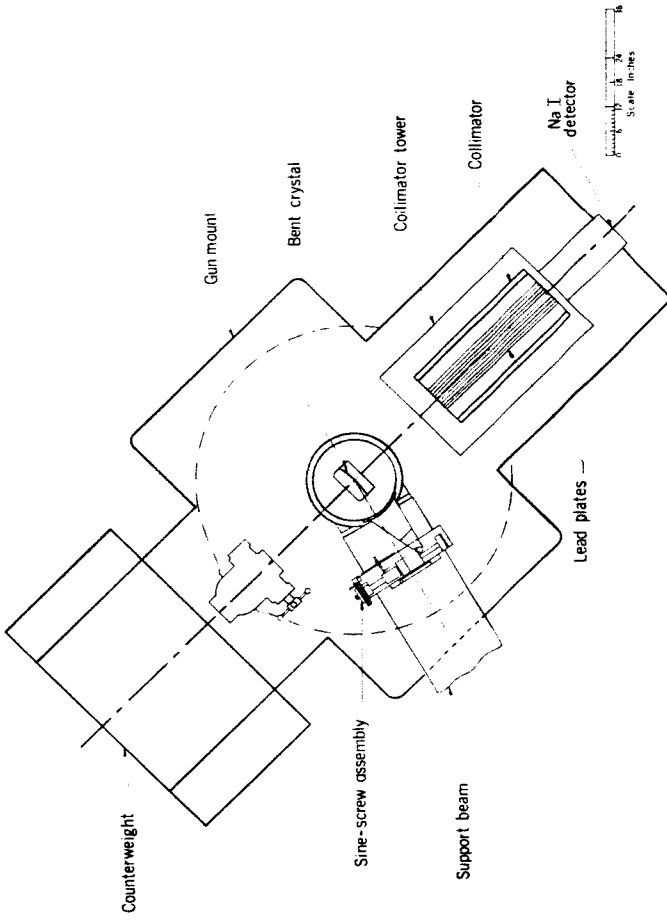


Figure 2. Gamma detection experimental layout.

AU-36737

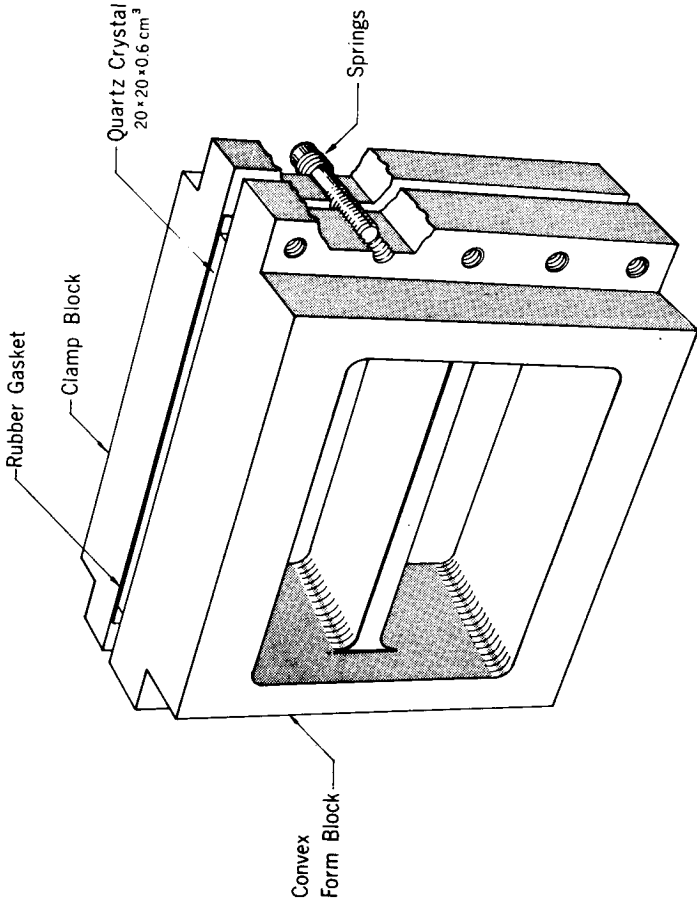


Figure 3. Crystal holder assembly.

## Pi-Mesic X-rays

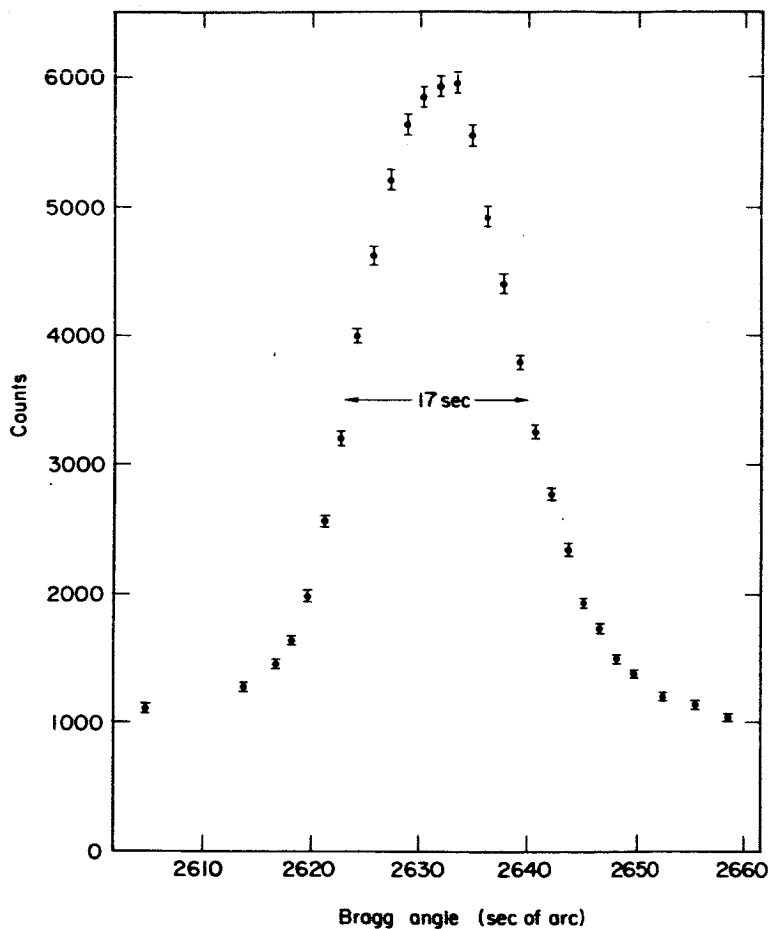


Figure 4. Measurement of crystal quality. Full width at half maximum is 17' of arc.

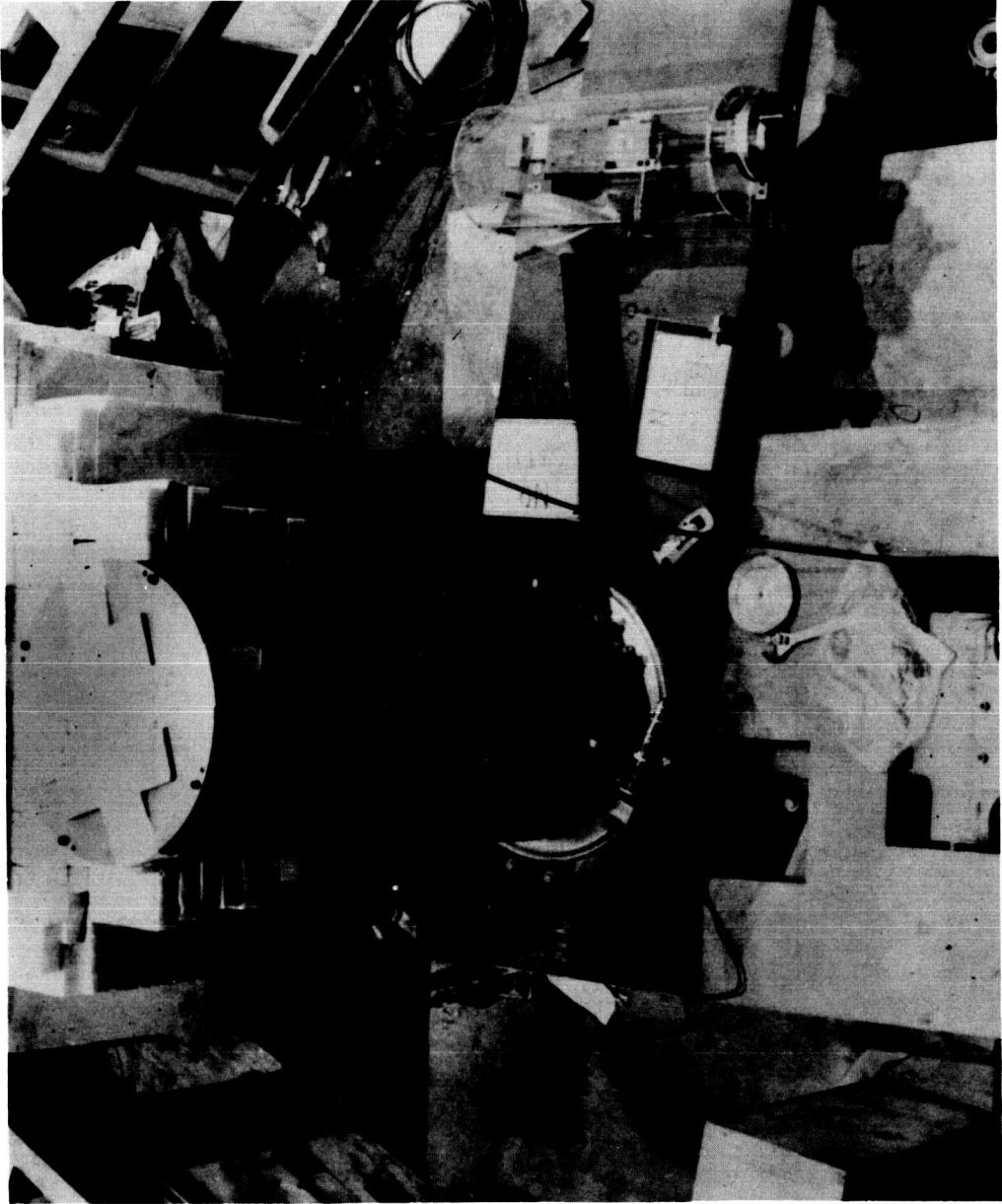


Figure 5. View of tower containing mounted crystal.



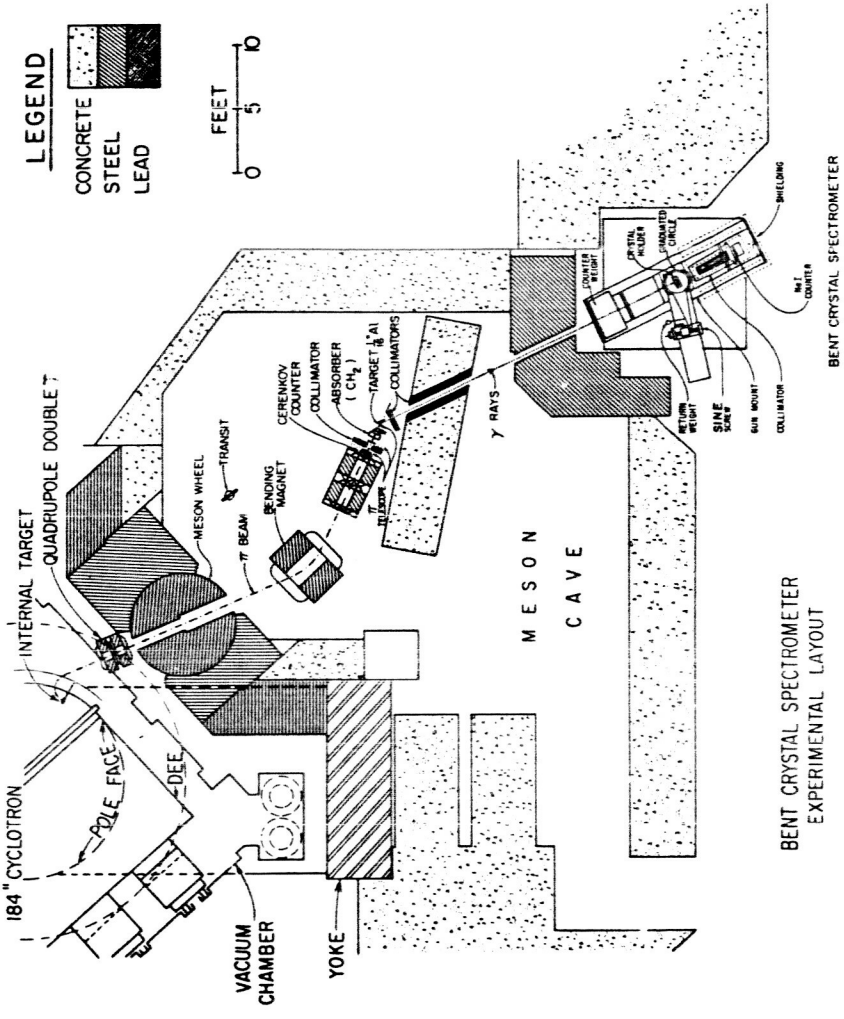
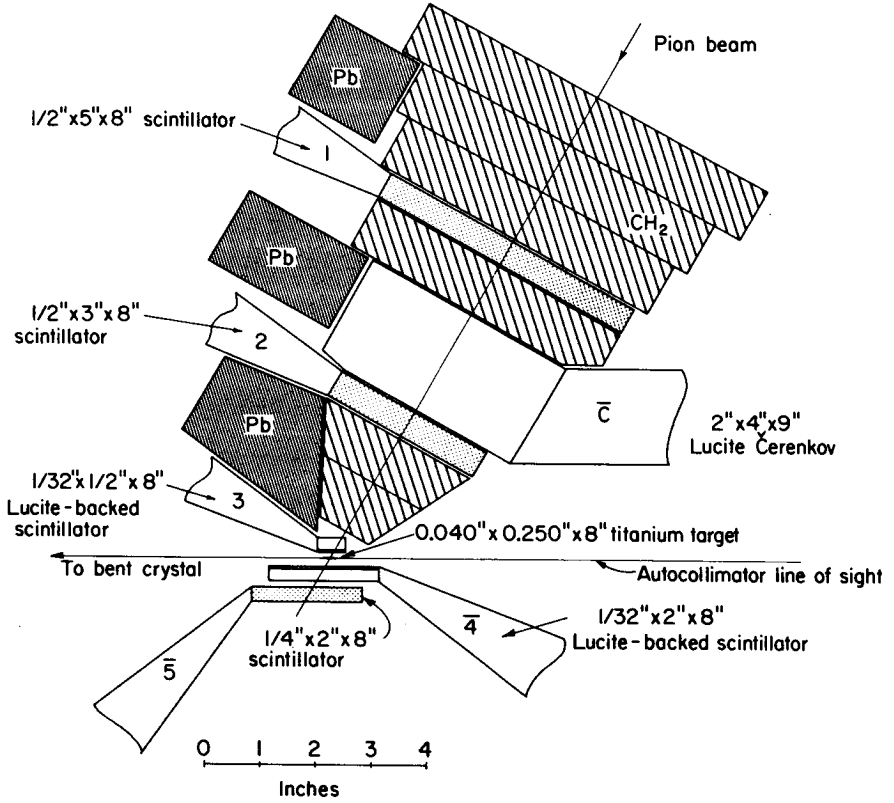


Figure 6. Overall experimental layout.



MUB-6015

Figure 7. Detail target layout.

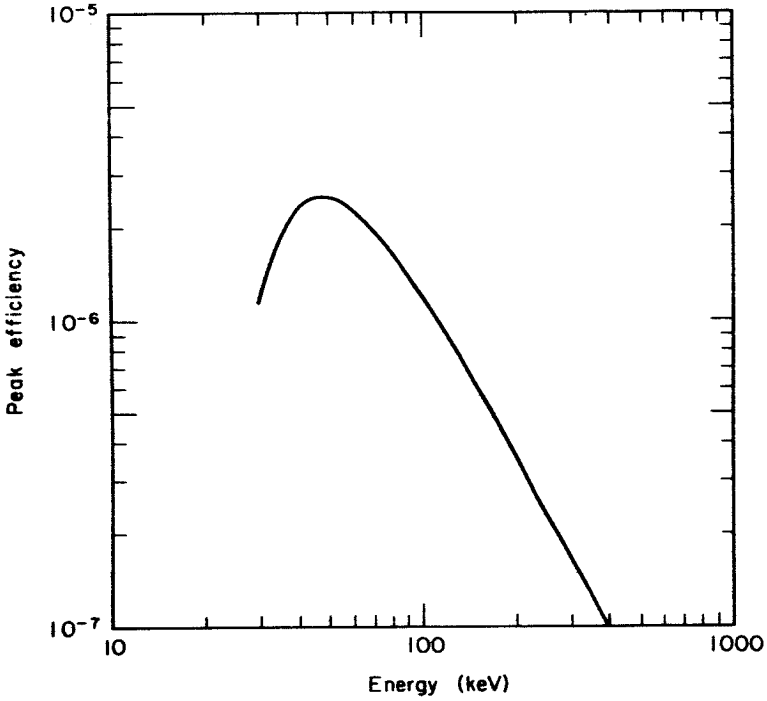
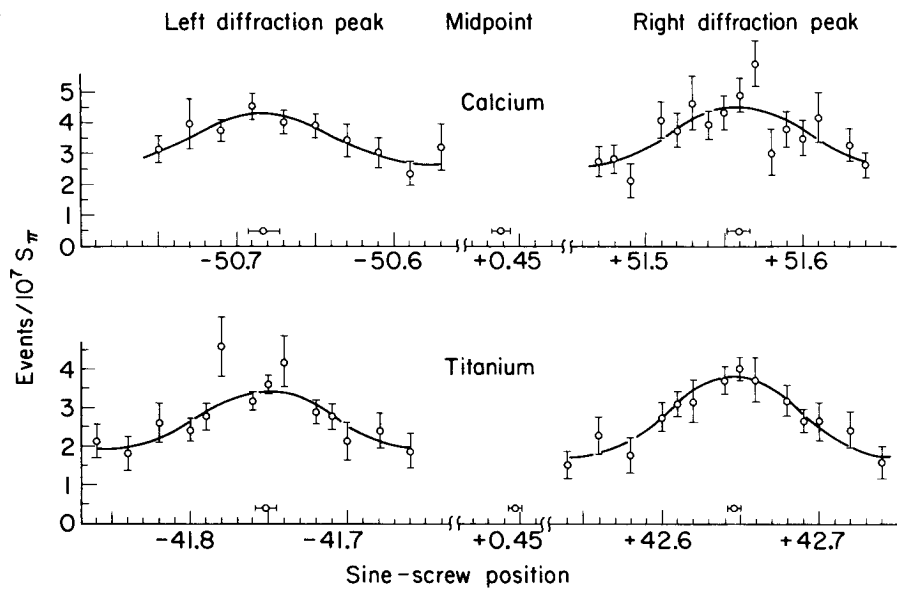


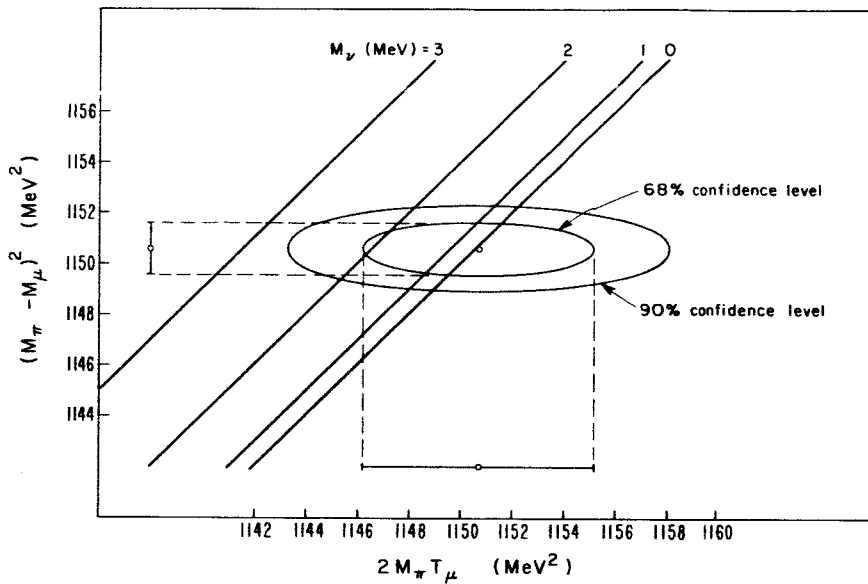
Figure 8. Efficiency of curved crystal spectrometer as a function of incident gamma energy.



MUB 6013

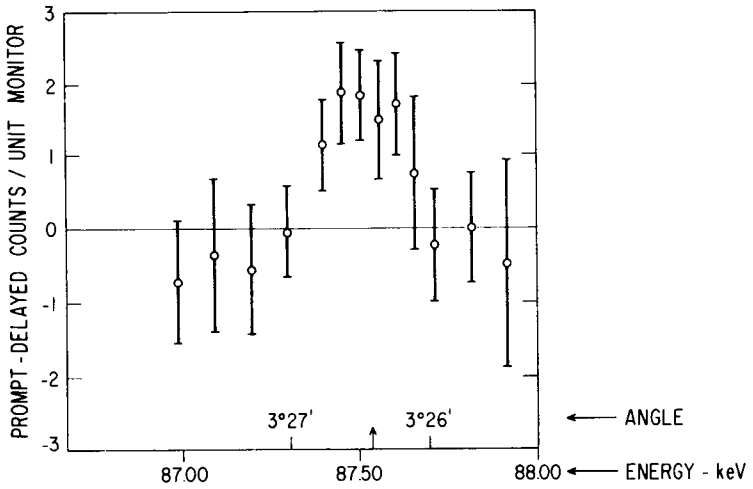
Figure 9. Measurements of the 4f-3d transition in Ca and Ti.

## Pi-Mesic X-rays



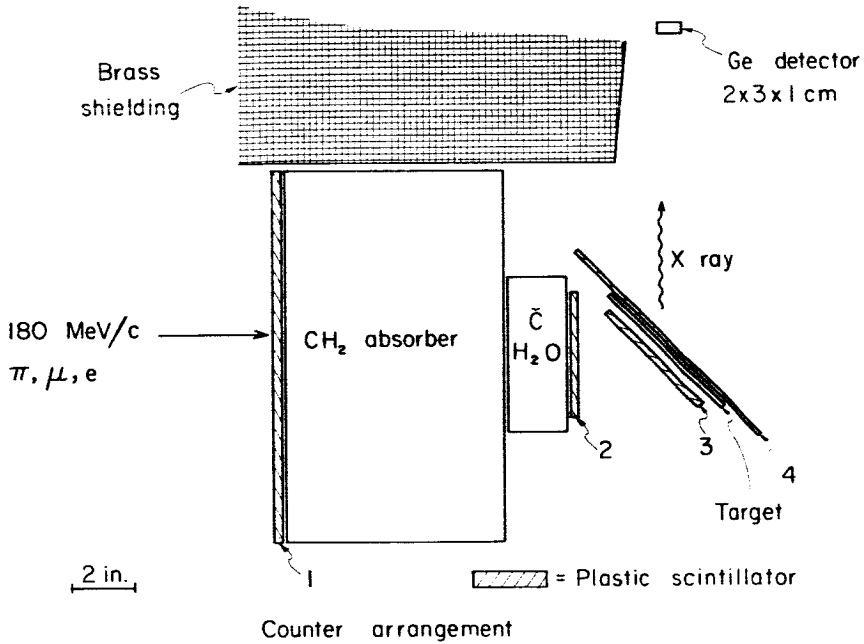
NUB 8510

Figure 10. Results of neutrino masses.



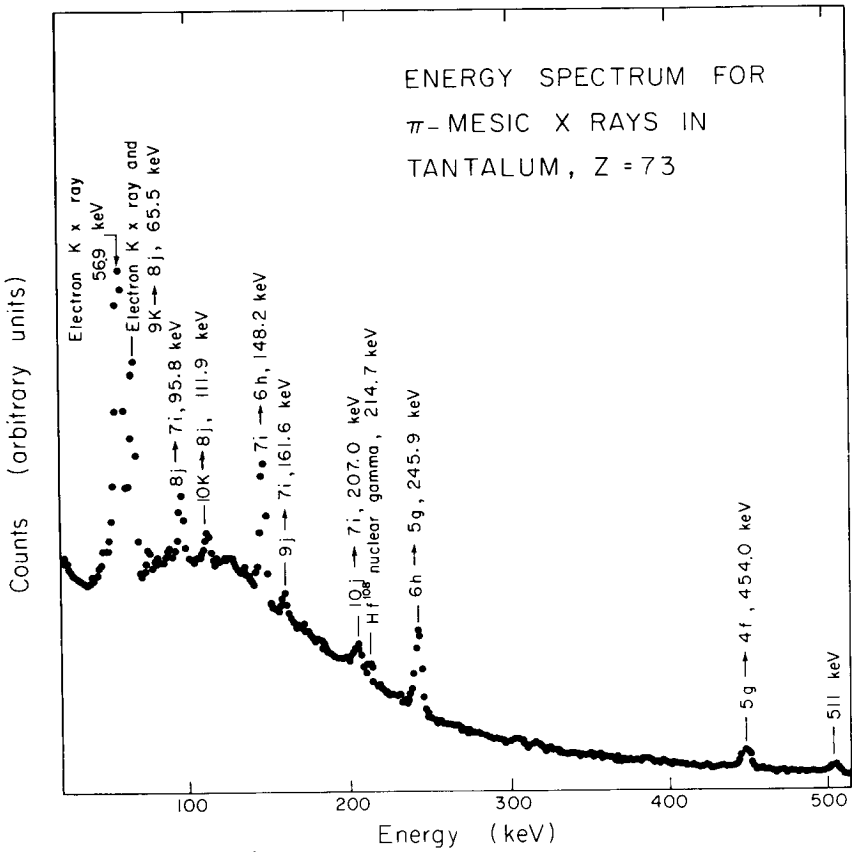
$\pi$  MESIC 3D-2P TRANSITION IN ALUMINUM  
 $\gamma$  COUNTING RATE VERSUS ANGLE  
 (POSITIVE AND NEGATIVE ANGLES COMBINED)

Figure 11



MUB-8377

Figure 12. Plan of Ge lithium drifted detector layout.



MUB-8374

Figure 13.



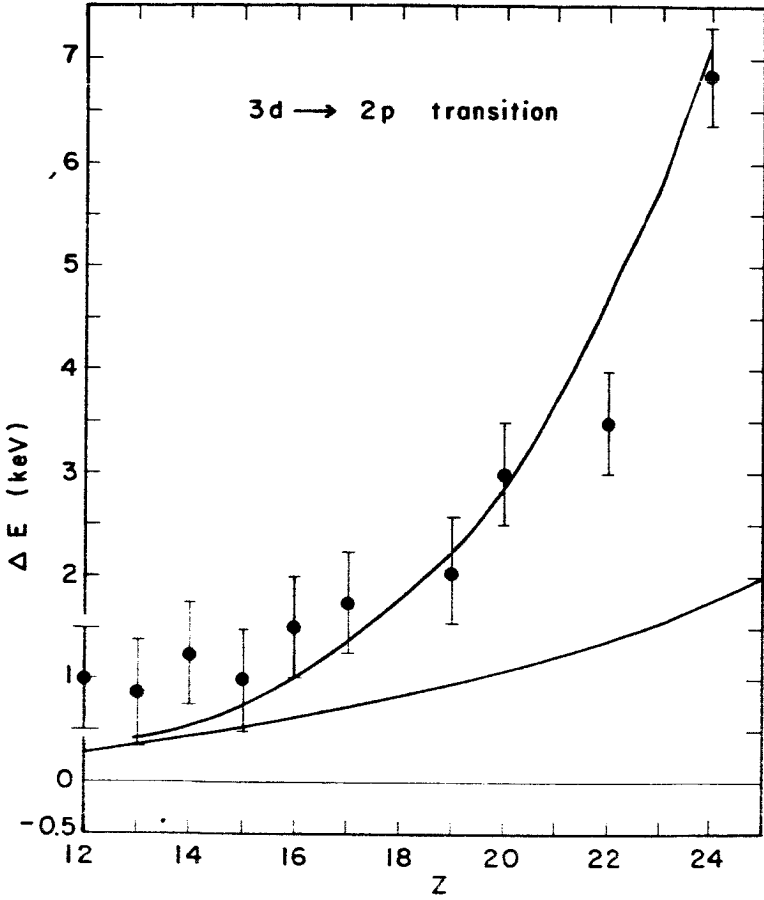
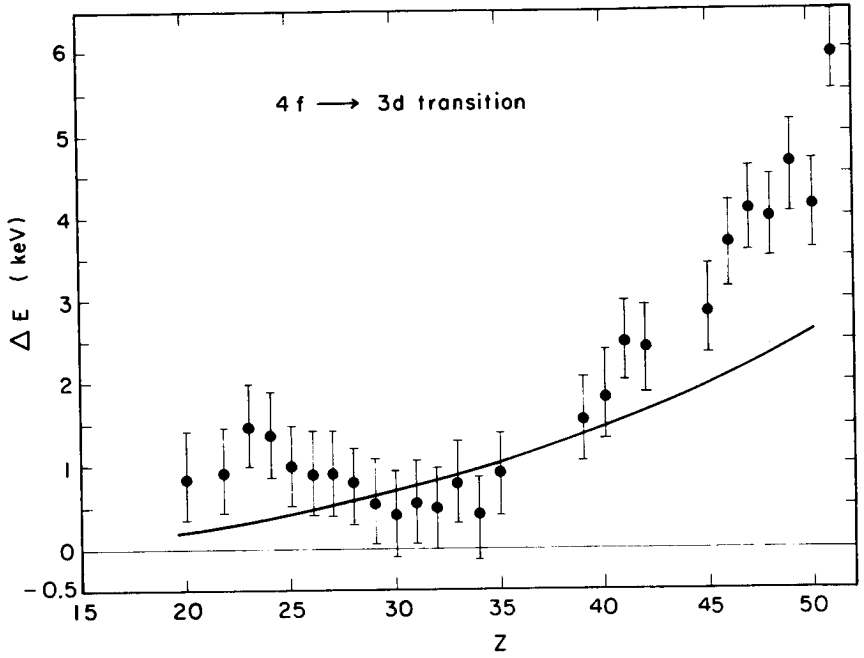


Figure 14. Difference between the calculated energy for the 3d-2p transition and the measured energy.



MUB-8379

Figure 15. Shift in the 4f-3d transitions.

## Pi-Mesic X-rays

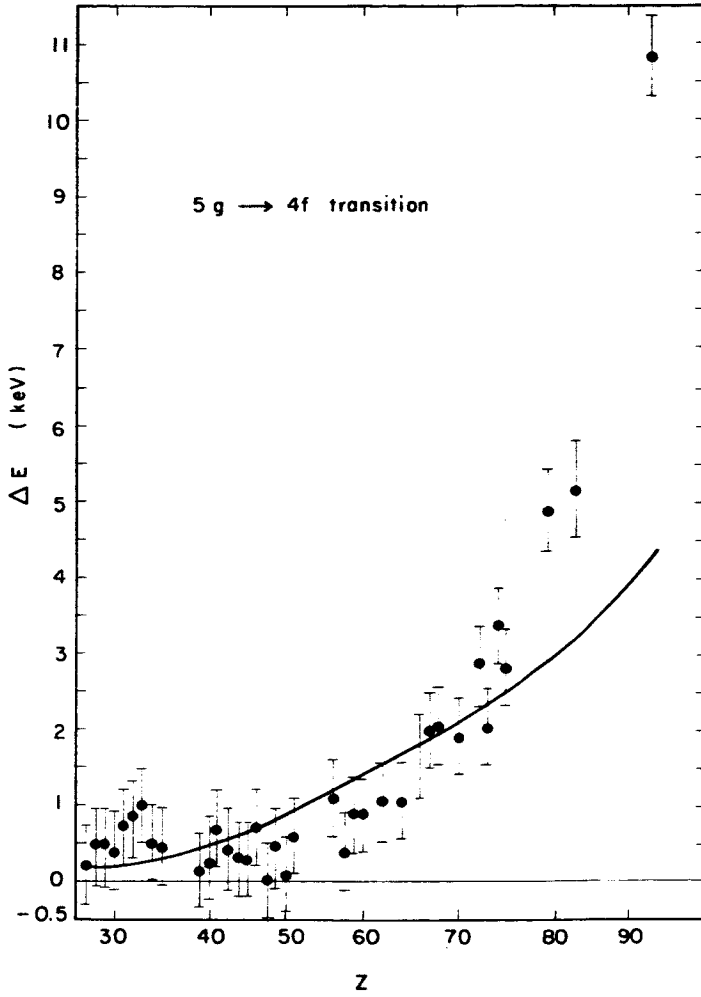
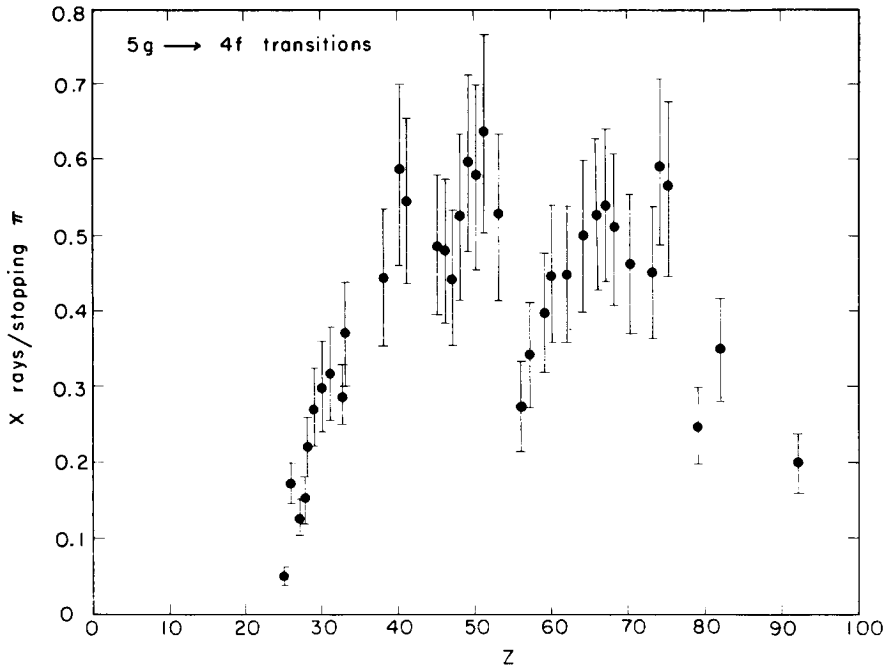


Figure 16. Presence of a residual shift in the 5g-4f transitions.



MUB-8380

Figure 17. Yield data obtained for the 5g-4f transitions.

TELEGDI: Why is it that, working in this energy range, you are not switching to a higher Z bent crystal like Ge or something that would have better effectiveness? Is it just a matter of size?

CROWE: The change to a different type of crystal is the next step. Getting a good quality crystal, the size that we need, is also difficult. What it does, in effect, is move that efficiency curve up so that the peak, instead of being about 80 kv, goes up to about 200 kv. For our measurements it's perfectly adequate; quartz is adequate. For 200 kv, we should have another detector.

ERICSON: Do you see any isotopic spin shifts in the elements as a function of Z in the 1s states.

CROWE: We haven't looked for them specifically yet. We've measured mainly the even-even isotopes.

ERICSON: I see and have all others been equal to zero?

CROWE: Yes, we have not done separate isotope studies yet, and I don't have anything to say about that.

ERICSON: These shifts are expected to be quite large.

CROWE: Yes.

POLARIZATION IN PION-PROTON SCATTERING

P. D. Grannis

University of California, Berkeley

N66 175  
32737

I wish to discuss two experiments measuring the polarization parameter in  $\pi$ -p scattering which are currently being completed in Berkeley. The first of these was done at the Berkeley 184 inch cyclotron with  $\pi^-$  beam momenta of 440, 460, and 515 MeV/c by Areus et. al. The second is still in progress at the Bevatron and will result polarization measurements in both  $\pi^-p$  and  $\pi^+p$  elastic scattering from 600 MeV/c to about 4000 MeV/c. Today I shall present some preliminary results for the energy region of 1 BeV and lower.

The primary objective of the lower energy measurement is, of course, to aid in the experimental reconstruction of pion-nucleon scattering amplitudes. Much progress has been made recently in the program of reducing the data to a set of phase shifts by Roper et. al. at Livermore, Awvil et. al. at London, Bransden et. al. at Rutherford, and Bareyre et. al. at Saclay; these solutions suggest some very interesting properties of the  $\pi$ -N interaction though there are several areas of disagreement. It is our hope that the present data will help resolve these differences and that we can begin on a similar analysis upward to 1.5 BeV. Of secondary interest to this conference is the objective of determining the spins and parities of some of the higher  $\pi$ -N resonant states.

The polarization parameter in  $\pi$ -p scattering is usually defined operationally as follows: let a pion beam be incident on an unpolarized proton target; the recoil proton is then analyzed for its component of polarization along the scattering normal - usually by a second scattering from carbon. This component of recoil proton polarization is defined as the polarization parameter P. An alterna-

PRECEDING PAGE BLANK NOT FILMED.

tive experiment can be performed in which the left-right asymmetry in scattering from a 100% polarized proton target is measured. This asymmetry,  $\epsilon$  - or, in the case of a target polarized to extent  $P_T$ ,  $(\epsilon/P_T)$  - defines another parameter  $P'$ .

The most general form of the  $\pi$ -p interaction can be written

$$M = g + \vec{h} \cdot \vec{\sigma}$$

In the case of a parity invariant interaction, this reduces to

$$M = g + h \hat{n} \cdot \vec{\sigma}$$

where  $\hat{n} = (\vec{k}_i \times \vec{k}_f) / |\vec{k}_i \times \vec{k}_f|$ , the normal to the scattering plane. In this case the two parameters  $P$  and  $P'$  are the same and become

$$P = \frac{2\text{Re } g^*h}{|g|^2 + |h|^2} .$$

It is clear at this point that there are distinct advantages in the use of a polarized target. Chief among these is that no second scattering is necessary so that the data can be collected more rapidly. Secondly, many of the sources for systematic error arising from alignment problems or poorly known analyzing power are removed and also, data may be collected at a wide range of angles at once. In  $\pi$ -p scattering there are further advantages in that the so-called "triple scattering experiments" now become possible - though not with the first generation of polarized targets.

The first figure[Figure 1 - "Experimental Arrangement"] shows the experimental arrangement in the current experiment. The pion beam is incident on the polarized target which is inside the tilted magnet. The target is stack of crystals ( $\text{La}_2\text{Mg}_3(\text{NO}_3)_{12} - 24 \text{W}_2\text{O}$ ) in which only the free protons in the waters of hydration are polarized. The magnitude of the target polarization is typically 50% and the direction is either in or out of the paper and can be reversed in 10 minutes.

Both final state particles are detected in counter hodoscopes above and below the beam. There are two arrays in each hodoscope corresponding to the  $\theta$  and  $\phi$  degrees of freedom; in each array the counters are overlapped to achieve a doubling in the number of bins. A hodoscope at the left measures the convergence angle in both planes of the incoming beam particle. The Cerenkov counter beneath the lower hodoscope distinguishes  $\pi^+$  from protons in the case that the kinematics are ambiguous between proton up or down.

The beam flux is typically  $10^6$   $\pi$ /pulse; in the case of the  $\pi^+$  beam, protons are eliminated by requiring a signal from a gas Cerenkov counter. Events satisfying rough constraints are coded in fast logic electronics and processed on line in a PDP-5 computer. Subsequent analysis proceeds first by requiring that the beam particle and the two final state particles define a plane to within rather close tolerances. This eliminates large fraction of the scattering from nucleons in the heavy target nuclei (which comprise 97% of the target crystals, by weight) since if the transverse component of the Fermi Momentum of the struck nucleon exceeds approximately 10 MeV/c, the coplanarity requirement is destroyed. For the remaining events, the elastic scattering peak stands out over the broad background of quasi-elastics by a factor varying from 5/1 to zero, dependent on the elastic differential cross section. At present we are capable of measuring the polarization if the cross section exceeds 30  $\mu\text{b}/\text{ster}$ . An accurate measure of the background is obtained by substituting a dummy target for the crystals, in which there are no free protons.

Before discussing the results of these experiments, I would like to summarize briefly some aspects of present knowledge of the  $\pi$ -N amplitudes. In particular I will refer to the work of Bareyre and co-workers in Saclay - not from any presumption that their solution is necessarily correct in all respects, but it is



representative and extends up to 1 BeV. The method they employ makes no assumption about the energy dependence of the amplitudes; rather they seek solutions at energies spaced at intervals of about 50 MeV. At some energies they achieve only one fit though more typically they do not; however by requiring that the various phase shifts and absorption parameters join smoothly at successive energies they have succeeded in identifying a unique solution. In their analysis they have used all available cross section data from  $\pi^-p$ ,  $\pi^+p$  and charge exchange, polarizations where they were available and dispersion relations for the forward amplitudes. I should point out that the polarizations are essential to the analysis due to the well known Minami ambiguity which states that the differential cross sections are invariant if all amplitudes are made to change their parities, while the polarizations change sign. In fact, it is one of the pleasant surprises of the analysis that one can get by without requiring the more difficult triple-scattering experiments.

Figure 2 shows a summary of the total cross sections in the 2 isotopic spin channels. In the  $I = 3/2$  channel the cross section shows the  $P_{33}$  resonance plus a shoulder at approximately 900 MeV. In  $I = 1/2$  channel there are bumps at about 600 and 900 MeV, normally attributed to resonant amplitudes  $D_{13}$  and  $F_{15}$  respectively (the notation is  $L_{2I,2J}$ ).

Turning now to the results of Bareyre, we see the  $F_{15}$  and  $D_{15}$  amplitudes in the complex plane, Fig. 3. The numbers parametrizing the locus of the amplitude is the invariant mass of the system and the circular boundary is the unitarity limit. The  $F_{15}$  shows the expected resonant behavior at 900 MeV; note, however, that the  $D_{15}$  amplitude is apparently resonating along with the  $F_{15}$ . Presumably the  $D_{15}$  resonance is masked in elastic channels by its high absorption. Figure 4 shows the  $S_{31}$  amplitude; here the amplitude is repulsive up to about 550 MeV at

which point it circles about in a clockwise direction. The interpretation is that there is a highly inelastic resonance in this channel superimposed on a repulsive non-resonant amplitude; this resonance at about 900 MeV could then explain the shoulder in the  $I = 3/2$  total cross section. Thus the indication is that 900 MeV the situation is somewhat more complex than expected with the presence of two overlapping resonances in the  $I = \frac{1}{2}$  state and a third in the  $I = 3/2$ .

Figure 5 shows the  $D_{13}$  and  $P_{11}$  amplitudes. The  $D_{13}$  shows the usual resonant behavior at 630 MeV with a width of 90 MeV. The  $P_{11}$  amplitude also shows evidence of resonating in this vicinity, but its large width (about 350 MeV) apparently precludes it from being observed in cross section measurements. This  $P_{11}$  resonance was first found by Roper in his analysis and has been the subject of some of the major disagreements among current phase shift solutions. There exists an alternative in which the  $P_{11}$  does not resonate but for which the phase shift merely becomes large in the vicinity of 600 MeV. It should be pointed out that the  $P_{11}$  is of special interest since its quantum numbers are identical to the nucleon. The final figure of this sequence (Fig. 6) shows the  $S_{11}$  amplitude which shows a relatively broad, elastic resonant behavior at about 950 MeV with superposition of a highly inelastic resonance at 650 MeV. Again at 600 MeV, the analysis discloses more structure than imagined previously - in this case there are perhaps three states resonating rather than one in the  $I = \frac{1}{2}$  state.

The data from the present experiment seeks to clarify the situation at both 600 and 900 MeV. The analysis is only preliminary at this time; we present the asymmetry rather than the polarization. The asymmetry should be multiplied by approximately 2 to get the polarization.

Figure 7 shows the results at 323 MeV from the cyclotron measurement of the  $\Pi^-p$  polarization, plotted with  $\cos \theta^*$  as the abscissa,  $\theta^*$  being the center

of mass pion scattering angle. When the target polarization is taken into account, the maximum in the polarization near  $\cos \theta^* = -.5$  is .58, in agreement with the phase shift solutions, and in disagreement with the value of about .8 of Vik and Ruge at 310 MeV. Figure 8 shows the results at 342 and 394 MeV which are similar to those at 323.

The next series (Fig. 9 & 10) give preliminary results for the  $\pi^-p$  backward angle polarizations in the vicinity of the 600 MeV resonances. First, at 675 MeV/c we see that there is a pronounced peak for angles near  $180^\circ$ ; at 750 and 825 MeV/c this peak has broadened and shifted toward smaller angles, and at 900 MeV/c there is again sharp peaking in the backward direction. The data for forward angles at these momenta have not yet been taken. Between 900 MeV/c and 2000 MeV/c we have no data for  $\pi^-p$ , this region having been studied by Duke et. al. at Rutherford Lab. and Suma et. al. at Argonne.

The final series (Fig. 11,12,13,14,15,& 16) show the asymmetry for  $\pi^+p$  scattering in the forward directions; in the sequence from 900 MeV/c to 1150 MeV/c the peak in the backward hemisphere is replaced with a peak near the forward direction. At 1280 and 1450 MeV/c, the polarization appears to go from its upper limit to lower limit as  $\cos \theta^*$  varies from 0.8 to 0.5. Finally at 1580 MeV/c, the minimum has washed out - a behavior which seems to extend to somewhat higher momenta.

In conclusion, we have observed rapid changes in the polarization in the region of the resonances in the  $\pi$ -N nucleon. It is to be hoped that with the aid of these measurements we might settle some of the differences in the analysis below 1 BeV and extend it to higher energy.

Polarization in Pion-Proton Scattering

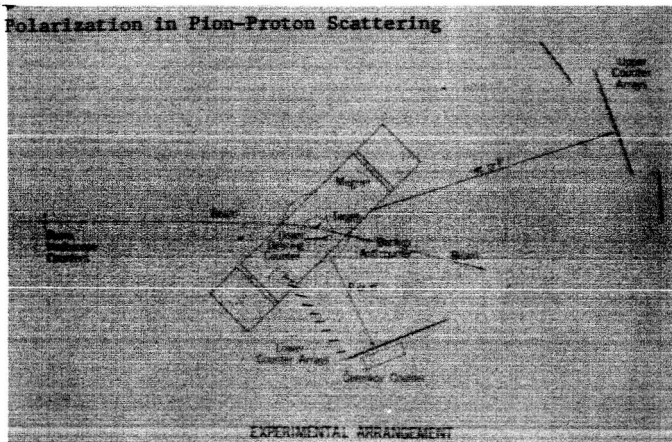


Figure 1

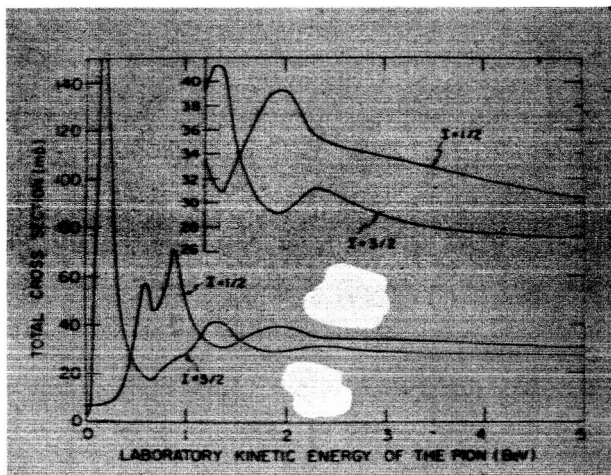


Figure 2 - Total  $\pi p$  cross sections for  $I=3/2, 1/2$

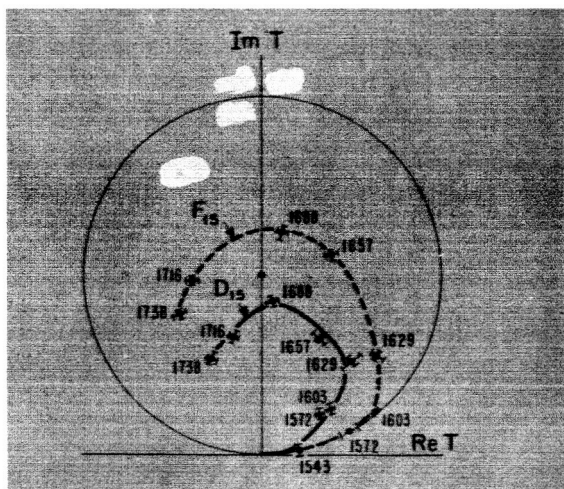


Figure 3 -  $F_{15}, D_{15}$  complex amplitudes.

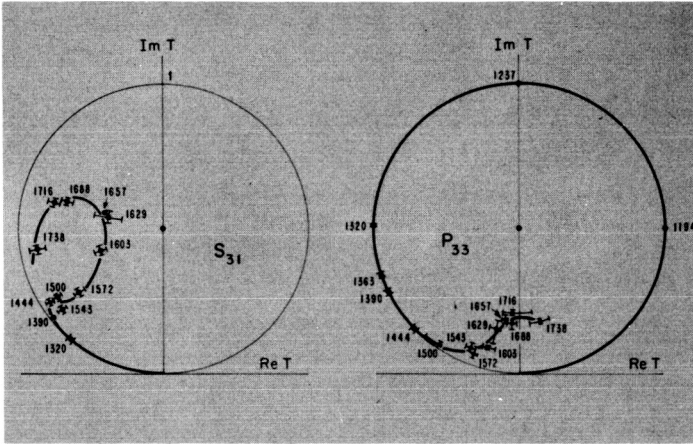


Figure 4 - Complex  $S_{31}$  amplitudes.

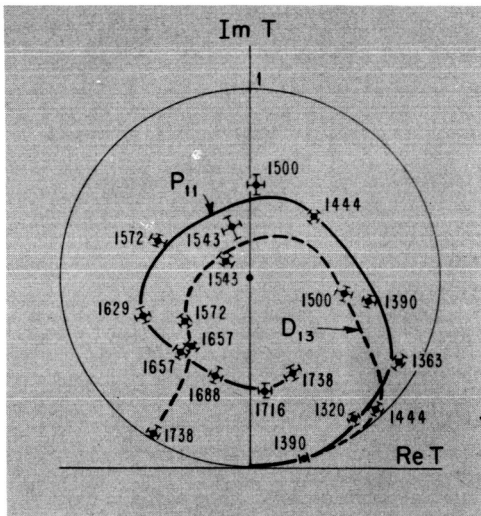


Figure 5 -  $D_{13}$  and  $P_{11}$  complex amplitudes.

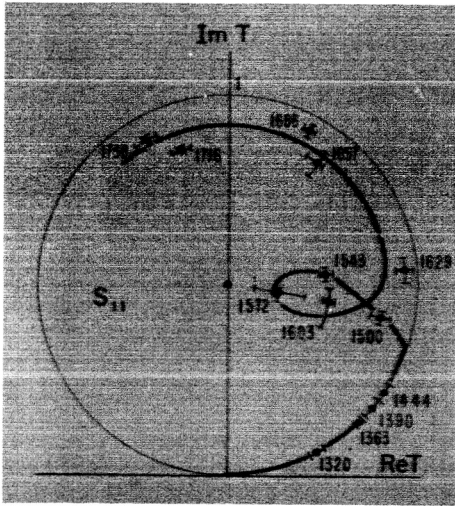


Figure 6 -  $S_{11}$  complex amplitude.

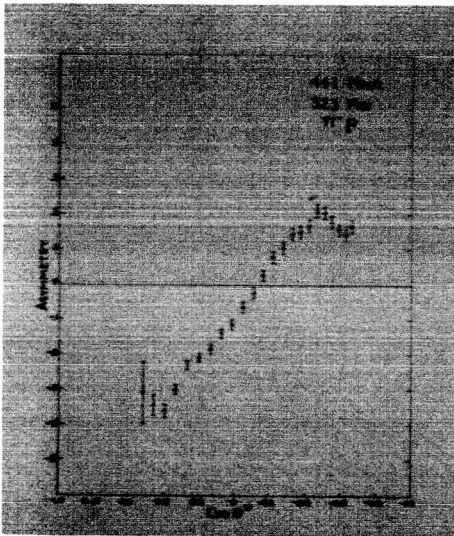


Figure 7 - Results at 323 Mev from the cyclotron measurement of  $\pi^-p$  polarization.

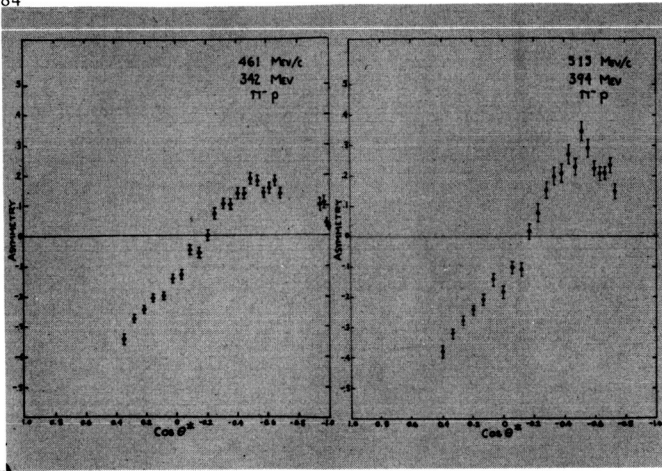


Figure 8. Results at 342 and 394 Mev from the cyclotron measurement of  $\pi^-p$  polarization.

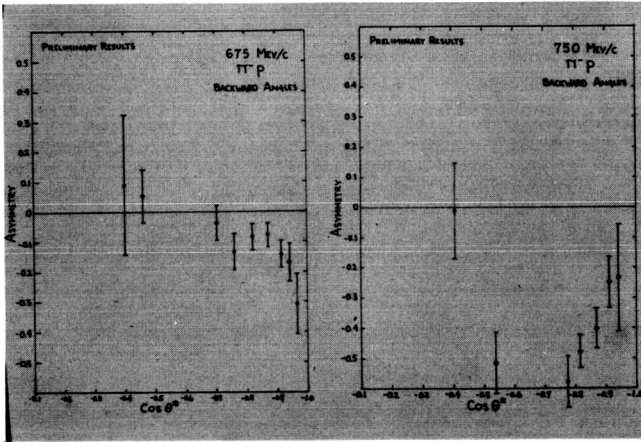


Figure 9. Preliminary results for the  $\pi^-p$  backward angle polarization in the vicinity of the 600 Mev resonances, and at 750 Mev resonances.

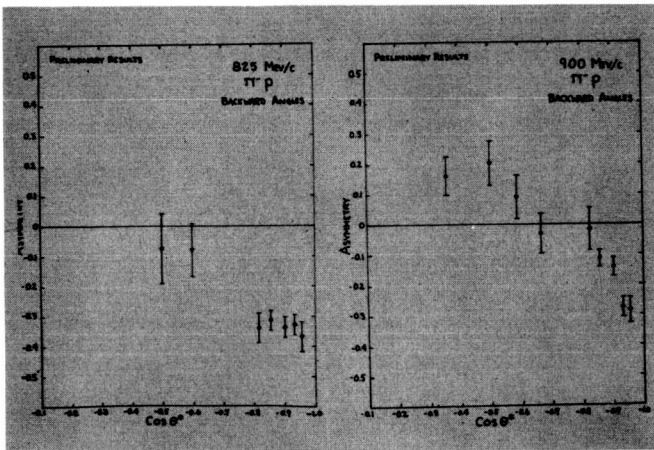


Figure 10. Preliminary results from the  $\pi^-p$  backward angle polarization in the vicinity of the 825 Mev resonances and the 900 Mev resonances.

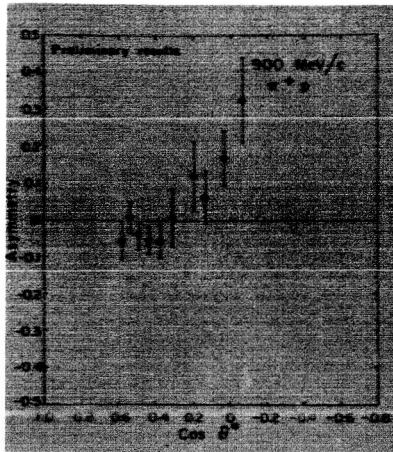


Figure 11 - at 900 Mev/c.

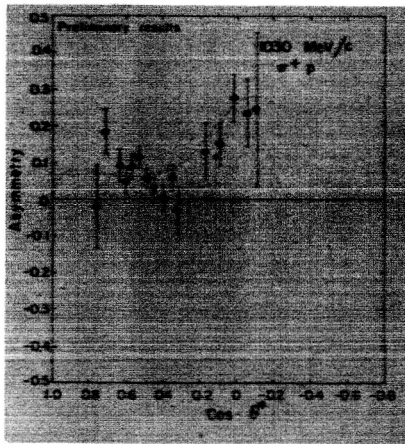


Figure 12 - at 1030 Mev/c

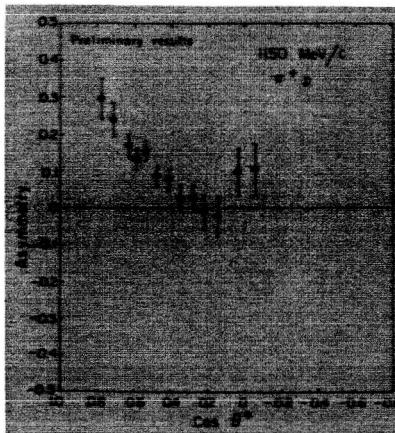


Figure 13 - 1150 Mev/c



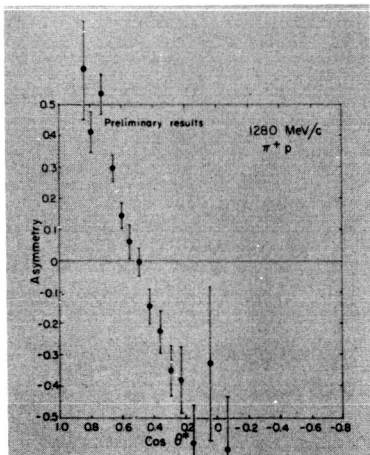


Figure 14 - at 1280 MeV/c/

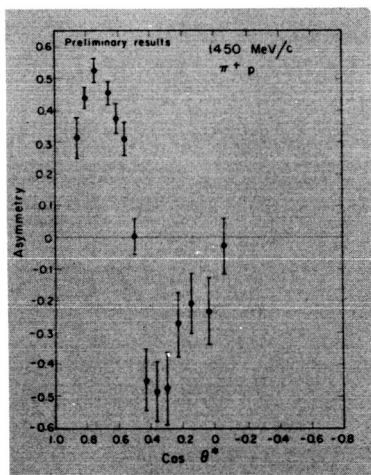


Figure 15 - at 1450 MeV/c.

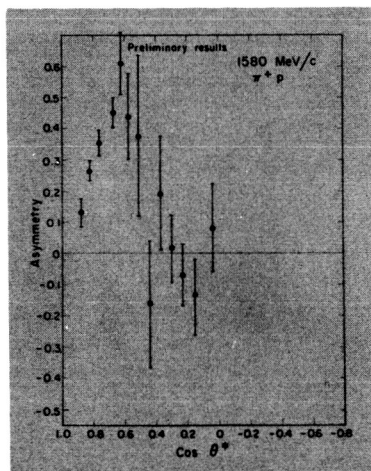


Figure 16 - at 1580 MeV/c.

PION INTERACTIONS WITH NUCLEI

T. E. O. Ericson

CERN

N66 187 32738

This report will mainly concern a study of the low energy elastic pion interactions with nuclei done in collaboration with my wife, Magda Ericson from the University of Lyon.<sup>1)</sup> We have become interested in this problem for two very different reasons. First, the field of pion interactions with complex nuclei begins now to emerge with pioneering experiments on  $\pi$ -mesic atoms,  $\pi$ -scattering and  $\pi$ -absorption. A proper understanding of the elastic interaction is then nearly a necessity for a description also of most inelastic processes, as we well know from the distorted wave approach in low energy nuclear physics. The understanding required for this is, however, mainly of a phenomenological nature. Our second and principal motivation is that low energy elastic  $\pi$  nuclear interactions are intimately and transparently related to  $(\pi N)$  interactions and to  $\pi$  production in  $(NN)$  collisions. Hence it becomes possible to obtain an optical model potential for a pion in a finite nucleus directly from elementary interactions and without free parameters. This one has wanted to do for a long time for nucleons without much success in the low energy region and moderate success only in the few hundred Mev region. Why should one expect this problem to work out more easily for pions? This is an interesting point which illustrates the great usefulness not to be confined to nucleons only in studying nuclei with elementary strongly interacting particles.

The mass of the nucleon is 7 times the mass of the pion. Hence, recoil corrections for pions become small; further the pion is even at low energies a light, fast particle interacting with heavy, nearly massive scatterers. This

transforms the whole problem into a nearly classical problem, which is an enormous simplification from all points of view. The difference in mass scale also implies that the range of the ( $\pi N$ ) interaction is shorter than the pion wave length at low energies, while the corresponding statement for nucleons rapidly is invalid. This permits us to make zero range approximations for the ( $\pi N$ ) interaction in the nucleus. Even at low energy the corresponding approximation cannot be made for nucleons due to the deuteron bound state and the singlet resonance; in contrast, the first ( $\pi N$ ) resonance is at 180 Mev. Finally, it should be mentioned that the pion does not pose any problems of identity between scatterer and projectile, as does the nucleon.

These are the principal points on which pions become easier to handle. Minor points could be added like the absence of a pion spin, but this is of much less importance.

The way in which we have tackled the multiple scattering problem is basically extremely simple, though we have made it look a bit complicated in the actual articles, so as to be able to make proper bookkeeping of all kinds of small corrections. The idea is this:

We first assume that the bound nucleons scatter pions in the same way as free nucleons. We take the interaction to be short ranged though we permit both s and p wave ( $\pi N$ ) interactions. This is thus an impulse approximation; it is not a high energy approximation, as we see easily from the well-known application of this approximation to coherent slow neutron diffraction in matter by Fermi's method.

Secondly, we have to put in the correct effective field for exciting a scatterer. Here people often say: OK, this will be fine if we just put in the typical average wave function locally. As we will discuss more in detail, we will

## Pion Interactions

have to worry at this point: pion scattering is largely dipole scattering. In the classical dipole scattering of an electromagnetic wave in a dense medium, one has to make an important and clear-cut distinction between the effective field exciting a scatterer and the average field in the medium as is well known from elementary physics. We will have to make the corresponding distinction in nuclei and the effect is sizable.

Let us briefly review the experimental background, but in a qualitative way only, since the present information is quite old (10 years or so) and will shortly be replaced by more detailed and extensive measurements. The information on the equivalent interaction in nucleon-nuclear scattering comes from elastic scattering experiments. In  $\pi$  nuclear interactions, suitable scattering experiments exist only at 70 - 90 Mev, which is a region that begins to be influenced by the (3/2, 3/2) ( $\pi$ N) resonance and which we thus want to avoid at present. Therefore we turn to the lowest energy scattering experiments of nuclear physics, mesic atoms. Just as the muon samples the nuclear charge distribution, reflecting it in the energy shifts of  $\mu$  mesic atoms, the pion samples the strong interaction mass distribution in an equivalent fashion. The pion can also make inelastic reactions by absorption on nucleons or by radiative capture: this reflects itself in absorption widths of levels as well as in level shifts. The mesic atoms give a very pedagogical demonstration of the main properties of  $\pi$  nuclear interaction in the following way:

in the 1s orbits of  $T = 0$  nuclei the x-ray transition energies are decreased, i.e., the interaction is opposite in sign to ordinary Coulomb interaction, so it is repulsive<sup>2)</sup>

in the 1s orbits of  $T = 1/2$ ,  $T_z = 1/2$  nuclei (adding a neutron) the energy

shifts become sizably more repulsive, indicating a very strong isospin dependence of the interaction.<sup>2)</sup>

In the 2p orbit of  $^{27}\text{Al}$  the energy shift (measured in a beautiful and difficult crystal spectrometer experiment at Berkeley) has become attractive.<sup>3)</sup> This is further confirmed by the Berkeley measurements on 2p, 3d and 4f energy shifts that Professor Crowe just showed us.

The conclusion out of the comparison of the 1s and the 2p energy shifts with different signs is that we will have to use a very strong ordinary local potential if we are to get this feature.

An absorption width has been directly measured in the  $^9\text{Be}$  1s level<sup>2)</sup> and it is of the order of the 1s level shift; indirect determinations of widths in 2p and 3d levels are obtained from intensity attenuation and known electromagnetic transition rates.<sup>4)</sup> These also indicate difficulties in using a local potential description, but less vividly so than energy shifts.

How can these properties be quantitatively obtained? Let us sketch the multiple scattering description in an oversimplified way. The ( $\pi\text{N}$ ) scattering operator is given roughly by

$$f_{\mathbf{i}}(r) = [b_0 + c_0 (k \cdot k')] \rho(r - r_{\mathbf{i}}) \quad (1)$$

in the short range approximation we will use. Here  $b_0$  and  $c_0$  are constants describing the intensity of s and p wave scattering:  $b_0$  is a linear combination of the s wave scattering lengths and  $c_0$  one of the p wave scattering volumes (also called scattering lengths by some people). Further,  $k, k'$  refer to ingoing and outgoing pion momenta,  $r$  and  $r_{\mathbf{i}}$  are the spatial co-ordinates of pion and its scatterer. The amplitude above depends both on isospin and spin in a way which gives rise to amusing final effects, but let us forget it. In much of the

detailed further discussion, we will put  $c_0 = 0$  for simplicity, just to get simpler expressions.

To discuss the multiple scattering, it is simpler to take a classical picture of static scatterers which is not so bad since nucleons are massive. We must remember that densities always mean expectation values, etc. All that part can be handled correctly and it is no more than a technical detail. Then the pion wave function at a given point  $\phi(r)$  can be written (for s wave scattering only, i.e.,  $c_0 = 0$ )

$$\phi(r) = \chi_0(r) + \sum_i b_0 g(r, r_i) \phi_{r_i}(r_i) \quad (2)$$

with  $\chi_0(r) =$  incident wave

$\phi_{r_i}(r_i) =$  tickling wave incident at a scatterer  $r_i$

$g(r, r_i) = \exp ik|r-r_i|/|r-r_i| =$  outgoing scattered wave

(Green function).

This equation can be read as follows: an incident pion comes in and gets re-scattered in an extremely complicated fashion on all the various scatterers  $i$ . This modifies the incident wave completely. We can, of course, ask for the average wave  $\phi(r)$  at some position (now we used an expectation value!). However this wave is the result of contributions of many small trickles of scattered waves from all the scatterers in the medium + the incident wave; that is the right-hand side of the equation. The only trouble is: what is the scattered wave from a scatterer? That is obviously proportional to the strength of the tickling field which is not equal to the average field; the reason is the average field contains also the scattered wave produced by the tickling field itself. Hence, if one wants to be consistent, one should make a clear distinction between these two concepts, which is indicated by the extra label on  $\phi_{r_i}(r_i)$  at the extreme left in Eq. (2).

We can write out the integral equation in differential form quite easily for

$$(\nabla^2 + k^2) \frac{\exp |r-r_i|}{|r-r_i|} = -4\pi\rho(r-r_i) \quad (3)$$

Hence, applying this to Eq. (2) and observing that  $(\nabla^2 + k^2) \chi_0(r) = 0$  we have

$$(\nabla^2 + k^2)\phi(r) = -4\pi b_0 \rho(r)\phi_p(r)$$

where  $\rho(r)$  is the density of scatterers at  $r$  (expectation value!)

There are now several easy approximations to the equation:

1. Let us say that the incident wave does hardly get modified by multiple scattering. Then  $\phi_p(r) \approx \chi_0(r)$ . This is just the single scattering perturbation approximation and it is usually not terribly good except at high energies.

2. A more sophisticated "bona fide" multiple scattering approximation which is very non-perturbative is to say: "OK, after all the medium is not terribly dense, or, OK, the scattering strength is not very great, so it will be fine to neglect the difference between the average wave  $\phi(r)$  and the effective exciting wave  $\phi_p(r)$ . Then the equation above depends only on  $\phi(r)$  and can be solved in terms of a potential  $V(r)$ ; it is just an ordinary wave equation.

$$V(r) = -\hbar^2/2m \cdot 4\pi b_0 \rho(r) \quad (4)$$

(We neglect effects of trivial kinematical factors, so as not to mess up things.)

This is often called the high energy approximation, but we all know it quite well from thermal neutron scattering in media, so it is not a high energy approximation. Let us apply it to pions. Then we have also p wave  $\pi N$  scattering, but that means in this spirit that we just replace momenta  $k$  by  $-iV$ .

$$\text{Thus } \tilde{V} = -\hbar^2/2m [4\pi b_0 \rho(r) - \nabla \cdot 4\pi c_0 \rho(r)\nabla] \quad (5)$$

We thus see that we have got an effective mass term in the potential which now is non-local, or if you so want, velocity dependent. This is the so-called Kisslinger potential.<sup>5)</sup>

The question is now: how good is this approximation? For our purposes, a good first orientation on this is given by the effective field description in a classical dielectric as given by Lorenz and Lorentz already about a 100 years ago. Just as dipole scattering is quite important in  $\pi N$  interactions, it is also dominant for electromagnetic scattering on atoms. If we look for the exciting field at a scatterer, the standard procedure is to cut out a little hole in the medium and put a test body in the middle. There will be induced dipole layers on the surface of the hole and the effectively measured field  $E_{\text{eff}}$  is related to the average electric field  $E$  by

$$E_{\text{eff}} = \left(1 + \frac{4\pi}{3} c_0 \rho\right)^{-1} E \quad (6)$$

in our notation. The constant  $c_0$  is called the electric polarizability of the atoms. For exactly the same reason, we may expect a similar effect in nuclei, which means the replacement of  $4\pi c_0 \rho(r)$  in Eq. (5) by

$$\left(1 + \frac{4\pi}{3} c_0 \rho(r)\right)^{-1} 4\pi c_0 \rho(r)$$

Numerically for pions this is a 30% correction, so we have good reasons to believe we have to go beyond the "high energy approximation". Neglecting terms of order  $A^{-1}$  this can be done as follows: look for the equation of  $\phi_{r_1}(r_1)$ , solve it and put it back in the original equation. Now we are lucky, for  $\phi_{r_1}(r_1)$  is the field measured at a scatterer (or at a test body if you so like). If we let  $\phi_{r_1}(r_1)$  have  $r_1 \rightarrow \infty$  we simply measure the wave function at infinity which to order  $A^{-1}$  is exactly the original wave function  $\phi(r)$  and which determines the scattering amplitude. Hence we will not have to solve two, but one equation.

The way of handling this problem is now to make an expansion into nucleon correlation functions, which we will break off at the level of two-nucleon correlations, i.e., one step beyond the ordinary density approximation. Just



as before

$$\phi_{r_i}^{(r_i)} = \chi_0^{(r_i)} + \sum_{i \neq j} b_0 g(r_i, r_j) \phi_{r_j}^{(r_j)} \quad (7)$$

The only difference between this and Eq. (2) is that the sum has  $i \neq j$  and that  $\phi_{r_j}^{(r_j)}$  is the field incident at  $r_j$  with the additional knowledge of a scatterer at  $r_i$ . We now neglect the difference in this last index, saying that the effective field is the same as before, an approximation that should be a vast improvement, since the auto-excitation of a scatterer by its own outgoing wave has been thrown out. Then we have an equation in  $\phi_r^{(r)}$  which can be solved. In expectation values, the equation depends on the pair correlation function  $G(r, r')$  between two scatterers, one at  $r$  and one at  $r'$ :

$$\phi_r^{(r)} = \chi_0^{(r)} + \int b_0 g(r, r') \rho(r') (1 + G(r, r')) \phi_{r'}^{(r')} dr' \quad (8)$$

The thing that matters about the nucleon pair correlation function (which has turned out to be very hard to get information on in its short range part) is that it is expected to go from -1 to 0 in about  $\approx 1F$  (Fig. 2). This fact simply reflects that two scatterers cannot be in the same spot, and that they get uncorrelated when they are large distances apart. Since the pion wave length is long compared to this distance of  $1F$  we can hope to be reasonably sensitive to this difference but not to the shape of the correlation function. This turns out to be exactly the case: the p wave  $\pi N$  scattering introduces a Lorenz-Lorentz effect just as in an ordinary dielectric and this effect is due to short range anticorrelations between scatterers. The occurrence of this effect is a detailed question of wave lengths in the medium, but when you go through it all you find it ought to be there. Hence the potential will become

$$V(r) = -\hbar^2/2m [4\pi b_0 \rho(r) - \nabla \cdot \frac{4\pi c_0 \rho(r)}{1 + \frac{4\pi c_0}{3} \rho(r)} \nabla]$$

There will be minor corrections in local term  $b_0$  from a) Fermi motion and

## Pion Interactions

b) a Lorenz-Lorentz s wave effect depending on the correlation length, but these are not so essential corrections.

Further, correlations in a medium depend on virtual excitations. The propagation of a scatterer is modified by this, but an investigation in detail shows that virtual excitation energies of the nucleus up to  $\sim 300$  Mev will give essentially identical results; this is so high that pair correlations can be correctly handled. Hence we have no restrictions imposed by this condition.

The main remaining point is nuclear absorption of pions. Here we do something that is slightly inconsistent, and which - though simple - will have to be improved on later on. Pions can of course get absorbed on nucleons by the process  $\pi + N \rightarrow N$  provided the necessary energy-momentum balance is furnished. The nucleus is a momentum source in principle, but the Fermi momentum of  $\sim 250$  Mev/c turns out to be quite insufficient. To make the process go we need in practice the presence of at least one other nucleon, so we deal rather with an effective process  $\pi + (2N) \rightarrow (2N)$ . The importance of this two-nucleon absorption process has been experimentally demonstrated by a number of experiments from various laboratories. We now do the following: we describe the two-nucleon absorption as a short-range process phenomenologically, without enquiring into its detailed structure.

This absorptive process induces a "scattering" process  $\pi + (2N) \rightarrow \pi + (2N)$  due to very short range interactions involving the two nucleons. We write down the most general amplitude for this, assuming: a) only s and p wave pions with respect to the two nucleons and b) that the two nucleons are in a relative s state. (This is a generalization of Wolfenstein's description of  $\pi$  production in NN collisions.) The amplitude depends on various spin, isospin and momenta, of course. It contains 10 complex constants to be determined experimentally.

We get the 10 imaginary parts by the optical theorem using  $\pi$  production data (5 of these are zero corresponding to closed channels). The remaining 10 real parts are not known, but we only need them roughly, so that we can control their magnitude. This we get: a) by observing that dispersion arguments tell us they will be repulsive and b) by taking them to be roughly equal to the imaginary part in magnitude (as is also indicated by dispersion arguments). From this point on, we simply say that two nucleons at short range behave as an additional type of scatterer and we put this straight into our previous treatment. Of course, we count some  $\pi N$  scatterings twice but, since the contribution of the real part of the two-nucleon scatterers is small, the total error due to this should not be very important. The quantities describing the s and p wave average scattering on nucleon pairs are denoted by  $B_0$  and  $C_0$  in analogy with  $b_0$  and  $c_0$  for  $\pi N$  scattering.

What do experiments tell us about these quantities, and what do  $\pi N$  scattering and  $\pi$  production predict? We start with the real part of the non-velocity dependent part of the potential. But for correction terms this is determined by  $b_0 = (\alpha_1 + 2\alpha_3)/3$  in terms of the singlet and triplet  $\pi N$  scattering lengths. Now a fluke happens: by accident these cancel heavily, so that all kinds of small perturbations matter. In addition, the scattering lengths, though very well determined, are no longer known well enough for our purpose. We get contributions also from Fermi motion, an s wave correlation effect between nucleons and from the normally quite small absorption terms. The predictions of Hamilton and Woolcock's scattering lengths<sup>6)</sup> - as compared to the recently proposed Samaranyake and Woolcock's ones<sup>7)</sup> - are as follows (units  $\hbar = m = c = 1$ )

## Pion Interactions

|              |                          | $\frac{a_1+2a_3}{3}$ |   | Fermi<br>Motion | Correlations | Absorption     | Total                |
|--------------|--------------------------|----------------------|---|-----------------|--------------|----------------|----------------------|
| $(b_0)_{th}$ | Hamilton-<br>Woolcock    | -0.002               | + | 0.004           | - 0.010      | - $\sim 0.006$ | $= -0.014 \pm 0.005$ |
|              | Samaranyake-<br>Woolcock | -0.012               | + | 0.004           | - 0.014      | - $\sim 0.006$ | $= -0.028 \pm 0.005$ |

$$(b_0)_{exp} \quad - 0.029 \pm 0.006$$

It is clear from this that we like the recent scattering lengths better, and in fact they came after we had finished our work. Still the question of scattering lengths should be cleared up by the elementary particle people. Anyway, we are not really unhappy even with the first version, since no cancellations would produce a  $b_0 \sim 0.1$ : hence also the first case from a multiple scattering point agrees to  $\sim 13\%$  which is excellent (This is just a statement that fractional errors become infinite if the prediction is zero, so that you have to use a proper scale to measure accuracy.)

One can similarly determine a coefficient  $b_1 \approx "(a_1-a_3)/3"$  for the isospin dependence of the local interaction, a term proportional to  $(t \cdot T)/A$  where  $t$  and  $T$  are the pion and nuclear isospin. The predictions are:

$$\text{H.W. :} \quad b_1 = -0.086$$

$$\text{S.W. :} \quad b_1 = -0.097 \pm 0.007$$

while the experiments, which have large uncertainties give

$$(b_1)_{exp} = -0.10 \pm 0.04$$

in good agreement, though this does not really constitute any test of the theory yet. There are no cancellations here, so there is no excuse for not making a good job.

The imaginary local potential is described by  $\text{Im}B_0$  which is predicted to be  $0.0055 \pm 0.0007$  using  $\pi$  production only: it should be slightly increased for radiative  $\pi$  capture. The only experimental information is an old measurement of

a level width in  ${}^9\text{Be}$  which yields  $0.0140 \pm 0.0030$ . There may be a discrepancy at this point. I insist, however, that there are big  $A^{-1}$  corrections in  ${}^9\text{Be}$  and further Professor Crowe informs me that at Berkeley they think the width of this time is at least 30% smaller from their own preliminary measurements. Obviously this point has to be settled.

For the non-local interactions the relevant parameters for the real and imaginary parts are  $c_0$  and  $\text{Im } C_0$ . They are in agreement with the present experiments assuming short range anticorrelations between nucleons. In Figure 1 the area A is the experimental 50% probability area using a Lorenz-Lorentz effect and B is the same without such an effect. The hatched square is the theoretical prediction including uncertainties in basic parameters. The present experiments do not yet give any clear preference for the one or the other case, but it would be exceedingly interesting to see a direct effect of nucleon pair correlations.

While I have not discussed this, the optical potential derived contains other terms induced by the spin and isospin dependence of the basic scattering amplitudes. For example, there is an isospin tensor interaction  $(t \cdot T)^2/A^2$  which can give rise to direct double pion charge exchange reactions between isobaric spin multiplets. Further there is an induced strong interaction hyperfine coupling between the nucleus spin  $I$  and the pion orbital angular momentum  $\ell$  by a term  $(I \cdot \ell)/A$  which gives rise to level splittings in mesic atoms.

At the present moment we can say that low energy pions qualitatively see the nucleus as a dielectric medium with parameters describing the wave motion in qualitatively good agreement with predictions. Further work will be required to show if the understanding is or can be made quantitative.

Finally I would like to end by briefly describing some work done by J. Delorme from Lyon and myself on radiative  $\pi$  capture in nuclei. About half a

year ago we were deeply impressed by some measurements of yields and spectra on the reaction  $\pi^- + (A,Z) \rightarrow \gamma + (A,Z-1)$  done at Liverpool.<sup>8)</sup> It was observed that typical branching ratios were of the order of several % with typical  $\gamma$  energies of about 110-120 Mev. This suggested to us that this might be a quasi-free  $\pi^- + p \rightarrow \gamma + n$  reaction. If we now take a look at the amplitude for photoproduction of pions at threshold this is dominated by an E1 transition + higher order terms in the pion momentum. It is therefore straightforward to use the non-relativistic photoproduction amplitude to write an effective Hamiltonian for radiative capture:

$$H_{\text{eff}} = 4\pi i \sum_{j=1}^A t_j^- \{ A(\sigma_j \hat{\epsilon}) + B(\sigma_j \hat{\epsilon})(q \cdot k) + C(\sigma_j k)(q \cdot \hat{\epsilon}) + Dq \cdot (k \times \hat{\epsilon}) \} \rho(r - r_j)$$

where A, B, C and D are constants simply related to the threshold limits of the photoproduction amplitudes. The quantities  $\hat{\epsilon}$ ,  $k$  and  $q$  refer to the photon polarization vector and momentum and to the pion momentum. Delorme has calculated how much the higher order terms in the pion momentum contribute to radiative  $\pi$  capture. These terms give rise to non-local interactions as in the optical potential. He finds for the ratio of non-local to local interactions in the 1s, 2p and 3d Bohr orbits:

T A B L E 1

| Orbit | Ratio non-local/local |
|-------|-----------------------|
| 1s    | ~ 0 %                 |
| 2p    | ~ 5 %                 |
| 3d    | ~ 12 %                |

Hence the radiative capture rates are quite dominated by the axial vector type interaction  $(\sigma_1 \cdot \epsilon) t_1^-$ . This is exceedingly interesting because exactly the same matrix element occurs in the  $\mu$  capture process  $\mu^- + p \rightarrow n + \nu$ ; hence we can crib the entire  $\mu$  capture theory word for word, statement by statement and apply it to radiative  $\pi$  capture with trivial kinematical changes.\*) The enormous difference is that a  $\gamma$  is easily measured while a neutrino is not. Therefore all the sad sighs that  $\mu$  capture neutrinos would be so interesting to see should now stop and one should look to the  $\gamma$ 's in  $\pi$  capture. I will not enter into any further details about the problems that can be studied in this way, since there is a full session on  $\mu$  capture. I only want to emphasize the importance of now being able to study, say those collective  $T = 1$  giant dipole supermultiplet states, which correspond to oscillations of neutrons versus protons with spin waves.<sup>9)</sup> It is also possible to study, say, the negative parity states in  ${}^4\text{H}$  with precision.<sup>10)</sup>

We have calculated the total radiative absorption rate in the closure approximation, i.e., summing over all final states. Since we know the spectrum of final states, we can easily correct the phase space factors (which is hard in  $\mu$  capture). We apply this to a Fermi gas (Primakoff Theory) which works extremely well for total  $\mu$  capture rates, after suitable modification to handle absorption also in 2p and 3d orbits. Then we find the following predicted radiative yields compared to the experimental ones:

---

\*) Several People have used the similarity of radiative  $\pi$  capture and  $\mu$  capture in  ${}^3\text{He}$  to deduce the nuclear transition matrix elements needed for a proper determination of weak interaction coupling constants.<sup>11)</sup>

T A B L E 2

Branching ratios of radiative capture  
(no  $A^{-1}$  corrections)

| Element         | Orbit | Theory % | Experiment %  |
|-----------------|-------|----------|---------------|
| ${}^6\text{Li}$ | 1s    | 5.0      | $3.3 \pm 0.2$ |
| ${}^7\text{Li}$ | 1s    | 2.5      | $1.9 \pm 0.2$ |
| C               | 1s    | 4.3 mean | $1.6 \pm 0.1$ |
|                 | 2p    | 1.7 1.9  |               |
| S               | 2p    | 1.7 mean | $1.8 \pm 0.1$ |
|                 | 3d    | 1.1 1.6  |               |
| Cu              | 2p    | 1.7 mean | $1.5 \pm 0.1$ |
|                 | 3d    | 1.2 1.4  |               |

The table is mainly self-explanatory. The following comments should be made: the mean value for capture out of two orbits simultaneously has been obtained from the observed relative absorption in the orbits. The theoretical yields for C, S and Cu are obtained using normalization to known electromagnetic transition rates and are thus rather trustworthy. For  ${}^6\text{Li}$  and  ${}^7\text{Li}$  the rate of absorption of pions into all nonradiative processes is not very well-known: we have estimated it from the optical model, but the  $A^{-1}$  corrections can be quite large for low A and they would decrease the radiative yield. The agreement between this first rough attempt of a theoretical description and the experiments is quite striking. It gives us a very strong impression that we understand the main features of the process and that we are on the right way for a more detailed exploitation of this process both for the understanding of nuclear structure and for a better understanding of  $\mu$  capture in nuclei.



- 1) M. Ericson and T. Ericson, *Annals of Physics* (N.Y.) to appear.
  - 2) See D. West, *Reports on Progress in Physics*, Vol. XXI, 271 (1958).
  - 3) A. Astbury, J. P. Deutsch, K. M. Crowe, R. E. Shafer and R. E. Taylor, "Congrès International de Physique Nucléaire - II" Dunod, Paris (1964), p. 225.
  - 4) P. Huguenin, *Z. Phys.* 167, 416 (1962).  
M. Ericson, *Compt. Rend.* 257 3831 (1963).
  - 5) L. Kisslinger, *Phys. Rev.* 98 761 (1955).
  - 6) J. Hamilton and W. S. Woolcock, *Revs. Modern Phys.* 35, 737 (1963).
  - 7) V. K. Samaranayake and W. S. Woolcock, *Phys. Rev. Letters* 15, 936 (1965).
  - 8) H. Davies, M. Muirhead and J. N. Wouds, *Nucl. Phys.*, to appear.
  - 9) J. Barlow, J. C. Sens, P. J. Duke and M. A. R. Kemp, *Phys. Letters* 9, 84 (1964).  
L. L. Foldy and J. D. Walecka, *Nuovo Cimento* 34, 1026 (1964).
  - 10) A. de-Shalit and J. D. Walecka, SLAC preprint No. 160.
  - 11) B. V. Struminsky, 1962 Int. Conf. on High Energy Physics at CERN, P. 17 Geneva (1962).  
A. Fujii and D. J. Hall, *Nucl. Phys.* 32, 224 (1962).
- See also
- A. M. L. Messiah, *Phys. Rev.* 87, 638 (1952).

## Pion Interactions

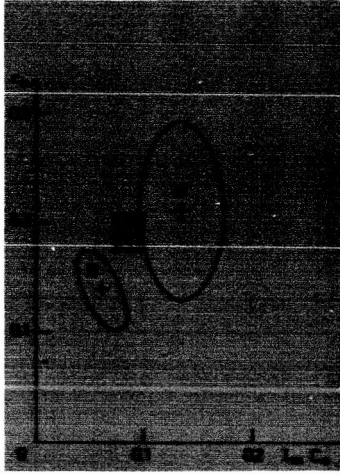


Figure 1 - Plot of  $c_0$  vs  $\text{Im } C_0$ . Hatched square is theoretical prediction.

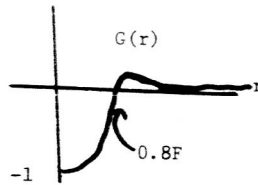
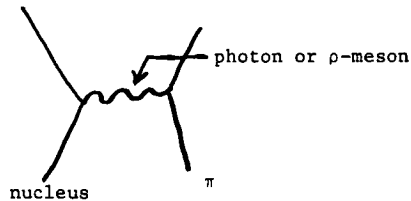


Figure 2 - Nucleon pair correlation function in a nucleus.

TELEGDI: I would like to make a point which Dr. Ericson referred to very briefly, and I'm sure only for the sake of brevity didn't discuss, but which I found in reading his papers very interesting and to which I would like to direct your attention. Namely, that if you have a pi mesic atom, of course having a scalar particle, you don't have such a thing as hyperfine structure except to the extent of the orbit of the meson interacts with the nuclear spin, which is a small electromagnetic effect. But, you can then sort of wonder is there a strong analog of the electromagnetic hyperfine structure?

Now you can draw this diagram twice - once you put in the photon and the other time you put in a rho meson.



The coupling constants here are known and then by a simple tautology you get immediately a sort of strong hyperfine effect; of course, which is  $a_1/A$ . Now in order to get the correct answer to this you've got to be very fancy and work out the wave functions at the nucleus, which I haven't been able to do and maybe you have numbers. But from the experimental point of view, it's just the restatement of the fact that there is a very strong spin dependence between the pion and the nucleon. It would be amusing to see if the strong hyperfine effect exists.

ERICSON: Thank you. This is a very interesting point and this way that you are doing it is a very pretty one seeing qualitatively that you must have necessarily a hyperfine effect of this kind. We did it the sordid way; we just got hold of

## Pion Interactions

the p-wave scattering lengths and plugged them in and went through, and we came out indeed with an interaction of the type  $\frac{i \cdot l}{A} \frac{1}{r} \frac{dl}{dr}$ . So that you get an effect of this kind with a certain coefficient to it. Now it is of course possible in principle to measure the hyperfine effect in pi-mesic atoms. This is a rather amusing thing if one could see this strong hyperfine interaction effect. But I don't know how feasible it is to see it. It should be of the order of at least say 5% of the level shift or something of this kind, and is thus not so terribly small.

N66 207  
32739

Two - Nucleon Emission Following Absorption of Stopped Negative Pions\*

M.E. Nordberg, Jr., K.F. Kinsey and R.L. Burman

Department of Physics and Astronomy  
University of Rochester, Rochester, New York

A B S T R A C T

A beam of negative pions was brought to rest in a variety of light element targets ranging from  $\text{Li}^6$  to  $\text{Al}^{27}$ . The angular distributions of neutron-proton and neutron-neutron pairs emitted in the subsequent pion capture process were measured. The protons were detected in a scintillation counter telescope and the neutrons were detected in a plastic scintillation counter with an anti-coincidence guard counter. The threshold requirements discriminated against low-energy evaporation nucleons. The angular distributions peak strongly at  $180^\circ$ . These distributions and the comparison of n-n to p-n rates are discussed and compared with other similar measurements and theoretical analysis.

PRECEDING PAGE BLANK NOT FILMED.

### Introduction

At the University of Rochester we have what is nearly the lowest energy pion producing facility in the world. We have been doing an experiment which comes naturally to low energy pions, namely, stopping negative pions in various materials and measuring the angular distributions of two emitted nucleons. A stopped pion has zero momentum but can introduce its 140 MeV rest mass energy upon capture by a nucleus. Therefore in order to conserve both energy and momentum the capture process is likely to occur on a pair of nucleons in the nucleus with their subsequent emission each carrying about half the energy in opposite directions. In principle the study of the n-n and p-n pairs emitted gives information on p-n and p-p correlations within the nucleus. Of course final state interactions with the residual nucleus and the momentum of the correlated pairs within the nucleus tend to smear out the simple  $180^\circ$  angular correlation.

### Apparatus

We have used several scintillation detector systems of coarse and fine angular resolution which measure the angular distribution of the coincident emission of p-n or n-n pairs following  $\pi^-$  capture. The coarse resolution apparatus was used to survey the angular distributions from several light elements. Then  $\text{Li}^6$  and  $\text{O}^{16}$  were studied in more detail with a finer resolution apparatus.

The p-n apparatus of fine resolution is shown in Fig. 1. The

incident beam of 32 MeV negative pions is defined by two scintillation detectors labeled  $\pi_a$  and  $\pi_b$  with a third detector in anti coincidence after the target. The energy of the beam is degraded so that a maximum number of pions stop in the target (about half the incident beam). The target is typically  $1/2 \text{ gm/cm}^2$  and is placed at  $45^\circ$  with respect to the beam. The proton detectors are located approximately perpendicular to the target to minimize the energy loss of the protons in the target. This loss is about 10 MeV for a 50 MeV proton. The three proton telescopes have a common front element in coincidence. A sharp 20 MeV proton threshold was considered in the calculations corresponding to half target thickness plus the front proton detector. Using the phase space energy distribution,  $90\% \pm 5\%$  of the proton in p-n emission are over 20 MeV. In actuality the threshold is smeared out. The three neutron detectors are made up of 4" long by 2" diameter scintillation detectors and front guard detectors in anti coincidence. They can be moved to any angle but they were not placed in the direct beam.

For the case of Fig. 1, electronic logic circuits (Chronetics, Inc.) formed 10 nsec coincidences of all 9 possible p-n pairs of detectors which are also in coincidence with a pion. Background was measured by removing the target but it is very small. The fine resolution n-n apparatus had a fourth neutron detector in place of the proton detectors. All six pairs of the four detectors were recorded. The coarse resolution apparatus used 6" long by 3" diameter neutron detectors closer to the target and only one proton detector. The three p-n and three n-n

pairs were recorded simultaneously as also were the randoms. The same relative p-n or n-n angle could be obtained with several combinations of detector positions. However, the tendency with four detectors is to have all the relative angles at about  $90^\circ$ . It proved awkward to evenly space the data points. Calibration of the pulse height of the thin detectors was done either by moving them into the beam or more conveniently was done in place with a  $\text{Bi}^{207}$  conversion electron source. Calibration of the neutron detectors was done with the  $\text{C}^{12}(n,\gamma)$  reaction from thermal neutrons of the machine background.

#### Data

For every pair of detectors an acceptance function of angle was obtained by integrating over the beam intensity distribution, target position, and detector areas. The coarse resolution was about  $25^\circ$  full width at half maximum and the fine resolution was about  $15^\circ$ . The centroid of these distributions defines an average angle at which the data is plotted in the following figures and listed in Tables I, II, and III.

The n-n data shown in Fig. 2 for  $\text{Li}^6$  and  $\text{O}^{16}$  were obtained with the apparatus with finer angular resolution. This resolution is shown for one point. The  $\text{Li}^6$  curve is sharply peaked at  $180^\circ$  whereas even for a nucleus as light as  $\text{O}^{16}$  the distribution is smeared out. There may be a slight increase at small angles but this is not definite from this data and would be surprising from a theoretical viewpoint. The data from the larger counters for many elements would fill in between



these curves with more or less a monotonic decrease in the  $180^\circ$  peaking as  $Z$  or  $A$  increases.

The p-n curves shown in Fig. 3 are similar but slightly less peaked.

A theoretical shell-model calculation by Kopaleishvili and Machabeli<sup>1</sup> for n-n emission from pion capture on  $\text{Li}^6$  gives an exponential peaking at  $180^\circ$  with a width to the  $1/e$  point of about  $40^\circ$ . An estimate by Koltun<sup>2</sup> gives a width about  $25^\circ$  for  $\text{O}^{16}$ . Our data are narrower than the former and broader than the latter. More complete analyses and more accurate data are needed to extract detailed information from these angular correlations.

From these data, the solid angles, and calculated neutron and proton detector efficiencies we can obtain the correlated emission rates. This is highly sensitive, however, to the sharpness of the peaking at  $180^\circ$ . The ratio of n-n to p-n emission is less sensitive since the curves are of similar shape. The calculated neutron detector efficiency appears inversely in this ratio. These efficiency calculations predict the number of pulses over the threshold setting from knock-on protons and breakup of  $\text{C}^{12}$  within the detector volume. These thresholds are 11 MeV and 7 MeV for the small and large detectors. The phase space energy distribution of the neutron is used in the calculation in lieu of more precise information. Our estimate of the possible errors in the neutron detectors' efficiencies is  $\pm 20\%$ . This results in the possibility of  $\pm 40\%$  systematic error in the number of correlated n-n emissions. With

the proton detector efficiency error this also leads to the possibility of a  $\pm 25\%$  systematic error in both the p-n rates and the ratio. This is the dominant source of error for all cases but Cu and Pb.

The correlated emission rates of Table IV are obtained by integrating the curves such as Figs. 1 and 2 over angles greater than  $120^\circ$  with a weighting equal to  $\sin \theta$  for the solid angle factor. In other words correlated emission is considered to be all those where the two particles are within  $60^\circ$  of antiparallel. The p-n curves are broader than the n-n so that this definition of correlated emission gives about  $2/3$  the value for the ratio of n-n to p-n emission as does defining the correlated emission to be the extrapolation of the curves at  $180^\circ$ . The value of the ratio is surprisingly independent of the target nucleus. Previously 5.0 and 3.9 had been reported for this ratio for  $O^{16}$  and  $Al^{27}$  by Ozaki et al.<sup>3</sup> Our results would be consistent with a constant for this ratio and the weighted average is 3.9 to 4.6. The differences between the two sets of data for  $Li^6$  and  $O^{16}$  are probably an indication of the inaccuracies of the efficiencies used for the neutron detectors.

The simplest model for calculating this ratio gives 3.0. This model assumes pion absorption on relative s-wave nucleons in the p-shell only with equal probability for a triplet pair as a singlet pair. For  $C^{12}$  Kohmura<sup>4</sup> has increased this ratio to 5 by assuming the range of the wave function for a triplet pair is shorter than for a singlet pair by about 5%. This violates charge independence. For  $O^{16}$  Koltun and Reitan<sup>5</sup> find that a larger ratio than 3 is obtained when one properly

includes pion charge-exchange rescattering in the matrix elements. The similarity of the results for  $\text{Li}^6$  and  $\text{Li}^7$  are puzzling.  $\text{Li}^6$  has only a p-n pair outside the  $\alpha$ -particle core and so  $\pi^-$ -absorption should lead only to n-n emission giving an infinite ratio.

The parameter missing from the previous data is the energy of the two particles. We have observed the proton energies in the p-n cases but there was no evidence of any structure. The distributions were nearly flat -- tapering off at high energy. What is of interest is the sum of the two particles energies since this gives directly the excitation remaining in the residual nucleus. Our intensity is too low and background too high to measure neutron energies by time of flight. Therefore the future plans are to perform  $\pi^+$  capture in flight, and look at the two protons emitted with spark chambers. We expect about 2 MeV energy resolution from range measurements. The momentum of the incoming pion must be considered in the kinematic analysis but introduces no major difficulty. A preliminary run with only counters indicates that the cross section is sufficiently high and the angular distribution is also peaked at  $180^\circ$ . It should provide a means to study two-hole states of the shell model theory as well as the momentum distribution of p-n pairs within the nucleus.

References

- \* Supported by the U.S. Atomic Energy Commission
1. T.I. Kopaleishvili and I.Z. Machabeli; private communication.
  2. D.S. Koltun; private communication.
  3. S. Ozaki, R. Weinstein, G. Glass, E. Loh, L. Neimala and A. Wattenberg; Phys. Rev. Lett. 4, 533 (1960).
  4. T. Kohmura; Prog. Theor. Phys. 34, 234 (1965).
  5. D.S. Koltun and A. Reitan; Phys. Rev. 141, No. 4 (1966).

TABLE I

Number of Coincidences per Million Stopped Pions

Large Counter n-n Data

$$\epsilon_{n_1} = \epsilon_{n_2} = 0.2, \quad \frac{\Omega_1 \Omega_2}{n_1 n_2} = 0.011$$

| Target $\theta_{nn}$ | 53°     | 60°     | 75°     | 120°    | 138°     | 142°    | 146°     | 159°     | 165°     |
|----------------------|---------|---------|---------|---------|----------|---------|----------|----------|----------|
| Li <sup>6</sup>      | 2.5±1.1 | .2±1.3  | .4±1.3  | 2.5±1.3 | 6.4±1.5  | 8.2±1.7 | 11.4±1.6 | 21.9±1.8 | 37.2±2.0 |
| Li <sup>7</sup>      | 1.2±2.3 | -.2±2.1 | -.2±1.8 | 6.3±2.2 | 4.5±2.1  | 9.5±2.6 | 13.2±1.5 | 22.5±2.9 | 33.1±2.9 |
| Be                   | 3.0±1.6 | 1.2±1.6 | -.1±1.5 | 2.5±1.7 | 4.8±1.3  | 7.1±1.8 | 9.9±1.5  | 11.8±1.9 | 22.8±1.9 |
| B <sup>10</sup>      | 0.6±2.0 | 1.3±1.6 | .2±1.7  | 3.0±2.1 | 3.5±2.3  | 4.1±2.6 | 5.5±2.0  | 9.0±2.6  | 10.0±2.1 |
| B                    | 0.3±1.7 | 1.5±1.6 | .9±1.1  | 2.2±1.9 | 4.8±1.7  | 5.8±1.9 | 8.2±2.0  | 9.2±1.9  | 12.3±1.9 |
| C                    | 2.5±1.4 | 2.5±1.4 | 1.0±1.2 | 3.5±1.3 | -1.7±1.7 |         | 5.8±1.8  |          | 11.8±1.8 |
| N                    | .9±1.0  | .9±1.0  | .9±.9   | 2.9±1.3 | 3.8±1.1  |         | 3.5±1.1  |          | 9.2±1.5  |
| O                    | 1.2±1.5 | 1.2±1.5 | .4±1.6  | 5.6±1.9 | 4.1±1.8  |         | 7.9±1.7  |          | 15.6±2.0 |
| Al                   | 1.9±1.8 | 1.9±1.8 | 1.5±1.5 | 4.1±1.7 | 2.9±1.6  |         | 2.3±1.7  |          | 4.9±1.8  |
| Cu                   | .2±1.8  | .2±1.8  | .4±2.5  | 1.7±1.5 | 1.1±2.5  |         | 1.6±2.7  |          | 4.5±2.1  |
| Pb                   | 2.6±1.8 | 2.6±1.8 | 1.0±1.7 |         |          |         |          |          | 2.8±1.8  |

TABLE II  
 Number of Coincidences per Million Stopped Pions

| Target $\theta_{nn}$ | Large Counter p-n Data |                    |  |            |            |            |             |             |             |             |
|----------------------|------------------------|--------------------|--|------------|------------|------------|-------------|-------------|-------------|-------------|
|                      | $\epsilon_n = 0.2$     | $\epsilon_p = 0.9$ | $\frac{\Omega_n \Omega_p}{n p} = 0.0049$ | $62^\circ$ | $77^\circ$ | $91^\circ$ | $119^\circ$ | $140^\circ$ | $157^\circ$ | $163^\circ$ |
| Li <sup>6</sup>      | 1.0±.5                 | .3±.5              | 1.1±.5                                   | 1.3±.3     | 1.6±.6     | 5.7±.7     | 9.8±.9      | 11.3±1.0    |             |             |
| Li <sup>7</sup>      | .2±.5                  | -.1±.8             | .7±.6                                    | 1.0±.4     | 2.2±.7     | 6.2±1.0    | 10.5±1.1    | 9.5±1.1     |             |             |
| Be                   | .7±.5                  | .1±.5              | 1.2±.5                                   | 1.1±.3     | 2.7±.5     | 3.9±.7     | 8.4±.8      | 10.5±1.0    |             |             |
| B <sup>10</sup>      | 1.5±.8                 | .8±.6              | .4±.8                                    | .8±.5      | 2.9±.9     | 5.5±1.1    | 4.3±.8      | 7.5±1.2     |             |             |
| B                    | 1.4±.6                 | .6±.5              | .3±.6                                    | 1.0±.4     | .9±.6      | 2.7±.8     | 3.7±.7      | 4.4±.9      |             |             |
| C                    | 1.3±.6                 | .8±.5              |  | 1.2±.6     | 2.2±.6     |            | 4.1±.8      | 5.9±.9      |             |             |
| N                    | .6±.4                  | 1.1±.5             |  | 1.0±.4     | 1.8±.5     |            | 2.8±.6      | 3.4±.7      |             |             |
| O                    | 1.2±.6                 | -.4±.7             |  | .2±.7      | 2.2±.7     |            | 4.8±.9      | 5.5±.9      |             |             |
| Al                   | .7±.5                  | 1.4±.5             |  | 1.5±.6     | 1.4±.5     |            | 2.7±.6      | 3.9±.8      |             |             |
| Cu                   | .2±.5                  | -.6±1.0            |  | .2±.8      | 1.7±.7     |            | 2.9±.9      | 3.5±.9      |             |             |
| Pb                   | .0±.6                  |                    |  |            | .3±.9      |            |             | 1.2±.8      |             |             |

TABLE III

Number of Coincidences per Million Stopped Pions

Small Counter n-n Data

$$\epsilon_{n_1} = \epsilon_{n_2} = 0.1 \quad \frac{\Omega_{n_1} \Omega_{n_2}}{n_1 n_2} = 0.0011$$

| Target $\theta_{nn}$ | $31^\circ$  | $38^\circ$  | $60^\circ$  | $90^\circ$  | $120^\circ$ | $135^\circ$ |
|----------------------|-------------|-------------|-------------|-------------|-------------|-------------|
| Li <sup>6</sup>      | .31±.05     | .24±.06     | .16±.05     | .16±.05     | .14±.05     | .46±.08     |
| 0                    | .15±.03     | .26±.05     | .07±.04     | .12±.05     | .15±.06     | .55±.08     |
|                      | $149^\circ$ | $156^\circ$ | $163^\circ$ | $169^\circ$ | $172^\circ$ |             |
| Li <sup>6</sup>      | .71±.10     | .83±.10     | 2.01±.17    | 2.50±.19    | 2.82±.20    |             |
| 0                    | .44±.10     | .61±.08     | .61±.08     | .56±.08     | .77±.14     |             |

Small Counter p-n Data

$$\epsilon_n = 0.1 \quad \epsilon_p = 0.9 \quad \frac{\Omega_n \Omega_p}{n p} = 0.00104$$

| Target $\theta_{pn}$ | $35^\circ$  | $51^\circ$  | $66^\circ$  | $90^\circ$  | $105^\circ$ | $120^\circ$ |
|----------------------|-------------|-------------|-------------|-------------|-------------|-------------|
| Li <sup>6</sup>      | .16±.06     | .08±.04     | .19±.07     | .31±.08     | .22±.07     | .31±.08     |
| 0                    | .17±.06     | .10±.05     | .15±.06     | .34±.07     | .21±.05     | .31±.07     |
|                      | $142^\circ$ | $149^\circ$ | $156^\circ$ | $163^\circ$ | $169^\circ$ | $172^\circ$ |
| Li <sup>6</sup>      | .79±.10     | 1.31±.13    | 1.51±.14    | 1.55±.14    | 2.46±.17    | 2.12±.16    |
| 0                    | .57±.07     | .52±.07     | .80±.08     | .77±.08     | 1.06±.09    | .90±.08     |

TABLE IV

Number of Correlated Emissions of Two Nucleons per Stopped Pion

| Nucleus   | n-n<br>(relative units) | p-n<br>(relative units) | ratio            | $\frac{n-n}{p-n}$ |
|---|-------------------------|-------------------------|------------------|-------------------|
| Li <sup>6</sup>   | 8.9 ± 3.6 (±.5)         | 2.4 ± .6 (±.17)         | 3.7 ± 1.0 (±.3)  |                   |
| Li <sup>6</sup> (smaller<br>detectors)                        | 20.7 ± 8.3 (±.9)        | 3.4 ± .9 (±.14)         | 6.1 ± 1.6 (±.4)  |                   |
| Li <sup>7</sup>   | 9.0 ± 3.7 (±.8)         | 2.5 ± .7 (±.18)         | 3.6 ± 1.0 (±.4)  |                   |
| Be  | 6.0 ± 2.4 (±.4)         | 2.1 ± .5 (±.14)         | 2.8 ± 0.7 (±.3)  |                   |
| B <sup>10</sup>   | 3.9 ± 1.6 (±.8)         | 1.8 ± .5 (±.20)         | 2.2 ± 0.6 (±.5)  |                   |
| B   | 4.6 ± 1.9 (±.6)         | 1.0 ± .3 (±.15)         | 4.4 ± 1.3 (±.9)  |                   |
| C   | 3.5 ± 1.4 (±.8)         | 1.5 ± .4 (±.20)         | 2.3 ± 0.8 (±.6)  |                   |
| N   | 3.5 ± 1.4 (±.6)         | 1.0 ± .3 (±.15)         | 3.7 ± 1.1 (±.9)  |                   |
| O   | 5.7 ± 2.3 (±.8)         | 1.5 ± .4 (±.21)         | 3.8 ± 1.2 (±.6)  |                   |
| O (smaller<br>detectors)                                      | 11.9 ± 4.8 (±.9)        | 2.0 ± .5 (±.09)         | 6.1 ± 1.6 (±.6)  |                   |
| Al  | 2.8 ± 1.3 (±.8)         | 1.0 ± .3 (±.13)         | 2.9 ± 1.0 (±1.0) |                   |
| Cu  | 1.7 ± 1.2 (±1.0)        | 1.0 ± .3 (±.21)         | 1.7 ± 1.1 (±1.1) |                   |
| Pb  | 1.3 ± 1.3 (±1.3)        | 0.3 ± .3 (±.35)         | 4.7 ± 4.7 (±4.7) |                   |
| Average weighted with overall errors                          |                         |                         | 3.9 ± 1.0        |                   |
| Average weighted with statistical errors in parenthesis above |                         |                         | 4.6 ± 1.1        |                   |



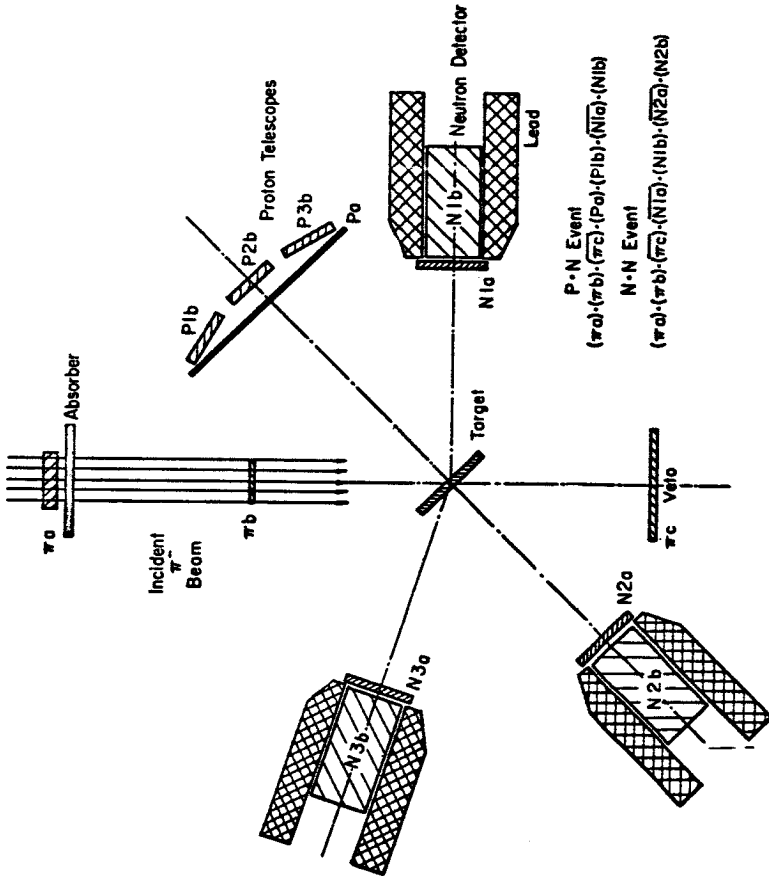


Figure 1.

Apparatus for measuring the angular correlation of p-n pairs emitted in  $\pi^-$  - absorption.

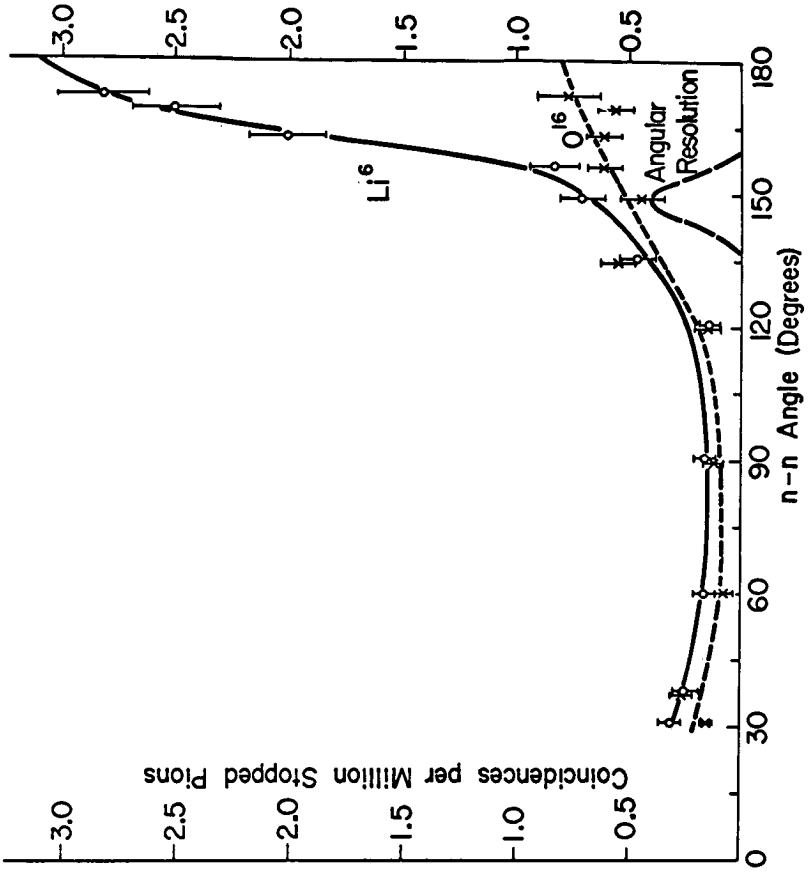


Figure 2. Angular correlation of  $n-n$  pairs from  $Li^6$  and  $O^{16}$ .

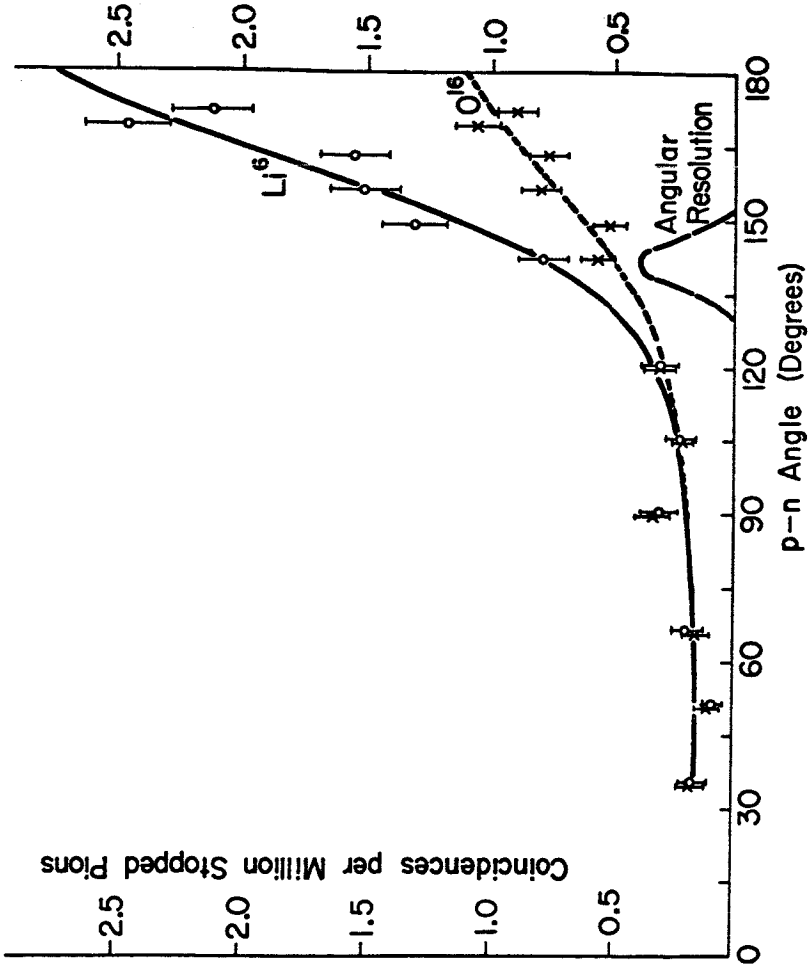


Figure 3. Angular correlation of p-n pairs from  $Li^6$  and  $O^{16}$

GOTTSCHALK: It is rumored that you have done preliminary experiments on  $\pi^+$  capture in flight. Could you comment on the counting rates that you get in such experiments?

NORDBERG: We have done preliminary experiments with this same apparatus just changing the coincidence requirement so that you detect protons in all counters rather than both neutrons and protons and this gives us, at a rough estimate, a feasible counting rate in the set-ups we are planning. I wouldn't say much beyond that, except that it's also peaked at  $180^\circ$ .

PHILLIPS: In the experimental point, you didn't show any measurement of the energies of the proton nor the energy of the neutron from time of flight. Do you have any comments on that - in particular do you know how many of these events of the angular correlations correspond to essentially a full energy event?

NORDBERG: No, we don't know how many are full energy. The proton threshold is determined by the range. The proton must get out of the target and through one scintillator to be counted in the second. The neutron threshold is determined by its pulse height in the neutron counter and, of course, anything higher than that can produce such a pulse, but one has to make calculation. We've assumed that the neutron energy distribution is the phase space distribution in order to make the efficiency calculations. This is just an approximation. In other words, the neutron energies are integrated over a certain threshold, that threshold is 7 Mev for the larger detectors and 11 Mev for the smaller. The precision on the ratio is almost entirely limited by this efficiency calculation which is about 25% - I'm sorry, I should have said for Cu and Pb the data is much, much poorer than for any of the others. The precision there is about 50%, from statistics.

N66 223  
32740

PION CAPTURE AND NUCLEAR STRUCTURE

H. Davis, H. Muirhead, and J. N. Wouds

University of Liverpool

[Paper presented by P. T. Andrews]

As there is a large amount of data from this experiment I shall simply run quickly through the results.

Figure 1 shows the counter arrangement. There were two neutron counters set at an angle near  $180^\circ$  and with these neutron energies could be measured by time of flight. There are anticoincidence counters in front of them so that charged particles are not counted. The counter telescope in the beam included a cerenkov counter and ensured that neutrons or gammas were observed only after a pion stopped.

The sodium iodide crystal was used for a separate measurement of gamma emission following pion capture. Again an anti-coincidence counter rejected charged particles entering the crystal and neutrons were rejected by their longer time of flight.

The measurements were done on  $\text{Li}^6$  and  $\text{Li}^7$  as these were expected to show differences in the number of correlated neutron proton pairs in the nucleus. Also as they are light nuclei negative pion capture is almost entirely from the S state.

Figure 2 shows the total kinetic energy of the two neutrons plotted against their total momentum for a  $^6\text{Li}$  target. There are no corrections for instrumental efficiency variation with energy nor background subtraction. All neutrons have been included which had energies greater than 8.5 Mev. The expected clustering of events around the total energy of 140 Mev and zero momentum transfer to the nucleus shows up very clearly. Fig. 3 shows a similar

plot obtained with a  ${}^7\text{Li}$  target. The clustering noticeable at 140 Mev is somewhat away from zero momentum transfer. This will show up more clearly in Fig. 9. In the case of the  ${}^7\text{Li}$  there is much less obvious clustering of the points around 140 Mev. than in the  ${}^6\text{Li}$  case.

Fig. 4 shows the total kinetic energy distribution for the two neutrons from  ${}^6\text{Li}$ . The total momentum is restricted to the 0-100 Mev/c range. The coincidence counters are at  $180^\circ$ . The ordinate is in pairs of particles/ Mev/c, ster, stopped pion. As was expected there is a large peak at an energy corresponding to the  ${}^4\text{He}$  being left in the ground state. There is also some indication of an excited state at 40 Mev. The distribution for  ${}^7\text{Li}$  shown in Fig. 5 indicates that the yield is less than for  ${}^5\text{Li}$  but is still mainly to the final ground state, in this case that of  ${}^5\text{He}$ .

Fig. 6 shows the distributions of total kinetic energy of the neutrons from capture in  ${}^6\text{Li}$  and  ${}^7\text{Li}$  again, but in this case when the total momentum is in the 100-200 Mev/c range. These are rather large momentum transfers to the nucleus and the distributions are different from those of Fig. 4 and 5. The nuclei are not left predominately in their ground states and the evidence for states at about 40 Mev excitation is stronger.

Fig. 7 shows the angular distribution of the neutrons relative to each other for  ${}^6\text{Li}$  and  ${}^7\text{Li}$ . The dotted line includes all events, the solid line is drawn using only events where the final nuclei were left in their ground states. (The peak picked out in Fig. 4). It is very obvious that these transitions to the ground state have more peaked distributions than when all events are included. The strong peaking of these distributions is good evidence that the captures take place on correlated nucleons. The distribution for  ${}^7\text{Li}$

is less strongly peaked than that for  ${}^6\text{Li}$ . On integrating over the solid angles it is found that capture of a pion on  ${}^6\text{Li}$  leads  $(37 \pm 10)\%$  to the ground state of  ${}^4\text{He}$  and capture on  ${}^7\text{Li}$  leads  $(50 \pm 12)\%$  to the ground state of  ${}^3\text{He}$ .

Fig. 8 shows the distribution of total neutron momentum from capture on  ${}^6\text{Li}$  and Fig. 9 that for  ${}^7\text{Li}$ . The solid curves are for those cases where the capture goes to a ground state and were selected by requiring the total kinetic energy to lie between 115 and 155 Mev. The dotted lines are for total kinetic energies between 80 and 110 Mev and may correspond to transitions to excited states in the final nuclei.

The solid curve in the  ${}^6\text{Li}$  case is a theoretical fit using a formula of Sakamoto. He derived this by using a model of  ${}^6\text{Li}$  as a cluster of an alpha particle and a deuteron in a relative S state. There is only one momentum variable and by giving this a value of  $48 \pm 6$  Mev/c the solid curve through the experimental points was obtained. Treating  ${}^6\text{Li} (p, pd) {}^4\text{He}$  as the quasi-elastic scattering of a proton off the deuteron in a cluster model  ${}^6\text{Li}$  Riou obtained a value of  $45 \pm 5$  Mev/c for the momentum parameter. This implies that the deuteron and alpha particle are about 4 Fermis apart, which is quite a large separation. Jackson obtained a p shell radius of 3.53 Fermis from an analysis of electron scattering on  ${}^6\text{Li}$ .

The momentum distribution of Fig. 9 for capture on  $\text{Li}^7$  shows a dip near zero momentum. This suggests that if one is capturing the  $\pi^-$  on a deuteron in  ${}^7\text{Li}$  that deuteron is not in a relative s state. Clearly one requires different pictures of the  ${}^6\text{Li}$  and  ${}^7\text{Li}$  nuclei.

The remaining figures show the data obtained from the NaI gamma counter. Two spectra are shown in Fig. 10. one is a calibration spectrum of gamma rays

from pion capture in a hydrogen target. The other is the spectrum from  $\pi^-$  capture on  ${}^6\text{Li}$ . These show that the energy resolution is not good. The hydrogen target spectrum provides a resolution function.

Fig. 11 shows the spectra of gammas following  $\pi^-$  capture in all the nuclei examined. They have in common a fairly narrow peak showing that the process is a very simple one. If there were any final state more complicated than one free neutron and a gamma ray, you would expect a much broader peak than given by the instrumental resolution. Fig. 12 is a table of the results which have been referred to by Dr. T. Ericson in his talk in which he successfully accounted for the yields.

The position of the peaks suggests one is observing a simple capture of a  $\pi^-$  on one nuclear proton leading to a free neutron and a gamma ray. Petrukin and Prokoshkin observed 9 Mev neutrons correlated with gammas of greater than 30 Mev energy when  $\pi^-$  were captured on nuclei. Their yield was about 2%.

Fig. 13 is an attempt to explain the energy spectrum by using a degenerate Fermi gas model for the nucleus  ${}^6\text{Li}$ .

No. 1 is the theoretical result. No. 2 has the actual experiment resolution folded in and no. 3 is a line through the experimental points.

This work will very soon be published in full in two papers in Nuclear Physics.



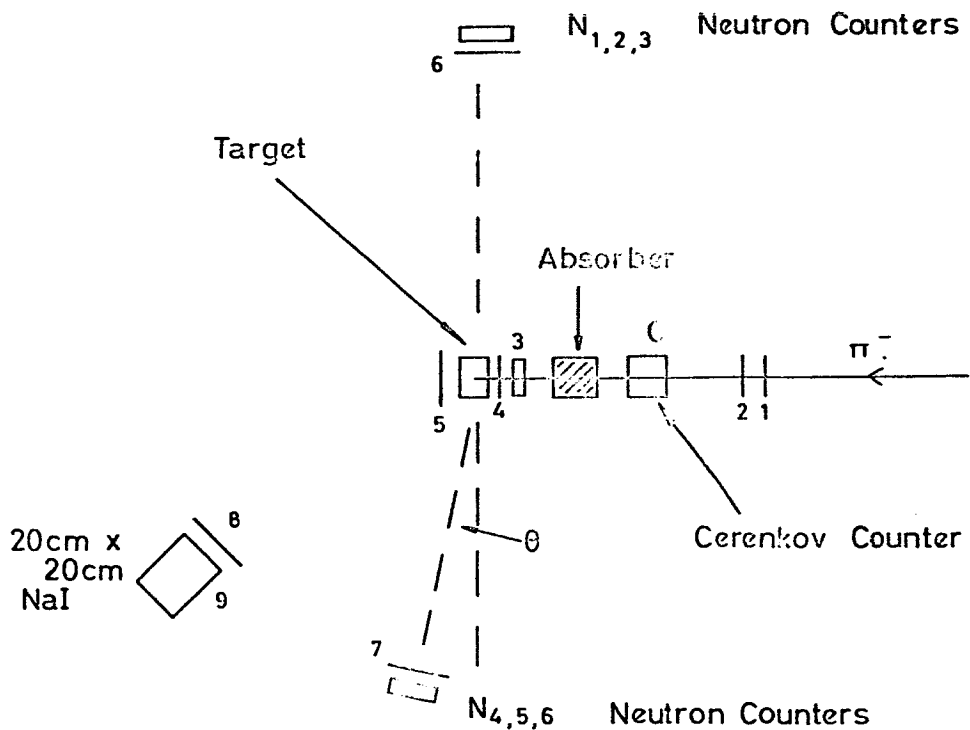


Figure 1. Experimental layout.

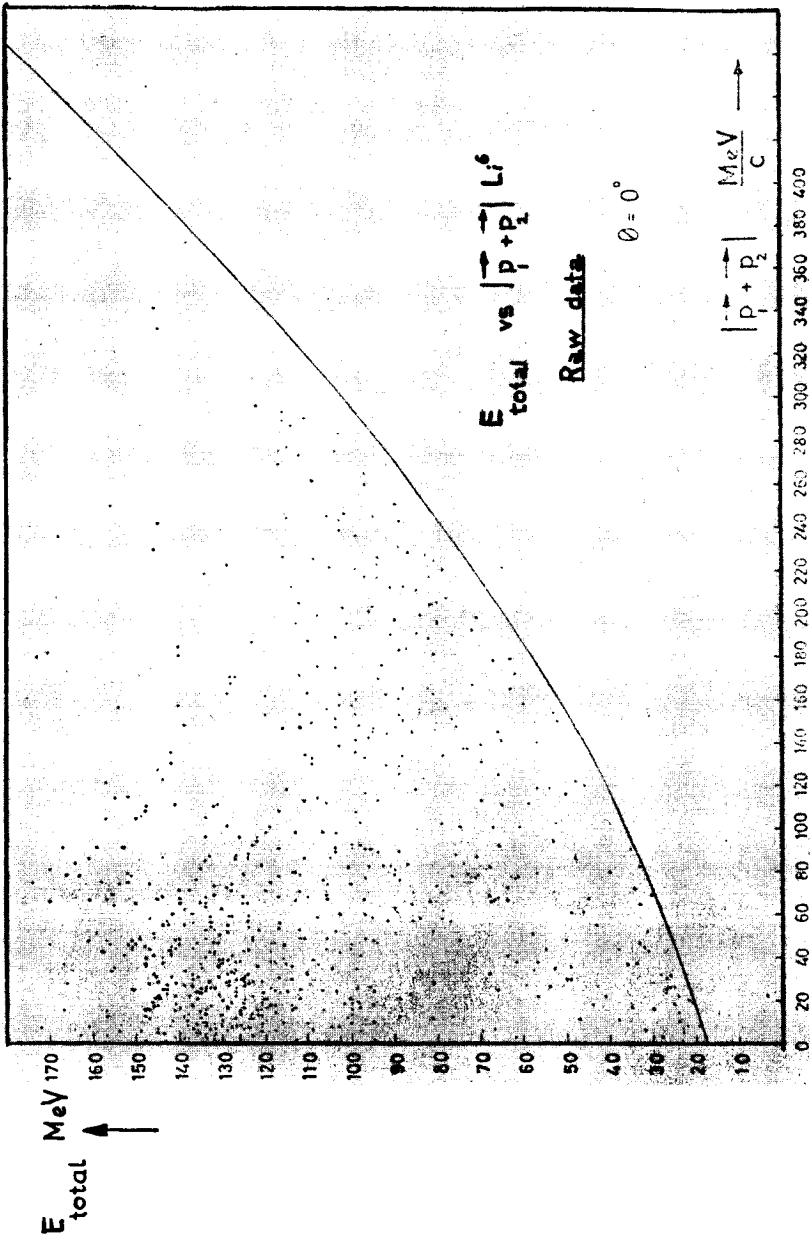


Figure 2. Energy-momentum plot for two neutrons from  $\pi^-$  capture in  $\text{Li}^6$ .

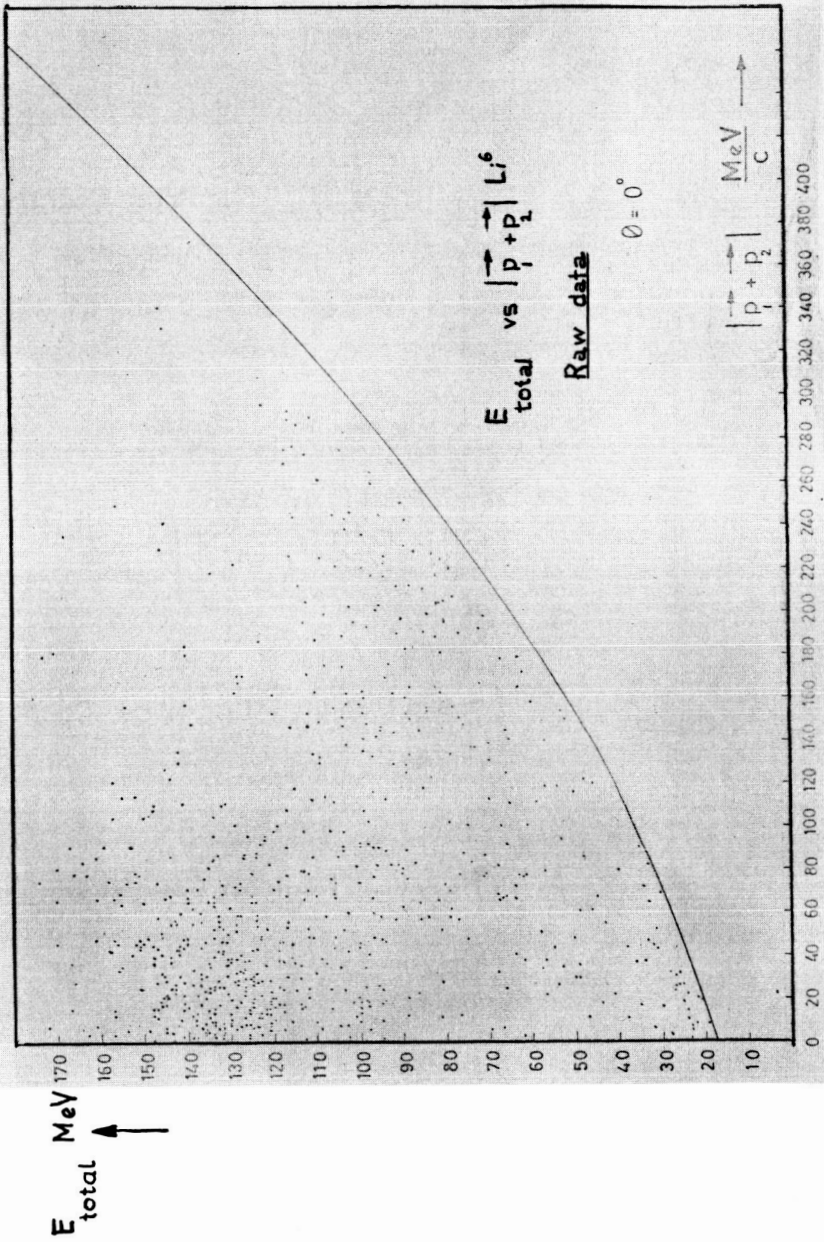
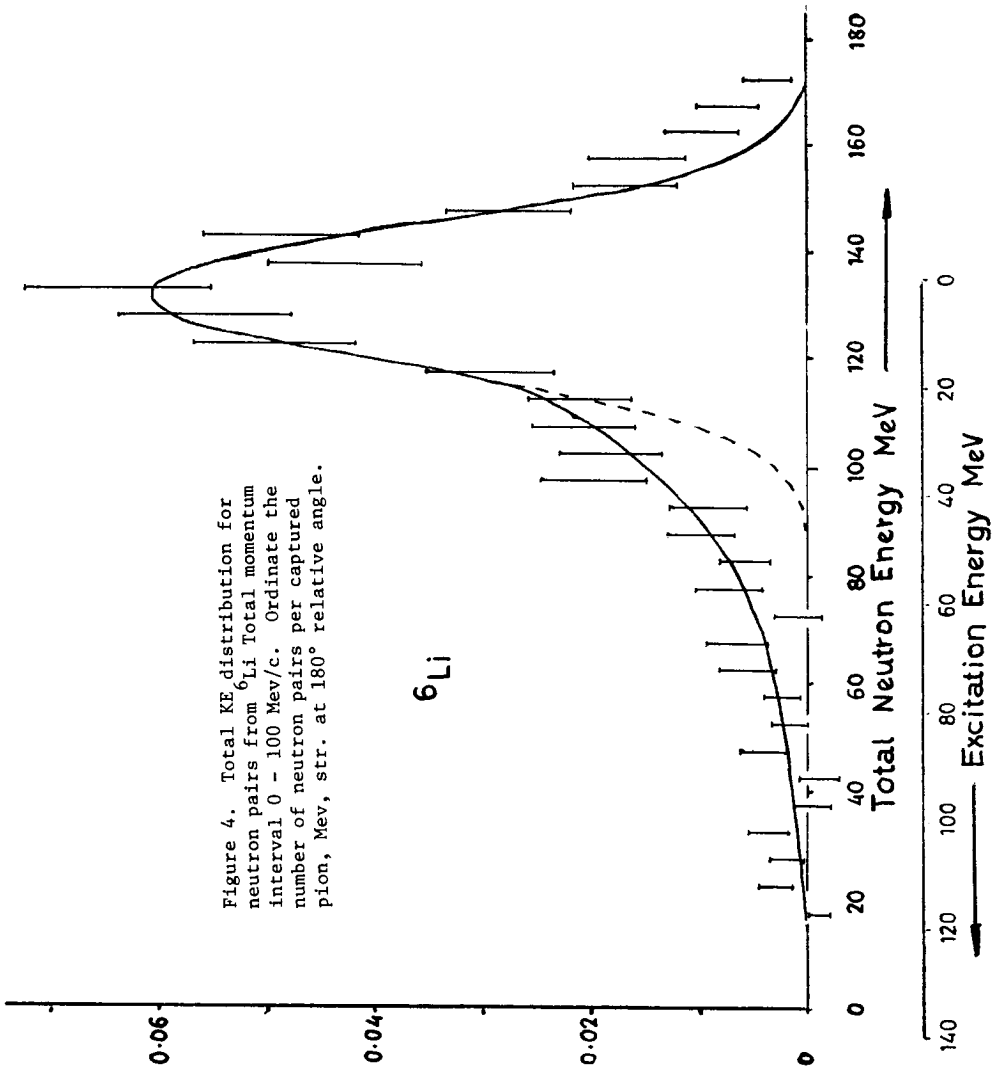


Figure 2. Energy-momentum plot for two neutrons from  $\pi^-$  capture in  $\text{Li}^6$ .



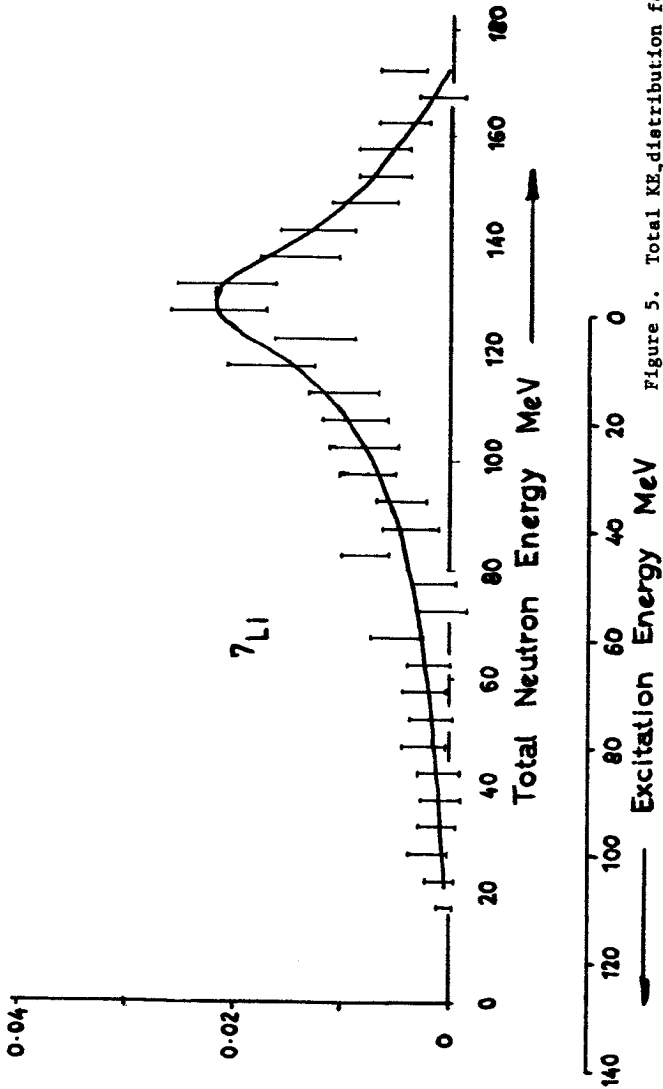
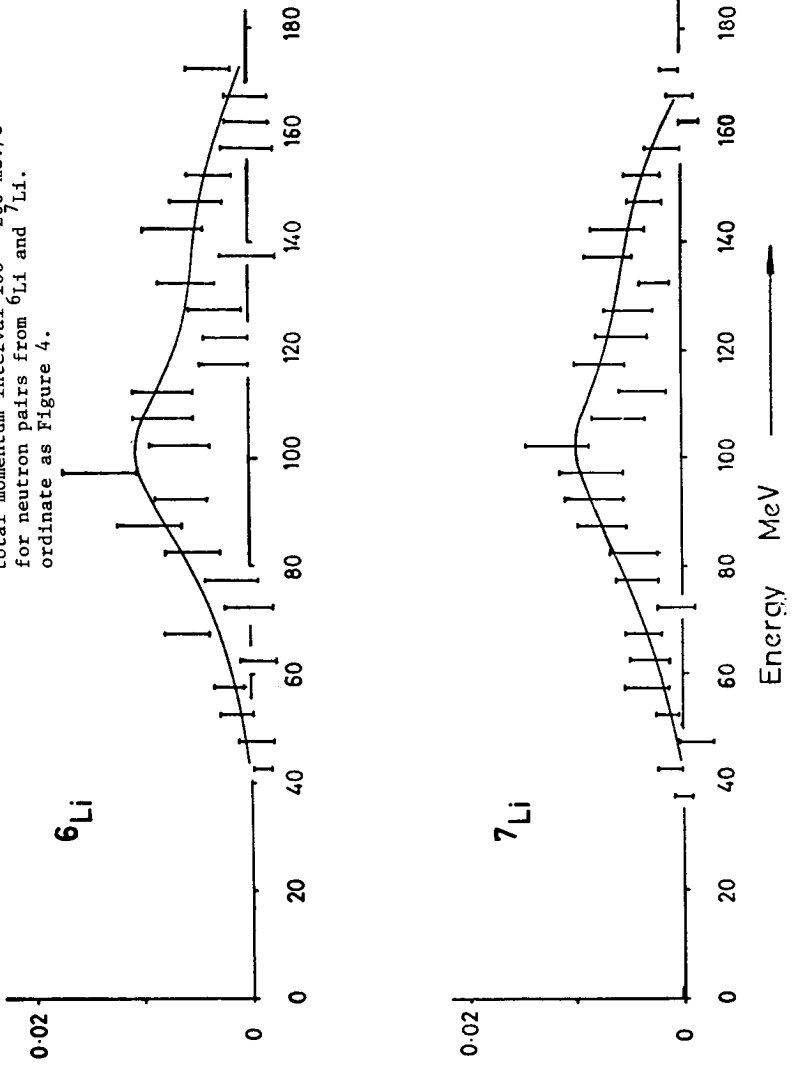


Figure 5. Total  $K\pi$  distribution for neutron pairs from  ${}^7\text{Li}$ . Total momentum interval 0 - 100 Mev/c.

Figure 6. Total KE distribution in total momentum interval 100 - 200 meV/c for neutron pairs from  ${}^6\text{Li}$  and  ${}^7\text{Li}$ . Ordinate as Figure 4.



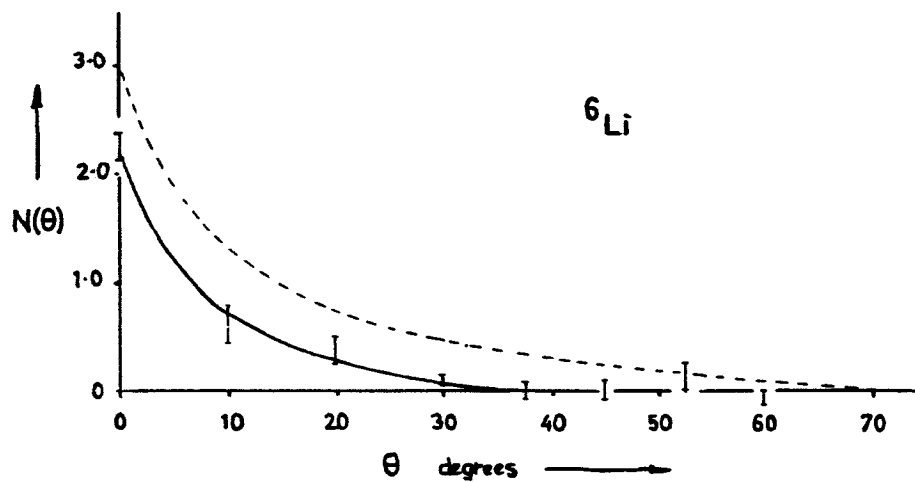
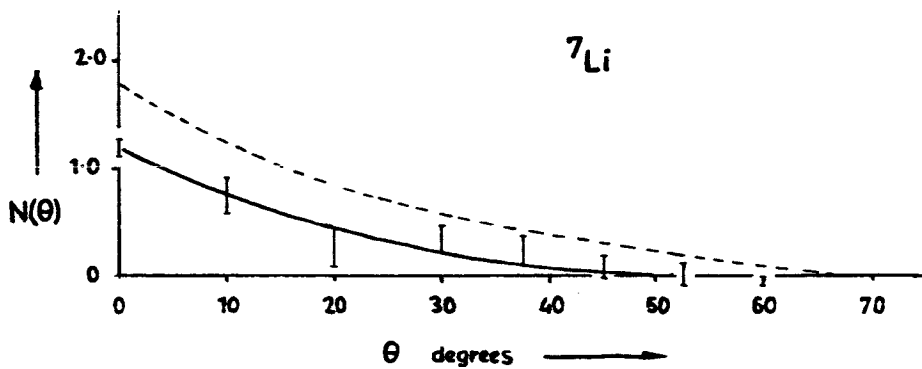


Figure 7. Relative angular distributions for neutron pairs from  ${}^6\text{Li} + \pi^-$  and  ${}^7\text{Li} + \pi^-$ . Dotted line includes all events; the solid line is those giving a final nucleus ground state.

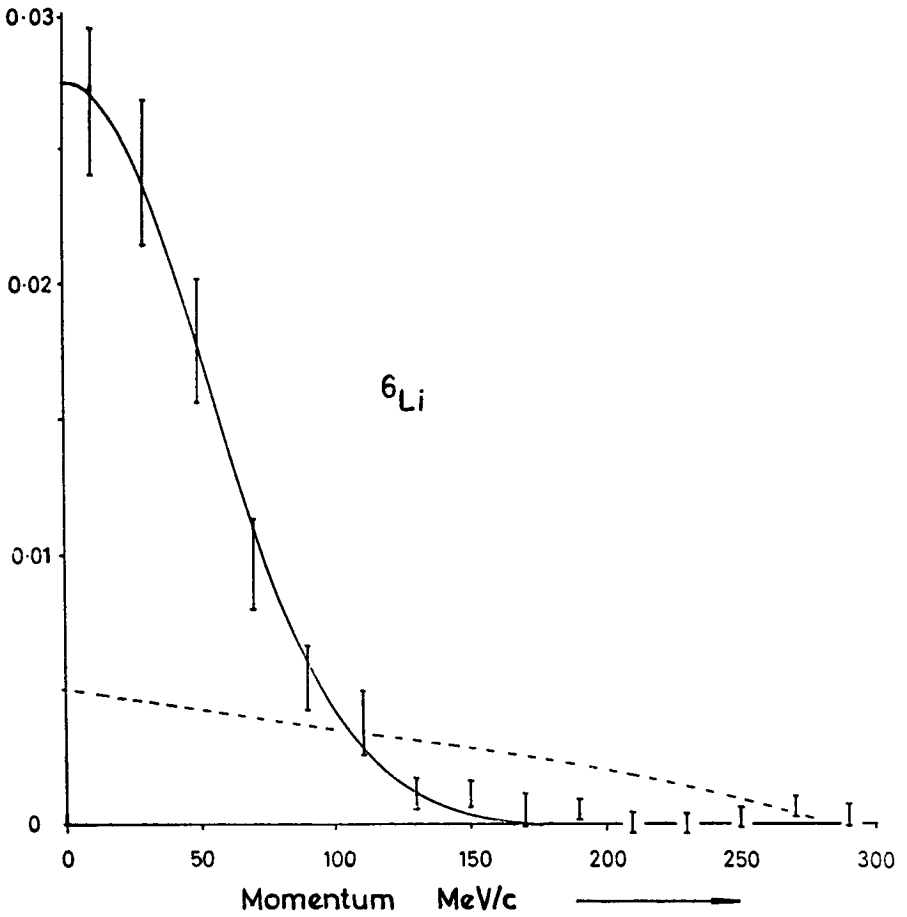


Figure 8. Momentum distribution of neutron pairs from  ${}^6\text{Li} + \pi^-$ . For explanation see text.



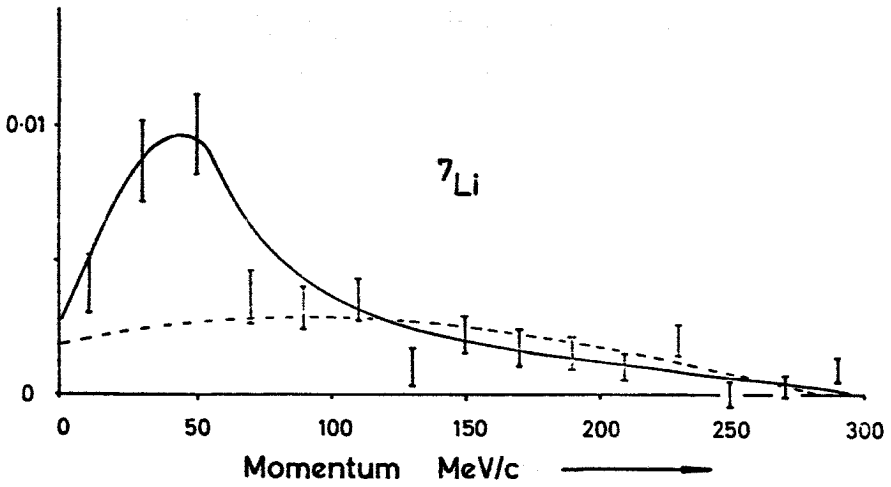


Figure 9. Momentum distribution of neutron pairs from  ${}^7\text{Li} + \pi^-$ . For explanation see text.

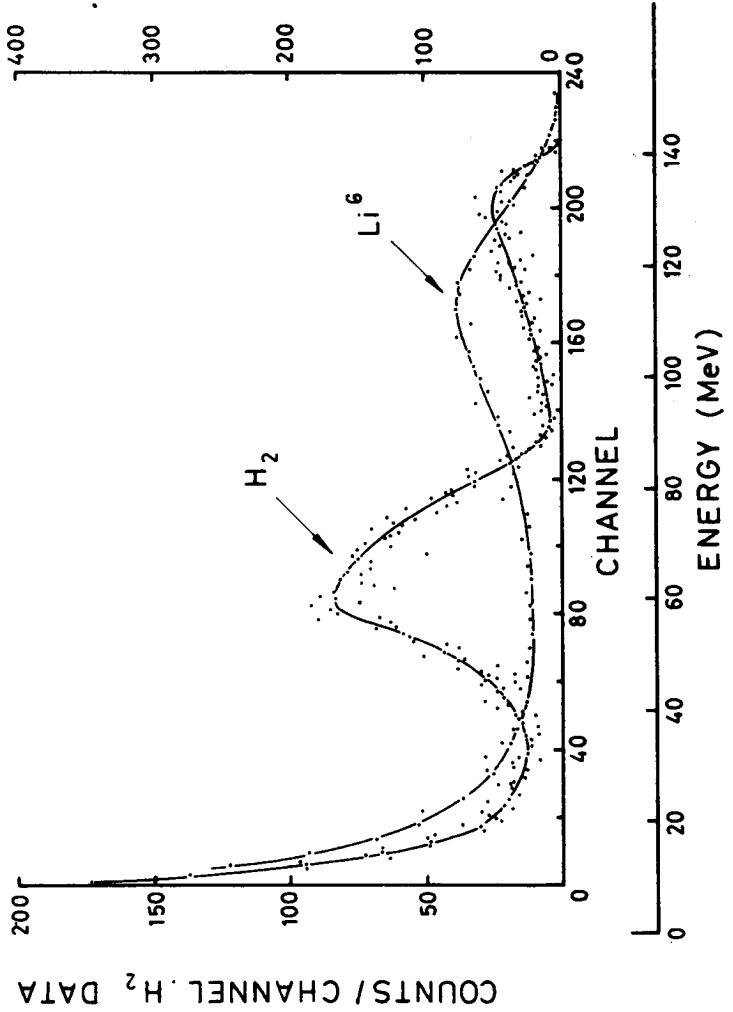
COUNTS / FOUR CHANNELS,  ${}^6\text{Li}$  DATA

Figure 10. Gamma ray spectra from  $\text{H} + \pi^-$  and  ${}^6\text{Li} + \pi^-$ .

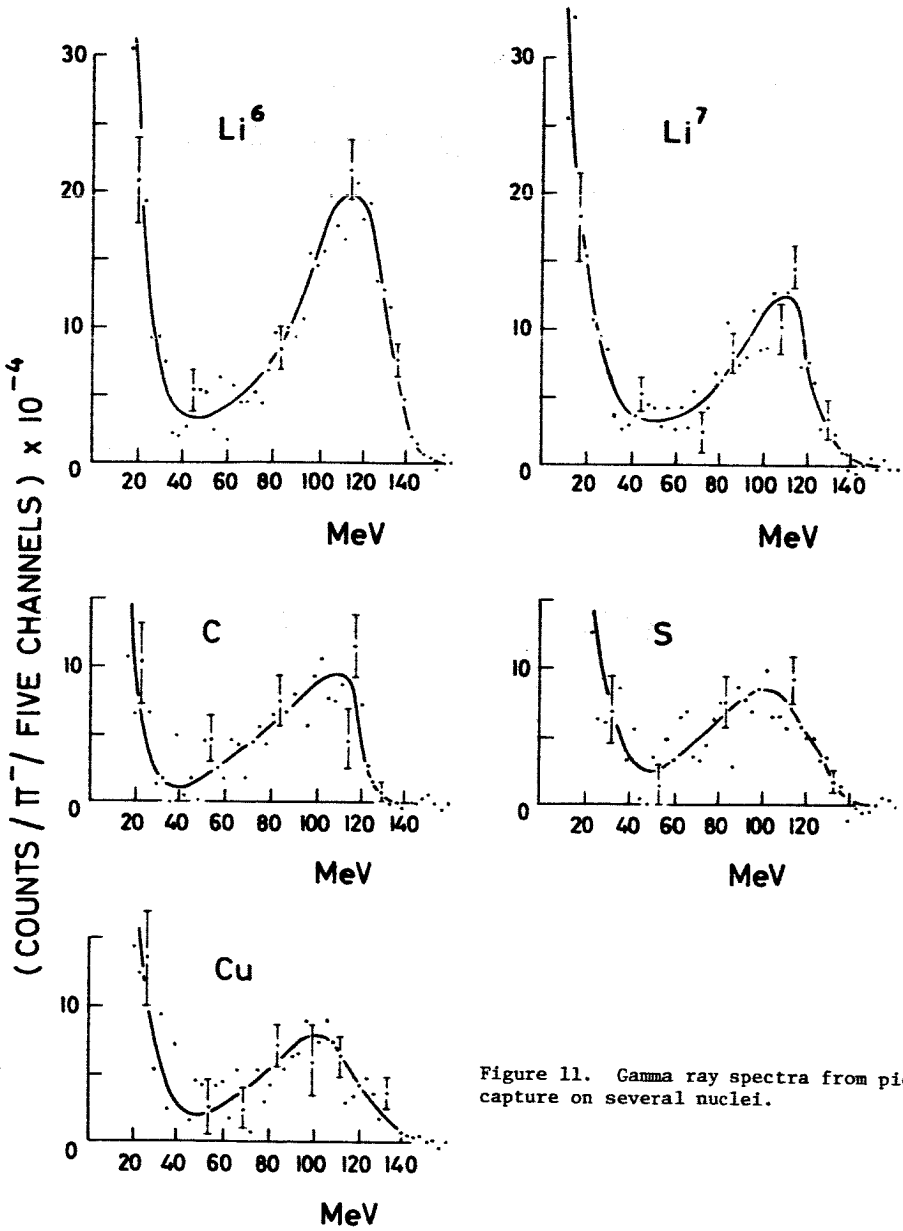


Figure 11. Gamma ray spectra from pion capture on several nuclei.

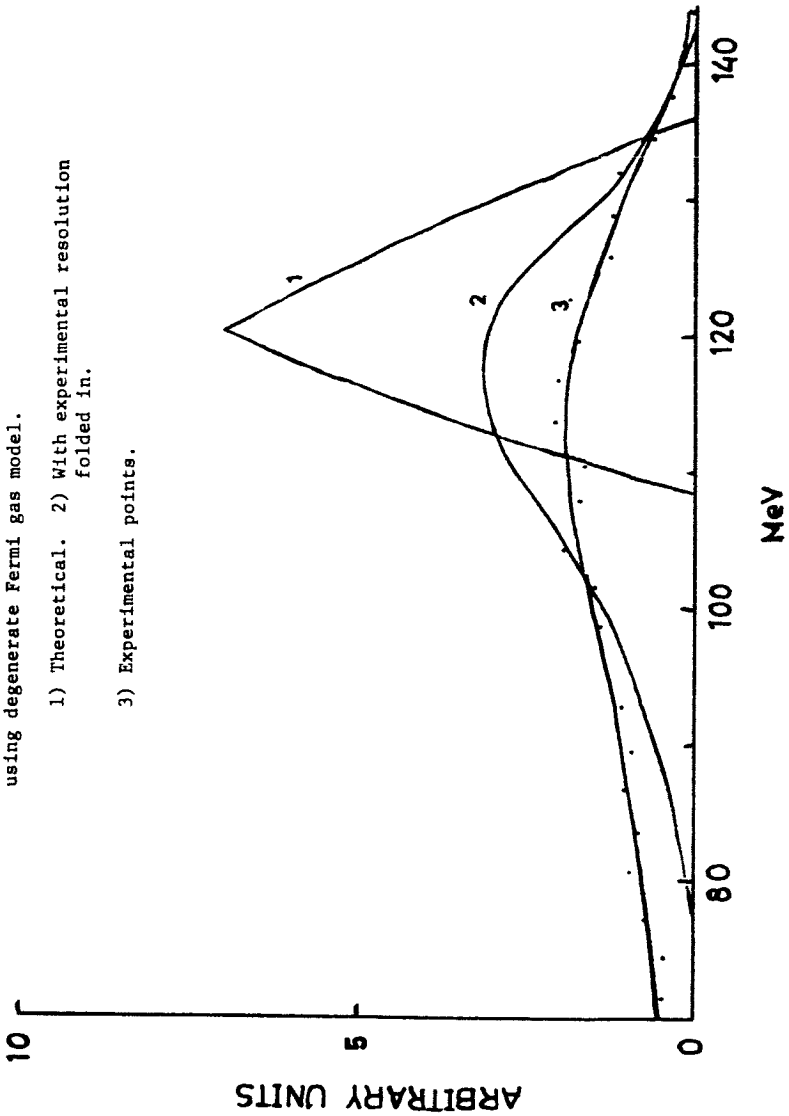
TABLE 1

| Target          | Position of peak | Full width<br>at half-height | Yield             |
|-----------------|------------------|------------------------------|-------------------|
| ${}^6\text{Li}$ | 114 MeV          | 44 MeV                       | $0.033 \pm 0.002$ |
| ${}^7\text{Li}$ | 109              | 41                           | $0.019 \pm 0.002$ |
| C               | 108              | 46                           | $0.016 \pm 0.001$ |
| S               | 102              | 56                           | $0.018 \pm 0.001$ |
| Cu              | 100              | 50                           | $0.015 \pm 0.001$ |

Figure 12. Table of results.

Figure 13. Calculation of gamma energy spectrum for  ${}^6\text{Li}$  using degenerate Fermi gas model.

- 1) Theoretical.
- 2) With experimental resolution folded in.
- 3) Experimental points.



KOLTUN: I have one question about  $\text{Li}^7$  data. In the rather striking difference in the distribution of summed momenta, the two particles coming out look quite different from the angular correlation of the two nucleons which shows no  $180^\circ$  dip. Yet the two are connected through integral forms.

ANDREWS: That is true. I'm not going to offer any explanation, though.

KOLTUN: Is the angular resolution poorer than momentum resolution?

ANDREWS: Angular resolution is poorer than momentum resolution. Just how much poorer, I don't know. That may very well be the explanation. I think the time of flight measurements are good enough to show the dip quite clearly. It's a very strong dip. If you put in the resolution function, it would make a much deeper dip.

ERICSON: I want to make a short comment on the  $\pi$ - $\gamma$  work. Because of the large similarity of this process to mu capture, studies of radiative pi capture also can be used as an empirical measurement of the distribution of excited states of mu capture. This has been a quantity one has always found very hard to get at, because the average energy of the neutrino in mu capture processes enters importantly in the theory.

N66-241  
32741

Theory of Pion Absorption on Light Nuclei

D. Koltun and A. Reitan

Department of Physics and Astronomy  
University of Rochester, Rochester, New York

We consider the absorption of a pion by a nucleus, with the emission of two fast nucleons, in the impulse approximation, such that only the two recoiling nucleons interact with the pion. Thus we neglect the interaction of the pion or fast nucleons with other target nucleons, but we do try to treat the direct process in some detail.

A theory which attempts to explain this process should be able to explain the simpler case of pion absorption by the deuteron, or, since this experimental information is not directly available, the time-and charge-reversed reaction  $p + p \rightarrow \pi^+ + d$  near threshold. It has been known for some time that the simple pseudovector pion-nucleon interaction applied to a simple s-state deuteron gives the right order-of-magnitude rate, but inclusion of the D-state in a better deuteron wave function almost cancels this out, giving much too small a rate. Woodruff<sup>1</sup> proposed that the theory can be improved by considering the first multiple scattering process which can occur: The pion first scatters in an s-wave from one nucleon, and is captured by the second. Thus, in addition to the pi-nucleon absorption interaction, one needs an interaction which scatters pions in s-waves; this latter is obtained phenomenologically from low energy pi-nucleon

scattering. (See Fig. 1.) We have applied this rescattering theory with some improvements to the deuteron reaction, using a variety of deuteron wave functions and final-state wave functions generated from phenomenological nucleon-nucleon potentials. Our result for the threshold cross section  $\sigma(p + p \rightarrow \pi^+ + d)$  agrees with experiment. See Table I.

We note that both the rescattering  $(K_3, K_4, K_5, K_6)$  and the deuteron D-state  $(K_2, K_4, K_6)$  contributions are essential. This work has just appeared in the Physical Review,<sup>2</sup> along with the calculation of  $\sigma(p + p \rightarrow \pi^0 + p + p)$ .

We have applied the same considerations to the absorption  $\pi^- + \text{Li}^6 \rightarrow \alpha + n + n$ , considering only interaction with the valence nucleons. Here the central problem is to obtain good wave functions for the nucleon motion, in particular with the D-state component mixed into, say, the Shell Model ground state ( ${}^3S_1$ ). We have so far made use of wave functions for relative motion in a harmonic oscillator well plus Hamada-Johnston interaction,<sup>3</sup> which have been generated by Y.E. Kim at Oak Ridge.<sup>4</sup> The final state is taken as the H.J.  ${}^3P_1$  relative state. We were stuck with the harmonic oscillator range parameter chosen by Kim, which is appropriate to most of the 1p shell, but not to  $\text{Li}^6$ .

For given final momenta of the absorbing nucleons, the amplitude is given by a combination of relative motion amplitudes (J) with c. of m. wave functions (in momentum space). For example, for emission at angle



## Pion Absorption

$\theta = \pi$  we can give the probability  $P(k_1 + k_2)$ , as shown in Table II. For our  $\Sigma$ , we get a distribution in  $K = k_1 + k_2$  reflecting the sum of oscillator functions  $u_{0s}(K) + u_{1s}(K)$ , while for no rescattering, we get only  $u_{1s}$ , and if there is no rescattering and no D-state, we get almost  $u_{0s}$  alone, as shown in Fig. 2. The scale is  $x = K/160$  MeV/c. This is the Shell Model  $K = \sqrt{3/2} K$  experimental, because of  $\alpha$ -recoil.

Experiments by Davies, Muirhead and Woulds (Liverpool)<sup>5</sup> giving  $P(K)$  at  $\theta = \pi$ , are shown in Fig. 3. The shape agrees with our full calculation, but the scale disagrees, which simply means we must use a different center of mass oscillator range (larger) than relative. The experiment on Li<sup>7</sup>, shown in Fig. 4, gives a strikingly different distribution which however seems to disagree with the angular correlation of neutrons, which is monotonic in  $\theta$ .

We have also extended our method to treat absorption by a  $^1S_0$  pair. If we can ignore absorption by  $L \neq 0$  states in light nuclei, for which we have some evidence, we can use the ratio of the amplitude for  $^1S_0$  absorption to that for  $^3S_1$  absorption, to give the ratio of n-n pairs to n-p pairs emitted in  $\pi^-$  absorption. This ratio has been measured by Ozaki et al<sup>6</sup> for  $\theta = \pi$  on C<sup>12</sup>, to be  $\approx 5$ , and also for various light elements by the Rochester group: Nordberg, Kinsey and Burman,<sup>7</sup> shown in article I, page I-10.

The simplest case to calculate is for O<sup>16</sup>, considered as a closed

shell nucleus. For equal amplitudes for  $^1S_0$  and  $^3S_1$ , as given in the pseudovector absorption theory without rescattering, the  $nn/np$  ratio is 3. However, we find that rescattering changes this to about 5.

---

#### References

1. A. E. Woodruff, Phys. Rev., 117, 1113 (1960).
2. D. S. Koltun and A. Reitan, Phys. Rev., 141, 1413 (1966).
3. T. Hamada and I. D. Johnston, Nuclear Phys., Vol 34, p. 382 (1962).
4. Y. E. Kim, Phys. Letters 19, 583 (1965), and private communication.
5. H. Davies, H. Muirhead and J. N. Woulds, to be published.
6. S. Ozaki, R. Weinstein, J. Glass, E. Loh, L. Neimala and A. Wattenberg, Phys. Rev. Letts., Vol. 4, 533 (1960).
7. M. E. Nordberg, Jr., K. F. Kinsey and R. L. Burman, to be published.

TABLE I. The cross section  $\sigma_a$  for the reaction  $p + p \rightarrow d + \pi^+$  with s-wave pions, and the rate  $R$  for the reaction  $\pi^- + d \rightarrow n + n$  with pions in the 1s orbit. The integrals  $K_l$  are defined in Eqs. (13) and (23), and the quantity  $\eta$  is the pion momentum in units of  $\mu c$ . The p-p or n-n wave functions have been obtained by using the potentials of Hamada and Johnston<sup>8)</sup> (H-J) and Gammel and Thaler<sup>9)</sup> (G-T), and the deuteron wave functions are those of Hamada and Johnston<sup>8)</sup> (H-J) and Gartenhaus<sup>13,14)</sup> (G).

| p-p or n-n Deuteron state | $K_1$  | $K_2$  | $K_3$ | $K_4$  | $K_5$  | $K_6$  | $\sum_{l=1}^6 K_l \frac{\sigma_l}{\eta} (10^3 \mu b)$ | $\frac{R}{10^{15} s^{-1}}$ |      |      |
|---------------------------|--------|--------|-------|--------|--------|--------|---|----------------------------|------|------|
| H-J                       | -0.080 | 0.083  | 0.002 | -0.004 | -0.126 | -0.035 | -0.160  | 146                        | 0.84 |      |
| H-J                       | G      | -0.087 | 0.087 | 0.003  | -0.004 | -0.129 | -0.033  | -0.163                     | 151  | 0.87 |
| G-T                       | H-J    | -0.079 | 0.086 | 0.001  | -0.004 | -0.129 | -0.036  | -0.161                     | 147  | 0.85 |
| G-T                       | G      | -0.089 | 0.090 | 0.003  | -0.004 | -0.134 | -0.034  | -0.168                     | 160  | 0.93 |

TABLE II. The partial transition amplitudes for the  $0_S$  and  $1_S$  states of relative motion.  $\Sigma$  is the sum of all processes, while  $\Sigma_{\text{grad}}$  includes only direct absorption. The contributions of the S and D parts of the wave functions are so labelled.

|                 | $J_1$    | $J_2$ | $J_3$     | $J_4$ | $\Sigma$ | $(\Sigma_{\text{grad}})$ |
|-----------------|----------|-------|-----------|-------|----------|--------------------------|
| $0_S$           | -.042    | .142  | -.193     | -.032 | -.125    | (.100)                   |
| $1_S$           | -.100    | .108  | -.128     | -.026 | -.142    | (.008)                   |
| relative motion | <u>S</u> |       | <u>S</u>  |       | <u>D</u> |                          |
|                 | grad     |       | rescatter |       |          |                          |

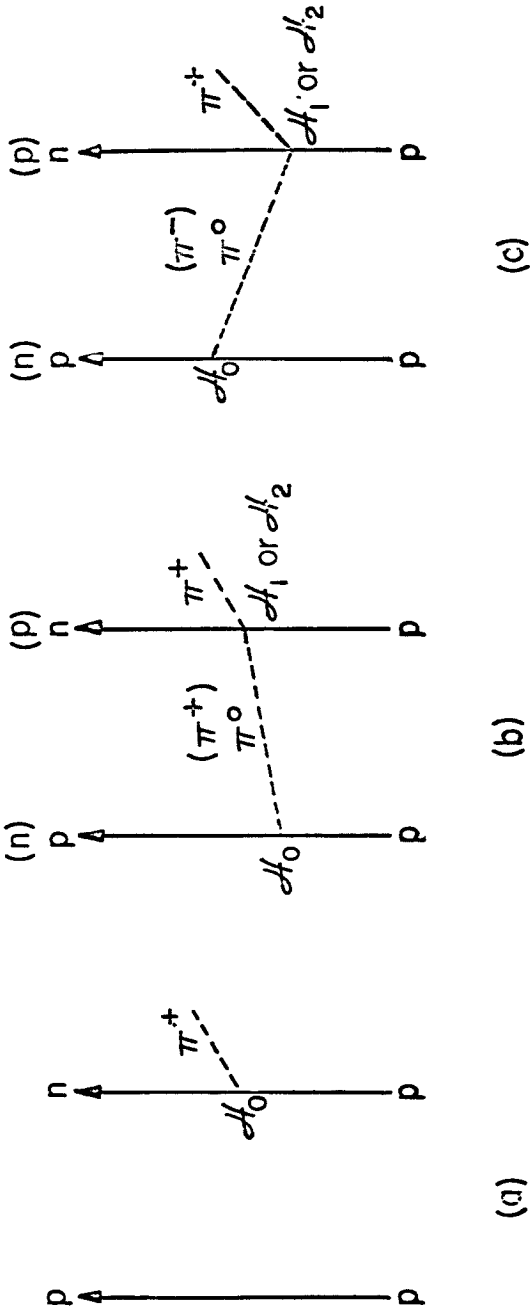


Fig. 1 Diagrams for the processes taken into account for the production process  $p + p \rightarrow d + \pi^-$ . For absorption, the arrows, denoting the direction of time, are reversed.

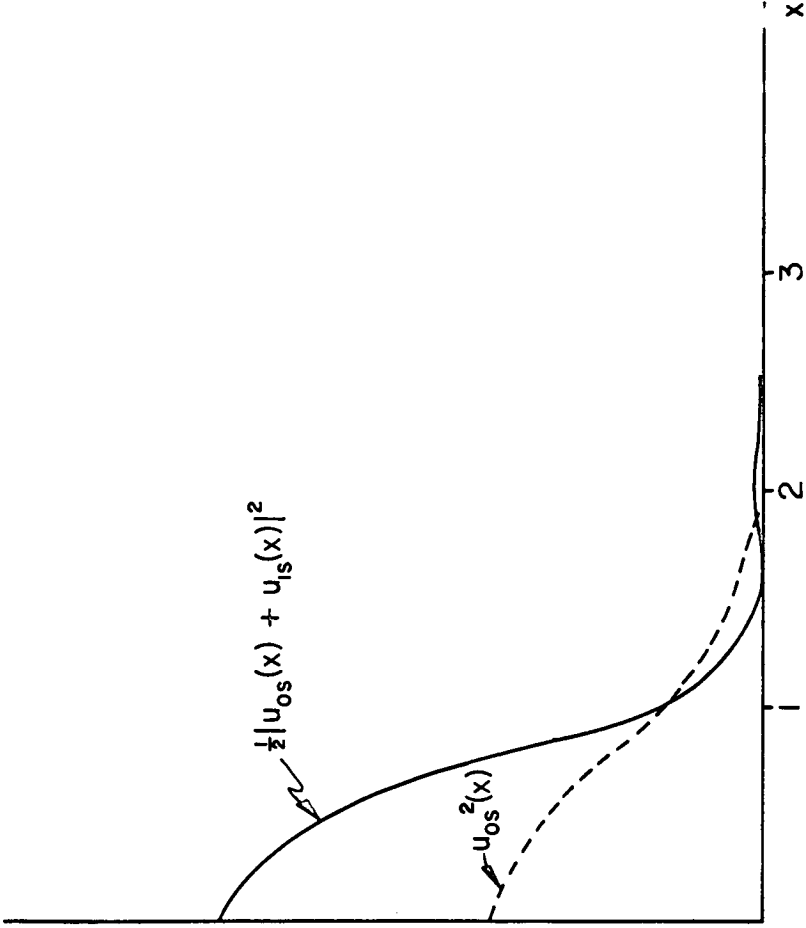


Fig. 2 Total Shell Model momentum distribution  $P(k)$  for equal  $\Sigma(0_s)$   $\Sigma(1_s)$ , in arbitrary units, compared to the distribution for  $\Sigma(1_s)$  alone. The momentum scale is in units of 160 MeV/c.

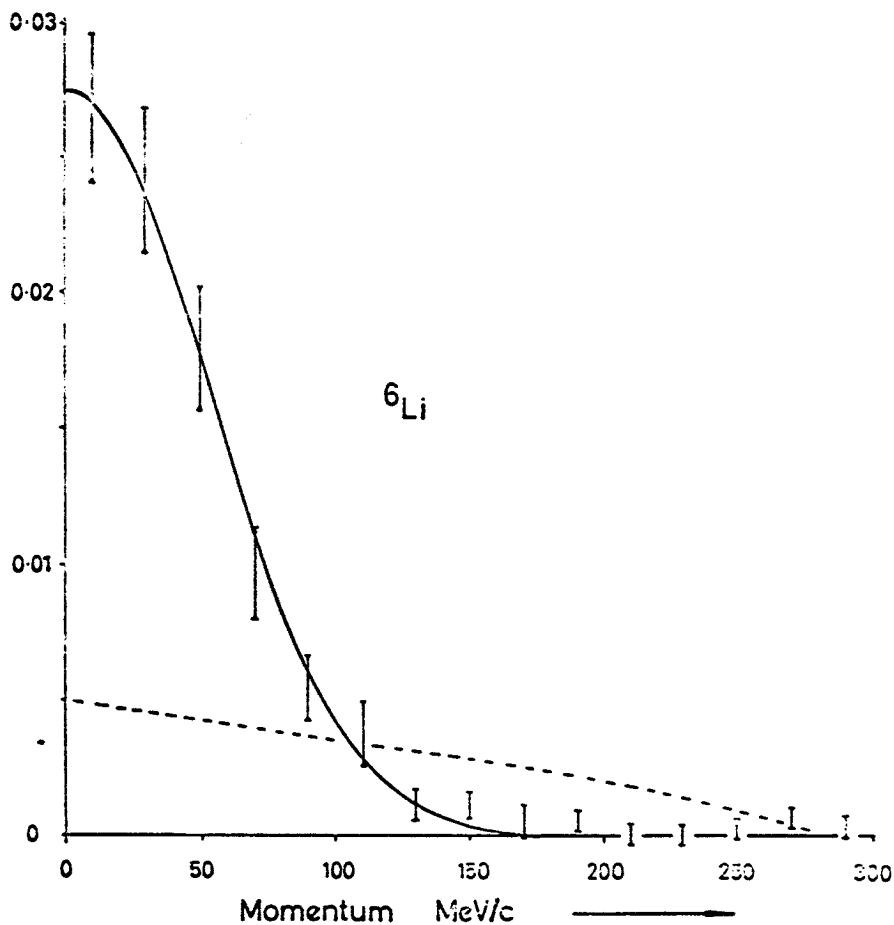


Fig. 3 Distribution of total momentum in the energy interval 115-155 MeV for  $\text{Li}^6$ . Ordinate, the number of neutron pairs emitted per captured pion per MeV/c per sterad. at a relative angle of  $180^\circ$ . The dotted curve shows the momentum distribution in the energy interval 80-110 MeV.

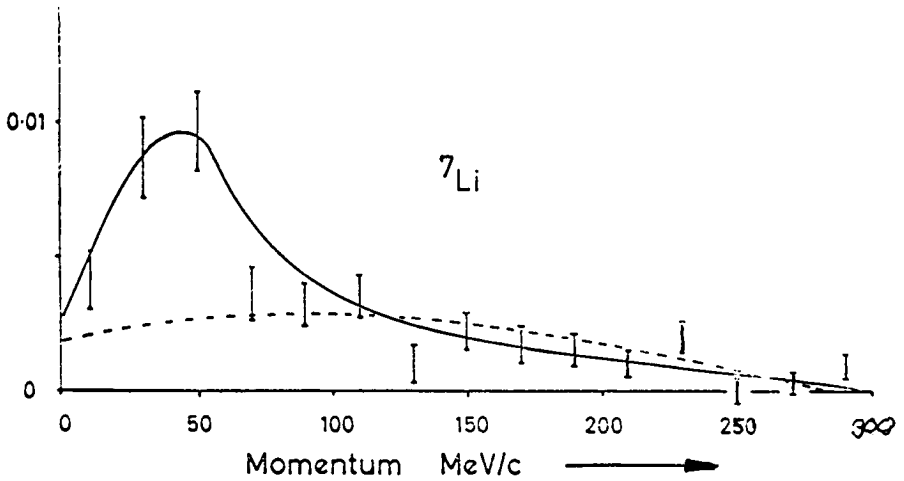


Fig. 4 Distribution of total momentum in the energy interval 110-150 MeV for  $\text{Li}^7$ . Ordinate, the number of neutron pairs emitted per captured pion per MeV/c per sterad. at a relative angle of  $180^\circ$ . The dotted curve shows the momentum distribution in the energy interval 80-110 MeV.



## Pion Absorption

CROWE: I'd like to know if you have ever tried to apply your rescattering calculations to the Panofsky ratio in  $\pi^-$  capture in deuterium? There was a discrepancy by Ryan several years ago.

KOLTUN: I haven't, Reitan has. The results aren't published. If I remember, the results were surprisingly good, that is, they were so surprisingly good that we didn't believe them and it's being reworked. We were looking at Ryan's results at the time.

CROWE: Do you consider it a direct check of your calculations? It's a very simple final state.

KOLTUN: It should be. I suppose the only question is whether you are fitting in the electro-magnetic effects correctly; you should be.

BLOCK: As I understand your rescattering, it is the physical equivalent of the pion being swallowed up by two nucleons - in somewhat simpler words. Your theory predicting the large ratio of n-n to p-n is essentially a restatement that the pion is preferentially absorbed on the deuteron-like structure - at  $\approx 0$  absorption.

KOLTUN: That's right. In fact, we coupled this calculation with another one that had not been done previously and the two of these have just appeared this week in fact in the Physical Review.  $p + p + \pi^0 + p + p$  is the other term. Now the point is that we get both of these within the experimental error. That's a safe statement because the experimental error is enormous, so we don't know whether we have as good a treatment one or the other.

ANDREWS: Can you say why you are surprised at a dip in  $Li^7$ ?

KOLTUN: We haven't done all the integrals you have to for  $\text{Li}^7$  because you can get relative motion d-states which don't appear in this problem. We have treated the relative motion s-states and also the relative  $3D_1$ . It's the only one of the d-states allowed, and that contribution is rather small. Just guessing, I'd say that I expect the other d-states to be small, too. I don't expect such a very large hump from what we see. In shell model terms - it may not be the valence nucleons alone. There is another problem with the shell model. You can take a particle out of the s-state and still leave an alpha particle because there's a spurious center of mass motion.

N66-253  
32742

RADIATIVE PION ABSORPTION IN COMPLEX NUCLEI\*

D. K. Anderson and J. M. Eisenberg

University of Virginia

We would like to discuss some results concerning a calculation of radiative pion absorption in complex nuclei. In particular, we consider absorption of a pion in  $O^{16}$  leading to  $N^{16}$  plus a high energy photon.

In order to obtain the transition operator for this reaction, we begin with the pseudoscalar interaction of the form

$$H_{\pi N} = G \bar{\psi} \gamma_5 \vec{\tau} \psi \cdot \vec{\phi} \tag{1}$$

Here  $\psi$  represents the nucleon operator,  $\phi$  refers to the pion field, and  $G$  is the pseudoscalar coupling constant. However, we want to discuss a process where the pions interact with nonrelativistic nucleons bound in a nucleus. In order to do this we use the equivalence theorem<sup>1</sup> which, in effect, states that to first order in the meson-nucleon coupling constant  $G$  the pseudoscalar interaction is equivalent to the pseudovector interaction given by

$$H_{\pi N} = \frac{f}{M_\pi} \bar{\psi} \gamma_5 \gamma_\mu \vec{\tau} \psi \cdot \nabla_\mu \vec{\phi}, \tag{2}$$

where  $f = \frac{M_\pi}{2M} G$  is the pseudovector coupling constant. In the presence of an electromagnetic field<sup>2</sup> this coupling leads in the nonrelativistic limit to an interaction having the form

$$H_{int} = e \frac{f}{M_\pi} \bar{\psi}^* \vec{\tau}^+ \frac{\sigma \cdot A}{M_\pi} \psi, \tag{3}$$

where we retain only that part involving negative pions. This is the

\* Work supported in part by the U. S. Atomic Energy Commission.

so-called gauge invariance term which leads to strong s-wave photo-production<sup>3</sup> of charged pions. Its contribution is shown diagrammatically in Fig. 1a.

There are also other terms which can contribute to the process we are considering. Terms which are of first order in the meson-nucleon coupling constant involve the current operators of the pions and nucleons. These lead to the diagrams shown in Figs. 1b-1d and we have estimated that they give corrections of about 10% in comparison with the gauge invariance term. Contributions of higher order in the coupling constant involve re-scattering corrections. At present there is no reliable way to estimate their importance. However, if one examines the process in the spirit of the impulse approximation using the Chew-Low amplitude<sup>3</sup> these terms also are small.

Taking the gauge invariance term to be the dominant part of the interaction we want to consider the absorption of pions from an atomic Bohr orbit. As the interaction in this process depends on the meson wave function and not on its gradient as would be true for two-nucleon emission, absorption from s states will predominate. In fact, radiative absorption from p states is smaller by a factor  $> 10^3$ . In this case we can also remove the meson wave function from the transition matrix element by defining a suitably averaged quantity.

It is clear from the form of the interaction that only  $T = 1$  excited states will contribute. Performing a multipole expansion of the electromagnetic field we can further classify our transitions according to the type of photon emitted. Results for the dipole cases are presented in Table 1. From this table, we see that the E1 transitions should be small

## Radiative Pion Absorption

for closed shell nuclei since the transition operator vanishes in the long wave length limit due to the exclusion principle. Thus, the only contributions come from retardation effects. On the other hand, the operator associated with M1 transitions (as well as the operator associated with E2 transitions) leads to the spin-isospin modes of nuclear excitations which have recently been studied in connection with muon capture<sup>4</sup>. Assuming contributions from higher multipoles are negligible, we are led to expect that these spin-isospin modes play a dominant role in radiative pion absorption.

Calculations confirm this expectation. In Table 2 we present the results of a partial transition calculation using the unperturbed particle-hole basis wave functions. From this table we see that the greatest part of the strength is in the  $J^\pi = 1^-, 2^-$ ;  $T = 1$  states as expected. Contributions from higher multipoles were found to be negligible.

Using the particle-hole formalism and  $O^{16}$  wave functions calculated by Gillet and Vinh Mau<sup>5</sup> we obtain the results presented in Table 3. This shows quite clearly that the spin-isospin modes play an important role in the radiative absorption process. The  $1^-$  and  $2^-$  levels of this character at 25.4 MeV and 20.2 MeV, respectively, contribute about 45% of the total  $1^-$ ,  $2^-$  strength. Also, since the  $J^\pi = 1^-, 2^-$ ;  $T = 1$  levels contribute about 80% of the total rate we conclude that more than 50% of the total strength will be concentrated in the energy range from 20 to 25 MeV. This peaking should be evident in the emitted photon spectrum. Moreover, since the  $1^-$  and  $2^-$  spin-isospin modes are separated by about 5 MeV, it may be possible to resolve them and thus verify the role played by these states in radiative absorption.

In concluding we would like to make a few remarks concerning the capture process itself. Thus far we have been concerned solely with the absorption of s state mesons. However, Messiah and Marshak<sup>6</sup> have pointed out that in elements heavier than lithium most captured mesons do not reach the 1s state. This is due to the fact that absorption from the 2p level is several times greater than the  $2p \rightarrow 1s$  radiative transition rate. Although it is difficult to estimate reliably the fraction of mesons which reach the 1s level it appears<sup>7,8</sup> that about 10% of them do. This, together with the estimated branching ratio  $10^{-2}$  for radiative absorption, should give a sufficient number of high energy photons to permit an experimental observation of the effects discussed here.

ERRATUM:

The branching ratio for radiative absorption from a 2p atomic level has been recalculated and found to be approximately the same as the 1s branching ratio instead of smaller by a factor of  $10^{-3}$  as reported above.

- 1) F. J. Dyson, Phys. Rev. 73 (1948) 929.
- 2) S. D. Drell and E. M. Henley, Phys. Rev. 88 (1952) 1053.
- 3) G. F. Chew, M. L. Goldberger, F. E. Low, and Y. Nambu, Phys. Rev. 106 (1957) 1345.
- 4) L. L. Foldy and J. D. Walecka, Nuovo Cimento 34 (1964) 1026.
- 5) V. Gillet and N. Vinh Mau, Nucl. Phys. 54 (1964) 321; 57 (1964) 698.
- 6) A. M. L. Messiah and R. E. Marshak, Phys. Rev. 88 (1952) 678.
- 7) M. Camac, A. D. McGuire, J. B. Platt, and H. J. Schulte, Phys. Rev. 99 (1955) 897.
- 8) Y. Eisenberg and D. Kessler, Phys. Rev. 123 (1961) 1472.

Radiative Pion Absorption

Table 1. Dipole Transitions

| Type | Transition            | Long Wavelength Limit of Operator                         |
|------|-----------------------|---|
| E1   | $0^+ \rightarrow 1^+$ | $\sum \tau^+ \sigma_M$                                    |
| M1   | $0^+ \rightarrow 1^-$ | $\sum \tau^+ (\underline{\sigma} \times \underline{x})_M$ |

Table 2. Partial Transition Strengths

| $J^\pi$ | Strength |
|---------|----------|
| $1^+$   | 9%       |
| $1^-$   | 44       |
| $2^+$   | 8        |
| $2^-$   | 39       |

Table 3.  $J^\pi = 1^-, 2^-; T = 1$  Strengths

| $1^-, T=1$ |          | $2^-, T=1$ |          |
|------------|----------|------------|----------|
| E          | Strength | E          | Strength |
| 25.4 MeV   | 48%      | 23.7 MeV   | 17%      |
| 22.7       | 24       | 20.2       | 40       |
| 19.6       | 9        | 19.1       | 13       |
| 18.1       | 14       | 17.7       | 1        |
| 13.6       | 5        | 13.0       | 29       |

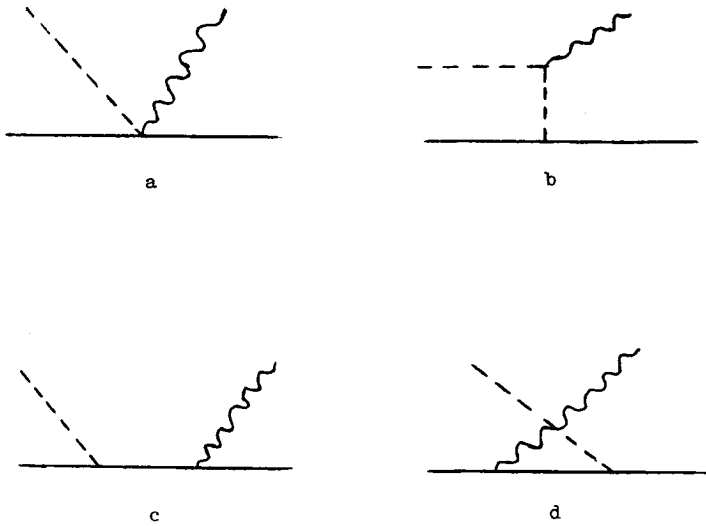


Figure 1 - Feynman Diagrams for the Radiative Absorption Reaction.

---

QUESTION: You have no experimental data?

ANDERSON: No, I wasn't aware of any experimental data at the time, so I wasn't able to compare it with anything.



$\pi^-$  ABSORPTION BY UNCORRELATED NUCLEONS IN  $O^{16}$ \*

Jean LeTourneur

University of Virginia

N66 259  
3C743

ABSTRACT

A study is made of the absorption from rest of  $\pi^-$  mesons by uncorrelated nucleons in  $O^{16}$ . The absorption probability is calculated for pions in the 1s and 2p orbits. The non-relativistic pion-nucleon interaction contains two terms, one of them involving the momentum of the nucleon, the other the momentum of the pion. The neglect of the latter is shown to be an unjustified procedure in the study of the absorption process. From the results of the present calculation, the absorption of a 2p pion by uncorrelated nucleons appears to be highly hindered with respect to the absorption process by a correlated pair, as could be expected from conservation principles.

\* Work supported in part by the U. S. Atomic Energy Commission

As early as 1951, it was suggested by Brueckner, Serber and Watson<sup>1)</sup> that the capture of negative pions from atomic orbits proceeds mainly through absorption by a pair of correlated nucleons. This suggestion is based on the fact that the meson carries essentially no momentum but releases a large amount of energy when it is annihilated, so that absorption by an uncorrelated nucleon may take place only if the nucleon happens to have a momentum considerably higher than the average momentum of a nucleon inside the nucleus. Such an occurrence is rather unlikely, and the meson is more likely to be absorbed by a correlated pair of nucleons which can share energy and momentum in such a way as to satisfy the conservation laws. Although this hypothesis has been confirmed by a certain amount of experimental evidence, the relative probability of the two absorption mechanisms has not yet been established quantitatively. It is therefore of interest to have some accurate theoretical predictions of the relative importance of the two mechanisms based on more than general qualitative considerations.

Partly because it is dominant and partly because it may yield some interesting information on the nuclear correlation function and the spectrum of the residual nucleus, the absorption by correlated pairs has attracted most of the theoretical attention so far, at the expense of the absorption by uncorrelated nucleons. The only explicit study of the latter, to the best of my knowledge, was made by Spector<sup>2)</sup> who, specifically, considered the capture on  $O^{16}$ . In this paper, I should like to report on an extension of Spector's work. This extension bears on two points. Firstly, it deals with the fact that in the non-relativistic limit the Hamiltonian describing the pion-nucleon interaction is a function of the relative velocity  $\frac{v_{\pi}}{c} - \frac{v_N}{c}$ .

Spector neglected the term involving  $\underline{v}_{\pi}$ . It will be shown that its contribution is not negligible. Moreover, Spector's study is limited to the absorption of a negative pion from a 1s Bohr orbit. Messiah and Marshak<sup>3</sup> indicated that the ratio of the absorption probability to the radiative transition probability should increase as  $Z^2$  for a meson in a 2p orbit. This prediction has been confirmed experimentally. Since the present calculation deals with  $O^{16}$ , the absorption probability for a pion in the 2p as well as the 1s shell will be considered.

In the non-relativistic limit, the pion-nucleon interaction takes the Galileo-invariant form

$$H = \frac{f}{\kappa} \left[ \underline{\sigma} \cdot \nabla (\underline{\tau} \cdot \underline{\phi}) - \frac{m}{M} \underline{\tau} \cdot \underline{\phi} \underline{\sigma} \cdot \nabla \right], \quad (1)$$

where  $\kappa = mc/\hbar$ ,  $m$  and  $M$  are the masses of the pion and the nucleon respectively and  $\underline{\phi}$  describes the field of charged and neutral pions. The coupling constant takes the value

$$\frac{f^2}{4\pi\hbar c} = 0.083. \quad (2)$$

According to first-order time dependent perturbation theory, the number of captures per second resulting in the ejection of a nucleon of momentum  $k$  is given by

$$\omega = \frac{ML^3}{(2\pi)^2 \hbar^3} k \int d\Omega \sum_f |K_f| |H_{if}|^2. \quad (3)$$

The angular integration takes place over the direction of  $\underline{k}$ . The state of the outgoing nucleon is assumed to be a plane wave normalized to unity in a volume  $L^3$ . Of course the final result is independent of this

volume. Under the assumption that the residual nucleus is left in a state lying at a well-defined energy  $\Delta E$  above the energy of the initial nuclear state,  $k$  is given in the non-relativistic limit by

$$mc^2 = \Delta E + \hbar^2 k^2 / 2M. \quad (4)$$

The recoil of the daughter nucleus is neglected.

We assume that initially the meson is in a Bohr orbit around the nucleus. It was shown by Huguenin<sup>4)</sup> that the pionic field  $\phi$  can be expanded in terms of the solutions of the Klein-Gordon equation for a pion in presence of the electric field of the nucleus. The matrix element of  $\underline{r} \cdot \nabla \phi$  between the ket  $|\alpha\rangle$  corresponding to one pion in the state  $\alpha$  and the vacuum  $|0\rangle$  is given by

$$\langle 0 | \underline{r} \cdot \nabla \phi | \alpha \rangle = \sqrt{2k^2} f_{\alpha}(\underline{r}), \quad (5)$$

where  $f_{\alpha}(\underline{r})$  is the eigenfunction of the Klein-Gordon equation corresponding to the state  $\alpha$ . In the non-relativistic limit  $f_{\alpha}(\underline{r})$  goes into  $(2E_{\alpha})^{-\frac{1}{2}} \phi_{\alpha}(\underline{r})$ , where  $\phi_{\alpha}(\underline{r})$  is the normalized non-relativistic hydrogen-like wave function corresponding to the eigenvalue  $E_{\alpha}$ . Equation (5) must therefore be replaced by

$$\langle 0 | \underline{r} \cdot \nabla \phi | \alpha \rangle = \sqrt{\frac{\hbar c^2}{E_{\alpha}}} \phi_{\alpha}(\underline{r}) \quad (6)$$

in the non-relativistic limit.

The evaluation of the nuclear part of the matrix elements is straight forward and will not be described in details. Let me just mention that very drastic assumptions are made about the nuclear physics of the problem. The

initial and final states of the nucleus are described by a single Slater determinant and no account is taken of the interaction between the outgoing nucleon and the residual nucleus.

In order to demonstrate the importance of the contribution from the  $v_{\pi\pi}$  term in the Hamiltonian, I will show the result of the calculation for the specific case where the pion is absorbed from a  $1s$  orbit with emission of a nucleon from the  $1p_{1/2}$  shell:

$$\int d\Omega \sum_i |\langle f | u | i \rangle|^2 = \left(\frac{k}{N}\right)^2 \frac{8\pi}{m} \frac{1}{313} \left[ \frac{m\nu}{M} I_4(00, 1/2) - I_1(00, 1/2) \right]^2, \quad (7)$$

where

$$I_1(\bar{l} l_\alpha l j) = \langle j_\beta(kr) | \left( \frac{d}{dr} - \frac{k}{r} \right) R_\alpha(r) | R_{n\ell}(r) \rangle$$

$$I_4(\bar{l} l_\alpha l j) = \langle j_\beta(kr) | R_\alpha(r) \left( \frac{d}{dr} + \frac{k}{r} \right) | R_{n\ell}(r) \rangle$$

$R_{n\ell}(r)$  and  $R_\alpha(r)$  are the radial parts of the wave functions of the absorbing nucleon and the pion respectively and  $j_\beta(kr)$  comes from the expansion of the plane wave into partial waves. An evaluation of the radial integrals using harmonic oscillator wave functions for the single nucleon wave functions yields:

$$I_1(001 \frac{1}{2}) = 0.205 \times 10^{-4} \text{fm}^{-1}$$

$$I_4(001 \frac{1}{2}) = 0.191 \times 10^{-3} \text{fm}^{-1}$$

Bearing in mind the fact that the first and second terms in eq. (7) come from the part of the Hamiltonian involving  $v_N$  and  $v_{\pi\pi}$  respectively, one sees that the contribution from the latter is by no means negligible.

The results of the calculation are shown in Table 1. The parameters were given essentially the same value as in Spector's paper.

As far as I know, the absorption probability for a  $\pi^-$  in the 1s orbit has not been determined experimentally; it results from the work of Stearns and Stearns<sup>5)</sup> that the absorption rate for a pion in the 2p orbit, being 20 times as large as the radiative transition probability, is of the order of  $1.5 \times 10^{16} \text{ sec}^{-1}$ . A calculation of the absorption probability by M. Ericson<sup>6)</sup>, using an optical model potential and assuming that the pions are absorbed by pairs of nucleons, yields transition probabilities of the order of  $5 \times 10^{18}$  and  $10^{16} \text{ sec}^{-1}$  for a pion in the 1s and the 2p shells respectively. This implies that our corresponding transitions probabilities for the absorption by an uncorrelated nucleon are smaller by 2 and 3 or 4 orders of magnitude. This result lends some theoretical confirmation to the prediction of Brueckner, Serber, and Watson and indicates that the absorption by uncorrelated nucleons is negligibly small.

- 
- 1) K. A. Brueckner, R. Serber and K. M. Watson, Phys. Rev. 84 (1951) 258
  - 2) R. M. Spector, Phys. Rev. 134 (1964) B101
  - 3) A. M. L. Messiah and R. E. Marshak, Phys. Rev. 88 (1952) 678
  - 4) P. Huguenin, Z. Phys. 167 (1962) 416
  - 5) M. Stearns and M. B. Stearns, Phys. Rev. 107 (1957) 1709
  - 6) M. Ericson, Compt. rend. 257 (1963) 3831

TABLE 1

Absorption probabilities for the various processes

| Shell              | 1s meson              | 2p meson              |
|--------------------|-----------------------|-----------------------|
| $1s_{\frac{1}{2}}$ | $3.51 \times 10^{16}$ | $2.90 \times 10^{12}$ |
| $1p_{\frac{3}{2}}$ | $2.27 \times 10^{16}$ | $3.03 \times 10^{12}$ |
| $1p_{\frac{1}{2}}$ | $4.14 \times 10^{14}$ | $1.01 \times 10^{12}$ |
| Total              | $5.8 \times 10^{16}$  | $6.94 \times 10^{12}$ |

JARMIE: There must be intermediate processes where the pion absorbs, say, on three or four nucleons, e.g., the pion is absorbed, not on two nucleons, not on the whole nucleus either, but on three or four nucleons. Do you think these would be significant?

LeTOURNEUX: I think that the whole approach is, in a way, a very unsimple one. I don't like, first of all, the idea of distinguishing between uncorrelated and correlated nucleons. What is exactly the meaning of such a process where your nucleon happens to have in the nucleus in the central field a very large momentum. How does it get its momentum? It is not the average momentum. It gets it if it has just interacted with another nucleon. This other nucleon has interacted with another nucleon just a bit later. When does this happen exactly? What you see is that they are not correlated.

KOLTUN: On the three-body correlation, there is one interesting experiment to do which has almost been done at Rochester, but not quite. It is absorption of  $\pi^-$  leading to the emission of two protons. Of course, this cannot be direct two-body; it must be three-body. There's evidence that it is and that it's probably down by a factor of 25 over the two-neutrons. That gives you an estimate of, say, three-body correlation or rescattering, whatever you want to call it over the two-body effects. The time-reverse of the process you've considered is interesting because it is the production of pions by a nucleon colliding with a nucleus and can be done as a function of energy for the pion. It might be looked at.

PHILLIPS: It seems to me that the very interesting paper BK1 by the Rochester group certainly must bear on this point. You may recall that one of their figures showed the n-n coincidences vs. angle and the p-n coincidences vs. angle. The n-n coincidences had a narrower width as I recall than did the p-n. If the



width of those peaks exceeds the angular resolution of the detectors, it must be an indication of the sharing of momentum with the other nucleons. That would bear upon Dr. Jarmie's point. Also, if there is a significant difference in those two peaks so that the n-n peak is narrower, this would imply that there are better correlations between neutron and proton pairs than between proton-proton pairs, which is indeed just what you'd expect from the scattering lengths of the fundamental nucleus.

N66 269  
32744

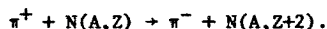
DOUBLE CHARGE EXCHANGE

J. Solomon

Princeton University and the Princeton-Pennsylvania Accelerator

I will discuss an experiment performed at the 184" Berkeley Cyclotron where-  
in a search was conducted for a  $\Delta T_z = -2$  Isobaric Analog State in Complex Nuclei  
produced through the double charge exchange scattering of  $\pi^+$  mesons.

The reaction is of the form



In the process two neutrons are changed into two protons and  $T_z$  changes by  $-2$ .  
These analog states as suggested by several others may be used in the study of  
nuclear level structure and isospin mixing.

Barshay and Brown have calculated the cross section and angular distribution  
for the production of the analog state for 210 MeV  $\pi^+$  scattering of  $\text{Ca}^{48}$ .  $\text{Ca}^{48}$   
has 8 neutrons in the F 7/2 shell and has no protons. They consider the process  
to go through the production of two  $T = 3/2$ ,  $J = 3/2$   $\pi$ -N isobars and an intermed-  
iate  $\pi^0$ . Harmonic oscillator functions were used for the nuclear wave functions.  
Since the only quantum number changed is  $T_z$  we may expect large overlap of the  
initial and final wave functions. Final mesons emerge with the incident energy  
less only the Coulomb energy of the two created protons. The cross section is  
large, because of a factor of 56, the number of neutron pairs which may be changed  
into protons. The analog state when formed should be stable against particle  
emission because it is inhibited by isospin conservation. This state should be  
narrow and may be observed in a narrow  $\pi^-$  peak in the momentum spectrum. The  
predicted cross sections are about 250  $\mu\text{b}/\text{sr}$  at  $0^\circ$  and 110  $\mu\text{b}/\text{sr}$  at  $15^\circ$ .

Since the world's supply of  $\text{Ca}^{48}$  was required by us to perform the measure-

PRECEDING PAGE BLANK NOT FILMED.

ment and since it wasn't available we chose  $V^{51}$  as a target. V has available 20 neutron pairs which may be changed into proton in the F 7/2 shell. We expected our measurements to be down by a factor of 3 from Brown and Barshay's calculation. We also made some measurements on  $Zr^{90}$  because of its large neutron excess in the outer shell and on Li in order to compare to a measurement of Gilly et al at the CERN Cyclotron.

Figure 1 shows the experimental lay-out. The  $\pi^+$  beam was produced in a Polyethylene Target in Physics cave of 184" cyclotrons and brought to a focus at the target position. The scattered  $\pi^-$  was detected with scintillation counters and the wire spark chambers were used to measure the momentum of the  $\pi^-$ . Electrons were rejected by a Propane Cerenkov Counter.

The momentum resolution of the chambers and spectrometer was about 1%. The wire spark chambers were read out with the aid of a Magnetostriction Delay Line system which directly digitized the spark information. Within 24 hours the events were processed and histograms of the data along with information about the efficiency of our chambers and electronics was made available.

The efficiency of the detector as a function of momentum was determined by making suspended wire measurements on the spectrometer and confirmed by calculation of orbits using the measured magnetic field. The data we present needed no correction for inefficiency except in the lowest momentum bins where 20% correction was applied.

The triggering rate was about 20 per hour for an incident beam of  $10^8\pi/\text{hr}$ . Of these 20 events about three or four were deemed acceptable by the analysis program. The ability to reject background was mainly due to the sharp momentum resolution of the spectrometer and spark chambers.

Our results for  $V^{51}$  at  $7.5^\circ$  and  $15^\circ$  in the lab is shown Figure 2.

We plot the number of events per 10 MeV/c bins versus the momentum of the detected  $\pi^-$ . The scale on the right is the cross section in  $\mu\text{b}/\text{sr MeV}$ . The analog state, if present, would show up in the V data as a large peak in the labelled bin. Adjusting Brown and Barshay's predictions for the V target at  $15^\circ$  we expected about  $30 \mu\text{b}/\text{sr}$ . We observe less than  $1 \mu\text{b}/\text{sr}$  in desired bins at both  $7.5^\circ$  and  $15^\circ$ . The integrated cross section over the whole measured momentum spectrum is at  $7.5^\circ$ ,  $49 \pm 8 \mu\text{b}/\text{sr}$  and at  $15^\circ$ ,  $28 \pm 4 \mu\text{b}/\text{sr}$ .

Our Zirconium data may be seen in Figure 3. The data has the same overall shape as the V data does, but has not as strong an angular dependence for the continuum. The integrated cross sections in this case are  $66 \pm 10$  at  $7.5^\circ$  and  $51 \pm 7 \mu\text{b}/\text{sr}$  at  $15^\circ$ . We do not observe any sign of the analog state for either.

Figure 4 shows Li data taken by us and by Gilly et al. The differences are:

- 1) Their incident energy was 190 MeV, ours is 200 MeV.
- 2) Their angle is  $0^\circ$  and ours  $15^\circ$ .
- 3) They used a Cerenkov Counter and were required to move the radiator in order to measure different energies. We took all our data simultaneously.

They contend that their data, evidenced by the drop off at low momenta, shows the same momentum shape as the incident beam (30 MeV) shifted to lower energies and thereby demonstrates that a considerable fraction of the double charge exchange process in Lithium occurs through two body channels. The observed peak is shifted from the expected position by 25 MeV. We see no evidence of a low energy drop off, but rather observe a broad continuum indicating multiple-body first states rather than 2 body final states.

We conclude that the excitation of  $\Delta T_z = -2$  isobaric analog states of two

nuclei expected to have favorable cross sections for the process does not compete significantly with other double charge exchange channels. Furthermore, the measured upper limit of these cross sections are better than order of magnitude smaller than indicated by the Barshay-Brown model. And lastly our data on the shape of the momentum spectrum of Lithium does not agree with that of the CERN group.

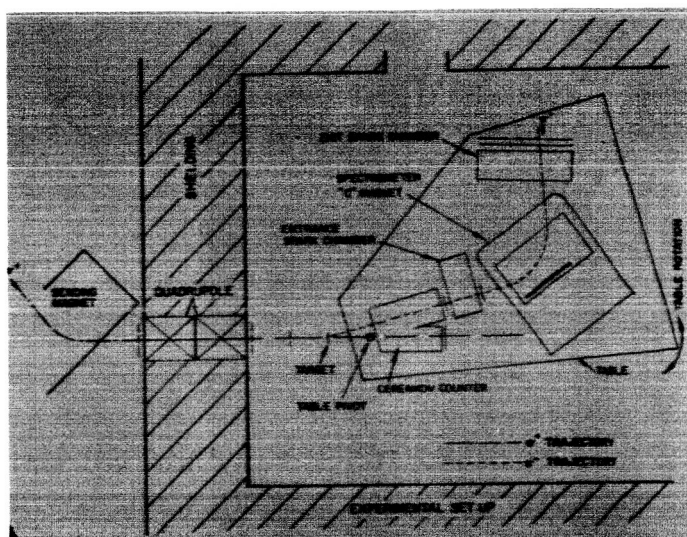


Figure 1

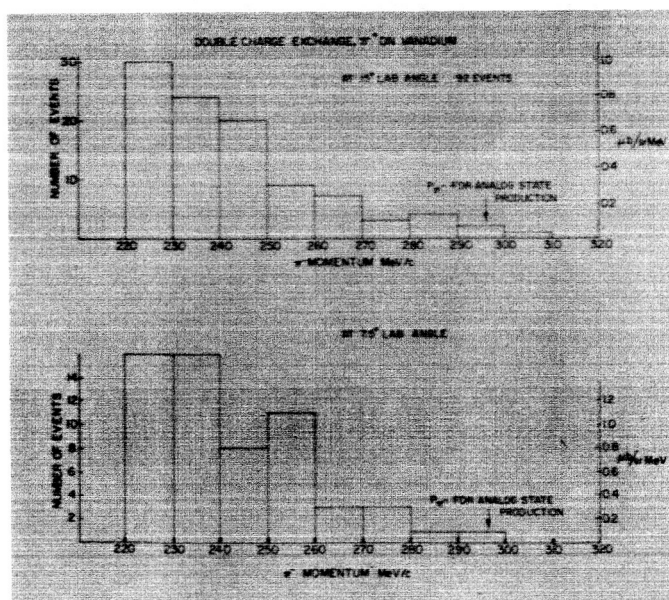


Figure 2

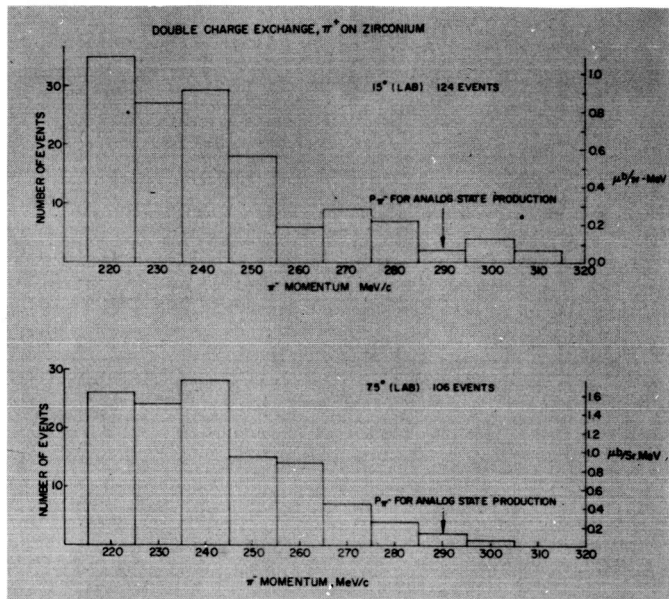


Figure 3

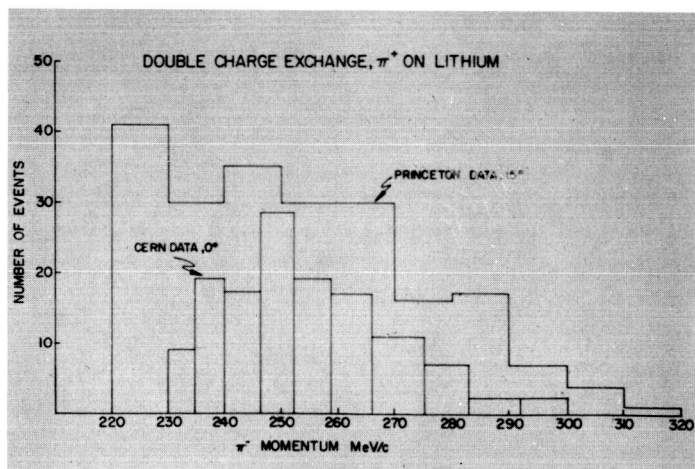


Figure 4

BLOCK: Would you care to give us the cross-section for your Li data:

SOLOMON: Integrated over our momentum range it was 40 millibarns/str. Gilley et al, has 100  $\mu$ /str. in that same range at 0°.

BLOCK: In other words, it was higher than with your heavier elements.

SOLOMON: No, it wasn't noticeably different, V was 25, Ar was 50, at 15°, Li was 40.

ERICSON: I have a solicited question from the CERN group which I was asked to carry on to you and that is: How do your integrated V and Zr cross-sections compared with the CERN and Russian measurements? The Russian measurements are essentially in agreement to the CERN ones.

SOLOMON: I'm sorry I don't know of them.

KOLTUN: Just one comment on the counting of pairs, to get the enhancement of the isobar state, the Brown & Barshay calculation may not be completely correct from this point of view. For the high energy double charge exchange, that is the correlation distances measured are reasonably short and instead of counting pairs, one should count the 0-coupled pairs using a seniority argument. It's only the closely associated pairs which are going to affect this and that's considerably lower than  $n(n-1)/2$ . By the way, I don't know why they always quote 56; the number of pairs is 28.

NEFKENS: How well can you separate out the muon from decays in flight?

SOLOMON: We do a momentum analysis, using the incoming track and one outgoing point of the two spark chambers. We can tell that a track is continuous for a



particular momentum to within  $1^{\circ}$ , so that if the track does not appear to be continuous within that angular uncertainty, we reject the track completely. In so doing, we actually throw away most of the  $\mu$ 's from the  $\pi$ 's and just make a correction for the  $\pi$  decay. Eventually, we'll do the analysis more carefully and find out how many we get back in that small angular acceptance, but right now we just throw them all away.

N66<sup>277</sup>  
32745

THE PRODUCTION OF CHARGED PIONS BY 600 MeV PROTONS ON VARIOUS NUCLEI

E. Heer\*, W. Hirt \*\*, M. Martin\*, E. G. Michaelis \*\*\*,  
C. Serre<sup>+</sup>, P. Skarek\*\*\*, B. T. Wright<sup>++</sup>

CERN, Geneva

1. Introduction

The work to be described forms part of a joint programme established with members of the University of California with the aim of measuring charged pion production cross-sections in the forward direction on various nuclei. The experiments were performed at the Berkeley 184" Synchrocyclotron and at the CERN Synchrocyclotron, that is at proton energies of 725 and 600 MeV respectively. The Berkeley data have been presented by Haddock et al<sup>1)</sup>.

In the present experiment we have measured production cross-sections on CH<sub>2</sub>, CD<sub>2</sub>, Be, C, Al, Cu, Ag and Pb at pion energies between 100 and 350 MeV and for production angles of 0.8 and 21.5°.

2. Method

2.1 General Principles

The experimental arrangement used by us is shown in fig. 1. The 600 MeV extracted proton beam of the CERN SC was focused by quadrupoles and directed on the production target by magnet M<sub>0</sub>. The secondary beam was deflected by magnet M<sub>1</sub> and was analyzed by M<sub>2</sub> after passing through a pipe in the 5-metre shielding wall surrounding the SC Hall. Counters C<sub>2</sub> - C<sub>4</sub> formed a time-of-flight telescope which permitted a clean separation of protons and heavier particles from mesons. A gas-Cerenkov counter C<sub>5</sub> identified electrons and a range-counter C<sub>6</sub>, shielded by a pion-range absorber, detected a fraction of the muons. By choosing suitable target positions and corresponding fields in M<sub>0</sub> and M<sub>1</sub> the pion production angle  $\omega$  could be varied from 0 to 50°.

This arrangement was largely determined by radiation safety requirements. It has the advantage of low background but various disadvantages arising from the long flight path of 13.5 m between the target and detectors.

\* University of Geneva.

\*\* Federal Polytechnic, Zurich.

\*\*\* European Organization for Nuclear Research (CERN).

+ University of Grenoble.

++ University of California, Los Angeles.

The differential pion production cross-section was calculated from

$$\frac{d^2\sigma}{d\Omega d\omega} = \frac{N_m(A, p, \omega)}{T K N_p D \beta_{\pi} p(\Delta p/p) \Delta \Omega \eta C_m C_{\mu} C_d F} \quad (1)$$

$N_m$  = number of mesons recorded by time-of-flight system.

$N_p$  = number of incident protons corresponding to  $N_m$ .

$\omega$  = production angle.

$A$  = target material.

$p$  = particle momentum,  $\Delta p$  = momentum interval of secondaries.

$T$  = thickness of target specimen,  $K$  thickness correction for oblique incidence of protons.

$D$  = pion decay correction.

$\beta_{\pi} c$  = pion velocity.

$\Delta \Omega$  =  $\Delta \theta_h \cdot \Delta \theta_v$  = solid angle.

$\Delta p/p$  = momentum resolution.

$\eta$  = secondary detection efficiency.

$C_m$  = multiple scattering correction.

$C_{\mu}$  = muon correction.

$C_d$  = dead-time correction.

$F$  = folding and target-thickness corrections.

The factors requiring particular attention were  $N_p$ ,  $N_m$ ,  $\omega$ ,  $\Delta \Omega$ ,  $\Delta p/p$ ,  $C_m$  and  $C_{\mu}$ .

## 2.2 The Number of Incident Protons $N_p$

The incident beam had an intensity of order  $10^{11}$  protons per second and a duty cycle between 10 and 20 %. The flux was measured relatively by two secondary emission chambers<sup>2)</sup> (SEC) whose output was amplified, integrated and converted to digital form.

The absolute calibration of the chambers was performed by activation measurements on carbon and aluminium. The data were finally evaluated by reference to the  $C^{12}$  (p, pn)  $C^{11}$  cross-section of  $30.8 \pm 1.5$  mb<sup>3)</sup>. A check of the absolute calibration was obtained by means of an adiabatic calorimeter, in which the temperature rise of a lead plate traversed by the beam was measured in terms of the SEC dose. In principle this method furnishes an upper limit of the proton flux. In practice this limit is close to the true value of the flux for a thin plate.

## 2.3 The Number of Mesons $N_m$

The principle of the time-of-flight system is indicated in fig. 2 and the complete electronic block diagram is shown in fig. 3. A time-to-voltage converter TVC forms the core of the system. Coincidences (34) gave "start" and counts (2) gave "stop" signals. The TVC output was fed into a 512 channel pulse-height analyzer, whose memory was split into four sections. Events (23456) comprising all particles except electrons and a fraction of the muons were stored in the first section, events (2345) - electrons - in the second section and events (23456) - a sample of the muons - in the third.

An example of a time-of-flight spectrum obtained with positive particles of 310 MeV/c momentum is in fig. 4 on a logarithmic scale. The meson peak is well separated from the peak of low energy protons present in the secondary beam. Pions and muons are not separated by the time-of-flight system except at the lowest energies. To evaluate  $N_m$  the contents of the appropriate channels in the pion and muon part of the memory were therefore added.  $N_m$  was obtained by subtracting background and target-out intensities and was then corrected for muon contamination by  $C_\mu$ .

#### 2.4 Production Angle $\omega$ , Solid Angle $\Delta\Omega$ and Momentum Resolution $\Delta p/p$

These quantities were calculated with a TRAMP programme and checked by floating wire measurements. Calculation and wire measurements agreed to better than 3%. For a given  $\omega$  the solid angle and momentum resolution were made independent of  $p$ . The values used are listed in table I.

Table I

| $\omega$<br>Nominal<br>(deg.) | $\omega$<br>True<br>(deg.) | $\Delta p/p$<br>(%) | $\Delta\theta_h \cdot \Delta\theta_v$<br>( $\mu$ sterad) |
|-------------------------------|----------------------------|---------------------|--|
| 0                             | 0.8                        | 3.82                | 46.9   |
| 10                            | 11.7                       | 3.89                | 39.8   |
| 20                            | 21.5                       | 4.08                | 35.4   |

\* The fast electronics used in the experiment was designed by Prof. D. Maeder. It consisted of DC coupled standard units. For a general description of this system see Proceedings of the Monterey Conference, National Academy of Science, NS Series No 40, Washington 1964.

#### 2.5 The Multiple Scattering Correction $C_m$

Multiple scattering between target and detectors was minimized by keeping the flight path in vacuum or helium. The scattering losses were therefore caused mainly by  $C_2$  (3 mm plastic scintillator). To estimate these losses additional thicknesses of scintillator were placed near  $C_2$ , and the decrease in meson flux was measured. In addition the expected loss was calculated using Molière scattering distributions and taking into account the focusing effect of  $M_2$ . Agreement between calculation and measurement was very poor when using the measured value of  $N_m$ . However, at low energies it was possible to evaluate the measurements separately for pions and muons and good agreement was found for pions. We think that the different behaviour of pions and muons is due to the fact that the muons come from an extended source and that scattering effects are largely compensated in that case.

The following calculated values of  $\frac{1}{C_m}$  were used in the evaluation:

|                 |     |      |      |      |      |      |
|-----------------|-----|------|------|------|------|------|
| $E_\pi$ (MeV)   | 100 | 150  | 200  | 250  | 300  | 350  |
| $\frac{1}{C_m}$ | 1.5 | 1.28 | 1.19 | 1.14 | 1.10 | 1.08 |

### 2.6 The Muon Correction $C_\mu$

To find the proportion of pions and muons in the meson channels of the time-of-flight spectrum we principally used the integral-range method. At low energies the ratio  $N_\pi/N_\mu$  was checked by the time-of-flight method and good agreement between the two methods was obtained. The measurements were performed at  $\omega = 21.5^\circ$  with positive particles from carbon. The results were used to calibrate the "muon-shift" events (23456). For other target materials, production angles and for negative pions  $C_\mu$  was obtained from the calibrated muon-shift.

The measured  $C_\mu$  values were as follows:

|               |      |      |      |      |      |      |
|---------------|------|------|------|------|------|------|
| $E_\pi$ (MeV) | 100  | 150  | 200  | 250  | 300  | 350  |
| $C_\mu$       | 1.52 | 1.37 | 1.16 | 1.11 | 1.06 | 1.04 |

### 2.7 Other Corrections

The decay correction D was calculated.  $C_d$  was obtained from the comparison of gated and ungated (234) coincidences and was kept above 0.7 by varying the beam intensity where necessary. No variation of the pion cross-section with either target thickness or beam intensity was observed.

$\eta$  was obtained experimentally and was close to unity. Folding and absorption in the counters were shown to affect the result by less than 1%.

### 2.8 Data Evaluation

The contents of all scalers and of the pulse height analyzer channels were recorded on punched tape. The time-of-flight spectra were plotted on an IBM 1620 (see fig. 4) and were used to determine the meson channels and the

target-in background. All relevant information was then transferred to cards, which were subjected to various checking routines to eliminate a few runs containing gross errors or inconsistencies. The cross-sections were then evaluated and plotted with the aid of the CDC 6600 computer. A total of about a thousand spectra were handled in this manner.

### 2.9 Errors

The error evaluation was performed by adding quadratically the relative errors of the individual factors entering into the cross-section formula. The important errors are due to the factors  $N_p$ ,  $N_m$ ,  $\Delta\Omega$ ,  $\Delta p/p$ ,  $C_m$  and  $C_\mu$ .

The error in  $N_p$  was principally due to variations in the SEC sensitivity and to the scatter of the results of the various calibration methods. The SEC sensitivity was checked by taking the ratio of the results recorded by the two chambers. In addition  $N_m/N_p$  was checked periodically under standard conditions to discover possible drifts. We have not included the error of the  $C^{11}$  cross-section in our estimate.

$N_m$  has only the statistical errors of the individual measurements, including errors arising from various subtraction procedures.

The errors of  $\Delta\Omega$  and  $\Delta p/p$  were obtained from the comparison of ray-tracing and floating wire measurements.

The possible variations of  $C_m$  were found by obtaining its derivatives with respect to different parameters entering into the calculation. In addition we attempted to find an upper limit to the error in  $C_m$  by fitting a polynomial to the measurements and extrapolating it to zero counter thickness.

The errors of  $C_\mu$  were obtained at lower energies from the comparison of time-of-flight and range data. At higher energies the parameters used to fit the range curves were varied to estimate the possible spread of  $C_\mu$ .

### 3. Results

The results of the cross-section measurements on elements from Be to Pb and at production angles of  $0.8^\circ$  and  $21.5^\circ$  are shown in figures 5 and 6. The hydrogen cross-sections for  $\pi^+$  production, obtained by  $\text{CH}_2 - \text{C}$  subtraction, are given in fig. 7. Fig. 8 shows the neutron cross-sections evaluated by  $\text{CD}_2 - \text{CH}_2$  subtraction. In figures 9 and 10 our carbon spectra are compared to the earlier results of Lillethun<sup>4)</sup>, Meshkovskii et al<sup>5)</sup>, Meshcheriakov et al<sup>6)</sup> and of Haddock et al<sup>1)</sup>.

The estimated errors are summarized in the following table, in which a common range of error is attributed to groups of measurements.

Table II

| Range of Errors | Cross-sections                                   |
|-----------------|--|
| 5 - 7 %         | $\pi^+$ and $\pi^-$ at 200, 250, 300 and 350 MeV |
| 7 - 10 %        | $\pi^+$ and $\pi^-$ at 150 MeV                   |
| 10 - 14 %       | $\pi^+$ and $\pi^-$ at 100 MeV                   |

The errors quoted are to be understood as the half-width of half maximum of the appropriate probability distribution. They apply *grosso modo* to all elements and to both the  $0.8^\circ$  and  $21.5^\circ$  results.

The hydrogen spectra show the characteristic deuteron peak. The pion energy at the peak allowed us to determine the kinetic energy of the incident protons. The result was found to be compatible with the nominal energy of 600 MeV at both angles.

### 4. Comparison with Other Data

Our results for the hydrogen cross-section agree well with earlier measurements by Meshcheriakov<sup>7)</sup>, Meshkovskii et al<sup>8)</sup>, Haddock et al<sup>1)</sup> and Gushavin et al<sup>9)</sup>. The carbon cross-sections for negative pions fall between



the results of Lillethun at 450 MeV and those of Haddock et al at 725 MeV proton energy, as one would reasonably expect. The results of Meshcheriakov et al<sup>6)</sup> have been normalized using the  $\pi^+/\pi^-$  ratio and the absolute value of the  $\pi^+$  cross-section given in Ref. 5).

The picture is less clear in the case of positive pions from carbon, where our integrated cross-section is lower than that given by earlier results. In view of our agreement with other work on the spectrum from hydrogen and the acceptable values of our negative cross-sections it is particularly surprising to note that the integrated  $\pi^+$  cross-section on carbon at  $21.5^\circ$  should be higher at a proton energy of 450 MeV than at 600 MeV.

### 5. Acknowledgements

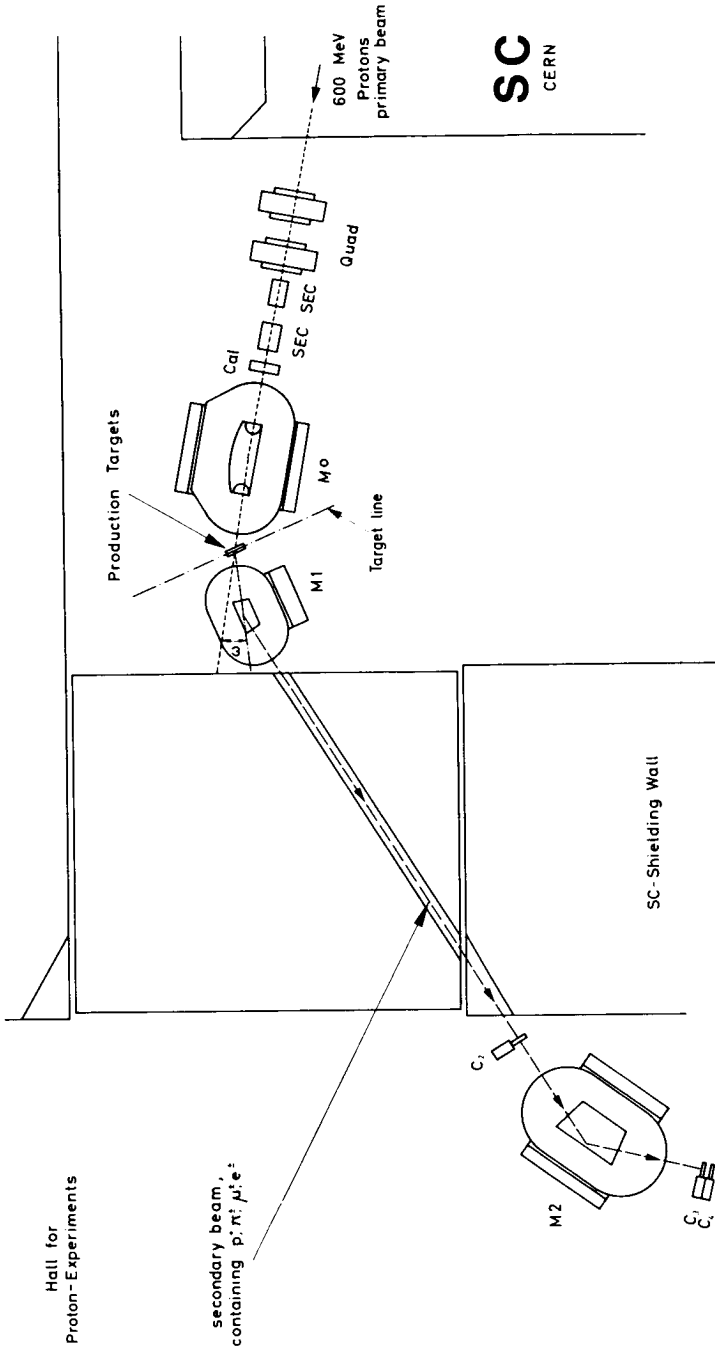
We thank Prof. R.P. Haddock (UCLA) for his help in the preparation of the project and his participation in a part of the experiment. Prof. D. Maeder (Geneva) gave invaluable help in providing our electronics. We gratefully acknowledge the assistance given by Dr. B. Levrat, Mr. C. Revillard, Mr. J.P. Boymont and Miss M. Flück of the University of Geneva and by Dr. D.F. Measday (CERN).

The Swiss National Science Research Fund supplied a great part of our equipment. We thank Profs. J.P. Blaser (ETH, Zürich) and R. Bouchez (Grenoble) for permitting members of the team (W. Hirt and C. Serre) to participate in the work. We have been encouraged by the interest and support of Drs. P. Lapostolle and G. Brianti, successive leaders of the CERN SC Division.

The effective service rendered by the MSC Operations Group, and in particular the help given by Mr. E. Leya, contributed greatly to the success of our work.

References

1. R.P. Haddock, M. Zeller and K.M. Crowe, UCLA (MPG) 64-2.
2. D. Harting, J.C. Kluyver and A. Kusumegi, CERN 60-17, 1960.
3. J.B. Cumming, Ann. Rev. Nucl. Sci. 13, 261 (1963).
4. E. Lillethun, PR 125, 665 (1962).
5. A.G. Meshkovskii, I.I. Shalamov and V.A. Shebanov, Soviet Physics JETP 7, 987 (1958).
6. M.G. Meshcheriakov, I.K. Vzorov, V.P. Zrellov, B.S. Neganov and A.F. Shabudin, CERN Symposium, Vol. 2, 357 (1956) and Soviet Physics JETP 4, 79 (1957).
7. M.G. Meshcheriakov, V.P. Zrellov, B.S. Neganov, I.K. Vzorov and A.F. Shabudin, JETP 4, 60 (1957).
8. A.G. Meshkovskii, I.I. Shalamov and V.A. Shebanov, Soviet Physics JETP 8, 46 (1959).
9. Gushavin et al, quoted by Yu.M. Kazarinov, Rapporteur's Report on Nucleon-Nucleon and Pion Nucleon Interactions below 1 GeV, JINR, P-1785, 1964.



Heer et al.

Figure 1. General Layout of the Pion Production Experiment.

- $M1$  } = Spectrometer Magnet
- $M2$  } = Magnet bending incident proton beam on production target
- $M0$  = Magnet bending incident proton beam on production target
- $C_1 + (C_2, C_3)$  = Time of flight system

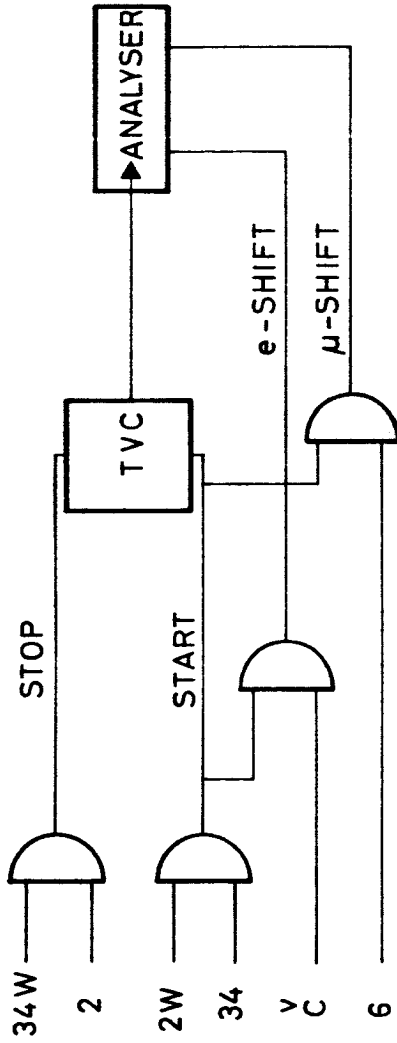


FIG. 2

Figure 2. Time-of-flight Detection System, Schematic Diagram.

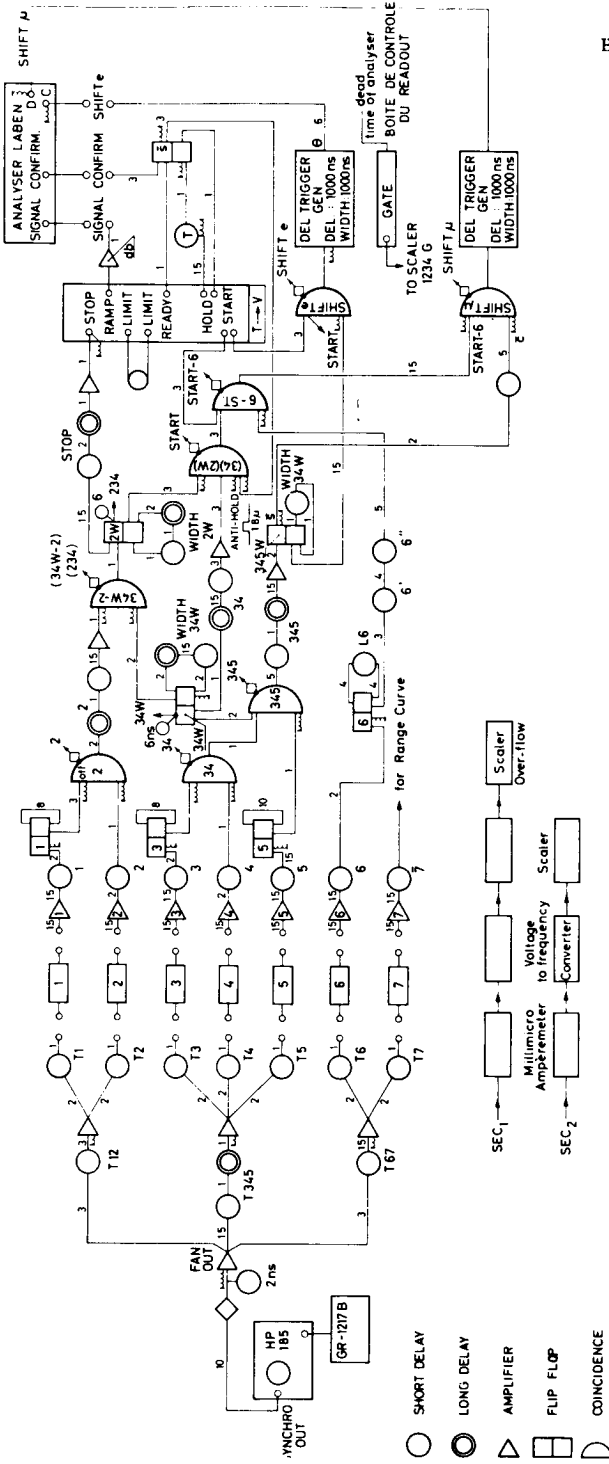


Figure 3. Pion Production Detection System, Block Diagram.

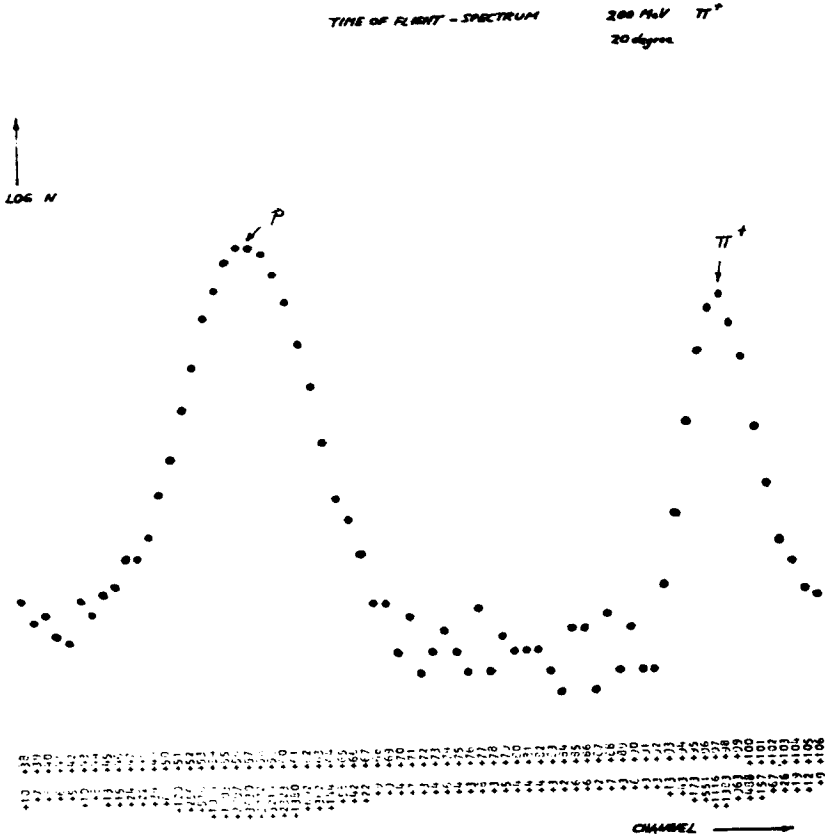


Figure 4. IBM 1620 Print-out of the time-of-flight spectrum of 310 MeV/c positive particles showing the proton and pion peaks on a log-linear scale.

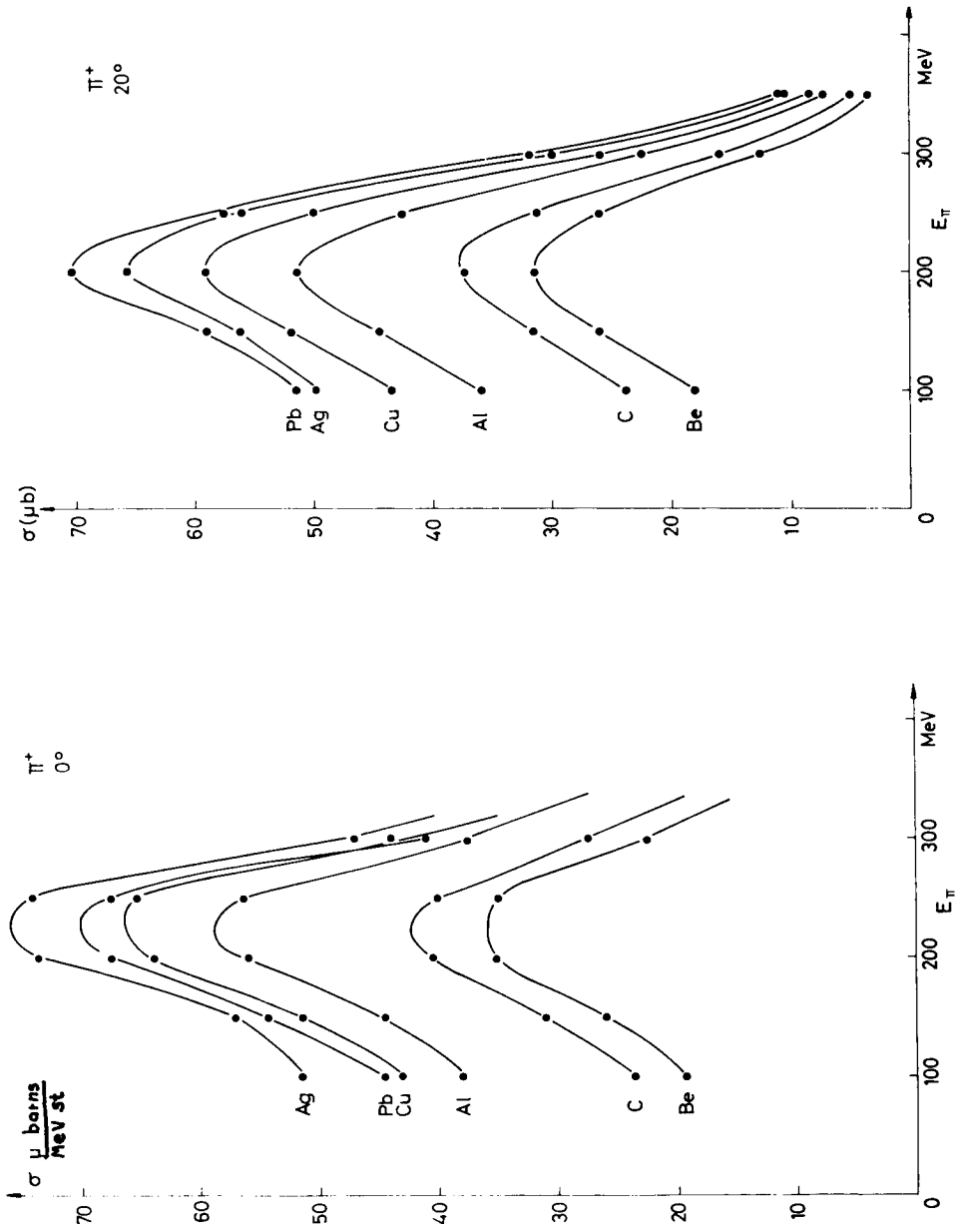


Figure 5.  $\pi^+$  spectra from Be, C, Al, Cu, Ag and Pb at  $0.8^\circ$  and  $21.5^\circ$  production angle.

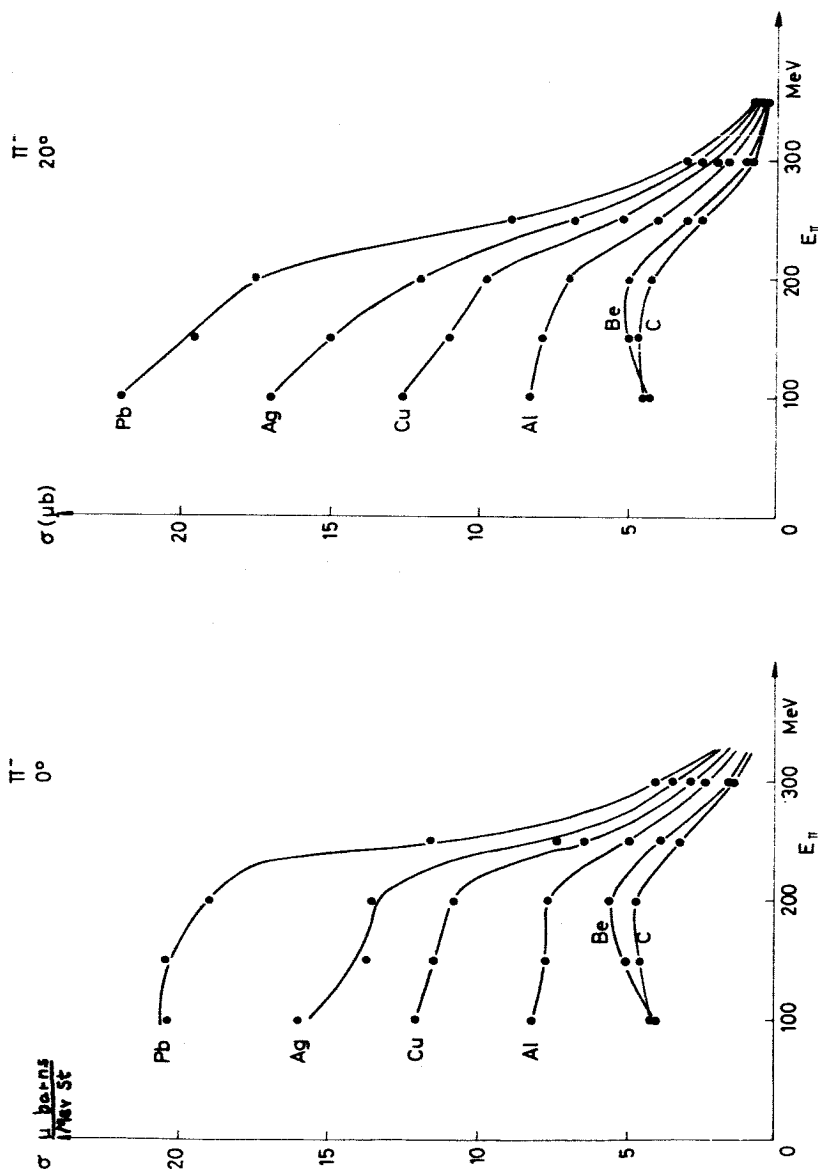


Figure 6.  $\pi^-$  spectra from Be, C, Al, Cu, Ag and Pb at  $0.8^\circ$  and  $21.5^\circ$  production angle.



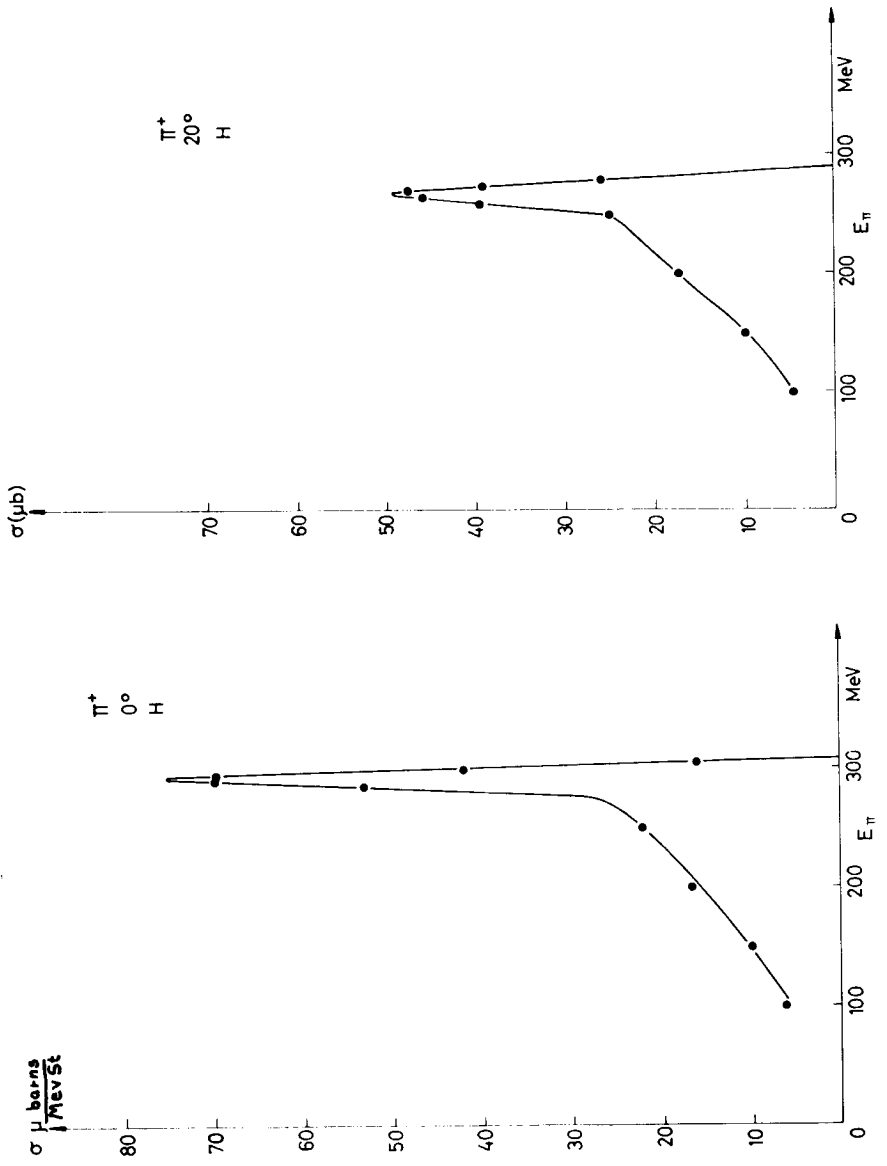
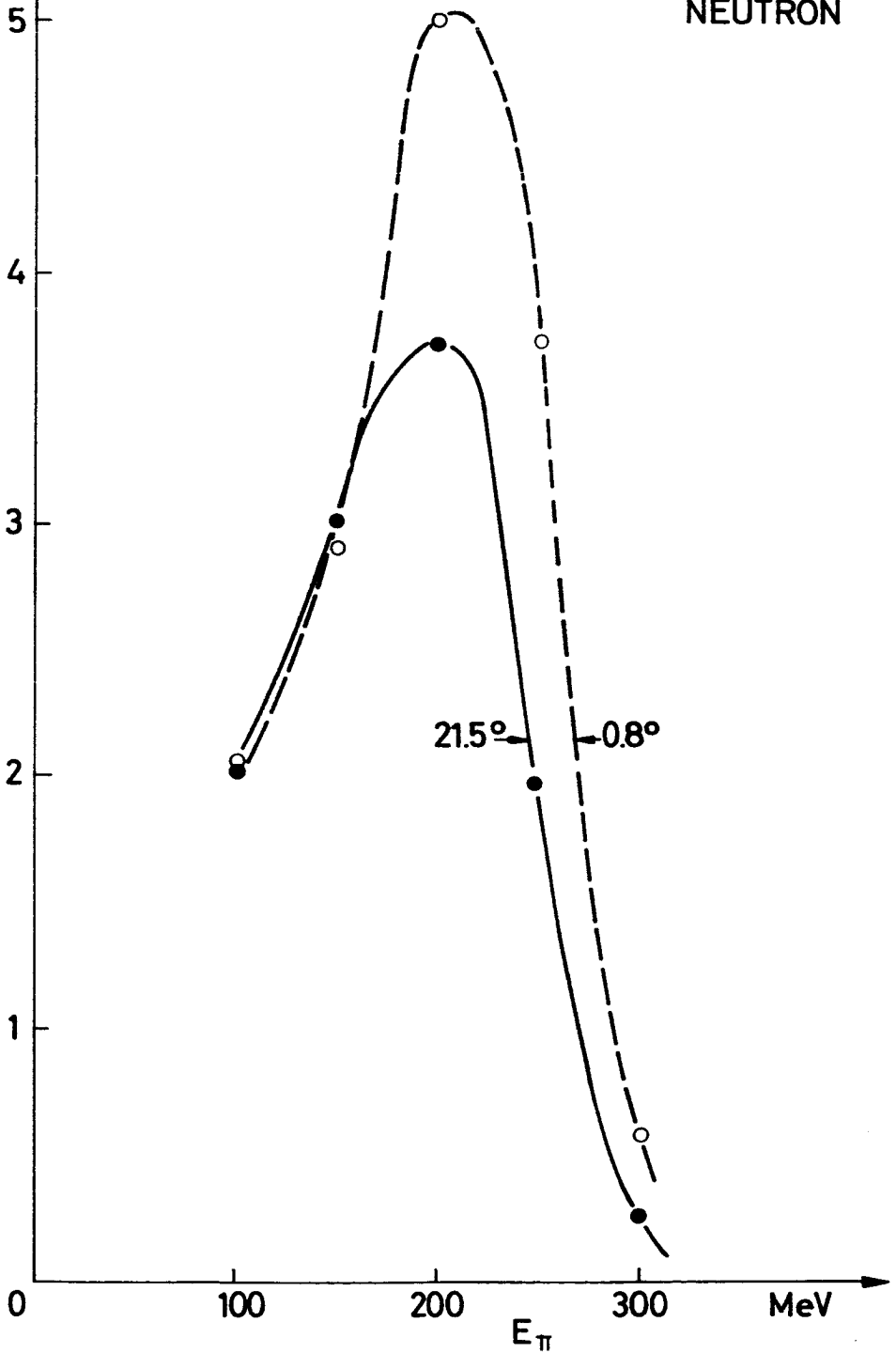


Figure 7. Positive pion spectra from proton-proton collisions at 0.8° and 21.5° lab angle.

$\sigma$   $\mu$  barns  
 Mev St

Pion spectra from p-n collisions/Figure 8.  
 at  $0.8^\circ$  and  $21.5^\circ$  lab angle.

$\pi^-$   
 NEUTRON



$$d^2\sigma/dE d\Omega$$

$$\frac{\mu \text{ barns}}{\text{MeV} - \text{st}}$$

- $P_c\pi^+$  21.5° LAB 450 MeV Lillethun 1962
- $P_c\pi^+$  19.5° LAB 660 MeV Meshkovski
- $P_c\pi^+$  0° LAB 725 MeV Haddock
- ▲  $P_c\pi^+$  21.5° LAB 600 MeV } CERN
- △  $P_c\pi^+$  0.8° LAB " " }

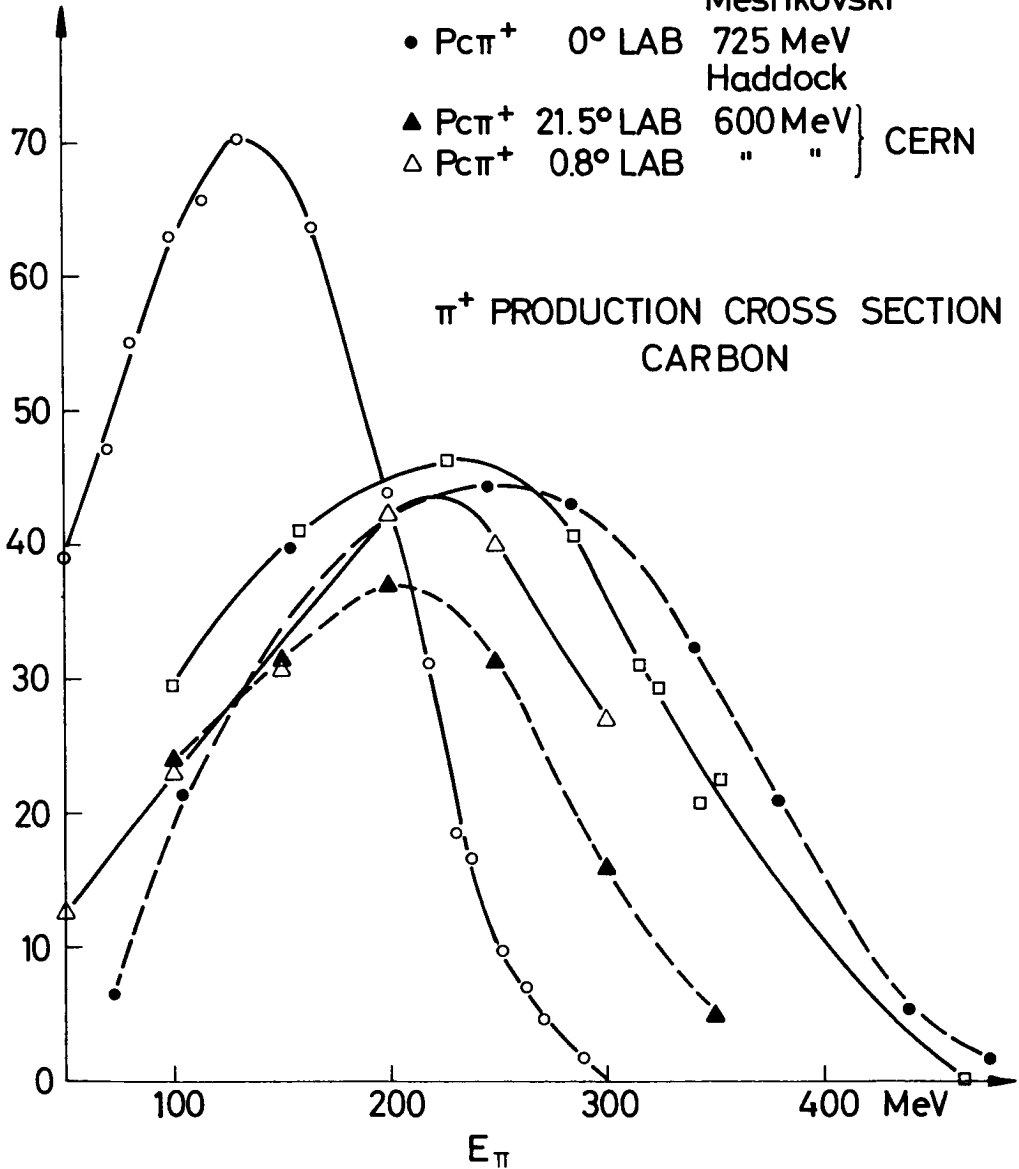


Figure 9. Positive pion spectra from pC collisions at various proton energies.

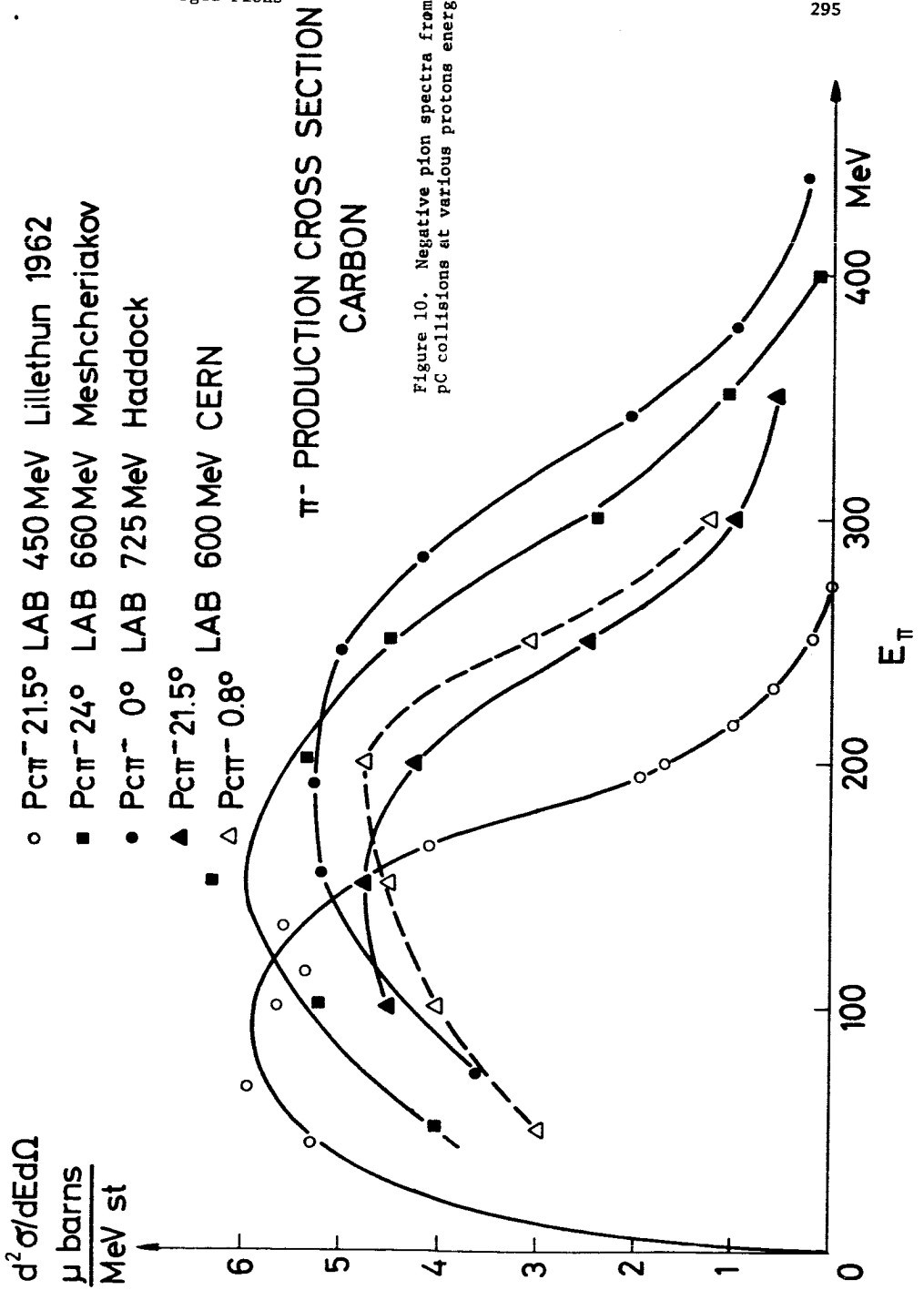


Figure 10. Negative pion spectra from pC collisions at various proton energies.

HADDOCK: I'd like to make just one small correction. The report to write for if you want the 725 MeV data is a UCLA report MPG 64-2.

PHILLIPS: Your ordinates on the last few graphs were called microbarns - I suppose it was microbarns per/str./MeV.

HADDOCK: Yes.

MUONS AND PIONS

Chairman, L. I. Foldy

N66 32746  
297

MUON CAPTURE AND NUCLEAR STRUCTURE

J. D. Walecka

Stanford University

Let me start by briefly refreshing your memory on some of the basic elements of muon capture in nuclei. (Figure 1) The fundamental process is

$$\mu^- + p \rightarrow \nu_\mu + n$$

The lifetime of the free muon against  $\beta$  decay is<sup>1)</sup>

$$\tau_\mu = 2.200 \pm .001 \times 10^{-6} \text{ sec.}$$

and therefore the  $\mu^-$  quickly cascades down into the 1s atomic orbit and sits there until it either decays or is captured by a proton. The Bohr radius for the muon is

$$A_\mu = \frac{1}{Z} \frac{Me}{M_\mu} A_0 \approx \frac{300 \times 10^{-13} \text{ cm}}{Z}$$

therefore the muon sits well inside the other atomic electrons, and still outside of the nucleus. I have indicated, roughly to scale, the situation in  $0^{16}$  on Slide 1. The capture rate is proportional to the probability of finding the muon at the nucleus and to the number of protons  $Z$ . Using the value of  $|\phi(0)|^2$  for a point charge  $Z$  we find that the capture rate follows the famous  $Z^4$  law. It is not until about  $\text{He}^{20}$  that the capture rate is equal to the free decay rate.

Since the  $\mu$  and the  $\nu_\mu$  couple locally in the weak interaction, the strong interaction part of the amplitude for muon capture on a free nucleon is summarized in a vertex function. (Figure 2) Using just Lorentz invariance and the Dirac equation we find that this vertex is characterized by six form factors. The conserved vector current theory tells us that we can take  $F_1$  and  $F_2$  from the isovector part of the electron scattering form factors. It also tells us  $F_3 = 0$ . Universality of the weak leptonic couplings tells us we can take  $F_A^\mu(0)$

from the  $\beta$  decay of the neutron while the Goldberger-Treiman relation and the assumption of the dominance of the one-pion-exchange pole in the induced pseudoscalar term,  $F_p$ , relates this quantity to  $F_A$  and gives<sup>2)</sup>

$$F_p(q^2) = \frac{2M}{M_\pi^2 + q^2} F_A(0) = \frac{M \cdot S}{M_\mu} F_A(0)$$

If we imagine starting with a basic weak coupling involving  $\bar{\chi}_\mu(1+\gamma_5)\chi$  for the bare nucleons and then turn on the strong interactions which are invariant under charge conjugation and isospin rotations we can never develop the terms  $F_S$  and  $F_T$ . These are called "second-class currents" by Weinberg.<sup>3)</sup>

The basic problem, then, is can we understand the nuclear physics in terms of this interaction? To get to the nuclear physics we reduce the Dirac Spinors to Pauli Spinors keeping terms of order  $1/M$  and then sum over all nucleons.<sup>†</sup> We find for the capture rate the result given in Figure 3. The  $G$ 's are linear combinations of the fundamental coupling constants and since the muon wave function varies only slowly over the nucleus, we have factored out the average of its square. ( $1/v_\mu$  is the muon Compton wavelength.) The nuclear physics is in the matrix element  $M_V^2$ ,  $M_A^2$ , and  $M_P^2$ . These are just the retarded Fermi or vector ( $\tau^-$ ) and Gamow-Teller or axial vector ( $\vec{\sigma}\tau^-$ ) matrix elements weighted with a phase space factor which is the square of the neutrino momentum,  $(v_{ab})^2$ , corresponding to a nuclear transition  $a \rightarrow b$ . The term  $\Lambda_{\mu c}^1$  represents the nucleon recoil corrections which go as  $(p/M)_{\text{nucleon}}$  and give corrections to the capture rate characteristically about 10 - 20%. The question then is how to feed an energy which can run up to the muon mass of 105 Mev and the corresponding momentum transfer

$$v_{ab} \stackrel{\Delta}{=} M_\mu - E_{ab}$$

<sup>†</sup> The  $1/M^2$  terms have been worked out by Friar at Stanford.



## Muon Capture

into a nucleus through the operators in  $M_V^2$ ,  $M_A^2$ , and  $M_P^2$ .

There are three basic types of nuclear physics that we can do:

1. We can try and extract information on the coupling constants by looking at the capture rates between distinct nuclear states. The most elementary process of this type, the capture on a free proton is unfortunately complicated by the fact that since the  $\mu$ -p system is neutral, p- $\mu$ -p molecules are readily formed in hydrogen and the theoretical discussion is clouded by the complications of the molecular physics. Only recently is reliable information becoming available on this part of the problem.<sup>5)</sup> Even the total capture rate in hydrogen gives us only one relation on the coupling constants, however. The difficulty with trying to do this in other nuclei is the well-known one of finding accurate enough nuclear wave functions. To some extent this problem can be bypassed by getting the nuclear matrix elements from other experiments. I will return to this point later. Once the coupling constants are determined, of course, one can turn the argument around and use the capture process to get very interesting information on the nuclear wave functions.

2. A second approach is to try and study the systematics of muon capture in heavy nuclei by assuming an average neutrino momentum and then using closure to evaluate the sum over nuclear states. The resulting two-particle correlation functions are then evaluated by using some model of nuclear matter. This was the approach used by Primakoff<sup>6)</sup>, and at least the qualitative features of the dependence on fractional neutron excess are understood.

3. A third approach, and the one I will spend most of my time discussing, is to try and calculate the total capture rates in nuclei where you think you have reliable knowledge of the structure. The hope is that in computing the total capture rates, uncertainties in any of the partial capture rates will average out.

The first study of this kind was that of Tiommo and Wheeler<sup>7)</sup>. Luyten, Rood, and Tolhoek<sup>8)</sup> (I will refer to this work as LRT) greatly extended this idea and carried out a systematic sum over all excitations in a single particle shell model of  $O^{16}$  and  $Ca^{40}$ . They found that their computed total capture rate was too high by a factor of two. Several features of their calculation are of particular interest. They start by using the result

$$M_V^2 = M_A^2 = M_P^2$$

which is true for the single-particle shell model without spin orbit splittings, and comes from the fact that adding a  $\sigma_f$  to the matrix element changes nothing in this simple model. Almost all previous work on muon capture also used this relation. It allows one to concentrate on evaluating  $M_V^2$ . Now for muon capture in nuclei up to  $Ca^{40}$  we have

$$\nu R \approx 1$$

and it makes sense to start expanding the neutrino wave function or the exponential in  $M_V^2$ . It is easy to see that the first term gives zero since we simply get the total isospin lowering operator and this annihilates the ground state. This means that most of the capture is "first-forbidden dipole" as was originally pointed out by Tiommo and Wheeler. In fact LRT found that the transitions to  $T = 1$ ,  $J^\pi = 1^-$  states accounted for 90% of  $M_V^2$  in  $O^{16}$  and 75% in  $Ca^{40}$ . It is therefore crucial to treat the dipole part of the capture correctly. Now working still within this model, Foldy and I<sup>4)</sup> observed the following: using isospin invariance and the Wigner-Eckart theorem the elements of  $\tau^-$  can be related to those of  $\tau^3$ . The leading term in the expansion of the exponential is now  $\tau^3 \bar{\chi}$  and this is exactly the same operator as governs the emission and absorption of electric dipole radiation. Thus we have the results of Figure 4. In the

first relation  $E_m$  is the maximum nuclear excitation energy measured with respect to the ground state of the initial nucleus. The second relation says that the retardation of the electric dipole contribution is contained in the ground state elastic form factor of the nucleus evaluated at the appropriate momentum transfer. This was found to be true to the order of a per cent by looking at the LRT calculation and has a very simple physical interpretation as we shall see.

At this point we see the inadequacy of the single particle harmonic oscillator shell model for it puts all the dipole resonance strength at an energy  $\hbar\omega = 10$  to 12 Mev in the LRT calculations. We know that in actual fact the electric dipole strength is concentrated in the giant dipole resonance which lies in the region 20 to 25 Mev in these light nuclei. We also understand theoretically from the work of Elliot and Flowers<sup>9)</sup> and Brown<sup>10)</sup> how the particle-hole interactions concentrate the electric dipole strength in a few levels which are pushed to an energy higher than  $\hbar\omega$ . It appears therefore to be crucial to treat the nucleus as an interacting system and examine the role of these collective modes.

Now Foldy and I argued, why can't we just turn these results around and use the formulae of the last slide to evaluate the total capture rates in terms of the experimentally measurable photo-excitation cross sections? The "guillotine factor"  $(E - E_m/E_m)^4$  coming from neutrino phase space means that only the well-known low-energy photo cross sections will be important. In this way we can empirically take into account the dynamical nuclear correlations. For the higher multipoles, since they are now correction terms to our main result we can simply use closure or the partial summations of LRT. Since, however, all of these results were derived on the basis of an independent particle model, it is necessary to go back and examine how they are modified by the presence of nuclear

interactions.

The most important relation is of course

$$M_V^2 = M_A^2 = M_P^2$$

We can get some insight here by assuming that the interaction forces are of the Wigner or Majorana type with only a weak spin dependence. This may not be so unreasonable since such a force can give the qualitative features of nucleon-nucleon scattering up to  $\sim 90$  Mev or so. In this case the Wigner supermultiplet theory<sup>11,4)</sup> applies. We define the familiar operators of Figure 5. They are closed under commutation and the transformations  $R(\omega)$  on the four-component spin-isospin nucleon wave functions form a group,  $SU(4)$ , the group of  $4 \times 4$  unitary unimodular matrices. If we furthermore assume that these operators commute with the Hamiltonian, then the eigenstates of  $H$  form a basis for an irreducible representation of the group  $SU(4)$ . If we concentrate on nuclei of the type  $A = 4n$  (i.e.,  $He^4$ ,  $C^{12}$ ,  $O^{16}$ ,  $Ca^{40}$  etc.) then if the forces are short range and attractive, one wants a spatial wave function of highest symmetry and therefore the ground state will belong to the identity representation of  $SU(4)$ . We can think of the giant dipole resonance, since it exhausts the dipole sum rule, as being very crudely just

$$(\sum \tau^3(i) \bar{\chi}(i)) |0\rangle$$

This suggests then that we assign it to the 15-dimensional representation of  $SU(4)$  for we could replace  $\tau^3$  by any one of the 15 other matrices and still have a degenerate state. This leads to the state shown in Figure 6.<sup>12)</sup> We note that they must have  $L = 1$ . These states have a very simple physical interpretation is one thinks back to the Goldhaber-Teller model of the giant dipole resonance where the neutrons oscillate against the protons<sup>13)</sup> for these other states are simply the corresponding oscillations of the different spin and isospin groups.

These modes have been considered previously by Glassgold, Heckrodt, and Watson and Fallieros, Ferrell, and Pal<sup>14)</sup> in a somewhat different context and Uberall will go into this in more detail in the next talk. It is easy to see, since  $\tau, \sigma$ , and  $\sigma\tau$  are treated on the same footing that SU(4) symmetry leads to the relation

$$M_V^2 = M_A^2 = M_P^2$$

One can ask how the actual spin dependent forces present in nuclei modify this result. Lewis and deForest have carried out calculations similar to those of Brown for C<sup>12</sup> and O<sup>16</sup>. The unperturbed particle-hole configuration energies were taken from neighboring nuclei and thus include the spin-orbit splitting. The nucleon force was taken from a fit to low energy scattering and therefore has the correct singlet-triplet spin dependence. The results are shown in the next few slides. Figure 7 shows the results of Lewis for the T = 1 states of O<sup>16</sup>15). D is the unretarded dipole strength and S is that of the tensor product of  $\sigma$  and  $\chi$ . The top two 1<sup>-</sup> states have most of the usual dipole strength as in the calculations of Elliot and Flowers. The interesting thing is that one state, the upper 1<sup>-</sup> also has most of the  $\vec{\sigma}_A \vec{\chi}$  strength while a giant 2<sup>-</sup> at 21 Mev and 0<sup>-</sup> at 27 Mev are also predicted. One finds here that even though the states are split and mixed by the spin-dependent forces

$$M_V^2 = M_A^2 \quad \text{to } 12\% \text{ (O}^{16}\text{)}$$

In Figure 8 are the results of deForest<sup>16)</sup> on C<sup>12</sup> and a very similar situation holds with respect to the 1<sup>-</sup> states. The state at 23 Mev has all the  $\tau^3 \vec{\chi}$  strength while its upper neighbor has all the  $\tau^3 \vec{\sigma}_A \vec{\chi}$  strength. Again a giant 2<sup>-</sup> is predicted at 20.7 Mev and 0<sup>-</sup> at 26 Mev. deForest finds

$$M_V^2 = M_A^2 = M_P^2 \quad \text{to } 8\% \text{ (C}^{12}\text{)}$$

We must also re-evaluate the assumption that the retardation of the dipole

contribution is given by the ground state elastic form factor of the nucleus evaluated at a neutrino momentum corresponding to nuclear excitation of the giant dipole resonance. We see by looking at deForest's particle-hole calculation (Figure 9) that the result holds in the presence of interactions to a few per cent.<sup>16)</sup> The physics is most clearly seen by thinking back to the Goldhaber-Teller model. To excite the giant dipole resonance and at the same time transfer momentum  $\nu$ , you must first catch hold of the ground state proton charge distribution and then shake it. This just costs you the elastic form factor.<sup>14,17)</sup> There is also experimental evidence on  $O^{16}$  from the work of Bishop and Isabelle that this relation is correct.<sup>18)</sup> Keeping the form factor under the integral is a few per cent correction.

We are therefore in a position to try and compute the total capture rates in these nuclei. Figure 10 gives you an idea of the size of the various contributions.  $R$  is the reduction of the square of the atomic muon wave function from its point Coulomb value.<sup>19)</sup>

$$|F_{e1}|^2 \text{ and } \int \left( \frac{E-E_m}{E_m} \right)^4 \frac{\sigma_{\gamma}(E)}{E} dE$$

we take from experiment. For the higher multipoles we use either closure or a sum over partial transition. We note that the role of these contributions has been enhanced by the suppression of the dipole. Unfortunately we have very little information on possible collective  $T = 1$  modes in these higher angular momentum states. For the correction  $\Lambda_{\mu c}^1$  we use the work of LRT and Primakoff. When we compare with the experimental capture rates we find the results on Figure 11. They are certainly consistent with our ideas about the universal Fermi interaction. The  $C^{12}$  value contains a contribution of  $.07 \times 10^5 \text{ sec}^{-1}$  from the allowed axial vector transition to the ground state of  $B^{12}$ . This large contribution casts some doubt on the applicability of our  $SU(4)$  analysis here.

The only trouble might be in  $\text{He}^4$ . Since it is so small, the first-forbidden contributions are greatly suppressed. Caine and Jones have estimated that one could have an additional allowed contribution of  $38 \pm 20 \text{ sec}^{-1}$  which has not been included in the theoretical rate.<sup>20)</sup> Note that the form factor and higher multipole effects are quite unimportant here.

I would like to spend a few minutes discussing the nuclear structure implications of these results. The agreement between the experimental and calculated total capture rates indicates that the axial vector strength is distributed in these nuclei in the same way as the vector strength and these results are strong, though rather indirect, evidence for some of the components of our supermultiplet of giant resonances. We can get additional information on some of these levels through inelastic electron scattering. The transverse electromagnetic multipole form factors can be seen by doing electron scattering experiments at  $180^\circ$  for example. These operators, which also govern real photon emission and absorption have the familiar long wavelength form shown on Figure 12. The second term in  $T_{LM}^{el}(q)$  is thrown away for photons but can become large for electrons where  $q$  is the momentum transferred to the nucleus for a given excitation energy. The effect of this term is seen quite clearly in the giant resonance region in  $\text{C}^{12}$  and  $\text{O}^{16}$ . (Figure 13) There is a pronounced dip in the transverse electric dipole form factor for the upper two  $1^-$  states corresponding to a transfer of dipole strength between these levels. This takes place over a relatively small  $q^2$  interval. These experiments are due to Barber, Goldemberg, and Vanpraet.<sup>22)</sup> The results for  $\text{O}^{16}$  are shown on Figure 14. These experiments show that there is a large component of  $\tau^3(\vec{\sigma}_\lambda \vec{\chi})$  strength in the giant dipole region. The form factor for pure charge oscillations is a decreasing function of  $q^2$  in this interval.

One of the most exciting predictions of our previous discussion is that

there should be giant magnetic quadrupole oscillations in these light nuclei.<sup>4,23)</sup> We saw that  $|\frac{T_{2M}^{mag}}{2M}|^2 \propto q^4$  and while magnetic quadrupole transitions are small for real photons, these states should show up strongly as the momentum transfer is increased. Sure enough, if one looks at the electron scattering data, there are peaks which shoot up as a function of  $q^2$  in the  $180^\circ$  data. Figure 15 shows the 65 Mev data on  $C^{12}$ .<sup>23)</sup> A giant M2 at 19.2 Mev had also been predicted independently by Brown and Vinh-Mau.<sup>10)</sup> The form factor for this state, Figure 16, shows the characteristic  $q^4$  growth. (There are two new experimental points at  $q = 81$  and 121 Mev that lie right on the solid line.)<sup>16)</sup>

As one last application let me return to the  $\alpha$  particle. According to our SU(4) considerations, there should be a 15 dimensional supermultiplet of negative parity excited states of which one member is the usual electric dipole resonance. deShalit and I have calculated where these states should lie.<sup>24)</sup> The position of the center of gravity of the supermultiplet is determined by the Wigner and Majorana parts of the force as we've seen from our general considerations while the splittings come from the spin-dependent parts of the force. Using a non-singular Serber force fit to low-energy nucleon-nucleon scattering and an empirical single-particle spin-orbit force determined from the  $0^- - 2^-$ ,  $T = 1$  splitting we find the results of Figure 17. The calculations are fit to the data at 22 Mev although the position of the center of gravity is predicted correctly to  $\sim 5\%$ . The energies of the recently observed levels are indicated in parenthesis. Using these results, Barrett, a student at Stanford, finds that<sup>25)</sup>

$$M_V^2 = M_A^2 = M_P^2 \quad \text{to } 12\% \quad (\text{He}^4)$$

lending some support to our muon capture predictions in this system.

Exactly the same nuclear physics considerations are applicable to the process of radiative muon capture. This process is of particular interest since one can



get to a momentum transfer  $q^2 \approx -m_\mu^2$  which is close to the pion pole and thus greatly enhances the role of the induced pseudoscalar coupling constant. Fearing,<sup>2,6)</sup> also a student at Stanford, has redone the Rood and Tolhoek calculation<sup>27)</sup> for  $\text{Ca}^{40}$  by making use of the appropriate integrals over the photoabsorption cross section. Since there are now two massless particles coming off, for a given energy transfer to the nucleus, one on the average transfers less momentum. This means the dipole matrix elements play an even larger role in radiative capture than in the total capture rates. Also, since the phase space weighting factors are different, the ratio of radiative to total capture rates is not model independent as hoped for by Rood and Tolhoek. Fearing's results, using the UFI coupling constants, are shown on Figure 18. The experiments on the high energy photon tail of Conversi, Diebold, and diLella<sup>29)</sup> required a larger rate or bigger value of  $F_p$  than the Goldberger-Treiman value. Fearing finds that a better treatment of the nuclear physics demands an even larger value and he concludes

$$\frac{M_\mu F_p}{F_A} = 16.5 \pm 3$$

There is obviously some difficulty here.

Let me turn briefly to the subject of muon capture between discrete nuclear states. Foldy and I<sup>30)</sup> noticed that there is one process, namely

$$\mu^- + C^{12} \rightarrow B^{12}(\text{g.s.}) + \nu_\mu$$

where one can get almost all the nuclear matrix elements from other experiments and thus get information on the coupling constants in an essentially model independent way. This capture rate, since it is  $0^+ \rightarrow 0^+$ ,  $T = 0 \rightarrow 1^+$ ,  $T = 1$  depends only very weakly on the vector, induced pseudoscalar, and possible tensor coupling constants and not at all on a possible scalar coupling. The empirical information we use are the  $F_{T\frac{1}{2}}$  value for the inverse  $\beta$  decay which is known very

accurately and the recent precise dipole form factor for exciting the analogue state at 15.1 Mev in  $C^{12}$ . By comparing the  $\sigma\tau$  matrix element obtained from the  $F\tau_{\frac{1}{2}}$  value with the transition magnetic dipole matrix element obtained by extrapolating the form factor shown in Figure 19 to zero momentum transfer one can separate the contribution of the spin and orbital angular momentum to the magnetic dipole form factor. The result is that the spin term makes up about 90% of the matrix element. After putting in some small corrections for second-forbidden contributions we can thus get  $M_A^2$  and  $M_P^2$  at the correct momentum transfer by normalizing to the  $F\tau_{\frac{1}{2}}$  value and using the electron scattering to give us the form factor. This procedure allows us to get the squares of the leading matrix elements to an accuracy of about 5%. If we assume the conserved vector current theory is correct, then we can use our results to determine  $F_A^u/F_A^\beta$ . The results are shown on Figure 20.<sup>31)</sup> The results are consistent with universality, and the accuracy, which is essentially limited by experiment, is comparable to that obtained in comparing the  $\frac{\pi \rightarrow e+\nu}{\pi \rightarrow \mu+\nu}$  branching ratio. If we assume  $F_A^u/F_A^\beta = 1$  then we can solve for the weak magnetism term and we get the results of Figure 21. We definitely have evidence for the presence of the weak magnetism term and the sign and magnitude are consistent with CVC. The accuracy is comparable to that obtained by comparing the  $\beta$  spectra of  $N^{12}$  and  $B^{12}$ .

Similar results have recently been obtained by Kim and Primakoff<sup>32)</sup> starting from a different approach which treats the various nuclear states as elementary particles.

Finally, then, let me try to make a summary of where things stand. From the results of capture in H, He<sup>3</sup>, and C<sup>12</sup> as well as some of the partial capture rates in O<sup>16</sup> the coupling constants are known to be fairly close to their UFI values.<sup>33)</sup> The exact magnitude of the induced pseudoscalar coupling constant is

not known but it appears to have the sign and order of magnitude of the Goldberger-Treiman value. One should not forget, however, that since the one-pion exchange process has a long range, there may be a real modification in nuclear matter. There is at present no evidence for the scalar and tensor couplings, unfortunately the evidence against the tensor coupling is not very strong since in any nuclear physics calculation only the combination  $M_{\mu}F_p - 2MF_T$  enters. As to the nuclear physics, there is rather strong evidence that the predominate capture process is through the supermultiplet of giant resonances and as we have seen there is independent evidence from electron scattering on the presence of the spin-isospin members of the multiplet. Several important questions remain unanswered, however, such as: Are these resonances present systematically throughout the periodic table? Are there  $T = 1, J^{\pi} = 0^{-}$ , and  $T = 0, S = 1, J^{\pi} = 0^{-}, 1^{-}, 2^{-}$  resonances present? What is the effect of strong spin dependences (for example the strong tensor force component present in most of the more sophisticated nucleon-nucleon potentials) on the giant magnetic resonances? Barrett<sup>25)</sup> has done some preliminary work on this. He is attempting to calculate particle-hole spectra with realistic nucleon-nucleon forces. For the  $\alpha$  particle, he finds the tensor force affects the  $0^{-}$  levels very strongly but that the relation  $M_A^2 = M_V^2 = M_P^2$ , though slightly worse, still holds to better than 20%. A lot of work remains to be done here.

In closing then just let me repeat that once the coupling constants are pinned down,  $\mu$  capture, since it is a weak probe with a known interaction, and since the relevant operators connect to very interesting states not always easily accessible to other experiments, is an extremely powerful tool for studying nuclear structure.

---

Discussion combined with next paper by H. Überall.

## REFERENCES

- 1) G. Feinberg and L. Lederman, Annual Review of Nuclear Science 13, 431 (1963).
- 2) M. L. Goldberger and S. B. Treiman, Phys. Rev. 111, 354 (1958).
- 3) S. Weinberg, Phys. Rev. 112, 1375 (1958).
- 4) L. L. Foldy and J. D. Walecka, Nuovo Cimento 34, 1026 (1964).
- 5) W. Roy Wessel and P. Phillipson, Phys. Rev. Letters 13, 23 (1964); A. Halpern, Phys. Rev. Letters 13, 660 (1964); P. K. Kabir, Phys. Letters 14, 257 (1965).
- 6) H. Primakoff, Rev. Mod. Phys. 31, 802 (1959). See however: H. A. Tolhoek, Nuclear Physics 10, 606 (1959); R. Klein and L. Wolfenstein, Phys. Rev. Letters 8, 327 (1963); J. S. Bell and J. Løvseth, Nuovo Cimento 32, 433 (1964); L. L. Foldy and J. D. Walecka, Nuovo Cimento 36, 1257 (1965).
- 7) J. Tiommo and J. A. Wheeler, Rev. Mod. Phys. 21, 153 (1949).
- 8) J. R. Luyten, H. P. C. Rood, and H. A. Tolhoek, Nuclear Phys. 41, 236 (1963).
- 9) J. P. Elliott and B. H. Flowers, Proc. Roy. Soc. 242A, 57 (1957).
- 10) G. E. Brown and M. Bolsterli, Phys. Rev. Lett. 3, 472 (1959); G. E. Brown, L. Castillejo, and J. A. Evans, Nuclear Physics 22, 1 (1961); N. Vinh-Mau and G. E. Brown, Nuclear Physics 29, 89 (1962).
- 11) E. Wigner, Phys. Rev. 51, 106 (1937).
- 12) J. D. Walecka, "Preludes in Theoretical Physics", p. 59, (North-Holland, 1965).
- 13) M. Golhaber and E. Teller, Phys. Rev. 74, 1046 (1948).
- 14) A. E. Glassgold, W. Heckrotte, and K. M. Watson, Annals of Physics 6, 1 (1959); S. Fallieros, R. Ferrell and M. K. Pal, Nuclear Physics 15, 363 (1960).
- 15) F. H. Lewis, Jr., Phys. Rev. 134, B331 (1964) and private communication.
- 16) T. deForest, Phys. Rev. 139, B1217 (1965).
- 17) J. Goldemberg, Y. Torizuka, W. C. Barber, J. D. Walecka, Nuclear Physics 43, 242 (1963).
- 18) G. R. Bishop and D. B. Isabelle, Nuclear Physics 45, 209 (1963).
- 19) J. C. Sens, Phys. Rev. 113, 679 (1958).
- 20) C. A. Caine and P. S. H. Jones, Nuclear Physics 44, 177 (1963).
- 21) J. M. Blatt and V. F. Weisskopf, "Theoretical Nuclear Physics", (Wiley, 1952).

## REFERENCES - (continued)

- 22) J. Goldemberg and W. C. Barber, Phys. Rev. 134, B963 (1964); G. Banpraet, Nuclear Physics 74, 219 (1965).
- 23) T. deForest, J. D. Walecka, G. Vanpraet, and W. C. Barber, Physics Letters 16, 311 (1965).
- 24) A deShalit and J. D. Walecka, Stanford University preprint ITP-193 (to be published).
- 25) B. Barrett, private communication.
- 26) H. Fearing, Stanford University preprint, ITP-197 (to be published).
- 27) H. P. C. Rood and H. Tolhoek, Nuclear Physics 70, 658 (1965).
- 28) W. E. Meyerhof, Stanford University preprint (to be published).
- 29) M. Conversi, R. Diebold, and L. Dilella, Phys. Rev. 136, B1077 (1964).
- 30) L. L. Foldy and J. D. Walecka, Phys. Rev. 140, B1339 (1965).
- 31) The experimental result is that of E. J. Maier, R. M. Edelman, and R. T. Siegel, Phys. Rev. 133, B663 (1964).
- 32) J. K. Kim and H. Primakoff, Phys. Rev. 140, B566 (1965).
- 33) H. P. C. Rood, CERN preprint 65/1417/5 th613; N. Drechsler and B. Stech, Z. fur Physik 178, 1 (1964); V. Gillet and D. A. Jenkins, Phys. Rev. 140, B32 (1965).

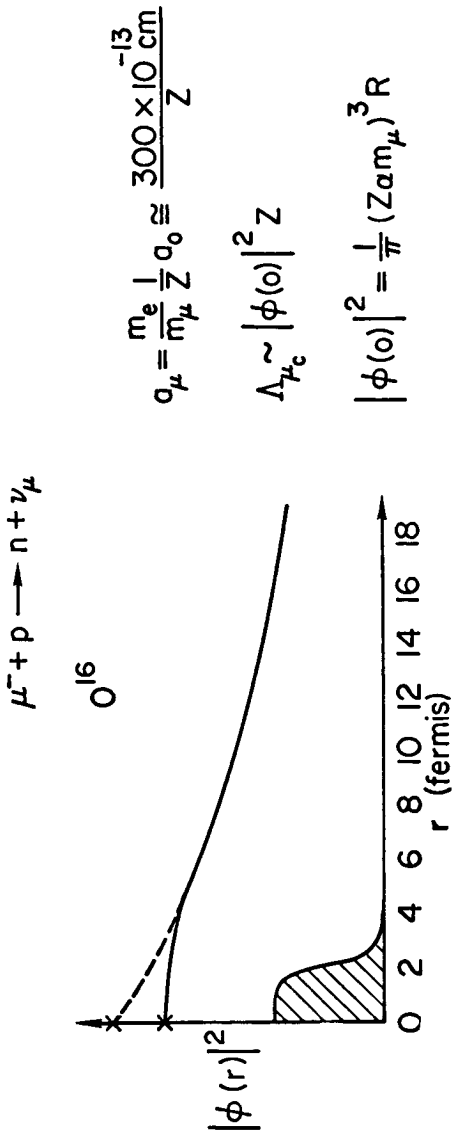
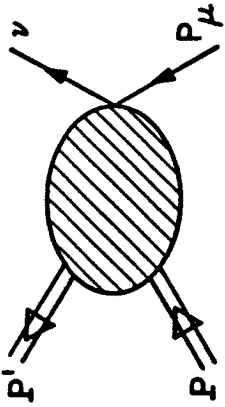


Figure 1. Some basic elements of muon capture.



$$q = P - P' = \nu - P_\mu$$

$$\langle P' | j_\mu(0) + j_\mu^5(0) | P \rangle = \bar{u}(P') \left\{ F_1(q^2) \gamma_\mu + F_2(q^2) \sigma_{\mu\nu} q_\nu + i F_S(q^2) q_\mu \right.$$

$$\left. + F_A(q^2) \gamma_5 \gamma_\mu - i F_P(q^2) q_\mu \gamma_5 - F_T(q^2) \sigma_{\mu\nu} q_\nu \gamma_5 \right\} \tau^{(-)} u(P)$$

Figure 2. The weak vertex for muon capture on a free nucleon

$$A_{\mu e} = \frac{v_{\mu}^2 |g_{\mu}|^2}{2\pi\hbar^2 c} [G_V^2 M_V^2 + 3G_A^2 M_A^2 + (G_V^2 - 2G_S G_A) M_S^2] + A'_{\mu e}.$$

$$M_V^2 = \overline{\sum_a} \sum_b \left( \frac{v_{ab}}{v_{\mu}} \right)^2 \int \frac{d\hat{v}}{4\pi} |\langle b | \sum_{i=1}^A \tau^{(-)}(i) \exp[-i\mathbf{v}_{ab} \cdot \mathbf{x}(i)] | a \rangle|^2,$$

$$M_A^2 = \frac{1}{3} \overline{\sum_a} \sum_b \left( \frac{v_{ab}}{v_{\mu}} \right)^2 \int \frac{d\hat{v}}{4\pi} |\langle b | \sum_{i=1}^A \tau^{(-)}\sigma(i) \exp[-i\mathbf{v}_{ab} \cdot \mathbf{x}(i)] | a \rangle|^2,$$

$$M_S^2 = \overline{\sum_a} \sum_b \left( \frac{v_{ab}}{v_{\mu}} \right)^2 \int \frac{d\hat{v}}{4\pi} |\langle b | \sum_{i=1}^A \tau^{(-)}(i) \hat{v} \cdot \sigma(i) \exp[-i\mathbf{v}_{ab} \cdot \mathbf{x}(i)] | a \rangle|^2.$$

Figure 3. The formulae for the muon capture rate in nuclei.<sup>4)</sup>



$$(M_V^2)_{\text{U.D.}} = \frac{\nu_\mu^2}{2\pi^2\alpha} \left(\frac{\nu_m}{\nu_\mu}\right)^4 \int_0^{E_m} \frac{(E_m - E)^4}{E_m^4} \sigma_\gamma(E) dE$$

$$(M_V^2)_D = (M_V^2)_{\text{U.D.}} \left| F_{el}(E_m - E_{res}) \right|^2$$

Figure 4. Relation of dipole capture matrix element to photo absorption. 4)

$$T^\alpha \equiv \frac{1}{2} \sum_{i=1}^A \tau^\alpha(i)$$

$$S_\lambda \equiv \frac{1}{2} \sum_{i=1}^A \sigma_\lambda(i)$$

$$Y_\lambda^\alpha \equiv \frac{1}{2} \sum_{i=1}^A \tau^\alpha(i) \sigma_\lambda(i)$$

$$\alpha, \lambda = 1, 2, 3$$

$$R(\omega) \phi_i \equiv [e^{i\omega_\alpha G_\alpha}]_{ji} \phi_j$$

$$[G^{(\alpha)}, H] = 0 \quad \alpha = 1, \dots, 15$$

Figure 5. Generators of SU(4).

"Degenerate" giant resonances

| L | S | $J^\pi$  | T |
|---|---|--|---|
| 1 | 0 | 1 <sup>-</sup>                                   | 1 |
| 1 | 1 | 0 <sup>-</sup> , 1 <sup>-</sup> , 2 <sup>-</sup> | 0 |
| 1 | 1 | 0 <sup>-</sup> , 1 <sup>-</sup> , 2 <sup>-</sup> | 1 |

Figure 6

| $J_\pi$        | Energy | $(1/\eta^2)D$ | $(1/\eta^2)S_0$ | $(1/\eta^2)S_1$ | $(1/\eta^2)S_2$ |
|----------------|--------|---------------|-----------------|-----------------|-----------------|
| 0 <sup>-</sup> | 27.28  | —             | 1.18            | —               | —               |
| 0 <sup>-</sup> | 14.41  | —             | 0.14            | —               | —               |
| 1 <sup>-</sup> | 26.63  | 0.93          | —               | 2.21            | —               |
| 1 <sup>-</sup> | 23.89  | 2.91          | —               | 0.79            | —               |
| 1 <sup>-</sup> | 21.01  | 0.02          | —               | 0.29            | —               |
| 1 <sup>-</sup> | 18.65  | 0.06          | —               | 0.43            | —               |
| 1 <sup>-</sup> | 14.63  | 0.07          | —               | 0.29            | —               |
| 2 <sup>-</sup> | 24.52  | —             | —               | —               | 1.27            |
| 2 <sup>-</sup> | 21.34  | —             | N <sup>o</sup>  | —               | 3.88            |
| 2 <sup>-</sup> | 20.01  | —             | —               | —               | 0.17            |
| 2 <sup>-</sup> | 18.69  | —             | —               | —               | 0.00            |
| 2 <sup>-</sup> | 13.85  | —             | —               | —               | 1.33            |

Figure 7. Vector  $\frac{1}{\eta^2}D\alpha|\langle\tau_3\mathbf{x}\rangle|^2$  and axial vector  $\frac{1}{\eta^2}S_J\alpha|\langle\tau_3[\sigma\otimes\mathbf{1}]_J\rangle|^2$  strengths for states in  $C^{12}(4,15)$

| C <sup>12</sup> |                         |  |  | C <sup>12</sup> (RPA)                                      |                |                         |  | O <sup>16</sup>  |  |                |                         |  |  |  |
|-----------------|-------------------------|--|--|--|----------------|-------------------------|--|--|--|----------------|-------------------------|--|--|--|
| J <sub>i</sub>  | E <sub>i</sub><br>(MeV) | (M <sub>V</sub> <sup>2</sup> ) <sub>D</sub> <sup>(1)</sup> | (M <sub>A</sub> <sup>2</sup> ) <sub>D</sub> <sup>(1)</sup> | (M <sub>T</sub> <sup>2</sup> ) <sub>D</sub> <sup>(1)</sup> | J <sub>i</sub> | E <sub>i</sub><br>(MeV) | (M <sub>V</sub> <sup>2</sup> ) <sub>D</sub> <sup>(1)</sup> | (M <sub>A</sub> <sup>2</sup> ) <sub>D</sub> <sup>(1)</sup> | (M <sub>T</sub> <sup>2</sup> ) <sub>D</sub> <sup>(1)</sup> | J <sub>i</sub> | E <sub>i</sub><br>(MeV) | (M <sub>V</sub> <sup>2</sup> ) <sub>D</sub> <sup>(1)</sup> | (M <sub>A</sub> <sup>2</sup> ) <sub>D</sub> <sup>(1)</sup> | (M <sub>T</sub> <sup>2</sup> ) <sub>D</sub> <sup>(1)</sup> |
| 0               | 25.66                   |  | 0.091  | 0.273  | 0              | 25.53                   |  | 0.087  | 0.260  | 0              | 14.41                   |  | 0.013  | 0.039  |
|                 | 35.78                   |  | 0.001  | 0.004  |                | 35.37                   |  | 0.002  | 0.006  |                | 27.28                   |  | 0.077  | 0.230  |
| 1               | 19.57                   | 0.023  | 0.013  |  | 1              | 19.76                   | 0.021  | 0.012  |  | 1              | 14.63                   | 0.016  | 0.024  |  |
|                 | 23.26                   | 0.472  | 0.017  |  |                | 23.08                   | 0.424  | 0.026  |  |                | 18.65                   | 0.016  | 0.040  |  |
|                 | 25.01                   | 0.000  | 0.197  |  |                | 24.95                   | 0.002  | 0.173  |  |                | 21.01                   | 0.002  | 0.021  |  |
|                 | 35.80                   | 0.072  | 0.010  |  |                | 35.61                   | 0.059  | 0.015  |  |                | 23.89                   | 0.638  | 0.060  |  |
|                 |                         |  |  |  |                |                         |  |  |  |                | 26.63                   | 0.184  | 0.147  |  |
| 2               | 18.91                   |  | 0.011  | 0.013  | 2              | 18.90                   |  | 0.010  | 0.012  | 2              | 13.85                   |  | 0.144  | 0.173  |
|                 | 20.76                   |  | 0.210  | 0.251  |                | 20.67                   |  | 0.190  | 0.228  |                | 18.69                   |  | 0.000  | 0.000  |
|                 | 23.94                   |  | 0.059  | 0.071  |                | 23.92                   |  | 0.053  | 0.064  |                | 20.01                   |  | 0.020  | 0.024  |
|                 |                         |  |  |  |                |                         |  |  |  |                | 21.34                   |  | 0.302  | 0.362  |
|                 |                         |  |  |  |                |                         |  |  |  |                | 24.52                   |  | 0.092  | 0.110  |

Figure 8. Capture matrix elements for states in C<sup>12</sup> and O<sup>16</sup>. <sup>16)</sup> R.P.A. means random phase approximation.

Square of the elastic form factor and ratios of the retarded to unretarded squared matrix elements.

| Nucleus               | $\frac{(M_V^2)_D}{(M_V^2)_{UD}}$ | $\frac{(M_A^2)_D}{(M_A^2)_{UD}}$ | $\frac{(M_T^2)_D}{(M_T^2)_{UD}}$ | $ F_{el}(v_{rel}) ^2$ |
|-----------------------|----------------------------------|----------------------------------|----------------------------------|-----------------------|
| C <sup>12</sup>       | 0.713                            | 0.713                            | 0.710                            | 0.719                 |
| C <sup>12</sup> (RPA) | 0.711                            | 0.711                            | 0.711                            | 0.719                 |
| O <sup>16</sup>       | 0.681                            | 0.664                            | 0.663                            | 0.676                 |

Figure 9. deForest's results on the retardation of the dipole matrix elements in the particle-hole model. <sup>16)</sup>

| Element          | $K$  | $(M_p^2)_{\text{v.d.}}$<br>[eq. (4.3)] | $E_m - E_{\text{cm}}$<br>(MeV) | $\frac{F_{\text{el}}(E_m - E_{\text{cm}})}{(-E_{\text{cm}})^2}$ | $\frac{F_{\text{el}}^2(E_m - E_{\text{cm}})}{(M_p^2)_{\text{v.d.}}}$ | $(M_p^2)_{\text{o.m.}}$                                    | $M_p^2$ | $\Lambda_{\mu\mu}^2$<br>[in $\text{s}^{-2}$ ] | $G\Lambda_{\mu\mu}^2$<br>[in $\text{s}^{-1}$ ] |
|------------------|------|--|--------------------------------|---|--|--|---------|---|--|
| $^{40}\text{Ca}$ | 0.44 | 2.73                                   | 91.5                           | 0.40  | 1.09   | 1.67 closure<br>1.16 partial trans. (*)<br>1.41 average    | 2.50    | $24.7 \cdot 10^6$                             | $3.6 \cdot 10^6$<br>ref. (*)                   |
| $^{16}\text{O}$  | 0.79 | 0.77                                   | 85                             | 0.63  | 0.485  | 0.231 closure<br>0.178 partial trans. (*)<br>0.204 average | 0.69    | $0.79 \cdot 10^6$                             | $0.16 \cdot 10^6$<br>ref. (*)                  |
| $^{12}\text{C}$  | 0.83 | 0.45                                   | 83                             | 0.72  | 0.324  | 0.073  | 0.40    | $0.20 \cdot 10^6$                             | $\sim 0.06 \cdot 10^6$                         |
| $^4\text{He}$    | 0.98 | 0.108                                  | 79                             | 0.87  | 0.094  | 0.004  | 0.098   | 195   | 54<br>ref. (**)                                |

Figure 10. Contributions to the total capture rate.<sup>4)</sup>

|                  | Theory                            | Experiment                                 |
|------------------|-----------------------------------|--|
| $\text{Ca}^{40}$ | $29 \times 10^5 \text{ s}^{-1}$   | $25.5 \pm 0.5 \times 10^5 \text{ s}^{-1}$  |
| $\text{O}^{16}$  | $0.95 \times 10^5 \text{ s}^{-1}$ | $0.98 \pm 0.05 \times 10^5 \text{ s}^{-1}$ |
| $\text{C}^{12}$  | $0.33 \times 10^5 \text{ s}^{-1}$ | $0.30 \pm 0.07 \times 10^5 \text{ s}^{-1}$ |
| $\text{He}^4$    | $252 \text{ s}^{-1}$              | $368 \pm 47 \text{ s}^{-1}$                |

Figure 11. Comparison of calculated and experimental capture rates.<sup>4)</sup>

$$T_{IM}^{\text{el.}}(q) \xrightarrow{q \rightarrow 0} \frac{\omega}{qc} \vec{x} - \frac{i(\lambda p - \lambda_n)}{2} \left( \frac{q}{2Mc} \right) \vec{\sigma}_\lambda \vec{x} \Big]_{IM} \tau_3$$

$$T_{2M}^{\text{mag}}(q) \xrightarrow{q \rightarrow 0} \left( \frac{iq}{2Mc} \right) q \left\{ \left[ (\lambda p - \lambda_n) \vec{\sigma} + \frac{2}{3} \vec{\ell} \right] \odot \vec{x} \right\}_{2M} \tau_3$$

Figure 12. Long wave-length reduction of the transverse E1 and M2 multipole operators.<sup>21)</sup>

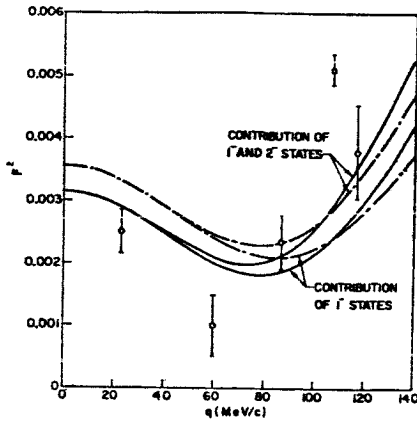


Figure 13. Transverse E1 form factor for the giant dipole resonance in  $^{12}\text{C}$ . 16)

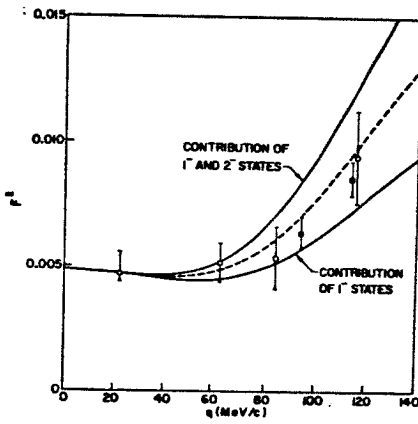
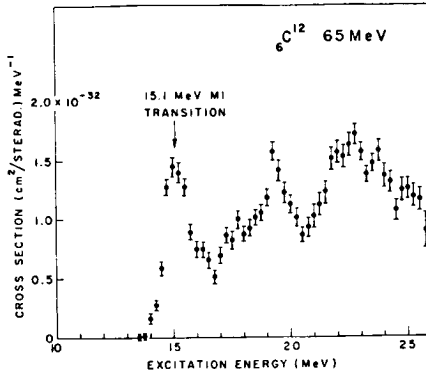


Figure 14. Transverse E1 form factor for the giant dipole resonance in  $^{16}\text{O}$ . 16)



Cross section for inelastic scattering of 65 MeV electrons at  $180^\circ$  from carbon, plotted as a function of the excitation energy.

Figure 15

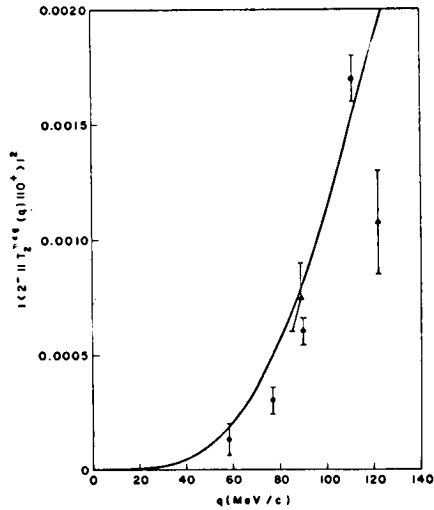


Figure 16. Form factor for the 19.2 MeV level in  $C^{12}$ . The solid line is the particle-hole model result [reduced by a factor of 2].<sup>22)</sup>



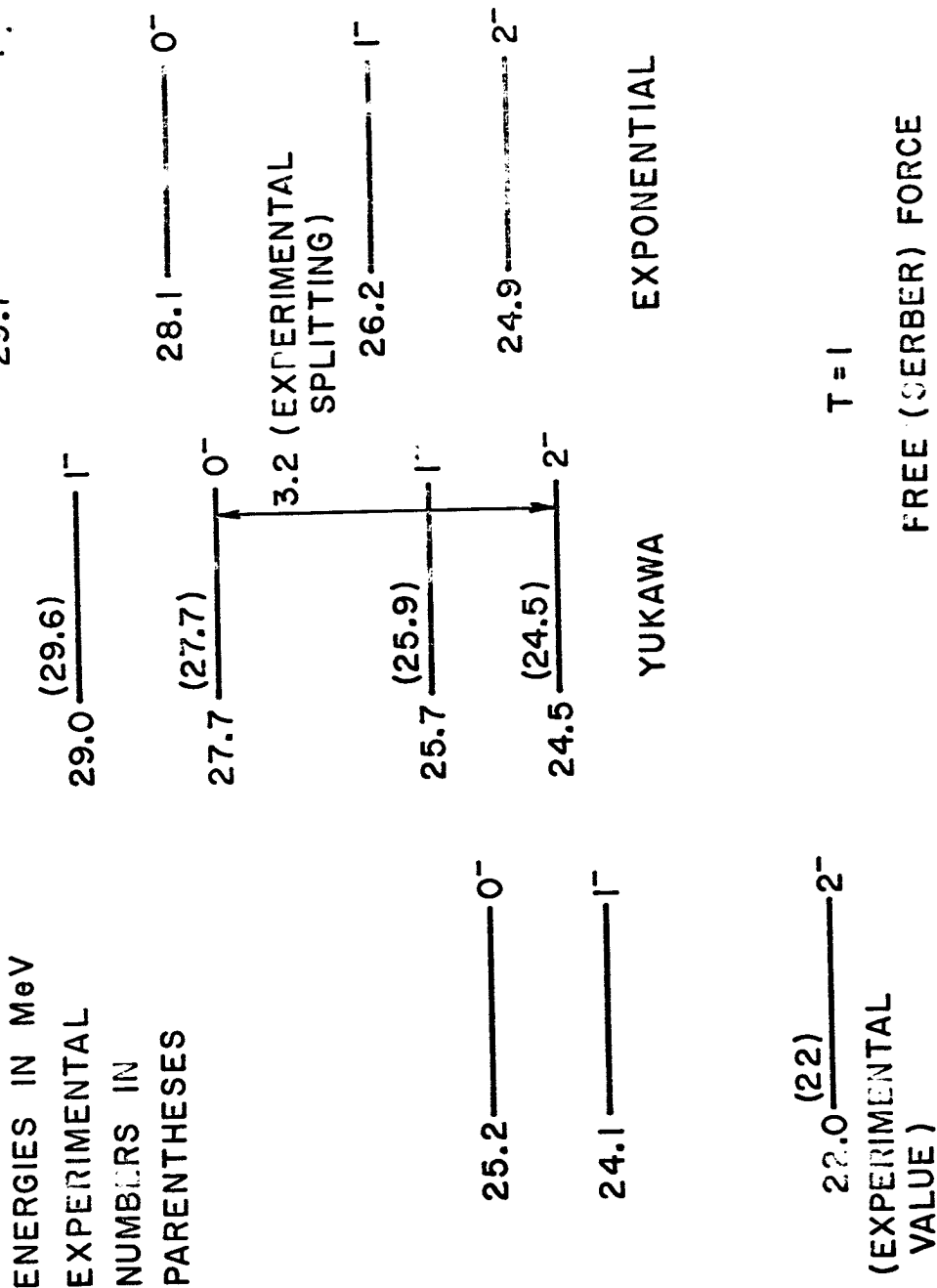


Figure 17. Spectrum of negative parity excited states of the  $\alpha$ -particle.

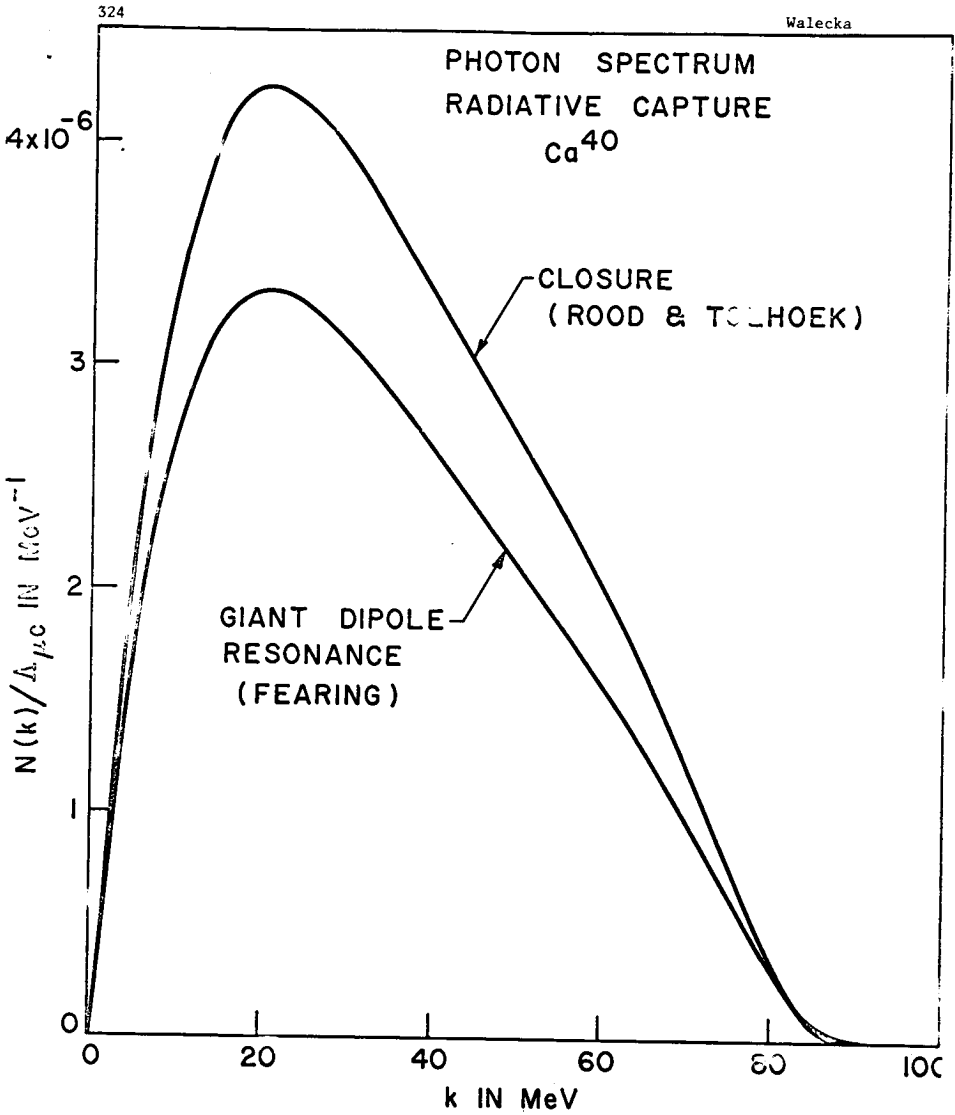


Figure 18. Photon spectrum for radiative muon capture in  $\text{Ca}^{40}$ . The result is normalized by the calculated total capture rate.<sup>26,27)</sup>

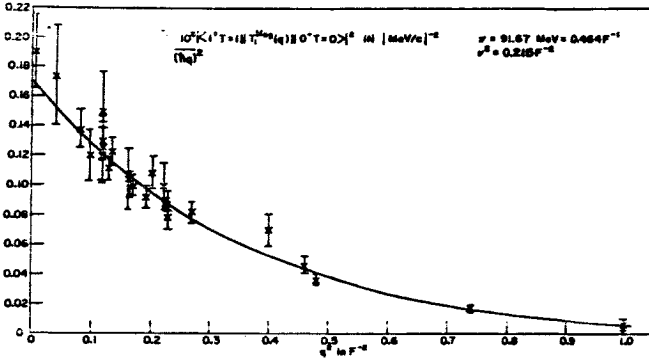
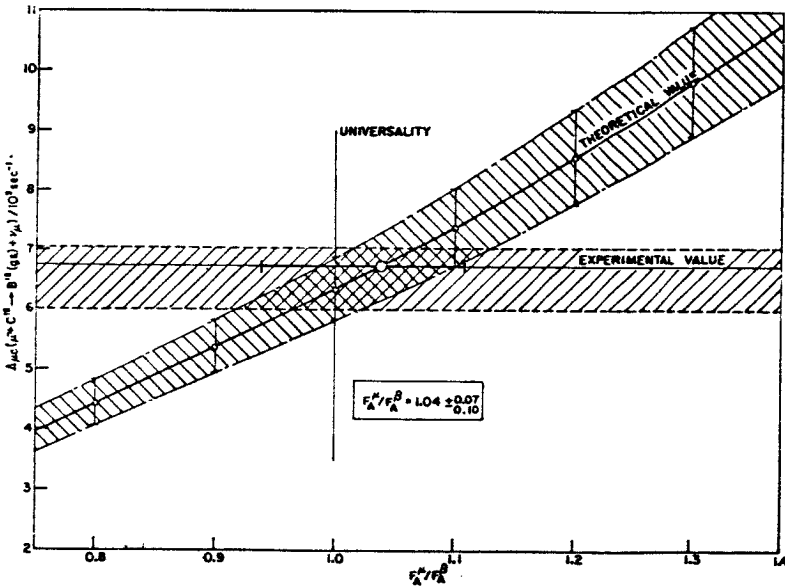
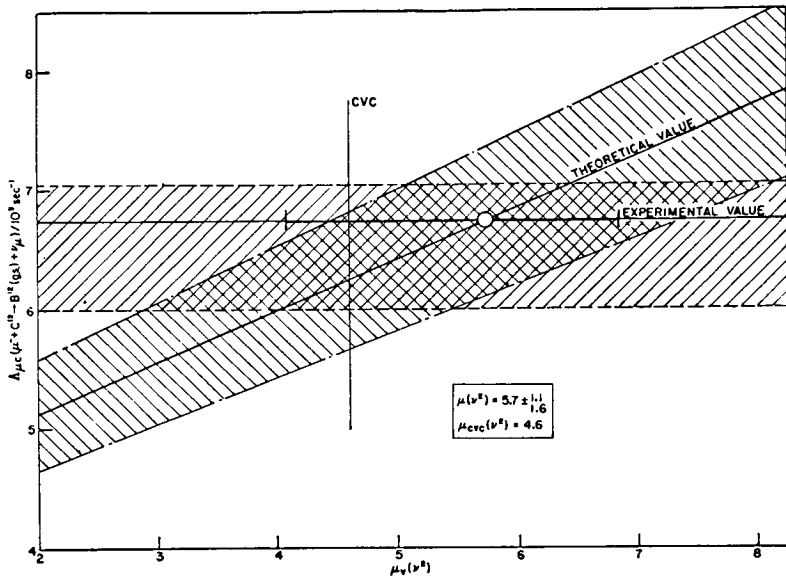


Figure 19. Best fit to the experimental values of the transverse magnetic dipole form factor for the 15.1,  $1^+$ ,  $T=1$  level in  $C^{12}$ . 30)



Experimental and theoretical values of the partial capture rate for the process (1) plotted against  $F_A^{\mu} / F_A^{\beta}$ , assuming  $\mu(\beta^2) = \mu c v c(\beta^2)$ .

Figure 20.



Experimental and theoretical values of the partial capture rate for the process (1) plotted against  $\mu(\nu^2)$ , assuming  $F_{\Delta^+}/F_{\Delta^0} = 1$ .

Figure 21.

N66<sup>327</sup> 32747

Muon Capture and Nuclear Giant Resonances.

H. Überall

Department of Physics

The Catholic University of America

Washington D.C.

Supported in part by the National Science Foundation.

It has often been said that muon capture in complex nuclei, besides providing the possibility of determining the coupling constants of the weak interaction, could also be used as a tool for probing the structure of the nucleus once the coupling constants are known (or assumed to be known, e.g. from universality). So far, not too much use has however been made of this attractive idea; most nuclear-structure dependent phenomena were still interpreted as means for determining coupling constants, such as the induced pseudoscalar (1-5). It has only recently been attempted, after one had realized the important role that giant resonance states play in muon capture (6,7), to introduce detailed properties of the giant dipole states (7-12) into the muon capture formalism, and to relate their excitation in muon capture to the excitation by other means (8,12). Since the giant resonances often are members of isotopic multiplets, they will occur in one or several of neighboring nuclei, and one can thus develop a unified picture of the excitation of all these states by weak or electromagnetic interactions (13), with or without change of  $T_3$ , with mutual interrelations provided by charge independence. Muon capture can therefore be used as a tool for studying the giant resonances in the same sense in which the conventional photonuclear and more recently electroexcitation processes have been used. As a matter of fact, more states can be reached this way, such as (starting with a  $O^+$ ,  $T = 0$  nucleus)  $2^-$  states which are fairly inaccessible for  $(\gamma, N)$  reactions, and  $O^-$  states which are inaccessible to both photo- and electroexcitation. Muon capture is however somewhat restricted, as is photonuclear excitation, by having its momentum transfer related to the energy transfer, whereas in electroexcitation, the momentum transfer can be varied independently. In any case, muon capture together with photo- and electroexcitation as well as neutrino absorption form a family of reactions by which the giant resonances may be excited, and which may complement each other in the study of these resonances. The present paper has as its main point a demonstration of this fact, and a discussion of its various aspects, as well as of any direct experimental evidence, which so far is only very scant as far as muon capture is concerned (14). We also take

the opportunity of discussing a simplified and therefore rather lucid picture of the various modes of collective nuclear vibrations that the giant dipole states represent, based on the Goldhaber-Teller model (15,16) and its completion by the introduction of spin waves (17). A classification of the resonance states is given in this picture, and various sum rules are discussed. The observation of the nuclear "breathing" collective mode states, which cannot be achieved through the previously discussed excitation mechanisms, will be touched upon in an appendix.

The realization of the important role played in muon capture by the giant dipole states arose from a discrepancy between experiment and calculation of total capture in  $^{16}\text{O}$  and  $^{40}\text{Ca}$  which Tolhoek et al (18) had performed using a simple version of the shell model, assuming the Universal Fermi Interaction. The theoretical values of the capture rates were by  $\sim 50\%$  higher than the experimental results. Barlow, Sens et al (6) confirmed this disagreement in  $^{16}\text{O}$  by a new measurement. Fig.1 shows their experimental result for the total capture rate,

$$\Lambda_{\text{capt}}(^{16}\text{O}) = (0.98 \pm 0.05) \times 10^5 \text{ sec}^{-1}, \quad (1)$$

and the theoretical values obtained by different methods. Luyten et al (18) had performed a sum over partial transitions to final states, whose energies were taken as the eigenstates of a harmonic oscillator or square well potential; the wave functions used for the calculation of the matrix elements were those of an independent particle shell model. In Table I, we exhibit the results of their calculation for the squared matrix elements,  $M^2$ , of the individual transitions which are classified by a multipole expansion (order  $\ell$ ). It is seen that the most important contribution by far ( $\sim 90\%$  of the total) is that leading from the  $0^+$  ground state to a  $1^-$  dipole state by  $\ell = 1$ , with matrix element

$$M^2 = \left| \langle T=1, 1^- \left| \sum_{i=1}^A \tau_i^- v_{ab} \right| T=0, 0^+ \rangle \right|^2. \quad (2)$$

The energies of this "giant dipole state" are 12.7 Mev for the oscillator, 13.3 Mev for the infinite square well potential. There is a

similarity with the giant dipole states of photonuclear<sup>(19)</sup> excitation, which are also  $T = 1$ ,  $J = 1^-$ , and in which most of the electric dipole excitation strength is concentrated; their experimental energy in  $^{16}\text{O}$  however lies at  $\sim 22$  Mev. The situation suggests strongly that these final states should be the isotopic analogues of each other (6,8) ( $T_3 = 0$  in photoabsorption,  $T_3 = -1$  in muon capture); then the low calculated energy of the dipole state most effective in muon capture should just be due to the shortcomings of the independent particle shell model, and could easily be "raised" using Elliott and Flowers'<sup>(20)</sup> method of configuration mixing by a residual particle-hole interaction. The situation in the  $^{16}\text{O}$  photonuclear effect is pictured (21) in Table II. For the single-particle excited configurations (in  $jj$ -coupling) of the first column, the unperturbed energies  $E$  are taken from states of neighboring closed-shell-plus-particle (or hole) nuclei, and one finds dipole strengths  $D^2$  (in % of the total) which are fairly uniformly distributed. Mixing of the configurations by the residual interactions leads to energies  $E'$  that are raised somewhat; but now the dipole strengths  $D'^2$  are concentrated in the states of highest energy.

Assuming, then, that for the dipole transitions, Luyten's (18) matrix elements could still be used, but that now it should refer to the state of dominant dipole absorption strength (at  $\Delta E_{ab} = 22.2$  Mev in Table II), Barlow et al (6) note that the corresponding neutrino momentum  $\nu_{ab} = m_\mu - \Delta E_{ab}$  would be decreased by  $\sim 10$  Mev, with a corresponding decrease of  $\Lambda_{\text{capt}}$  which is a sensitive function of  $\nu_{ab}$ ; they thus obtain a value

$$\Lambda_{\text{capt}} = 1.1 \times 10^5 \text{ sec}^{-1}, \quad (3)$$

in good agreement with experiment.

Foldy and Malecka (3) extended this procedure and related muon capture rates in  $^4\text{He}$ ,  $^{12}\text{C}$ ,  $^{16}\text{O}$  and  $^{40}\text{Ca}$  to experimentally measured photonuclear cross sections. The muon capture matrix elements were written as a weighted integral over energy of the experimentally measured photonuclear excitation cross sections. The results



are very satisfactory for all these nuclei. For  $^{16}\text{O}$ , e.g., the theoretical value for the capture rate thus obtained is

$$\Lambda_{\text{capt}} = (0.95 \pm 0.05) \times 10^5 \text{ sec}^{-1} \quad (4)$$

We may take the agreement of this phenomenological theory of refs. 6 and 8 as an indirect confirmation of the predominant role that transitions to the photonuclear giant dipole states play in muon capture.

The way how to obtain a direct confirmation of this mechanism is suggested by the work of a group of Russian authors (7), who discovered the giant resonance effect in muon capture independently, and in a different way. After the particle-hole model of the dipole states had been applied (22) to  $^{40}\text{Ca}$  in order to calculate the photonuclear absorption, and the subsequent single-nucleon emission from the decay of these states, it had been realized that muon capture should proceed to the giant resonance states in an entirely analogous fashion, and a corresponding calculation was made by Kabachnik (23) in  $^{40}\text{Ca}$ , and by Balshov et al (7) in  $^{16}\text{O}$ , using the standard particle-hole formalism (20,24,25). Fig.2 (top) shows the  $T = 1$ ,  $J = 0^-, 1^-$  and  $2^-$  states in  $^{16}\text{N}$  (the  $T_3 = -1$  isotopic analogue states of those in  $^{16}\text{O}$ ,  $T_3 = 0$ ) obtained in this way; the numbers on the right of each level indicate the partial muon capture rates. The subsequent neutron decay to the single-hole states of  $^{15}\text{N}$  is also indicated, and the partial decay widths, leading to the branching ratios indicated in Fig.2) were calculated by R matrix theory (26,27). The neutron spectrum thus obtained is shown in Fig.3 (bottom). Here, the widths were arbitrarily taken as 2 Mev each. It seems to be indicated that a peak around 4 Mev and a smaller one around 10 Mev in the neutron spectrum should be present, the latter due to transitions from the high  $1^-$  states of  $^{16}\text{N}$  to the  $^{15}\text{N}$  ground state, the former due to transitions from both the low  $2^-$  state to  $^{15}\text{N}_{\text{gd}}$  and from the high  $1^-$  states to the excited negative-parity state of  $^{15}\text{N}$ . An accurate experimental measurement of the spectrum of neutrons emitted after muon capture showing these features should be a good direct confirmation of the giant resonance mechanism in muon capture. The only relevant experimental results existing so far seem to be those of Hagege(14); Fig.3 presents his neutron spectra in  $^{27}\text{Al}$  (top) and

$^{40}\text{Ca}$  (bottom), and indeed, the indicated features of the neutron spectrum given by the resonance mechanism seem to be present qualitatively. The continuous curve in Fig.2 (bottom) represents the spectrum of directly emitted neutrons after muon capture as calculated with a direct-interaction optical model (28). Their small yield compared to the line spectrum of neutrons demonstrates again the importance of the resonance mechanism in muon capture.

One can give a general view of the giant resonance states as members of isotopic multiplets, and describe muon capture as one out of a family of weak and electromagnetic interactions which can excite different members of the multiplets, and which may be used for a study of the giant resonances, complementing each other for this purpose. Such an approach will put the muon capture reaction into its proper perspective, and will indicate its relation with other processes. For simplicity, we shall consider only light nuclei with  $T = 0$ ,  $0^+$  ground states such as  $^4\text{He}$ ,  $^{12}\text{C}$ ,  $^{16}\text{O}$  and  $^{40}\text{Ca}$ .

Figs.4 and 5 outline the relations between the various interactions mentioned. Fig.4 shows the levels of concern to us in  $^{12}\text{C}$ , Fig.5 those in  $^{16}\text{O}$ . The observed giant resonance levels show sometimes a considerable degree of fine structure; the gross features of the giant resonance levels can however be reproduced in a very simple way by the collective Goldhaber-Teller model (15), which we shall use predominantly for the sake of its simplicity and its ensuing pedagogical merits. The energies of the various Goldhaber-Teller states must be taken from experiment; in  $^{12}\text{C}$ , e.g., (Fig.4), they form a group of one  $J = 1^-$  vector level (V) at  $\sim 22.5$  Mev, and of three axial vector (A) levels of  $J = 0^-$ ,  $1^-$ , and  $2^-$  at  $\sim 26.0$ ,  $25.5$ , and  $19.0$  Mev (our designation V, A refers to the type of muon capture matrix element to which they contribute); the situation in  $^{16}\text{O}$  (Fig.5) is very similar. Since all of these states have  $T = 1$ ,  $T_3 = 0$ , there must exist in the two neighboring nuclei  $^{12}\text{B}$  ( $T_3 = -1$ ) and  $^{12}\text{N}$  ( $T_3 = +1$ ) exact analogues of these states with which they form members of isotopic triplets (indicated in Figs.4 and 5), which are only shifted somewhat by the Coulomb energy. We have taken this shift roughly from the energy difference between the  $15.1$  Mev,  $J = 1^+$ ,  $T = 1$  state of  $^{12}\text{C}$  and the  $^{12}\text{B}$ ,  $^{12}\text{N}$  ground states which are its  $T_3 = \mp 1$  analogues.

The earliest way to study the excitation of these states was by photon absorption, with observation of total cross sections or of partial ( $\gamma, p$ ) or ( $\gamma, n$ ) cross sections, or by the inverse of the latter, i.e. ( $p, \gamma$ ) or ( $n, \gamma$ ) reactions. Consider e.g. the excitation process

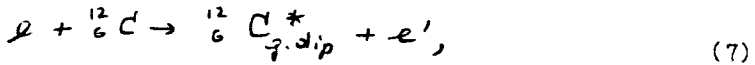


From kinematics, it follows that the nuclear recoil momentum  $q$  equals in magnitude the excitation energy  $\delta = E_{g, \text{dip}} - E_{gd}$ ,

$$q = \delta. \quad (6)$$

We shall see later that photon absorption leads predominantly to a transition from the ground state to the  $1^-$  V state in the same nucleus so that an excitation curve should essentially show just one large peak. In Fig.6, we present the results of a total cross section measurement of Koch et al (29) in  ${}^{12}\text{C}$  (top) and  ${}^{16}\text{O}$  (bottom); both cases roughly exhibit these peaks which possess a considerable width and a certain fine structure.

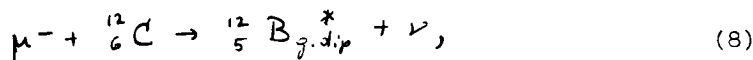
The excitation of the giant resonance states by electrons has also been studied; as in the photonuclear case, transitions within the same nucleus are induced only. The kinematics of the reaction, e.g.



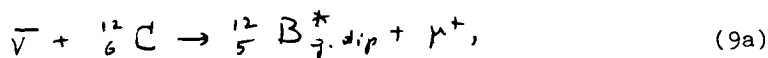
shows that now the momentum transfer  $q$  is not fixed to the excitation energy, but may be varied independently by varying the incident electron energy  $E_1$  or the electron scattering angle  $\theta = \angle(k_1, k_2)$  where  $k_1, k_2$  are the momenta of  $e, e'$ . The electron scattering process is thus inherently richer than photoabsorption since it allows the measuring of the nuclear form factors as functions of  $q$ , not just at the fixed value  $q = \delta \sim 22$  Mev. Even better, it turns out that as  $q$  is increased away from  $\delta$ , the magnetic axial (A) states come in whose strength was too small in photoexcitation to be observable. For this reason, inelastic electron scattering seems to be the most powerful tool for studying the giant resonances, superior to photoexcitation. The spectrum of  $e'$  was obtained in such an experiment by Vanpraet and shows directly the level scheme of the giant resonances,

if measured from the elastic peak on downwards. Fig. 7 shows these excitation curves, the top portion (30) for  $^{12}\text{C}$  at  $E_1 = 65$  Mev, the remaining portions (31) for  $^{16}\text{O}$  at  $E_1 = 43$  (center) and 69 Mev (bottom). For  $^{12}\text{C}$ , we notice the excitations of the  $1^+$  state at 15.1 Mev, of the  $2^-(A)$  state at 19.2 Mev and of the  $1^-(V)$  state at 25.5 Mev (the latter being the only giant state which gets substantially excited by photons). For  $^{16}\text{O}$ , there is much fine structure, and the details are less clear. One notices, however, that the peak about 22.5 Mev decreases with increasing  $q$  (at  $E_1 = 43$  Mev,  $q \approx 65$  Mev/c, and at  $E_1 = 69$  Mev,  $q \approx 115$  Mev/c), whereas the peaks around 19 or 20 Mev, which for photoexcitation ( $q \sim 22$  Mev/c) would be quite invisible, grow in relative importance. This behavior is characteristic for a  $V$  or an  $A$  state, respectively, as will be discussed later, and we made our assignment of Figs. 4, 5 on this basis. Further, the 19 Mev state was assigned  $2^-$ , the 25 Mev state  $1^-$  as suggested by the particle-hole model (25,32, 33). The  $0^-(A)$  state cannot be excited by electron scattering since the electromagnetic multipole expansion starts with  $J = 1$ .

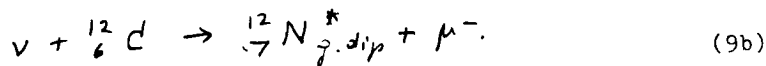
If one uses a  $0^+$  nucleus as a target, the giant resonance states in the same nucleus can thus be excited by photons or electrons. The other members of the isotopic giant resonance triplets can be excited and studied by the weak interactions whose matrix elements contain  $\tau^\pm$ : muon capture (7,11,34) or neutrino (antineutrino) excitation (17). Muon capture will e.g. give



and so does antineutrino excitation:



whereas neutrino excitation leads to the other member of the isotopic triplet:



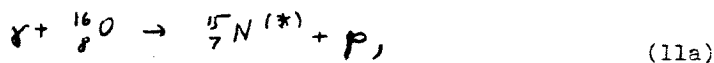
These transitions are illustrated in Fig. 4 and 5 also. In muon capture as in photoexcitation, the momentum transfer is fixed and related to the excitation energy:

$$q = m_{\mu} - \Delta E; \quad (10)$$

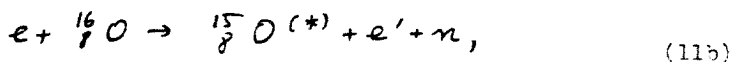
but whereas for the dipole states, photoabsorption had  $q \sim 22 \text{ Mev}/c$ , muon capture has  $q \sim 90 \text{ Mev}/c$  so that, since the matrix elements are similar, both V and A states are strongly excited in muon capture; this includes the  $G^{-}(A)$  state which cannot be reached in electroexcitation. Muon capture should thus, in spite of its fixed momentum transfer, also be a rather useful probe into the giant resonance states.

Neutrino excitation has the same matrix elements as muon capture and the additional advantage of a variable momentum transfer, but of course the very small reaction cross section will hardly render it suitable for a tool of nuclear structure research, at least for the time being.

The question of course arises as to how to study the individual resonance states participating in muon capture; an excitation curve cannot be obtained since the muons are captured at rest. The investigation must thus use the decay mechanism of the resonance states, which is already well known in photo- and electroexcitation. It is illustrated for this case in Fig 8 for  $^{16}\text{O}$ . If this nucleus is irradiated by a continuous bremsstrahlung spectrum, or, what amounts to the same thing, with electrons which are not observed after the scattering, the decay nucleons from the reactions which are now essentially e.g. a  $(\gamma, p)$  reaction,



or, e.g., a  $(e, e'n)$  reaction,



will form spectra with distinct peaks. At the high end, the peaks will correspond to highly excited  $\rightarrow$  ground state transitions; lower energy peaks are a mixture of less highly excited  $\rightarrow$  ground state and highly excited  $\rightarrow$  excited transitions. Thus, the highly excited giant resonance states will appear clearly near the upper end of the spectrum.

Fig.9 (top) presents another illustration of the  $(\gamma, n)$  decay scheme in  $^{16}\text{O}$ , and Fig.9 (bottom) the corresponding observed photo-

neutron spectrum in  $^{150}\text{Sm}$  when irradiated with 25 keV bremsstrahlung (33). Due to the ground state transition, the  $I(V)$  and  $I(A)$  peaks are exhibited very clearly at 22.5 and 24.5 keV, with some important fine structure. The  $I(A)$  level, which cannot be reached in photoexcitation according to the Goldhaber-Teller model, does have a certain dipole strength in the particle-hole model with residual interaction, cf. Table II.

Another detailed study of these states was made by Dodge and Barber (36), observing the (e, e'p) reaction. Fig. 10 presents their proton spectra from carbon (top) and oxygen (bottom), and one can again see the large  $I(V)$  peak at 22.5 keV, the smaller  $I(A)$  peak at 25 keV excitation energy.

For muon capture, the situation is quite analogous, as shown in Fig. 11. The capture leads to the dipole states of the  $\mu^- = -1$  nucleus  $^{150}\text{Sm}$ , populating all  $V$  and  $A$  states strongly. The decay to  $^{150}\text{Sm}$  with neutron emission has been indicated; proton decay to  $^{149}\text{Sm}$  is not possible energetically, see figure. In practice, the ground states transition to  $^{150}\text{Sm}$  is present only, as suggested by the particle-hole model (27), and confirmed experimentally (37). The corresponding peaks in the neutron spectrum indicate then directly the  $0^+$ ,  $1^-$  and  $1^-$  states of  $^{150}\text{Sm}$  and are represented in Fig. 11 by rectangles of 2 keV width. It is however possible to calculate their actual width using Wigner D matrix theory (26,27), and we obtained in this way (33)  $\Gamma_{0A} \approx 8.3$  keV,  $\Gamma_{1V} \approx 8.2$  keV,  $\Gamma_{1A} \approx 3.1$  keV (where we used particle-hole state assignments and the corresponding wave functions of Gillet (25) for these states). This comes out larger than an analogous calculation of Becker (27) for (twice) the neutron widths in the identical situation of  $^{150}\text{Sm} \leftarrow ^{149}\text{Sm} + n$  decay, for which he found  $\Gamma_{1V}(B) \approx 5.2$  keV,  $\Gamma_{1A}(B) \approx 2.3$  keV. We therefore adopted values in between. The corresponding spectrum is shown in Fig. 11 at its low end, there is undoubtedly a large background of evaporation neutrons to be superimposed which rises as  $U$  decreases. One sees that it may be deceptive to use a spectrum with arbitrarily assigned widths. In Fig. 12, we present the analogous situation for muon capture in  $^{40}\text{Ca}$ , with excitation of the  $40\text{Z}$  giant resonance

levels (34). If there is a large proportion of ground state transitions present, then one would feel tempted to identify the peaks in Vagge's (14) neutron spectrum, shown alongside in Fig. 12, with the  $40\text{K}$  giant resonance levels as indicated. More experimental (and theoretical) work should be done on these neutron spectra.

A final remark should indicate that in the  $40\text{Ca}$  case, proton decay from  $40\text{K}$  to  $39\text{Ar}$  is energetically possible; and this is also true for the  $0^-$  and  $1^-$   $\Lambda$  states of  $16\text{N}$  in the  $16\text{O}$ - muon capture case. The  $39\text{Ar}$  ground state is probably a (1f  $7/2$ ) state with two extra holes. If therefore, emitted protons are observed with an energy corresponding to the ground state transition, this would constitute a check for the presence of 2-particle, 2-hole states in the giant-dipole configuration; concerning this, there has recently been some argument in the case (39, 40) of  $16\text{O}$ .

We shall now present expressions for the matrix elements of the various transitions (indicating their similarities), and their values found on the basis of the Goldhaber-Teller model with its spin-wave generalization. Table III lists the total cross section for photon absorption integrated over one absorption line (32), and the differential cross section for inelastic electron scattering, (32) in terms of multipole matrix elements ("nuclear form factors")  $\mathcal{M}_J$  and  $\mathcal{T}_J$ . Here,  $\alpha = 1/137$ ,  $J_i$  is the initial nuclear spin,  $\hat{J}_i = (2J_i + 1)^{1/2}$ ,  $\Delta^2$  is the squared four momentum transfer, and the electrons have been assumed extremely relativistic.  $V_\ell(\theta)$  and  $V_t(\theta)$ , where  $\theta = \angle(\underline{k}_1, \underline{k}_2)$ , are kinematical factors of which  $V_\ell$  has the property

$$V_\ell(180^\circ) = 0. \quad (12)$$

The last line lists the partial muon capture rate (18) corresponding to the nuclear transition from state a to state b, with  $\underline{v}$  the momentum of the emitted neutrino,  $m$  the nucleon mass, and  $G_V, G_A$  and  $G_P$  the vector, axial vector, and induced pseudoscalar coupling constant, in terms of the vector (Fermi) and axial vector (Gamow-Teller) matrix elements  $M_V$  and  $M_A$ . All these matrix elements are listed in Table IV; matrix elements giving rise to corresponding transitions are put into the same line. Electron scattering matrix

elements are written for the particular transition to the states of the Goldhaber-Teller model to which they give rise. The "longitudinal" matrix element  $\mathcal{M}_{JM}$  is due to the Coulomb interaction between electron and nuclear charge, and depends on the nuclear transition charge distribution  $\rho(\underline{r})$ . It usually dominates the electron scattering process, except at  $\theta = 0^\circ$ , and at  $180^\circ$  due to Eq.(12). For  $180^\circ$  electron scattering, one can best observe the two "transverse" matrix elements  $\mathcal{T}_{JM}$  containing the nuclear transition charge current density  $\underline{j}(\underline{r})$  ( $Y_{JL}^M$  is a vector spherical harmonic), corresponding to both electric (e) and magnetic (m) multipoles (the latter vanishing for the transition to  $J = 1^-$  from parity). For photon absorption, exactly the same matrix element enters and causes the giant electric dipole transition. For muon capture, it is the vector matrix element  $M_V$  ( $\phi_\mu$  being the wave function of the bound muon) in the third column which due to its similarity with  $\mathcal{T}_{JM}^{ej}$  causes nuclear transitions to the V giant dipole states also (18): it may be rewritten as

$$M_V = \int d^3r e^{-i\underline{q}\cdot\underline{r}} \rho^-(\underline{r}) \phi_\mu(\underline{r}), \quad (13)$$

where

$$\rho^-(\underline{r}) = \langle b | \sum_i \tau_i^- \delta(\underline{r} - \underline{r}_i) | a \rangle \quad (14)$$

is a  $T_3 = -1$  analogue of the transition charge (or current) density. Finally, there are two transverse matrix elements due to the nuclear transition magnetic moment density  $\underline{\mu}(\underline{r})$  (also best observed for  $180^\circ$  electron scattering), which for photon absorption with recoil  $q = J$  become very small, and which have their muon capture analogue in the Gamow-Teller matrix element  $M_{GT}$ , as becomes obvious when considering the expression for the magnetic moment density operator

$$\underline{\mu} = (4m)^{-1} (\mu_p - \mu_n) \sum_i \underline{\sigma}_i \tau_i^3, \quad (15)$$

where  $\mu_p, \mu_n$  are the proton (neutron) anomalous magnetic moments.

For the schematic Goldhaber-Teller model and its spin-wave generalization, which satisfactorily describe the gross features of the giant resonance states (41), the correspondence between the matrix



elements and the various states to which they exclusively contribute is exhibited in Fig.13. The original Goldhaber-Teller model (15,16) considers the neutrons and the protons with their original distribution rigidly displaced against one another, and oscillating back and forth. In Fig.13, this is indicated as the "isospin mode", and it clearly gives rise to a large "collective" electric dipole moment, thus absorbing photons strongly through the electric dipole form factor  $\mathcal{T}_1^{ej}$ , and contributing strongly also to the other matrix elements in the first line of Fig.13; the corresponding  $1^-$  state to which a transition from the ground state is induced in this way is what we called the vector state (V). One may introduce a density matrix  $\rho(\underline{r})$ , with the help of which, nuclear densities of a spin and isospin operator  $\hat{\sigma}$  may be expressed as

$$\rho_0(\underline{r}) = \text{Tr } \hat{\sigma} \phi(\underline{r}). \quad (16)$$

The density matrix of the isospin mode of oscillation is then:

$$\phi_i(\underline{r}) = \frac{1+i\tau_3}{2} \frac{1}{2} \rho_0(\underline{r} - \frac{1}{2} \underline{d}) + \frac{1-i\tau_3}{2} \frac{1}{2} \rho_0(\underline{r} + \frac{1}{2} \underline{d}), \quad (17)$$

where  $\rho_0(\underline{r})$  is the ground state proton density satisfying

$$\int \rho_0(\underline{r}) d^3r = Z. \quad (18)$$

If one considers  $\underline{d}$ , the displacement vector of the protons against the neutrons, as the coordinate variable of a harmonic oscillator which is subsequently quantized, and becomes a creation operator, one finds in an expansion to first order of  $\underline{d}$  the transition density matrix

$$\phi_i(\underline{r}) = -\frac{1}{4} \tau_3 \underline{d} \cdot \nabla \rho_0(\underline{r}). \quad (19)$$

With its help, one obtains the reduced matrix element of  $\kappa_{JM}$ ,

$$\langle T=1, 1^- \| \kappa_1 \| T=0, 0^+ \rangle = \frac{2}{4\pi} \left( \frac{2\pi}{Am\delta} \right)^{1/2} F(\underline{q}), \quad (20a)$$

or of  $\mathcal{T}_{JM}^{ej}$ ,

$$\langle T=1, 1^- \| \mathcal{T}_1^{ej} \| T=0, 0^+ \rangle = -\frac{5}{4\pi} \left( \frac{4\pi}{Am\delta} \right)^{1/2} F(\underline{q}), \quad (20b)$$

or the vector matrix element

$$\langle T=1, 1^- \| M_1 \| T=0, 0^+ \rangle = i_2 \left( \frac{4\pi}{3Am\delta} \right)^{1/2} F(\underline{q}) Y_{1M}^*(\underline{q}), \quad (20c)$$

in terms of the ground state form factor

$$F(\underline{q}) = \int d^3r e^{i\underline{q}\cdot\underline{r}} \rho_0(\underline{r}). \quad (21)$$

In order to describe the A states in this model, one notices that theories of vibrations of nuclear matter (42-44) had predicted four different types of modes of vibrations in a hydrodynamic picture: the four interacting fluids consisting of  $p\uparrow$ ,  $p\downarrow$ ,  $n\uparrow$  or  $n\downarrow$  (the arrow indicating spin) may vibrate in the four modes indicated by Fig.13. The previous formalism may again be used, with the results for the A states:

$$\phi_{si}(\underline{r}) = -\frac{1}{4} \tau_3 \sigma_m \underline{d} \cdot \nabla \rho_0(\underline{r}), \quad (22)$$

$$\phi_s(\underline{r}) = -\frac{1}{4} \sigma_m \underline{d} \cdot \nabla \rho_0(\underline{r}) \quad (23)$$

for the spin-isospin and spin wave density matrix, respectively. The model is essentially an LS coupling model, with total orbital angular momentum L being given by the oscillator transition, whereas the nucleon spins in the Goldhaber-Teller state couple to total spin  $S = 0$  (in  $\phi_i$ ) or  $S = 1, m$  (in  $\phi_{si}, \phi_s$ ). Therefore the A states can couple to  $J = 0^-, 1^-$  and  $2^-$  which may either be  $T = 0$  (for  $\phi_s$ ) or  $T = 1$  (for  $\phi_i, \phi_{si}$ ). Altogether, this leads to fifteen states (counting the  $T_3$  substates) classified as follows:

3 isospin states  $T = 1$  with  $J = 1^-$  (V states) (i)

9 spin-isospin states  $T = 1$  with  $J = 0^- 1^- 2^-$  (A states) (si)

3 spin wave states  $T = 0$  with  $J = 0^- 1^- 2^-$ . (s)

A final sixteenth state is provided by the breathing mode:

1 breathing state  $T = 0, J = 0^+$  (b)

The matrix elements containing spin and isospin operators contribute strongly to the A states as indicated in Fig.13; one finds e.g.

$$\langle T=1, 1^- \| \mathcal{T}_1^{em} \| T=0, 0^+ \rangle = -\frac{q^2}{m} \frac{\mu_p - \mu_n}{2} \frac{F(q)}{4\pi} \left( \frac{2\pi}{A-m} \right)^{1/2}, \quad (24)$$

or

$$\langle T=1, 2^- \| \mathcal{T}_2^{em} \| T=0, 0^+ \rangle = -i \frac{q^2}{m} \frac{\mu_p - \mu_n}{2} \frac{F(q)}{4\pi} \left( \frac{2\pi}{A-m} \right)^{1/2}, \quad (25)$$

for the only non-vanishing transitions. Note the factor  $q^2$  which makes the matrix elements of the A states increase more strongly with  $q$  than that of the V state, as was mentioned before. The transitions to spin-wave states are negligible since the matrix elements would contain  $(\mu_p + \mu_n)$ , and one has  $(\mu_p + \mu_n)^2 / (\mu_p - \mu_n)^2 = 0.035$ . There are no muon capture transitions to the spin wave states as they have  $T = 0$ . (Strong interactions of course may reach these states). The breathing mode may be reached by the  $\mathcal{M}_0$  monopole Coulomb matrix element in electron scattering.

The energies of these states are not determined in the Goldhaber-Teller model. We shall take them from experiment, but we ignore a possible configuration mixing which the spin dependence of the nuclear Hamiltonian, that removes the degeneracies of these states in Wigner's supermultiplet theory (8), would also cause, and which results e.g. in a photoexcitation of the  $1^-$  A state.

In Fig. 14, we show predictions (41) of the Goldhaber-Teller model for the  $130^\circ$  electron scattering cross section in  $^{12}\text{C}$ , at various momentum transfers. At  $q \approx 100$  Mev/c, the data of Vanpraet (30) are entered, and show reasonable agreement. Also exhibited in the figure are the excitation strengths of the individual states (solid lines), and further (broken lines) the excitation strengths of the states of a particle-hole model (11); we have marked its  $2^-$  states with a dot. Apart from giving a certain fine structure, and being partly shifted up in energy, the particle-hole states may be easily identified with the Goldhaber-Teller states by their  $q$ -dependence; this identification is indicated in parentheses in Fig.14, and we have also entered the principal configuration of the particle-hole states corresponding to  $1^-$  V,  $1^-$  A and  $2^-$  A next to the respective levels. These configurations, together with the small components given by the particle-hole model, were used for a computation of the width from R matrix theory (38,41). One can see that the predictions of the Goldhaber-Teller model are reasonably good; they have also been used for obtaining the muon capture rates in Fig.11.

We finally show in Table V various sum rules for the electromagnetic and weak transitions considered so far, and investigate

to what extent they are satisfied by our model. One can first of all derive sum rules in the dipole approximation,  $qR \ll 1$ , where  $R$  is the nuclear dimension. The classical example is the Thomas-Reiche-Kuhn sum rule of the electric dipole transition, which occurs in photo- or electroexcitation. It was shown that in the Goldhaber-Teller model, this sum rule is satisfied (45), and furthermore, the weak interaction analogue of this sum rule containing the vector matrix element is also satisfied (17). A magnetic counterpart of the TRK dipole sum rule has also been established, and shown to be satisfied by the Goldhaber-Teller model (45). This means that the vector and the axial states of the model alone completely exhaust the sum rules and leave no room for other states to be excited. Since experimentally, other dipole transitions are present and the observed giant dipole resonance e.g. does not exhaust the sum rule ( a considerable amount of dipole strength occurs at  $\approx 30$  Mev due to short-range correlations), we expect the collective model to overestimate the actual results.

For general  $q$ , i.e. not in the dipole approximation, a relation between vector and axial vector weak interaction matrix elements was established by Tolhoek et al(18), presented in Table V, which was shown by them to hold in a shell model in which at least a neutron (or proton) subshell is closed. Foldy and Walecka (8) proved the validity of a generalization of this sum rule in supermultiplet theory, and it was shown by them (8, 11) and by Rho (46) that it also holds approximately (within 12%) for the particle-hole model. The relation was also proved (17) for the Goldhaber-Teller model. This relation is important because it ties the  $A$  to the  $V$  states and, from the observation of the giant resonance in photoabsorption, already implies the existence of giant spin resonances e.g. in Gamow-Teller transitions of muon capture or in magnetic quadrupole transitions of electron scattering even before they have been seen experimentally.

It seems that the most interesting task as far as muon capture is concerned would be a direct verification of the giant resonance mechanism. For this purpose, the measurements of neutron spectra following muon capture (14) should be repeated with great

ter accuracy and with narrower energy intervals in order to confirm the structure found so far and improve the resolution; the measurements should also be extended to lighter nuclei ( $O^+$  and others). The positions and widths of the levels should (apart from the Coulomb shifts) agree with those in  $(\gamma, n)$  reactions. Fig. 15 presents the situation in  $^{12}C$  again. In this figure, we have also entered the widths used for drawing the levels in the neutron spectrum, and the neutron polarization which is expected (34) from the decay of the  $1^- A$  state to the  $1^1 B$  ground state, having longitudinal component

$$P_{n1} \approx 0.2 P_{\mu} \cos \theta \quad (26)$$

along the direction  $\underline{p}_n$  of the emitted neutron momentum, with  $\theta = \angle(\underline{p}_n, \underline{s}_{\mu})$  where  $\underline{s}_{\mu}$  is the polarization direction of the captured muon (degree of polarization  $P_{\mu}$ ), and a transverse component:

$$P_{nt} \approx -0.1 P_{\mu} \sin \theta, \quad (27)$$

along  $\underline{p}_n \times (\underline{s}_{\mu} \times \underline{p}_n)$ . No polarization is expected from the  $0^- A$  and  $1^- V$  state decay neutrons.

Another indication for the excitation of the giant resonance states in muon capture may be the observation of photon decay of the 20.5 Mev level ( $1^- V$ ) in  $^{12}B$ . The corresponding photon of 7.1 Mev could be very characteristic. Excitation of the lower excited states of  $^{12}B$  by muon capture has been investigated (47), and the corresponding gamma rays have been found (48); the 7.1 Mev gamma ray has not been looked for. Since the  $1^- V$  state is particle-unstable, gamma emission has to compete with the large amount of neutron decay, but the transition goes to the  $1^+$  ground state and is therefore a relatively large E1. We have estimated (33) its decay rate, again on the basis of the Goldhaber-Teller model, and find

$$\Gamma_{\gamma} \sim 0.8 \text{ kev}, \quad (28)$$

which compared to the neutron width  $\Gamma_n \sim 3 \text{ Mev}$ , shows that about one out of 4000 decays should produce a photon emission; this should be experimentally observable.

In conclusion, we have demonstrated the interrelation of giant

resonance excitations by muon capture with other electromagnetic and weak excitations, and have shown that due to the isospin dependence and to the particular structure of the weak and electromagnetic matrix elements, a variety of different states may be excited in neighboring nuclei. This permits a study of the giant resonances by electrons, muons (49) and photons, whose results should complement each other and thus lead to a more complete understanding of the giant resonance states. Our discussion has been simplified, we feel, by the predominant use of the Goldhaber-Teller model of the giant dipole state and its spin wave generalization (17), which owing to its property of describing all essential features of the spin and isospin vibrations by the simplest possible means, gives a highly instructive view of an otherwise rather complicated situation.

#### Appendix.

The breathing mode completes the sixteen states of the collective nuclear vibrations. A Goldhaber-Teller type model can also be established (50) for this state and shall be sketched here, although the excitation cannot occur by muons and photons, but only by the monopole matrix element  $M_0$  of electron scattering. The vibration can be visualized as a scale-vibration of the nuclear ground state density

$$\rho(\underline{r}, t) = N(\eta) \rho_0\left(r \frac{R-\eta}{R}\right), \quad (29)$$

with  $R$  the r.m.s nuclear radius,  $\eta$  its displacement. One may represent to first order in  $\eta$

$$\rho(\underline{r}, t) - \rho_0(\underline{r}) \approx -\frac{\eta}{Rr^2} \frac{d}{dr} (r^3 \rho_0(r)), \quad (30)$$

consider  $\eta$  as the position variable of a harmonic oscillator which one quantizes, and finds a transition form factor

$$F_{in}(\eta) = (2m A \delta)^{-1/2} \frac{\eta}{R} \frac{dF(\eta)}{d\eta} \quad (31)$$

in terms of a derivative of the ground state form factor  $F(\eta)$ , Eq.(2

The differential inelastic electron scattering cross section is then

$$\frac{d\sigma}{d\Omega} = \sigma_M(\theta) |F_{in}(q)|^2, \quad (32)$$

where  $\sigma_M(\theta)$  is the Mott cross section.

It has been attempted to explain the 20.4 Mev  $0^+$  level in  $^4\text{He}$  recently observed in electron scattering (51) in terms of this collective model. Since the 20.4 Mev state lies  $\sim 0.5$  Mev above the  $t + p$  and  $\sim 0.3$  Mev below the  $^3\text{He} + n$  threshold, the width and level shift in the equation

$$\frac{d\sigma}{d\Omega dE_1} = \frac{1}{\pi} \frac{\frac{1}{2}\Gamma}{(E_2 + \Delta - E_1)^2 + \frac{1}{4}\Gamma^2} \frac{d\sigma}{d\Omega} \quad (33)$$

are rapidly varying functions of  $E_1$  which have been obtained previously (52), and using them, the Lorentz factor in Eq.(33) integrates to  $\cong 3/4\pi$  instead of to unity. In Fig. 16, we show a comparison between theory and experiment for the quantity  $R(q) = F_{in}(q)/(1 - F(q)/Z)$  and for the differential cross section. The excess of a factor 2 in the theory is not unsatisfactory (11). It can also be shown that our collective model exhausts Ferrel's (53) monopole sum rule

$$\sum_{\underline{J}} \int | \langle 0^+ | \sum_i \frac{1}{r_i} \tau_i^z | 0^+ \rangle |^2 = R^2 A / 2m. \quad (34)$$

The 20.4 Mev level has also been observed in inelastic proton scattering (54) by  $^4\text{He}$ , see Fig. 17. The same curve shows the  $2^-$  state of  $^4\text{He}$  at 22.2 Mev. If this state has  $T = 1$ , it would show up as the dashed curve in Fig.17 in electron scattering due to a magnetic quadrupole transition ( $2^-$  A state). Since it is not seen there, we identify it with the  $T = 0$ ,  $2^-$  member of the spin-wave mode of the giant resonance.

- (1) R.C.Cohen, S.Devons, and A.D.Kanaris, Nucl Phys.57,255(1964)
- (2) T.Ericson, J.C.Sens, and H.P.C.Rood, Nuovo Cimento 34, 51(1964)
- (3) H.P.C.Rood, thesis, University of Groningen(1964), unpublished
- (4) H.P.C.Rood, CERN report 65/1417/5-TH.613, Oct.1965,unpublished
- (5) V.Gillet and D.A.Jenkins, Phys.Rev. 140, B32 (1965)
- (6) T.Barlow, J.C.Sens, P.J.Duke, and M.A.R.Kemp, Phys. Letters 9, 84 (1964)
- (7) V.V.Balashov, V.B.Beyaev, R.A.Eramjian, and N.M.Kabachnik, Phys.Letters 9, 168 (1964)
- (8) L.L.Foldy and J.D.Walecka, Nuovo Cimento 34, 1026 (1964)
- (9) H. Überall, Phys.Rev. 139, B1239 (1965)
- (10) H. Überall, Nuovo Cimento 38, 669 (1965)
- (11) T.de Forest, Jr., Phys. Rev. 139, 1217 (1965)
- (12) L.L.Foldy and J.D.Walecka, Phys. Rev. 140, B1339 (1965)
- (13) Their excitation by strongly interacting particles is possible also, but cannot be calculated accurately and will therefore not be considered by us.
- (14) D.E.Hagge, Univ.of Calif. Radiation Laboratory Report No. UCRL-10516, 1963 (unpublished)
- (15) M.Goldhaber and E.Teller, Phys. Rev. 74, 1046 (1948)
- (16) See also J. Goldemberg, Y. Torizuka, W.C.Barber and J.D.Walecka, Nucl. Phys. 43, 242 (1963)
- (17) H. Überall, Phys. Rev. 137, B502 (1965)
- (18) J.R.Luyten, H.P.C.Rood, and H.A.Tolhoek, Nucl. Phys.41,236(1963)
- (19) E. Hayward, Revs. Mod. Phys. 35, 324 (1963)
- (20) J.P.Elliott and B.H.Flowers, Proc.Roy.Soc.(London) A242,57(1957)
- (21) E.Hayward, Lecture Notes on Photonicuclear Reactions (Scottish Universities' Summer School, 1964), unpublished
- (22) V.V.Balashov, V.G.Shevchenko, and N.P.Yudin, Nucl.Phys.27, 323 (1961)
- (23) N.M.Kabachnik, Thesis, Moscow State University 1962, unpublished
- (24) G.E.Brown, L.Castillejo, and J.E.Evans, Nucl.Phys. 22,1(1961)
- (25) V.Gillet, Thesis, University of Paris, 1962, unpublished
- (26) H.E.Gove, in Nuclear Reactions, edited by P.W.Engt and W.Demeur, (North-Holland Publishing Co., Amsterdam, 1959) Vol.1, p.259
- (27) E.Boeker, Thesis, University of Amsterdam, 1963, unpublished



- (28) E.I. Dolinski and L.D. Blokhintsev, J. Exptl. Theor. Phys. (USSR) 35, 1498 (1958)
- (29) J.M. Wyckoff, B. Ziegler, H.W. Koch, and R. Uhlig, Phys. Rev. 137, 38 (1965)
- (30) T. de Forest, J.D. Walecka, G. Vanpraet, and W.C. Barber, Phys. Letters 16, 311 (1965)
- (31) G. Vanpraet, Nuclear Phys. (to be published)
- (32) F.H. Lewis, Jr., and J.D. Walecka, Phys. Rev. 133, B849 (1964)
- (33) F.H. Lewis, Jr., Phys. Rev. 134, B331 (1964)
- (34) H. Überall, Phys. Rev. 139, B1239 (1965)
- (35) F.W.K. Firk, Nucl. Inst. Meth. 28, 205 (1964)
- (36) W.R. Dodge and W.C. Barber, Phys. Rev. 127, 1746 (1962)
- (37) S. Penner and J.E. Leiss, Phys. Rev. 114, 1101 (1959)
- (38) H. Überall, Nuovo Cimento 38, 669 (1965)
- (39) P.F. Yergin, R.H. Augustson, N.N. Khaushal, F.A. Medicus, W.R. Moyer, and E.J. Winhold, Phys. Rev. Letters 12, 733 (1964)
- (40) R.C. Morrison, J.K. Stewart, and J.S.O'Connell, Phys. Rev. Letters 15, 367 (1965)
- (41) H. Überall, Nuovo Cimento (in press)
- (42) W. Wild, Bayr. Akad. Wiss. Math.-Naturw. Klasse 18, 371 (1956)
- (43) A.E. Glassgold, W. Heckrotte, and K.M. Watson, Ann. Phys. (N.Y.) 6, 1 (1959)
- (44) S. Fallieros, R.A. Ferrell, and M.K. Pal, Nucl. Phys. 15, 363 (1960)
- (45) J.D. Walecka, Preludes in Theoretical Physics (to be published)
- (46) M. Kho, Phys. Letters 16, 161 (1965)
- (47) M. Ruel and J.G. Spennan, Phys. Rev. 129, 866 (1963)
- (48) E.J. Maier, R.M. Edelstein, and R.T. Siegel, Phys. Rev. 133, B663 (1964)
- (49) It would of course also be possible to excite the giant resonances by inelastic muon scattering, which would have the advantage over electron scattering of the relative absence of a disturbing background from the radiation tail.
- (50) C. Werntz and H. Überall, to be published
- (51) R. Frosch, R.E. Rand, M.R. Yearian, H.L. Crannell, and L.R. Suelzle, Phys. Letters 19, 155 (1965)
- (52) C. Werntz, Phys. Rev. 133, B19 (1957)
- (53) R.A. Ferrell, Phys. Rev. 107, 1631 (1957)
- (54) L.E. Williams, Phys. Rev. Letters 15, 170 (1957)

Results for the total matrix elements  $M^2$  and matrix elements for partial transitions  $M^2_{n_a l_a n_b l_b ; l}$  for  $^{16}\text{O}$

| Partial transition                | A) harm. osc. well<br>( $b = 1.80$ fm) | B) infinite potential well<br>( $R_\infty = 4.55$ fm) |                   |                             |
|-----------------------------------|--|---|-------------------|-----------------------------|
| $n_a l_a \rightarrow n_b l_b ; l$ | $E_{ab}$<br>(MeV)                      | $M^2_{n_a l_a n_b l_b ; l}$                           | $E_{ab}$<br>(MeV) | $M^2_{n_a l_a n_b l_b ; l}$ |
| 1 0 1 2 2                         | 25.5                                   | 0.021   | 23.5              | 0.030                       |
| 1 0 2 0 0                         | 25.5                                   | 0.010   | 29.6              | 0.007                       |
| 1 1 1 2 1                         | 12.7                                   | 1.107   | 13.3              | 1.048                       |
| 1 1 1 2 3                         | 12.7                                   | 0.010   | 13.3              | 0.006                       |
| 1 1 2 0 1                         | 12.7                                   | 0.174   | 19.4              | 0.095                       |
| 1 1 1 3 2                         | 25.5                                   | 0.082   | 29.1              | 0.056                       |
| 1 1 2 1 0                         | 25.5                                   | 0.042   | 39.8              | 0.009                       |
| 1 1 2 1 2                         | 25.5                                   | 0.013   | 39.8              | 0.003                       |
| 1 1 2 2 1                         | 38.2                                   | 0.004   | 62.7              | 0.004                       |
| $M^2$                             |  | 1.463   |                   | 1.258                       |

Table I

Squared matrix elements of partial transitions for muon capture in  $^{16}\text{O}$ , obtained from an independent particle shell model <sup>24</sup>.

Transitions in  $O^{16}$ 

| Transition                        | $D^2(\%)$ | $E(\text{MeV})$ | $E'(\text{MeV})$ | $D'^2(\%)$ |
|-----------------------------------|-----------|-----------------|------------------|------------|
| $1 p_{3/2} \rightarrow 2 s_{1/2}$ | 11        | 18.53           | 19.6             | 2          |
| $1 p_{3/2} \rightarrow 1 d_{5/2}$ | 50        | 17.65           | 22.2             | 73         |
| $1 p_{1/2} \rightarrow 1 d_{3/2}$ | 28        | 16.58           | 18.1             | 1          |
| $1 p_{1/2} \rightarrow 2 s_{1/2}$ | 5.5       | 12.38           | 13.5             | 4          |
| $1 p_{3/2} \rightarrow 1 d_{3/2}$ | 5.5       | 22.73           | 25.2             | 20         |

Table II

Energy levels and squared electric dipole absorption strengths in % before (E, D) and after ( $E^1$ ,  $D^1$ ) configuration mixing by a residual interaction, obtained from a jj coupling shell model<sup>28</sup>.

$$\text{Photons: } \int \sigma dE = \frac{(2\pi)^3 \alpha}{\delta \hat{J}_i^2} \sum_J \left\{ |J_J^e|^2 + |J_J^m|^2 \right\}_{q=\delta}$$

$$\text{Electrons: } \frac{d\sigma}{d\Omega} = \frac{\hbar^2 8\pi\alpha^2}{\hbar, \Delta^4 \hat{J}_i^2} \left\{ V_l(\vartheta) \sum_{J=0} |K_J|^2 + \right. \\ \left. + V_t(\vartheta) \sum_{J=1} (|J_J^e|^2 + |J_J^m|^2) \right\}$$

where

$$J_J^{(e,m)} = J_J^{(e,m)} j + J_J^{(e,m)} \mu$$

$$\text{Muons: } \Lambda_{a \rightarrow b} = \frac{v^2}{2\pi \hat{J}_a^2} \frac{1}{1 + \frac{v}{Am}} \sum_{M_f, M_i} \int \frac{d\hat{v}}{4\pi} \left\{ G_V^2 |M_V|^2 + \right. \\ \left. + G_A^2 |\vec{M}_A|^2 + (G_P^2 - 2G_P G_A) |\hat{v} \cdot \vec{M}_A|^2 \right\}$$

Table III

Cross sections for photo- and electro excitation  
of nuclear states, and partial muon capture rate.

| $\gamma$                 | Electrons   | Muons   |
|--------------------------|---|---|
| —                        | $\mathcal{K}_{1M} = \int d^3r \varrho(\vec{r}) j_1(qr) Y_{1M}$  | —   |
| same $\rightarrow$       | $\left\{ \begin{array}{l} \mathcal{J}_{1M}^{ej} = i\sqrt{\frac{2}{3}} \int d^3r j_0(qr) \vec{j}_1 \cdot \vec{Y}_{101}^M \\ \mathcal{J}_{1M}^{mj} \equiv 0 \end{array} \right.$  | $M_V = \langle b   \sum_i \tau_i^- e^{-i\vec{v} \cdot \vec{r}_i} \phi_\mu   a \rangle$                      |
| $\sim 0$ at $q = \delta$ | $\left\{ \begin{array}{l} \mathcal{J}_{1M}^{e\mu} = q \int d^3r j_1(qr) \vec{\mu} \cdot \vec{Y}_{111}^M \\ \mathcal{J}_{2M}^{m\mu} = \int d^3r \vec{\mu} \cdot \vec{\nabla} \times j_2(qr) \vec{Y}_{221}^M \end{array} \right.$ | $\vec{M}_A = \langle b   \sum_i \tau_i^- e^{-i\vec{v} \cdot \vec{r}_i} \phi_\mu \vec{\sigma}_i   a \rangle$ |

$$\vec{\mu} = \frac{1}{4m} (\mu_p - \mu_n) \sum_i \vec{\sigma}_i \tau_i^3$$

Table IV

Detailed matrix elements occurring in photon (first column) and electron (second column) excitation of the Goldhaber-Teller giant resonance states. Last column: Corresponding general matrix elements for muon capture.

## A. Dipole Sum Rules ( $qR \ll 1$ ):

1.) Thomas-Reiche-Kuhn:  $2 \sum_{M, J} \delta | \langle 1^- | \sum_i^A \tau_i^3 x_i^{M_1} | 0^+ \rangle |^2 = \frac{3A}{m}$   
 holds for Goldhaber-Teller (Walecka)

Its  $\mu$ -analogue holds for G-T (Überall):

$$\lim_{q \rightarrow 0} \sum_{M, J} \frac{\delta}{q^2} | \langle 1^- | M_V | 0^+ \rangle |^2 = \frac{NZ}{mA}$$

## 2.) Magnetic Analogue of TRK (Walecka):

$$2 \sum_{M, J} \delta | \langle J^- | \sum_i^A \tau_i^3 [\sigma_i \otimes x_i]_{JM} | 0^+ \rangle |^2 = (2J+1) \frac{A}{m}$$

holds for G-T (Walecka)

## B. Sum Rules for General $q$ :

$$\sum_{ab} v_{ab}^2 \int d\hat{v} | \vec{M}_A |^2 = 3 \sum_{ab} v_{ab}^2 \int d\hat{v} | M_V |^2$$

holds a.) in shell model with closed subshell (Tolhoek)

b.) in Wigner supermultiplet theory ( $SU_4$  invariance)

(Foldy-Walecka):  $\sum_M | \langle E_n M | \sum_i^A \tau_i^3 \omega_i | 0^+ \rangle |^2 = \sum_M | \langle E_n M | \sum_i^A \tau_i^3 \sigma_i^z \omega_i | 0^+ \rangle |^2$   
 ( $\omega_i$ : any fn. of  $x_i$ )

c.) within 12% for particle-hole model (Foldy, Rho)

d.) for G-T model (Überall):

$$\sum_m | \langle \vec{M}_A \rangle |^2 = 3 | \langle M_V \rangle |^2$$

Table V

List of electric and magnetic sum rules in dipole approximation, and of sum rules for muon capture.

$$\lambda_{\text{capt}} = \frac{V_{\text{ab}}^2}{2\pi} |\phi_{\mu}|_{\text{av}}^2 (G_F^2 + 3G_{\text{GT}}^2) M^2$$

$$M^2 = |\langle T=1, 1 | \sum_i \tau_i^- i v_{\text{ab}} Z | T=0, 0^+ \rangle|^2$$

$$v_{\text{ab}} \cong m_{\mu} - \Delta E_{\text{g.res}}$$

### Oxygen 16

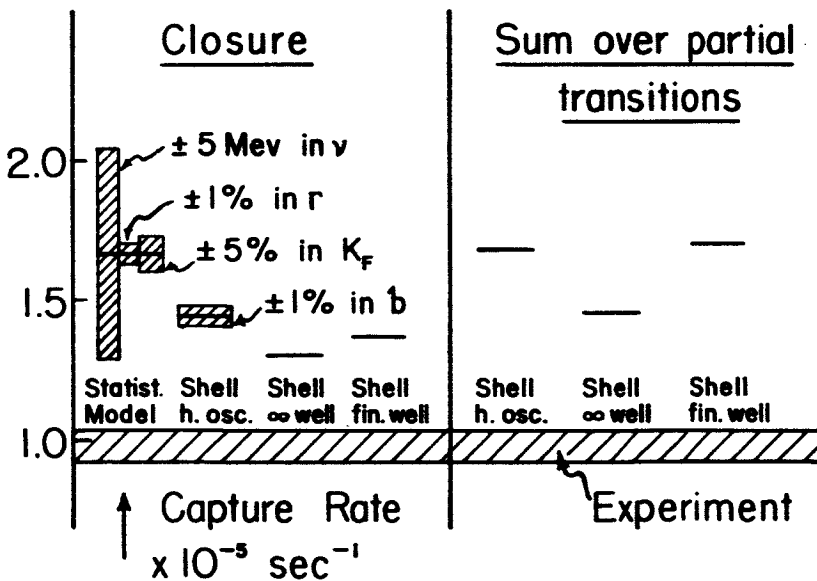


Figure 1

Top: Formula for the partial muon capture rate to giant resonance states.  
 Bottom: Comparison of Experimental <sup>12</sup> and theoretical <sup>24</sup> results for the total muon capture rate in <sup>16</sup>O.

Figure 2

Top: Level scheme and neutron decay mechanism of the giant resonance states in  $^{16}\text{N}$  (as obtained from a particle-hole calculation<sup>13</sup>) after their excitation by muon capture in  $^{16}\text{O}$  (numbers on right: partial muon capture rates). Bottom: Neutron spectrum obtained from the decay of the giant resonance levels in  $^{16}\text{N}$ . The width of each state has arbitrarily been taken as 2 Mev.

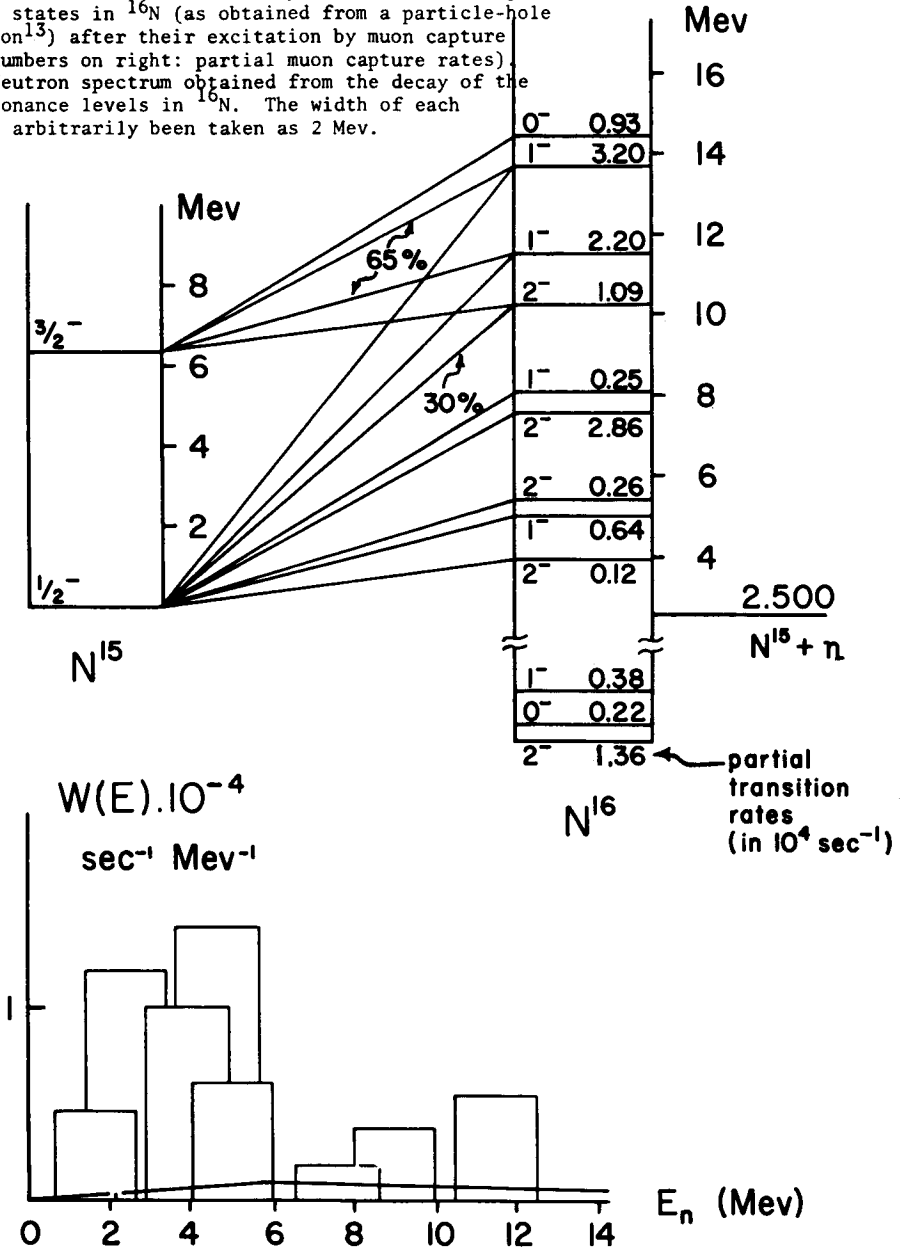
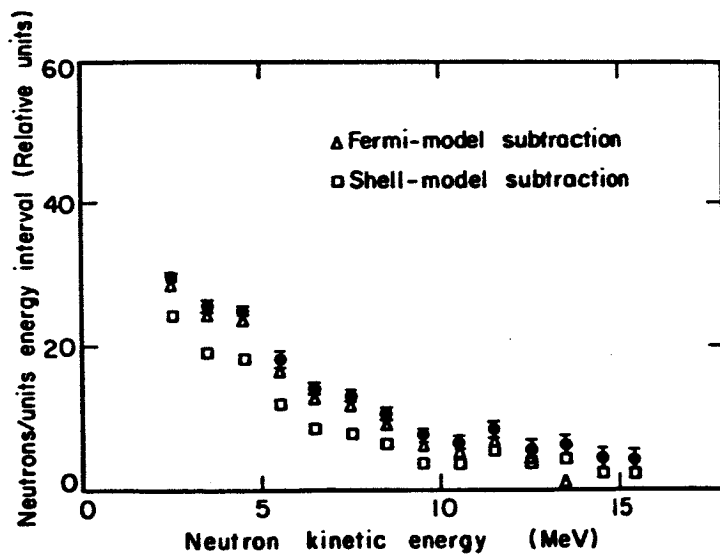
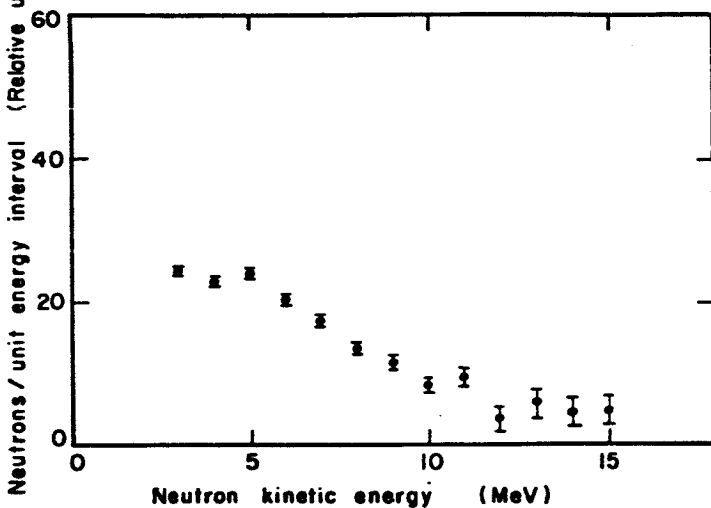




Figure 3

Measured  $^{20}\text{Ne}$  spectra of neutrons emitted after muon capture in  $^{27}\text{Al}$  (top), and  $^{40}\text{Ca}$  (bottom).



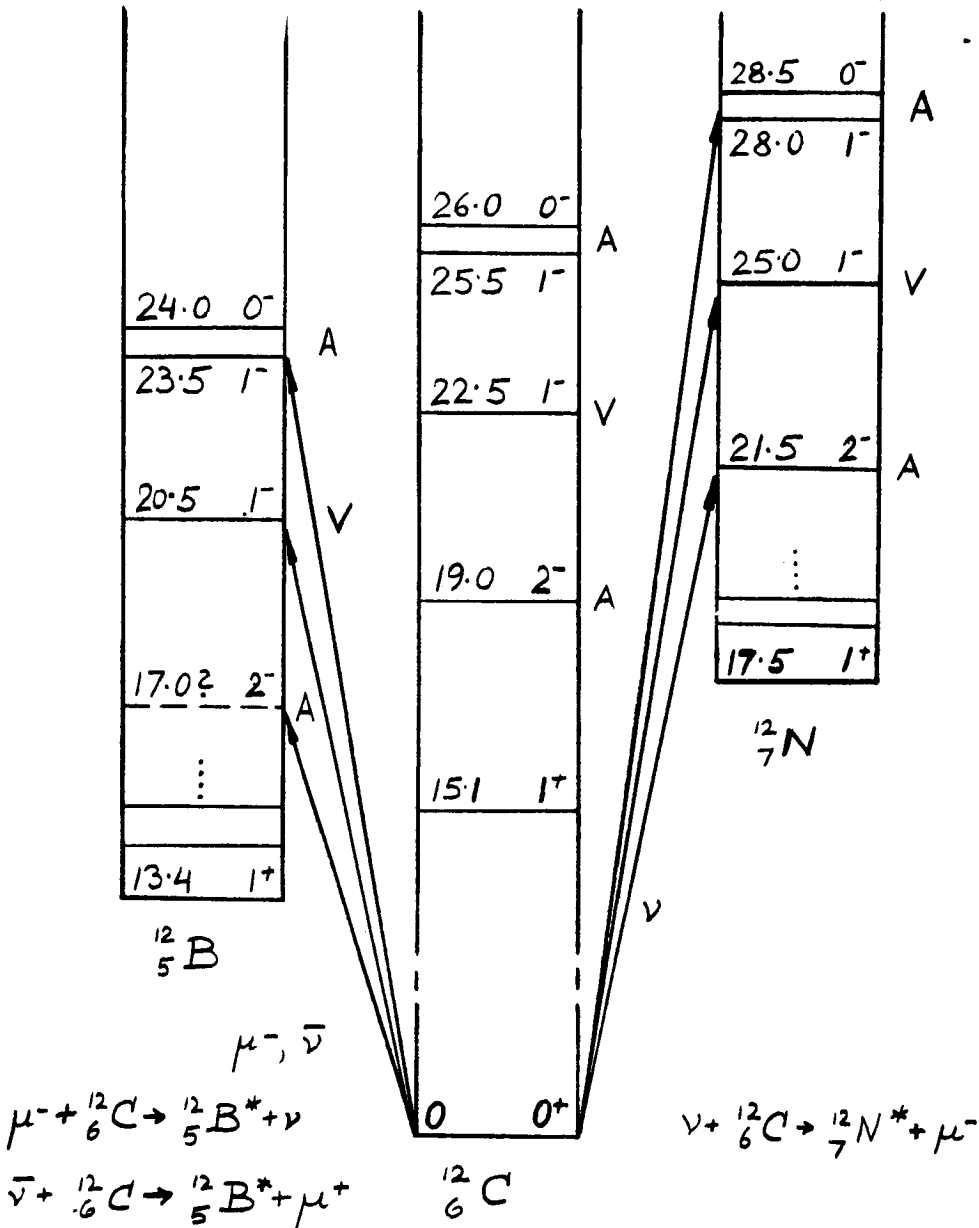
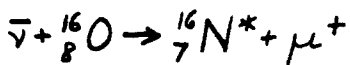
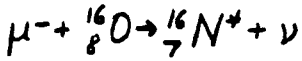
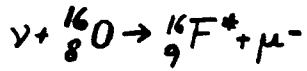
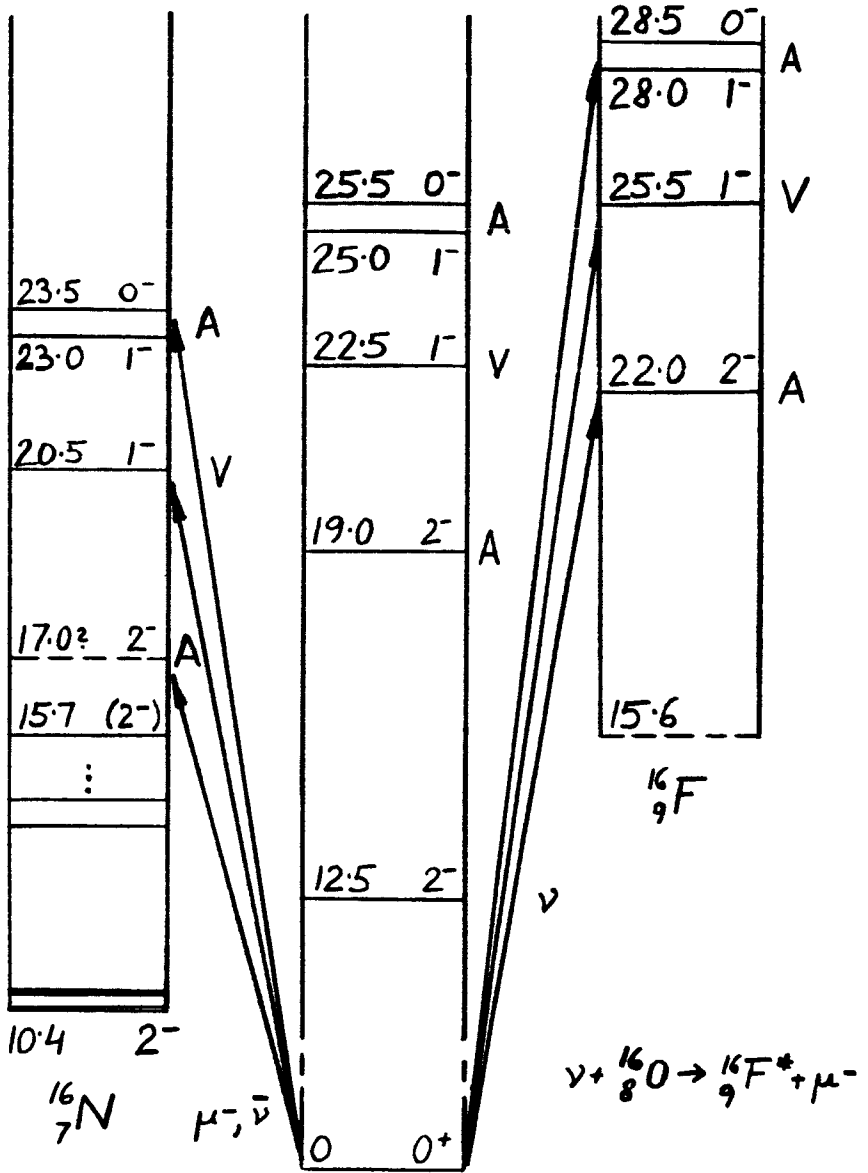


Figure 4

Schematic level structure of the giant resonance states in  $^{12}\text{C}$  and in the neighboring nuclei  $^{12}\text{B}$  and  $^{12}\text{N}$ .



$^{16}_8\text{O}$

Figure 5

Schematic level structure of the giant resonance states in  $^{16}\text{O}$  and in the neighboring nuclei  $^{16}\text{N}$  and  $^{16}\text{F}$ .

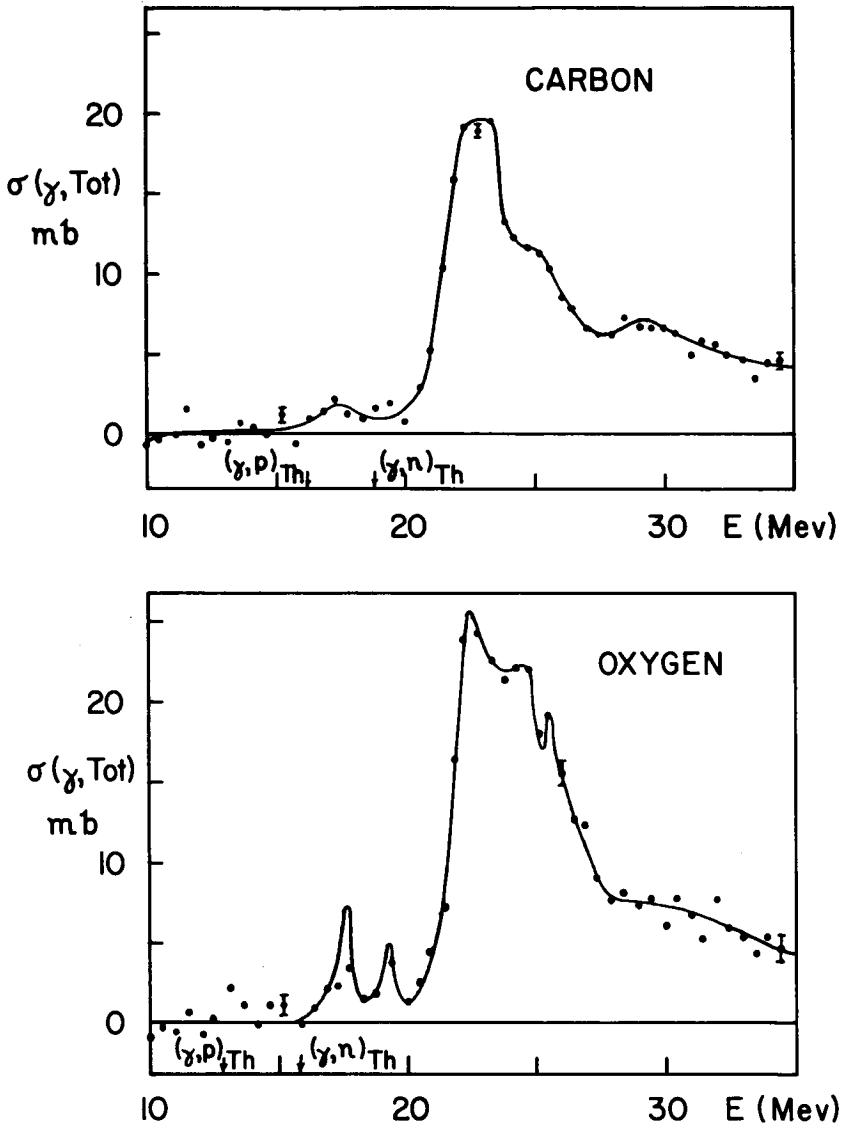


Figure 6

Total photon absorption cross sections vs. excitation energy in  $^{12}\text{C}$  and  $^{16}\text{O}$ .

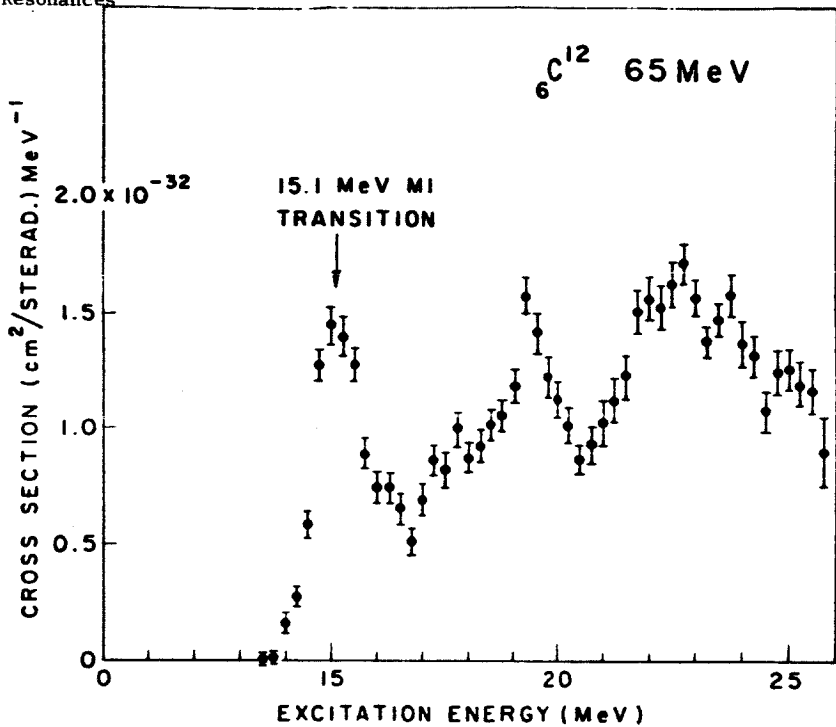


Figure 7

Excitation curve of the giant resonance states by  $0^\circ$  electron scattering. p<sup>39</sup>: in  ${}^{12}\text{C}$  with 65 MeV electrons; center and bottom<sup>40</sup>: in  ${}^{16}\text{O}$  with 43 and 69 MeV electrons.

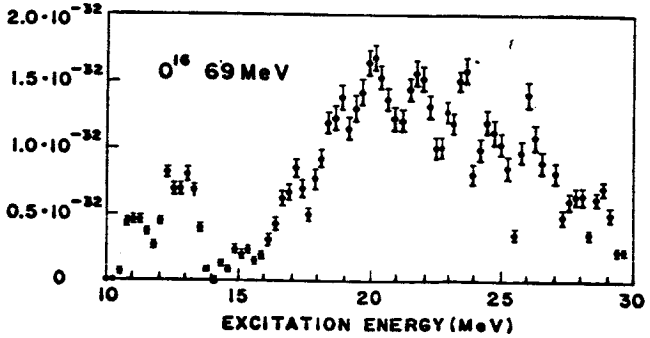
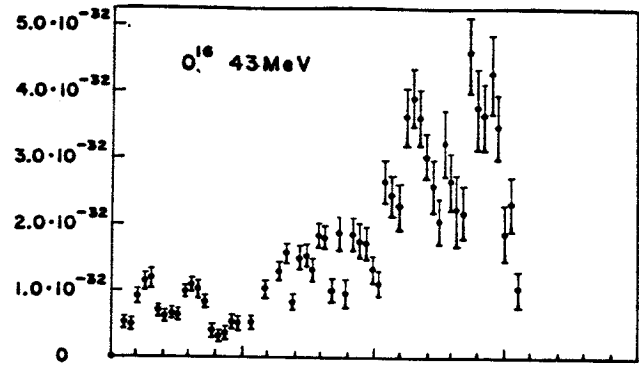


Figure 8

Nucleon decay schemes of the giant resonance states in  $^{16}_8\text{O}$  after photo-or electroexcitation.

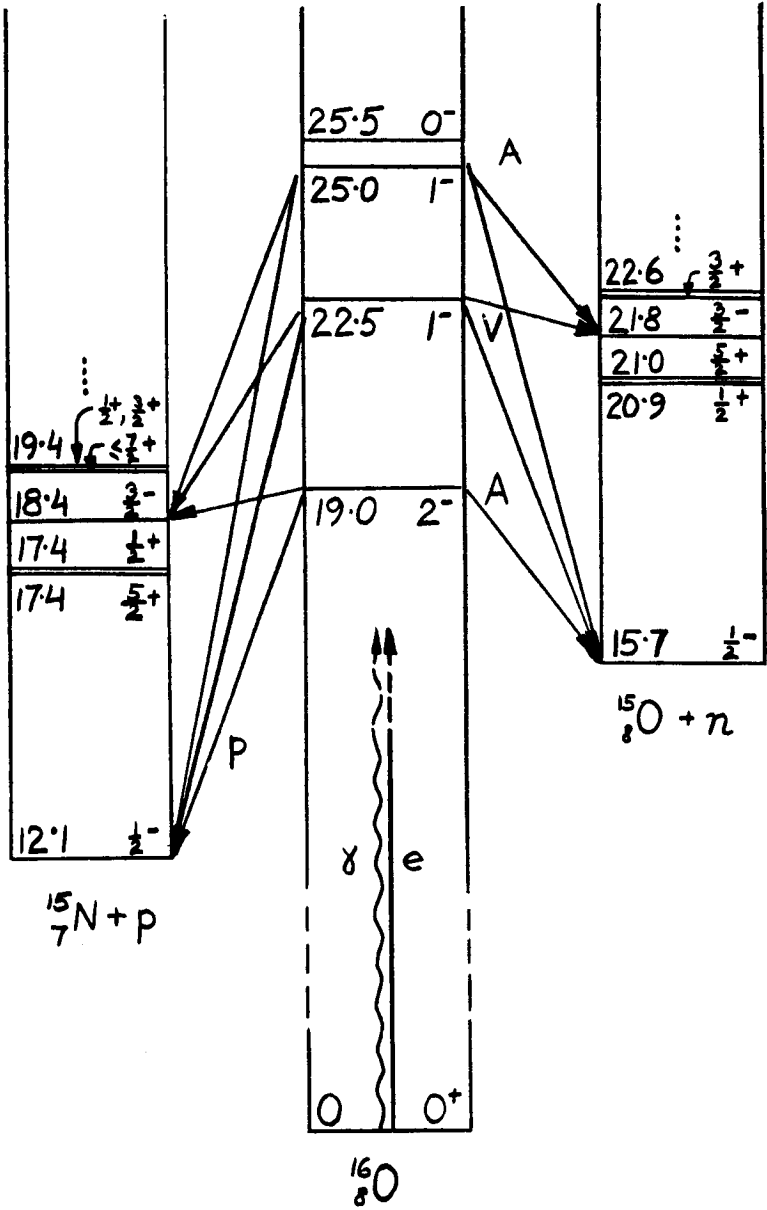
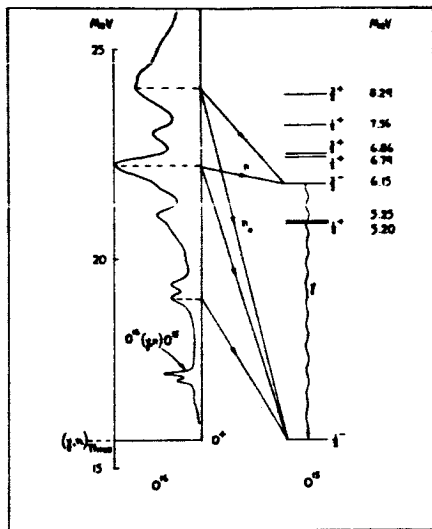


Figure 9

Top: Level scheme for neutron decay of the giant dipole states in  $^{16}\text{O}$ .

Bottom: Photoneutron spectrum from  $^{16}\text{O}$  irradiated with 25 Mev Bremsstrahlung (after Firk 44).



ENERGY LEVELS IN  $O^8$  AND  $O^6$

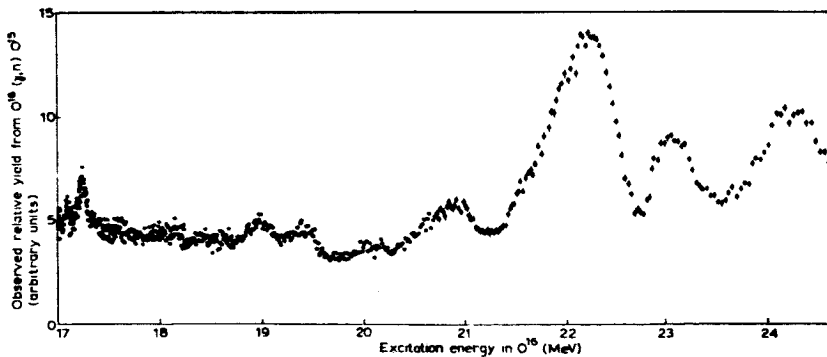


Figure 10

Proton spectra from the  $(e, e'p)$  reaction in  $^{12}\text{C}$  (top) and  $^{16}\text{O}$  (bottom) with 30 Mev electrons; protons observed at  $76^\circ$  emission angle. After Dodge and Barber <sup>45</sup>.

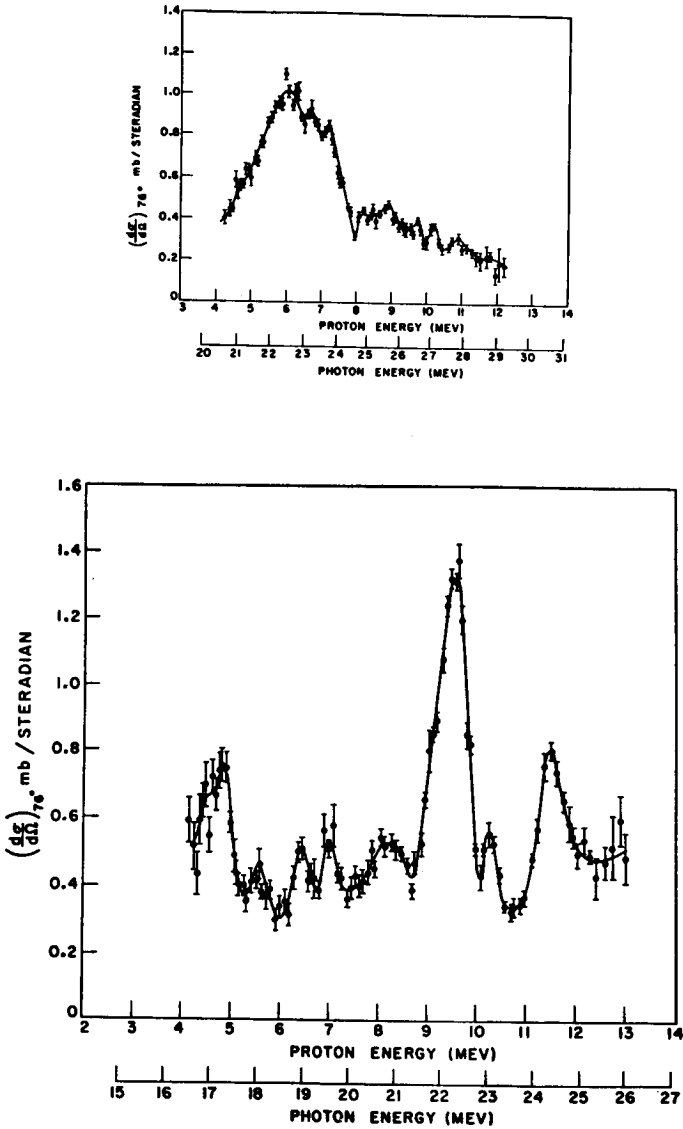
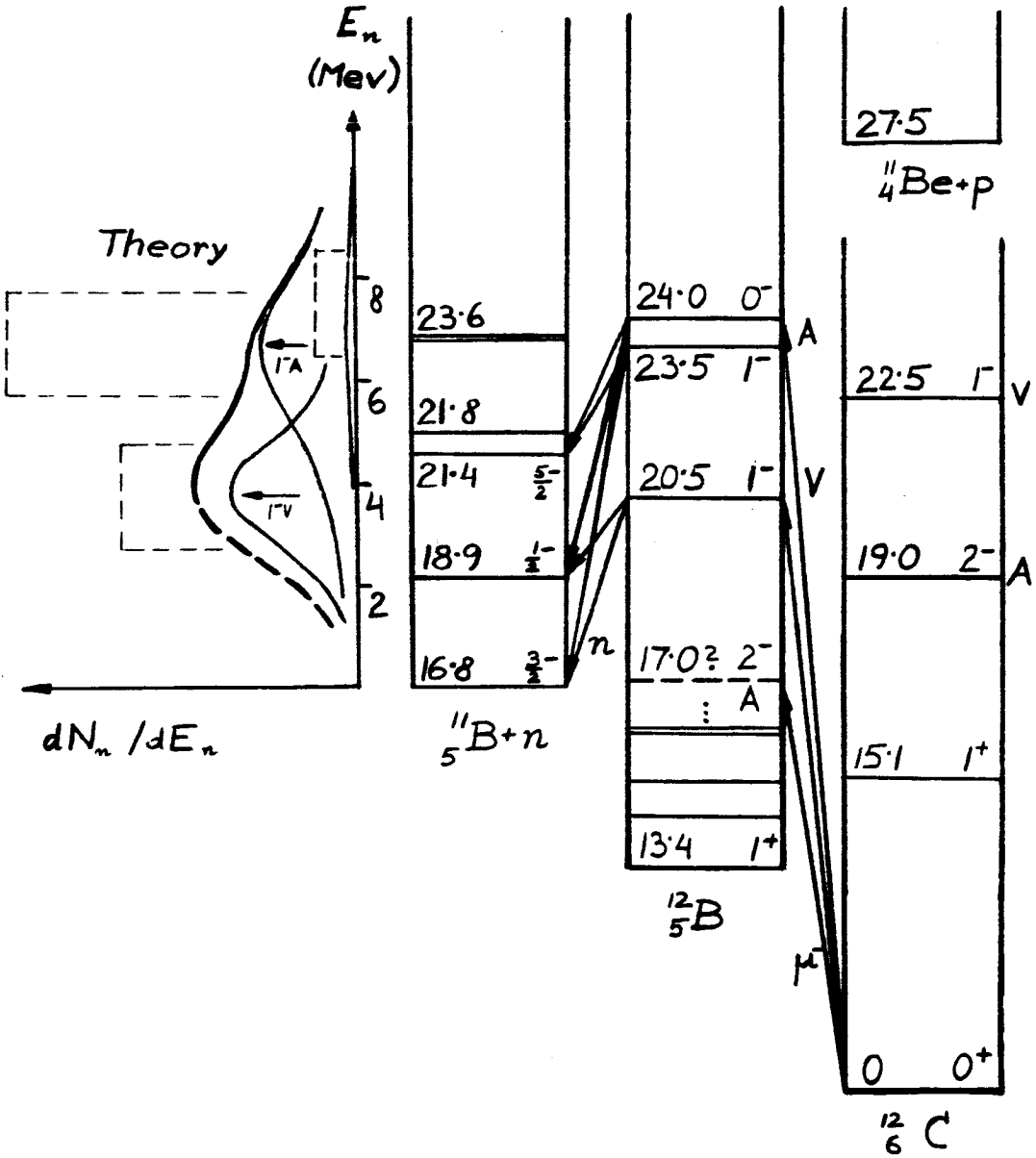




Figure 11

Level scheme for muon capture in  $^{12}\text{C}$  leading to  $^{12}\text{B}^*$  dip and subsequent neutron decay, with theoretical neutron spectrum.



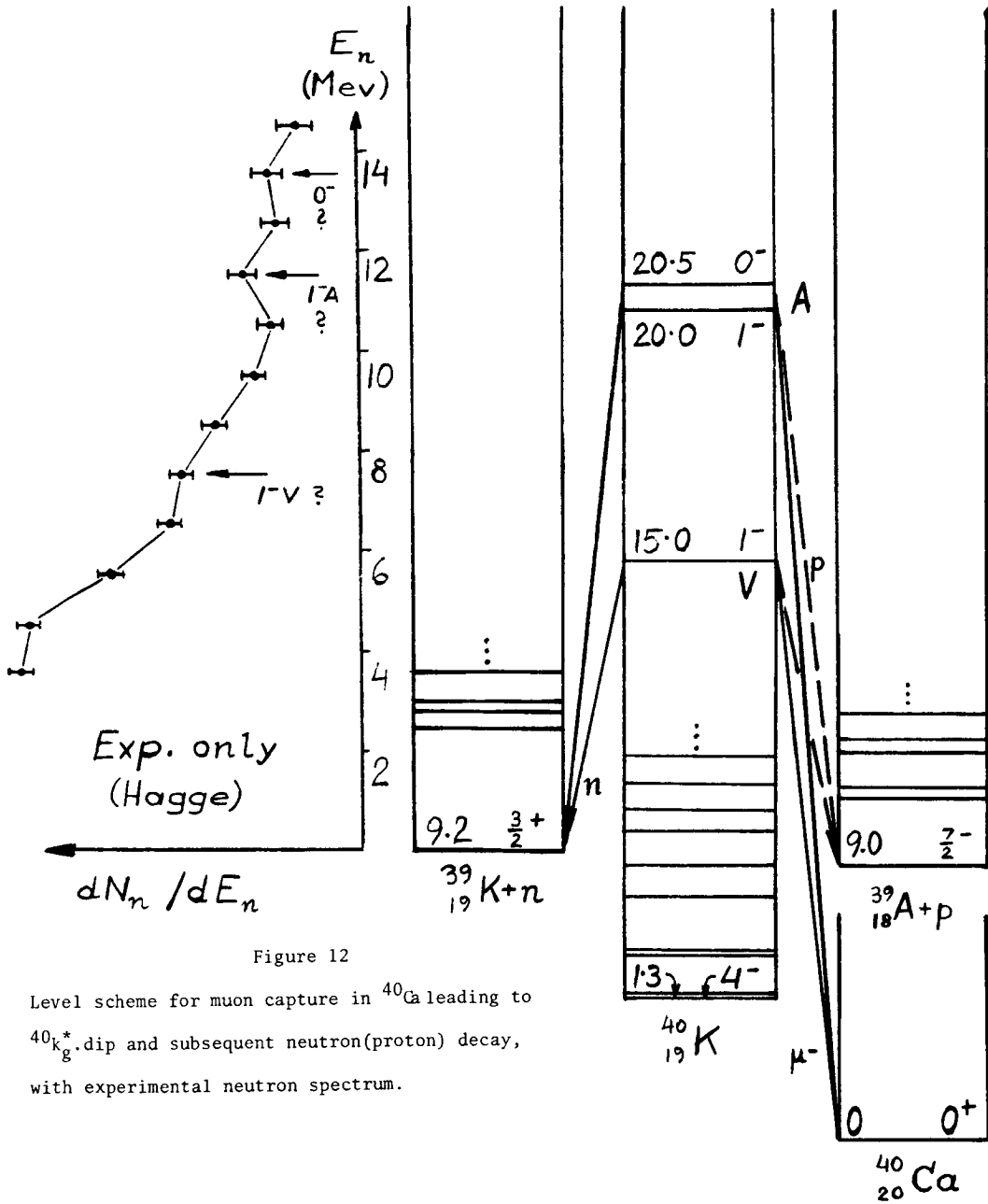


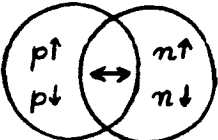
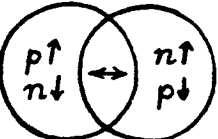
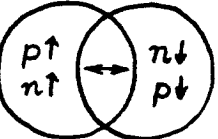
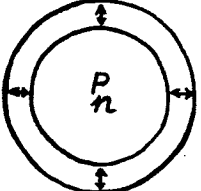
Figure 12

Level scheme for muon capture in  $^{40}\text{Ca}$  leading to  $^{40}\text{K}_g^*$  and subsequent neutron(proton) decay, with experimental neutron spectrum.

Figure 13

The possible modes of collective vibrations in the Goldhaber-Teller model, and list of the matrix elements which exclusively contribute to the corresponding states.

### Goldhaber-Teller Model

| modes  | # | $\gamma$   | J     | e                             | J                                 | $\mu$       | J                       |
|--|---|--|-------|-------------------------------|-----------------------------------|-------------|-------------------------|
|  <p>isospin<br/>(<math>T=1, J=1^-</math>)</p>            | 3 | $J_1^{ej}$   | $1^-$ | $\mathcal{M}_1$<br>$J_1^{ej}$ | $1^-$                             | $M_V$       | $1^-$                   |
|  <p>spin-isospin<br/>(<math>T=1, J=0^-1^-2^-</math>)</p> | 9 | $\sim 0$ at<br>$q=\delta$  |       | $J_1^{e\mu}$<br>$J_2^{m\mu}$  | $1^-$<br>$2^-$                    | $\vec{M}_A$ | $0^-$<br>$1^-$<br>$2^-$ |
|  <p>spin wave<br/>(<math>T=0, J=0^-1^-2^-</math>)</p>   | 3 | $\sim 0$ as $\left(\frac{\mu_p + \mu_n}{\mu_p - \mu_n}\right)^2 \ll 1$ |       |                               | none<br>( $M_{V,A} \sim \tau^-$ ) |             |                         |
|  <p>breathing<br/>(<math>T=0, J=0</math>)</p>          | 1 | —  |       | $\mathcal{M}_0$               | $0^+$                             | —           |                         |

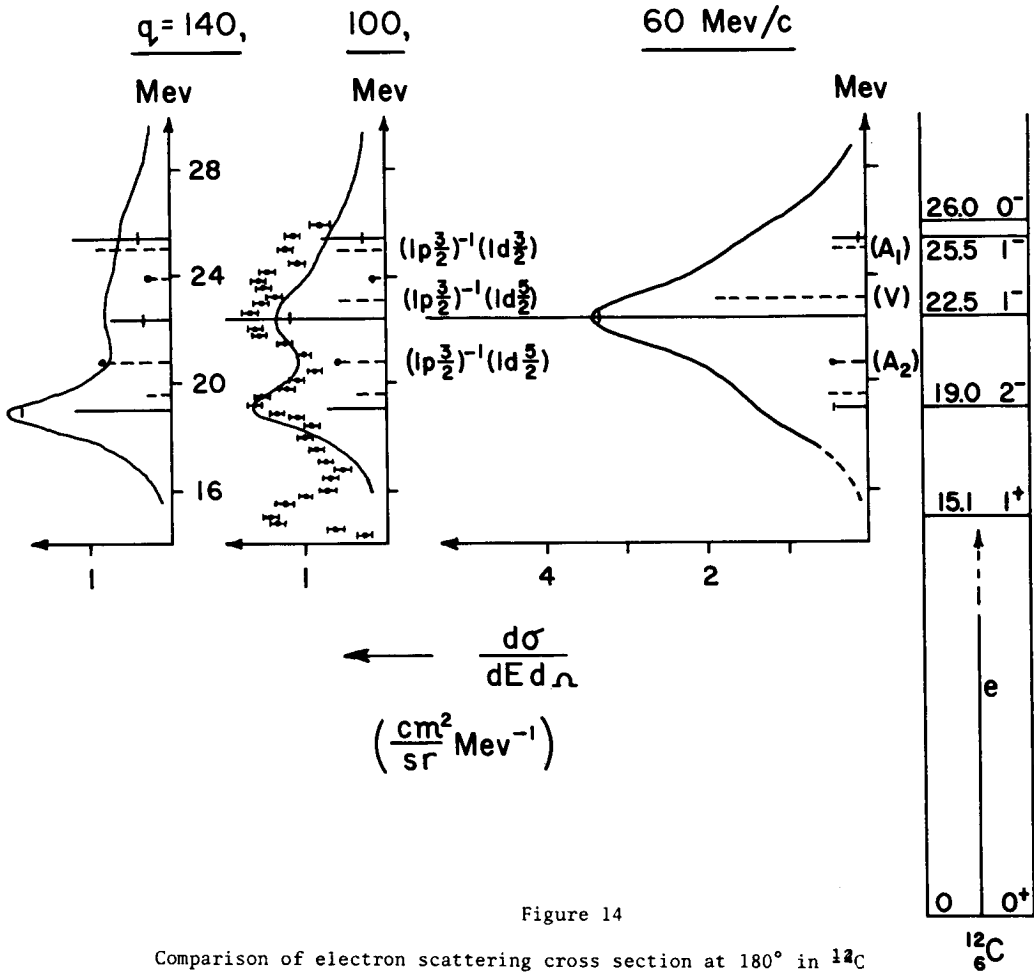


Figure 14

Comparison of electron scattering cross section at 180° in  $^{12}\text{C}$  as predicted by the Goldhaber-teller model with experiment, and identification of collective and particle-hole states.

Figure 15

Neutron and gamma decay spectra of giant resonance states of  $^{12}\text{B}$  following their excitation by muon capture in  $^{12}\text{C}$ . Decay width and neutron polarizations are indicated.

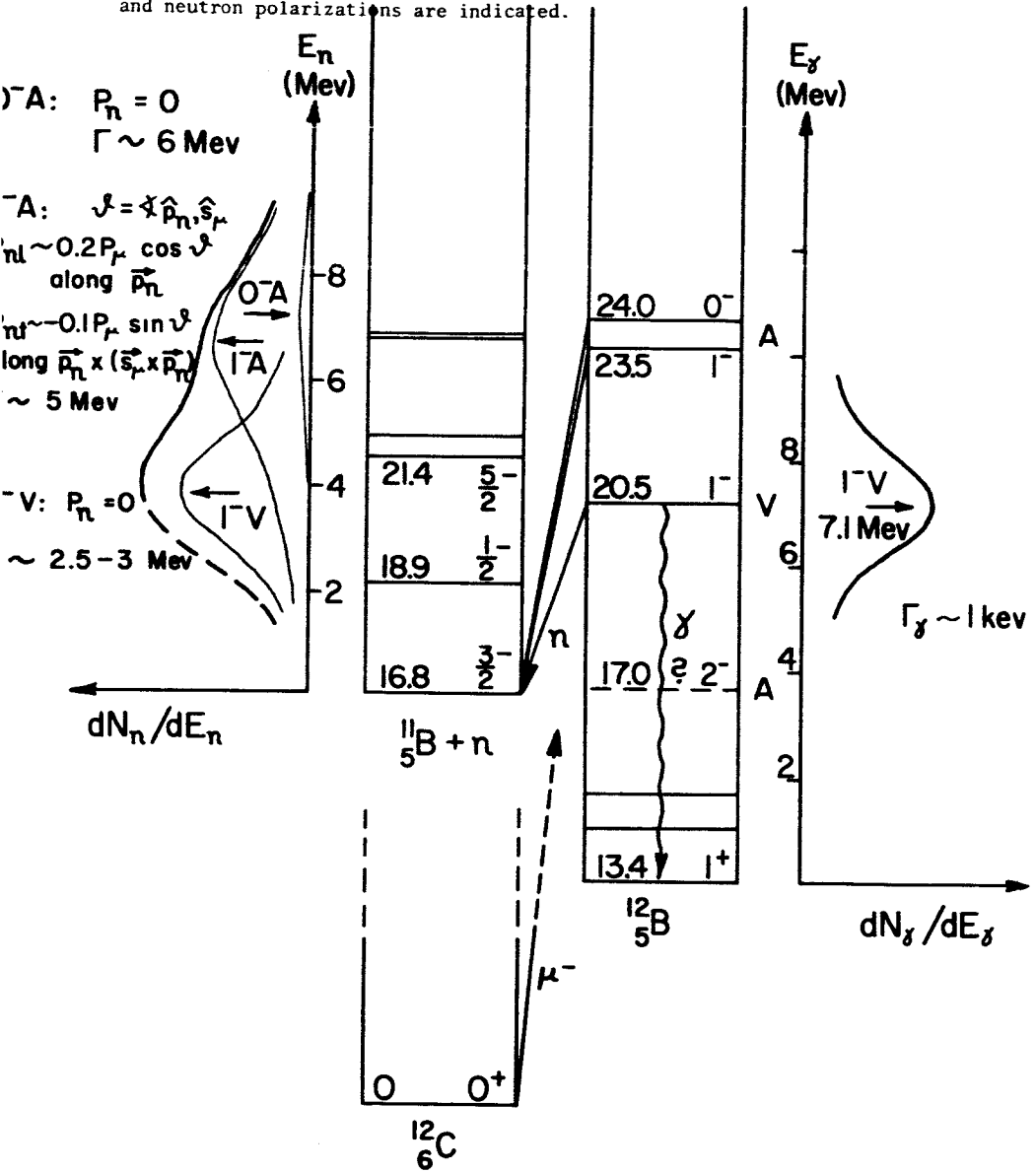


Figure 16

Inelastic electron scattering cross section for the 20.4 Mev state in  ${}^4\text{He}$  and function  $R(q)$ : comparison of experiment with breathing mode collective model.

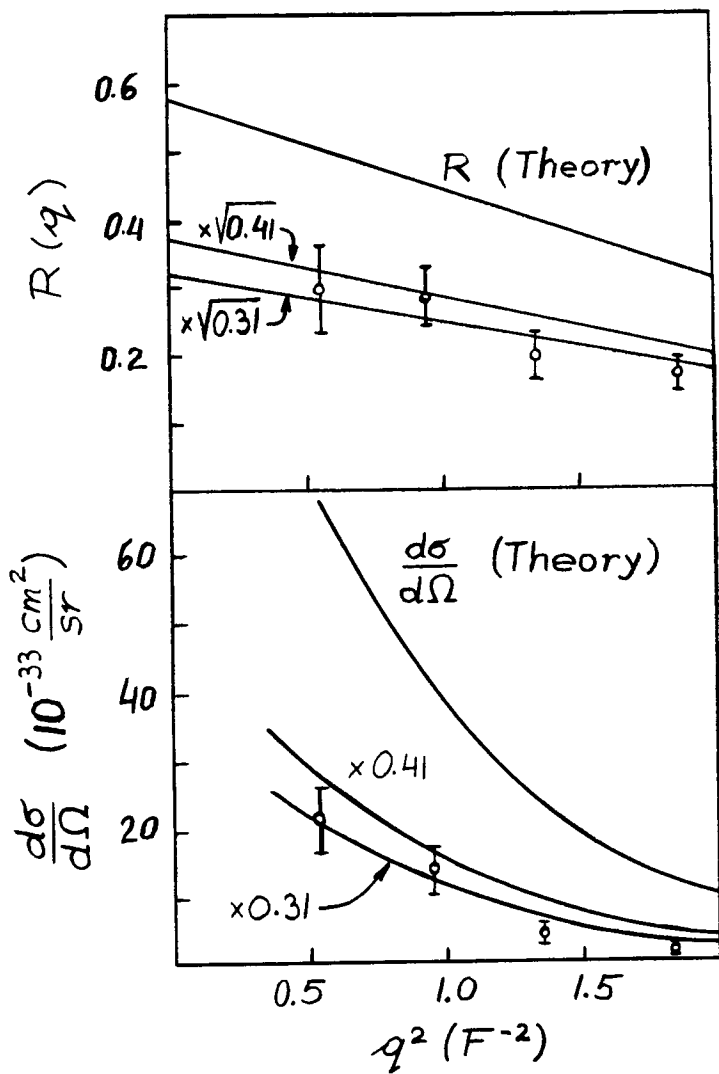
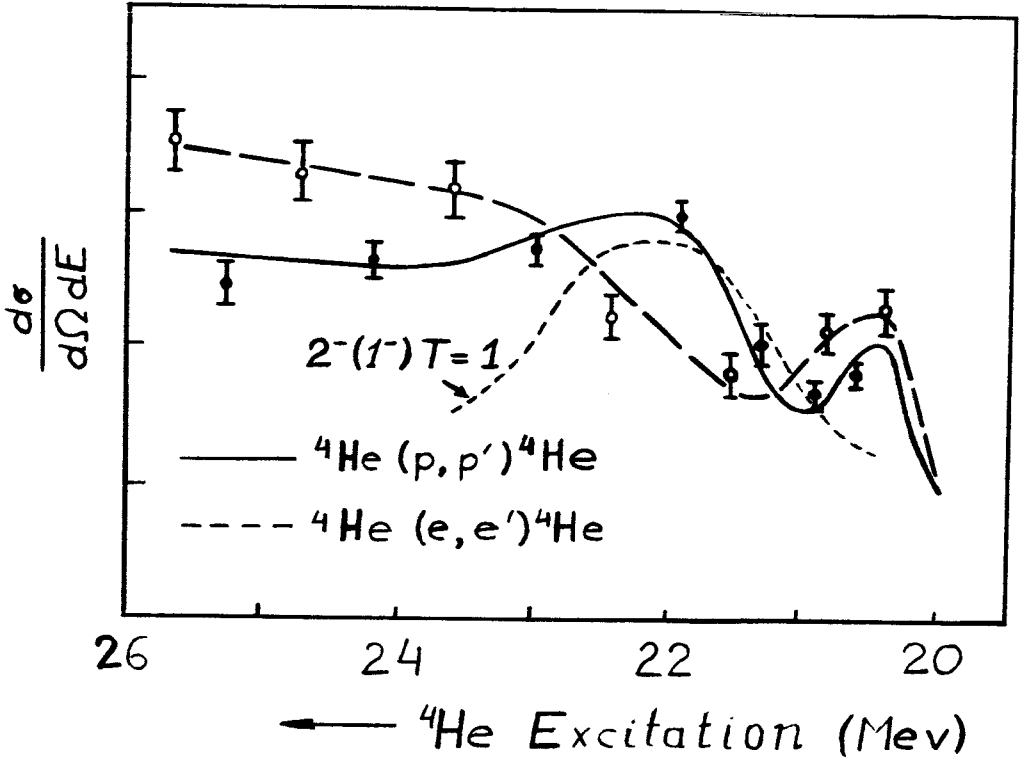


Figure 17

Excitation functions of  ${}^4\text{He}$  states by inelastic proton (solid curve) and electron (dashed curve) scattering.



EISENBERG: I think this is perhaps directed to Dr. Walecka. The electron scattering evidence for the appearance of a  $1^-$  spin-isospin vibration is spotty to say the least, and in fact I think no level of that character is observed in experiments of Isabell and Goldemberg. In fact, they find that in order to get the kind of closure result which you indicate, the curve with the dip, they actually have to sum over a considerable range of energy, something like 10 Mev. This, of course, could be because the level is broad, as I think Dr. Uberall indicates, or it could be because there is two particle-two hole admixture in this region. But, in any event, since the muon capture is so sensitive to the excitation energy, perhaps it would be misleading in that situation.

WALECKA: The data that I showed was integrated over a region about 4 Mev, I think, and that was from two or three different experiments. There certainly is a rise in the total cross-section in that region. Those are the points I showed on the graph. You could argue this with other multipoles. The best we can do is just calculate all the other multipoles we know. If we added in the  $2^-$  that was also shown on the curve, the contribution would be small. It certainly was not integrated over 10 Mev, but, I think, about 4 Mev. And that is the total strength. Now, it is true that you don't see the detailed shift of dipole strength from the lower level. We say it should shift up by about 2 Mev, but it's a puzzle. Uberall pointed out that the upper level is broader. We've done some calculations on a continuum model and it is true that the upper level is much broader and the shift is not as great as you would expect on a simple bound state picture.

WERNTZ: I'd like to direct a question or maybe a comment to Professor Walecka. We've done some continuum calculations on helium and I think they're in semi-quantitative agreement with the more complicated phase-shift analyses of Tombrello.



The results seem to be that the  $T=1$  dipole states of the alpha particle are no true resonances in the sense the phase shifts go through 90 degrees. And, furthermore, the  $T=0$  phase shift is considerably smaller than the others. I was wondering whether this might, therefore, reduce that  $M_V$  in comparison with  $M_A$ . That would explain why the experimental muon capture rate is much larger than the theory indicated.

WALECKA: Yes, that's an interesting point. Actually, in the spectrum I showed on the alpha particle, we find that the dipole strength in the two  $1^-$  levels are actually reversed. In our calculation, we find the upper state has about twice the electric dipole strength as the lower state. Now, experimentally, the peak in the photo-absorption cross section is in the lower state. We tried to play with that, and put the strength in as experimentally observed and also as calculated and it only made the comparison with the muon capture worse. There was no way of significantly improving our predictions for the muon capture. I think the predictions for the first forbidden contributions to muon capture are probably pretty good, probably good to something like 15% or so, in the alpha particle. Now, you can turn the argument around if you want. You can say that the muon capture is therefore the world's best measurement of admixtures into the ground state of the alpha particle. I don't know any numbers here. All I know is that Kane and Jones estimated how big the allowed contribution should be and it was nowhere near big enough to explain the discrepancy. It would be interesting, of course, to try to put an admixture in and see if this contradicted any other experiments. I don't know whether it would or not. Also, as long as I've got a microphone in my hand, let me suggest that anybody that can think up clever ways of trying to see these  $T=1$  or  $T=0$ ,  $0^-$  states, would be very welcome. They're very hard to see, to really pick out, and some of these should have all the strength concentrated in them.

TELEGDI: I have two questions to Professor Walecka and one to Professor Uberall. Let me preface my questions by saying that they are in no way directly related to the specific model on which you spent most of your time, this  $SU_4$  scheme. First question is, what is the opinion of theorists about our present knowledge of the deuteron wave function and similar things that would enter into mu capture in deuterium? After all, you said yourself the hydrogen gives one number, the  $He^3$  gives another, and that's far from an overdetermination. Now there are many experimental difficulties in doing mu capture in deuterium into which I shall not go, but assuming one can overcome these, wouldn't the theorists say that we don't know the deuteron wave function at close distances sufficiently well to do this? Or, is there an aura of optimism on this topic; this is question number one. Question number two is that there has been a very detailed experimental study in at least two labs of the partial capture rates in  $O^{16}$  and one tried to squeeze these data for a lot of information. But when you look at the calculations, they are still very model dependent and for some states, in rather violent disagreement with the experiment, which makes you believe that you shouldn't attach too much importance to the agreement in other states. Now, this great trade of electric versus weak matrix elements cannot be applied to this situation. These are my two questions to Professor Walecka. When he has answered, I will ask Professor Uberall something else.

WALECKA: There are people certainly much more qualified than me to talk about the deuteron wave function and maybe Professor Breit could comment on that. I do know that the elastic electron scattering experiments on the deuteron are very sensitive to details. For example, recent experiments of Ericson, at large momentum transfers, show the presence of a hard core. If you leave out a hard core you get completely

wrong curves. That's the one point. The second point was the partial capture rates in oxygen. There is a nice paper recently by Kim. There was always a discrepancy with the  $2^-$ . I think this is the ground state of  $N^{16}$ . He took the form factor, which is known only very crudely, from the electron scattering experiments but which disagrees with the shell model calculation for that particular state. He found within the experimental errors that he could match the rates. There's a big error on that, though, so I don't know how seriously that should be taken. Some of the other states you want to give information on the coupling constants. For example, the transition to the  $0^-$  state was this induced pseudoscalar analyzer. It turns out Ericson was the first one to show this, that roughly 3/4 of the capture rate comes from these nucleon recoil correction terms, which, of course, are model-dependent.

FOLDY: One of the problems in the  $O^{16}$  and the  $N^{16}$  is just the fact that since the giant dipole resonance tends to dominate the transition, the sensitivity with which you can calculate contributions to other states is impaired. They have their transition strength robbed by the giant resonance. It is a lot more sensitive to small details.

TELEGDI: All partial capture rates will be of order  $1/Z$ , or what have you. But I was careful in saying that I wanted to have this discussion outside the giant resonance model but rather see what you could do specifically with magnetic transitions. Do you see what I mean? I know that this is a small residual as compared to the main transitions. Now, as to Professor Uberall, first of all, I don't understand what's meant by the Goldhaber-Teller model. Fifteen years ago I thought I did. Well, what I can understand from the argument you showed is that one has to have four different vibrations in the  $SU_4$ . Then part of the argumentation as I

understood it didn't seem to prove to me anything in particular. Namely, you showed a certain number of states with specific spins,  $1^-$ ,  $2^-$ , the ones that you wanted to find. You then assume that those exist and have been proven to have the quantum numbers such as desired by such a theory. If one takes  $SU_4$  as a suitable starting basis it is unavoidable that such states exist somewhere. Once those states have been localized, then you have said what would happen to them in their electro-excitation. Now, as I understand these arguments, it simply rests on seeing which operators have Q's in which form. The vector part has a Q in a damping factor, the magnetic part requires velocity dependent q's in a way that makes them rise. So if I don't know any theoretical physics whatsoever, except the form of the operators, I know that excitations of certain states do manifest themselves through the momentum dependence of the operators in this advertised fashion. And, what else do I prove?

UBERALL: The Goldhaber-Teller Model is first a classification of the states which occur according to the spins and isotopic spins and, secondly, it tells you which of the multipole operators.....

TELEGDI: That's set by spin alone. Spin and isospin tell you that uniquely.

UBERALL: Yes, sure, but first you have to classify the states on the basis of the Goldhaber-Teller model.

TELEGDI: In any reasonable model that is spin independent of the Wigner type, those states would be produced, that's clear. What Walecka calls in a very refined manner the 15 dimensional representation makes it obvious that such states occur.

UBERALL: I want to say that any reasonable model should of course give you these

features. The Goldhaber-Teller model was chosen because it depicts these features in an especially simple and a lucid fashion because you see exactly what states are there and how the relative energy varies. If you take the particle-hole model, some of the states are split off, satellites are split off, and the picture doesn't become so clear anymore. So, this, I feel, is the simplest description of a more complicated situation and one has to go into more sophisticated models to describe it better, but, this is the starting point of description.

BLOCK: My question is addressed to Walecka. Having had a loose liason with helium over the years, this comment that you can find the D-wave admixture by reversing the argument strikes me as an extremal statement. The amount of D-wave, if I recall, estimated by Kane and Jones was supposed to be an upper limit, nowhere close to what they would even consider a reasonable value. Trying to somehow or other bound the answer, they estimated 35. If I recall the number from your slide, you would then have a D-wave admixture in the order of 10% or so, if you turn the argument around. Could it not be that the model is inapplicable? Is this the best way to find the D-wave admixture?

WALECKA: Well, the only thing I can say, is, I think that our estimate of the first forbidden contributions, by integrating over photoabsorption, are fairly reliable. I think our assumptions relating the axialvector and pseudoscalar to the vector are fairly reliable. The contribution of the other multipoles and the form factor is small. Now, the only thing you have left is the possibility of large admixtures in the ground state, unless I'm missing something.

KOLTUN: I have one comment on Telegdi's question, on the Goldhaber-Teller model. There are microscopic models of Goldhaber-Teller based on shell model considera-

tions and so on. The crucial question isn't whether there is a state or not, the question is what's the width of the state. And the point is, you can produce in reasonable models Goldhaber-Teller-like states with reasonable widths. If the width is small, you say the state is there. Now, in relation to this, I'd like to ask Dr. Uberall a question on the sum rules - the TRK sum rule and its extension by you and by Tolhoek. Are these based on single particle considerations or do you go the whole way as the TRK sum rule has gone in nuclear physics to looking at the exchange character of the forces and its effect on the sum rules?

UBERALL: No, that doesn't enter. You use the matrix element, which is provided by the Goldhaber-Teller model and you put it into the sum rule. No single-particle considerations enter and therefore no exchange forces either.

KOLTUN: There must be a generalization, just as there is to TRK.

UBERALL: Yes, it is well known that Levinger's sum rule gives you the exchange forces. This has not been used here.

KOLTUN: It'll be a different term here, that's the interesting thing. Because of the different isospin-spin character, there will be a different term of the two-body force.

UBERALL: Well, I don't know of any investigation of this point in the literature.

RECENT EXPERIMENTS ON MUONIUM

V. W. Hughes, J. Amato, R. Mobley, J. Rothberg, and P. Thompson

Gibbs Laboratory, Yale University-

166  
97  
32748

I would like to talk about two topics involving muonium on which some progress has been made in the past year. As you know, muonium is the misnomer for the atom consisting of a positive muon and an electron. The possibility for studying muonium comes about because of parity nonconservation in the production and decay of the muon. The decay of the positive pion at rest ( $\pi^+ \rightarrow \mu^+ + \nu_\mu$ ) produces a positive muon with its spin in the direction opposite to its linear momentum. The decay of the positive muon ( $\mu^+ \rightarrow e^+ + \nu_e + \bar{\nu}_\mu$ ) occurs with an angular asymmetry favoring positron emission in the direction of the muon spin. Hence polarized muonium can be formed, and changes in muon polarization, which accompany changes in muonium state associated with magnetic resonance transitions or collisions, can be observed through the change in the angular distribution of the decay positrons.

The first topic is a new measurement of the hyperfine structure of muonium which has been done by observing an induced transition at weak magnetic fields. The hyperfine structure interval in the ground state is of interest essentially

for quantum electrodynamic reasons. Muonium is the simplest system involving the muon and the electron, and hence a very suitable one for studying muon electrodynamics and the interaction of the muon and the electron. The second topic is muonium chemistry or the interaction of muonium with atoms and molecules.

#### Hyperfine Structure of Muonium.

With reference to the first topic, Figure 1 shows the simple energy level diagram of the hyperfine structure levels in the ground state of muonium. At zero field there are two states, the singlet state with  $F = 0$  and the triplet state with  $F = 1$ . The quantity  $x$  is a parameter proportional to the magnetic field. In the presence of a magnetic field the triplet state splits into its three magnetic substates. In previous work<sup>1</sup> we studied the transition shown by the arrow at a high magnetic field and used the theory of the energy level diagram (the Breit-Rabi formula) to obtain  $\Delta\nu$  (the zero-field hfs splitting). In a run we had just a few months ago we have been able to observe<sup>2</sup> transitions in a very weak field between the  $F = 0$  and the  $F = 1$  states, in particular both the transitions  $(F, M_F) = (1, 1) \leftrightarrow (0, 0)$  and  $(1, -1) \leftrightarrow (0, 0)$ .

Figure 2 shows the theoretical expression for the hyperfine structure interval in muonium. It is based on treating the muon as a heavy Dirac particle and is an expansion in powers in the fine structure constant,  $\alpha$ , and of the ratio of the electron mass to muon mass,  $m_e/m_\mu$ . The value for  $\alpha$  comes from the deuterium fine structure measurements of Lamb and his colleagues.<sup>3</sup>



The value of  $\alpha^2$  is known to about 18 ppm, and contributes the principal uncertainty to  $\Delta\nu(\text{theor})$ . The ratio of the muon magnetic moment to the proton magnetic moment, which is obtained from muon precession frequency experiments done at Columbia,<sup>4</sup> contributes an uncertainty of 13 ppm. Hence  $\Delta\nu(\text{theor}) = 4463.15 \pm 0.10 \text{ Mc/sec.}$ <sup>5</sup>

Figure 3 will remind you of the simple Hamiltonian involved. The relevant part of the muonium Hamiltonian includes the hyperfine structure interaction, and the interactions of the electron magnetic moment and of the muon magnetic moment with the external magnetic field. The usual expression for the energy levels is given.<sup>6</sup>

The general method of the experiment involves bringing muons into a gas where they are stopped and form polarized muonium. In a weak magnetic field with the incident muon spin direction in the direction of the external field, (the quantization direction), the relative populations of the hfs states will be:

$$(F = 1, M_F = 1) = 1/2$$

$$(F = 1, M_F = 0) = 1/4$$

$$(F = 0, M_F = 0) = 1/4$$

$$(F = 1, M_F = -1) = 0.$$

If no microwave frequency is applied, then the angular distribution of the decay positrons will be characteristic of the net polarization of the muons in these states. If we apply a microwave frequency so that a transition occurs, for example from

the ( $F = 0, M_F = 0$ ) state in which the muons are unpolarized to the ( $F = 1, M_F = +1$ ) state in which the muons are polarized, then the angular distribution of the decay positrons will be changed, thus serving as the detection for the occurrence of the transition.

Figure 4 summarizes the theory of the line shape. It is based on the time-dependent Schroedinger equations for the state amplitudes  $a_p$  and  $a_q$ , in which the muon decay rate  $\gamma$  is introduced phenomenologically. Matrix elements  $V_{pq}$  of the Hamiltonian term involving the microwave magnetic field  $\vec{H}rf$  connect the two levels. The initial conditions are  $a_p = 1, a_q = 0$ , at  $t = 0$ . We calculate  $|a_q(t)|^2 = P_{pq}$ . The signal observed is the change in angular distribution of the decay positrons and is proportional to the quantity  $P_q$ . The line-shape is Lorentzian.

Figure 5 shows the experimental arrangement. The incoming muon beam passes through counters numbered 1, 2, and 3 and stops in a high pressure target, filled with argon at some 35 atmospheres. Positrons are detected by the scintillation counter telescope 45 in a time interval of about 3  $\mu$ sec after the muon arrives. A principal technical problem was the achievement of a small, homogeneous and stable magnetic field on the floor of the Nevis synchrocyclotron, where the fringing magnetic field from the cyclotron is about 10 gauss and the field inhomogeneity is about one gauss per foot. The requisite magnetic field with a homogeneity of better than 0.05 G and a stability

of better than 0.01 G was achieved with the use of a structure involving three large moly-permalloy shields surrounding a solenoid and associated correction coils. The static magnetic field was monitored and mapped with a  $\text{Rb}^{85}$  optical pumping magnetometer.

Figure 6 shows the microwave system. Without going into detail, fundamentally the frequency is referred back to a crystal oscillator. There are various amplification and harmonic generation stages and eventually about 3 watts of power is fed into a resonant cavity with a Q of 12000, operating in the  $\text{TM}_{220}$  mode, which has the virtues of having convenient dimensions for a gas target used in the Nevis meson beam and of having a microwave magnetic field perpendicular to the static field.

The data consist of observations of the gated positron counts as a function of the microwave frequency with a fixed static magnetic field. The cavity is retuned as the microwave frequency is varied.

One of the three resonance curves obtained thus far is shown in Figure 7 for the transition  $(F, M_F) = (1, -1) \leftrightarrow (0, 0)$  at a static magnetic field of 2.7 G, which is well resolved from the other observable nearby transition  $(F, M_F) = (1, 1) \leftrightarrow (0, 0)$ . The signal is the difference between the ratio of the number of gated positron counts with the microwaves on to the

number with the microwaves off minus 1. The error bars indicate one standard deviation for the counting statistics. The solid curve is a fitted curve based on the theoretical line shape,  $P_q$ , given in Figure 4. The amplitude of the resonance curve is 0.7%, which is the expected value relative to that of about 3.5% for the strong field experiment. The resonance signal is predicted to be a factor of 5 smaller than for the strong field  $(M_J, M_\mu) = (1/2, 1/2) \leftrightarrow (1/2, -1/2)$  experiment due to the relative populations of the hfs states and to the change in polarization accompanying the transition. The linewidth is about 0.3 Mc/sec due to the power broadening and the muon lifetime. Note that the resonance frequency is at about 4458.9 Mc/sec. The contribution of the Zeeman effect to the transition frequency is -3.8 Mc/sec and the hfs pressure shift, taken from the strong field result, is -0.45 Mc/sec.

On the basis of two resonance curves for the  $(F, M_F) = (1, -1) \leftrightarrow (0, 0)$  transition and one resonance curve for the  $(1, 1) \leftrightarrow (0, 0)$  transition, we obtain

$$\Delta\nu(\text{expt}) = 4463.18 \pm 0.12 \text{ Mc/sec}$$

where the error (one standard deviation) is due to counting statistics (0.11 Mc/sec) and uncertainty in the pressure shift (0.05 Mc/sec). In a longer run planned for this summer we hope to improve the accuracy by a factor of two. The experimental accuracy is severely limited by the intensity of the muon beam.

This value agrees well with the value of  $\Delta\nu(\text{expt}) = 4463.15 \pm 0.06$  Mc/sec obtained from the high field experiment. Combining the experimental values for  $\Delta\nu$  from the strong field and weak field experiments, we obtain

$$\Delta\nu(\text{expt}) = (4463.16 \pm 0.05) \text{ Mc/sec}$$

An alternative view of the high and low field measurements is that the low field measurement determines  $\Delta\nu$  directly and the high field measurement can be used to determine  $g_\mu/g_p$ . At present the high field experiment determines  $g_\mu/g_p$  only to an accuracy of about 2 parts in  $10^4$  because the interaction of the external magnetic field with the muon magnetic moment contributes only about 5 per cent to the transition energy for the  $(M_J, M_\mu) = (1/2, 1/2) \leftrightarrow (1/2, -1/2)$  transition. However, in future more precise experiments (perhaps one using a much higher external magnetic field) the quantity  $g_\mu/g_p$  could be determined in this way. The value so obtained would not be subject to uncertainties about magnetic shielding as is the experiment involving muons in water from which  $g_\mu/g_p$  is presently determined.<sup>4</sup>

The agreement between the experimental value for  $\Delta\nu$  given and the theoretical value is excellent. This agreement provides further proof that the muon is a heavy Dirac particle obeying modern quantum electrodynamics, in particular for the atom in which the muon and the electron are bound together.

In view of the fact that the experimental value for  $\Delta\nu$  is known as well as, or perhaps even somewhat better than, the

theoretical value, which is limited principally by our knowledge of  $\alpha$  based on the experimental measurement of the fine structure of deuterium,<sup>3</sup> we can assume that the theoretical expression for  $\Delta v(\text{theor})$  given in Figure 2 is correct, and use the value of  $\Delta v(\text{expt})$  to determine an independent value for  $\alpha$ . This procedure gives:

$$\alpha^{-1} = 137.0388 (\pm 9 \text{ ppm})$$

If this value of  $\alpha$  is combined with that from the deuterium fs measurement, we obtain the new value

$$\alpha^{-1} = 137.0388 (\pm 6 \text{ ppm})$$

Apart from the desirability of having a better value of  $\alpha$  as one of the fundamental constants,<sup>7</sup> the value of  $\alpha$  is of critical importance to the comparison of the theoretical<sup>5</sup> and experimental values for the hfs of hydrogen. (See Figure 8) The most precise experimental value for  $\Delta v$  of hydrogen is obtained from measurements with the hydrogen maser.<sup>8</sup> The measurement of  $\Delta v$  for <sup>muonium</sup> / provides a confirmation of the value of  $\alpha$  determined from the fine structure of deuterium and hence confirms the outstanding discrepancy between the experimental and theoretical values for the hfs of hydrogen. It seems likely that this interesting discrepancy is due to an inadequate theoretical treatment of the effects of proton structure and recoil (the term  $\delta_p$ ).<sup>9,10</sup> Two unconventional attempts to explain the discrepancy have been made by Nambu and his colleagues. One introduced an axial vector meson<sup>11,12</sup> in the interaction of the electron and proton and the other involved a quark model of the proton's structure in a theory similar to that of the hfs anomaly for electronic atoms.<sup>13</sup> More recently

Drell and his colleagues have been considering in detail the effects of dynamic proton polarization.<sup>14</sup>

### Hyperfine Structure of Muonic Hydrogen

The hyperfine structure interval of the muonic hydrogen atom would be a most interesting quantity to measure. This is particularly true because of the present discrepancy between the theoretical and experimental values for the hfs interval of hydrogen. As mentioned above, the calculation of the effect of proton structure and proton recoil included in the term  $\delta_p$  is ambiguous. This term is of order  $\alpha \frac{m_e}{m_p}$  for hydrogen and hence  $\sim 0.5/10^5$ , but for muonic hydrogen/of order  $\alpha \frac{m_\mu}{m_p}$  or  $\sim 1/10^3$ ; hence the ambiguous term is relatively much more important in muonic hydrogen and indeed so large that its effect could not be masked by uncertainties in  $\alpha$  and other constants appearing in the expression for  $\Delta v$  of  $\mu^-p$ . The theoretical expression for  $\Delta v$  of muonic hydrogen is given in Figure 9. The interval of 6.79 microns is in the infra red wavelength range.

An experiment to measure  $\Delta v$  of muonic hydrogen can be imagined but would be very difficult. The general method of the experiment would be similar to that of the muonium hfs experiment. Negative muons would be stopped in  $H_2$  gas at sufficiently low pressure so that  $\mu^-p$  would exist in the lowest  $F = 0$  hfs level for a time interval of the order of the muon lifetime. If polarized infra red light at the wavelength of 6.79 microns is applied, a transition can be induced from  $(F, M_F) = (0, 0)$  to  $(1, 1)$ . This transition could be detected

through the change in angular distribution of the decay electrons.

The transition is a magnetic dipole transition which must be induced within a time interval of 2  $\mu$ sec (the muon mean life). The required amplitude of the time-varying magnetic field is about 100 G. Since the natural, non-power-broadened linewidth is 0.14 Mc/sec and the transition frequency is  $4 \times 10^{13}$  cps, the fractional linewidth will be 1 part in  $3 \times 10^8$ . These factors clearly imply an extremely high power and extremely high stability infra red light source. Only a laser appears to have the potential for this problem. The wavelength is in a reasonable range for laser operation.<sup>15</sup> However, the line is very narrow (power broadening would probably require excessive power); the exact location of the line is uncertain theoretically due to the  $a m_\mu/m_p$  term; and tunability is required. With an optical cavity of reasonable size ( $10^3$  cm<sup>3</sup>) to contain a H<sub>2</sub> gas target for stopping negative muons (or negative pions), having a reflectance of 0.99, a peak power level of 1 megawatt is required at the repetition rate of the meson source (say 60 cps for the Nevis synchrocyclotron). Clearly all these requirements on the laser are extreme, though not ridiculous. Perhaps by the time meson factories and meson factorettes become available an appropriate laser source will be available.



### Muonium Chemistry

Muonium chemistry may not be in the field of intermediate energy physics, but chemistry played a negative role in some of the early experiments, including our own, in which a search for the characteristic muonium precession frequency was undertaken. The absence of a signal in some cases was probably due to the subsequent chemical interaction that muonium had with molecules that were present.

Muonium will behave as a light isotope of hydrogen with regard to its atomic interactions and chemical reactions since the muon mass is 207 times the electron mass and since the muon mean lifetime of 2.2  $\mu\text{sec}$  is long compared to electron atomic orbital times. Muonium interactions with various molecules which produce changes in the muon spin direction have been studied.

The direct interactions of muonium with various molecules can be studied by one of two related methods.<sup>16</sup> For both, polarized muons are stopped in argon gas to form muonium atoms and effects due to the admixture of small fractional amounts of various molecules as impurities are observed. The first method involves the study of the intensity of the resonance signal for the transition  $(M_J, M_\mu) = (1/2, 1/2) \leftrightarrow (1/2, -1/2)$  as a function of the impurity content in argon. Results are shown in Figure 10. Decrease in the signal implies collisions which remove muonium from the resonant states. These data are analyzed to yield an effective cross section,  $\sigma_1$ , for such a collision

and the results are given in table 1. For the paramagnetic molecules NO and O<sub>2</sub> an electron spin exchange collision which transfers muonium from one hfs magnetic substate to another is probably the reaction mechanism.<sup>17,18.</sup> For C<sub>2</sub>H<sub>4</sub>, which is an unsaturated hydrocarbon, a muonium-containing molecule may be formed. No reaction is observed with H<sub>2</sub> (or with N<sub>2</sub>), which is consistent with the facts that H<sub>2</sub> is not paramagnetic and that the chemical reaction  $M + H_2 \rightarrow MH + H$  is forbidden on energetic grounds for thermal muonium due to the high vibrational energy of MH. This interesting case illustrates that the chemical behavior of M and H can be quite different and confirms that it is not safe to claim that the muon in water will necessarily experience the same diamagnetic shielding as the proton in water.

The second method involves the measurement of the polarization of the muons as a function of time and of impurity concentration by use of a precision digital time analyzer following the scintillation counters for the positrons.<sup>19</sup> Such data are shown in Figure 11 for NO. These data are analyzed to yield an effective cross section  $\sigma_2$ , for depolarizing collisions (see table 1). The cross sections  $\sigma_1$  are much larger than the cross sections  $\sigma_2$ . For an electron spin exchange reaction occurring in a strong magnetic field this difference is due to the fact that the most probable transitions are between two hfs substates with different directions of the electron spin but the same direction of the muon spin (such as states 1 and 4

Table 1

Muonium-Molecule Cross Sections

| Gas                           | $\sigma_1$<br>( $10^{-16} \text{cm}^2$ ) | $\sigma_2$<br>( $10^{-16} \text{cm}^2$ ) | $\sigma_1 / \sigma_2$ |
|-------------------------------|--|--|-----------------------|
| NO                            | $3.2 \pm 1.5$                            | $0.27 \pm 0.08$                          | $12 \pm 7$            |
| O <sub>2</sub>                | $5.4 \pm 2.5$                            | $0.31 \pm 0.08$                          | $17 \pm 9$            |
| C <sub>2</sub> H <sub>4</sub> | $0.29 \pm 0.16$                          | $0.024 \pm 0.006$                        | $12 \pm 7$            |

of Figure 1), and this type of collision results in a decrease in the resonance signal but not in depolarization, which occurs only in transitions between two hfs substates with different directions of the muon spin (such as states 1 and 2 of Figure 1). The ratio of the cross sections for electron spin exchange transitions between different states depends only on the spin eigenfunctions for muonium. It can be shown that the ratio of  $\sigma_1/\sigma_2$  is

$$\sigma_1/\sigma_2 = \frac{1}{4s^2c^2}$$

where the amplitudes  $s$  and  $c$  are defined by

$$\chi_{1,0}(H) = c \alpha_e \beta_\mu + s \beta_e \alpha_\mu$$

$$\chi_{0,0}(H) = c \beta_e \alpha_\mu - s \alpha_e \beta_\mu$$

The static magnetic field was about 5200 G, so  $s^2 = 0.02$  and  $c^2 = 0.98$  and hence  $\sigma_1/\sigma_2 = 12$ , in agreement with the results of table 1.

A more detailed study of the nature of the depolarizing collisions has been made by observation of the depolarization rate (or cross section) as a function of the magnetic field. If an electron spin exchange mechanism is involved, the depolarization rate  $\lambda_2$  should be proportional to the quantity  $s^2c^2$ . Figure 12 shows such data for NO. The molecule NO has a ground  $^2\pi$  state with two fine structure states,  $^2\pi_{3/2}$  and

$^2\pi_{1/2}$ , separated by 0.013 eV and is, of course, paramagnetic. Hence we expect that an electron spin exchange mechanism will be involved. The solid curve has the form

$$\lambda_2 = \lambda_0 s^2 c^2$$

where  $\lambda_0$  is a constant chosen to fit the data. Agreement of the solid curve with the experimental data confirms the electron spin exchange nature of the depolarizing collisions. The corresponding electron spin exchange cross section<sup>18</sup> for H collisions with NO is about three times larger than that for muonium, which may be due to the fact that fewer partial waves are important for the muonium collisions.<sup>20</sup>

Our work on what may be called muonium chemistry is still in an early stage. Further studies of other molecules, analyses of the possible collision mechanisms, and comparison with corresponding hydrogen cross sections are in progress.

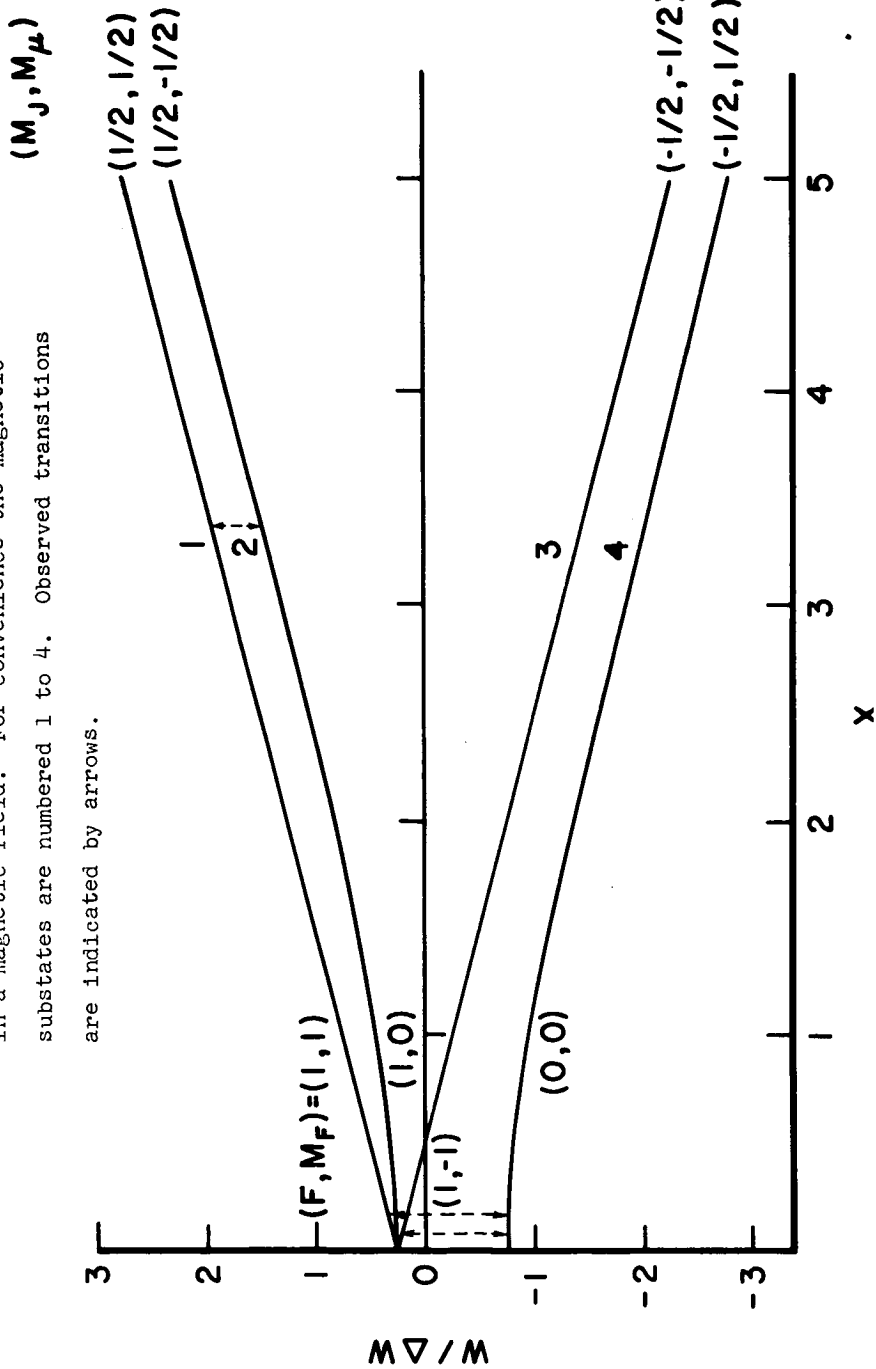
References

1. Cleland, W.E., Bailey, J.M., Eckhause, M., Hughes, V.W., Mobley, R.M., Prepost, R., and Rothberg, J.E., Phys. Rev. Letters 13, 202-205 (1964).
2. Thompson, P., Amato, J., Hughes, V.W., Mobley, R., and Rothberg, J., Bull. Am. Phys. Soc. 11, 343 (1966).
3. Dayhoff, E.S., Triebwasser, S., and Lamb, W.E., Phys. Rev. 89, 106-115 (1953).
4. Hutchinson, D.P., Menes, J., Patlach, A.M., and Shapiro, G., Phys. Rev. 131, 1362-1367 (1963).
5. Brodsky, S.J. and Erickson, B.W., "Radiative Level Shifts III. Hyperfine Structure in Hydrogenic Atoms." (preprint) Partial calculation of  $\alpha^3$  term. Their result is not incorporated in formula given for  $\Delta v(\text{theor})$ .
6. Kusch, P. and Hughes, V.W., "Atomic and Molecular Beam Spectroscopy," Encyclopedia of Physics, Vol. 37/1, ed. by Springer-Verlag/Berlin (1959), pp. 1-172.
7. Cohen, E.R. and DuMond, J.W.M., Rev. Mod. Phys. 37, 537-594 (1965).
8. Crampton, S.B., Kleppner, D., and Ramsey, N.F., Phys. Rev. Letters 11, 338-340 (1963).
9. Hughes, V.W., Proceedings of the International Conference on Nucleon Structure, 1963, edited by R. Hofstadter and L.I. Schiff (Stanford University Press, Stanford, California, 1964) pp. 235-244.

## References (continued)

10. Iddings, C.K., Phys. Rev. 138, B446-B458 (1965).
11. Fenster, S., Koberle, R., and Nambu, Y., Phys. Letters 19, 513-515 (1965).
12. Sullivan, J.D. and Drell, S.C., Phys. Letters 19, 516-518 (1965).
13. Fenster, S. and Nambu, Y., Progr. Theoret. Phys. Suppl.  
.(Extra Number, Yukawa commemoration issue, 1965), pp. 250-260.
14. Drell, S.D., Bull. Am. Phys. Soc. 11, 304 (1966).
15. Bennett, W.R., Jr., Applied Optics (Supplement 2: Chemical Lasers) p. 3-33 (1965).
16. Mobley, R.M., Bailey, J.M., Cleland, W.E. Hughes, V.W., and Rothberg, J.E., Fourth International Conference on the Physics of Electronic and Atomic Collisions, pp. 194-197, Science Bookcrafters, Inc., New York (1965); Bull. Am. Phys. Soc. 10, 80 (1965); J. Chem. Physics (to be published).
17. Purcell, E.M. and Field, G.B., Astrophys. J. 124, 542-549 (1956).
18. Berg, H.C., Phys. Rev. 137, A1621-A1634 (1965).
19. Meyer, S.L., Anderson, E.W., Bleser, E., Lederman, L.M., Rosen, J.L., Rothberg, J., and Wang, I-T, Phys. Rev. 132, 2693-2698 (1963).
20. Glassgold, A.E. and Lebedeff, S.A., Annals of Physics 28, 181-219 (1964).

Fig. 1. Energy level diagram of the muonium ground state in a magnetic field. For convenience the magnetic substates are numbered 1 to 4. Observed transitions are indicated by arrows.





$$\Delta\nu = \left( \frac{16}{3} \alpha^2 c R \omega \frac{\mu_\mu}{\mu_0} \right) \left( 1 + \frac{m_e}{m_\mu} \right)^{-3} \left( 1 + \frac{3}{2} \alpha^2 \right) (1 + a_e) (1 + a_\mu) (1 + \epsilon_1 + \epsilon_2) (1 - \delta_\mu)$$

where

$$\delta_\mu = \frac{3}{\pi} \alpha \frac{m_e}{m_\mu} \ln \frac{m_\mu}{m_e}$$

$$a_e = \frac{\alpha}{2\pi} - 0.328 \frac{\alpha^2}{\pi^2} \quad \epsilon_1 = -\alpha^2 \left( \frac{5}{2} - \ln 2 \right)$$

$$a_\mu = \frac{\alpha}{2\pi} + 0.75 \frac{\alpha^2}{\pi^2} \quad \epsilon_2 = -\frac{8\alpha^3}{3\pi} \ln \alpha \left( \ln \alpha + \frac{37}{96} + \frac{1}{5} - \ln 4 \right)$$

$$\begin{aligned} \mu_e / \mu_p &= 658.2106 \text{ (1 ppm)} & \alpha^{-1} &= 137.0388 \text{ (9 ppm)} \\ R \omega &= 109,737.31 \text{ cm}^{-1} \text{ (0.1 ppm)} & \mu_\mu / \mu_p &= 3.18338 \text{ (13 ppm)} \\ c &= 2.997925 \times 10^{10} \text{ cm/s (1 ppm)} & m_\mu / m_e &= 206.765 \text{ (13 ppm)} \end{aligned}$$

giving

$$\begin{aligned} \Delta\nu &= 2.632936 \times 10^7 \alpha^2 (\mu_\mu / \mu_p) \text{ Mc/s (1.5 ppm)} \\ \text{or } \Delta\nu &= 4463.15 \pm 0.10 \text{ Mc/s } (\pm 22 \text{ ppm}) \end{aligned}$$

Figure 3.

### Energy Levels and Transition Frequency

$$\mathcal{K} = a\vec{I} \cdot \vec{J} + \mu_0 g_J \vec{J} \cdot \vec{H} + \mu_0 g_\mu \vec{I} \cdot \vec{H}$$

$$W_F = \frac{1}{2} \pm \frac{1}{2}, m = -\frac{\Delta W}{4} + \mu_0 g_\mu H m \pm \frac{\Delta W}{2} (1 + 2mx + x^2)$$

$$x = \frac{(g_J - g_\mu) \mu_0 H}{\Delta W}$$

$$\nu [(1,1) - (1,0)] = \frac{\Delta \nu}{2} [1 + x - \sqrt{1+x^2}] + \frac{\mu_0 g_\mu H}{h}$$

$$\nu_P = \frac{\mu_0 g_P H}{h}$$

$$x = \left( \frac{g_J}{g_P} - \frac{g_\mu}{g_P} \right) \frac{\nu_P}{\Delta \nu}$$

Figure 4.

Theoretical Line Shape

$$\begin{aligned} \dot{a}_p &= -i a_q b e^{+i\omega t + i\omega_0 t} - \frac{\gamma}{2} a_p & \text{----- } p \\ \dot{a}_q &= -i a_p b^* e^{-i\omega t - i\omega_0 t} - \frac{\gamma}{2} a_q & \text{----- } q \end{aligned}$$

$W_p - W_q = \hbar \omega_0$

Initial Conditions:  
 $a_p = 1, a_q = 0$  at  $t = 0$

Decay Rate of Both  
 States p and q is  $\gamma$

$$\mathcal{H}' = \mu_0 g_J \vec{J} \cdot \vec{H}_{rf} + \mu_0 g_\mu \vec{I}_\mu \cdot \vec{H}_{rf}$$

$$V_{pq} = \langle p | \mathcal{H}' | q \rangle = \hbar b e^{+i\omega t}$$

$$P_{p,q}(t) = e^{-\gamma t} \frac{|2b|^2}{|2b|^2 + (\omega_0 - \omega)^2} \sin^2 \left\{ \frac{1}{2} \left[ |2b|^2 + (\omega_0 - \omega)^2 \right]^{\frac{1}{2}} t \right\}$$

$$P_q = \int_0^\infty \gamma P_{pq}(t) dt, \text{ probability of decay from state } q$$

$$P_q = \frac{2|b|^2}{4|b|^2 + \gamma^2 + (\omega - \omega_0)^2}$$

$$\delta\nu = \frac{1}{\pi} \sqrt{4|b|^2 + \gamma^2}, \text{ half width}$$

$$\delta\nu (\text{natural width}) = \frac{\gamma}{\pi} = 0.14 \text{ Mc/s}$$

### Experimental Layout (Low Field)

Figure 5.

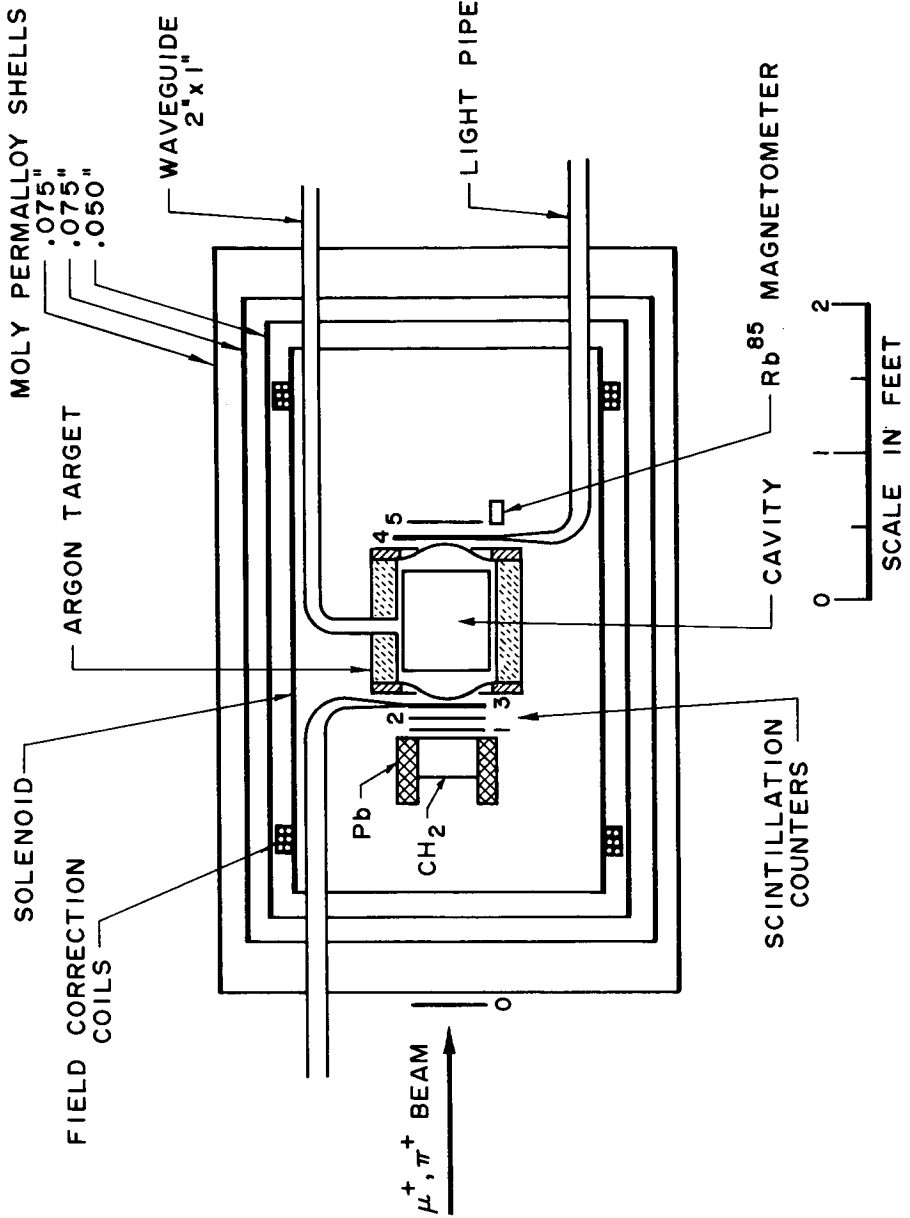


Figure 6. Microwave System (Low Field)

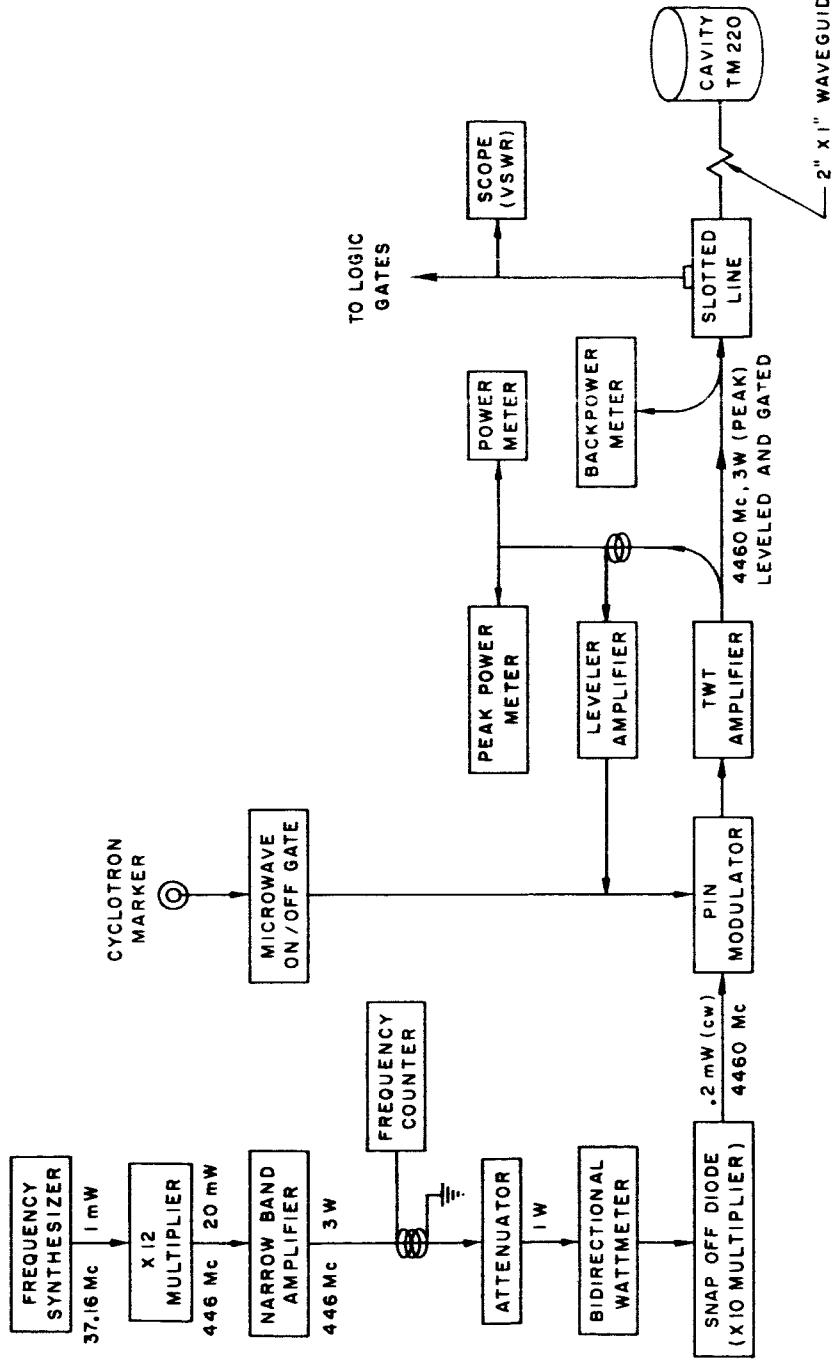


Fig. 7. Resonance curve for the transition  $(F, M_F) = (1, -1) \leftrightarrow (0, 0)$ , showing signal as a function of microwave frequency. The value of the static magnetic field was 2.7 G.

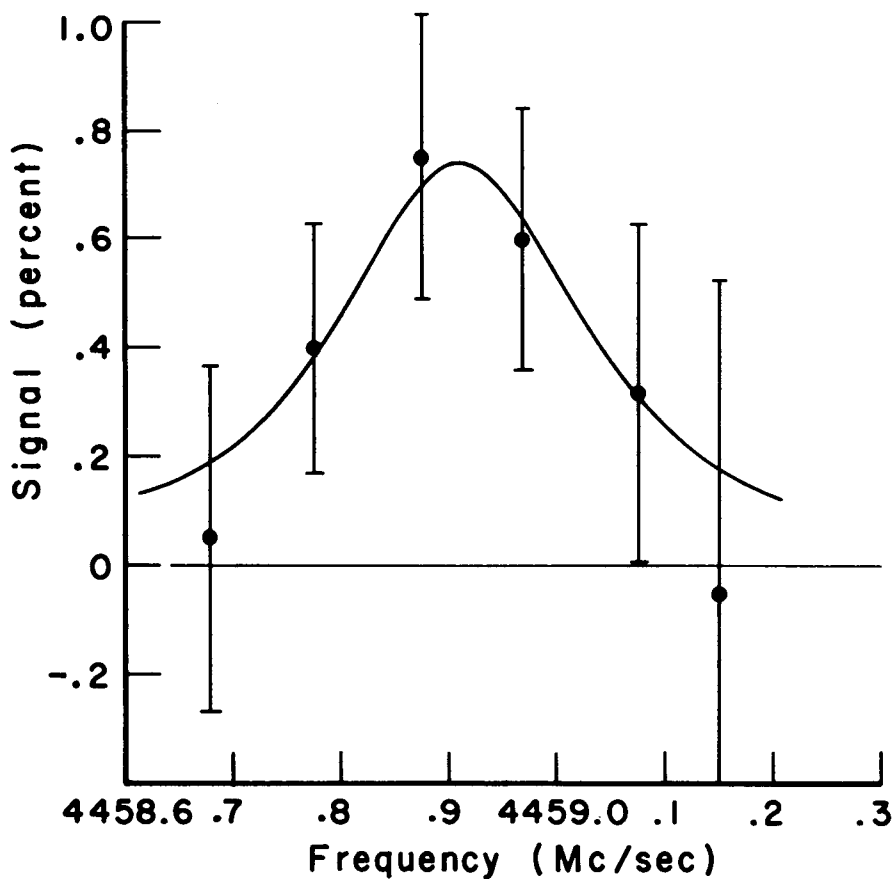


Figure 8

### Theoretical Formula for Hyperfine Structure Interval for Hydrogen

$$\Delta\nu = \left(\frac{16}{3} \alpha^2 c R\omega \frac{\mu_P}{\mu_e}\right) \left(1 + \frac{m_e}{m_P}\right)^{-3} \left(1 + \frac{\alpha}{2\pi} - 0.328 \frac{\alpha^2}{\pi^2}\right)^2 \left(1 + \frac{3}{2} \alpha^2\right)$$

$$\left(1 + \mathcal{E}_1 + \mathcal{E}_2\right) \left(1 - \delta_P\right)$$

$$\mathcal{E}_1 = -\alpha^2 (5/2 - \ln 2)$$

$$\mathcal{E}_2 = -\frac{8\alpha^3}{3\pi} \ln \alpha \left(\ln \alpha + \frac{37}{96} + \frac{1}{5} - \ln 4\right)$$

$$\delta_P = 35 \times 10^{-6} \text{ (Proton Recoil and Proton Structure)}$$

$$\left[ \begin{array}{l} \alpha^{-1} = 137.0388 \pm 0.0008 \\ c = (2997925 \pm 4) \times 10^4 \text{ cm/s} \\ R\omega = (109,737.309 \pm 0.012) \text{ cm}^{-1} \\ \mu_e / \mu_P = 658.2106 \pm 0.0007 \\ m_P / m_e = 1836.12 \pm 0.02 \end{array} \right.$$

$$\Delta\nu \text{ (theor.)} = 1420.342 \pm 0.019 \text{ Mc/s (21 ppm)}$$

$$\Delta\nu \text{ (expt.)} = 1420.405751800 \pm 0.000028 \text{ Mc/s}$$

$$\frac{\Delta\nu \text{ (expt.)} - \Delta\nu \text{ (theor.)}}{\Delta\nu \text{ (expt.)}} = 45 \pm 13 \text{ ppm}$$

Figure 9.

$$\Delta\nu_{\mu p} = \left(\frac{16}{3} \alpha^2 c R_{\mu} \frac{\mu_p}{\mu_0}\right) \left(1 + \frac{m_{\mu}}{m_p}\right)^{-3} \left(1 + \frac{3}{2} \alpha^2\right) (1 + \Delta_{\mu p}^E) (1 - \delta_p^{\mu p})$$

where  $\Delta_{\mu p}^E = (1 + a_{\mu} + \epsilon_1 + \epsilon_2)$

$$a_{\mu} = \frac{\alpha}{2\pi} + 0.75 \frac{\alpha^2}{\pi^2}$$

$$\epsilon_1 = -\alpha^2 \left(\frac{5}{2} - \ln 2\right)$$

$$\epsilon_2 = -\frac{8\alpha^3}{3\pi} \ln \alpha \left(\ln \alpha + \frac{37}{96} + \frac{1}{5} - \ln 4\right)$$

$$\delta_p^{\mu p} = O\left(\alpha \frac{m_{\mu}}{m_p}\right)$$

$$R = \frac{\Delta\nu_{\mu p}}{\Delta\nu_H} = \left(\frac{m_{\mu}}{m_e}\right)^2 \frac{\left(1 + \frac{m_e}{m_p}\right)^3}{\left(1 + \frac{m_{\mu}}{m_p}\right)^3} \frac{(1 + \Delta_{\mu p}^E)}{(1 + \Delta_H^E)} \frac{(1 - \delta_p^{\mu p})}{(1 - \delta_p^H)}$$

$$\Delta\nu_{\mu p} \simeq 4.42 \times 10^{13} \text{ cps or } \lambda_{\mu p} \simeq 6.79 \text{ micron or } 67,900 \text{ \AA}$$



Figure 10. Resonance signal for the transition ( $M_J, M_I$ ) = (1/2, 1/2)  $\leftrightarrow$  (1/2, 1/2) at 5200 G vs impurity concentration. The fitted curves are of the form

$$S = S_0 [ (\bar{v} + \lambda_1) + 4|b|^2 ]^{-1}$$

in which the symbols are defined in Figure 4 and  $\lambda_1 = n \bar{V}_{rel} \sigma_1$ , where  $\sigma_1$  is the fitted cross section,  $n$  is the impurity concentration and  $\bar{V}_{rel}$  is the mean relative velocity of muonium and impurity atom.

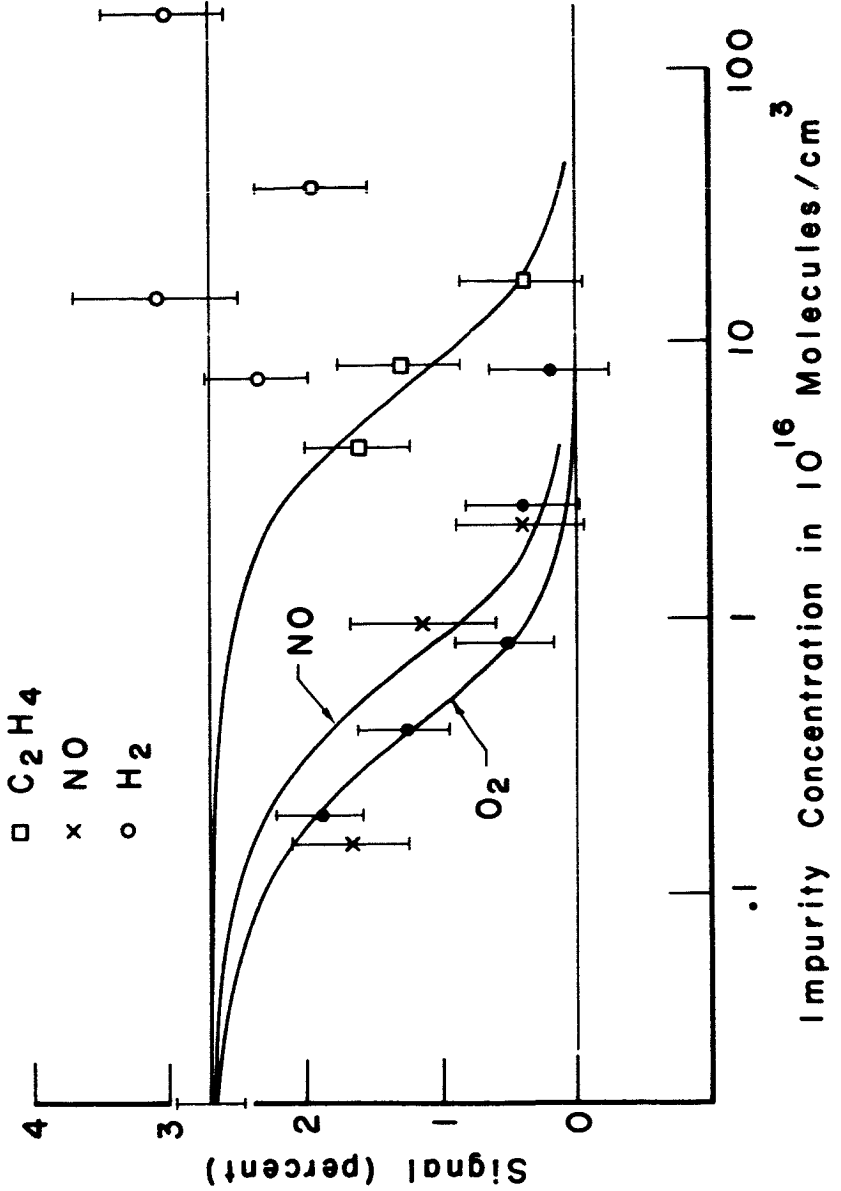
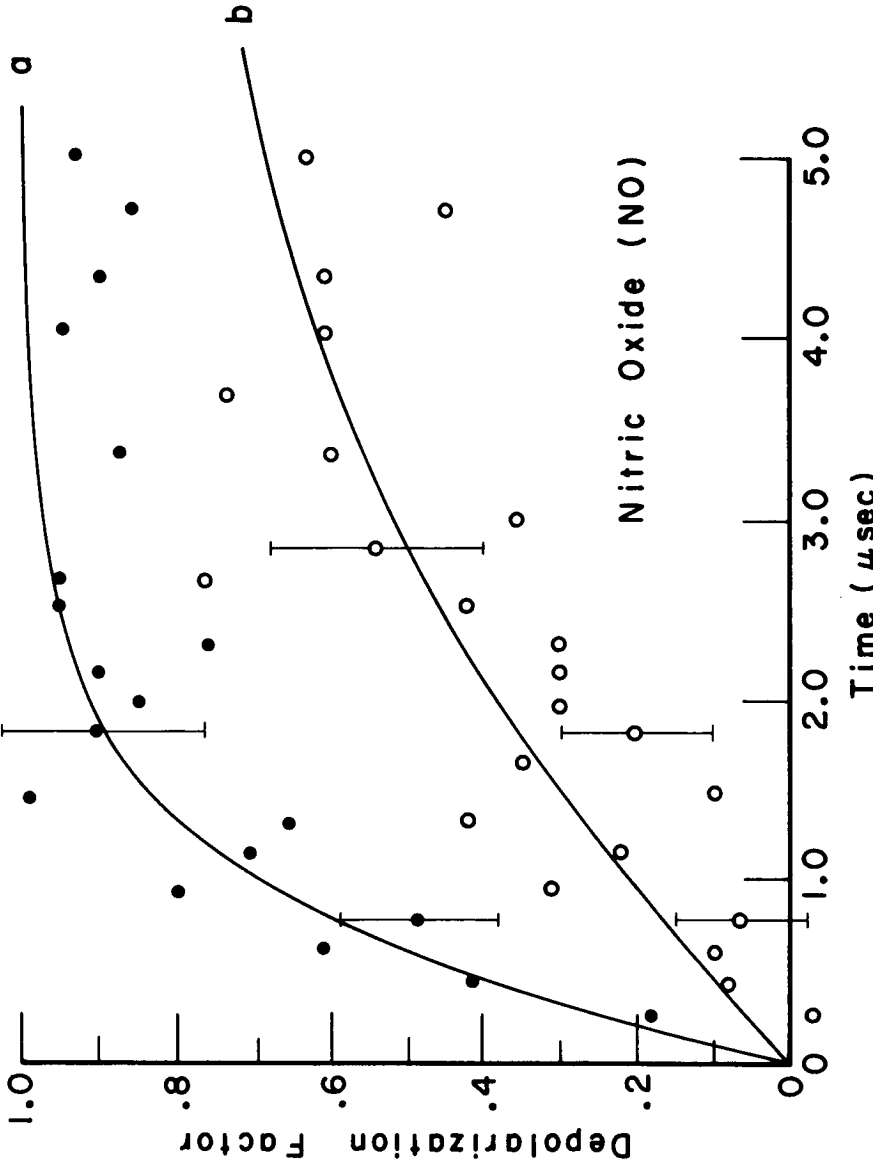


Figure 11. Depolarization factor,  $1 - e^{-\lambda_2 t}$ , vs time, where  $\lambda_2$  is the fitted depolarization rate, under the assumption that the muon polarization varies as  $P = P_0 e^{-\lambda_2 t}$ . The partial pressures of NO are 0.37 mm of Hg for curve a and 0.13 mm of Hg for curve b.



# NO Molecule

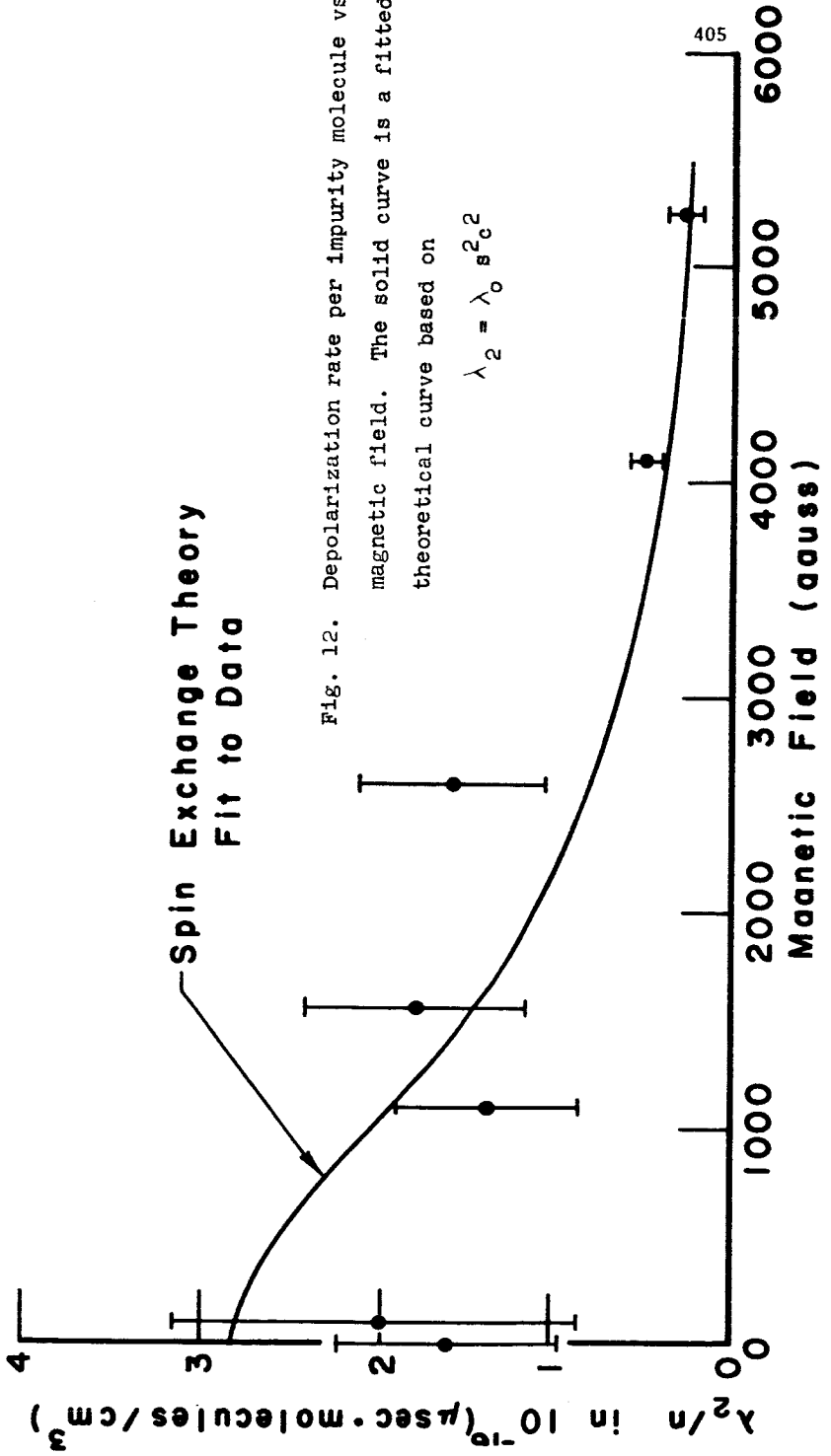


Fig. 12. Depolarization rate per impurity molecule vs magnetic field. The solid curve is a fitted theoretical curve based on

BREIT: I'm just wondering whether in muonium there might not be a somewhat different situation regarding the distortion of the wave function of the electron close to the muon, speaking in the approximation of considering the muon as being fixed. I remember working on that in connection with hyperfine structure in hydrogen in connection with the anomaly of the magnetic moment. The formula has to be modified somewhat on account of those effects, and I wonder whether you have estimated them?

HUGHES: For a point charge in both cases, but with different masses.

BREIT: Well, of course, they wouldn't be exactly point charges. I mean particularly point magnetic dipole. It's a very strong field close to the point, but, of course, a muon is not a point. On the other hand it is perhaps more a point than a proton.

HUGHES: Well, I think those effects would come from modifications due to vacuum polarization-like effects and so on. I believe they would be already in the  $\alpha^2$  order of correction.

BREIT: I don't mean vacuum polarization. I mean the simpler problem of adjusting the electron in the field of a point dipole.

FOLDY: It would be second order in the magnetic point dipole.

BREIT: I don't know that one can really calculate them just in expansion properly, but one can calculate them.

HUGHES: I recall now, those things have been talked about at various time. I think the estimates are that those are small, aren't they?

BREIT: They are certainly small, but now that you are getting down to such very small numbers, the question might come up. I'm not clear on the discrepancy as you stated it. Your last measurement seems to check the theory according to what you have on the board.

HUGHES: Yes, this is all muonium itself and that's in good shape. And all this is used for is to get  $\alpha$  - the viewpoint that I'm taking.

BREIT: It's only in the comparison with hydrogen that there is 43 parts per million or so.

HUGHES: That's right.

TELEGDI: I would like you to offer us your latest thoughts on the matter of pressure-shift and related unsavory topics. What do you think is the importance of it and what's the worthwhile effort to go to lower pressures? This seems to me the fundamental experimental problem here.

HUGHES: Yes, I quite agree with you. To go to lower pressures is totally a question, as you know, of muon rates. There's an improvement program at Nevis which claims it's going to get a factor of 100 to 1000 more muons in three or five years. I know Chicago and certain other places have more muons now. There's some further work, not on muonium itself to try to understand the pressure shift. Hidden in this number is a correction of about a half a megacycle to a megacycle. If one observes  $\Delta\nu$  as a function of the pressure of the argon gas, there's a big dependence, which amounts to something like  $\frac{1}{2}$  to 1 megacycle. We measured it at many pressures in our high field work and it seemed to be fit by a linear curve, that is, many body collisions were not

important. We compared our muonium pressure shift with hydrogen pressure shift which Pipkin and his students had measured in optical pumping experiments and the agreement there was fairly good. There could have been a difference. Pipkin, and also we, are redoing these optical pumping type experiments for the various isotopes of hydrogen. There are two questions. One is whether there might be an isotope dependence of the pressure shift, which is a kind of a sophisticated thing, perhaps, and measurements are going to be made of the three hydrogen isotopes that are easily available to look at this. And, then, the second question is whether there is non-linearity in the curves that we're concerned with and attempts are going to be made to go to as high pressures as possible in the optical pumping experiments to look for that. And then when more muons become available, one will not have to work at 30 atmospheres, we can work at one atmosphere or so and things will be very much better.

TELEGDI: One possible way to get around this sticky point of pressure shift - I'm not trying to imply that you didn't correct properly, but it is a sticky point - is to make use of the fact observed in the atomic work of Pipkin, et. al., and others, that the pressure shift goes in one of two directions, positive and negative, in different noble gasses, and anytime I have contemplated joining you in this field, I thought that it would perhaps be a good idea to go into those mixtures of the noble gasses where the two pressure shifts of the two components are cancelled. Do you think this is madness?

HUGHES: We have considered that, and we don't really see that you gain anything by it. It is true that you certainly can get a mixture of neon and argon. That should give you more or less a straight line, but I think it

doesn't matter whether that's a horizontal line or a line with a slope. In either case you have to know it.

TELEGDI: The slope should be zero.

HUGHES: That's right. Of course, you can say how do you know it's zero for muonium. You might say, well, if it's zero for hydrogen, it's zero for muonium. Maybe that would be good, but if it's sloping for hydrogen, it's the same as for muonium; that should be just as good. I don't think one really gains anything by that.

N66 411  
32749

MUON CAPTURE RATES IN COMPLEX NUCLEI\*

R. E. Welsh, M. Eckhause and R. T. Siegel

College of William and Mary, Williamsburg, Virginia

T. A. Filippas\*\*

Carnegie Institute of Technology, Pittsburgh, Pennsylvania

We wish to summarize the results of a series of experiments to measure negative muon disappearance rates in complex nuclei. The most recent of these<sup>(1)</sup> involved exposure of about 30 targets (each weighing about a pound), most of them natural targets except for two separated isotopes, one Sr<sup>88</sup> and the other Cu<sup>63</sup>. The experiment was performed at the Carnegie Tech cyclotron and the experimental arrangement is shown in Figure 1. Since we were operating in the "medium" Z range, it was advantageous to signal the muon disappearance by detecting a neutron which resulted from muon capture. Thus a pair of liquid scintillation detectors five inches in diameter by five inches in height were employed to detect neutrons. They were protected from charged particles entering on the target sides by the plastic scintillants (No. 5 and No. 6). Pulse shape discrimination was employed in the neutron detectors. The arrival muon signature was  $123\bar{4}$  and the neutron following muon capture was signalled by N<sub>1</sub> or N<sub>2</sub> with neither 5 nor 6. The elapsed time between muon arrival and detection of a neutron following muon capture was then timed using a 100 MC digital timer.<sup>(2)</sup> The raw timing data followed a curve of the form

\* Work supported in part by the national Aeronautics and Space Administration and the U. S. Atomic Energy Commission.

\*\* Present Address: Greek Atomic Energy Commission, Athens, Greece, and CERN.



$A \exp(\lambda t) + B$ , where the exponential slope should be the muon disappearance rate. The muon disappearance rate is then the sum of the muon capture and decay rates and in order to get the capture rate one subtracts the "free" muon decay rate as corrected for Z dependence using the theory of Huff.<sup>(3)</sup> The muon capture rates so obtained are shown in Table 1.

The capture rates so obtained were fitted to the Primakoff formula as modified by the suggestions of Klein, Neil and Wolfenstein.<sup>(4)</sup> The form of the fit used was

$$\lambda_c(Z, A) = \gamma \lambda(1, 1) Z_{\text{eff}}^4 (0.97) (1 + \beta_a) [1 - \delta(A - Z)/2A]$$

The quantity  $\lambda(1, 1)$  represents the spin-averaged muon capture rate on a proton,  $\gamma$  is a measure of the relative phase space available to the neutrino, and  $\delta$  is a nucleon-nucleon correlation parameter whose value from a closure approximation is estimated by Primakoff<sup>(5)</sup> to be 3. Since the relativistic modification given by  $\beta_a$  varies only slightly in magnitude throughout the periodic table, an average value of  $\beta_a = 0.15$  was chosen.

An analysis of the data was also made using a Fermi gas model<sup>(6)</sup> for the nuclear ground state and a closure approximation in the sum on excited states, with all contributions from terms linear in the proton and neutron momenta included. As in the Primakoff formula, the Fermi gas model provides a two-parameter fit of the data, with  $\gamma \lambda(1, 1)$  and the average neutrino energy,  $\nu$ , as the parameters to be determined by a least-squares fit of the data to the model. The effective nuclear charge,  $Z_{\text{eff}}$ , has recently been calculated by Clark, Herman, and Ravenhall<sup>(7)</sup> for elements throughout the periodic table. They have made these calculations in two ways: (1) assuming a Fermi distribution which fits electron elastic scattering data well throughout the periodic table, and (2) assuming a charge density enhanced at the edge of the nucleus. The latter charge density was chosen to be that resulting from differentiation of the Fermi

distribution. The  $Z_{\text{eff}}$ 's calculated by method (2) will be denoted by " $Z_{\text{edge}}$ ".

The " $Z_{\text{edge}}$ " calculations were motivated by the recent work of Foldy and Walecka, (8) in which the  $\mu$ -capture reaction leads primarily to nuclear transitions from the ground state to the giant resonance states. In the electric dipole contribution, for example, the overlap of the nuclear wave functions produces a weighting factor which emphasizes the muon wave-function contributions from the surface of the nucleus. Although this tends to disappear on using closure for the nuclear final states, it is interesting to calculate the average muon probability density, which is usually expressed in terms of  $Z_{\text{eff}}^4$ , also using a weighting proportional to  $\partial\rho/\partial r$ , to see how important such an effect might be. This "edge average" is called  $Z_{\text{edge}}^4$ . (9)

The results of statistical fits of the data to the Fermi gas and Primakoff formulas are shown in Tables 2 and 3 respectively. We attach no significance to the absolute values of  $\chi^2$  obtained, but consider the relative improvement in the fit using  $Z_{\text{edge}}$  to be significant.

## References

- (1) M. Eckhause, R. T. Siegel, R. E. Welsh and T. A. Filippas, Nuclear Physics, to be published (1966).
- (2) M. Eckhause, R. T. Siegel, and R. E. Welsh, Nuc. Inst. and Meth., to be published (1966).
- (3) R. W. Huff, Annals of Physics 16, 288 (1961).
- (4) R. Klein, T. Neal and L. Wolfenstein, Phys. Rev. 138, B86, (1965).
- (5) H. Primakoff, Revs. Mod. Phys. 31, 802 (1959).
- (6) R. H. Klein, Thesis, Carnegie Institute of Technology, Pittsburgh (1963).  
We are indebted to Dr. Klein for suggestions and assistance in making these comparisons.
- (7) B. C. Clark, R. Herman and D. G. Ravenhall (private communication).  
We are indebted to these authors for communicating their results to us prior to publication.
- (8) L. I. Foldy and J. D. Walecka, Nuovo Cimento 34, 1026 (1964).
- (9) We are indebted to Professor Ravenhall for helpful discussions and communications concerning this calculation.

Table 1

| Z  | Element                    | Mean Lifetime, $\tau_m^{\#}$<br>(nsec) | Capture Rate, $\lambda_c^{\#}$<br>( $10^6 \text{ sec}^{-1}$ ) | (A-Z)/2A |
|----|----------------------------|--|---|----------|
| 12 | Mg                         | 1021 $\pm$ 25                          | 0.52 $\pm$ 0.02   | 0.25319  |
| 14 | Si                         | 758 $\pm$ 20                           | 0.86 $\pm$ 0.04   | 0.25076  |
| 16 | S                          | 567.4 $\pm$ 8.4                        | 1.31 $\pm$ 0.03   | 0.25050  |
| 22 | Ti                         | 327.3 $\pm$ 4.5                        | 2.60 $\pm$ 0.04   | 0.27026  |
| 23 | V                          | 282.6 $\pm$ 3.2                        | 3.09 $\pm$ 0.05   | 0.27425  |
| 24 | Cr                         | 264.5 $\pm$ 3.2                        | 3.33 $\pm$ 0.06   | 0.26922  |
| 25 | Mn                         | 225.5 $\pm$ 2.3                        | 3.98 $\pm$ 0.05   | 0.27247  |
| 26 | Fe                         | 206.7 $\pm$ 2.4                        | 4.40 $\pm$ 0.05   | 0.26722  |
| 27 | Co                         | 184.0 $\pm$ 1.7                        | 4.96 $\pm$ 0.05   | 0.27093  |
| 28 | Ni                         | 159.4 $\pm$ 3.1                        | 5.83 $\pm$ 0.11   | 0.26151  |
| 29 | Cu                         | 163.5 $\pm$ 2.4                        | 5.67 $\pm$ 0.09   | 0.27182  |
| 29 | Separated Cu <sup>63</sup> | 162.1 $\pm$ 1.4                        | 5.72 $\pm$ 0.05   | 0.26958  |
| 30 | Zn                         | 161.2 $\pm$ 1.1                        | 5.76 $\pm$ 0.05   | 0.27059  |
| 31 | Ga                         | 163.0 $\pm$ 1.6                        | 5.70 $\pm$ 0.06   | 0.27767  |
| 32 | Ge                         | 167.4 $\pm$ 1.8                        | 5.54 $\pm$ 0.06   | 0.27971  |
| 33 | As                         | 153.8 $\pm$ 1.7                        | 6.07 $\pm$ 0.07   | 0.27977  |
| 34 | Se                         | 163.0 $\pm$ 1.2                        | 5.70 $\pm$ 0.05   | 0.28478  |
| 37 | Rb                         | 136.5 $\pm$ 2.7                        | 6.89 $\pm$ 0.14   | 0.28353  |
| 38 | Sr                         | 130.1 $\pm$ 2.3                        | 7.25 $\pm$ 0.14   | 0.28314  |
| 38 | Separated Sr <sup>88</sup> | 142.0 $\pm$ 5.5                        | 6.61 $\pm$ 0.27   | 0.28386  |
| 40 | Zr                         | 110.8 $\pm$ 0.8                        | 8.59 $\pm$ 0.07   | 0.28076  |
| 42 | Mo                         | 103.5 $\pm$ 0.7                        | 9.23 $\pm$ 0.07   | 0.28078  |
| 45 | Rh                         | 95.8 $\pm$ 0.6                         | 10.01 $\pm$ 0.07  | 0.28135  |
| 46 | Pd                         | 96.0 $\pm$ 0.6                         | 10.00 $\pm$ 0.07  | 0.28389  |
| 47 | Ag                         | 88.6 $\pm$ 1.1                         | 10.88 $\pm$ 0.14  | 0.28232  |
| 52 | Te                         | 105.5 $\pm$ 1.2                        | 9.06 $\pm$ 0.11   | 0.29629  |
| 72 | Hf                         | 74.5 $\pm$ 1.3                         | 13.03 $\pm$ 0.21  | 0.29811  |
| 74 | W                          | 74.3 $\pm$ 1.2                         | 13.07 $\pm$ 0.21  | 0.29834  |
| 80 | Hg                         | 76.2 $\pm$ 1.5                         | 12.74 $\pm$ 0.26  | 0.30000  |
| 82 | Pb                         | 73.2 $\pm$ 1.2                         | 13.27 $\pm$ 0.22  | 0.30214  |

# Errors quoted are statistical standard deviations only.

Table 2 -

Computed results of Fermi gas fits to muon capture rates

| Number of Elements | Effective Nuclear Charge | Avg. Neutrino Energy | $\gamma\lambda(1,1)$ | $\chi^2$ |
|--------------------|--------------------------|----------------------|----------------------|----------|
| 57                 | $Z_{\text{eff}}$         | 66.4 Mev             | 184/sec              | 2000     |
| 57                 | $Z_{\text{edge}}$        | 81.2 Mev             | 158/sec              | 1300     |

Table 3 -

Computed results of Primakoff fits to muon capture rates

| Number of Elements | Effective Nuclear Charge | $\gamma\lambda(1,1)$ | $\delta$ | $\chi^2$ |
|--------------------|--------------------------|----------------------|----------|----------|
| 57                 | $Z_{\text{eff}}$         | 151/sec              | 3.14     | 2100     |
| 57                 | $Z_{\text{edge}}$        | 140/sec              | 3.01     | 1300     |

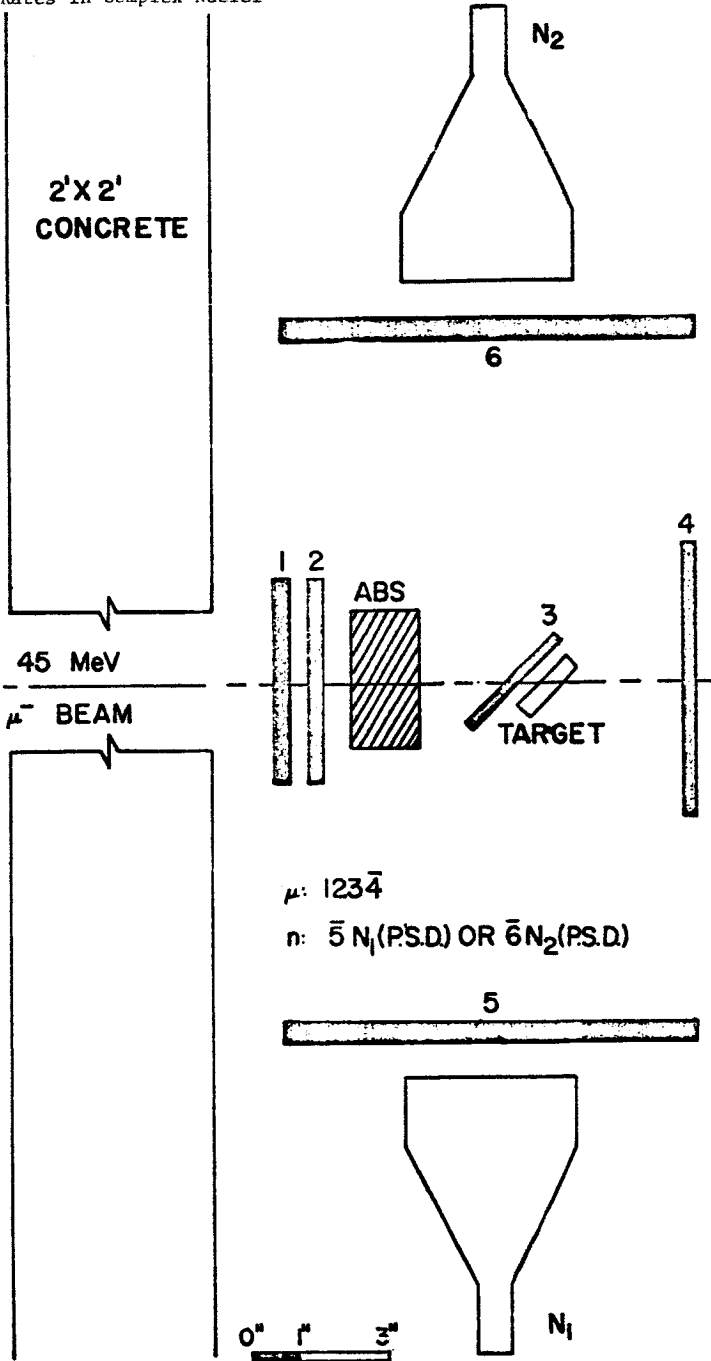


FIGURE 1: Counter arrangement.

BLOCK: How do these data fit with earlier data on this subject experimentally?

WELSH: There were a few disagreements. Perhaps three or four elements in which quoted errors on this experiment and quoted errors on previous experiments did not overlap, but for the most part they agreed well. In each of our three runs we repeated some elements, lead for example, and we achieved consistent results to within accuracies of the order of a nanosecond.

TELEGDI: The novelty as I see it is in this proposed Z edge which is a factor in front of the Pauli Exclusion principle bracket. One point that I don't understand clearly is the philosophy of a chi-squared fit to something which is in no way a law of nature like the Balmer formula. I mean that the Delta inside the Primakoff Formula is not meant to be constant except in a very raw sense, so that if one has a law which contains an unfixed parameter, the interpretation of its validity or its test by statistical hypothesis through chi-squared is something which I do not fully comprehend.

WELSH: Perhaps the strongest statement I would make is that if one assumes Delta to be constant over the range of elements above  $Z = 10$  and omits Al, Na and P which might show large hyperfine effects, then it is probably not without meaning to comment on relative goodness of fit.

\*COMPARISON OF THE LIFETIMES OF POSITIVE AND NEGATIVE PIONS\*

David S. Ayres, Richard D. Eandi<sup>†</sup>, Arthur S. Greenberg, Robert W. Kenney, Richard J. Kurz, and Burns Macdonald<sup>††</sup>, Lawrence Radiation Laboratory, Berkeley, California; David O. Caldwell, University of California at Santa Barbara; and Brenton F. Stearns, Tufts University.

We describe here an experiment currently in progress at the Berkeley 184-in. synchrocyclotron and designed to measure the total lifetimes of positive and negative pions and the ratio of these lifetimes. Results presented here are based on a preliminary analysis of the data accumulated thus far.

CPT invariance is a sufficient but not a necessary condition for the equality of the total lifetimes and masses of particle and antiparticle. In view of the possible large violations of C and CP invariance we may use such equalities as evidence for CPT invariance.

The present upper limit on the experimental error in the ratio of the lifetimes of particle and antiparticle is 0.1% for  $\pi^+$  but is only 10%, approximately, in the cases of  $\pi^0$  and  $K^0$ . The present experimental values for  $\pi^+$  and  $\pi^-$  lifetimes is summarized in Table I. (Slide 1)

Obviously the lack of precision in the ratio of lifetimes comes from the experimental difficulty in measuring the lifetime of negatively charged particles, although we note that there are discrepancies between the three most recent determinations of the  $\pi^+$  lifetime.

In the case of positively charged particles an accurate measurement of the lifetime may be made by stopping the particle in scintillator and observing the decays of the particle at rest. The capture and subsequent absorption of strongly-interacting, negative particles at rest makes this type of measurement

\*Work performed under the auspices of the U. S. Atomic Energy Commission.  
†Present address: DESY, Hamburg, Germany.  
††Present address: Virginia Polytechnic Institute, Blacksburg, Virginia.

N66 32750  
419



impossible. For  $\mu^-$  the very low absorption rate due to the weak interaction in hydrogen has allowed an accurate  $\mu^-$  lifetime determination. Thus it is necessary to perform the lifetime measurement for negative particles in flight.

In our experiment the  $\pi^+$  lifetimes are determined by measuring the attenuation due to decay as a function of distance of nearly identical beams of  $\pi^+$  and  $\pi^-$ . The layout of the pion beam is shown in Fig. 1 (Slide 2). The pions are produced in collisions of the external proton beam ( $T = 732$  MeV) with a 6 in. long Be target. At this energy the number of  $\pi^+$ 's produced per incident proton is about five times the number of  $\pi^-$ 's produced. Therefore the  $\pi^+$  rate relative to the background resulting from the proton beam is also five times the  $\pi^-$  rate relative to background. The beam momentum is analyzed by the bending magnets  $M_1$  and  $M_2$  and geometrically defined by five thin scintillators,  $S_1$  to  $S_5$ , and four anticoincidence scintillators,  $A_1$  to  $A_4$ , which are simply counters with a 1 in. hole in the center. The entire trajectory after  $S_2$  is in vacuum. The central momentum of the beam is 315 MeV/c and the full width at the base of the momentum distribution is 2%. The angular spread of the beam is less than  $\pm 1$  deg. The  $\pi^+$  beam contains approximately 6%  $\mu^+$  and 1%  $e^+$  and the  $\pi^-$  beam contains approximately 6%  $\mu^-$  and 3%  $e^-$ . The  $\pi^+$  rate is 50/sec and the  $\pi^-$  rate is 10/sec. At this time all of these numbers are preliminary and further measurements of these quantities will be made. The polarity of the beams is changed by reversing the fields in the magnets of the beam transport system.

The determination of the exponential attenuation of the beams is accomplished by measuring the number of pions in the beam as a function of distance along the beam trajectory. Measurements are made without the quadrupole, Q, up to 17 ft past  $A_4$  and with the quadrupole up to 36 ft past its exit end. At the beam

momentum used this maximum distance corresponds to 0.77 mean lifetimes in the pion rest frame.

The pion detector is a velocity-selecting, liquid hydrogen Cerenkov counter. A schematic diagram of the counter is shown in Fig. 2 (Slide 3). The Cerenkov light produced by a particle which traverses the radiator is focused by the optical system in a ring at the ring aperture, A. The diameter of this ring focus is a function of the angle of emission of the Cerenkov light and hence of the velocity of the particle. A cylindrical mirror whose axis is parallel to the optical axis of the lenses is contained in the hydrogen flask in order to have full efficiency across the 4-inch diameter of the radiator. In order to reject particles with trajectories inclined to the optical axis of the counter, the coincidence ring is surrounded by a concentric anticoincidence ring. The momentum resolution of the counter is  $\pm 3\%$  (HWHM) and the angular resolution is  $\pm 3$  deg (HWHM).

In this experiment the ring aperture which masks the coincidence photomultiplier has a diameter which corresponds to the 11 deg Cerenkov emission angle of 315 MeV/c pions ( $\beta = 0.913$ ). Momentum analyzed electrons and muons in the beam have higher velocities and hence are not counted. Muons from 315 MeV/c pion decays have a range of velocities that includes  $\beta = 0.913$ , however, these muons are emitted at 7 deg with respect to the beam direction.

Thus far the data have been taken at 7 points after the quadrupole.  $\pi^+$  and  $\pi^-$  data are taken at each point alternately. The logarithm of the ratio <sup>of</sup> pion counts/beam counts as a function of distance along the beam trajectory is fitted with a straight line by the least squares method in order to determine the slope of the curve. This slope is equal to  $m_\pi/v_\pi c\tau_\pi$ . At the present time we have the following results:

$$\pi^+ \text{ slope} = 1.429 \pm 0.005 \times 10^{-3} \text{ in.}^{-1}$$

$$\pi^- \text{ slope} = 1.454 \pm 0.012 \times 10^{-3} \text{ in.}^{-1}$$

The quoted errors are statistical only because complete studies of systematic errors have not been made yet. At this point multiplying the errors by a factor of two would be prudent. If we assume that our preliminary value of 315 MeV/c for the beam momentum is correct these correspond to

$$\pi^+ \text{ lifetime} = 26.26 \pm 0.08 \text{ nsec.}$$

$$\pi^- \text{ lifetime} = 25.80 \pm 0.21 \text{ nsec.}$$

Because possible systematic effects have not been completely studied we prefer not to give a value for the ratio of lifetimes with an error, but rather to state that the upper limit on the error in the ratio is about 2% at present. We feel that continued datataking and more complete analysis will yield an eventual accuracy of about 0.3% to 0.5%.

| $\pi^+$ Lifetime (sec) |   |
|------------------------|---|
| $25.46 \pm 0.32$       | Abell et al., Phys. Rev. 102, 115 (1956)    |
| $25.01 \pm 0.04$       | McLerran et al., Phys. Rev. 102, 115 (1956) |
| $24.94 \pm 0.02$       | Lucas et al., Phys. Rev. 102, 115 (1956)    |
| $\pi^-$ Lifetime (sec) |   |
| $28.5 \pm 2.5$         | McLerran et al., Phys. Rev. 102, 115 (1956) |
| $29.5 \pm 1.7$         | Burba et al., Phys. Rev. 102, 115 (1956)    |
| $\pi^0$ Lifetime (sec) |   |
| $0.99 \pm 0.01$        | McLerran et al., Phys. Rev. 102, 115 (1956) |
| $1.04 \pm 0.11$        | Burba et al., Phys. Rev. 102, 115 (1956)    |

Table I. The experimental values for  $\pi^+$  and  $\pi^-$  lifetimes.



KAPLAN: Do you attribute any significance to the present difference or could it be instrumental?

MacDONALD: This could be instrumental after perhaps a correction for the cyclotron fringing field. There's no reason to suspect that they shouldn't be the same in our experiment. The bending magnets were kept to within .05% measurement of the magnetic field. So, there's no problem with that.

WELSH: Is there any mechanism other than decay that could preferentially remove minuses rather than pluses. There is gas in you path, right; it's not a vacuum pipe.

MacDONALD: I beg your pardon. I neglected to say that there is a vacuum pipe in the path. The vacuum pipe is after the second scintillator, well in front of the second bending magnet.

WELSH: I see, so, all of the path over which you consider the decay is vacuum.

MacDONALD: Yes. The vacuum pipe was added as we moved the Cerenkov counter down the stream.

N66 32751  
427

A Measurement of the Lifetime of the Positive Pion

K.F. Kinsey, L. Lobkowitz, M.E. Nordberg, Jr.

Department of Physics and Astronomy  
University of Rochester, Rochester, New York

Considering its position as one of the fundamental particles of physics, some of the properties of the pion are rather poorly known. The mean life, in particular, prior to our undertaking this experiment, was known to a stated accuracy of 1%. This number was, moreover, based on the analysis in all experiments of a total of about 10,000 pion decays. Fast electronic techniques and good low energy pion beams have made possible a re-determination of the lifetime, using an essentially unlimited number of decay events.

In this experiment we have measured the decay of about  $10^8$  positive pions.

The counter array is shown in Fig. 1. A stopped pion is indicated by a 1 2 3  $\bar{4}$  coincidence. The decay muon has a short range and does not leave No. 3, so produces a 3( $\bar{2}$  or  $\bar{4}$ ). As a further tag on the identification of the decay, the beta decay of the muon was detected, being identified by a 3( 2 or 4 ) coincidence.

The electronic apparatus is shown in Fig. 2. The crucial part of the circuitry is in the top two lines: The  $\pi$  pulse initiates one 350 nsec pulse, the  $\mu$  initiates the second. The time overlap of these pulses is converted to an amplitude by the time to pulse height converter and recorded

PRECEDING PAGE BLANK NOT FILMED.

in the 400 channel analyzer. The rest of the circuitry is responsible for detecting the electron in a 5  $\mu$ sec gate after the  $\mu$  pulse and for suppressing analysis if a second beam particle entered the apparatus.

To provide a time calibration a source of pulse pairs was provided and substituted for the signals from the No. 3 phototube. This source was produced by gating a continuous chain of pulses from an oscillator as shown in Fig. 3. The oscillator frequency was counted with a crystal controlled EPUT meter while the calibration point was being recorded. A set of 23 points was recorded before and after each data run. Several other checks on system gain and stability were made during the experiment.

The calibration was linear to within 1% and the non linearity was taken into account by fitting the calibration data with a cubic polynomial fit. In addition the non-linearity was primarily at the extreme ends of the range. In analysis involving only a limited range of data the calibration curve was recalculated including only the region of interest.

The most serious problem was that of recovery of the number 3 counter, so that its response to the muon pulse would be unaffected by the previous pion pulse. Effects of ringing, reflections, etc. in the system would show up as irregularities on the decay curve. These effects could not be completely eliminated, but they could be minimized. We also took pains to reduce the background to a minimum so that the decay curve could be followed to later times.

Several parameters were varied for different runs to test for systematic



effects. None of these systematic tests showed any statistically significant effect.

### Analysis

The direct expression for the mean life could not be used because of the background. In principle the time dependence of the background should be taken into account. However the background per channel in this experiment was about 4 or 5 decades below the real counting rate. The primary source was the dead time of No. 3 which let about half of the  $\pi$ 's decay undetected. The logic for these decays could be completed by a random " $\mu$ " count followed by the electron decay from the real  $\mu$  or by the electron imitating a  $\mu$ , followed by a random "electron". Since both of these effects were small and had a decay time  $\sim 100$  times the  $\pi$  decay time, the background was treated in the analysis as though it were a constant.

The data for each run was fit by a search program which found the values of the mean lifetime and the background which gave the lowest chi-squared. This was done several times for each run cutting off the data at different early times. For each run there was a "best" value corresponding to the lowest error. These best values are displayed in Fig. 4. They are consistent with a random distribution of the same mean deviation as the uncertainty on each run. The mean is 26.38 nsec. A subset of 21 runs was combined into a consolidated run and analyzed to give a value of 26.41 nsec: Fig. 5. A different subset of 25 runs was selected, eliminating runs for which the value of  $\tau$  vs. lower cutoff was not quite self consistent.

The results are shown in Fig. 6. The mean of the best values was 26.41 nsec.

We chose  $26.40 \pm 0.08$  as our value. The uncertainty is larger than statistics would suggest, but this takes into account the small dependence on the low cutoff. Within this range, the lifetime is constant over several mean lives.

This number disagrees with the earlier value of  $26.51 \pm 0.26$  nsec. and with the recent report of Eckhause et al<sup>1</sup> of  $26.01 \pm 0.02$  nsec. The latter is the more serious discrepancy. There are several differences in technique between the two experiments, but no obvious grounds for a disagreement of this order.

---

Reference

1. M. Eckhause, R. J. Harris, Jr., W. B. Shuler, R. T. Siegel, R. E. Welsh; Phys. Letters 19, 4, 348 (1965).

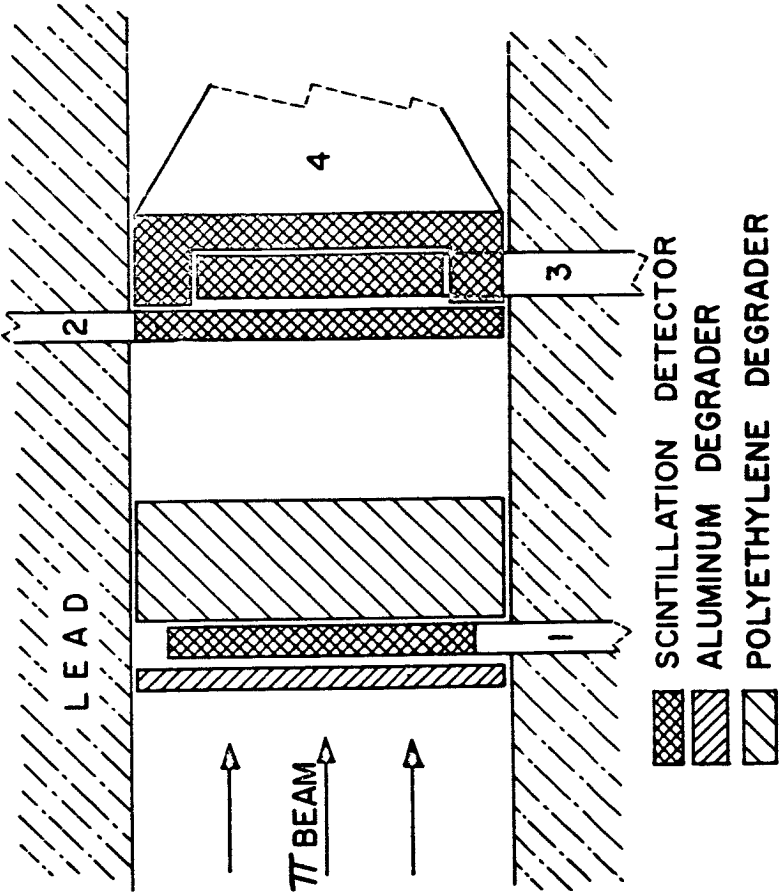


Figure 1. Experimental Counter Array.

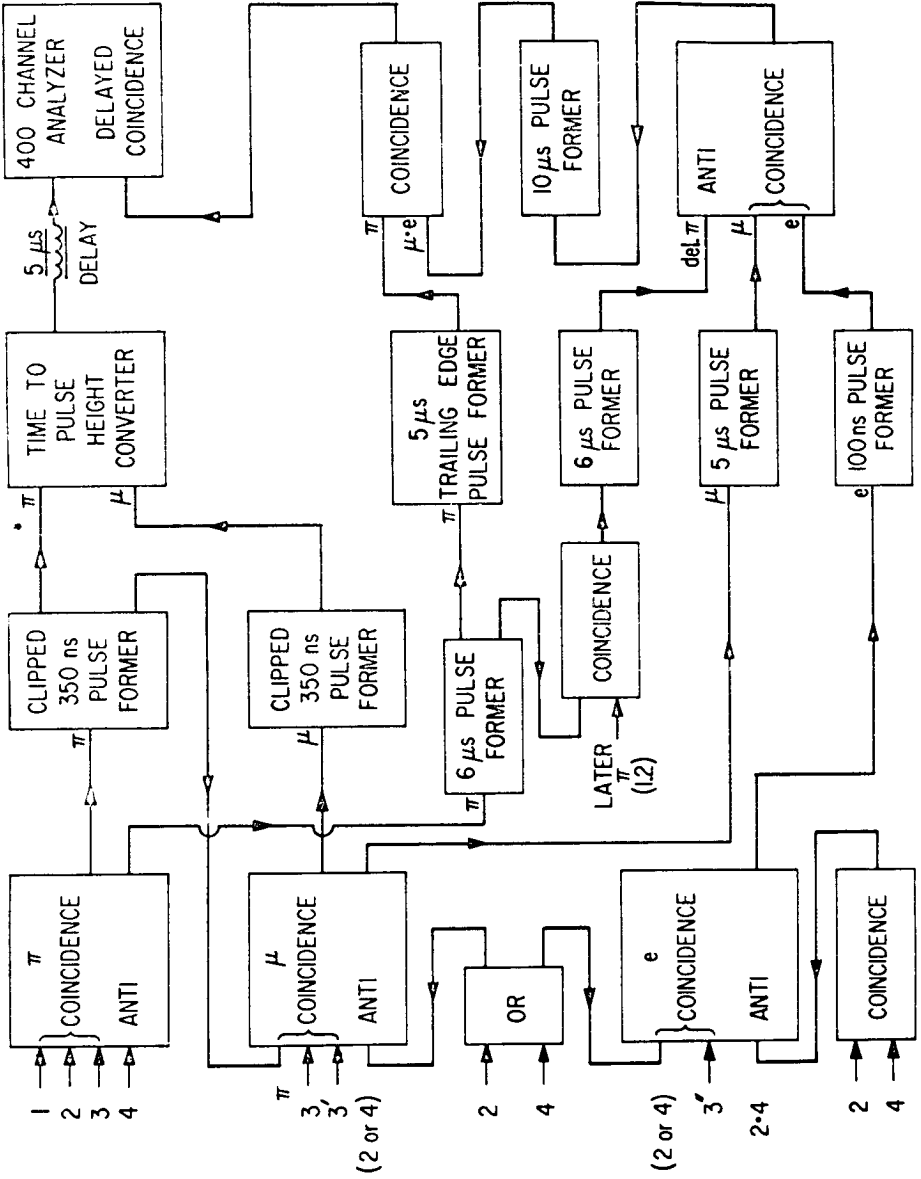


Figure 2  
Electronic Apparatus logic diagram.

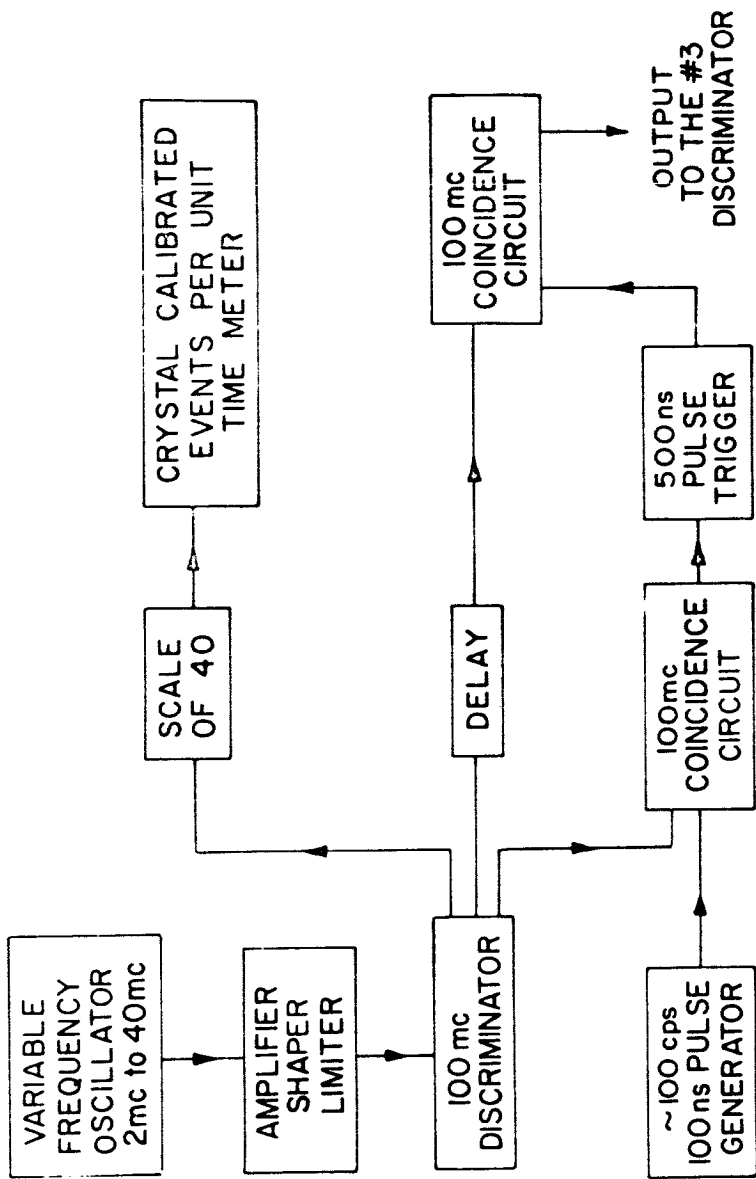


Figure 3  
Electronic logic circuit for time calibration.

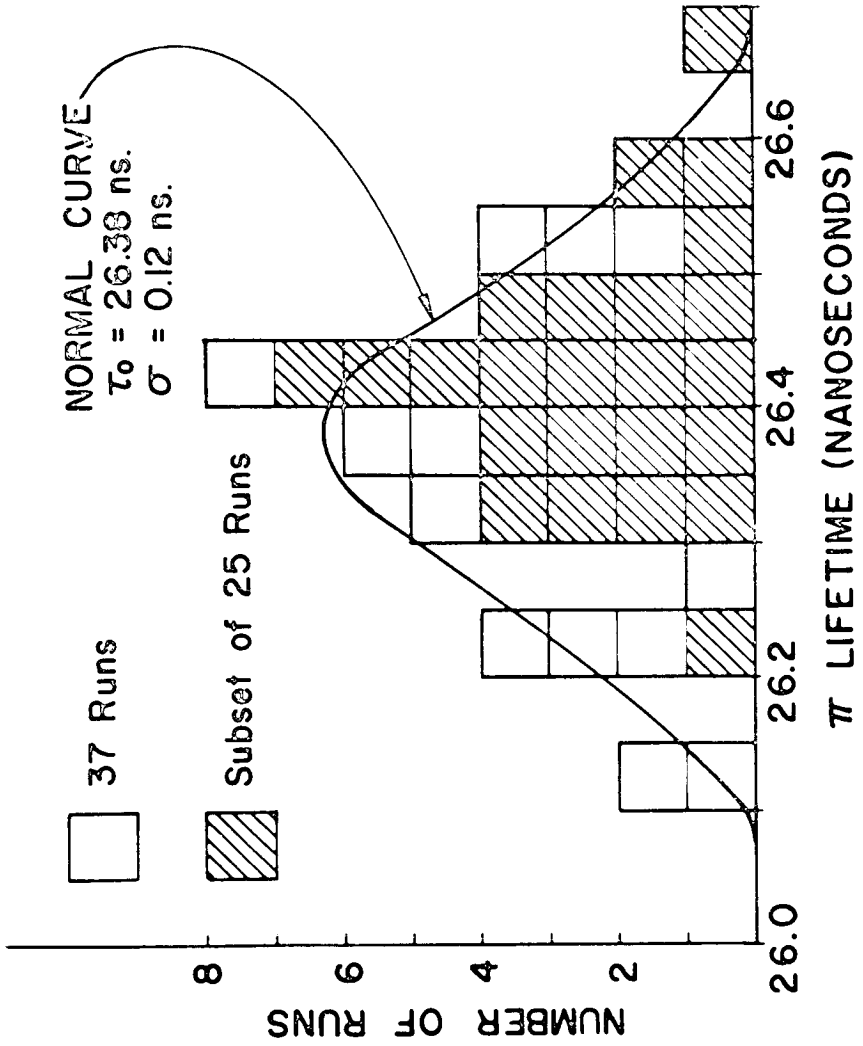


Figure 4  
Histogram of lifetime runs.

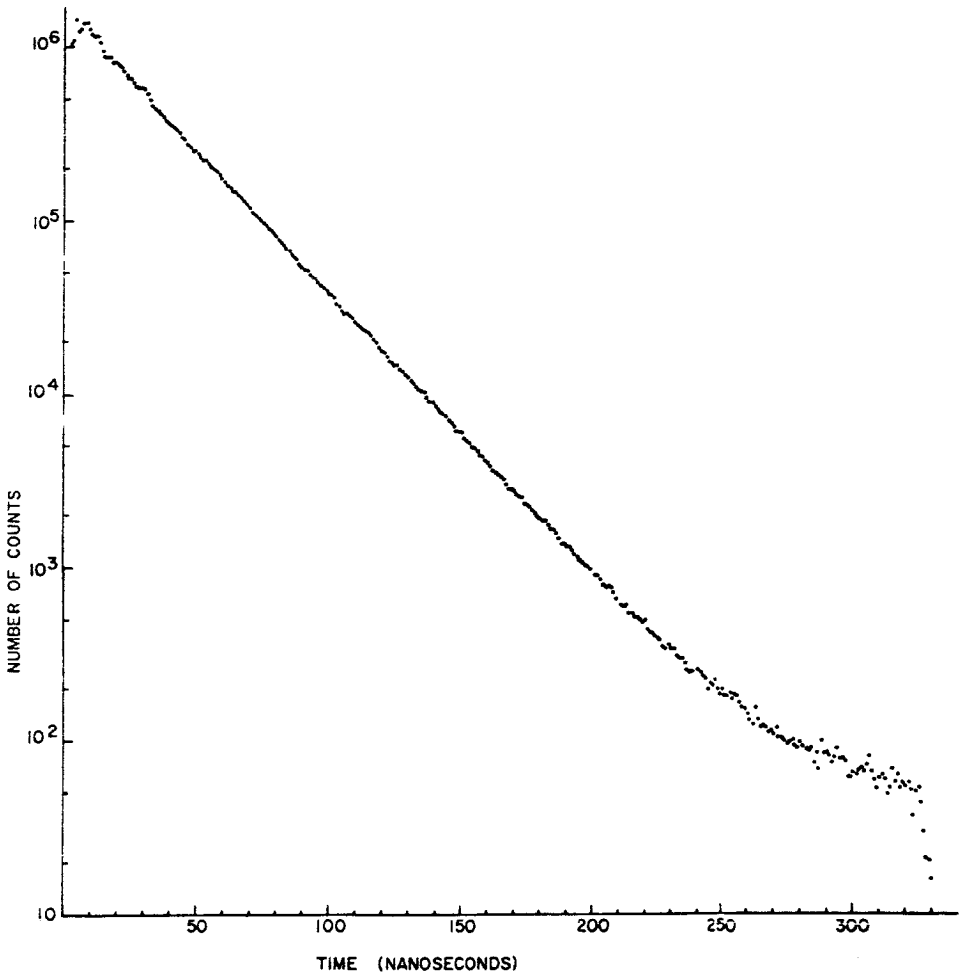


Figure 5  
Typical lifetime run spectrum.

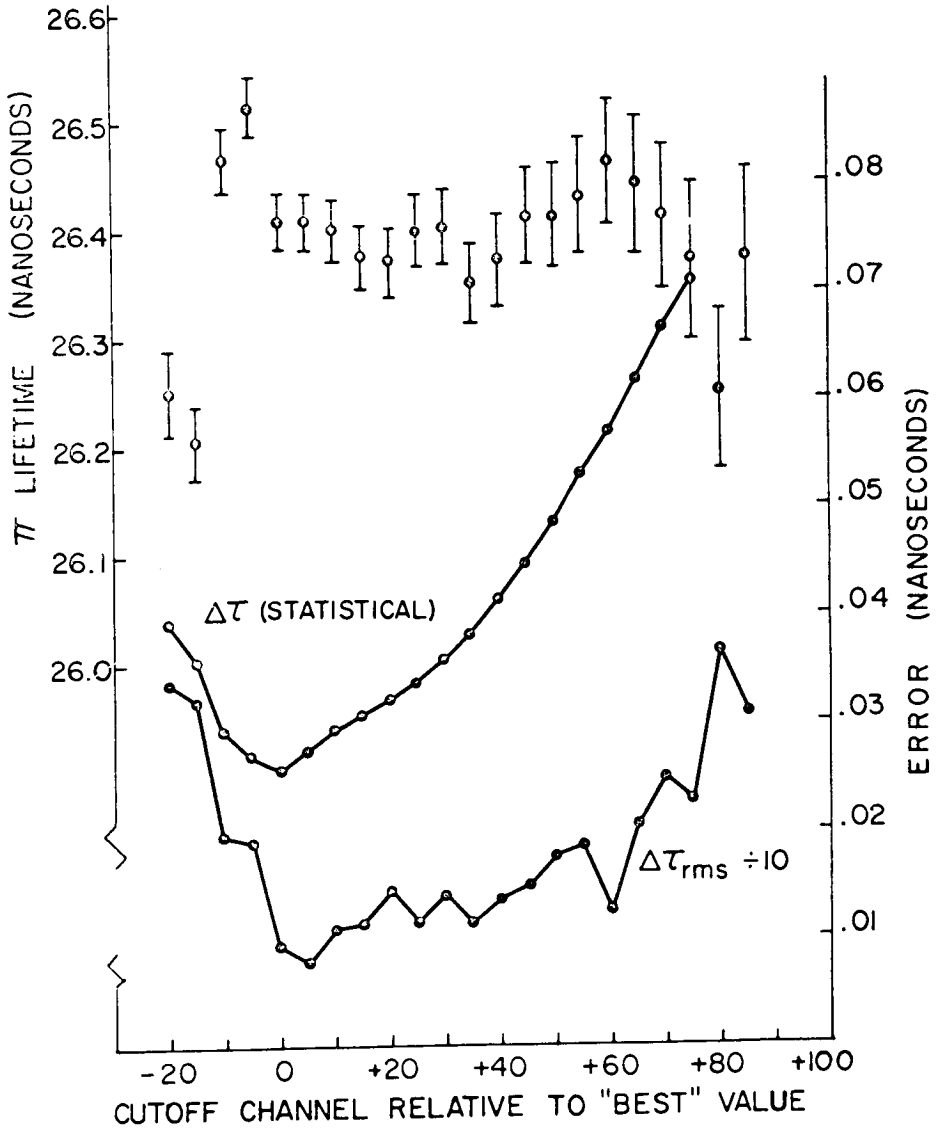


Figure 6  
Effects of varying cut off channel on  $\pi$  lifetime.



WELSH: It appears that counter two is triggered by the stopping  $\pi$  and also serves as an anti-coincidence for detection of the decay  $\mu$ on. This means that were there to be any ringing in counter two, then the stopping  $\pi$  giving ringing could anti-coincidence its own decay  $\mu$  at later times and so might show systematic effects on the lifetime. I was wondering if you looked for effects like this in counter two or if perhaps you took lifetime curves versus high voltage on counter two or something like that.

KINSEY: We did do high voltage lifetime checks. Also, I point out that this effect is essentially the same one as the counter number three tests, and that actually our analysis, due to very low background, could be started about two mean lives, 50 nanoseconds after time zero by which time everything non-exponential was gone.

WELSH: Yes, it is the same as the tests you made on counter three. I just wondered if the same tests were made on counter two because you hadn't mentioned it, and, as I recall, your preprint hadn't mentioned it.

KINSEY: We did look at this. We didn't worry quite as much about it as we did for three, but it was handled the same way, and the problems are essentially the same.

WELSH: The second question I wanted to ask concerned the logic. It is true, is it not, that if a second pion stopped anytime within the maximum time analysis range and not just before detection of the decay  $\mu$ , you would throw out that event and not analyze it.

KINSEY: Right. If another particle came down the beam path, it didn't have to

stop, the second incident particle vetoed analysis of the whole event.

WELSH: Even though the decay muon might have already been detected from the first stopped pion?

KINSEY: Right.

## OPTICAL MODELS FOR PION-NUCLEUS SCATTERING

M. M. Sternheim\*

University of Massachusetts, AmherstE. Auerbach<sup>+</sup>Massachusetts Institute of Technology

In this paper we will review the problem of calculating the elastic scattering of pions by nuclei, and will discuss some optical model calculations which are still in progress. Preliminary results will be presented.

We can approach this problem in two related ways. We can start with some information about the pion-nucleon interaction and nuclear structure, and calculate the pion-nucleus scattering. Assuming we may trust the necessary approximation, this affords a test of our understanding of the pion-nucleus system. This approach has been taken by Watson<sup>1</sup> and others and has had semiquantitative success.

Alternatively, we can fit the pion-nucleus data with a phenomenological model and try to extract some new information from this model. In particular, we can attempt to obtain the pion form factor, as was recently suggested.<sup>2</sup> The optical model is the most promising way to implement this idea.

\* Work supported in part by the National Science Foundation.

+ Work supported in part by the U. S. Atomic Energy Commission.

N66 32752

Watson has shown that the amplitude for pion-nucleus scattering can be written as a multiple scattering expansion. He takes

$$H = H_0 + \sum_{\alpha=1}^A V_{\alpha} \quad ,$$

where

$$H_0 = \text{K.E.}_{\pi} + H_{\text{nucleus}} \quad ,$$

and defines the amplitude for scattering of a pion by a bound nucleon to be a solution of

$$t_{\alpha} = V_{\alpha} + V_{\alpha} \frac{1}{a} t_{\alpha} \quad ,$$

$$\frac{1}{a} = \frac{1}{E - H_0 + i\epsilon} = P \frac{1}{E - H_0} - i\pi\delta(E - H_0).$$

Then the pion-nucleus scattering amplitude is given by

$$T = \sum t_{\alpha_1} + \sum' t_{\alpha_1} \frac{1}{a} t_{\alpha_2} + \sum' t_{\alpha_1} \frac{1}{a} t_{\alpha_2} \frac{1}{a} t_{\alpha_3} + \dots \quad (1)$$

where  $\sum'$  means that  $\alpha_i \neq \alpha_{i+1}$  in the sums. Thus  $T$  is a sum of single scattering terms, plus double scattering terms, etc.

If this series converges rapidly enough, a few terms can provide a good approximation. Making small angle approximations, neglecting the off-the-energy shell (principal value) terms, and setting the bound  $t_{\alpha}$ 's equal to the free  $t_{\alpha}$ 's, we obtained<sup>3</sup> reasonable agreement with small angle  $\pi^{-} - C$ ,  $\pi^{+} - Li$  and  $\pi^{-} - 0$  elastic scattering data near 80 Mev. Similarly, we crudely estimated the effect of the pion form factor on  $\pi^{+} - \alpha$  scattering and found appreciable contributions to  $T$  near the minimum.<sup>2</sup>

Watson also showed that if one assumes  $A$  is large and neglects effects of virtual nuclear excitations, summing the series for  $T$  is equivalent to solving a Schrodinger equation containing an optical potential given by

$$(\underline{q}' | v | \underline{q}) = A(\underline{q}' | t | \underline{q}) \rho(\underline{q}' - \underline{q}), \quad (2)$$

where  $\rho(\underline{q})$  is the Fourier transform of the nuclear density. Since  $\rho(\underline{q})$  drops off rapidly with increasing  $q$  for a large nucleus, it is plausible to set  $(\underline{q}' | t | \underline{q}) = (\underline{q} | t | \underline{q})$  in (2), leading to

$$v(\underline{r}) = \text{constant} \cdot f(0) \rho(\underline{r})$$

Cross sections obtained from this simple model fit reasonably well at small angles, but are much too small at large angles.

Kisslinger<sup>4</sup> suggested that since the  $\pi$ - $n$  amplitude is mostly  $p$ -wave, a better approximation is

$$(\underline{q}' | v | \underline{q}') = A(a + bq \cdot \underline{q}') \rho(\underline{q}' - \underline{q}),$$

or, in coordinate space

$$v(\underline{r}) \psi(\underline{r}) = C_0 F \psi - C_1 \nabla \cdot (F \nabla \psi) \quad (3)$$

where  $F(\underline{r}) = \rho(\underline{r})/\rho(0)$ . This gives a wave equation of the form

$$\nabla^2 \psi = (1 + C_1 F)^{-1} [ C_0 F - C_1 \nabla F \cdot \nabla - (E - V_{\text{coul}})^2 ] \psi$$

Rainwater et al<sup>5</sup> noted  $\text{Re } C_1 F = -1$  for some  $r$  value, so that  $(1 + C_1 F)^{-1}$  becomes pure imaginary there. They chose to write this instead as

$$\frac{1}{1 + C_1 F} = 1 - C_1 F + \dots$$

and dropped higher terms. They were able to find parameters which

yielded excellent fits, but could not directly compare their C's with theory. The Saxon-Woods shape was used, with radius  $R = 1.08A^{1/3}f$  (in agreement with electron scattering data) and thickness parameter  $a = .25f$  (half the electron value).

We have applied the original Kisslinger model, without the Rainwater modification. The existing ABACUS optical model program<sup>6</sup> has been modified to take into account the derivative potentials and the relativistic kinematics. We are using the nuclear shell model density function

$$F(r) = \left(1 + \frac{(Z-2)r^2}{3a^2}\right)e^{-r^2/a^2}$$

Electron scattering data gives  $a = 1.6$  for C and 0, 1.65 for He, and 1.7 for Li. For a specific choice of  $C_0$  and  $C_1$ , this shape gives results slightly different from those obtained with the corresponding Saxon-Woods shape.

Our preliminary results indicate that the best fit for  $\pi^- - C$  at 80 Mev is obtained with

$$a = 1.575$$

$$C_0 = .1 - .1i$$

$$C_1 = -1.05 - .47i$$

The corresponding theoretical C's were calculated from Anderson's  $\pi$ -n phase shifts and are

$$C_0 = .1 - .08i$$

$$C_1 = -1.43 - .41i$$

This fit is quite good, with the calculated curve passing through most of the experimental points, but it is not quite so good as Rainwater's fit.

## Optical Model Calculations

These best fit parameters were also used to calculate  $\pi^- - C$  scattering at 69.5 Mev and 87.5 Mev, and  $\pi^- - O$  at 87.5 Mev. The results are in fairly good agreement with the data, and slightly different parameters should give very good fits.

It therefore appears that this model can give a good fit to pi-nucleus scattering, using parameters fairly close to their theoretical values. Arguments can be given to explain the differences. In general, the correct large angle behavior can be obtained, in contrast to the case where no derivative terms are included.

Can we now expect to extract the pion form factor from  $\pi-\alpha$  scattering? We do not yet have a clear answer. Using the best fit 80 Mev carbon C's above we calculated  $d\sigma/d\Omega$  for  $\pi^+ - \alpha$  at 100 Mev. The qualitative features of our earlier estimates again appeared: a very deep minimum and a considerable dependence upon the pion form factor for angles near the minimum. However,  $d\sigma/d\Omega$  was considerably larger at small angles than is indicated in the preliminary experimental data.<sup>7</sup> Hopefully, the work in progress will clarify whether the pion form factor can be determined from  $\pi-\alpha$  scattering, and will indicate the most appropriate energies.

1. K. M. Watson, Phys. Rev. 105, 1388 (1957); Rev. Mod. Phys. 30, 565 (1958); also earlier papers given here.
2. M. M. Sternheim and R. Hofstadter, Il Nuovo Cimento 38, 1854 (1965).
3. M. M. Sternheim, Phys. Rev. 135, B912 (1964).
4. L. S. Kisslinger, Phys. Rev. 98, 761 (1955).
5. Baker, Byfield, and Rainwater, Phys. Rev. 112, 1773 (1958); Edelstein, Baker, and Rainwater, Phys. Rev. 122, 252 (1961).
6. E. Auerbach, BNL Report #6562.
7. K. Crowe, private communication.

ELTON: If I understood you correctly, you said that Rainwater made this modification because he feared embarrassment at the 0 of the coefficient of  $\nabla^2 x$ . You did not make that modification and this did not lead to any embarrassment.

STERNHEIM: Well, the theoretical parameter that goes into  $C_1$  is  $-1.4 - .4i$ . Now, if you take these numbers, you see that the imaginary part is not so small and so it doesn't get too near 0. It may not have physical interpretation. You'd get an imaginary mass if you look at the  $\delta^2$  terms in a sort of effective mass way; just go ahead and calculate and see if you get in trouble and the answer is you don't. As long as you have imaginary parts that are fairly substantial, you don't find that there is any abnormal sensitivity to the mesh size in the calculation or anything else. This seems to behave all right. If you talk to experts in numerical analysis, they can't find any reason why it shouldn't go through if that parameter is not too small.

ELTON: I'm not quite clear about why the embarrassment should be anyway. Of course, if you interpret it in terms of a mass, you'll find it in an infinite mass; but surely the mere fact that the coefficient of  $\nabla^2 x$  is zero, doesn't necessarily lead to a discontinuity in the wave function.

STERNHEIM: I think it's a physical objection rather than a mathematical objection that has lead the earlier workers to make that approximation. If you start out in momentum space you can state that the p-wave part is  $\bar{q} \cdot \bar{q}'$  times a constant. That may be a good fit in certain energy regions, but it is clearly crazy if you go to high enough momentum, for you'd still get an infinite answer instead of the unitary limit. So, somehow you should be cutting things off. That's the argument. Well, you can make an argument that the procedure that they followed in coordinate-space is a way of taking care of the anomalous high energy behavior. This was the argument that they gave, and I think there is



some logic to it. The only trouble is it's too hard to compare the results for the parameters with the so-called theoretical parameters.

WINTER: You use the so-called shell-model density which has an essentially gaussian drop-off at large distances. Of course, we all know that that's really wrong. Wave-functions do have to go like an exponential eventually. Furthermore, the pion nucleus interaction might be affected very heavily by what goes on in the surface. Therefore, might it not be more convincing to use a different density even though this shell-model density is good phenomenology for some purposes?

STERNHEIM: Certainly, it is a question we can study. I think once we do get a region of fit - to the He data for example - we will try making a variety of assumptions about density functions to answer that kind of question. I think indications are that it would not be terribly significant. For example, Saxon-Woods, which really does have an exponential drop off, does give roughly the same kind of results - as the gaussian term. So I don't think empirically there is going to be a big effect, but it will be checked.

ERICSON: I should like to make a remark on the parameters in this optical model. I notice that the parameter that you call  $C_1$ , and I call something else, is for you -1.05 and the theoretical one which you got out of phase shift analysis I suppose is -1.43. Now it's extremely interesting that that is exactly what we get also (provided we make this Lorentz-Lorenz effect I was talking about in my talk previously). We are getting very close to your value; you have not included it and therefore we have a kind of effective value. Also, how did you get the theoretical values for  $C_0$ ?

STERNHEIM: We took some phase-shifts, which are not the best available ones, but some old ones that we happened to have at hand and added up what we got. I

wouldn't be amazed if you told me that if I used some newer values I'd get a different answer, because there are the cancellations which you mentioned yesterday, and the error bars on the phase-shifts are rather large. I haven't bothered to carry through the error bars to the theoretical value yet, but I suspect they are comparable to the theoretical value.

ERICSON: This is also an effective value which I think, in that case, came out by accident to be very close...

STERNHEIM: Empirically, it was very insensitive to what we chose for  $C_0$ . It changed about a factor of 2. It didn't much matter in the final results because  $C_0$  is small, so it doesn't do much as long as you keep it small.

N66-32753

PHASE SHIFT ANALYSIS FOR ELASTIC  $\pi^+ - \text{He}^4$  SCATTERING IN THE ENERGY  
INTERVAL 100-160 MEV/c

M. M. Block, I. Kenyon, J. Keren, D. Koetke, P. K. Malhotra

R. Walker, H. Winzeler

Northwestern University

Introduction

This report concerns a continuing experiment on the phase shift analysis of  $\pi - \text{He}^4$  elastic scattering being performed by the Northwestern University Helium Bubble Chamber Group. The recently completed 20" Helium Bubble Chamber was exposed last fall to  $\pi$ -meson beams at the Chicago Cyclotron. 150,000 pictures were taken with  $\pi^+$  incident and 150,000 pictures with  $\pi^-$  incident, at a beam momentum of  $137 \pm 12$  Mev/c. Figure 1 shows a typical elastic scattering event. The active volume of the chamber is 20" long in the beam direction, 10" high and 12" deep: in the experiment the applied field was 15 kilogauss.

There are two interests in this analysis. The first is the study of nuclear-coulomb interference effects at high momentum transfer with the eventual objective of measuring the  $\pi$ -meson form factor. To get an idea of the size of effect to be expected we write the elastic scattering amplitude in a simple minded way:

$$a(\theta) = \frac{1}{k} \left\{ \frac{Z\alpha}{B(1-\cos\theta)} F_{\pi}(g^2) F_{\alpha}(g^2) + \delta_0 + 3\delta_1 \cos\theta \right\}$$

where  $k$  is the momentum,  $\delta_0$  and  $\delta_1$  the phase shifts for pure nuclear scattering and  $F_{\pi}(g^2)$  and  $F_{\alpha}(g^2)$  the form factors of the  $\pi$ -meson and  $\alpha$  particle at momentum transfer  $g$ . Thus at  $90^\circ$  the ratio of the interference term in the differential elastic cross-section to the purely nuclear term is:

$$D_{90^\circ} = \frac{2Z\alpha}{B\delta_0} F_{\pi} F_{\alpha}$$

which for the present experiment gives

$$D_{90^0} = 0.022/\delta_0$$

if we take  $F_\pi \approx 1$ .  $1/\delta_0$  then appears as an amplification factor. It is desirable to have a low value of  $\delta_0$  and for the non-coherent scattering to be small. Spin 0 targets have the tremendous advantage that there is no spin-flip amplitude: this term contributes to the denominator of D but not to the numerator because its amplitude is incoherent with the coulomb scattering amplitude. Among the available spin zero targets the  $\text{He}^4$  nucleus has the unique position of having no low lying excited states, the first being at 20 Mev. This means in the present experiment that with 60 Mev  $\pi$ -mesons incident the elastically scattered pions have 60 Mev energy and the inelastically scattered  $\pi$ -mesons have 40 Mev energy at most. The experimental distinction of the elastic events is very clear-cut. Sternheim and Hofstadter have suggested making the difference experiment, that is to measure both the  $\pi^+ - \text{He}^4$  and the  $\pi^- - \text{He}^4$  differential elastic cross-sections and take one from the other leaving the coulomb - nuclear interference part. This is the line of attack we are pursuing.

The second interest of the phase shift analysis program is connected with the projected studies of light hypenuclei to be made using the Northwestern Helium Bubble Chamber. For the decay  $\text{H}^4 \rightarrow \pi^- + \text{He}^4$ , the rate calculation requires knowledge of the final state effects. As all the particles involved have spin zero this requires the s-wave phase shift alone. The pion momentum is 133 Mev/c.

### Experimental Results

Our data so far are based on 4000 frames. In Figure 2 the differential elastic cross-section is shown for the events below the median momentum, of the beam (141 Mev/c). This bin has an average momentum of  $126 \pm 11$  Mev/c which is

conveniently close to the momentum of the pion in the hypernucleus problem mentioned above. Two sets of phase-shifts are possible and these differ essentially by the interchange of the sign of the phase shifts. Obviously we need increased statistics before we can pick out the correct phase shifts. In the fits the imaginary parts of the phase shifts have been obtained from the inelastic cross-section which is discussed in paper CK-8. Figure 3 shows a similar duality of fits for the upper momentum bin,  $151 \pm 10$  Mev/c.

Since the various solutions at present acceptable all have phase shifts of very similar magnitude we can get an estimate of D which is a kind of figure-of-merit of the difference experiment. In Figure 4  $|D|$  is plotted against  $\cos^2 \theta$ . It shows a region where  $|D|$  is 20% near  $90^\circ$ . For one choice of the phase shifts the first part of the curve has D positive and the second part has D negative. The reverse is true for the second choice of phase shifts.

In conclusion we can say that with increased statistics the S- and P-wave phase shifts will be determined: however on the basis of present results it is not yet clear what information the difference experiment will give on the  $\pi$ -meson form factor.

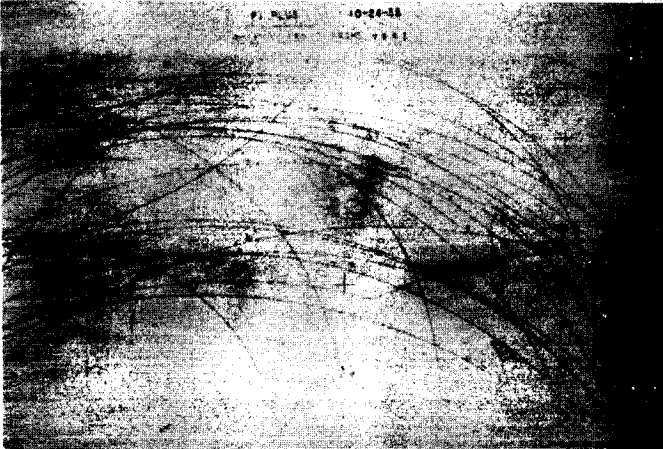


Figure 1 - Typical elastic scattering event in 20" He bubble chamber

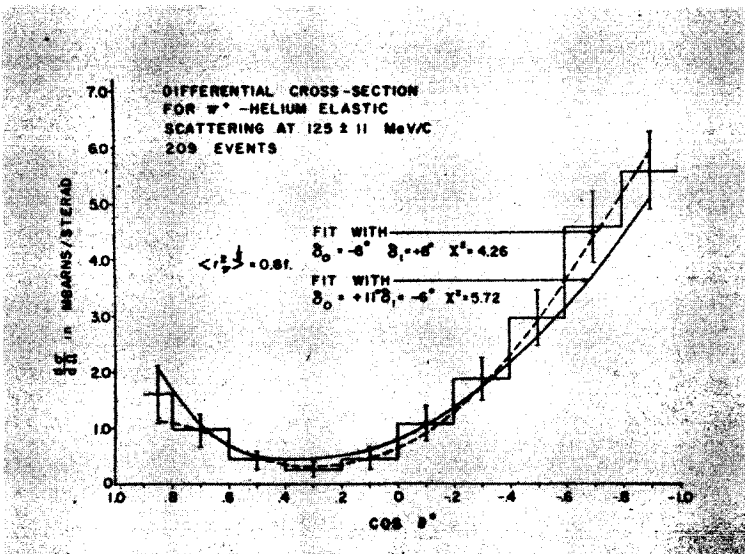


Figure 2

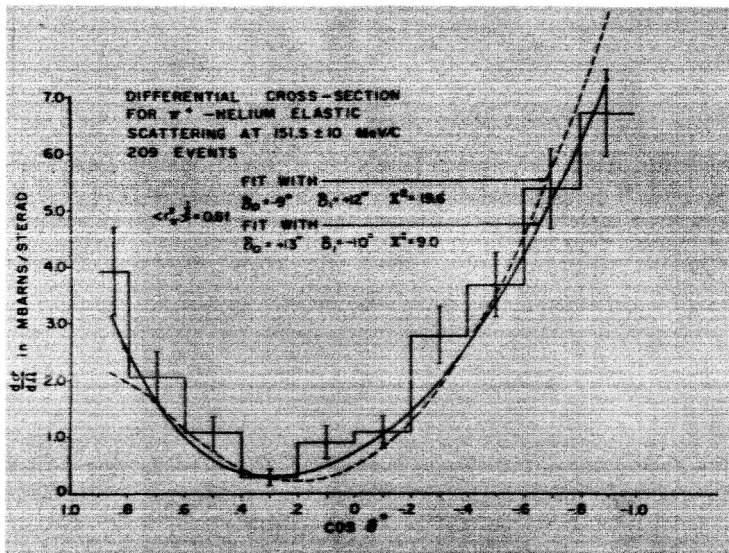


Figure 3

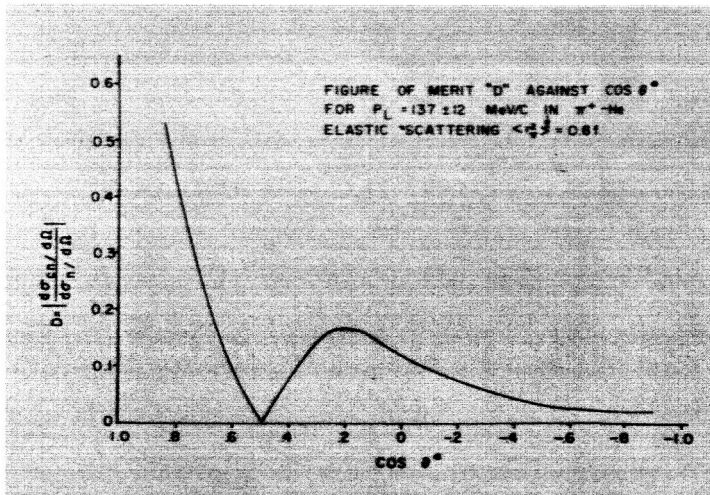


Figure 4

CROWE: I wonder if Dr. Kenyon would tell me the size of the cross-section at its minimum with the different choices. What's the minimum value of the cross-section you get for those four different phase-shift choices? What's the smallest of all the fits you get in milibarns?

BLOCK: To the best of my recollection it's about .4 milibarns.

CROWE: That agrees quite well with our measurement.

ERICSON: I have an impression from this data that there is a very sizeable contribution of elastic events; you are quoting here 40 milibarns. But still in the talk by Dr. Sternheim, I seem to recollect that the analysis was done with purely real phase shifts. Is that correct?

BLOCK: The argument that was given by Dr. Kenyon to show that the effects might be there, took into account the approximation at that point that there was a real phase shift. On the contrary, the analysis that was done for the phase shifts had an imaginary part to  $\delta_0$  and  $\delta_1$  and these imaginary parts were basically fitted by measuring the reaction cross-section which we measure simultaneously here. On the other hand, when you interpret these reaction cross-sections back into imaginary parts, an approximate fit is obtained with both the  $\delta_0$  and  $\delta_1$  imaginary parts being about .04 in absolute units, thus, corresponding to the order of a degree. So they don't change the effect of phase shift from a real phase shift fit very much. But this has been taken into account because one must worry very critically what the behaviour will be in the minimum with the interference terms as to how the imaginary parts come into play. One of the choices of this energy interval, I might add, parenthetically, was because the imaginary portions would be relatively small. Another reason, for example, though it wasn't mentioned by



Elastic  $\pi^+$  -  $\text{He}^4$  Scattering

Kenyon, that you might get very little interference is that your imaginary part became dominant, all your phase shifts effectively go to pure imaginary and, therefore, there would be no Coulomb interference with the nuclear scattering. So that you have to be very cautious in this type of approach to be in an energy region in which the imaginary portions are small. Furthermore, you have to be in an energy region where the exponential form factor, for example, for the alpha particle, doesn't damp the complete reaction so much that that, in turn allows you to have very little interference. So you're rather bounded in the kind of energy that you can use in this type of experiment.

MORAVSICK: In the elastic case, how did you decide to stop with S and P waves in the nuclear part. From what I was, the S and P phases were up at the same order of magnitude, in which case, there is no reason why you should stop at the P phases, right?

BLOCK: In principal you're absolutely correct. The program just came out and we put S and P waves in before we put D in. On the other hand, the information that we got last night from the computer which had done a more varied search, was that the chi squared that we had at the level of our data was sufficiently small that putting in P wave would be meaningless. In other words, we've gotten as good a fit as we could expect statistically from just the introduction of S and P waves, so that any question of whether D wave is present or not will have to be answered experimentally by essentially measuring all other events and we'd just begun to do that.

STERNHEIM: We've done optical model calculations at 100 Mev, not at 50 Mev, but even there we find that you only need 4 or 5 partial waves to get any effect at

all. You're down to  $10^{-5}$  or so if you go to sic partial waves at 100 Mev, so chances are you don't need more than about three at your energy.

NORDBERG: We've analyzed some pi-alpha scattering and get the sign of the  $\delta_0$ . We get  $-4.45 \pm 0.11$  degrees for that real part and 2.7 degrees  $\pm .2$  for the imaginary part. For the P wave we have 3 degrees  $\pm .09$  with an imaginary part of  $\frac{1}{2}$  degree  $\pm \frac{1}{2}$  degree and a D wave turned out to be very small; it's .05 degrees  $\pm .05$  degrees. This energy is slightly less; it's 86 Mev/c in momentum or 24 Mev in the Lab. I might mention since we have both  $\pi^+$  and  $\pi^-$  the data could yield a pi form factor.

N66 32754<sup>455</sup>

INELASTIC  $\pi^+$ -He<sup>4</sup> REACTIONS IN THE MOMENTUM RANGE 100-160 MeV/c

M. M. Block, I. Kenyon, J. Keren, D. Koetke, P. K. Malhotra,  
P. Mazur, R. Walker, H. Winzeler

Northwestern University

When a  $\pi^+$  passes through the liquid helium in the bubble chamber it can undergo four types of reactions

- (i)  $\pi^+ \text{He}^4 \rightarrow \pi^+ + \text{He}^4$  ; elastic
- (ii)  $\rightarrow \pi^+ + \text{nucleons}$ ; inelastic
- (iii)  $\rightarrow$  nucleons;  $\pi$  absorption
- (iv)  $\rightarrow \pi^0 + \text{nucleons}$ ; charge exchange
- (iv')  $\rightarrow \pi^- + \text{nucleons}$ ; double charge exchange

The elastic reactions have been discussed in the previous paper. In this paper we would like to discuss some aspects of the inelastic reactions.

The first question is how do we find the inelastic events and separate them from the elastic ones. Reaction (ii), in which there is a  $\pi^+$  in the final state, may look similar to an elastic event, but the separation between the two types is clean on the basis of kinematics; it takes at least 20 MeV to break up the  $\alpha$  particle, and thus the  $\pi^+$  which has characteristically 60 MeV of K. E. before the reaction, emerges at most with 40 MeV of K. E. Reaction (iii) in which the  $\pi^+$  is absorbed and the single charge exchange events in which an  $\pi^0$  is emitted look alike. We estimate the number of  $\pi^0$  events from the observed events which contain Dalitz pairs\* and then obtain the number of  $\pi^+$  absorption events by subtraction. The double charge exchange events are easily found (apart from their scarcity) because only these events can give a negative (non-electron) track in a picture.

\* (See Figure 1 for Dalitz pair event)

The only double charge exchange event that we found is shown in Figure 2. In this slide we note the incoming  $\pi^+$  track, two energetic protons emitted from the vertex, and two very short "evaporation" protons. The track proceeding downwards with a "hook" on its end is the emitted  $\pi^-$  which has interacted with a He nucleus. This event has been measured, and it gives  $35 \pm 3$  MeV as the break up energy of the  $\alpha$  particle. The agreement with the theoretical value (32 MeV) is an indication that this event has been correctly interpreted.

In Figure 3 we show the preliminary results of the experiment, based on the small fraction of the film so far analyzed. These cross sections are meant to be used as a guide in planning the analysis of the rest of the film rather than as final values.

The  $\pi$  absorption reaction which makes up about 75% of the inelastic cross section is interesting because it makes it possible to investigate the mechanism responsible for the  $\pi$  absorption. It is known that the radiationless absorption of a  $\pi$  is a multinucleon process. Thus here the  $\pi^+$  could be absorbed on an n-n pair, an n-p pair or on more than two nucleons. A preliminary analysis of the absorption events has shown that in over 2/3 of the cases there are two energetic ( $KE > 20$  MeV) protons emitted. This indicates that the  $\pi^+$  is preferentially absorbed on an n-p pair rather than on an n-n pair. It is consistent with our present data that all  $\pi^+$  are absorbed on n-p pairs. This problem is being investigated further. We also hope to learn something about the angular momentum states involved in the absorption process from the angular distribution of the final state nuclei.

In conclusion we would like to observe that the bubble chamber, which is not often used in this energy regions, has certain characteristics which make experiments with it interesting. We can obtain detailed information about events without the detailed statistics of counter experiments and thus we are able to complement that technique.

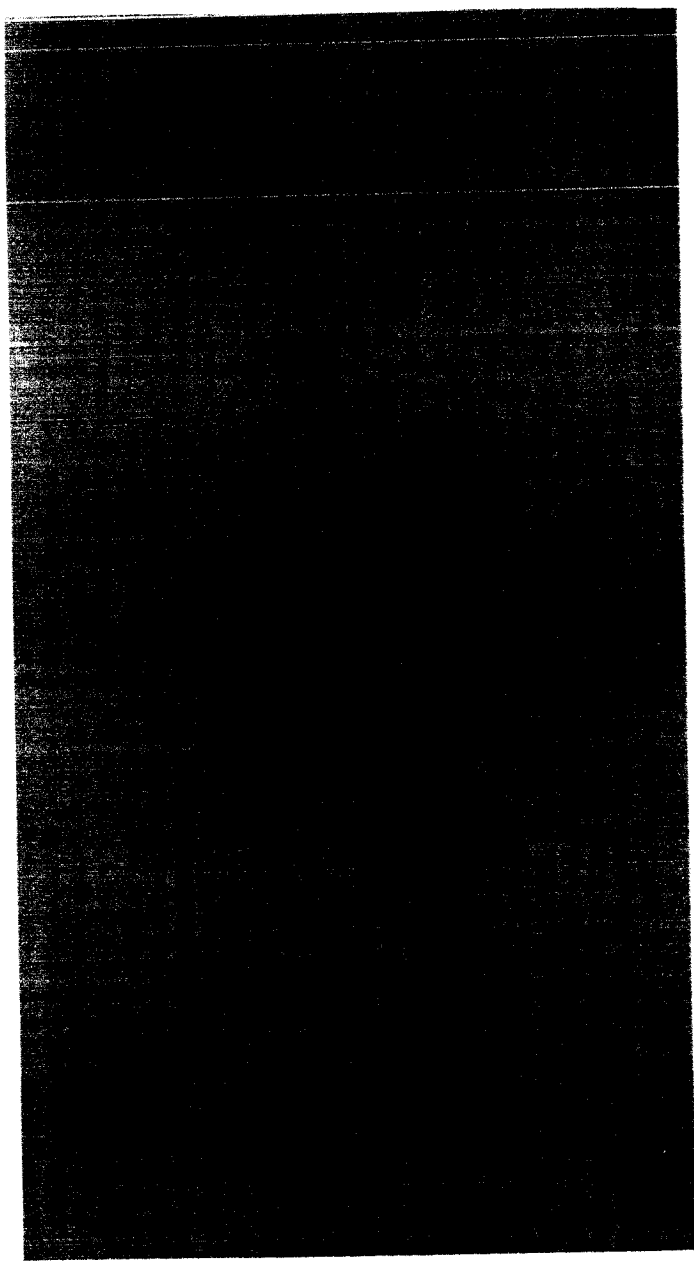


Figure 1 - Reaction occurs just below center in above figure, giving rise to spiraling  $e^+$  at right center.

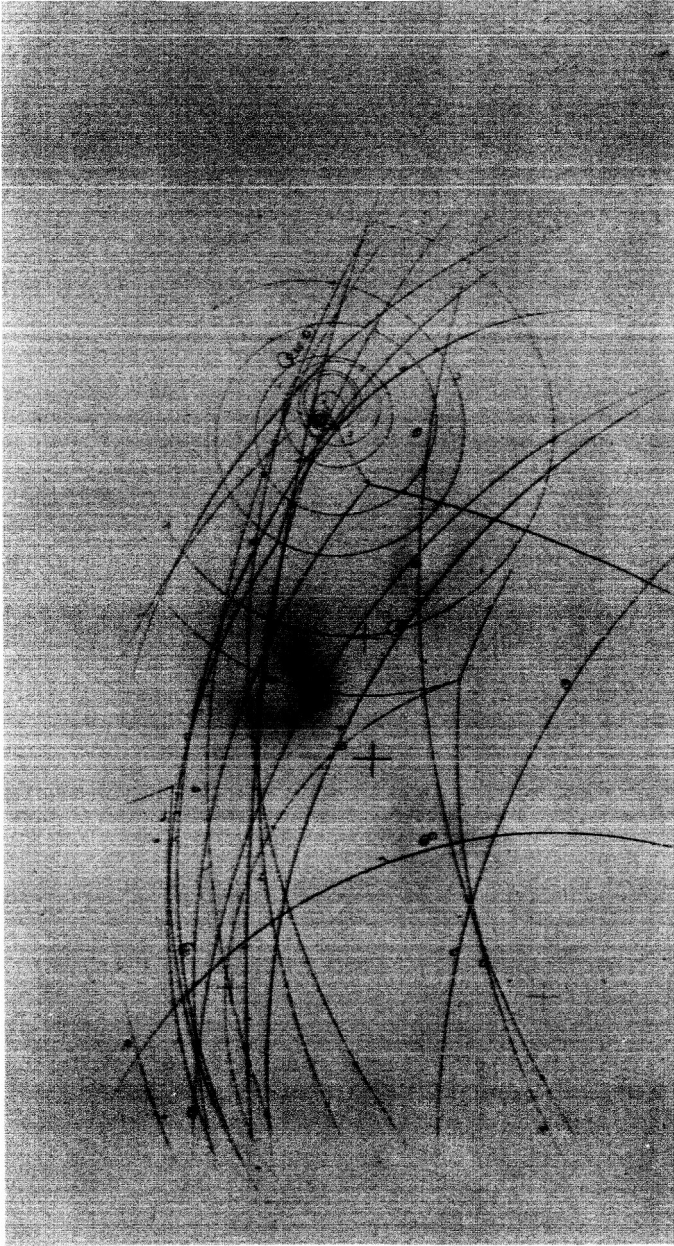


Figure 1 - Reaction occurs just below center in above figure, giving rise to spiraling  $e^+$  at right center.

## INELASTIC EVENTS

| TYPE                        | NUMBER        | TRACK LENGTH                     | CROSS SECTION PER He ATOM |
|-----------------------------|---------------|----------------------------------|---------------------------|
| $\pi^+ \rightarrow$ NO PION | 656           | $9.5 \times 10^9$ cm             | $(31 \pm 1)$ m barn       |
| $\pi^+ \rightarrow \pi^+$   | 282           | "                                | $(9 \pm 1)$ m barn        |
| ALL INELASTIC               | 838           | "                                | $(40 \pm 2)$ m barn       |
| $\pi^+ \rightarrow \pi^0$   | $2 \times 80$ | $(2.25 \pm 0.25) \times 10^7$ cm | $360 \pm 360$ $\mu$ barn  |
| $\pi^+ \rightarrow \pi^-$   | 1             | "                                | $2 \pm 1$ $\mu$ barn      |

$10^6$  cm of TRACK  
 $\approx 12.5$   $\mu$  barn / event

Figure 3

## Participants

PARTICIPANTS AT THE WILLIAMSBURG CONFERENCE  
ON INTERMEDIATE ENERGY PHYSICS

- |  |  |
|--|--|
| <p>H. L. Acker<br/>University of Virginia<br/>Charlottesville, Virginia</p> <p>D. K. Anderson<br/>University of Virginia<br/>Charlottesville, Virginia</p> <p>H. L. Anderson<br/>Enrico Fermi Institute for<br/>Nuclear Studies<br/>University of Chicago<br/>Chicago, Illinois</p> <p>P. T. Andrews<br/>University of Liverpool<br/>Liverpool, England</p> <p>G. Backenstoss<br/>CERN<br/>Geneva, Switzerland</p> <p>W. C. Barber<br/>Stanford University<br/>Stanford, California</p> <p>S. W. Barnes<br/>University of Rochester<br/>Rochester, New York</p> <p>R. Barrett<br/>University of California<br/>Berkeley, California</p> <p>G. A. Bartholomew<br/>Atomic Energy of Canada Limited<br/>Ontario, Canada</p> <p>M. M. Block<br/>Northwestern University<br/>Evanston, Illinois</p> <p>A. R. Bodmer<br/>Argonne National Laboratory<br/>Argonne, Illinois</p> | <p>E. T. Boschitz<br/>NASA, Lewis Research Center<br/>Cleveland, Ohio</p> <p>G. Breit<br/>Yale University<br/>New Haven, Connecticut</p> <p>R. L. Burman<br/>University of Rochester<br/>Rochester, New York</p> <p>R. A. Carrigan, Jr.<br/>Carnegie Institute of Technology<br/>Pittsburgh, Pennsylvania</p> <p>B. C. Clark<br/>General Motors Research<br/>Laboratory<br/>Warren, Michigan</p> <p>R. L. Clarke<br/>Atomic Energy of Canada Limited<br/>Ontario, Canada</p> <p>R. E. Coté<br/>Argonne National Laboratory<br/>Argonne, Illinois</p> <p>K. M. Crowe<br/>Lawrence Radiation Laboratory<br/>Berkeley, California</p> <p>C. Daum<br/>CERN<br/>Geneva, Switzerland</p> <p>S. R. Deans<br/>Vanderbilt University<br/>Nashville, Tennessee</p> <p>S. Devons<br/>Columbia University<br/>New York, New York</p> |
|--|--|



- I. P. Duerdoth  
Nevis Cyclotron Laboratory  
Irvington-on-Hudson, New York
- M. Eckhause  
College of William and Mary  
Williamsburg, Virginia
- J. M. Eisenberg  
University of Virginia  
Charlottesville, Virginia
- L. R. B. Elton  
Battersea College of  
Technology  
London, England
- T. E. O. Ericson  
CERN  
Geneva, Switzerland
- R. J. Esterling  
Enrico Fermi Institute for  
Nuclear Studies  
Chicago, Illinois
- S. Fallieros  
Bartol Research Foundation  
Swarthmore, Pennsylvania
- T. Foelsche  
NASA, Langley Research Center  
Hampton, Virginia
- L. L. Foldy  
Case Institute of Technology  
Cleveland, Ohio
- J. H. Fregeau  
National Science Foundation  
Washington, D. C.
- J. L. Friedes  
Brookhaven National Laboratory  
Upton, L. I., New York
- H. O. Funsten  
College of William and Mary  
Williamsburg, Virginia
- W. A. Gibson  
Oak Ridge Associated Universities,  
Incorporated  
Oak Ridge, Tennessee
- Maj. J. E. Gorrell  
Air Force Office of Scientific  
Research  
Washington, D. C.
- K. Gotow  
Virginia Polytechnic Institute  
Blacksburg, Virginia
- B. Gottschalk  
Northeastern University  
Boston, Massachusetts
- B. Goulard  
Laval University  
Quebec, Canada
- P. D. Grannis  
Lawrence Radiation Laboratory  
Berkeley, California
- P. C. Gugelot  
Virginia Associated Research Center  
Newport News, Virginia
- R. P. Haddock  
University of California  
Los Angeles, California
- C. K. Hargrove  
National Research Council of Canada  
Ottawa, Canada
- W. Hirt  
Federal Polytechnic  
Zurich, Switzerland
- D. Hitlin  
Columbia University  
New York, New York
- W. C. Honaker  
NASA, Langley Research Center  
Hampton, Virginia

## Participants

- D. Hopp  
Virginia Associated Research  
Center  
Newport News, Virginia
- J. Hüfner  
University of Heidelberg  
Heidelberg, Germany
- V. W. Hughes  
Yale University  
New Haven, Connecticut
- G. J. Igo  
Brookhaven National  
Laboratory  
Upton, L. I., New York
- M. Ijaz  
Virginia Polytechnic Institute  
Blacksburg, Virginia
- N. Jarmie  
Los Alamos Scientific  
Laboratory  
Los Alamos, New Mexico
- O. N. Jarvis  
Lawrence Radiation Laboratory  
Berkeley, California
- J. R. Kane  
College of William and Mary  
Williamsburg, Virginia
- S. N. Kaplan  
Lawrence Radiation Laboratory  
Berkeley, California
- I. Kenyon  
Northwestern University  
Evanston, Illinois
- J. Keren  
Northwestern University  
Evanston, Illinois
- K. F. Kinsey  
University of Rochester  
Rochester, New York
- R. H. Klein  
Case Institute of Technology  
Cleveland, Ohio
- E. A. Knapp  
Los Alamos Scientific  
Laboratory  
Los Alamos, New Mexico
- D. Koltun  
University of Rochester  
Rochester, New York
- A. J. Kromminga  
Calvin College  
Grand Rapids, Michigan
- J. LeTourneux  
University of Virginia  
Charlottesville, Virginia
- R. Lombard  
Laboratoire de Physique Theorique  
Orsay, France
- B. Macdonald  
Virginia Polytechnic Institute  
Blacksburg, Virginia
- E. R. Macagno  
Columbia University  
New York, New York
- I. E. McCarthy  
University of Oregon  
Eugene, Oregon
- H. McManus  
Michigan State University  
East Lansing, Michigan
- P. F. Meads  
William M. Brobeck &  
Associates  
Berkeley, California
- E. Merzbacher  
University of North  
Carolina  
Chapel Hill, North Carolina

- R. Mobley  
Yale University  
New Haven, Connecticut
- R. G. Moorhouse  
Theoretical Physics Center  
Stanford, California
- M. J. Moravcsik  
University of California  
Livermore, California
- D. E. Nagle  
Los Alamos Scientific  
Laboratory  
Los Alamos, New Mexico
- B. M. K. Nefkens  
University of Illinois  
Urbana, Illinois
- P. Nemethy  
Nevis Cyclotron Laboratory  
Irvington-on-Hudson, New York
- M. E. Nordberg, Jr.  
University of Rochester  
Rochester, New York
- P. J. O'Donnell  
University of Toronto  
Toronto, Canada
- H. Palevsky  
Brookhaven National  
Laboratory  
Upton, L. I., New York
- C. F. Perdrisat  
University of Illinois  
Urbana, Illinois
- V. Perez-Mendez  
University of California  
Berkeley, California
- G. C. Phillips  
Rice University  
Houston, Texas
- H. Quinn  
NASA  
Washington, D. C.
- J. Rainwater  
Columbia University  
New York, New York
- D. G. Ravenhall  
University of Illinois  
Urbana, Illinois
- A. Reetz  
NASA  
Washington, D. C.
- E. M. Rimmer  
University of Oxford  
Oxford, England
- E. Rind  
NASA, Langley Research Center  
Hampton, Virginia
- W. S. Rodney  
National Science Foundation  
Washington, D. C.
- L. D. Roper  
Kentucky Southern College  
Louisville, Kentucky
- B. Rose  
Atomic Energy Research  
Establishment  
Harwell, Didcot, Berkshire,  
England
- M. E. Rose  
University of Virginia  
Charlottesville, Virginia
- J. Rothberg  
Yale University  
New Haven, Connecticut
- K. W. Rothe  
University of Rochester  
Rochester, New York

- K. Runge  
Columbia University  
New York, New York
- J. E. Russell  
University of Cincinnati  
Cincinnati, Ohio
- R. E. Segel  
Argonne National Laboratory  
Argonne, Illinois
- K. K. Seth  
Northwestern University  
Evanston, Illinois
- P. Shepard  
Princeton University  
Princeton, New Jersey
- R. T. Siegel  
College of William and Mary  
Williamsburg, Virginia
- P. Signell  
Michigan State University  
East Lansing, Michigan
- R. Silbar  
Catholic University  
Washington, D. C.
- W. D. Simpson  
Rice University  
Houston, Texas
- J. J. Singh  
NASA, Langley Research Center  
Hampton, Virginia
- D. D. Smith  
NASA, Langley Research Center  
Hampton, Virginia
- M. I. Sobel  
Brooklyn College  
New York, New York
- S. Sobottka  
University of Virginia  
Charlottesville, Virginia
- J. Solomon  
The Accelerator  
Princeton, New Jersey
- M. M. Sternheim  
University of Massachusetts  
Northampton, Massachusetts
- R. Sunderlin  
Carnegie Institute of  
Technology  
Pittsburgh, Pennsylvania
- R. Sutter  
Brookhaven National Laboratory  
Upton, L. I., New York
- A. Suzuki  
Carnegie Institute of  
Technology  
Pittsburgh, Pennsylvania
- H. Talkin  
NASA  
Washington, D. C.
- C. A. Taylor  
Virginia State College  
Norfolk, Virginia
- V. L. Telegdi  
 Enrico Fermi Institute for  
Nuclear Studies  
University of Chicago  
Chicago, Illinois
- M. N. Thompson  
University of Illinois  
Champaign, Illinois
- E. H. Thorndike  
University of Rochester  
Rochester, New York
- C. C. Trail  
Brooklyn College  
Brooklyn, New York
- H. Überall  
Catholic University  
Washington, D. C.

- H. Valk  
National Science Foundation  
Washington, D. C.
- J. Wachter  
Oak Ridge Associated Universities,  
Incorporated  
Oak Ridge, Tennessee
- Rev. R. Wagner  
Augustinian College  
Washington, D. C.
- J. D. Walecka  
Stanford University  
Stanford, California
- N. S. Wall  
University of Maryland  
College Park, Maryland
- E. Weigold  
Air Force Office of Scientific  
Research  
Washington, D. C.
- R. E. Welsh  
College of William and Mary  
Williamsburg, Virginia
- C. Werntz  
Catholic University  
Washington, D. C.
- L. Wilets  
Washington University  
Seattle, Washington
- D. H. Wilkinson  
University of Oxford  
Oxford, England
- J. G. Wills  
Indiana University  
Bloomington, Indiana
- R. Winter  
College of William and Mary  
Williamsburg, Virginia
- H. Winzeler  
Northwestern University  
Evanston, Illinois
- L. Wolfenstein  
Carnegie Institute of  
Technology  
Pittsburgh, Pennsylvania
- C. S. Wu  
Columbia University  
New York, New York
- K. O. Ziock  
University of Virginia  
Charlottesville, Virginia
- A. Zucker  
Oak Ridge Associated  
Universities, Incorporated  
Oak Ridge, Tennessee

## INDEX OF CONTRIBUTORS

## Vol. I and Vol. II

In the entries below, "I" indicates a paper in Vol. I and "II" indicates paper in Vol. II.

|             |              |                     |             |
|-------------|--------------|---------------------|-------------|
| L. Acker    | I 91, I 99   | D. O. Caldwell      | I 419       |
| Amato       | I 377        | R. A. Carrigan, Jr. | I 51        |
| K. Anderson | I 253        | D. M. Corley        | II 749      |
| L. Anderson | I 1          | R. E. Cote'         | I 51        |
| T. Andrews  | I 223        | G. F. Cox           | II 595      |
| Auerbach    | I 439        | K. M. Crowe         | I 145       |
| S. Ayres    | I 419        | J. B. Czirr         | II 569      |
| Backenstoss | I 99         | C. Daum             | I 99        |
| T. Bardin   | I 135        | H. Davis            | I 223       |
| Barrett     | I 135        | S. R. Deans         | II 551      |
| W. Bennett  | II 749       | S. Devons           | I 15, I 135 |
| M. Block    | I 447, I 455 | S. A. deWit         | I 99        |
| Breit       | II 471       | R. D. Eandi         | I 419       |
| L. Burman   | I 207        |                     |             |

- G. H. Eaton II 595  
M. Eckhause I 411  
J. M. Eisenberg I 253  
L. R. B. Elton II 731  
T. E. O. Ericson I 187  
S. Fallieros II 743  
T. A. Filippas I 411  
J. L. Friedes II 749  
A. Gaigalas I 51  
B. Gottschalk II 649, II 703  
B. Goulard II 743  
P. D. Grannis I 175  
A. S. Greenberg I 419  
R. P. Haddock II 569  
C. K. Hargrove I 1  
E. Heer I 277  
E. P. Hincks I 1  
W. Hirt I 277  
D. Hitlin I 135  
W. G. Holladay II 551  
J. Hüfner I 87  
T. A. Hughes II 743  
V. W. Hughes I 377  
O. N. Jarvis II 595  
R. W. Kenney I 419  
I. Kenyon I 447, I 455  
J. Keren I 447, I 455  
K. F. Kinsey I 207, I 427  
P. F. M. Koehler II 677  
D. Koetke I 447, I 455  
D. Koltun I 241  
R. J. Kurz I 419  
J. LeTourneux I 259  
L. Lobkowicz I 427

## Index of Contributors

- E. R. Macagno I 135  
B. Macdonald I 419  
P. K. Malhotra I 447, I 455  
D. Marker II 667  
M. Martin I 277  
P. Mazur I 455  
R. J. McKee I 1  
E. G. Michaelis I 277  
R. Mobley I 377  
R. G. Moorhouse II 545  
M. J. Moravcsik II 517  
H. Muirhead I 223  
C. Nissim-Sabat I 135  
M. E. Nordberg, Jr. I 207, I 427  
D. R. Nygren II 569  
H. Palevsky II 749  
G. C. Phillips II 749  
W. J. Prestwich I 51  
S. Raboy I 51  
J. Rainwater I 135  
D. G. Ravenhall I 37  
N. W. Reay II 691  
A. Reitan I 241  
L. D. Roper II 495  
B. Rose II 595, II 603  
J. Rothberg I 377  
K. W. Rothe II 677  
K. Runge I 135  
R. M. Salter, Jr. II 569  
J. C. Sens I 99  
C. Serre I 277  
W. J. Shlaer II 649, II 703  
R. T. Siegel I 411  
P. Signell II 667  
W. D. Simpson II 749  
P. Skarek I 277



- J. Solomon I 269  
D. Spalding II 691  
B. F. Stearns I 419  
R. L. Stearns II 749  
M. M. Sternheim I 439  
K. Strauch II 703  
R. J. Sutter II 749  
R. B. Sutton I 51  
A. Swift II 731  
V. L. Telegdi I 77  
A. R. Thomas II 691  
P. Thompson I 377  
E. H. Thorndike II 677, II 691  
C. C. Trail I 51  
H. Überall I 327  
C. P. Van Zyl II 595  
J. D. Walecka I 297  
R. Walker I 447, I 455  
N. S. Wall II 719, II 749  
K. H. Wang II 649, II 703  
R. E. Welsh I 411  
D. H. Wilkinson II 757  
H. Winzeler I 447, I 455  
L. Wolfenstein II 775  
J. N. Woulds I 223  
B. T. Wright I 277  
C. S. Wu I 135  
M. Zeller II 569